STUDIES OF NOVEL TARGETED DRUG DELIVERY SYSTEMS AND MOLECULAR PROBES OF CANCER BIOLOGY

By

Kelsey E. Knewtson

Submitted to the graduate degree program in Medicinal Chemistry and the Graduate Faculty of the University of Kansas in partial fulfillment of the requirements for the degree of Doctor of Philosophy.

_____

Chairperson Dr. Blake R. Peterson

_____

Dr. Mark Farrell

_____

Dr. Robert Hanzlik

_____

Dr. Michael F. Rafferty

_____

Dr. Teruna Siahaan

Date Defended: April 19, 2019

The Dissertation Committee for Kelsey E. Knewtson

certifies that this is the approved version of the final dissertation:

STUDIES OF NOVEL TARGETED DRUG DELIVERY SYSTEMS

AND MOLECULAR PROBES OF CANCER BIOLOGY

_____

Chairperson Dr. Blake R. Peterson

Date Approved: April 19, 2019

ABSTRACT

Cancer is a complex family of diseases. As our understanding of cancer biology has improved, so has our ability to treat the pathology associated with this condition. Traditional anticancer therapeutics lack selectivity and cause many side effects. These side effects can reduce the quality of life of the patient and limit the doses of drugs that need to be used to fully eradicate cancer cells. In recent years, a deeper understanding of cancer has led to the development of targeted therapies that exploit molecular differences between cancer cells and healthy cells. These newer targeted therapies often have reduced side-effects compared with traditional drugs, to the great benefit of patients.

Sections of this dissertation focus on a specific class of targeted anticancer therapeutics called antibody drug conjugates (ADCs). ADCs combine the targeting power of antibodies with the cell killing mechanisms of potent toxins. These therapies can overcome some of the resistance that can emerge against therapeutic antibodies, and the low therapeutic index of associated toxins, but there is still room for improvement. Many patients treated with ADCs experience severe side effects. Additionally, most ADCs are generated by attaching the toxins to the antibody in a random manner, generating very heterogenous mixtures of therapeutics. In this dissertation, a system that combines ADCs with endosome disruptive peptides is explored as a possible method to improve the therapeutic index of ADCs. This system employs ADCs composed of poorly membrane permeable toxins whose toxicity is triggered by endosome disruptive peptides that allow these toxins to reach the cytoplasm. A novel approach to generate more homogenous ADCs is also described. This method takes advantage of the binding of

Protein A from *Staphylococcus aureus* to human antibodies to direct the labeling of the antibody with small molecules.

This dissertation also describes basic cancer biology research related to the cellular production of reactive oxygen/nitrogen species. Control of the levels of oxidants and reductants is very important for the normal function of cells and imbalances are linked to many disease states including cancer. We describe the development and use of novel fluorescent sensors of the important biological oxidant peroxynitrite. These sensors are able to detect endogenous production of peroxynitrite by macrophages upon phagocytosis of opsonized beads, a process that previously reported sensors are unable to detect. Better sensors of peroxynitrite such as those discussed here could aid the study of this oxidant and its role in cancer and other diseases.

ACKNOWLEDGMENTS

I owe a great debt of gratitude to everyone who has helped me reach this point. This trip has not been easy, and I would not have made it nearly this far without having many, many people helping me along the way.

I would like to thank my advisor, Dr. Blake R. Peterson, for his guidance over the past several years. He has helped me to mature as a scientist and has taught me many valuable lessons. Thank you to the entire Medicinal Chemistry Department. It has been an experience, that's for sure. I greatly appreciate the guidance and contributions of my committee members, Dr. Mark Farrell, Dr. Robert Hanzlik, Dr. Michael Rafferty, and Dr. Teruna Siahaan. Additionally, I would like to thank Dr. Stevan Djuric and Dr. Aleksandra Baranczak for giving me the wonderful opportunity of an internship within the Discovery Chemistry and Technology group at AbbVie.

Thank you to the entire Peterson Lab, past and present. Specifically, I would like to thank Dr. Chamani Perera, Dr. Digamber Rane, Zhe Gao, Dr. Molly Lee, and Dr. David Hymel for their contributions to this work and for their friendship and advice. Additionally, I am grateful to Sahishna Phaniraj, Yuwen Yin, Angelo Andres, Tomas Smith, Dr. Matt Meinig, and Dr. Bailin Lei for their friendship and helpful discussions.

A heart-felt thank you to everyone who helped me during my sister Hailey's sickness and eventual death. Hailey was my best friend and that time was incredibly hard for me. It meant so much to know that my absences would be forgiven, that my cat would be fed, and that there was always someone I could talk to. I miss Hailey more than I can say.

Finally, I would like to thank my family, especially my parents, Mary and Kevin, and my younger siblings, Abby and Isaac, for always being there and for keeping me from taking myself too seriously. And to my fiancé Daniel's family for becoming my second family. Thank you to Sarah Westenkirchner and Sami Moores for years of friendships and hours of conversation. And to Daniel, thank you for keeping me sane and sharing the burden.

TABLE OF CONTENTS

LIST OF FIGURES

LIST OF TABLES

LIST OF SCHEMES

LIST OF ABBREVIATIONS AND ACRONYMS

2-CTC	2-Chlorotrityl resin
3NT	3-Nitrotyrosine
ABC	ATP-binding cassette
ADC	Antibody drug conjugate
ADCC	Antibody-dependent cellular cytotoxicity
Aib	Aminoisobutyric acid
ATP	Adenosine triphosphate
BP	Band-pass filter
BRCA1/2	Breast-cancer-associated protein 1/2
CAF	Cancer associated fibroblast
CDC	Complement-dependent cytotoxicity
CGC	Cancer Gene Census
CME	Colchinol methyl ether
CML	Chronic mylogenous leukemia
COSMIC	Catalogue of Somatic Mutations in Cancer
CPK model	Corey, Pauling, Koltun model; space-filling model
CSC	Cancer stem cell
DAR	Drug to antibody ratio
DAST	Diethylaminosulfur trifluoride
DCM	Dichloromethane
DIEA	*N,N*-Diisopropylethylamine
DM1	Emtansine for antibody conjugation
DMF	Dimethylformamide
DMSO	Dimethyl sulfoxide
DNA	Deoxyribonucleic acid
DNP	6-(2,4-dinitrophenylamino)-hexanoic acid
DOL	Degree of labeling
DSB	Double stranded break
DTT	Dithiothreitol

ED	Endosome disruptor
EDC	1-Ethyl-3-(3-dimethylaminopropyl)carbodiimide
EGF	Epidermal growth factor
EGFR	Epidermal growth factor receptor
ER	Endoplasmic reticulum
ERK	Extracellular signal-regulated kinase
ESI	Electrospray ionization
Fab	Antigen-binding fragment
FBS	Fetal bovine serum
Fc	Fragment crystallizable
FDA	United States Food and Drug Administration
Fl-B	Fluorescein boronate
Fmoc	Fluorenylmethyloxycarbonyl protecting group
FRET	Förster Resonance Energy Transfer
GILT	Gamma-interferon-inducible lysosomal thiol reductase
GSH	Glutathione
HATU	Hexafluorophosphate azabenzotriazole tetramethyl uronium
HBSS	Hank’s balanced salt solution
HER2	Human epidermal growth factor receptor 2
HIF	Hypoxia inducible factor
HPF	Hydroxyphenyl fluorescein
HPLC	High pressure liquid chromatography
HRMS	High resolution mass spectrometry
IFN-γ	Interferon γ
IgG	Immunoglobulin G
LPS	Lipopolysaccharides
LRMS	Low resolution mass spectrometry
Lys	Lysine
mAB	Monoclonal antibody
MK	Megakaryocyte
MS	Mass spectrometry

mTORC1	Mechanistic target of rapamycin complex 1
NADPH	Nicotinamide adenine dinucleotide phosphate
NHS	*N*-hydroxysuccinimidyl
NMR	Nuclear magnetic resonance
NOS	Nitric oxide synthase
P-gp	P-glycoprotein
PARP	Poly(adenosine diphosphate-ribose) polymerase
PB	Pacific Blue
PBS	Phosphate buffered saline
PDB	Protein Data Bank
PEG	Polyethylene glycol
PG	Pennsylvania Green
PI	Propidium iodide
PI3K	Phosphatidylinositol-3-kinase
PMT	Photomultiplier tube
PRR	Pathogen recognition receptor
PTP	Protein tyrosine phosphatase
QSAR	Quantitative structure activity relationship
Ras-MAPK	Ras-mitogen activated protein kinase
ROS	Reactive oxygen species
RT	Room temperature
SAR	Structure activity relationship
SDS-PAGE	Sodium dodecyl sulfate-polyacrylamide gel electrophoresis
SIN-1	3-morpholinosydnonimine
SOD	Superoxide dismutase
SpA	Protein A
SPPS	Solid phase peptide synthesis
SSB	Single stranded break
TAM	Tumor associated macrophage
T_c	Cytotoxic T cell
TFA	Trifluoroacetic acid

TFE	Trifluoroethanol
T_H	T helper cell
THF	Tetrahydrofuran
TIPS	Triisopropylsilane
TLC	Thin-layer chromatography
TNF-α	Tumor necrosis factor α
Treg	Regulatory T cell
Trp	Tryptophan
Tyr	Tyrosine
UPR	Unfolded protein response
UV	Ultraviolet
VEGF	Vascular endothelial growth factor

Chapter 1

Introduction

1-1. The complexity of cancer

Cancer is a broad term that describes diseases characterized by abnormal cell growth with the potential to spread into surrounding tissues. There are over 100 different named cancers classified by the type of tissue involved and its location in the body,[1] but each cancer is a heterogenous mix of diseases caused by different combinations of genetic aberrations. Even a single tumor can be composed of groups of cells each containing different mutations. This heterogeneity makes each individual patient's cancer difficult to characterize and even more difficult to treat.

Decades have been spent understanding, characterizing, and categorizing the genetic changes that drive cancers in order to improve treatment. Hanahan and Weinberg published a seminal article in 2000[2] and an update in 2011[3] describing the Hallmarks of Cancer, traits that most, if not all cancers, share (Figure 1-1). These articles emphasize the complexity of cancer and attempt to simplify its study by outlining basic principles. However, some believe that these articles over-simplify carcinogenesis and might be detrimental to cancer research. These opponents argue that cancer is a tissue-level disease[4] and that five of the original six Hallmarks are common to both benign and malignant tumors.[5] Regardless, the Hallmarks of Cancer have been widely acclaimed as an important contribution to the study of cancer; without simplification, cancer can appear to be too complex to comprehend.

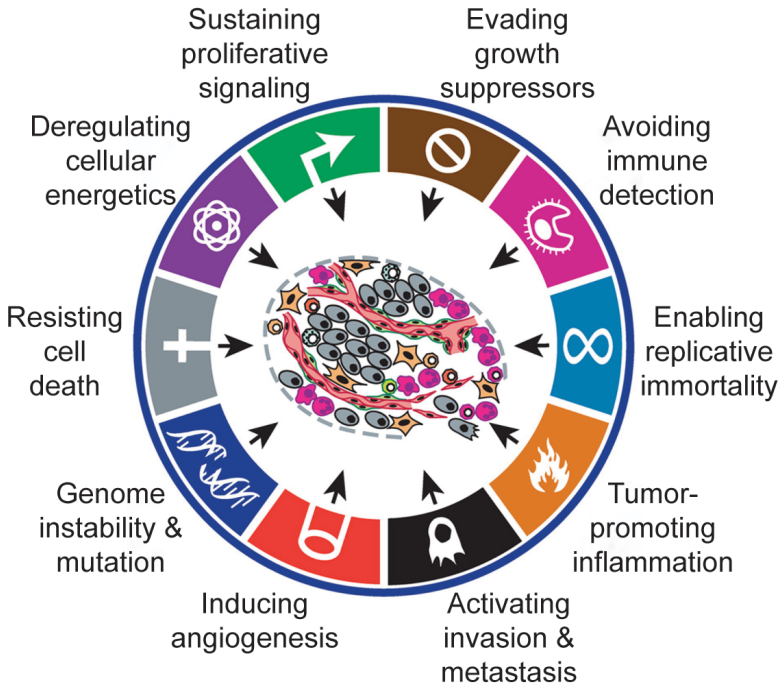

Figure 1-1. The Hallmarks of cancer. Hanahan and Weinberg proposed that most, if not all, cancers have these traits in common.[2,3] Genome instability and mutation and tumor-promoting inflammation are listed as enabling characteristics in the original articles, but these ten traits are frequently referred to jointly as the hallmarks. Figure adapted from Hanahan *et. al*.[3]

The Catalogue of Somatic Mutations in Cancer (COSMIC) provides some perspective on the complexity of cancer. COSMIC is a database of millions of mutations found in thousands of cancers. The Cancer Gene Census (CGC) is a resource within COSMIC that, as of August 2018, contains summaries of 719 cancer-driving genes. Genes in the CGC are categorized by their functional role as oncogenes: activated genes that can drive cancer, tumor suppressor genes: genes that normally slow cell proliferation whose loss can lead to cancer, or fusion genes: the combination products of two genes that individually do not drive cancer but can when fused. Genes are also categorized by their connection to the Hallmarks of Cancer.[6] The selection criteria for the CGC is

stringent, so it is likely that 719 is an underestimate of the number of genes that are capable of driving cancer.

Tumors are, of course, more than the underlying mutations within each individual cancer cell. Cancer cells interact with each other and with neighboring healthy cells. Research is revealing how heterogenous cancer cells within a single tumor are. Most tumors are composed of many distinct subpopulations of cells, each containing unique mutations and aberrations.[7,8] This heterogeneity makes it difficult to define clinically useful biomarkers of cancer. It also makes treatment challenging, given that it is often difficult to pinpoint which mutations are driving a particular tumor, and that there could be subpopulations of cells within a tumor that are resistant to a given treatment. Such subpopulations could repopulate the tumor after other cells die, leading to relapse (Figure 1-2).[9,10]

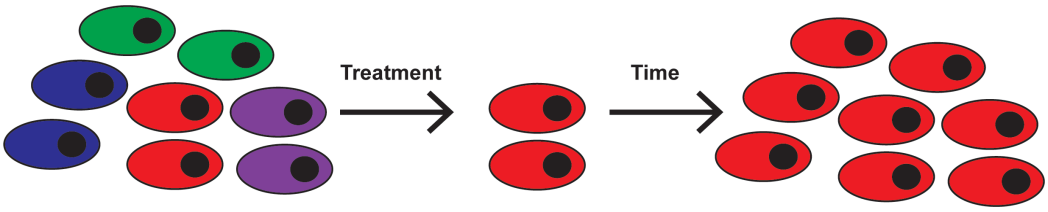

Figure 1-2. Tumor repopulation after treatment. Though the tumor initially responds to treatment, it contains a subpopulation of resistant cells (red). Over time, these cells are able to repopulate the tumor, generating a tumor that is resistant to therapy.

Cancer stem cells (CSCs) are one of the cell types within a tumor that can be most difficult to kill. In 2006, the American Association for Cancer Research Workshop on Cancer Stem Cells defined a CSC as “a cell within a tumor that possess the capacity to self-renew and to cause the heterogeneous lineages of cancer cells that comprise the tumor.”[11] CSCs are more resistant to radiation therapy than other cells, possibly because of decreased susceptibility to the DNA damage radiation inflicts due to increased ability

to cope with reactive oxygen species (ROS, discussed further later in this chapter),[12] or because of increased DNA repair ability.[13] CSCs also appear to be more resistant to traditional chemotherapeutics such as 5-fluorouracil and etoposide,[14,15] partially due to expression of ATP-binding cassette (ABC) transporters such as P-glycoprotein (P-gp) that are able pump drugs out of the cell.[16] Evidence suggests that if CSCs survive treatment, they are able to repopulate the tumor, leading to disease relapse.[15,17] It has even been shown that other cancer cells can de-differentiate and replace lost CSCs.[15] This de-differentiation depends upon signals from the tumor microenvironment.

The microenvironment of a tumor is a complex system composed of many tissue types, including blood vessels, fibroblasts, and immune cells, and other materials including the extracellular matrix and many signaling molecules (Figure 1-3).[18] Various immune cells can be found within tumors, some attacking the tumor and others promoting its survival. Cytotoxic T cells (T_c) and T helper cells (T_H) work together to attack malignant cells; high counts of these cells within a tumor are associated with a good prognosis for the patient.[19] Regulatory T cells (Tregs), on the other hand, secrete immunosuppressive signals that inhibit the function of other immune cells that could otherwise kill the tumor.[18] High numbers of these cells are associated with a poor prognosis for the patient in many types of cancer.[20,21] Tumor-associated macrophages (TAMs) can also be associated with a poor prognosis.[22] TAMs are associated with invasion and metastasis,[23] as well as angiogenesis.[24] The tumor microenvironment contains many chemokines secreted by TAMs and other cells that stimulate angiogenesis. The vasculature that grows to support the tumor is very irregular; the vessels are chaotic and leaky, leading to high interstitial fluid pressure and uneven blood flow.[25] This poor blood supply to tumors often leads to

necrotic centers, and it can also make delivering anticancer drugs into tumors problematic. Cancer associated fibroblasts (CAFs) are another part of the tumor microenvironment that can promote tumor growth. These cells secrete growth factors[26] and immunosuppressive signals.[27] They can also promote metastasis.[27] The complexity of the tumor microenvironment increases the difficulty of both understanding and treating cancer.

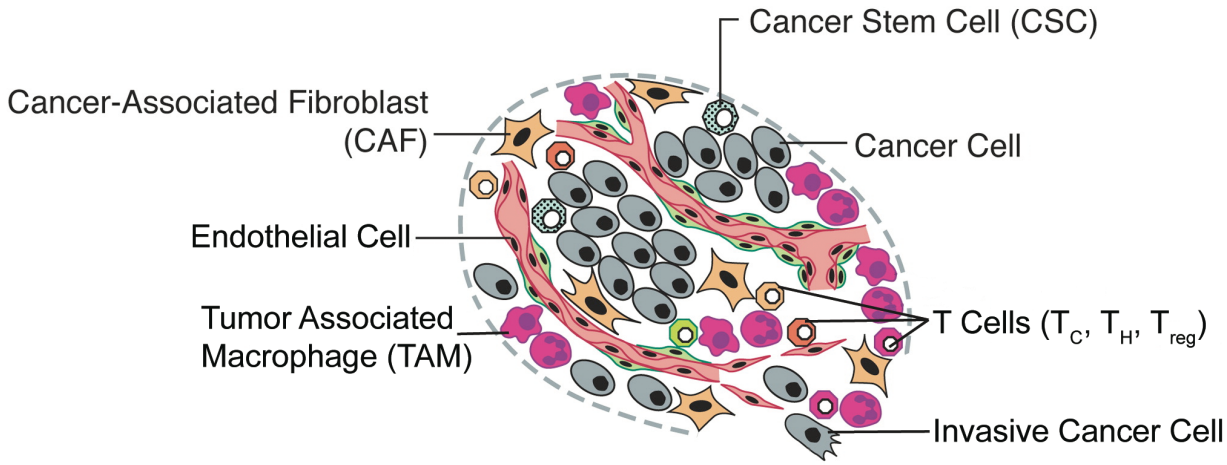

Figure 1-3. Tumor microenvironment. The tumor microenvironment is very complex and is composed of not only cancer cells, but also immune cells, fibroblasts, and endothelial cells. Figure adapted from Hanahan *et. al*. [3]

The complexity of cancer makes it a challenging group of diseases to treat. When new data suggests the promise of a new treatment, the application of that new treatment generally reveals shortcomings. This search for effective ways to treat cancer is not a new one, and it is a search that will continue for the foreseeable future.

1-2. Identifying exploitable differences between healthy and cancer cells

Cancer has been plaguing humans and people have been searching for cures for all of recorded history. Descriptions of cancer and its treatments have been found in

ancient documents such as the Ebers Papyrus, an Egyptian medical document dating to about 1550 BCE. Mastectomy was described by Roman encyclopedist Aulus Cornelius Celsus in the 1st century CE.[28] German neurologist Heinrich Lissauer's use of a solution of potassium arsenite, known as Fowler's solution, to treat a patient with chronic myelogenous leukemia (CML) in 1865 is considered by some to be the first effective use of chemotherapy to treat cancer,[28] though others argue that arsenic has been used to treat cancer since ancient times.[29] It wasn't until the 1960s, though, that there was evidence that it was possible to cure cancer using drugs.[30] During this period, combination therapies combining agents such as tubulin binders, antimetabolites, nitrogen mustards, and steroids were shown to be able to cure 50% of children with acute lymphocytic leukemia[30] and 60% of adults with Hodgkin's lymphoma.[31] Until this time surgery and radiation therapy were the mainstays of cancer treatment.[28,30]

Such successes were only possible due to advances in cancer research. The early 1900s saw the development of improved mouse models of cancer and more standardized and higher throughput screening of potential anticancer agents.[29,30] Observations that mustard gas depleted the bone marrow and lymph nodes of men exposed to the agent during World War I led to the development of the first real class of chemotherapeutics, the nitrogen mustards[28-30] (Figure 1-4). These molecules readily react with many biological molecules including DNA and proteins, and cellular susceptibility to these drugs is directly related to proliferative activity. Nitrogen mustards effectively treated Hodgkin's lymphoma, but caused many side effects, and remissions did not last.[32] Around the same time, it was observed that folic acid was necessary for bone marrow function, though the mechanism was not fully understood. Analogues of folic acid (Figure 1-5) were

synthesized and tested, and it was discovered that aminopterin and amethopterin (now methotrexate), the first antimetabolites used to treat cancer, could inhibit the production of folic acid and be used to treat leukemia in children.[30,33] However, the remissions caused by monotherapy with aminopterin were temporary, and treatment was accompanied by many dose-limiting side effects.[33] These discoveries were generally based more on chance observations than on a thorough understanding of cancer biology. In order to develop drugs that are truly selective for cancer cells, a deeper understanding of the disease is needed.

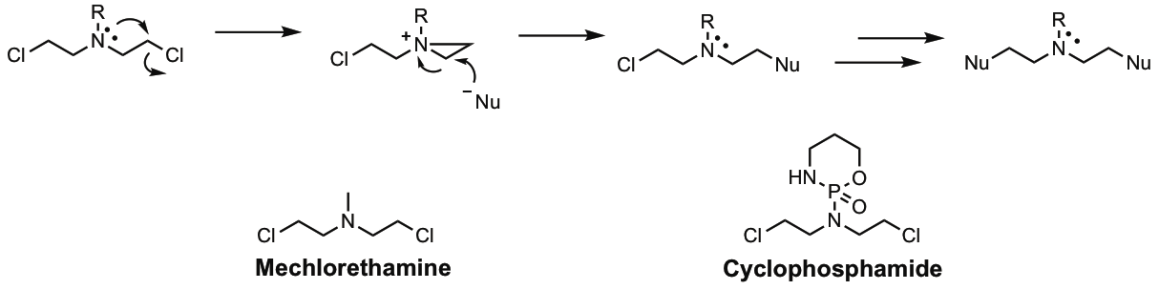

Figure 1-4. Nitrogen mustards are electrophiles that alkylate DNA, with the DNA base guanine most commonly acting as the nucleophile. Mechlorethamine, the original nitrogen mustard, and cyclophosphamide, a less toxic analogue, are shown.

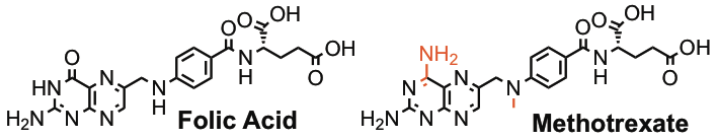

Figure 1-5. The antimetabolite methotrexate is structurally very similar to folic acid (differences are highlighted in red). Methotrexate binds competitively to dihydrofolate reductase, preventing the synthesis of folic acid, which is needed for the synthesis of DNA and RNA.

German physician Paul Ehrlich is credited with developing the concept of targeted therapies for treating human diseases. He coined the phrase “magic bullet” in the early 1900s to refer to molecules designed to act on their targets within a pathogen without harming healthy tissues. This concept was quickly applied to treating many diseases,

including cancer.[34] Early anticancer agents such as the DNA alkylating agent cyclophosphamide are targeted in the sense that they kill rapidly dividing cells to a greater extent than quiescent cells. However, healthy cells such as blood cells in the bone marrow and the lining of the digestive tract also divide rapidly, whereas some cancers are slow growing, leading to side effects and lack of efficacy. Dose-limiting side effects can include leukopenia and vomiting, in addition to an increased future risk of cancer.

Advances in cancer genetics and biology in the 1970s and 1980s were essential for the development of truly targeted therapies directed at specific mutations that make cancer cells unique. During this time, studies on retroviruses lead to the discovery of the first oncogenes. Studies on the Rous sarcoma virus, a virus that causes cancer in chickens, found that one of its genes, *v-src*, was a chicken gene that had been hijacked by the virus and used to drive cancer formation.[35,36] When it was discovered that this gene was present in mammals including humans,[37] the possibility that human cancers could be driven by corrupted genes that otherwise serve essential purposes arose.[38,39] The discovery of many other oncogenes such as *myc*, *erbB*, and *ras* from avian and murine tumor viruses followed quickly.[39] This deeper understanding of the drivers of cancer made it possible to develop therapies that more specifically target cancer cells.

In the 1980s, the *BCR-ABL* oncogene was discovered as the driver behind many cases of chronic myelogenous leukemia.[40,41] This discovery allowed for the development of imatinib (Gleevec, Figure 1-6)[42] to treat this disease. *BCR-ABL* is the result of a reciprocal chromosomal translocation that fuses a portion of the *BCR* gene to *ABL*, a gene encoding a tyrosine kinase.[40] This fusion leads to the constitutive activation of Abl, favoring its dimerization and autophosphorylation. It also disrupts the normal cycling of

Abl between the cytoplasm and nucleus because Bcr-Abl localizes to the cytosol. The increased phosphorylation and cytosolic location of Bcr-Abl allows it to interact with many signaling pathways, enhancing cellular proliferation and survival.[43] Bcr-Abl has been shown to be sufficient and necessary to maintain the leukemia phenotype of CML.[44,45] Gleevec binds in the ATP binding site of Abl, blocking its tyrosine kinase activity and stopping cell proliferation. Abl does not appear to be necessary for normal cell proliferation, thanks at least in part to the redundancy of signaling pathways, and Gleevec is relatively selective for Abl, although it also binds to the platelet derived growth factor receptor.[42] Consequently, the side effects associated with Gleevec are relatively minor, even over 5 years of treatment, with the most common being edema (60%), muscle cramps (49%), and diarrhea/nausea (50%). Grade 3 or 4 adverse events were relatively rare, with the most common being neutropenia (17%) and thrombocytopenia (9%).[46] After 5 years, 83% of patients can expect event-free survival.[46]

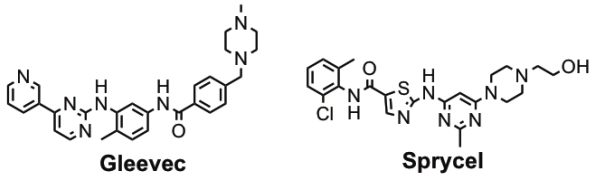

Figure 1-6. Inhibitors of Bcr-Abl. Gleevec was the first inhibitor of Bcr-Abl available to treat CML. Sprycel followed as a next generation drug that is more potent and less selective than Gleevec.

Unfortunately, 15-20% of patients develop resistance to Gleevec, a common issue for targeted therapies.[47] Several mechanisms have been found for this resistance, including point mutations that directly block the binding of Gleevec, or that change the conformation of Bcr-Abl, and different splice variants of Bcr-Abl that are not susceptible to Gleevec therapy.[47,48] This resistance can be overcome to some extent using next

generation Bcr-Abl inhibitors such as dasatinib (Sprycel, Figure 1-6) and combination therapy.[43] Though Gleevec is not a perfect drug, it exemplifies that targeting specific differences between cancer cells can generate effective treatments with improved side effects compared to traditional chemotherapy.

Other advances in the 1970s and 1980s allowed for the development of therapeutic antibodies to treat cancer. These advances include the development of monoclonal antibodies (mAbs) in 1975[49] and the discovery of cell surface receptors that are overexpressed on malignant cells and expressed by few healthy cell types. Therapeutic antibodies function by binding to specific antigens on targeted cells (Figure 1-7). They elicit therapeutic effects through many mechanisms including recruiting immune cells to kill the targeted cell and blocking proliferative signaling. They are discussed further in Chapter II.

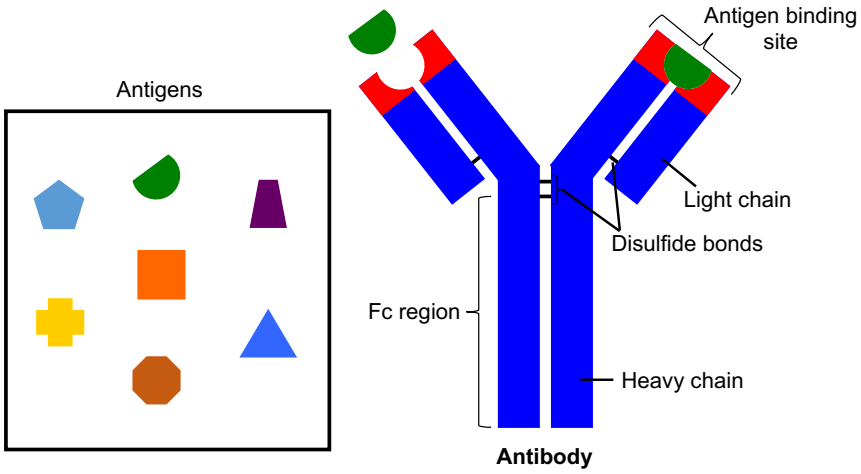

Figure 1-7. Illustration of an immunoglobulin G (IgG) antibody. Each IgG consists of two identical light chains and two identical heavy chains stabilized into a Y-shaped molecule by disulfide bonds between cysteine residues. The Fc region binds to Fc receptors on immune and other cell types, enhancing activation of immune responses and increasing residence time in vivo. The antigen binding site of an IgG recognizes and binds a single antigen, giving these macromolecules selectivity that makes them attractive therapeutics.

In 1997, the first targeted therapeutic antibody, chimeric CD20-targeted rituximab (Rituxan) for the treatment of non-Hodgkin lymphomas, was approved by the United States Food and Drug Administration (FDA). CD20 was discovered as a specific B-cell marker in 1980,[50] and it has since been shown to be expressed on malignant B-cells, normal B-cells, and developing B-cells, but not on hematopoietic stem cells or differentiated antibody-secreting plasma cells.[51] This expression pattern means that therapies targeting CD20 should have minimal effects on non-targeted cells, should not disrupt humoral immunity, and should allow for the repopulation of B-cells after treatment.

The function of CD20 is not fully understood, but it is a membrane protein that appears to modulate calcium release.[51] The mechanisms of action of Rituxan are not fully elucidated, but its binding to CD20 triggers antibody-dependent cellular cytotoxicity (ADCC), antibody-dependent phagocytosis, complement-dependent cytotoxicity (CDC), and possible direct initiation of apoptosis involving reactive oxygen species (ROS) generation.[52,53] The outcomes for patients treated with Rituxan vary depending on the disease being treated, but an overall response rate of 38-47% is typically seen in clinical trials of patients on monotherapy with non-Hodgkin's lymphoma. Combination with chemotherapy is also effective at treating other related cancers.[52] The most common side effects seen with Rituxan are infusion-related reactions such as flushing and low blood pressure. These are usually managed well using slow infusion rates and antihistamines. Other side effects include infections as a result of a compromised immune system and hematological events such as neutropenia and leukopenia, which are generally mild and reversible.[52] The success of Rituxan paved the way for the development of many other therapeutic antibodies.

In 1998, trastuzumab (Herceptin), a humanized monoclonal antibody targeting human epidermal growth factor receptor 2 (HER2), was approved by the FDA for the treatment of HER2+ breast cancer. This is very quick turnaround, given that HER2 was first identified as an oncogene in 1981.[54] The gene was then cloned and expressed, and found to be related to the epidermal growth factor receptor (EGFR).[55,56] HER2 was quickly linked to human breast cancer, was found to be overexpressed in 25-30% of cases, and its expression is associated with a poor prognosis.[57,58] Treatment of patients with Herceptin in combination with chemotherapy is relatively well tolerated and increases overall survival by 5 months as compared to treatment with chemotherapy alone.[59] Side effects and resistance to Herceptin are discussed further in Chapter II.

After the 1980s, advances in cancer research have led to the identification of multiple exploitable differences between cancer cells and normal cells, leading to new classes of targeted cancer therapies. Such therapies include inhibitors of signaling cascades, inhibitors of angiogenesis, hormone therapies, modifiers of gene expression, and antibody drug conjugates (ADCs). These therapies target specific proteins and/or pathways that are more likely to disrupt the function of cancer cells than that of normal cells.

Many of these therapies, including therapeutic antibodies, work by inhibiting cell signaling cascades that promote cellular proliferation and survival. One example is everolimus (Zortress, Figure 1-8), which is used to treat certain brain, breast, and kidney cancers. Zortress, an analogue of the natural product rapamycin, selectively targets the mechanistic target of rapamycin complex 1 (mTORC1), a protein kinase that regulates many cellular processes including protein translation and autophagy.[60] mTORC1 is part

of several signaling pathways, including the phosphatidylinositol-3-kinase (PI3K) pathway and the Ras-mitogen activated protein kinase (Ras-MAPK) pathway. Aberrant activity of mTORC1 is associated with several diseases including cancer.[61] Lapatinib (Tykerb, Figure 1-8) is a tyrosine kinase inhibitor similar to Gleevec that is used to treat HER2-positive breast cancer. Tykerb selectively inhibits EGFR and HER2,[62] which are both overexpressed in a variety of cancers. As mentioned above, both proteins are members of the epidermal growth factor (EGF) receptor family, a family of transmembrane proteins that dimerize upon ligand binding, transphosphorylate, and initiate signaling cascades that play key roles in cell survival and proliferation. One of the mechanisms of action of Herceptin is blocking these signaling cascades by binding to HER2 on cell surfaces.

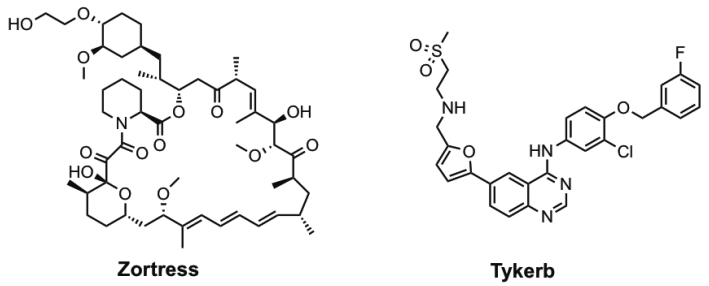

Figure 1-8. Examples of anticancer therapies that target signaling cascades involved in cellular proliferation and survival.

Other targeted therapies engage other aspects of cancer. Therapies such as the antibody bevacizumab (Avastin) and the tyrosine kinase inhibitor sorafenib (Nexavar, Figure 1-9) inhibit angiogenesis by blocking signaling through the vascular endothelial growth factor (VEGF) pathway.[63] Angiogenesis is turned off in most adult tissues, but is activated by many tumors to fuel their growth,[3] making this process an ideal one to target. Such therapies are complicated, though, by their own mechanism of action: decreasing blood flow to a tumor makes it more difficult to deliver drugs into the tumor and potentially

leads to resistance and even increased metastasis due to increased hypoxia.[63] Side effects of these drugs tend to be related to the circulatory system and include hypertension, an increased risk of bleeding, and slower wound healing.

Other therapies target cancers that use hormones to drive their growth. These therapies either block the production of hormones or interfere with hormonal signaling. An example of the former is anastrazole (Arimidex, Figure 1-9), which reversibly binds to aromatase and inhibits the conversion of androgens to estrogens.[64] Tamoxifen (Nolvadex, Figure 1-9) is an example of the latter. It binds to the estrogen receptor after being activated by cytochrome P450 and prevents estrogen from binding. Nolvadex is a selective estrogen receptor modulator, meaning that it has different effects in different tissues.[65] Both hormone therapies, like many therapies in this class, have side effects that are hormonal in nature, such as hot flashes and altered moods, along with cardiovascular effects.[64,65]

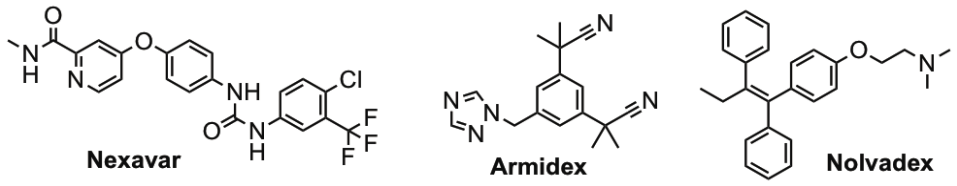

Figure 1-9. Examples of therapies targeting angiogenesis and hormone pathways.

Antibody drug conjugates (ADCs), another class of targeted therapies, use the targeting power of monoclonal antibodies to deliver potent toxins into cells. As of April 2019, there are four FDA approved ADCs: gemtuzumab ozogamicin (Mylotarg), brentuximab vedotin (Adcetris), trastuzumab emtansine (Kadcyla), and inotuzumab ozogamicin (Besponsa) (Figure 1-10). Each ADC consists of three distinct parts that must each be optimized: the mAb, linker, and toxin. The mAb itself must be human or

humanized to avoid immunogenicity and should target a protein expressed to a greater degree on the targeted cells as compared to healthy cells to avoid side effects. The targeted protein also must have an extracellular domain amenable to antibody binding and, in most cases, be internalized so the toxin can be delivered to the cell. The internalization method and the fate of the target after internalization are also important factors.[66,67] The linker needs to be stable in the plasma as to not release the toxin too early, but able to efficiently release the toxin within cells.[68] Of the FDA approved ADCs, one (Kadcyla) has a non-cleavable linker and requires lysosomal degradation of the antibody for toxin release.[69] The other three ADCs use cleavable linkers, two (Mylotarg[70] and Besponsa[71]) use an acid-labile hydrazone, while one (Adcetris[72]) employs a cathepsin-cleavable linker. Only a small fraction of the dosed toxin of an ADC ever reaches its targeted cells, so these toxins must be very potent, usually with sub-nanomolar IC_{50} values. In the FDA approved ADCs, the toxins target DNA (the calicheamicin derivative found on Mylotarg and Besponsa) and tubulin (the maytansine derivative found on Kadcyla and the auristatin found on Adcetris).[66] These therapies will be further discussed in Chapters II and IV.

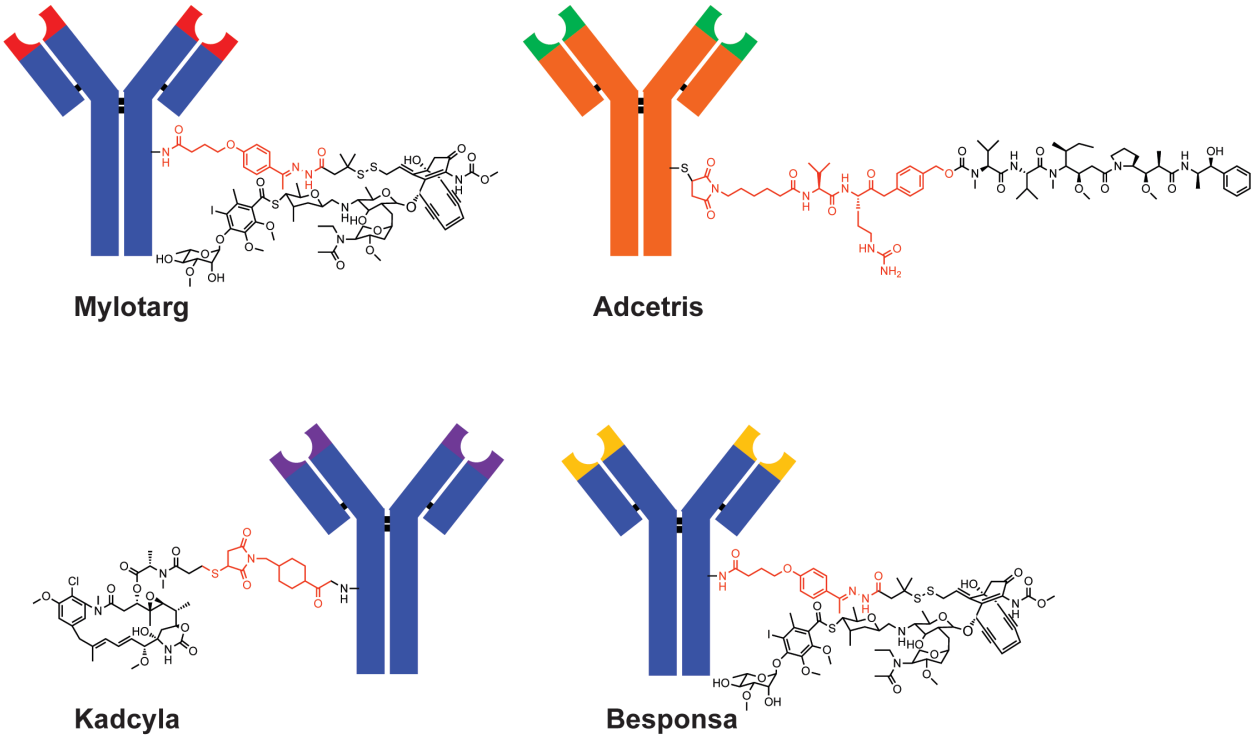

Figure 1-10. Structures of FDA approved antibody drug conjugates. Each ADC consists of an antibody (blue for humanized, orange for chimeric), a linker (red), and a toxin (black). Mylotarg and Besponsa have the same linker and toxin but different targets.

As our understanding of cancer and carcinogenesis have improved, so has our ability to develop therapies that selectively kill cancer cells. These therapies target proteins and pathways that cancer cells rely on, but that are less essential to the majority of normal cells. Targeted therapies cause side effects that are distinct and typically less severe from those caused by traditional chemotherapies.

1-3. Relevance of redox to cancer biology and targeted drug delivery

In healthy cells, oxidants and reductants are balanced. Reactive oxygen species (ROS) are generated and eliminated continuously to maintain this homeostasis. The disruption of this balance in favor of oxidants, known as oxidative stress, is related to cancer, heart disease, and neurodegeneration. Redox homeostasis is a complicated, multi-component system that is still being explored.

ROS are generated continuously in cells. The majority of ROS generated in most cell types is generated in mitochondria as part of normal metabolism.[73,74] During ATP generation, electrons are passed down the electron transport chain, eventually culminating in the reduction of molecular oxygen to water. One-electron reduction of oxygen generates the ROS superoxide.[75] Stimulation of cells by cytokines such as epidermal growth factor,[76] tumor necrosis factor α,[77] and platelet-derived growth factor[78] can activate NADPH oxidase, causing further generation of superoxide. Phagocytosis by immune cells can also activate NADPH oxidase and other ROS generating enzymes to combat invading pathogens, as will be further discussed in Chapter III. Other enzymes such as nitric oxide synthase, xanthine oxidase, and cytochrome P450s generate other ROS such as nitric oxide and hydrogen peroxide.[73,79] ROS such as hydrogen peroxide and peroxynitrite can decompose through various processes to yield secondary oxidants such as the hydroxyl radical and nitrogen dioxide.[80,81]

In order to maintain redox homeostasis, cells have many ways of eliminating ROS. These include enzymatic and non-enzymatic antioxidants. Humans, for example, have three different forms of superoxide dismutase (SOD) found in the cytoplasm, mitochondria, and extracellular space.[74] SOD catalyzes the dismutation of superoxide into hydrogen peroxide and oxygen.[82] Hydrogen peroxide produced by SOD or other methods is reduced to water by catalase[83] and glutathione peroxidase.[84] Other antioxidant enzymes include peroxiredoxin and thioredoxin.[74] Humans also use many non-enzymatic antioxidants. These include vitamins such as vitamins C and E, β-carotene, glutathione, and uric acid (Figure 1-11).[74,85] For example, vitamin C, also known as ascorbic acid, is able to donate electrons to many reactive species such superoxide,

hydroxyl radical, and hypochlorite, rendering them much less reactive. It also acts as an electron donor for several enzymes.[86,87] Antioxidant defenses also include those enzymes and systems that repair the damage of oxidants, such as DNA repair machinery and the proteasome.

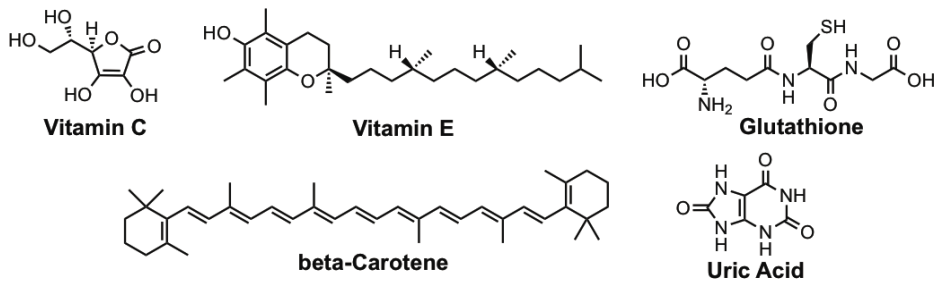

Figure 1-11. Structures of biologically relevant antioxidants.

When oxidants overwhelm the system's ability to neutralize them, widespread damage can occur. Hydroxyl and peroxyl radicals can abstract a hydrogen from polyunsaturated fatty acids, generating a lipid radical and beginning cascades of radical reactions that can damage lipid membranes by altering membrane permeability and fluidity.[88] These radical cascades can also generate side products such as aldehydes that can damage other biomolecules including proteins and DNA.[88,89] Such damage is related to many diseases, including neurodegenerative disorders and atherosclerosis.

Oxidants, especially the hydroxyl radical, can also cause extensive DNA damage. Damage occurs through addition to double bonds of DNA bases and abstraction of hydrogen atoms from DNA bases and backbone sugars. Damage to DNA bases can lead to point mutations in DNA and to DNA crosslinks. For example, oxidation of guanine generates 8-oxoguanine, a common DNA lesion that can result in pairing with adenine instead of cytosine. Damage to the backbone can lead to strand breaks. DNA oxidation is linked to diseases such as cancer, Parkinson's, and psoriasis.[90]

Biological oxidants are also able to damage proteins, causing widespread effects throughout cells. Electrophilic radicals such as the hydroxyl radical can abstract hydrogen atoms from the α-carbon of peptide backbones, potentially leading to protein fragmentation.[91,92] Many amino acid side chains, such as those of methionine, cysteine, and aromatic amino acids such as tyrosine can be oxidized, leading to inactivation or modification of the activity of enzymes.[91] An example is the formation of 3-nitrotyrosine from the reaction of tyrosine with nitrogen dioxide, which can be generated from other oxidants such as peroxynitrite.[93] Such aberrant protein activity is linked to many diseases, including cancer.[94]

Oxidants do more than cause damage within cells; they also play vital roles in normal cell function. Evidence has been emerging since the 1990s supporting the existence of redox dependent signaling and the important roles that oxidants such as hydrogen peroxide play. Early studies noted the necessity of ROS for signal transduction induced by cytokines such as platelet derived growth factor and determined that ROS were able to inactivate protein tyrosine phosphatases (PTPs).[76-78] Later studies have since expanded on this mechanism of action (Figure 1-12). As mentioned above, the binding of various cytokines to their cognate receptors leads to the activation of NADPH oxidases and thus the generation of superoxide.[73] Superoxide can dismutate to hydrogen peroxide, either spontaneously or through catalysis by SOD. Hydrogen peroxide then reversibly oxidizes the catalytic cysteine of PTPs to sulfenic acid, inactivating these enzymes[95,96] and tipping the balance between the activity of tyrosine kinases and phosphatases towards the kinases. This increase in tyrosine phosphorylation is the basis of many cell signaling cascades. Reduction of the sulfenic acid form of PTPs by various,

not fully understood systems restores catalytic activity and the balance between phosphatases and kinases and terminates the signal. Cysteine residues act as a redox-controlled switch in other types of proteins such as transcription factors as well, controlling many cellular systems. The oxidation and reduction of methionine can also be used as a switch in various redox signaling pathways.[97,98] New roles of oxidants as signaling molecules are constantly emerging, and they have already been shown to control cell proliferation, differentiation, and apoptosis.

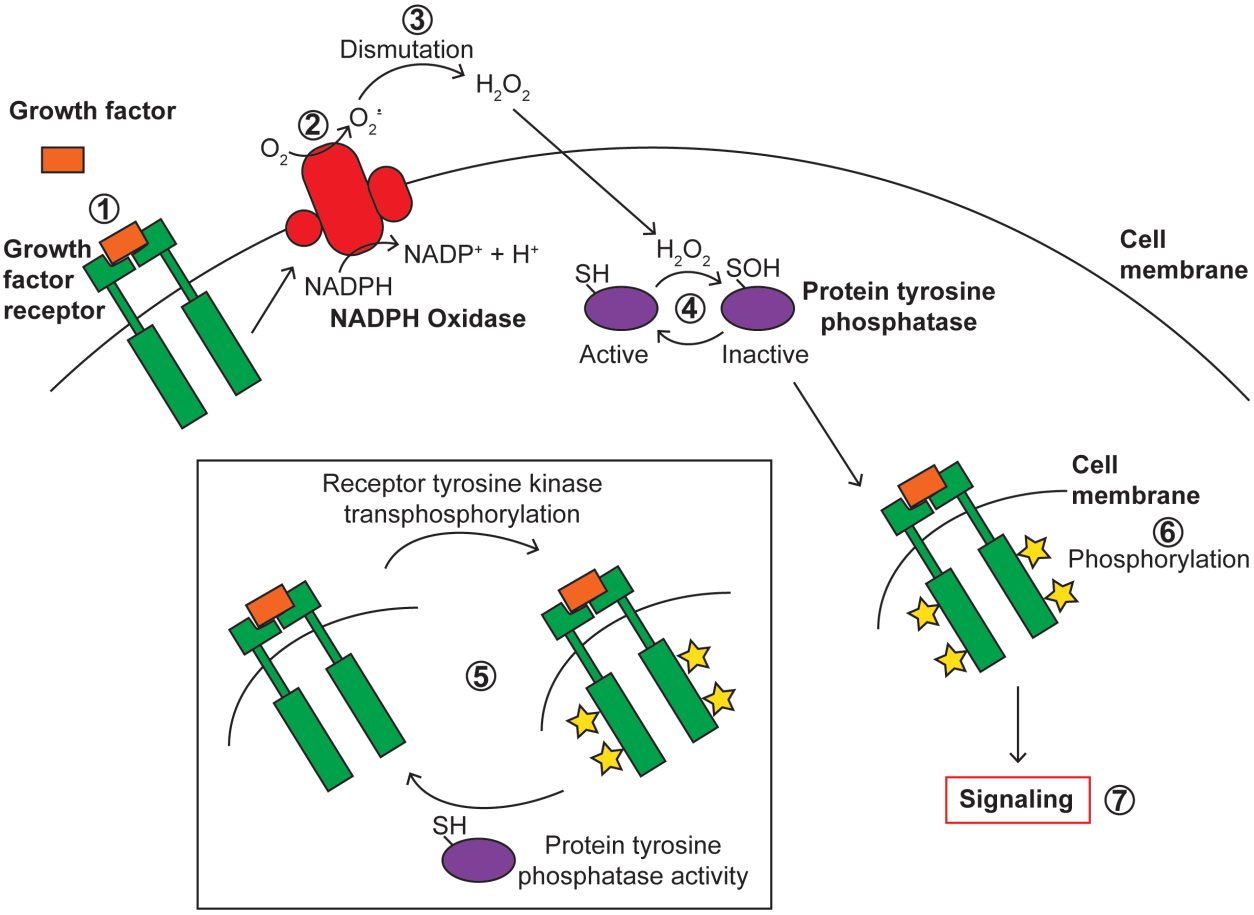

Figure 1-12. Example of redox signaling. The binding of a growth factor to its cognate receptor (1) stimulates the production of superoxide by NADPH oxidase (2). Superoxide is dismutated to hydrogen peroxide (3) which moves into the cell. Inside the cell, hydrogen peroxide oxidizes the active site cysteine of protein tyrosine phosphatases, leading to inactivation (4). This tips the equilibrium (5) between kinases and phosphatases in favor of kinases, leading to an increase of phosphorylation of many proteins (6) and signal transduction (7).

As we learn more about the complex roles redox homeostasis and ROS play in the function of healthy cells, it becomes clear that the roles of redox in cancer are equally complex. It has long been known that elevated levels of ROS are linked to and probably causal in cancer initiation and progression. As discussed above, many oxidants are able to cause widespread damage to DNA, resulting in mutations and strand breakage. Many cancers develop in areas of chronic inflammation, which contain elevated levels of ROS,[99] while other cancers can be initiated in part by mutations that lead to increased ROS generation. In this way, ROS contribute to the genetic instability[100,101] that is recognized as an enabling characteristic necessary for the initiation and progression of cancer.[3]

The contribution of redox to cancer is more complex than simple genetic instability. As mentioned above, many oxidants reversibly effect enzyme activity and act as signaling molecules. Cancer cells generate higher levels of oxidants than healthy cells through mechanisms involving altered signaling pathways, particularly those involved in metabolism.[102] This increases redox signaling through pathways such as hypoxia inducible factors (HIFs), phosphoinositide 3-kinase (PI3K), and extracellular signal-regulated kinase (ERK), leading to angiogenesis, improved survival, and growth.[103,104] Because excessive levels of oxidants can lead to cell death, cancer cells must balance increased oxidant levels by generating more antioxidants such as peroxiredoxin and superoxide dismutase.[102] By maintaining levels of oxidants that are high enough to initiate beneficial signaling but not high enough to trigger apoptosis, cancer cells can use redox to thrive (Figure 1-13).

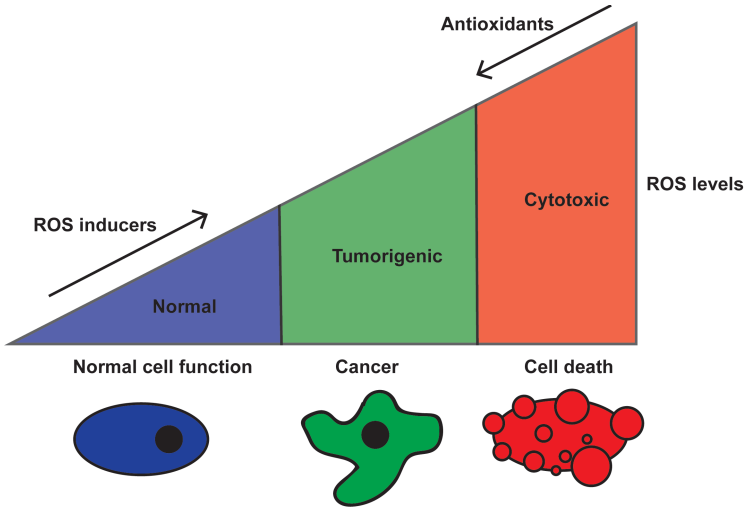

Figure 1-13. Redox homeostasis in cancer cells. Cancer cells use inducers of ROS production and antioxidants to maintain a rate of ROS production that is high enough to promote tumor growth but not so high as to trigger apoptosis. Figure adapted from Glasauer *et. al*. [102]

Researchers are attempting to alter redox homeostasis in order to target cancer cells. The altered redox state of cancer cells is linked to multidrug resistance through several mechanisms, making redox a tempting target. These mechanisms include modulating the expression and function of multidrug resistance proteins such as P-glycoprotein (P-gp)[105,106] and an increased ability to overcome oxidative stress generated by anticancer drugs such as paclitaxel (Taxol) and etoposide (Etopophos).[105,107] Additionally, the fine balance cancer cells maintain between high enough oxidant levels to maintain beneficial signaling but low enough to not induce apoptosis is believed to make them more susceptible than healthy cells to changes in redox.

To selectively kill cancer cells, attempts have been made to reduce ROS levels. This could block the increased redox signaling that cancer cells require. Alternatively, increasing ROS levels could force cancer cells into apoptosis, whereas reducing antioxidant levels could have the same effect. Dosing with antioxidants or disrupting ROS

production has potential for preventing or treating cancer.[102,108] However, these experiments have had little success, and in some cases treatment with antioxidants actually increased tumor growth or metastasis in mouse models,[109,110] or increased the risk of certain cancers among certain human subpopulations.[111-113] More success has been achieved by increasing ROS in cancer cells, although selectivity and resistance can still be an issue when using this strategy.[102] Several FDA approved drugs such as procarbazine (Matulane, Figure 1-14),[114] doxorubicin (Adriamycin, Figure 1-14),[115] Taxol (Figure 1-14),[116] and Rituxan[53] all use ROS generation as part of their mechanism of action. Many molecules are being investigated to eliminate or inhibit antioxidants such as GSH, thioredoxin, and SOD, but as of 2017 no such drugs have been approved by the FDA.[102,117]

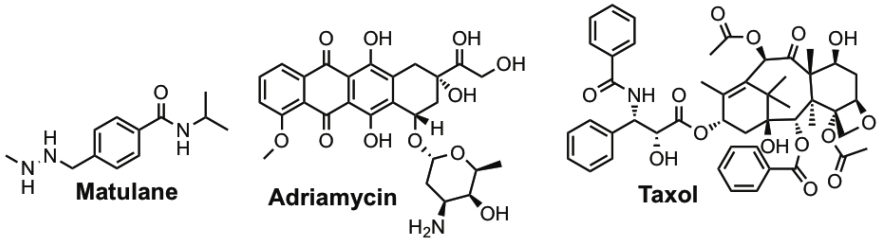

Figure 1-14. Structures of FDA approved drugs that generate ROS.

There is a continual search for more selective and potent anticancer therapeutics. As researchers learn more about cancer biology, they better understand why drugs fail and gain insight into how to improve future therapeutics. This is a circular process: a new understanding of cancer biology allows for improved therapeutics, and the shortcomings of improved therapeutics lead to a deeper understanding of cancer biology.

1-4. Outline of this dissertation

Cancer is a very complex, multi-faceted group of diseases. My research has focused on two main areas: 1) developing systems to improve antibody drug conjugates in the hope of reducing the side effects of cancer treatment, and 2) investigating tools to detect a biological oxidant that is linked to immunology and cancer. In this dissertation, Chapter II focuses on the synergistic use of antibody drug conjugates and endosome disruptive peptides to target and kill cancer cells. Advances in the design of endosome disruptive peptides are discussed, along with the optimization of an antibody-based system we termed synthetic lethal targeting. Chapter III describes novel fluorescent sensors of the biological oxidant peroxynitrite. These sensors become localized in the endoplasmic reticulum, which contributes to their ability to detect endogenous peroxynitrite generated by macrophages upon phagocytosis. Finally, Chapter IV discusses attempts at using proximity driven bioconjugation to generate more homogenous antibody drug conjugates.

1-5. References

(1) "What Is Cancer?" *National Cancer Institute.* February 9, 2015. <https://www.cancer.gov>.

(2) Hanahan, D.; Weinberg, R. A., The hallmarks of cancer. *Cell* **2000**, *100*, 57.

(3) Hanahan, D.; Weinberg, R. A., Hallmarks of cancer: the next generation. *Cell* **2011**, *144*, 646.

(4) Sonnenschein, C.; Soto, A. M., The aging of the 2000 and 2011 Hallmarks of Cancer reviews: a critique. *J. Biosci.* **2013**, *38*, 651.

(5) Lazebnik, Y., What are the hallmarks of cancer? *Nat. Rev. Cancer* **2010**, *10*, 232.

(6) Sondka, Z.; Bamford, S.; Cole, C. G.; Ward, S. A.; Dunham, I.; Forbes, S. A., The COSMIC Cancer Gene Census: describing genetic dysfunction across all human cancers. *Nat. Rev. Cancer* **2018**, *18*, 696.

(7) Gerlinger, M.; Rowan, A. J.; Horswell, S.; Math, M.; Larkin, J.; Endesfelder, D.; Gronroos, E.; Martinez, P.; Matthews, N.; Stewart, A.; Tarpey, P.; Varela, I.; Phillimore, B.; Begum, S.; McDonald, N. Q.; Butler, A.; Jones, D.; Raine, K.; Latimer, C.; Santos, C. R.; Nohadani, M.; Eklund, A. C.; Spencer-Dene, B.; Clark, G.; Pickering, L.; Stamp, G.; Gore, M.; Szallasi, Z.; Downward, J.; Futreal, P. A.; Swanton, C., Intratumor heterogeneity and branched evolution revealed by multiregion sequencing. *N. Engl. J. Med.* **2012**, *366*, 883.

(8) Yap, T. A.; Gerlinger, M.; Futreal, P. A.; Pusztai, L.; Swanton, C., Intratumor heterogeneity: seeing the wood for the trees. *Sci. Transl. Med.* **2012**, *4*, 127ps10.

(9) Su, K. Y.; Chen, H. Y.; Li, K. C.; Kuo, M. L.; Yang, J. C.; Chan, W. K.; Ho, B. C.; Chang, G. C.; Shih, J. Y.; Yu, S. L.; Yang, P. C., Pretreatment epidermal growth factor receptor (EGFR) T790M mutation predicts shorter EGFR tyrosine kinase inhibitor response duration in patients with non-small-cell lung cancer. *J. Clin. Oncol.* **2012**, *30*, 433.

(10) Pao, W.; Miller, V. A.; Politi, K. A.; Riely, G. J.; Somwar, R.; Zakowski, M. F.; Kris, M. G.; Varmus, H., Acquired resistance of lung adenocarcinomas to gefitinib or erlotinib is associated with a second mutation in the EGFR kinase domain. *PLoS Med.* **2005**, *2*, e73.

(11) Clarke, M. F.; Dick, J. E.; Dirks, P. B.; Eaves, C. J.; Jamieson, C. H.; Jones, D. L.; Visvader, J.; Weissman, I. L.; Wahl, G. M., Cancer stem cells--perspectives on current status and future directions: AACR Workshop on cancer stem cells. *Cancer Res.* **2006**, *66*, 9339.

(12) Diehn, M.; Cho, R. W.; Lobo, N. A.; Kalisky, T.; Dorie, M. J.; Kulp, A. N.; Qian, D.; Lam, J. S.; Ailles, L. E.; Wong, M.; Joshua, B.; Kaplan, M. J.; Wapnir, I.; Dirbas, F. M.; Somlo, G.; Garberoglio, C.; Paz, B.; Shen, J.; Lau, S. K.; Quake, S. R.; Brown, J. M.; Weissman, I. L.; Clarke, M. F., Association of reactive oxygen species levels and radioresistance in cancer stem cells. *Nature* **2009**, *458*, 780.

(13) Bao, S.; Wu, Q.; McLendon, R. E.; Hao, Y.; Shi, Q.; Hjelmeland, A. B.; Dewhirst, M. W.; Bigner, D. D.; Rich, J. N., Glioma stem cells promote radioresistance by preferential activation of the DNA damage response. *Nature* **2006**, *444*, 756.

(14) Takaishi, S.; Okumura, T.; Tu, S.; Wang, S. S.; Shibata, W.; Vigneshwaran, R.; Gordon, S. A.; Shimada, Y.; Wang, T. C., Identification of gastric cancer stem cells using the cell surface marker CD44. *Stem Cells* **2009**, *27*, 1006.

(15) Batlle, E.; Clevers, H., Cancer stem cells revisited. *Nat. Med.* **2017**, *23*, 1124.

(16) Szakacs, G.; Paterson, J. K.; Ludwig, J. A.; Booth-Genthe, C.; Gottesman, M. M., Targeting multidrug resistance in cancer. *Nat. Rev. Drug Discov.* **2006**, *5*, 219.

(17) Ajani, J. A.; Song, S.; Hochster, H. S.; Steinberg, I. B., Cancer stem cells: the promise and the potential. *Semin. Oncol.* **2015**, *42 Suppl 1*, S3.

(18) Balkwill, F. R.; Capasso, M.; Hagemann, T., The tumor microenvironment at a glance. *J. Cell Sci.* **2012**, *125*, 5591.

(19) Fridman, W. H.; Pages, F.; Sautes-Fridman, C.; Galon, J., The immune contexture in human tumours: impact on clinical outcome. *Nat. Rev. Cancer* **2012**, *12*, 298.

(20) Bates, G. J.; Fox, S. B.; Han, C.; Leek, R. D.; Garcia, J. F.; Harris, A. L.; Banham, A. H., Quantification of regulatory T cells enables the identification of high-risk breast cancer patients and those at risk of late relapse. *J. Clin. Oncol.* **2006**, *24*, 5373.

(21) Curiel, T. J.; Coukos, G.; Zou, L.; Alvarez, X.; Cheng, P.; Mottram, P.; Evdemon-Hogan, M.; Conejo-Garcia, J. R.; Zhang, L.; Burow, M.; Zhu, Y.; Wei, S.; Kryczek, I.; Daniel, B.; Gordon, A.; Myers, L.; Lackner, A.; Disis, M. L.; Knutson, K. L.; Chen, L.; Zou, W., Specific recruitment of regulatory T cells in ovarian carcinoma fosters immune privilege and predicts reduced survival. *Nat. Med.* **2004**, *10*, 942.

(22) Bingle, L.; Brown, N. J.; Lewis, C. E., The role of tumour-associated macrophages in tumour progression: implications for new anticancer therapies. *J. Pathol.* **2002**, *196*, 254.

(23) Condeelis, J.; Pollard, J. W., Macrophages: obligate partners for tumor cell migration, invasion, and metastasis. *Cell* **2006**, *124*, 263.

(24) Lin, E. Y.; Li, J. F.; Gnatovskiy, L.; Deng, Y.; Zhu, L.; Grzesik, D. A.; Qian, H.; Xue, X. N.; Pollard, J. W., Macrophages regulate the angiogenic switch in a mouse model of breast cancer. *Cancer Res.* **2006**, *66*, 11238.

(25) Jain, R. K., Normalization of tumor vasculature: an emerging concept in antiangiogenic therapy. *Science* **2005**, *307*, 58.

(26) Spaeth, E. L.; Dembinski, J. L.; Sasser, A. K.; Watson, K.; Klopp, A.; Hall, B.; Andreeff, M.; Marini, F., Mesenchymal stem cell transition to tumor-associated fibroblasts contributes to fibrovascular network expansion and tumor progression. *PLoS One* **2009**, *4*, e4992.

(27) Erez, N.; Truitt, M.; Olson, P.; Arron, S. T.; Hanahan, D., Cancer-Associated Fibroblasts Are Activated in Incipient Neoplasia to Orchestrate Tumor-Promoting Inflammation in an NF-kappaB-Dependent Manner. *Cancer Cell* **2010**, *17*, 135.

(28) Papac, R. J., Origins of cancer therapy. *Yale J. Biol. Med.* **2001**, *74*, 391.

(29) Morrison, W. B., Cancer chemotherapy: an annotated history. *J. Vet. Intern. Med.* **2010**, *24*, 1249.

(30) DeVita, V. T.; Chu, E., A History of Cancer Chemotherapy. *Cancer Res.* **2008**, *68*, 8643.

(31) Devita, V. T., Jr.; Serpick, A. A.; Carbone, P. P., Combination chemotherapy in the treatment of advanced Hodgkin's disease. *Ann. Intern. Med.* **1970**, *73*, 881.

(32) Gilman, A.; Philips, F. S., The biological actions and therapeutic applications of the B-chloroethyl amines and sulfides. *Science* **1946**, *103*, 409.

(33) Farber, S.; Diamond, L. K., Temporary remissions in acute leukemia in children produced by folic acid antagonist, 4-aminopteroyl-glutamic acid. *N. Engl. J. Med.* **1948**, *238*, 787.

(34) Strebhardt, K.; Ullrich, A., Paul Ehrlich's magic bullet concept: 100 years of progress. *Nat. Rev. Cancer* **2008**, *8*, 473.

(35) Martin, G. S., Rous sarcoma virus: a function required for the maintenance of the transformed state. *Nature* **1970**, *227*, 1021.

(36) Stehelin, D.; Varmus, H. E.; Bishop, J. M.; Vogt, P. K., DNA related to the transforming gene(s) of avian sarcoma viruses is present in normal avian DNA. *Nature* **1976**, *260*, 170.

(37) Spector, D. H.; Varmus, H. E.; Bishop, J. M., Nucleotide sequences related to the transforming gene of avian sarcoma virus are present in DNA of uninfected vertebrates. *Proc. Natl. Acad. Sci. U. S. A.* **1978**, *75*, 4102.

(38) Bishop, J. M., The discovery of proto-oncogenes. *FASEB J.* **1996**, *10*, 362.

(39) Bister, K., Discovery of oncogenes: The advent of molecular cancer research. *Proc. Natl. Acad. Sci. U. S. A.* **2015**, *112*, 15259.

(40) de Klein, A.; van Kessel, A. G.; Grosveld, G.; Bartram, C. R.; Hagemeijer, A.; Bootsma, D.; Spurr, N. K.; Heisterkamp, N.; Groffen, J.; Stephenson, J. R., A cellular

oncogene is translocated to the Philadelphia chromosome in chronic myelocytic leukaemia. *Nature* **1982**, *300*, 765.

(41) Bartram, C. R.; de Klein, A.; Hagemeijer, A.; van Agthoven, T.; Geurts van Kessel, A.; Bootsma, D.; Grosveld, G.; Ferguson-Smith, M. A.; Davies, T.; Stone, M.; et al., Translocation of c-ab1 oncogene correlates with the presence of a Philadelphia chromosome in chronic myelocytic leukaemia. *Nature* **1983**, *306*, 277.

(42) Druker, B. J.; Tamura, S.; Buchdunger, E.; Ohno, S.; Segal, G. M.; Fanning, S.; Zimmermann, J.; Lydon, N. B., Effects of a selective inhibitor of the Abl tyrosine kinase on the growth of Bcr-Abl positive cells. *Nat. Med.* **1996**, *2*, 561.

(43) Cilloni, D.; Saglio, G., Molecular pathways: BCR-ABL. *Clin. Cancer. Res.* **2012**, *18*, 930.

(44) Daley, G. Q.; Van Etten, R. A.; Baltimore, D., Induction of chronic myelogenous leukemia in mice by the P210bcr/abl gene of the Philadelphia chromosome. *Science* **1990**, *247*, 824.

(45) Heisterkamp, N.; Jenster, G.; ten Hoeve, J.; Zovich, D.; Pattengale, P. K.; Groffen, J., Acute leukaemia in bcr/abl transgenic mice. *Nature* **1990**, *344*, 251.

(46) Druker, B. J.; Guilhot, F.; O'Brien, S. G.; Gathmann, I.; Kantarjian, H.; Gattermann, N.; Deininger, M. W.; Silver, R. T.; Goldman, J. M.; Stone, R. M.; Cervantes, F.; Hochhaus, A.; Powell, B. L.; Gabrilove, J. L.; Rousselot, P.; Reiffers, J.; Cornelissen, J. J.; Hughes, T.; Agis, H.; Fischer, T.; Verhoef, G.; Shepherd, J.; Saglio, G.; Gratwohl, A.; Nielsen, J. L.; Radich, J. P.; Simonsson, B.; Taylor, K.; Baccarani, M.; So, C.; Letvak, L.; Larson, R. A., Five-year follow-up of patients receiving imatinib for chronic myeloid leukemia. *N. Engl. J. Med.* **2006**, *355*, 2408.

(47) Berman, E.; Jhanwar, S.; Hedvat, C.; Arcila, M. E.; Wahab, O. A.; Levine, R.; Maloy, M.; Ma, W.; Albitar, M., Resistance to imatinib in patients with chronic myelogenous leukemia and the splice variant BCR-ABL1(35INS). *Leuk. Res.* **2016**, *49*, 108.

(48) Shah, N. P.; Sawyers, C. L., Mechanisms of resistance to STI571 in Philadelphia chromosome-associated leukemias. *Oncogene* **2003**, *22*, 7389.

(49) Kohler, G.; Milstein, C., Continuous cultures of fused cells secreting antibody of predefined specificity. *Nature* **1975**, *256*, 495.

(50) Stashenko, P.; Nadler, L. M.; Hardy, R.; Schlossman, S. F., Characterization of a human B lymphocyte-specific antigen. *J. Immunol.* **1980**, *125*, 1678.

(51) Marshall, M. J. E.; Stopforth, R. J.; Cragg, M. S., Therapeutic Antibodies: What Have We Learnt from Targeting CD20 and Where Are We Going? *Front. Immunol.* **2017**, *8*, 1245.

(52) Salles, G.; Barrett, M.; Foa, R.; Maurer, J.; O'Brien, S.; Valente, N.; Wenger, M.; Maloney, D. G., Rituximab in B-Cell Hematologic Malignancies: A Review of 20 Years of Clinical Experience. *Adv. Ther.* **2017**, *34*, 2232.

(53) Bellosillo, B.; Villamor, N.; Lopez-Guillermo, A.; Marce, S.; Esteve, J.; Campo, E.; Colomer, D.; Montserrat, E., Complement-mediated cell death induced by rituximab in B-cell lymphoproliferative disorders is mediated in vitro by a caspase-independent mechanism involving the generation of reactive oxygen species. *Blood* **2001**, *98*, 2771.

(54) Shih, C.; Padhy, L. C.; Murray, M.; Weinberg, R. A., Transforming genes of carcinomas and neuroblastomas introduced into mouse fibroblasts. *Nature* **1981**, *290*, 261.

(55) Schechter, A. L.; Stern, D. F.; Vaidyanathan, L.; Decker, S. J.; Drebin, J. A.; Greene, M. I.; Weinberg, R. A., The neu oncogene: an erb-B-related gene encoding a 185,000-Mr tumour antigen. *Nature* **1984**, *312*, 513.

(56) Coussens, L.; Yang-Feng, T. L.; Liao, Y. C.; Chen, E.; Gray, A.; McGrath, J.; Seeburg, P. H.; Libermann, T. A.; Schlessinger, J.; Francke, U.; et al., Tyrosine kinase receptor with extensive homology to EGF receptor shares chromosomal location with neu oncogene. *Science* **1985**, *230*, 1132.

(57) Slamon, D. J.; Clark, G. M.; Wong, S. G.; Levin, W. J.; Ullrich, A.; McGuire, W. L., Human breast cancer: correlation of relapse and survival with amplification of the HER-2/neu oncogene. *Science* **1987**, *235*, 177.

(58) Slamon, D. J.; Godolphin, W.; Jones, L. A.; Holt, J. A.; Wong, S. G.; Keith, D. E.; Levin, W. J.; Stuart, S. G.; Udove, J.; Ullrich, A.; et al., Studies of the HER-2/neu proto-oncogene in human breast and ovarian cancer. *Science* **1989**, *244*, 707.

(59) Slamon, D. J.; Leyland-Jones, B.; Shak, S.; Fuchs, H.; Paton, V.; Bajamonde, A.; Fleming, T.; Eiermann, W.; Wolter, J.; Pegram, M.; Baselga, J.; Norton, L., Use of chemotherapy plus a monoclonal antibody against HER2 for metastatic breast cancer that overexpresses HER2. *New Engl. J. Med.* **2001**, *344*, 783.

(60) Arriola Apelo, S. I.; Neuman, J. C.; Baar, E. L.; Syed, F. A.; Cummings, N. E.; Brar, H. K.; Pumper, C. P.; Kimple, M. E.; Lamming, D. W., Alternative rapamycin

treatment regimens mitigate the impact of rapamycin on glucose homeostasis and the immune system. *Aging Cell* **2016**, *15*, 28.

(61) Kim, L. C.; Cook, R. S.; Chen, J., mTORC1 and mTORC2 in cancer and the tumor microenvironment. *Oncogene* **2017**, *36*, 2191.

(62) Wood, E. R.; Truesdale, A. T.; McDonald, O. B.; Yuan, D.; Hassell, A.; Dickerson, S. H.; Ellis, B.; Pennisi, C.; Horne, E.; Lackey, K.; Alligood, K. J.; Rusnak, D. W.; Gilmer, T. M.; Shewchuk, L., A unique structure for epidermal growth factor receptor bound to GW572016 (Lapatinib): relationships among protein conformation, inhibitor off-rate, and receptor activity in tumor cells. *Cancer Res.* **2004**, *64*, 6652.

(63) Lin, Z.; Zhang, Q.; Luo, W., Angiogenesis inhibitors as therapeutic agents in cancer: Challenges and future directions. *Eur. J. Pharmacol.* **2016**, *793*, 76.

(64) Tremont, A.; Lu, J.; Cole, J. T., Endocrine Therapy for Early Breast Cancer: Updated Review. *The Ochsner journal* **2017**, *17*, 405.

(65) Shagufta; Ahmad, I., Tamoxifen a pioneering drug: An update on the therapeutic potential of tamoxifen derivatives. *Eur. J. Med. Chem.* **2018**, *143*, 515.

(66) Beck, A.; Goetsch, L.; Dumontet, C.; Corvaia, N., Strategies and challenges for the next generation of antibody-drug conjugates. *Nat. Rev. Drug Discov.* **2017**, *16*, 315.

(67) Thomas, A.; Teicher, B. A.; Hassan, R., Antibody-drug conjugates for cancer therapy. *Lancet Oncol.* **2016**, *17*, e254.

(68) Lu, J.; Jiang, F.; Lu, A.; Zhang, G., Linkers Having a Crucial Role in Antibody-Drug Conjugates. *Int. J. Mol. Sci.* **2016**, *17*, 561.

(69) Lewis Phillips, G. D.; Li, G.; Dugger, D. L.; Crocker, L. M.; Parsons, K. L.; Mai, E.; Blattler, W. A.; Lambert, J. M.; Chari, R. V.; Lutz, R. J.; Wong, W. L.; Jacobson, F. S.; Koeppen, H.; Schwall, R. H.; Kenkare-Mitra, S. R.; Spencer, S. D.; Sliwkowski, M. X., Targeting HER2-positive breast cancer with trastuzumab-DM1, an antibody-cytotoxic drug conjugate. *Cancer Res.* **2008**, *68*, 9280.

(70) Bross, P. F.; Beitz, J.; Chen, G.; Chen, X. H.; Duffy, E.; Kieffer, L.; Roy, S.; Sridhara, R.; Rahman, A.; Williams, G.; Pazdur, R., Approval summary: gemtuzumab ozogamicin in relapsed acute myeloid leukemia. *Clin. Cancer. Res.* **2001**, *7*, 1490.

(71) Uy, N.; Nadeau, M.; Stahl, M.; Zeidan, A. M., Inotuzumab ozogamicin in the treatment of relapsed/refractory acute B cell lymphoblastic leukemia. *J. Blood Med.* **2018**, *9*, 67.

(72) Scott, L. J., Brentuximab Vedotin: A Review in CD30-Positive Hodgkin Lymphoma. *Drugs* **2017**, *77*, 435.

(73) Holmstrom, K. M.; Finkel, T., Cellular mechanisms and physiological consequences of redox-dependent signalling. *Nat. Rev. Mol. Cell Biol.* **2014**, *15*, 411.

(74) Birben, E.; Sahiner, U. M.; Sackesen, C.; Erzurum, S.; Kalayci, O., Oxidative stress and antioxidant defense. *World Allergy Org. J.* **2012**, *5*, 9.

(75) Murphy, M. P., How mitochondria produce reactive oxygen species. *Biochem. J* **2009**, *417*, 1.

(76) Bae, Y. S.; Kang, S. W.; Seo, M. S.; Baines, I. C.; Tekle, E.; Chock, P. B.; Rhee, S. G., Epidermal growth factor (EGF)-induced generation of hydrogen peroxide. Role in EGF receptor-mediated tyrosine phosphorylation. *J. Biol. Chem.* **1997**, *272*, 217.

(77) Lo, Y. Y.; Cruz, T. F., Involvement of reactive oxygen species in cytokine and growth factor induction of c-fos expression in chondrocytes. *J. Biol. Chem.* **1995**, *270*, 11727.

(78) Sundaresan, M.; Yu, Z. X.; Ferrans, V. J.; Irani, K.; Finkel, T., Requirement for generation of H2O2 for platelet-derived growth factor signal transduction. *Science* **1995**, *270*, 296.

(79) Zangar, R. C.; Davydov, D. R.; Verma, S., Mechanisms that regulate production of reactive oxygen species by cytochrome P450. *Toxicol. Appl. Pharmacol.* **2004**, *199*, 316.

(80) Denicola, A.; Freeman, B. A.; Trujillo, M.; Radi, R., Peroxynitrite reaction with carbon dioxide/bicarbonate: kinetics and influence on peroxynitrite-mediated oxidations. *Arch. Biochem. Biophys.* **1996**, *333*, 49.

(81) Lymar, S. V.; Hurst, J. K., Rapid reaction between peroxonitrite ion and carbon dioxide: Implications for biological activity. *J. Am. Chem. Soc.* **1995**, *117*, 8867.

(82) McCord, J. M.; Fridovich, I., Superoxide dismutase. An enzymic function for erythrocuprein (hemocuprein). *J. Biol. Chem.* **1969**, *244*, 6049.

(83) Loew, O., A New Enzyme of General Occurrence in Organisms. *Science* **1900**, *11*, 701.

(84) Mills, G. C., Hemoglobin catabolism. I. Glutathione peroxidase, an erythrocyte enzyme which protects hemoglobin from oxidative breakdown. *J. Biol. Chem.* **1957**, *229*, 189.

(85) Mironczuk-Chodakowska, I.; Witkowska, A. M.; Zujko, M. E., Endogenous non-enzymatic antioxidants in the human body. *Adv. Med. Sci.* **2018**, *63*, 68.

(86) Padayatty, S. J.; Katz, A.; Wang, Y.; Eck, P.; Kwon, O.; Lee, J. H.; Chen, S.; Corpe, C.; Dutta, A.; Dutta, S. K.; Levine, M., Vitamin C as an antioxidant: evaluation of its role in disease prevention. *J. Am. Coll. Nutr.* **2003**, *22*, 18.

(87) Buettner, G. R.; Jurkiewicz, B. A., Catalytic metals, ascorbate and free radicals: combinations to avoid. *Radiat. Res.* **1996**, *145*, 532.

(88) Gaschler, M. M.; Stockwell, B. R., Lipid peroxidation in cell death. *Biochem. Biophys. Res. Commun.* **2017**, *482*, 419.

(89) Esterbauer, H.; Schaur, R. J.; Zollner, H., Chemistry and biochemistry of 4-hydroxynonenal, malonaldehyde and related aldehydes. *Free Radic. Biol. Med.* **1991**, *11*, 81.

(90) Cooke, M. S.; Evans, M. D.; Dizdaroglu, M.; Lunec, J., Oxidative DNA damage: mechanisms, mutation, and disease. *FASEB J.* **2003**, *17*, 1195.

(91) Stadtman, E. R., Protein oxidation and aging. *Free Radic. Res.* **2006**, *40*, 1250.

(92) Davies, M. J., Protein oxidation and peroxidation. *Biochem. J.* **2016**, *473*, 805.

(93) Bartesaghi, S.; Radi, R., Fundamentals on the biochemistry of peroxynitrite and protein tyrosine nitration. *Redox Biol.* **2018**, *14*, 618.

(94) Moldogazieva, N. T.; Lutsenko, S. V.; Terentiev, A. A., Reactive Oxygen and Nitrogen Species-Induced Protein Modifications: Implication in Carcinogenesis and Anticancer Therapy. *Cancer Res.* **2018**, *78*, 6040.

(95) Denu, J. M.; Tanner, K. G., Specific and reversible inactivation of protein tyrosine phosphatases by hydrogen peroxide: evidence for a sulfenic acid intermediate and implications for redox regulation. *Biochemistry* **1998**, *37*, 5633.

(96) Meng, T. C.; Fukada, T.; Tonks, N. K., Reversible oxidation and inactivation of protein tyrosine phosphatases in vivo. *Mol. Cell* **2002**, *9*, 387.

(97) Hung, R. J.; Spaeth, C. S.; Yesilyurt, H. G.; Terman, J. R., SelR reverses Mical-mediated oxidation of actin to regulate F-actin dynamics. *Nat. Cell Biol.* **2013**, *15*, 1445.

(98) Erickson, J. R.; Joiner, M. L.; Guan, X.; Kutschke, W.; Yang, J.; Oddis, C. V.; Bartlett, R. K.; Lowe, J. S.; O'Donnell, S. E.; Aykin-Burns, N.; Zimmerman, M. C.; Zimmerman, K.; Ham, A. J.; Weiss, R. M.; Spitz, D. R.; Shea, M. A.; Colbran, R. J.; Mohler, P. J.; Anderson, M. E., A dynamic pathway for calcium-independent activation of CaMKII by methionine oxidation. *Cell* **2008**, *133*, 462.

(99) Mittal, M.; Siddiqui, M. R.; Tran, K.; Reddy, S. P.; Malik, A. B., Reactive oxygen species in inflammation and tissue injury. *Antioxid. Redox Signal.* **2014**, *20*, 1126.

(100) Jackson, A. L.; Loeb, L. A., The contribution of endogenous sources of DNA damage to the multiple mutations in cancer. *Mutat. Res.* **2001**, *477*, 7.

(101) Storz, P., Reactive oxygen species in tumor progression. *Front. Biosci.* **2005**, *10*, 1881.

(102) Glasauer, A.; Chandel, N. S., Targeting antioxidants for cancer therapy. *Biochem. Pharmacol.* **2014**, *92*, 90.

(103) Weinberg, F.; Chandel, N. S., Reactive oxygen species-dependent signaling regulates cancer. *Cell. Mol. Life Sci.* **2009**, *66*, 3663.

(104) Cairns, R. A.; Harris, I. S.; Mak, T. W., Regulation of cancer cell metabolism. *Nat. Rev. Cancer* **2011**, *11*, 85.

(105) Kuo, M. T., Redox regulation of multidrug resistance in cancer chemotherapy: molecular mechanisms and therapeutic opportunities. *Antioxid. Redox Signal.* **2009**, *11*, 99.

(106) Polimeni, M.; Gazzano, E., Is redox signaling a feasible target for overcoming multidrug resistance in cancer chemotherapy? *Front. Pharmacol.* **2014**, *5*, 286.

(107) Victorino, V. J.; Pizzatti, L.; Michelletti, P.; Panis, C., Oxidative stress, redox signaling and cancer chemoresistance: putting together the pieces of the puzzle. *Curr. Med. Chem.* **2014**, *21*, 3211.

(108) Weinberg, F.; Hamanaka, R.; Wheaton, W. W.; Weinberg, S.; Joseph, J.; Lopez, M.; Kalyanaraman, B.; Mutlu, G. M.; Budinger, G. R.; Chandel, N. S., Mitochondrial metabolism and ROS generation are essential for Kras-mediated tumorigenicity. *Proc. Natl. Acad. Sci. U. S. A.* **2010**, *107*, 8788.

(109) Sayin, V. I.; Ibrahim, M. X.; Larsson, E.; Nilsson, J. A.; Lindahl, P.; Bergo, M. O., Antioxidants accelerate lung cancer progression in mice. *Sci. Transl. Med.* **2014**, *6*, 221ra15.

(110) Sceneay, J.; Liu, M. C.; Chen, A.; Wong, C. S.; Bowtell, D. D.; Moller, A., The antioxidant N-acetylcysteine prevents HIF-1 stabilization under hypoxia in vitro but does not affect tumorigenesis in multiple breast cancer models in vivo. *PLoS One* **2013**, *8*, e66388.

(111) Klein, E. A.; Thompson, I. M., Jr.; Tangen, C. M.; Crowley, J. J.; Lucia, M. S.; Goodman, P. J.; Minasian, L. M.; Ford, L. G.; Parnes, H. L.; Gaziano, J. M.; Karp, D. D.; Lieber, M. M.; Walther, P. J.; Klotz, L.; Parsons, J. K.; Chin, J. L.; Darke, A. K.; Lippman, S. M.; Goodman, G. E.; Meyskens, F. L., Jr.; Baker, L. H., Vitamin E and the risk of prostate cancer: the Selenium and Vitamin E Cancer Prevention Trial (SELECT). *JAMA* **2011**, *306*, 1549.

(112) The effect of vitamin E and beta carotene on the incidence of lung cancer and other cancers in male smokers. *N. Engl. J. Med.* **1994**, *330*, 1029.

(113) Brasky, T. M.; White, E.; Chen, C. L., Long-Term, Supplemental, One-Carbon Metabolism-Related Vitamin B Use in Relation to Lung Cancer Risk in the Vitamins and Lifestyle (VITAL) Cohort. *J. Clin. Oncol.* **2017**, *35*, 3440.

(114) Renschler, M. F., The emerging role of reactive oxygen species in cancer therapy. *Eur. J. Cancer* **2004**, *40*, 1934.

(115) Kotamraju, S.; Chitambar, C. R.; Kalivendi, S. V.; Joseph, J.; Kalyanaraman, B., Transferrin receptor-dependent iron uptake is responsible for doxorubicin-mediated apoptosis in endothelial cells: role of oxidant-induced iron signaling in apoptosis. *J. Biol. Chem.* **2002**, *277*, 17179.

(116) Conklin, K. A., Chemotherapy-associated oxidative stress: impact on chemotherapeutic effectiveness. *Integr. Cancer Ther.* **2004**, *3*, 294.

(117) Kirkpatrick, D. L.; Powis, G., Clinically Evaluated Cancer Drugs Inhibiting Redox Signaling. *Antioxid. Redox Signal.* **2017**, *26*, 262.

Chapter 2

Synthetic Lethal Targeting: A New Anticancer Strategy

2-1. Introduction

Many traditional anticancer agents lack selectivity, leading to side effects for patients. Studies tracking side effects self-reported by cancer patients receiving chemotherapy in Australia[1] and the United States[2] indicate that more than 85% of cancer patients receiving chemotherapy experience at least one side effect, with 67% experiencing six or more and 62% experiencing at least one serious (grade III or IV) side effect.[1] The most common side effect reported is fatigue, followed by pain and nausea and/or vomiting.[1,2] Surveys of patients reveal that these side effects greatly reduce the quality of life of patients, and that even seemingly minor side effects such as hair loss and fatigue are big detractors.[3-6]

These side effects have spurred a constant search for more selective cancer therapies. Early anticancer agents such as the DNA alkylating agent cyclophosphamide are targeted in the sense that they kill rapidly dividing cells. Healthy cells such as blood cells in the bone marrow and the lining of the digestive tract also divide rapidly, and some types of cancer do not, leading to side effects and lack of efficacy. These side effects include leukopenia and vomiting, in addition to an increased future risk of cancer.

Advances in cancer biology have identified exploitable differences between cancer cells and healthy cells, as discussed in Chapter 1. These discoveries have allowed for the development of more targeted cancer therapies including both small molecules and

biologics. One promising class of cancer therapeutics are monoclonal antibodies (mAbs). Therapeutic mAbs selectively bind to receptors that are overexpressed on the surface of cancer cells. They kill targeted cells through many different mechanisms including receptor downregulation, antibody-dependent cell-mediated cytotoxicity, complement-dependent immunocytotoxicity, and/or inhibition of receptor-linked signaling pathways (Figure 2-1).[7] These newer therapies still cause side effects, but they are typically of a different sort and tend to be more manageable than those caused by traditional cancer therapeutics.

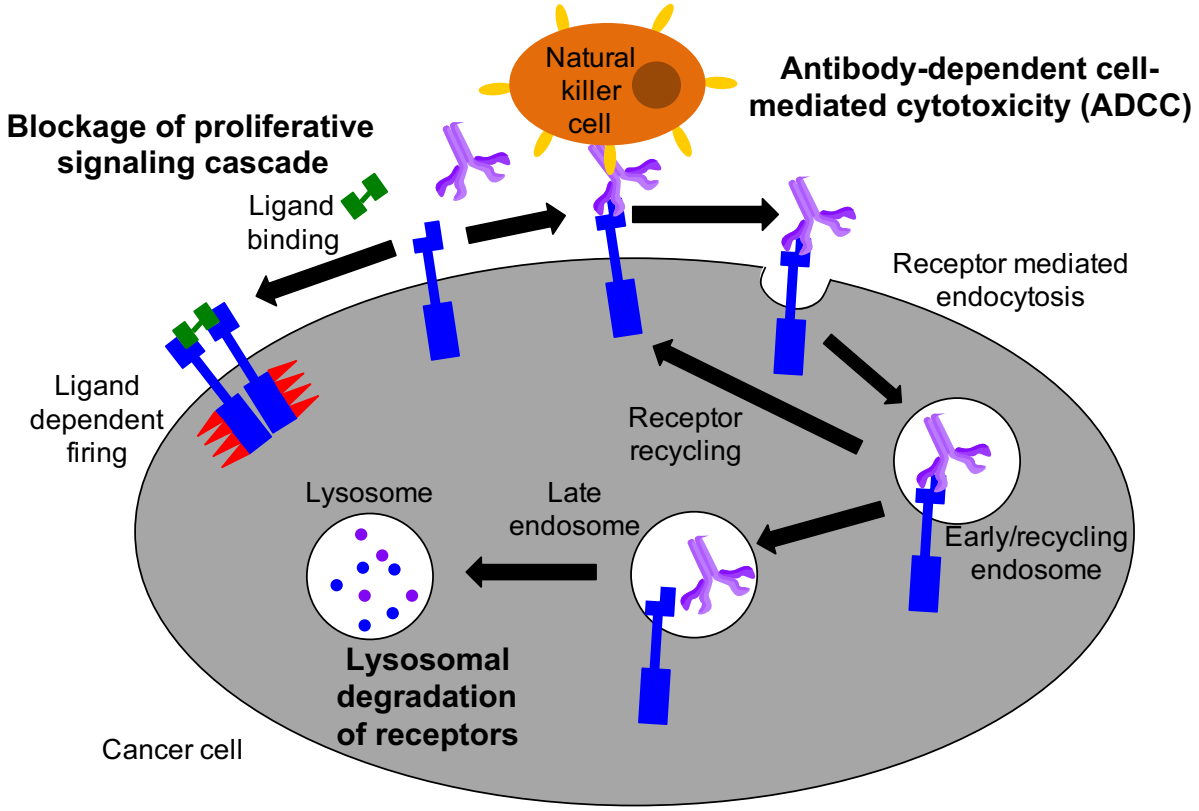

Figure 2-1. Representative mechanisms of action of therapeutic antibodies.

The side effects of FDA approved therapeutic antibodies are different than those associated with more traditional chemotherapies. The most common of these side effects are caused by the infusion of large amounts of antibody into the body and are relatively

minor, for example fever and chills.[8-10] These infusions can cause more serious side effects such as cytokine release syndrome and anaphylaxis, but these can generally be avoided by using slow infusion rates and prophylactic treatment with other agents to treat the anticipated side effects.[8] Other side effects of therapeutic antibodies are on-target in that they arise from a mAb binding to its targeted receptor on a non-targeted cell. For example, cardiac dysfunction has been seen in up to 4% of women treated with trastuzumab (Herceptin), a therapeutic antibody used to treat HER2+ breast cancer.[11] This side effect, which is commonly reversible and asymptomatic, is caused by Herceptin blocking HER2 signaling on cardiac muscle cells.[8,11] Such on-target side effects can be difficult to predict, but they are frequently reversible and less severe than side effects seen with traditional chemotherapeutics.

Though therapeutic antibodies offer improvements compared to traditional chemotherapeutics for treating cancer as far as side effects go, they do have limitations. As with all cancer therapeutics, resistance is a major concern for therapeutic antibodies. Many patients do not respond to mAbs at all, and of those that do, many develop resistance. For example, less than 35% of HER2+ breast cancer patients respond to Herceptin, and of those, 70% develop resistance within one year.[12] The mechanisms behind this primary and acquired resistance are not fully understood, but they seem to include signaling compensation through other receptors, constitutive amplification of the signaling pathway without HER2 activation, and HER2 mutation.[12,13] Similar resistance mechanisms are seen for other therapeutic antibodies.

The linkage of cytotoxins to therapeutic antibodies to form antibody-drug conjugates (ADCs) is one method to overcome this resistance. Trastuzumab emtansine

(Kadcyla), for example, is a conjugate of the HER2-targeted antibody trastuzumab (Herceptin) and the tubulin binding agent emtansine (DM1), a derivative of the natural product maytansine (Figure 2-2). DM1 is more potent *in vitro* than the anticancer drug Taxol, but has dose-limiting toxicities that limit its use *in vivo*.[14] Kadcyla can overcome some of the resistance observed in patients treated with Herceptin.[15,16] Unfortunately, severe side effects are seen in about 40% of patients, with fatigue being the most common and thrombocytopenia and elevation of liver transaminases being of greatest concern.[17] The causes of these side effects are not fully understood, but a mechanism has been proposed for the thrombocytopenia. Kadcyla binds to FcγRIIa receptors on megakaryocyte (MK) progenitors. This allows for the intracellular release of DM1, resulting in inhibition of MK differentiation and decreased platelet production.[18] In general, the toxicities of ADCs can be caused by the antibody and/or the toxin. On-target toxicities can be observed when the ADC binds to its target receptor on non-target cells or is taken up by non-target cells expressing Fc receptors. Alternatively, toxins can be released prematurely from ADCs or toxins can diffuse from targeted cells into neighboring cells.[19]

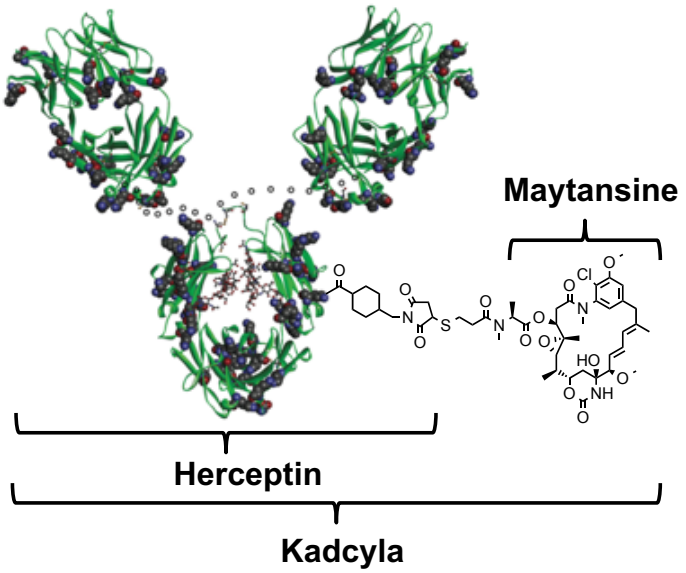

Figure 2-2. Model of the antibody drug conjugate Kadcyla. Model based on PDBs 1N8Z and 1HZH. Lysines are highlighted as CPK models. Carbohydrates are shown as balls and sticks. The highly mobile hinge region connecting the Fab and Fc fragments is represented as a chain of circles.

Premature release of toxins from ADCs is of greatest concern when the toxin is highly cell permeable. Cell permeable toxins can diffuse into nearby cells, damaging healthy tissues and potentially causing side effects. Alternatively, cell impermeable toxins may exhibit fewer side effects,[20-22] but these toxins are unlikely to reach cytoplasmic or nuclear targets due to the mechanism of uptake of therapeutic antibodies like Kadcyla (Figure 2-3). After a therapeutic antibody binds to its targeted receptor, it is internalized with the receptor through receptor mediated endocytosis. Small portions of the plasma membrane bud off to form small vesicles that fuse with each other to form early endosomes. Once delivered to early endosomes, receptor-bound antibodies are either recycled back to the cell surface or delivered to lysosomes for degradation.[23] If a toxin is cell impermeable, it may not be able to escape the endocytic system and reach the cytosol even after it is released from the antibody, since the compartments of this system are enclosed by membranes. Even-cell permeable toxins are not always efficiently released into the cell cytosol. A recent publication from Genentech[24] highlights this downfall. In that study, antibodies targeting HER2 and tomoregulin were linked to DM1 payloads similar to that of Kadcyla. The presence of fluorophores on the payload allowed for its tracking and revealed that much of the payload remained in intracellular vesicles of cancer cell lines even after 15 h of treatment.

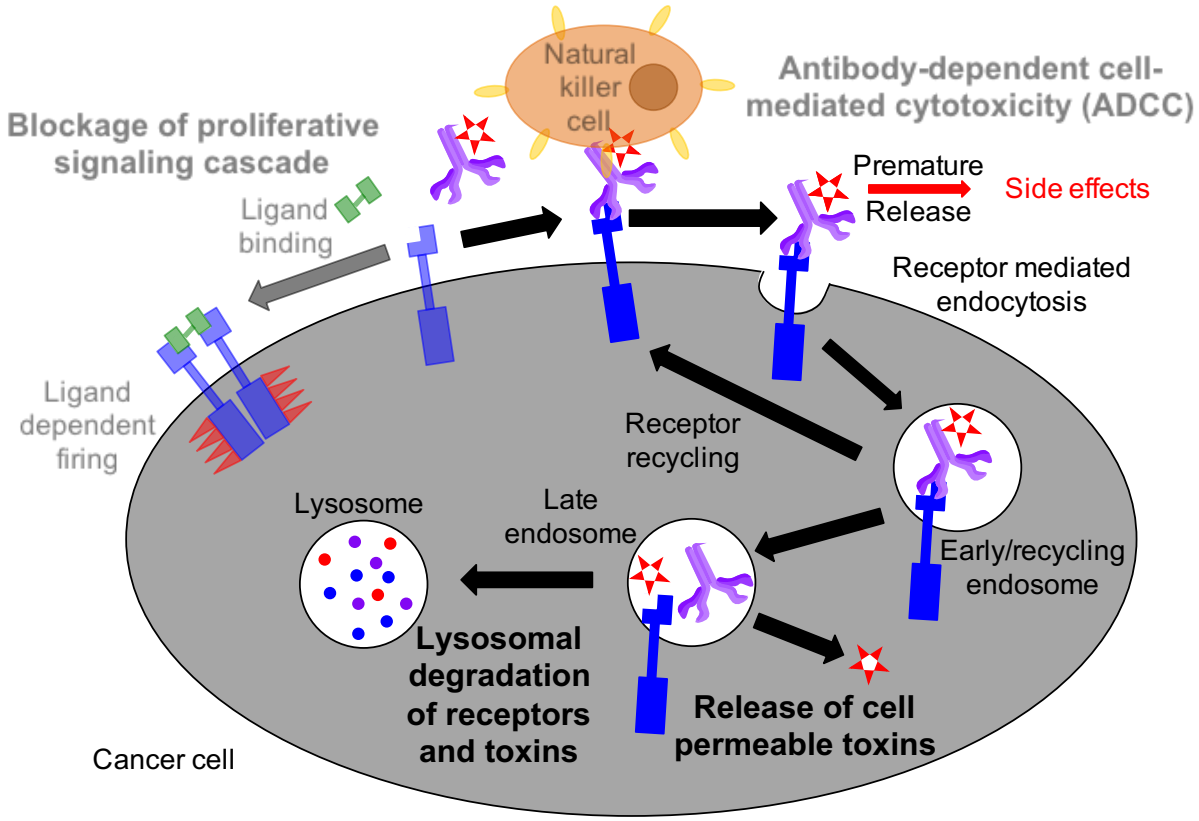

Figure 2-3. Mechanisms of action of antibody drug conjugates. ADCs add the mechanism of their toxins to those of therapeutic antibodies. Toxins can be released prematurely, which can lead to side effects if the toxins are cell permeable and able to reach non-targeted cells. If the toxins are cell impermeable, it is likely that they will become trapped within the endocytic system and be degraded in lysosomes.

One method to circumvent this issue could be the disruption of the endosomal membrane to allow for the release of cell impermeable toxins. Many viruses and bacteria disrupt endosomes to gain access to the cell cytosol, inspiring researchers to develop methods to do the same. Our lab has previously reported[25] the use of peptides anchored to cholesterol derivatives to selectively disrupt the membranes of early endosomes and a fluorescence-based assay to detect this disruption (Figure 2-4). Endosome disruption to improve cellular delivery of bioactive molecules has been reviewed.[26] Various methods of endosome disruption have been developed to release nucleic acids,[27,28] fluorophores,[29] and toxins[30] into the cytosol. Toxin release from early endosomes could

be advantageous since some potential targets of ADCs, such as HER2, are mostly recycled back to the cell surface and do not reach the lysosome to a great extent.[31] Additionally, the ability to use cell impermeable toxins could reduce side effects by preventing unwanted diffusion into non-targeted cells, and could potentially allow toxins to accumulate to a greater extent within targeted cells.

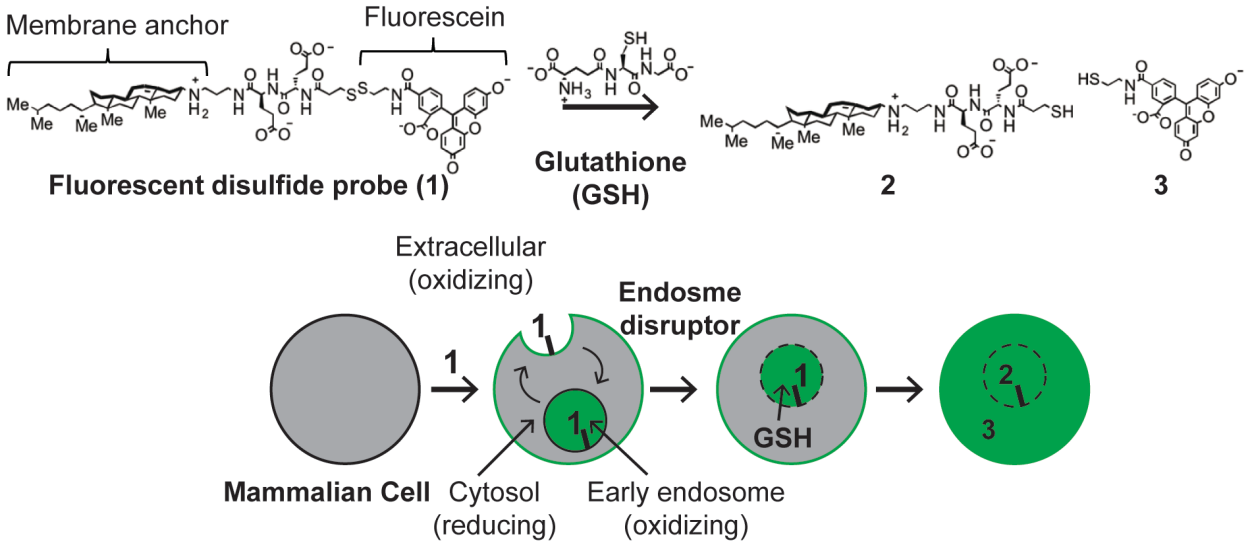

Figure 2-4. Fluorescence-based assay to detect endosome disruption. As previously reported,[25] the assay is based on a cholesterylamine-anchored fluorescent disulfide probe (**1**). This probe inserts into the cell membrane and then cycles between the cell surface and early endosomes, generating localized green fluorescence at these locations. Both the extracellular space and the early endosomes are reported to be oxidizing environments, suggesting that the disulfide will be cleaved slowly. Additionally, even when the disulfide is cleaved, the fluorescein thiol (**3**) is cell impermeable and trapped within endosomes. Upon addition of an endosome disruptor, the integrity of the endosomal membrane is lost, and reducing agents such as glutathione may enter endosomes to accelerate cleavage of the disulfide bond. The fluorescein thiol (**3**) can pass through compromised endosomal membranes, generating dispersed fluorescence throughout the cytosol and nucleus.

The Peterson Lab has synthesized and tested many endosome disruptive peptides. The exact mechanism of disruption of endosomes by these peptidomimetics is not completely understood, but we have found that the most efficacious of these

endosome disruptors contain a cholesterol mimic. Previous studies of structurally related fluorescent cholesteryl carbamates[32] and the endosome disruptive peptide cholesterylamine-PC4[25] support the hypothesis that the insertion of the cholesterol mimic of these compounds into plasma membranes allows them to engage an endocytic trafficking pathway that leads to their accumulation in early and recycling endosomes. We hypothesize that the hydrophobic peptide portion of the endosome disruptor then inserts into the endosomal membranes to form pores that allow small molecules to cross the membrane. This hypothesis and the experiments supporting it are discussed in greater detail in the PhD dissertation of Dr. David Hymel (University of Kansas, 2014).

One goal of this research was to attempt to improve the selectivity of ADCs using a two-component system. Each component is designed to be non-toxic and uses a commercially available antibody to target a distinct growth factor receptor that drives the proliferation of cancer. The components are designed to act synergistically and only kill cancer cells that express both targeted receptors, while sparing normal cells. We termed this approach synthetic lethal targeting, borrowing the term from the genetic concept of synthetic lethality.

Synthetic lethality arises when the loss of function of two genes through mutation or lack of expression leads to cell death, but the loss of the function of either gene alone is not lethal.[33] This concept has been applied to cancer treatment, with researchers searching for differences between cancer cells and healthy cells that make the cancer cells uniquely susceptible to a particular treatment. A well-known example is the use of poly(adenosine diphosphate-ribose) polymerase (PARP) inhibitors to treat cancers deficient in breast-cancer-associated protein 1 or 2 (BRCA1/2). PARP is a family of

enzymes involved in repairing single stranded breaks (SSBs) in DNA. In the presence of a PARP inhibitor, these SSBs progress to double stranded breaks (DSBs), which are normally repaired by homologous recombination aided by BRCA1/2. In cancer cells that lack active BRCA1/2, the DSBs are not repaired and the cells are forced into apoptosis (Figure 2-5).[33,34] Thus, neither the PARP inhibitor nor the BRCA1/2 deficiency is lethal on its own, but the combination of these two situations is lethal. There are currently several PARP inhibitors in clinical trials, and three have been approved by the FDA for the treatment of ovarian cancer by the FDA. The first to reach the clinic was Olaparib (Lynparza),[35] which was approved in 2014.

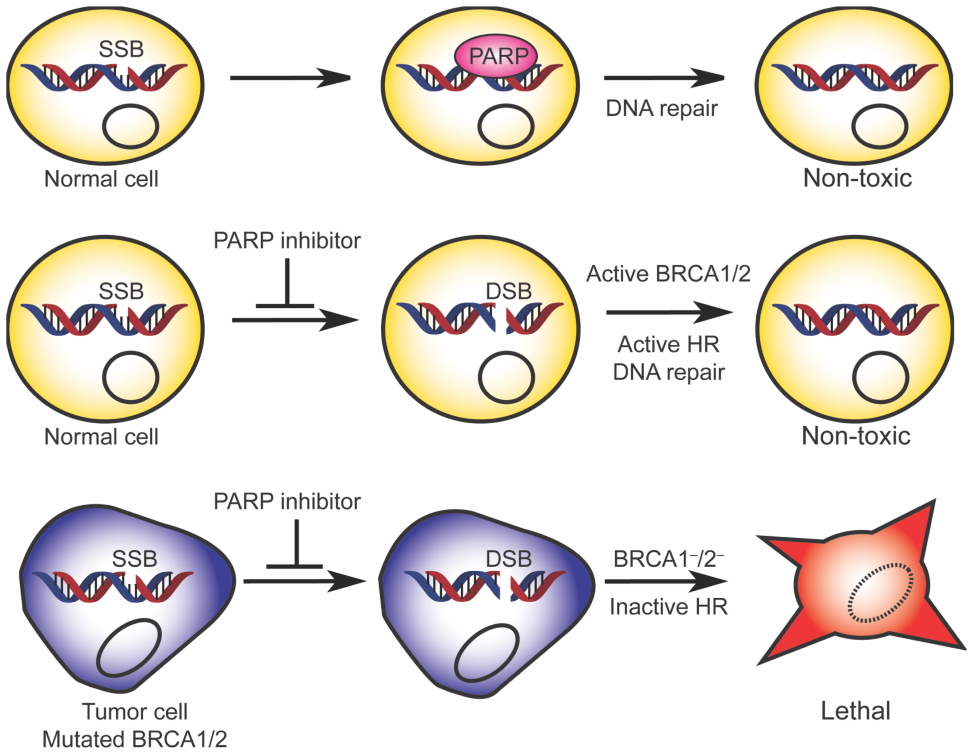

Figure 2-5. Synthetic lethality applied to cancer treatment. When a normal cell is treated with a PARP inhibitor, single stranded breaks (SSBs) progress to double stranded breaks (DSBs), but BRCA1/2 is able to repair the damage. In cells that lack active BRCA1/2, treatment with PARP inhibitors can be lethal. Figure adapted from Polyak *et. al.*[33]

Our approach was to create pairs of antibodies that synergistically target growth factor receptors and selectively kill targeted cancer cells (Figure 2-6). To enable this cytotoxic synergy, one targeting antibody was proposed to be linked via a disulfide linker to a cell-impermeable cytotoxin that is incapable of unaided passage across cellular membranes. When this first antibody binds a specific growth factor receptor on the cell surface, and is internalized by endocytosis, we hypothesize that the stability of the disulfide, in conjunction with the cell-impermeability of the cytotoxin, would cause entrapment in membrane-sealed endosomes. This entrapment would prevent toxicity unless membranes of these endosomes are disrupted by co-administration with a secondary agent. To synergistically kill cancer cells, this antibody conjugate would be co-administered with a second anti-growth factor antibody linked to a non-toxic endosome disruptive peptide. Release of this peptide from the second antibody could form pores in endosomal membranes. These pores might enable cytosolic reducing agents to enter endosomes, speed the breakage of the disulfide bond linking the toxin to the first antibody, and activate toxicity by enabling escape of the cytotoxin into the cytoplasm. These unique antibody conjugates were designed to provide high selectivity for killing specific cancer cells that express two distinct cell surface receptors without affecting normal cells that express one of these two target proteins. This chapter describes research progress toward this goal.

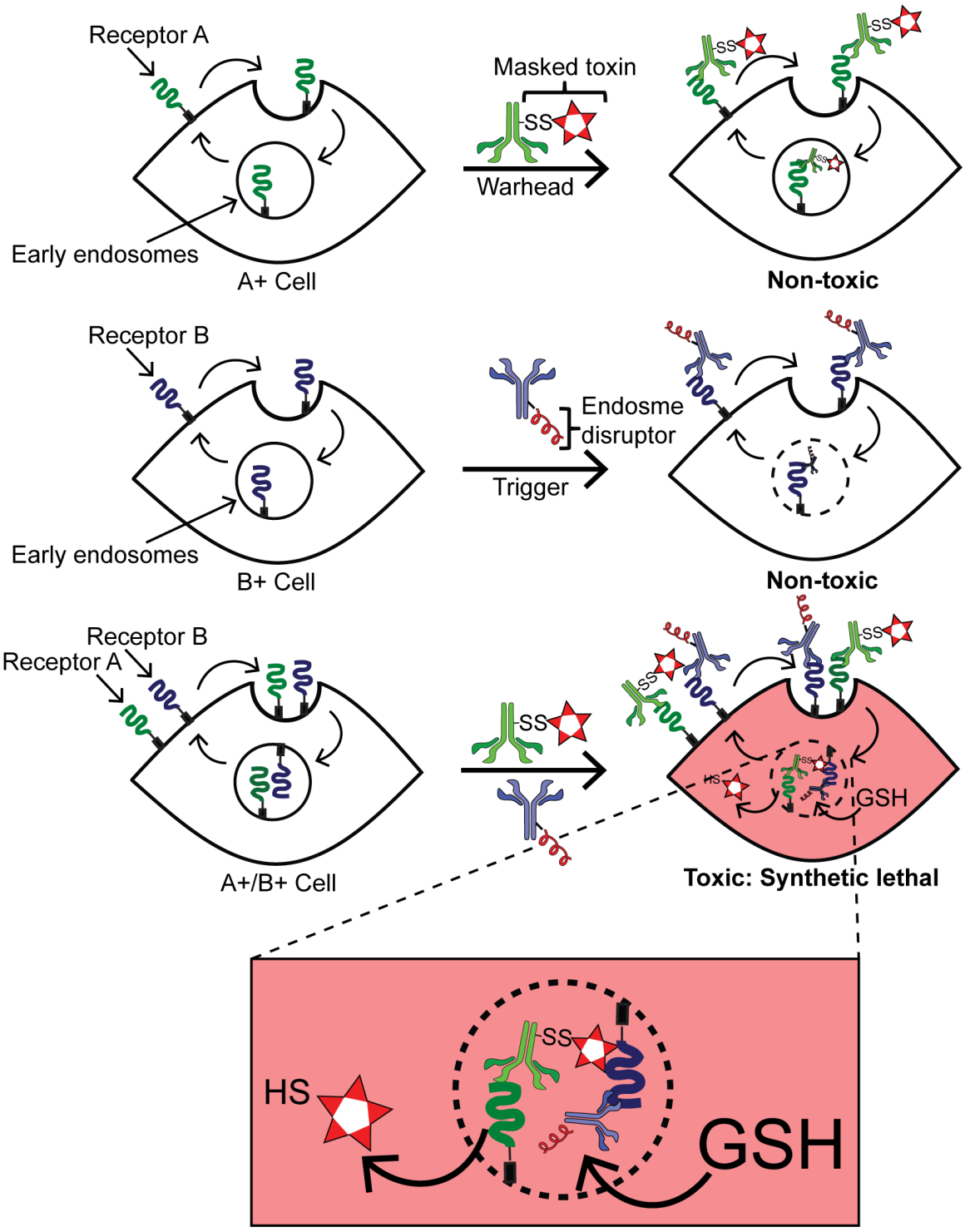

Figure 2-6. Synthetic lethal targeting. Cells expressing Receptor A or Receptor B would only take up one of the components of the system, both of which are non-toxic on their own. Only cells expressing both targeted receptors would take up both components, allowing the trigger to initiate the toxicity of the warhead, killing the cell. The insert shows an enlarged view of what might occur within endosomes of targeted cells.

2-2. Endosome disruption strategies and recent developments

We have made many advances in endosome disruption since the publication of our first paper on the subject in 2008.[25] Dr. Chamani Perera and Dr. David Hymel, both previous Peterson Lab members, worked together to synthesize and test many of these analogues, and some of this research is described in the PhD dissertation of Dr. Hymel. One of the outcomes of these studies was the development of endosome disruptors that are more efficacious and less toxic than the compounds reported in 2008.[25] In the 2014 dissertation of David Hymel, structure-activity studies are described that modify our previously published[25] cholesterylamine derivative of the membrane-lytic peptide PC-4 peptide originally identified by Weber and co-workers using a phage display library.[36] Alanine scanning and rational modifications designed to increase the helicity of these peptides were used to identify endosome disruptive peptides that are more potent and less toxic than the originally published cholesterylamine-PC4 peptide. Dr. Hymel showed that, in general, endosome disruptors that contain the cholesterol membrane anchor are 50 to 200-fold more potent than parent peptide alone. Molecular modeling revealed that the endosome disruptors likely adopt a 3_{10}-helix conformation, prompting the addition of 3 amino acids to the peptide sequence to extend the helix by one full turn and possibly provide more stability. All of these advances led to the development of **4**, an endosome disruptor that has become the gold standard for studies of effects on adherent cell lines in our laboratory (Figure 2-7). The related acetylated peptide **5**, lacking the membrane anchor, is capable of disrupting endosomes of suspension cell lines such as Jurkat and THP-1 but does not appear to be active in most adherent cell lines for reasons that are not clear.

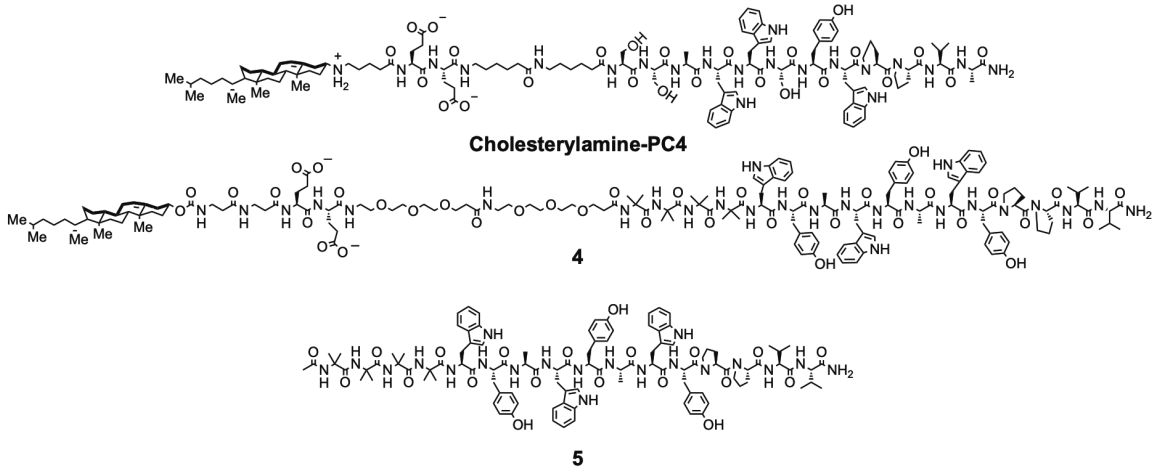

Figure 2-7. Structures of optimized endosome disruptors **4** and **5** compared to the previously reported **cholesterylamine-PC4**.[25] The short peptide **5** is active in suspension cell lines such as Jurkat and THP1, but the cholesteryl-derived membrane anchor is needed for activity in most adherent cell lines.

More recently, additional studies of the SAR of endosome disruptors have been conducted. Peptides **6** and **7** were synthesized to test the necessity of the four aminoisobutyric acid (Aib) residues, which promote helix formation,[37] by replacing them with alanine. Endosome disruptors without these residues would be simpler and more economical to synthesize. These studies demonstrated that the Aib residues are necessary for the activity of simple endosome disruptive peptides that lack the cholesterol anchor. However, they can be replaced by alanine in the cholesterol derivative **7** (Figure 2-8).

(A) Structures of fluorescent probe **1** and endosome disruptors

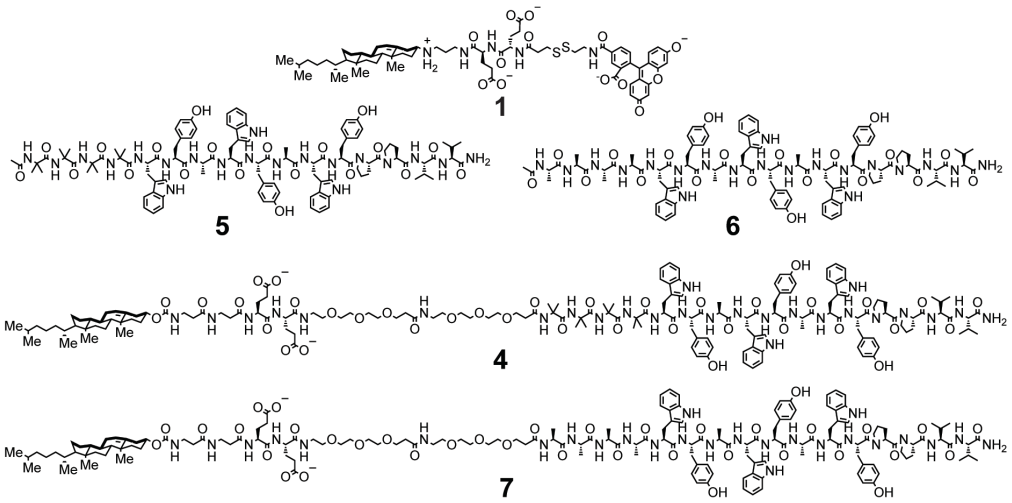

(B) Efficacy in Jurkats after treatment for 14 h

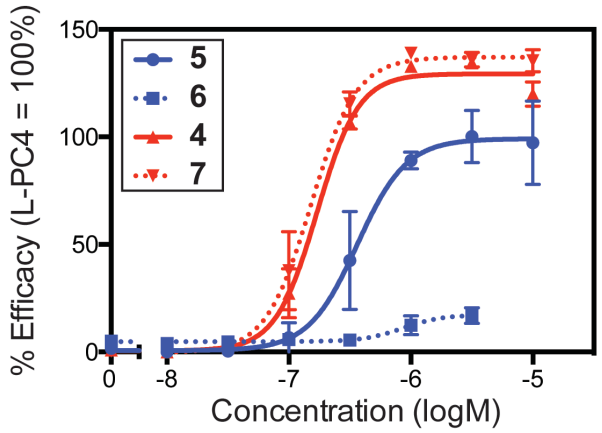

Figure 2-8. Structures and activity of **6** and **7**, as compared to their AIB containing counterparts, **5** and **4**. (A) Structures of fluorescent probe **1** and endosome disruptors (EDs). (B) Efficacy of release of disulfide probe **1** in Jurkats after treatment for 14 h. The Aib residues are needed for activity in the simpler ED (**6**), but these residues can be replaced by alanine without loss of activity in the cholesteryl carbamate derivative. The green fluorescence intensity of cells was measured then normalized to the activity of the published cholesterylamine-PC4.[25]

Analogues of the short peptide **5** were also synthesized to facilitate future structural studies of potential pore assemblies that might form in endosomal membranes. Dr. Chamani Perera synthesized analogues where a single hydroxyl group of each tyrosine residue was replaced by either fluorine (**8-10)** or an amino group (**11-13**) (Figure 2-9),

potentially enabling fluorine or ^{15}N NMR for structural studies. Unfortunately, none of these compounds showed comparable activity to **5** (Figure 2-9). The inactivity of these analogues speaks to the relatively narrow SAR of these types of endosome disruptors.

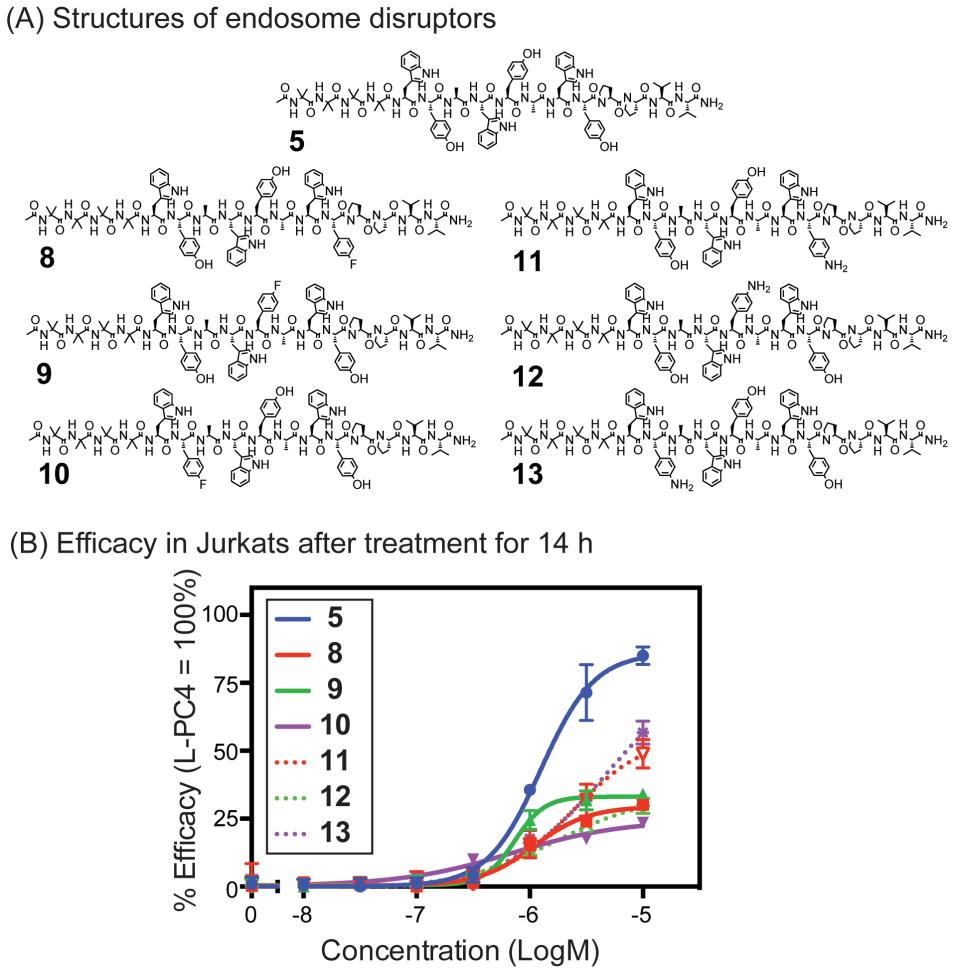

Figure 2-9. Structures and endosome disruptive activity of 5, **8-10** and **11-13**. (A) Structures of **5** and related analogues. (B) Potency and efficacy of endosome disruptive activity using disulfide probe **1** in Jurkat lymphocytes after treatment for 14 h. The replacement of even a single hydroxyl group of tyrosine by fluorine or an amino group is not well tolerated. The activity of analogues containing fluorine are plotted as solid lines, while their amino group containing counterparts are plotted as dotted lines. The green fluorescence intensity of cells was measured then normalized to the activity of the published cholesterylamine-PC4.[25]

One analogue that replaces the Trp residues of **4** with Tyr (**14**) showed surprising potency. This endosome disruptor was active at sub-nanomolar concentrations (Figure

2-10), but further studies of this compound were not extensively pursued. The SAR data obtained by studies of these additional analogues provided a basis for efforts to conjugate endosome disruptive peptides to antibodies as targeted delivery systems.

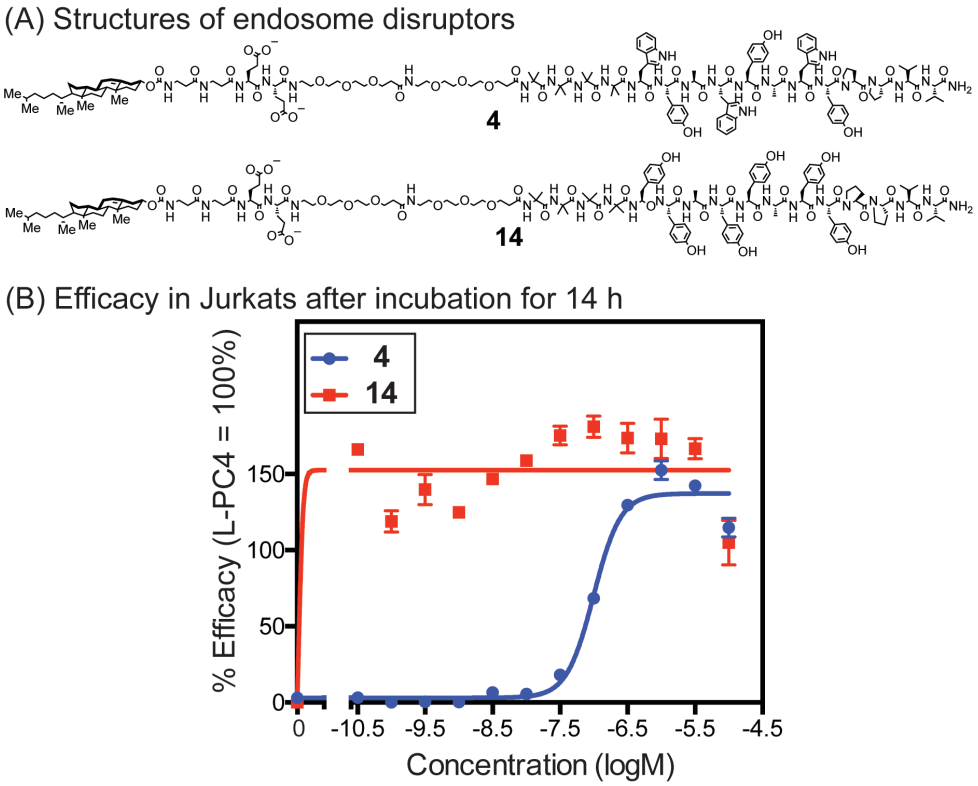

Figure 2-10. Unusually high potency of the tyrosine-rich analogue **14** as an endosome disruptive peptide. (A) Structures of **4** and **14**. (B) Efficacy of release of disulfide probe **1** in Jurkat lymphocytes after treatment for 14 h.

2-3. Targeted fluorescence-based model systems that combine antibodies with endosome disruptors

To optimize the synthetic lethal targeting system, we developed a fluorescence-based model system based on the fluorescence-based assay developed in our previous publication (Figure 2-11).[25] In this model system, the masked toxin is replaced by the green fluorophore fluorescein. This allows visualization and quantification of the release of the cargo into cells using confocal microscopy and flow cytometry.

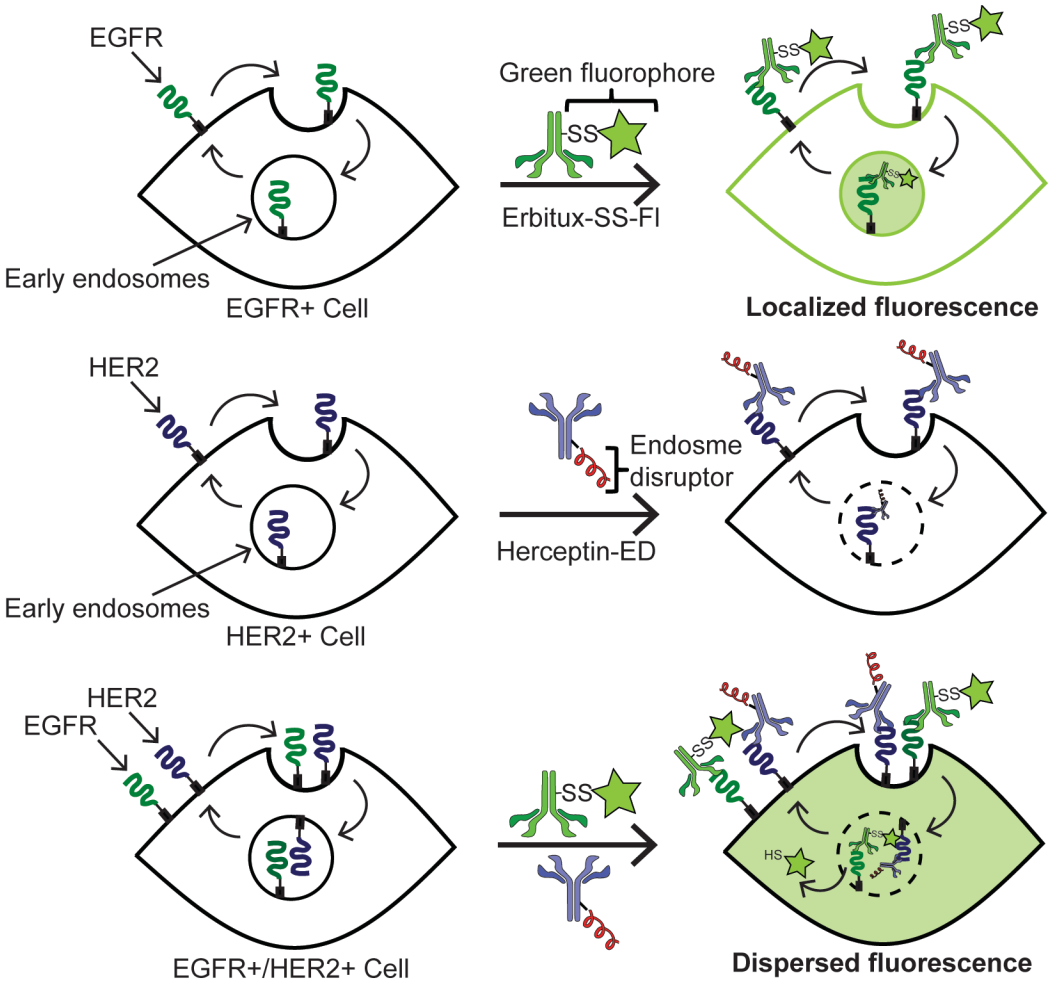

Figure 2-11. Synthetic lethal targeting model system. Cells expressing only EGFR or treated only with Erbitux-SS-Fl would show green fluorescence localized to the cell membranes and early endosomes. Only cells expressing both targeted receptors would take up both components, allowing the trigger (endosome disruptor) to promote the dispersed fluorescence.

To simplify the system for optimization, we broke it into its component parts and studied those individually. We began by investigating the delivery of the fluorophore into various cell lines using different antibodies to determine which combinations provided the best delivery and release using the optimized cholesterol-linked endosome disruptor **4**. Various endosome disruptor designs were explored to identify those that are most efficiently delivered by an antibody to release the fluorescein from the previously

described cholesterylamine-SS-fluorescein probe (**1**).[25] Once the individual components were optimized, the system as a whole was evaluated.

For these studies, antibody conjugates were generated by randomly labeling antibody lysines using *N*-hydroxysuccinimidyl (NHS) esters (Figure 2-12). Other methods of labeling antibodies with small molecules will be discussed in Chapter IV. This method provides relative simplicity of conjugation and requires only a single step.

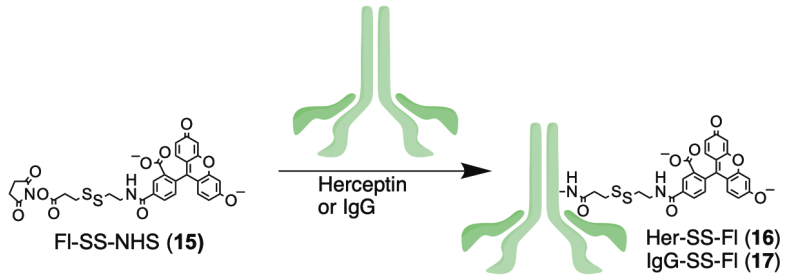

Figure 2-12. Preparation of antibody conjugates **16** and **17**. All of the antibody conjugates described in this chapter were generated similarly by randomly labeling lysines with NHS esters.

2-3-1. Optimization of the delivery and release of fluorescein

We explored several different mAbs for the delivery of a fluorescein disulfide into cancer cells followed by release of the fluorophore from endosomes with **4**. A summary of these trials is shown in Table 2-1, and the use of Herceptin for this delivery in SkBr3 breast cancer cells is shown in Figure 2-13. We found that **4** is an effective endosome disruptor in most of the cell lines tested. Interestingly, **4** is less efficacious in certain cell lines, such as the breast cancer line MDA-MB-231 and the gastric cancer cell line NCI-N87. The reasons for this are unknown, but they could be related to changes in the trafficking of the receptor, antibody, or endosome disruptor, or relate to differences in properties of endosomes of these cell lines. In the lymphoma cell line Raji, endosome disruptor **4** is able to release fluorescein from the cholesterylamine-SS-fluorescein probe

(**1**), but it is not able to release it from the antibody Rituximab. This may relate to the known[38] slow uptake of Rituximab by CD20-mediated endocytosis, limiting accumulation of the antibody and the endosome disruptor together in endosomes of this cell line. It has been shown[24] that different cell lines can show differential trafficking of the same receptor.

Cell Line	Antibody (Target)	Released by 4?
SkBr3	Herceptin (HER2)	Yes
	Erbitux (EGFR)	Yes
MDA-MB-231	Erbitux (EGFR)	Minimal
	Anti-CD44	No
MDA-MB-468	Erbitux (EGFR)	Yes
NCI-N87	Herceptin (HER2)	No*
	Erbitux (EGFR)	No*
Mia-Paca-2	Erbitux (EGFR)	Yes
Raji	Rituxan (CD20)	No
Ramos	Rituxan (CD20)	Yes

Table 2-1. Summary of release of fluorescein into cancer cell lines using antibody-fluorescein disulfides and the endosome disruptor **4**. Asterisks (*) indicate that **4** was also unable to release fluorescein-SH (**3**) from the cholesterylamine-SS-fluorescein probe (**1**) in this cell line.

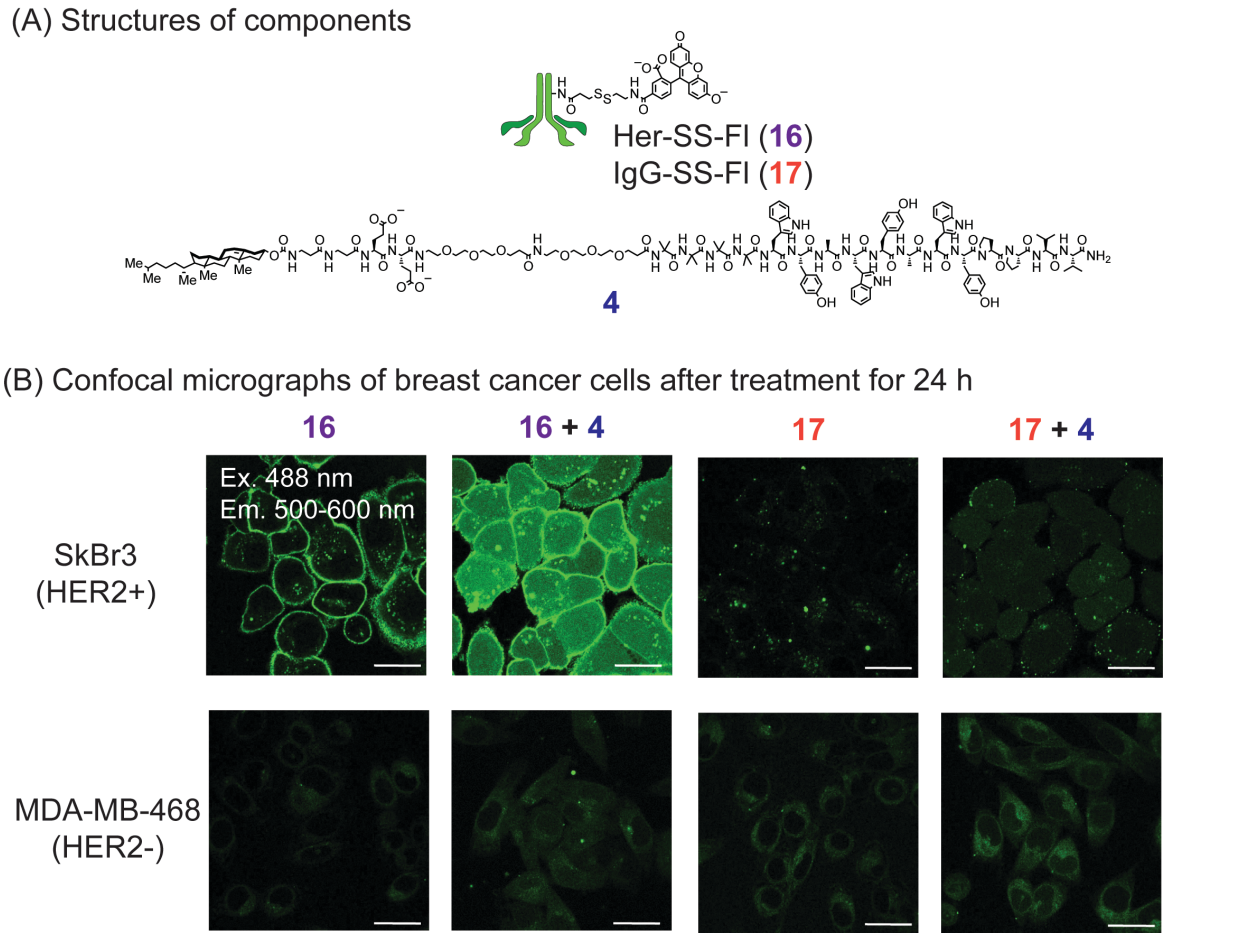

Figure 2-13. Delivery and release of fluorescein into SkBr3 breast cancer cells. (A) Structures of the antibody-delivered fluorescein and endosome disruptive peptide **4**. Herceptin (Her) targets HER2, which is expressed by SkBr3 cells but not by MDA-MB-468 cells. IgG is a non-targeted control antibody from human serum. (B) Confocal micrographs of SkBr3 and MDA-MB-468 cells treated with **16** or **17** (1 μM, **16** DOL 4.6, **17** DOL 4.5) and **4** (2 μM) for 24 h. Controls with **17** and the MDA-MB-468 cell line establish that delivery of fluorescein by **16** requires targeting to HER2+ cells. Bright, dispersed fluorescence is only seen in SkBr3 cells treated with **16** + **4**. White scale bars = 25 μm.

For continued studies we chose to focus on Herceptin and Erbitux. These antibodies are both commercially available, extensively studied, and target two different receptors, HER2 and EGFR, that are overexpressed on the breast cancer cell line SkBr3. These receptors exhibit different intracellular trafficking routes after internalization. HER2 mostly recycles to the cell surface,[24,31] whereas EGFR is mostly trafficked to the lysosome

for degradation.[39] Despite the low extent of lysosomal trafficking of HER2, the ADC Kadcyla[15] undergoes lysosomal degradation to release an active toxin.[40] Studies of FRET-based analogues of Kadcyla showed that HER2-targeted ADCs containing either cathepsin-cleavable or poly-L-alanine linkers (not recognized by cathepsins) are ~40% cleaved after incubation for 20 h in SkBr3 cells.[24]

These differences in receptor trafficking could have profound effects on our system, so it is interesting to note that the targeting of both receptors by antibody-delivered fluorophores can lead to release of the fluorophore into the cytosol by endosome disruptors directed to early endosomes with a mimic of cholesterol. This could be of potential interest for future studies.

2-3-2. Optimization of endosome disruptors for delivery by antibodies

The optimization of the antibody-delivered endosome disruptor proved to be challenging. Antibody-delivered endosome disruptors tested were synthesized as NHS esters for random labeling of lysines of antibodies. The fluorophore Pacific Blue (PB) was incorporated into these conjugates to allow estimation of the degree of labeling (DOL) of the antibody. These calculations compared the absorbance of PB at 425 nm to that of the antibody at 280 nm to determine their respective concentrations. Herceptin was chosen for most of these studies in part because it was supplied as a powder and could be readily reconstituted at the desired concentration. In contrast, Erbitux was supplied as a 2 mg / mL (~13 μM) solution that required concentration before conjugation. Additionally, when both antibodies were used to deliver the same ED in the experiments described below, the Herceptin conjugates performed as well if not better than the Erbitux conjugates.

Since the tyrosine-rich peptide **14** had shown potent activity, this all tyrosine design was applied to antibody-delivered endosomes in a series of analogues containing linkers of increasing length (Figure 2-14). It was hoped that these linkers would provide sufficient distance of the endosome disruptor from the antibody to allow activity. **22** was found to be the most active of these compounds (Figure 2-13), supporting this hypothesis. The mini-PEG linker also enhances solubility of the endosome disruptors. This was important because conjugation of some analogues caused precipitation of the antibody-endosome disruptor conjugate. However, none of these endosome disruptors were considered sufficiently active, and alternative designs were pursued to improve their activity.

(A) Structures of endosome disruptors for antibody conjugation

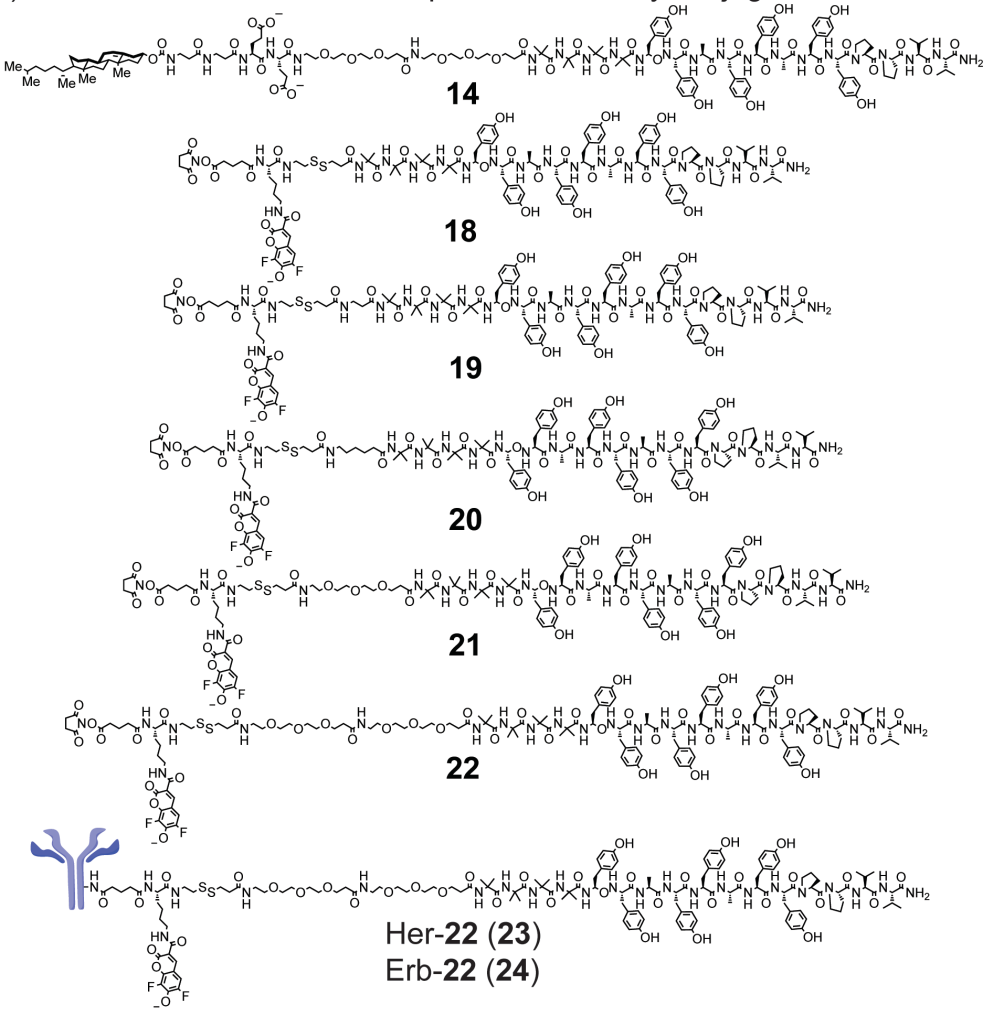

(B) Activity of conjugates of **22** in SkBr3 cells after 24 h of incubation

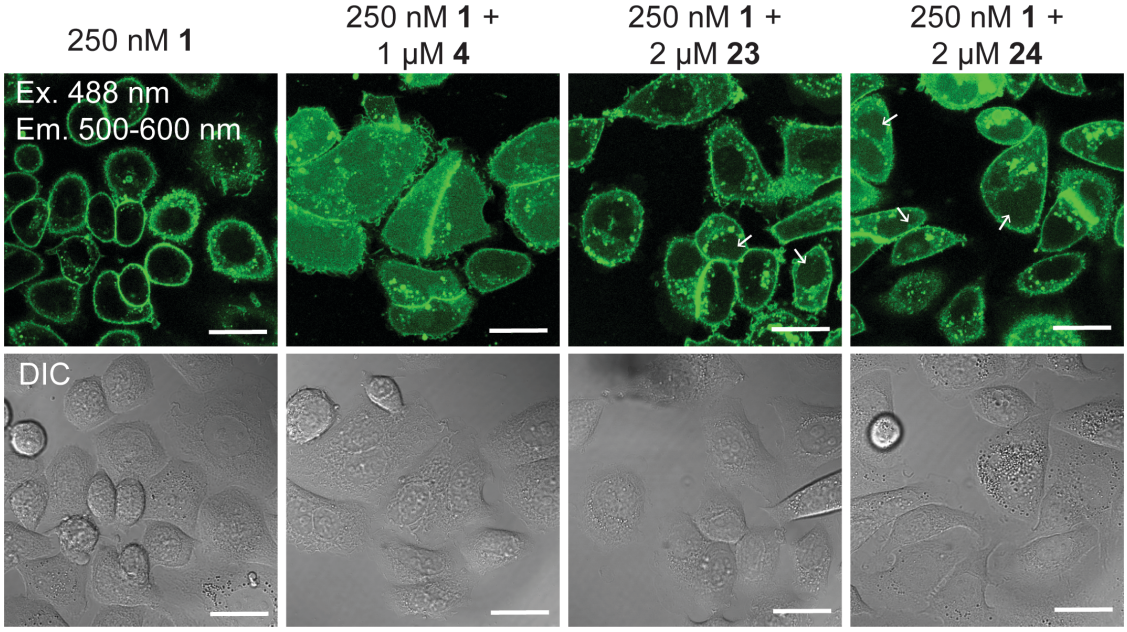

Figure 2-14. Structures and activities of antibody-endosome disruptor conjugates. (A) Comparison of the structure of cholesterol-derivative **14**, NHS esters used for antibody conjugation, and two antibody conjugates. Antibodies **23** and **24**, derived from **22** with the longest linker segment, showed the most activity. (B) Confocal micrographs of SkBr3 breast cancer cells treated with fluorescent probes and conjugates for 24 h. The results of endosome disruption by **22** conjugates are subtle compared to **4**, but some green fluorescence was observed to be dispersed throughout the cytosol and nucleus of cells treated with these conjugates, but not in cells treated with only fluorescent disulfide **1**. White arrows indicate cell nuclei where the dispersed fluorescence is especially clear. White scale bars = 25 μm. **23** DOL 3.7, **24** DOL 3.6.

We hypothesized that these endosome disruptors (EDs) were not efficiently inserting into the membranes. As previously discussed, cholesterol mimics such as *N*-alkyl-3β-cholesterylamines and cholesteryl carbamates were found to improve the activity of endosome disruptors in adherent cell lines. We hypothesized that such a membrane anchor might also improve the activity of our antibody-delivered endosome disruptors. Consequently, Dr. Chamani Perera synthesized **25** and provided this material for evaluation. This endosome disruptor contains the PEG-derived linkers previously shown to improve activity as well as a cholesteryl carbamate membrane anchor (Figure 2-15). This endosome disruptor conjugate proved more challenging to purify than previous analogues. Superfine Sephadex G50 was used to purify previous analogues by size exclusion chromatography, but free **25** was found to pass through the Sephadex with the antibody-ED conjugate. To overcome this issue, ω-aminopentyl agarose was used to purify these conjugates. The hydrocarbon side chain of the resin was hypothesized to interact with the peptide through hydrophobic interactions and retain the free peptide, whereas IgG has previously been shown to not bind to this resin.[41] This method was successful for purification, and as shown in Figure 2-15, the HER2-targeted conjugate **26** was able to extensively release fluorescein into HER2 positive SkBr3 cells. Unfortunately,

the non-targeted control conjugate **27** was active as well, even using a much lower DOL than **26**. Concentrations as low as 0.1 μM of antibody conjugate were tested, but no concentration was identified where **26** was active and **27** was not. For this reason, we concluded that this conjugate was active but not targeted. We believe the cholesteryl carbamate provides such a strong membrane anchor that it binds cells despite the absence of interactions of the antigen with the antibody.

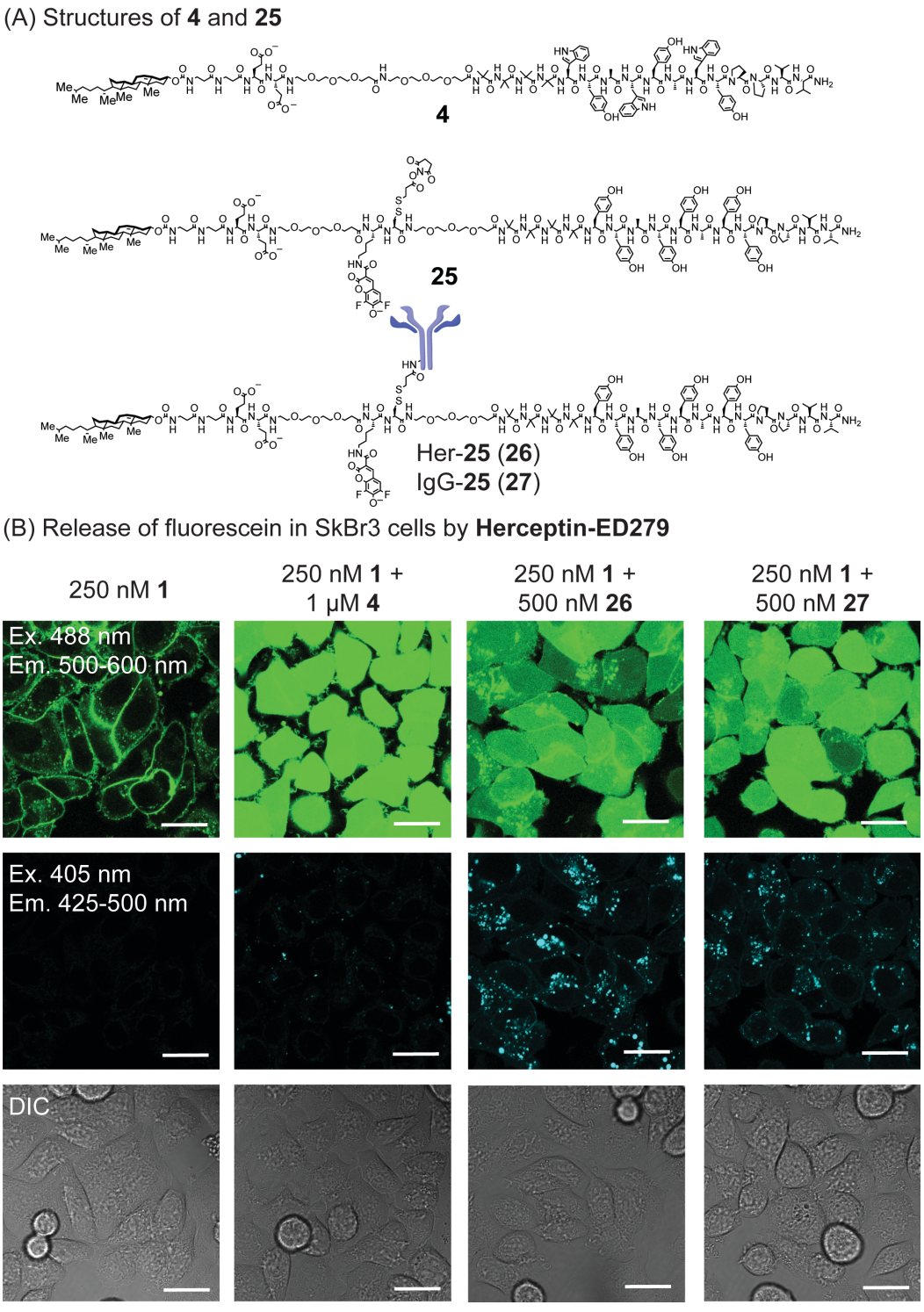

Figure 2-15. Structures and activities of cholesterol-linked endosome disruptors and conjugates. (A) Comparison of the structures of **4** and **25**. The cholesteryl carbamate was hypothesized to assist with insertion of the endosome disruptive peptide into cellular membrane. (B) Confocal micrographs of SkBr3 cells treated as indicated for 24 h. Release of fluorescence from endosomes is observed with both the targeted (**26**) and the

non-targeted (**27**) conjugates. Fluorescence from the 405 nm channel indicates that both conjugates are taken up by cells. The cholesteryl carbamate appears to be active enough to drive uptake into cells irrespective of the antibody used. White scale bars = 25 μm. **26** DOL 0.9, **27** DOL 1.1.

As an approach to overcome this lack of targeted endosome disruption, Dr. Perera synthesized **28** (Figure 2-16) and provided this compound for evaluation. This analogue contains palmitic acid in place of the cholesteryl carbamate of **25**. We hypothesized that this less hydrophobic hydrocarbon chain might interact with cellular membranes to increase the activity of this conjugate but not severely interfere with the targeting of the antibody. As can be seen in Figure 2-15, this hypothesis was supported by microscopy. The HER2 targeted conjugate (**29**) is able to release fluorescein into the cytosol of the targeted SkBr3 cells, but the non-targeted control **30** is not. The DOL of **29** was higher than that of **30** (1.7 vs 0.9) but based on the data in Figure 2-17, where the DOLs are more similar (0.8 vs 0.9), we do not believe that this difference fully accounts for the difference in activity. However, **29** was not as active as **26** or the non-targeted EDs. Additionally, this ED proved to be difficult to conjugate to antibodies. Under the conditions used to prepare the other antibody-ED conjugates, a maximum DOL of 0.5 was obtained. In order to improve this DOL to 1.0 or higher, it was necessary to add 0.4% Triton X-100 detergent to the labeling reaction, requiring purification of the conjugate with both Detergent Removal Spin Columns (Pierce) and Sephadex G50.

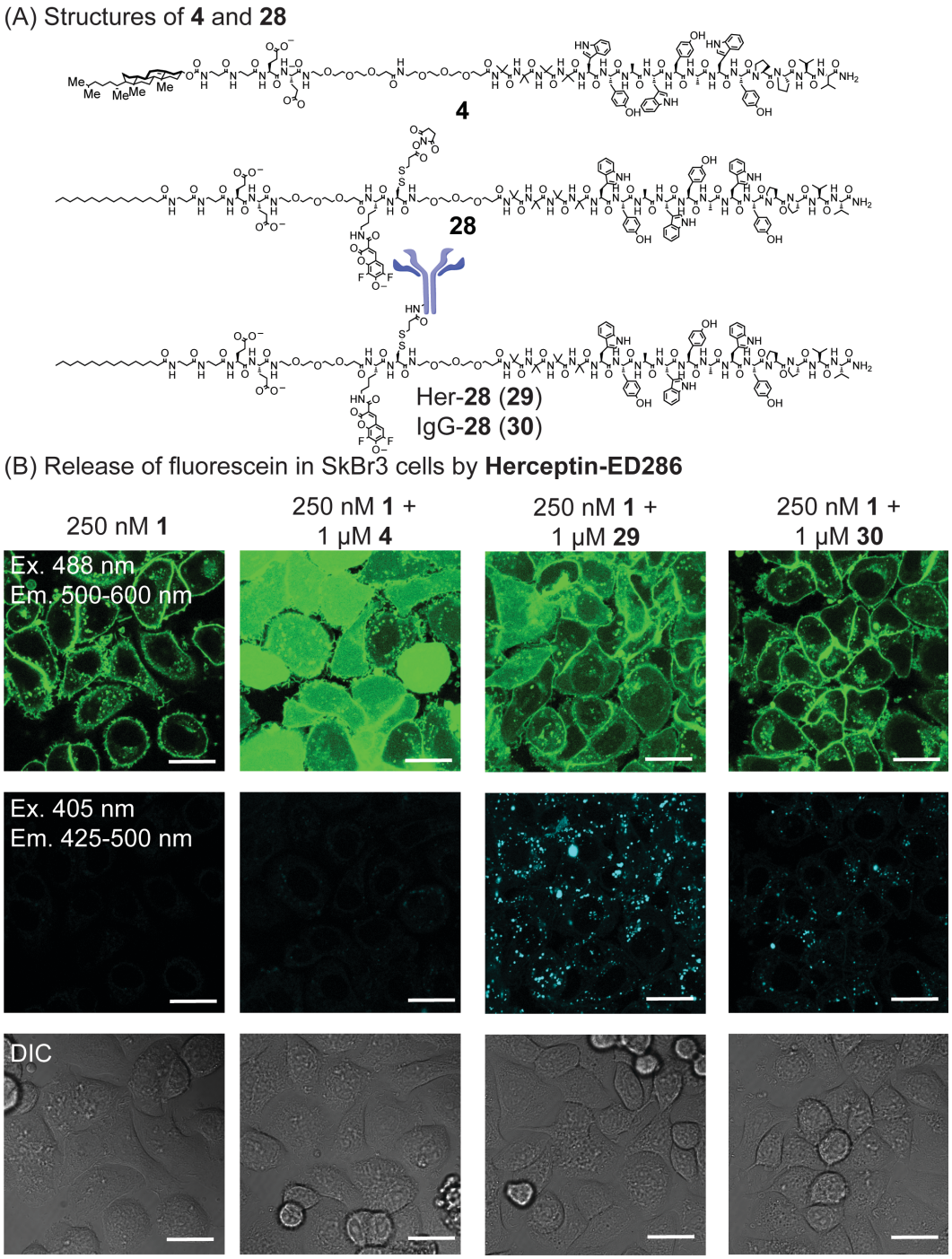

Figure 2-16. Structures and activities of palmitic acid-linked endosome disruptors and conjugates. (A) Comparison of structures of **4** and **28**. The cholesteryl carbamate of **25** was replaced with palmitic acid in **28** to aid the insertion into cellular membranes but not disrupt targeting by the antibody. (B) Confocal micrographs of SkBr3 cells treated for 24 h. Release of fluorescence is observed with the targeted conjugate **29** but not with the non-targeted **30**. Fluorescence from the 405 nm channel indicates that the targeted conjugate is taken up to a greater extent than the non-targeted conjugate. White scale bars = 25 μm. **29** DOL (degree of labeling) 1.7, **30** DOL 0.9.

2-3-3. Studies of combinations of antibodies bearing fluorescein and endosome disruptors

After optimizing the antibody-delivered fluorophores and EDs separately, we investigated a full two-antibody system. To do this, we used Erbitux to deliver fluorescein into cells and Herceptin to deliver the ED in most cases. When this labeling was reversed, activity was not improved (data is not shown).

As expected, antibody-ED conjugates that did not effectively release cholesterol-delivered fluorescein did not release antibody-delivered fluorescein. Conjugate **23** (Her-**22**) appears to cause some release of fluorescein from **31**, but the results were not impressive (Figure 2-17).

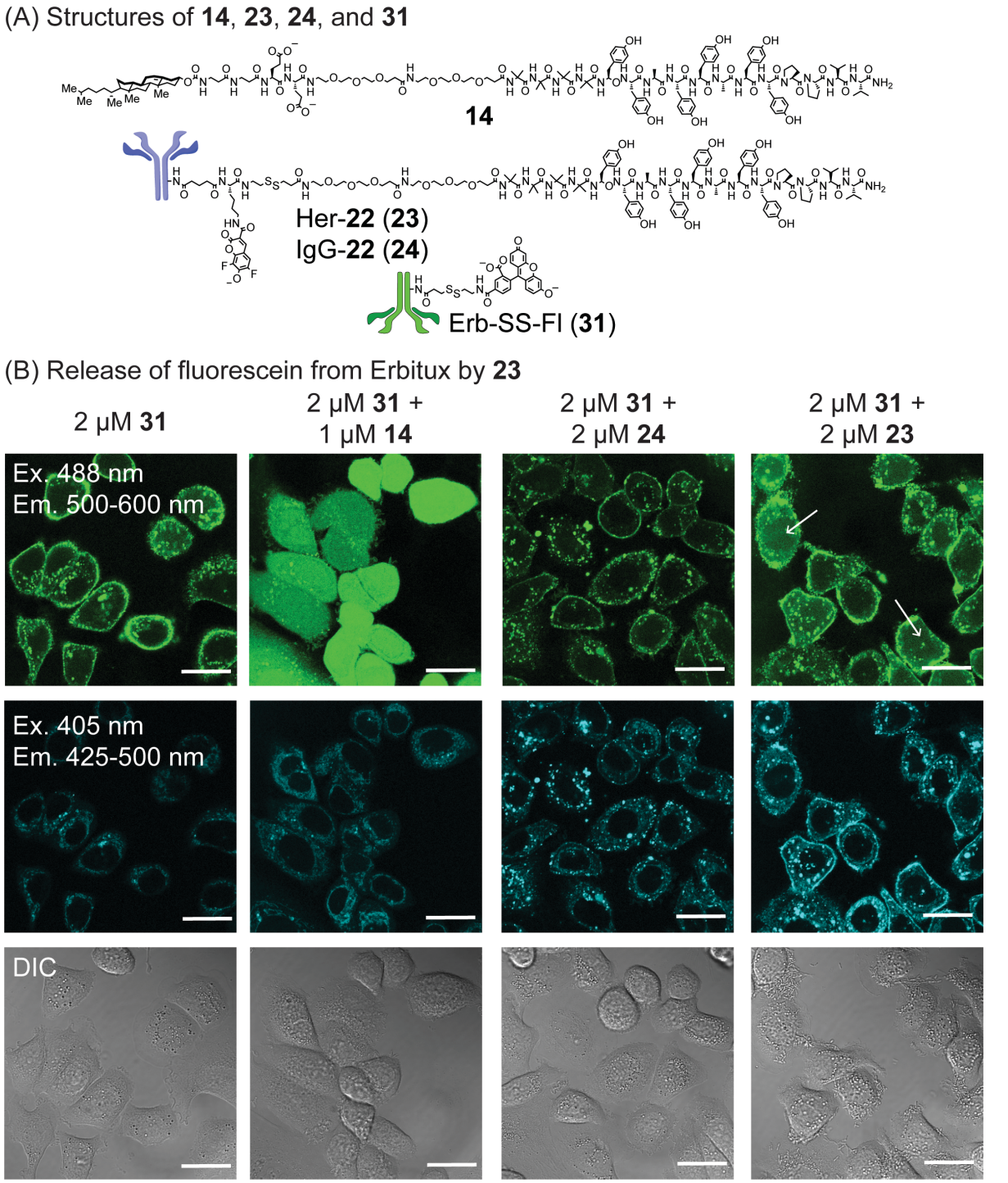

Figure 2-17. Structures and activities of conjugates used in a dual antibody system targeting both HER2 and EGFR in SkBr3 cells. (A) Structures of **14**, **28**, and **31**. (B) Confocal micrographs of SkBr3 cells treated for 24 h. Erbitux effectively delivers fluorescein into these cells, as evidenced by the accumulation of green fluorescence. Conjugate **23** is taken into cells much more than **24**, as indicated by the blue fluorescence.

White arrows indicate apparent release of some fluorescein into the nucleus. White scale bars = 25 μm. **31** DOL 3.9, **23** DOL 3.7, **24** DOL 3.9.

The HER2-targeted cholesteryl-derived conjugate **26**, was found to clearly release fluorescein from Erbitux-Fl into the cytosol and nucleus of SkBr3 cells (Figure 2-18). However, the non-targeted **27** was similarly active, indicating that the cellular uptake of this conjugate is not under the control of the antibody. The palmitic acid-derived conjugate **29** releases fluorescein into the cytosol and nucleus to a lesser extent than **26**, but its activity appears to be at least partially targeted (Figure 2-18).

(A) Structures of **26**, **27**, **29**, and **30**

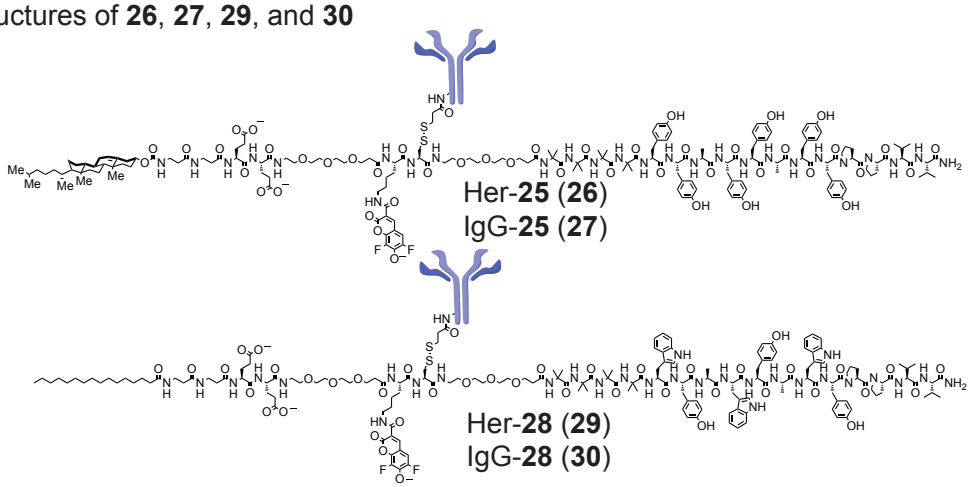

(B) Release of fluorescein from Erbitux into SkBr3 cells

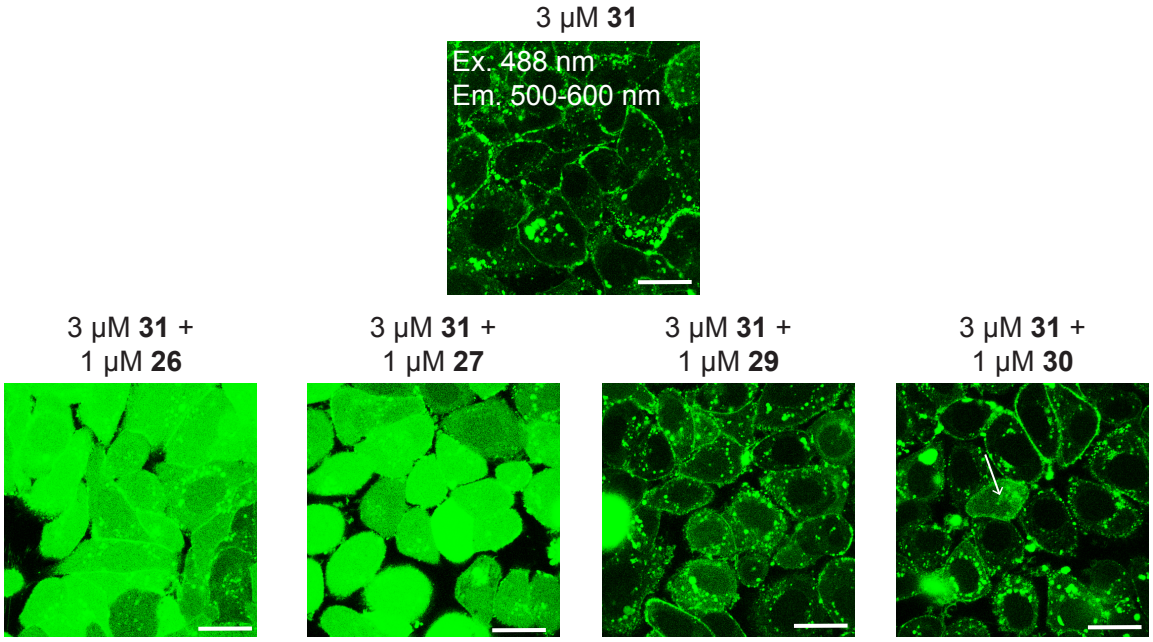

Figure 2-18. Structures and activities of lipid-linked conjugates used in a dual antibody system targeting both HER2 and EGFR in SkBr3 cells. (A) Structures of **26**, **27**, **29** and **30**. (B) Confocal micrographs of SkBr3 cells treated for 24 h. Erbitux effectively delivers fluorescein to these cells upon treatment with **31**, as indicated by the accumulation of green fluorescence. The difference in release of fluorescein with **30** compared to **29** indicates that this conjugate is targeted, whereas the conjugates of **25** are not. White arrows indicate some apparent release of fluorescein. White scale bars = 25 μm. **31** DOL 3.8, **27** DOL 1.4, **26** DOL 0.7, **30** DOL 0.9, **29** DOL 0.8.

The images shown in Figure 2-18 indicate that it is possible to use an endosome disruptor delivered by an antibody to release a fluorophore delivered by a second antibody into the cytosol and nucleus of cells. This fluorescence-based model of the synthetic lethal targeting system suggests that this approach has merit. Additionally, the optimization revealed that **29** is the most promising conjugate for future studies. However, **29** appears to be less efficacious than the simpler cholesterol-delivered EDs. More optimization will be necessary to generate a targeted antibody-ED conjugate with activity comparable to simpler lipopeptides such as **4**.

2-4. Synthetic lethal targeting in cancer cell lines

Studies of a fluorescence-based model system indicated that synthetic lethal targeting is likely to be possible. These studies also identified useful cell lines and antibodies to investigate this strategy. To further investigate effects on an antibody-delivered toxin, cholesterol-derived EDs were explored. The antibody-delivered toxins were generated by randomly labeling the lysines of the antibody with an NHS ester of the toxin (Figure 2-19). The toxin used was colchinol methyl ether (CME), an analogue of the natural product colchicine. This natural product inhibits mitosis by binding tubulin.[42] In CME, the tropone ring of colchicine is contracted to form a benzene, resulting in greater affinity for tubulin and decreased off-target effects.[43,44]

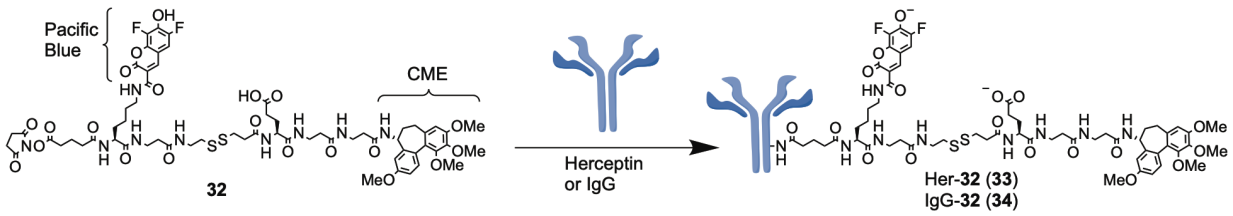

Figure 2-19. Labeling of antibodies with the CME derivative **32**.

2-4-1. Synergistic cytotoxicity of cholesterol-delivered endosome disruptors and antibody-delivered toxins

We investigated combinations of the optimized cholesterol-linked ED **4** and the targeted ADC **33** (Figure 2-20). The NHS ester **32** was synthesized by Dr. Chamani Perera and Zhe Gao of the Peterson Lab and provided for evaluation. As controls, we included non-targeted human IgG labeled with the toxin (**34**) at a degree of labeling (DOL) similar to that of the targeted conjugate (**33**). Additionally, we ran the same toxicity assay using the same conjugates in the HER2-negative breast cancer cell line MDA-MB-468. The lack of expression of HER2 was expected to result in uptake of similar amounts of the non-targeted IgG conjugates and the targeted Herceptin conjugates. We hypothesized that the ED **4** and the antibody-toxin conjugates would be relatively non-toxic individually towards these cell lines, but that the combination of **4** and **33** would synergistically kill HER2+ SkBr3 cells without affecting HER2– MDA-MB-468 cells. As shown in Figure 2-20, this pattern of activity was observed. The CME-cholesterylamine derivative **35** was used as a control for delivery of the toxin in a non-targeted manner to all cells.

(A) Structures of compounds

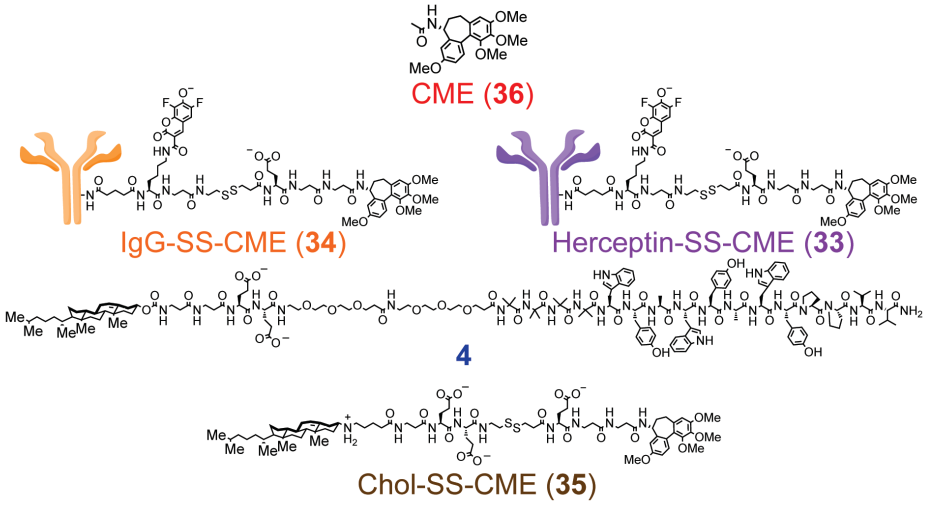

(B) 72 h cytotoxicity assays

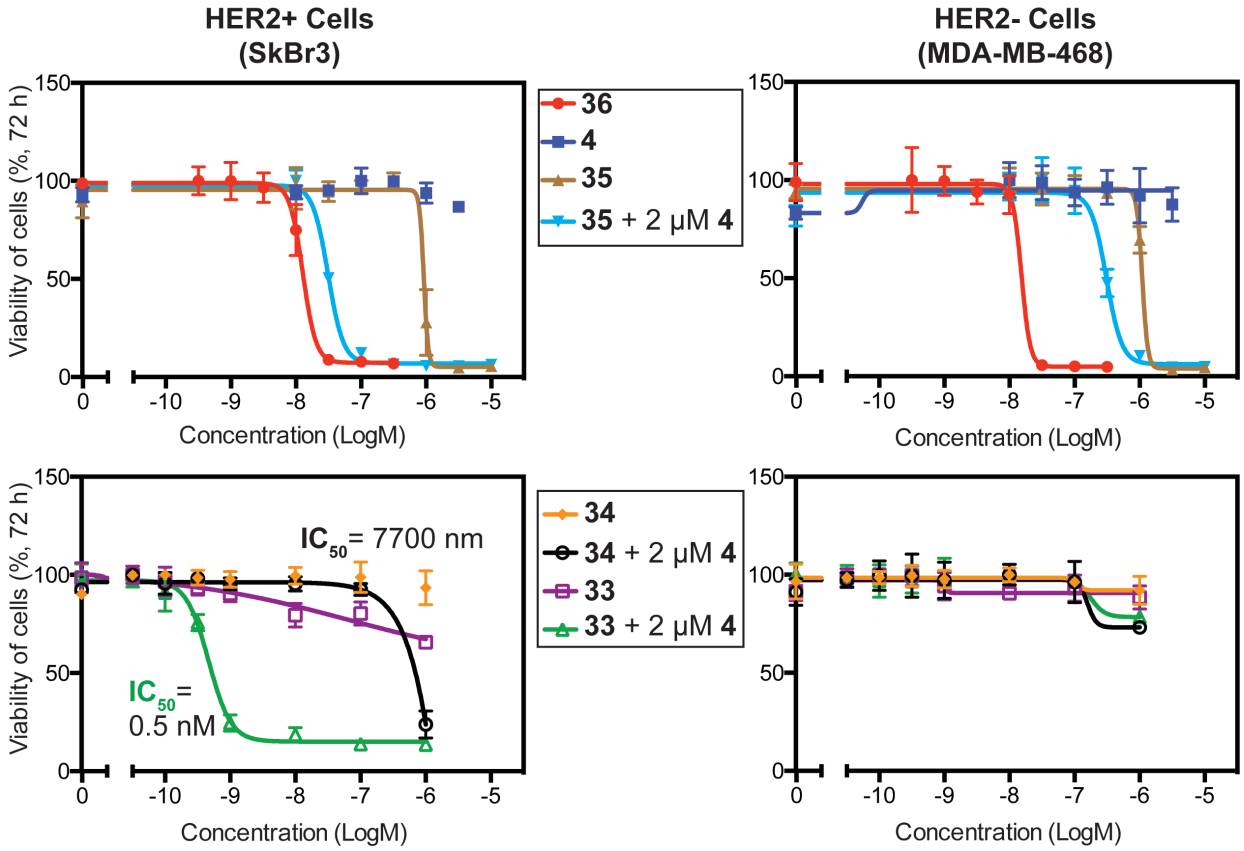

Figure 2-20. Structures of conjugates and controls and synergistic cytotoxicity of **4** and **33** towards SkBr3 cells (A) Structures of conjugates and controls. (B) Toxicity assays run after treatment of HER2+ SkBr3 cells and HER2- MDA-MB-468 cells for 72 h. The controls are shown in the graphs on the top. CME (**36**) and the cholesterol derivative **35** + **4** is toxic towards both cell lines. ED **4** and the targeted conjugate **33** synergistically kill only HER2+ SkBr3 breast cancer cells with high potency and selectivity. **34** DOL 6.3, **33** DOL 6.1.

A similar assay is shown in Figure 2-21. The difference here is that the toxin that would be released by the cleavage of the disulfide bond of **33** and **34** is used without and with **4** as a control. As expected, compound **37** showed little toxicity in either cell line because **37** should be poorly cell permeable and only small amounts would be expected to reach tubulin within the cell cytosol. This lack of toxicity indicates that premature cleavage of the linker of the ADC should spare non-targeted cells, which would be beneficial for the synthetic lethal targeting strategy. As expected, the non-targeted IgG conjugate **34** exhibited relatively low toxicity alone (IC_{50} (SkBr3) > 1 μM) towards either cell line. When combined with the essentially non-toxic ED **4** (IC_{50} (SkBr3) > 10 μM) held at a fixed concentration of 2 μM, this combination was also of relatively low toxicity (IC_{50} (SkBr3) ~ 0.7 μM). The HER2-targeted Herceptin conjugate **33** also exhibited relatively low toxicity alone (IC_{50} (SkBr3) > 1 μM, (MDA-MB-468) > 10 μM). In contrast, when SkBr3 cells were treated with a combination of the HER2-targeted conjugate **33** and ED **4**, this combination synergistically killed more than 90% of cells with sub-nanomolar potency (IC_{50} (SkBr3) = 0.12 ± 0.01 nM), while maintaining low toxicity towards MDA-MB-468 cells (IC_{50} (MDA-MB-468) > 1 μM). Consequently, ED **4** enhanced the toxicity of **33** towards HER2+ SkBr3 cells by more than 5,000-fold, but it did not appreciably enhance the toxicity of **33** towards HER2- MDA-MB-468 cells.

(A) Structures of compounds

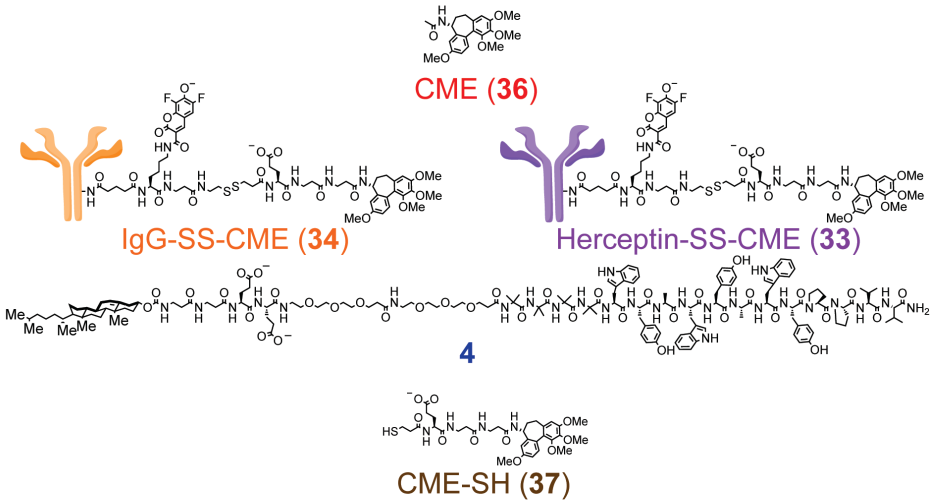

(B) 72 h cytotoxicity assays

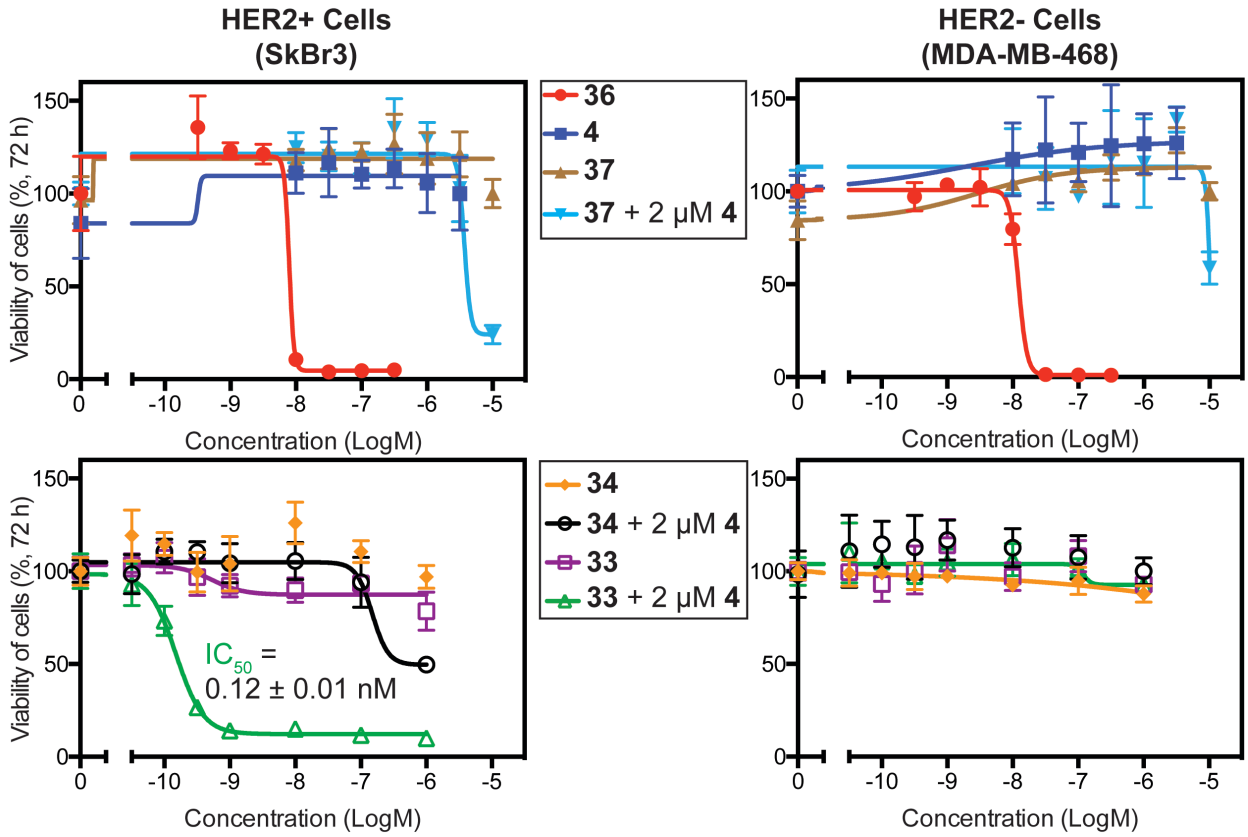

Figure 2-21. Structures of conjugates and controls and synergistic toxicity of **4** and **33,** including the released toxin (**37**) as a control. (A) Structures of conjugates and controls. (B) Toxicity assays in both HER2+ cells (SkBr3) and HER2- cells (MDA-MB-468) after treatment for 72 h. The controls are shown in the graphs on the top. CME (**36**) is toxic towards both cell lines. The more polar derivative **37** shows little toxicity even when co-treated with **4**. ED **4** and the targeted conjugate **33** synergistically kill only HER2+ SkBr3 breast cancer cells with high potency and selectivity. **34** DOL 5.7, **33** DOL 5.9.

Although the cholesterol-delivered ED was used in this assay, these results are very promising. The system is targeted in that the Herceptin conjugate is toxic only when cells are co-treated with **4**, and only when cells overexpress HER2. It is possible that this system would offer advantages over current ADCs given that it would be possible to use cell impermeable toxins and avoid toxicities related to premature release of the toxin. Additionally, the cell impermeability of the toxins prevents diffusion of the delivered toxins back out of the cell, potentially allowing the toxin to accumulate to a greater extent within the cytoplasm and nucleus. A pre-targeting strategy might also be applied to this system to further decrease off target effects. In this approach, animals would first be treated with the antibody-delivered toxin, which would then be given time to clear from the bloodstream and non-targeted tissues before the ED was added. Such strategies have been used for radioimmunodetection and radioimmunotherapy in preclinical and clinical trials, but these methods have not yet been approved by the FDA.[45-47] Further studies beginning with animal models will be needed to test this hypothesis.

2-4-2. Study of the toxicity of antibody-delivered endosome disruptor and toxin

The toxicity of the Herceptin-delivered ED **29** and the Herceptin-delivered toxin **33** were evaluated individually and combined (Figure 2-22). We hypothesized that this combination was likely to be less toxic than that of **33** and **4** given that conjugate **29** is less effective at releasing fluorescein into the cytosol of SkBr3 cells than **4**. This supposition proved to be correct, and the combination of **29** and **33** was found to be non-toxic to cells (Figure 2-22). However, this assay would have been better controlled if a treatment of **33** with **4** was included for comparison. We conclude that a more active

antibody-ED conjugate than **29** is needed for a dual-antibody synthetic lethal targeting system to show synergistic cytotoxicity.

(A) Structures of compounds

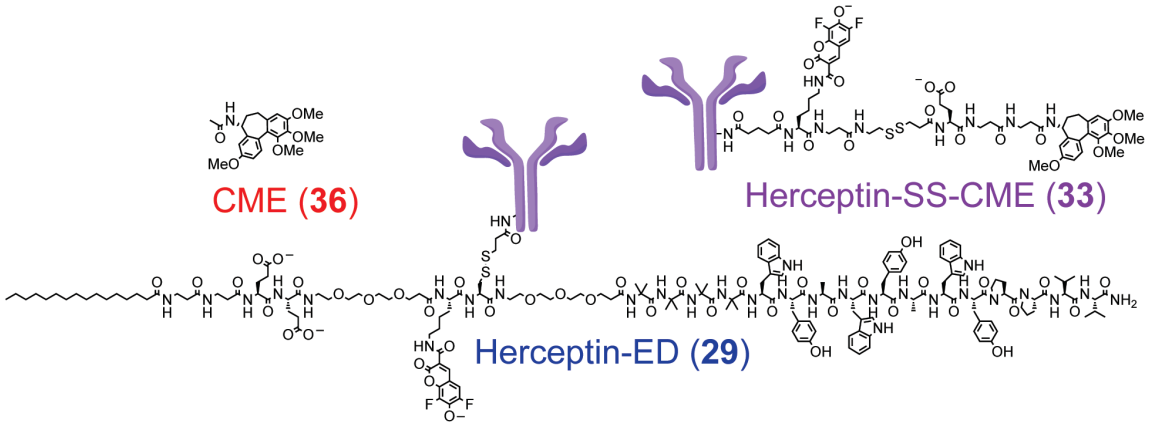

(B) 72 h toxicity assy in SkBr3 cells

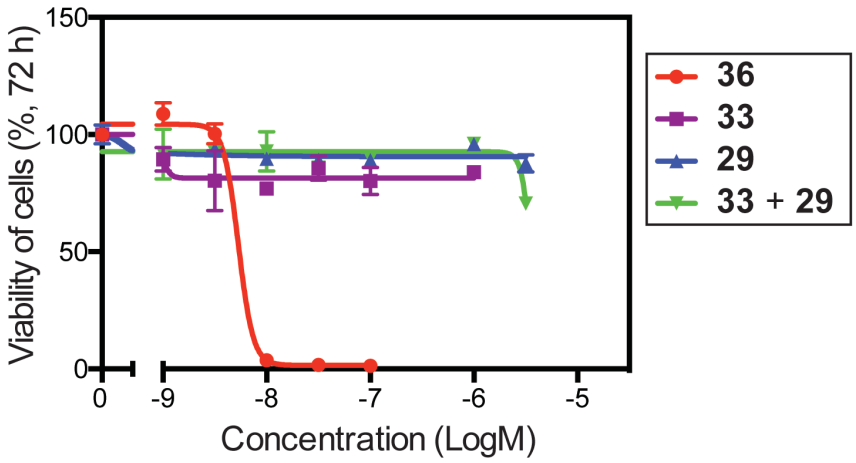

Figure 2-22. Structures of conjugates and controls and cytotoxicity of conjugates **29** and **33**. (A) Structures of conjugates and controls. (B) Toxicity towards SkBr3 cells after treatment for 72 h. No cytotoxic synergy was observed between these two antibody conjugates. **33** DOL 4.9, **29** DOL 1.8.

2-5. Studies of a FRET probe as a mimic of an antibody-delivered toxin

We showed that **4** exhibited cytotoxic synergy with the Herceptin conjugate **32**. To investigate whether **4** increased the rate of the cleavage of the disulfide linker of **32**, we synthesized the Förster Resonance Energy Transfer (FRET) probe **38** (Figure 2-23) with

the assistance of Zhe Gao. This probe was designed to mimic **32** as closely as possible in terms of clogP and size by replacing the toxin of **32** with the fluorophore Pennsylvania Green.[48,49] The combination of two fluorophores was designed to allow simultaneous visualization and quantification of both the antibody tethered fragment and the released probe in cells. Other related coumarin-fluorescein pairs have previously been shown to undergo FRET.[50,51]

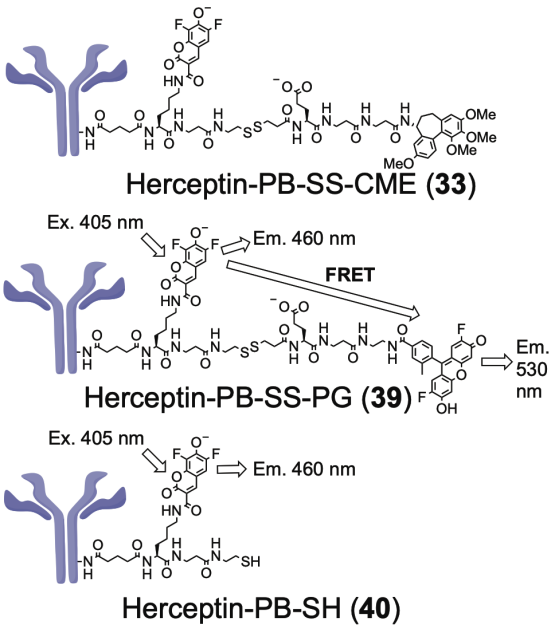

Figure 2-23. Structure of Herceptin-PB-SS-PG (**39**) compared to Herceptin-PB-SS-CME (**33**). **39** was designed to be as structurally similar to **3e** as possible. **40** is generated by cleaving the linker of **39** using DTT. It is used as a control for complete cleavage of **39**.

As predicted, FRET was seen between the Pacific Blue and Pennsylvania Green of **39** (Figure 2-24, C). When **39** is incubated in aqueous buffer in the presence of the reducing agent dithiothreitol (DTT), an increase in blue fluorescence signal is seen over time as the disulfide bond cleaves and the FRET signal and quenching caused by Pennsylvania Green are lost. An increase in green fluorescence intensity was also observed over time as FRET was lost. An increase in blue fluorescence intensity was

also seen for the Herceptin-SS-CME conjugate **33** as its disulfide was cleaved and Pacific Blue was no longer quenched by CME (Figure 2-24, C). This phenomenon was used to determine the *in vitro* half-times of the cleavage of each probe (Figure 2-24). The values were very similar (307 $\pm$ 24 s for **39** and 274 $\pm$ 26 s for **33**), validating **39** as a mimic of the cleavage of **33**.

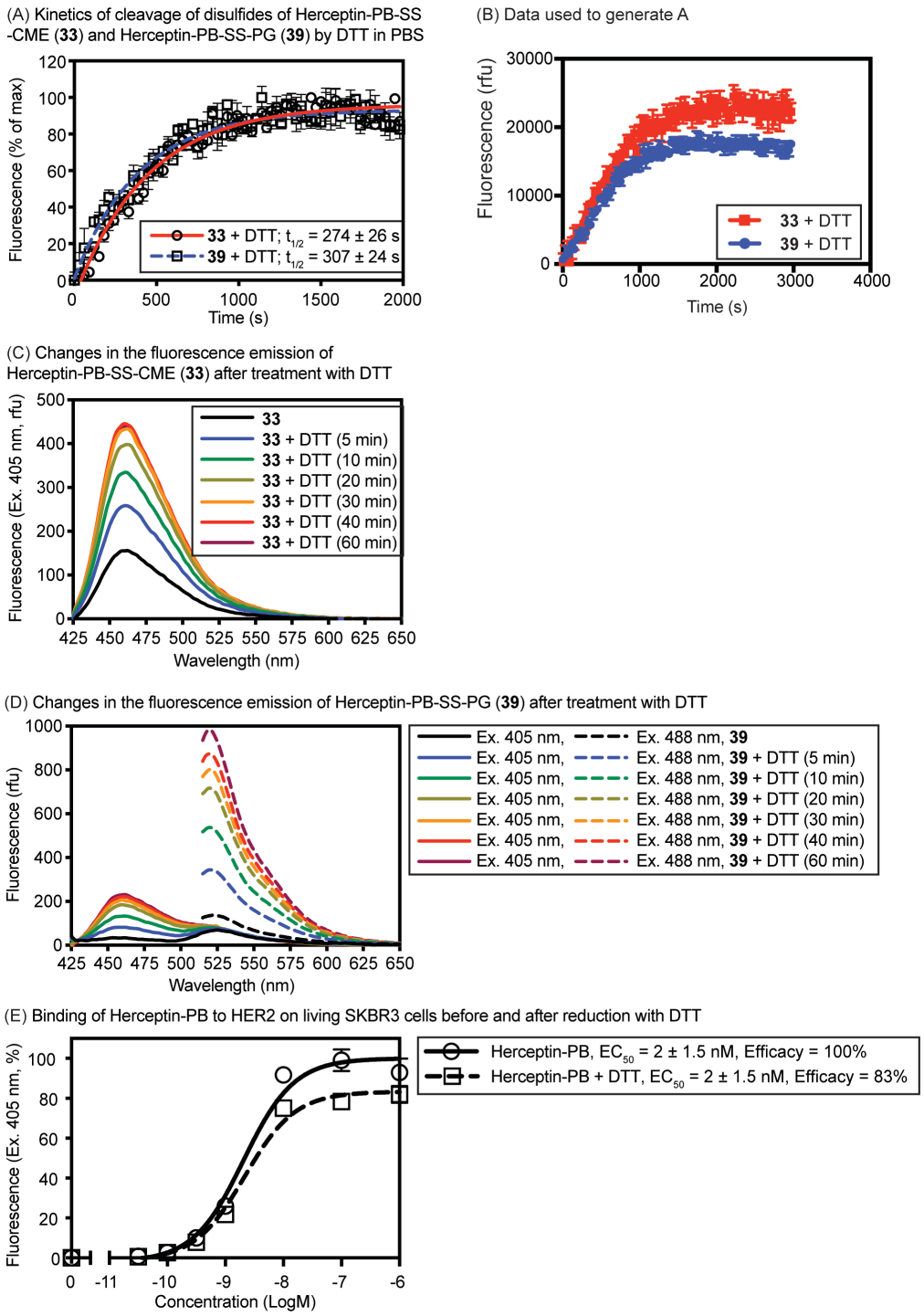

Figure 2-24. Cleavage of disulfides of Herceptin-SS-CME (**33**, 25 nM), Herceptin-PB-SS-PG (**39**, 25 nM), and Herceptin-PB by DTT (1 mM). (A) Conjugates **33** and **39** were treated with DTT in PBS (pH 7.4, 37 °C) under pseudo-first-order conditions, and fluorescence (Ex. 405 nm) was measured as a function of time on a 96-well plate. (B) Data used to generate A. The differences in intensity can be explained by differences in degree of labeling. (C-D) Emission spectra of **33** and **39** over time. For **33**, cleavage of the disulfide resulted in increased blue fluorescence due to reduced quenching by CME. For **39**,

cleavage of the disulfide resulted in increased blue (Ex. 405 nm, solid lines) and green (Ex. 488 nm, dashed lines) fluorescence from loss of FRET and reduced fluorescence quenching. (E) Binding of trastuzumab-PB to HER2 on SKBR3 cells before and after reduction with DTT and purification by SEC under conditions used to generate trastuzumab-PB-SH. DOL(degree of labeling, **33**) = 5.2; DOL(**39**) = 1.6. DOL(Herceptin-PB) = 1.8.

SkBr3 cells were incubated with **39** without and with **4** and analyzed over time by both flow cytometry and confocal microscopy. **40** (Figure 2-23), used as a control for complete cleavage of **39**, was generated by incubating **39** with DTT and then purifying using size exclusion chromatography and the loss of green fluorescence and increased blue fluorescence was confirmed by fluorescence spectroscopy (data not shown). Analysis of a related trastuzumab-PB conjugate by flow cytometry under the same conditions demonstrated that this treatment did not adversely affect potency for HER2 on SKBR3 cells, but binding efficacy was reduced by 17% (Figure 2-24, E), and this difference was factored into the analysis of the kinetics of disulfide cleavage in cells.

The blue fluorescence signal of SkBr3 cells treated with **39** was compared to that of cells treated with **40** at various time points without and with endosome disruptor **4** to determine the half-life of the cleavage reaction in cells (Figure 2-25 A). No significant difference was found between the half-times of **39** without (8 ± 2 h) and with (7 ± 2 h) **4**, indicating that **4** is not needed for the cleavage of **39** and does not significantly contribute to the rate of cleavage. The data also indicate that probe was not fully cleaved during the course of the assay, with a maximum cleavage of about 30%. Similar results were seen when cells were pretreated for 24 h with **4** before addition of **39** (data not shown). These results agree with previous studies reported by others. Yang *et. al.* found that a FRET-based probe with a disulfide linker targeted to the folate receptor has a 6 h half-life in KB

cells.[52] Lee *et. al.* showed that FRET-based antibody conjugates targeted at HER2 were only cleaved ~40% after incubation for 20 h in SKBR3 cells, though the linker in this report was cathepsin-cleavable rather than a reducible disulfide.[24] A report by Erickson *et. al.* found that after an incubation of 20 h in HER2 positive breast cancer cells, a trastuzumab emtansine analogue with a disulfide linker was less than 50% processed.[53]

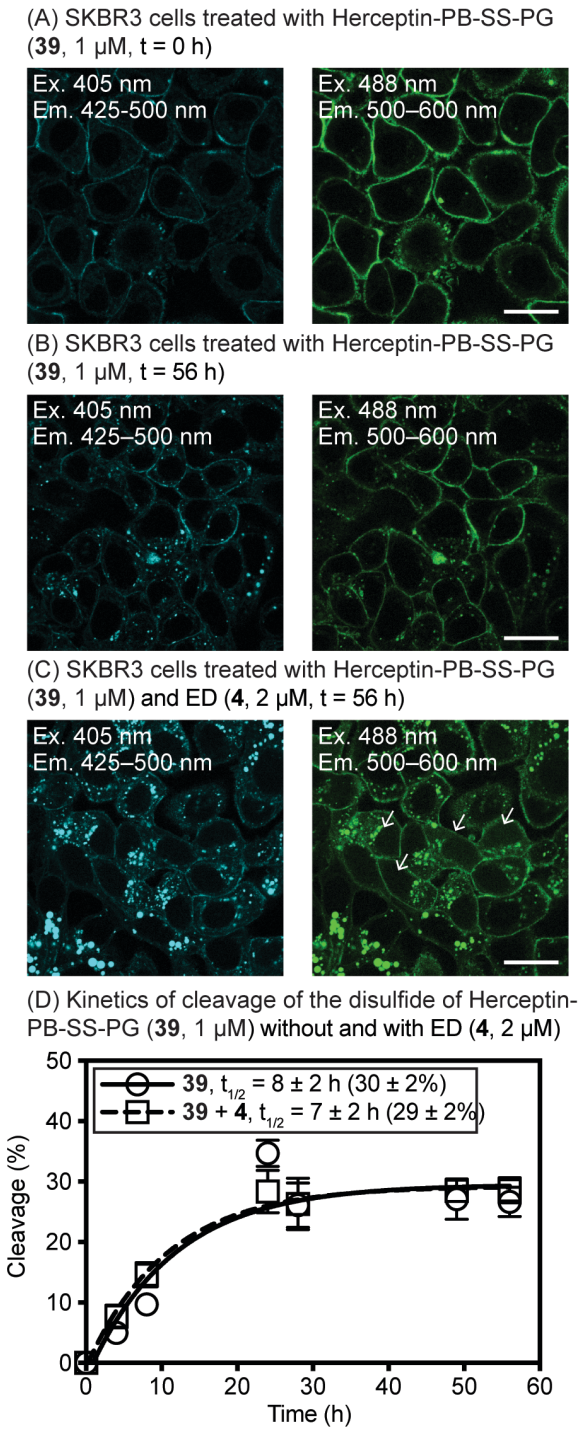

Figure 2-25. (A–C) Confocal micrographs of living SKBR3 cells treated with Herceptin-PB-SS-PG (**39**, 1 μM). In panel A, cells were treated at 4 °C for 0.5 h prior to washing and imaging. Panels B–C: Cells were treated at 4 °C for 0.5 h prior to washing and incubation at 37 °C for 56 h in the absence (B) and presence (C) of ED (**4**, 2 μM). In panel C, white arrows illustrate cells with dispersed green fluorescence resulting from endosome disruption and increased localization of blue and green fluorescence in endosomes/lysosomes. Scale bar = 25 μm. (D) Analysis of the kinetics of cleavage of the

disulfide of **39** by flow cytometry. The half-time of cleavage of the disulfide of **39** (± SEM) is not significantly altered by co-administration with **4**.

Confocal micrographs of SkBr3 cells treated with **39** without and with endosome disruptor **4** revealed more about the mechanism of synergy (Figure 2-25). At t = 0 the conjugates were located entirely at the cell membrane. Over time, more fluorescence was found within endosomes as the conjugates were endocytosed and cycled through the cells. The micrographs show that the green fluorescence was only released into cells that were treated with **39** and **4**; cells only treated with **39** show the localized green fluorescence expected of cells with intact endosomal membranes. This phenomenon is less obvious than the release of more polar fluorescein derivatives that are better retained within the cell, but it is still clear. Additionally, **4** appears to alter the trafficking of **39**. Without **4**, **39** is located mostly at the cell surface with minimal accumulation within internal vesicles. This correlates well with the previously reported extensive endosomal recycling of HER2 back to the cell membrane.[24,31] Cotreatment of **39** with **4** leads to more accumulation within vesicles of the endolysosomal system based on colocalization studies with LysoTracker Red DND-99 (Figure 2-26). The mechanism of the change in trafficking is unknown but could be beneficial for the release of the cargo of the antibody conjugate.

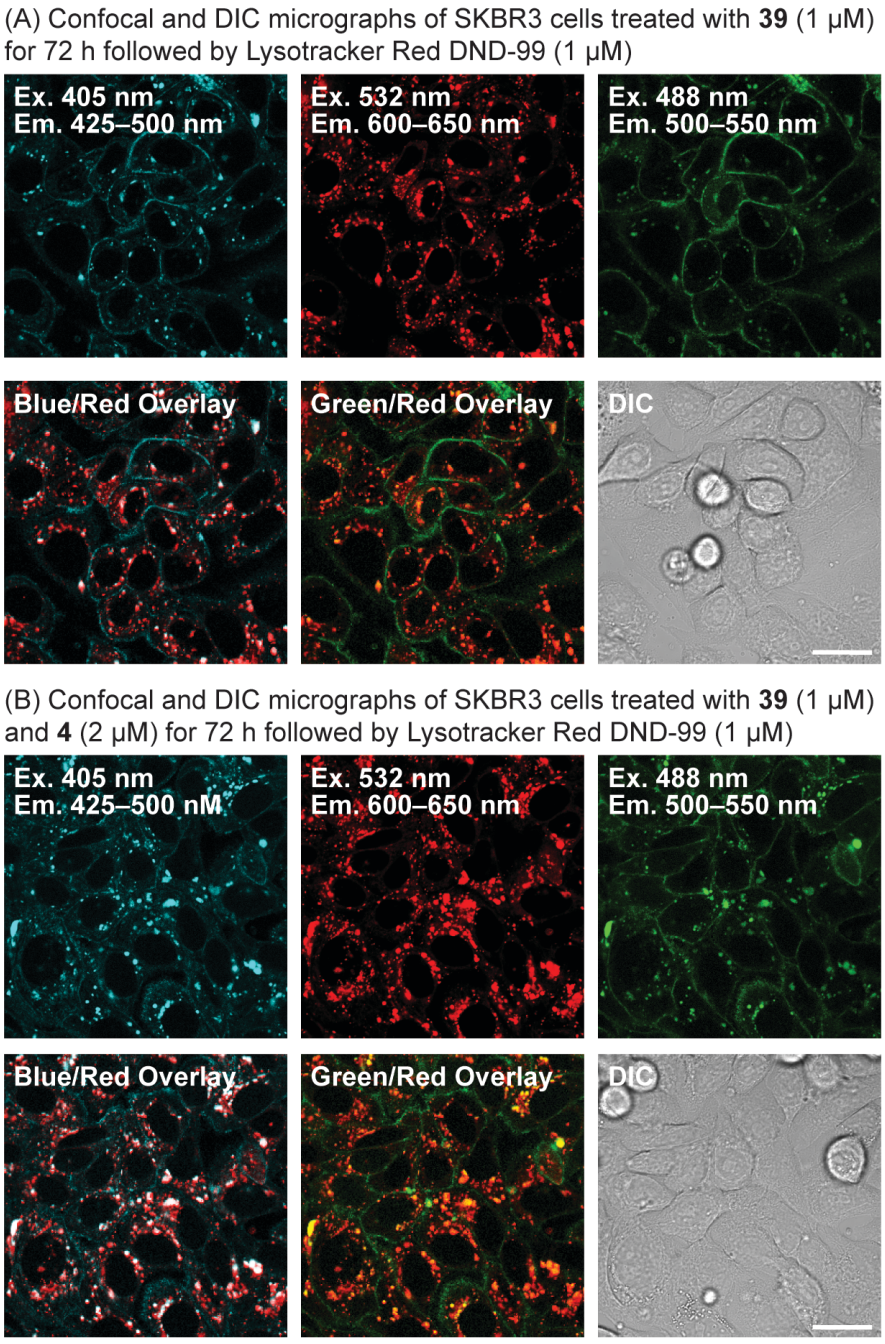

Figure 2-26. (A, B) Confocal and DIC micrographs of SkBr3 cells treated with Herceptin-PB-SS-PG (**39**, 1 μM) for 72 h followed LysoTracker Red DND-99 (1 μM) for 0.5 h. In panel B, cells were co-treated with **4** (2 μM) for 72 h prior to imaging. The blue and green fluorescence of **39** co-localizes with LysoTracker to a greater extent in the presence of **4**. Scale bar = 25 μm.

Together, these data reveal much about the mechanism of the synergy between ED **4** and the Herceptin-delivered toxin **33**. Endosome disruptor **4** is not needed for the cleavage of the disulfide linker of **33**. This leaves the exact mechanism of cleavage of the linker in the oxidizing environment of the endosome[54] undetermined, though we hypothesize that cellular thiol reductases such as gamma-interferon-inducible lysosomal thiol reductase (GILT)[55] could be responsible. Reduction could also occur in the lysosome, though this compartment has also been found to be oxidizing.[54] Release of the cargo from the antibody could also be caused by proteolysis. The products of both proteolytic cleavage and disulfide reduction have been previously seen in cells treated with an antibody conjugate with a disulfide linker.[53] Regardless, endosome disruptor **4** is necessary for appreciable amounts of the cell impermeable cargo to escape from the endocytic pathway.

This new information requires a revision to our hypothesized method of cargo release proposed in the Introduction of this chapter (Figure 2-4). We hypothesized that an endosome disruptive peptide would form pores in the endosomal membrane and allow reducing agents such as glutathione to enter the endosome and speed the rate of cleavage of a disulfide linker within the endosome. The new evidence indicates that addition of the endosome disruptor does not change the rate or extent of cleavage, but it is necessary for cargo release into the cytosol. For this reason, we have removed glutathione from the mechanism graphic. As discussed previously, other methods of reduction are more likely. Given the relatively high hydrophobicity of the peptide moiety of EDs such as **4**, and the very high polarity of GSH, the high energetic cost of desolvation

of GSH may limit its ability to pass through relatively hydrophobic pores in endosomal membranes. The new hypothesized mechanism is illustrated in Figure 2-27.

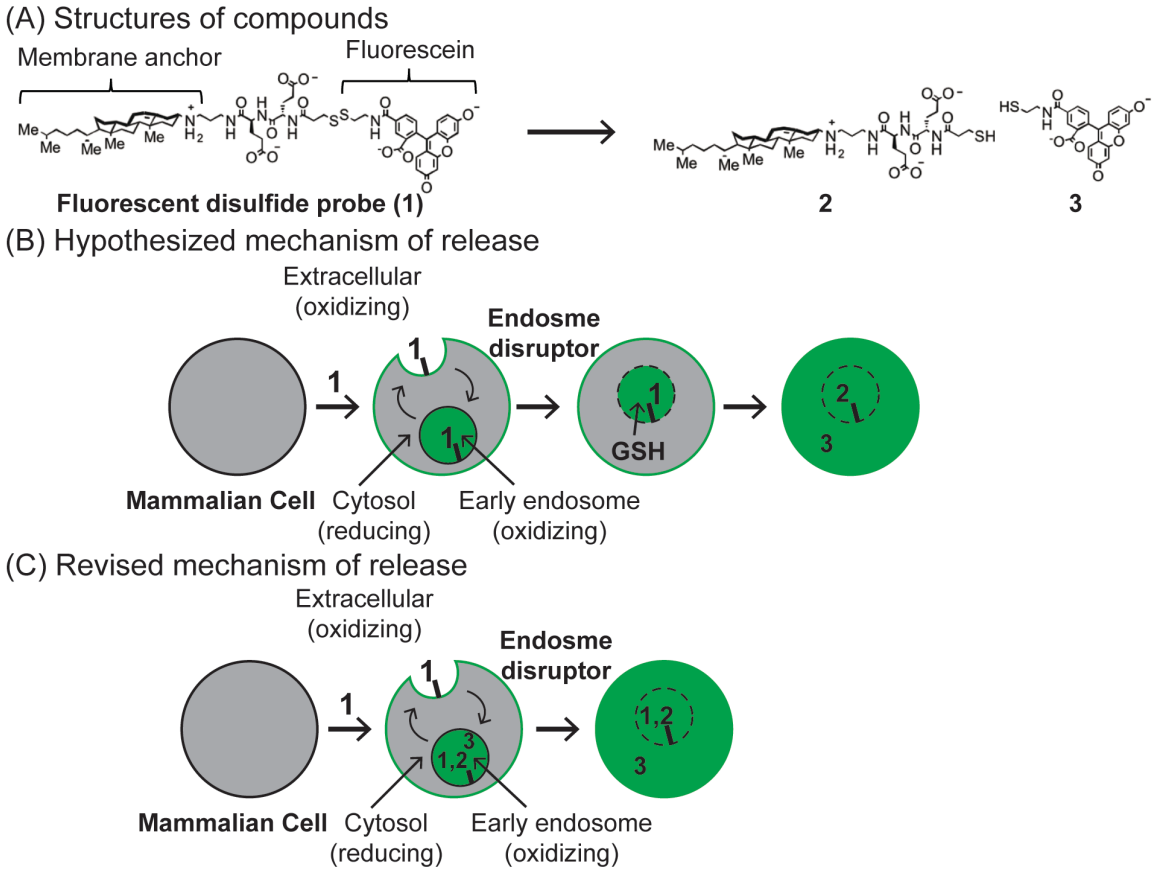

Figure 2-27. Revised hypothesis of the mechanism of release. The data presented in this chapter indicates that addition of an ED has no effect on the cleavage of a disulfide linker in the endosome. For this reason, we no longer believe that addition of an ED allows glutathione to enter the endosome and speed the cleavage of the disulfide. Instead, we hypothesize that the disulfide is cleaved by mechanisms independent of the ED, but that the ED is necessary for the release of the cleaved cargo into the cytosol.

2-6. Conclusions and future directions

In this chapter, we have presented an update on the progress that has been made in the development of endosome disruptive peptides. Since the dissertation of Dr. David Hymel (University of Kansas, 2014), cholesterol-delivered endosome disruptors have been optimized to yield **4**, an ED that works well in many adherent cell lines. Additionally,

a fluorescence-based model system has been developed to optimize the delivery of fluorophores and endosome disruptors into cells using antibodies. This system was used to optimize the structure and properties of each component individually and then to demonstrate that it is possible to release antibody-delivered cargo into the cytosol of a cell using an antibody-delivered endosome disruptor. The optimized components of this system were then used to deliver and release toxins into HER2+ breast cancer cells. Targeted, synergistic toxicity was observed between ED **4** and the Herceptin-CME conjugate (**33**), which together exhibited more than a 5,000-fold enhancement in toxicity compared to conjugate **33** alone. Unfortunately, even the most active Herceptin-endosome disruptor conjugate (**29**) was not active enough to cause similar synergy.

The FRET probe conjugate (**39**) was used to better understand the synergy of endosome disruptors and ADCs. It revealed that though EDs do not contribute to the rate of release of the cargo from the ADC, they are necessary for entry of the cell impermeable cargo into the cell cytosol. Additionally, EDs alter the trafficking of at least Herceptin-based ADCs, causing them to localize more heavily to endosomes and lysosomes.

Due to the lack of necessary activity and the complexity of the antibody-endosome disruptors conjugates, we are unlikely to continue attempting to optimize that component of the system. Instead, we will focus on using cholesterol-delivered EDs such as **4** to release the antibody-delivered toxin. Therefore, in the future, we plan to perform animal studies to explore the hypothesis that HER2+ tumors in mice treated with Herceptin-SS-Fl (**16**) and **4** would be more fluorescent than those of mice treated with only Herceptin-Fl. We would also expect the HER2+ tumors to be more fluorescent than HER2– tissues in the mice, given that the fluorophore is expected to be taken up to a greater extent by

HER2+ cells. If these hypotheses prove to be valid, we would move on to studying the synergy between an antibody-delivered toxin and an ED in a mouse model, possibly exploring the benefits of pre-targeting. It is our hope that this system could provide improvements in selectivity and efficacy over current ADCs for cancer treatment.

2-7. Experimental

2-7-1. General experimental section

Chemical reagents were purchased from Aapptec, Acros, Aldrich, Alfa Aesar, EMD Biosciences, or TCI America, and were used without further purification. Solvents were from Aldrich or Fisher Scientific. The fluorescent disulfide probe (**1**),[25] **36** and **CME,**[56,57] Fmoc-protected 3-((2-aminoethyl)disulfanyl)propanoic acid,[25] 3-((((Cholester-3-yl)oxy)carbonyl)amino)propanoic acid,[58] and Pacific Blue NHS ester[59] were prepared as previously described. Chol-SS-CME (**35**) was synthesized by Zhe Gao but was originally made by Ning Yang. Its synthesis and characterization are provided in Mr. Yang's Master's thesis. All endosome disruptor compounds and toxins were synthesized by Dr. Chamani Perera and Zhe Gao and provided with >90% purity based on analytical HPLC profiling. Column chromatography employed Silica Gel (SiliCycle, 40-63 μm). Preparative HPLC employed an Agilent 1200 Series preparative pump / gradient extension with a Hamilton PRP-1 (polystyrene-divinylbenzene) reverse-phase preparative column (10-12 μm particle size, 21.5 mm x 25 cm) with a flow rate of 25.0 mL/min. HPLC fractions containing water were dried using a Labconco FreeZone 4.5 lyophilizer. Compounds containing basic amines were isolated as TFA salts. Analytical HPLC traces were acquired using an Agilent 1220 Series binary pump and an Agilent PLRP-S reverse phase analytical column (8 μm particle size, 4 mm x 25 cm) with diode-array detection at 254

nm. Chromatograms were acquired at RT or 45 °C for peptides containing proline residues to minimize rotational isomers and employed a gradient elution of H_2O:CH_3CN (90:10 to 0:100) with added TFA (0.1%) over 20 min and a 100% CH_3CN wash for an additional 5 min. Purity was determined by integration of the chromatogram. Low-resolution mass spectra (LRMS) were obtained using a Waters Micromass ZQ instrument with ESI+ or ESI-. Peaks are reported as *m/z*.

2-7-2. Synthetic procedures and compound characterization data

General procedure for solid phase peptide synthesis (SPPS).

SPPS was performed on a Mettler Toledo MiniBlock reactor (Model No: Bohdan 2080; 12-well block with glass reaction vessels, 600 rpm) utilizing standard Fmoc chemistry employing Rink amide MBHA resin (0.05 mmol). The resin was swelled in DMF for 2 h and the Fmoc group removed by agitating with deblocking solution (20% piperidine in DMF (2 mL), 2 x, for 4 minutes each). The resin was washed 4x with DMF (2 mL) to remove any traces of piperidine, and treated with Fmoc-amino acids (4 eq.), HATU coupling reagents (3.8 eq.), and DIEA (8 eq.) in 2 ml of DMF with agitation until coupling was completed by Kaiser Test (3, 6, 12, or 16 h). Once the coupling was complete, the reaction solution was drained, and resin was washed four times with DMF (2 mL). This coupling protocol was repeated for each additional Fmoc-amino acid. The hindered 2-aminoisobutyric acid (Aib) was coupled via acid fluoride chemistry. Fmoc-Aib-F was synthesized using DAST chemistry.[60] Fmoc-Aib-F (4 eq.) was dissolved in 0.5 mL of DMF, added to the resin, and agitated for 6 h. For acetylated peptides, the final amine was capped by agitating with acetic anhydride/DIEA/DMF (1:2:7) for 1 h. Cleavage from Rink amide MBHA resin was done using a mixture of TFA/H_2O/TIPS (95/2.5/2.5) with agitation

for 2 h. 2-Chlorotrityl resin (0.1 mmol) was swelled in DCM for 10 min and then loaded with the first Fmoc amino acid (4 eq) in the presence of DIEA (8 eq) as a base in dry DCM (4 mL) overnight on the MiniBlock. After washing with DCM (4 mL, 4x), MeOH (4 mL) was added and stirred for 10 min to cap unreacted 2-CTC resin. Then solvent was filtered through, and the resin was washed with DMF (4 mL, 4x). Further couplings were performed as for Rink amide resin. Cleavage from 2-Chlorotrityl resin was done by treatment with a mixture of DCM/TFE/acetic acid (7:2:1) with shaking for 2 h. The resin was removed by filtration and washed with DCM (2 mL, 3x) or DMF (2 mL, 3x). The filtrates were combined and concentrated under vacuum to give crude products. Purification was done using preparative reverse-phase HPLC (gradient: 90/10 H_2O/MeCN to 100% MeCN over 20 min with 0.1% TFA added).

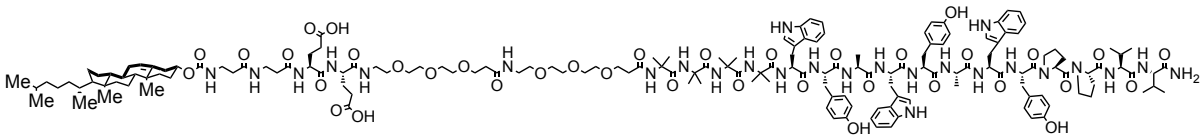

((3β-Cholest-5-en-3-yl)carbonyl)-β-Alanyl-β-Alanyl-L-Glutamyl-L-Glutamyl-mPEG-mPEG-Aminoisobutyl-Aminoisobutyl-Aminoisobutyl-Aminoisobutyl-L-Tryptophyl-L-Tyrosyl-L-Alanyl-L-Tryptophyl-L-Tyrosyl-L-Alanyl-L-Tryptophyl-L-Tyrosyl-L-Prolyl-LProlyl-L-Valyl-L-Valinamide (4). Using the general SPPS procedure, 0.05 mmole Rink amide resin was used to produce **4** as a white solid (35.2 mg, 21%). LRMS (ESI+) m/z calcd for $C_{164}H_{232}N_{26}O_{37}$ $[M+H]^+$: 3159.8, found: $[(M+2Na)/2]^+$: 1601.9.

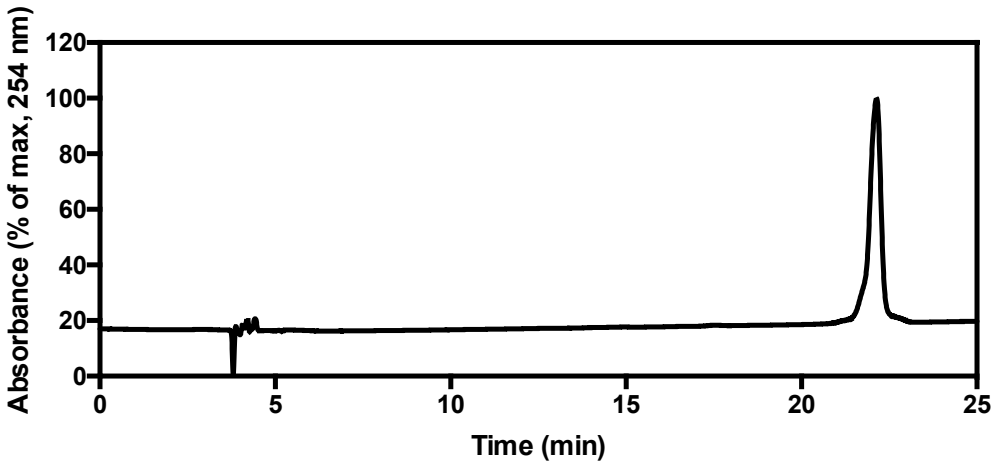

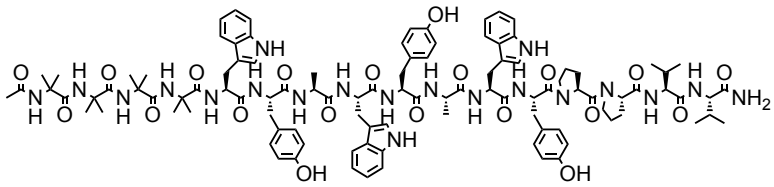

***N*-(Acetyl)-Aminoisobutyl-Aminoisobutyl-Aminoisobutyl-Aminoisobutyl-L-Tryptophyl-L-Tyrosyl-L-Alanyl-L-Tryptophyl-L-Tyrosyl-L-Alanyl-L-Tryptophyl-L-Tyrosyl-L-Prolyl-L-Prolyl-L-Valyl-L-Valinamide (5).** Using the general SPPS procedure, Rink amide resin was used to produce **5** as a white solid. LRMS (ESI-) m/z calcd for $C_{104}H_{132}N_{20}O_{20}$ $[M-H]^-$: 1982.3, found: 1982.0.

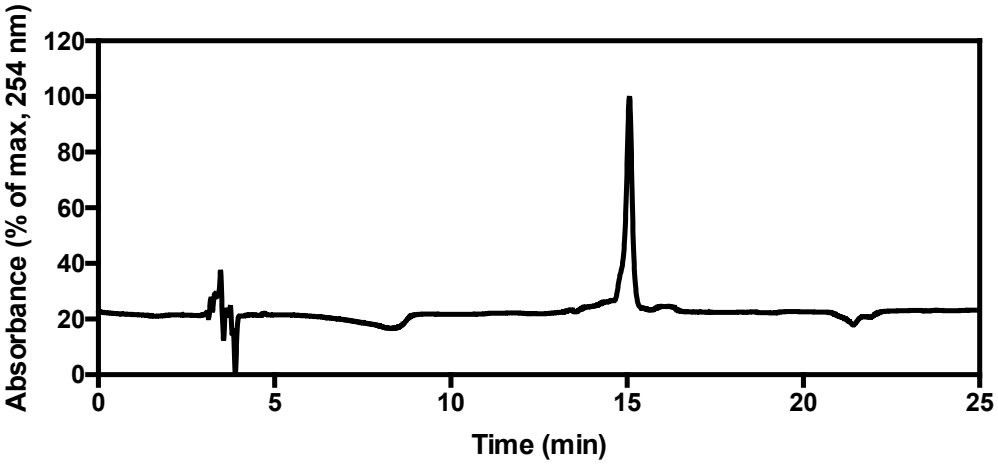

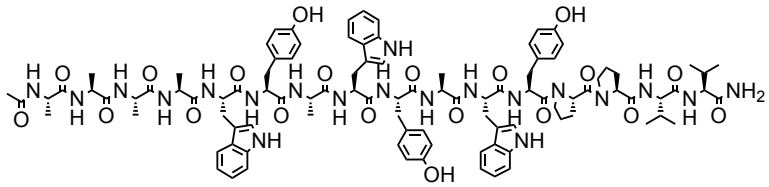

***N*-(Acetyl)-L-Alanyl-L-Alanyl-L-Alanyl-L-Alanyl-L-Tryptophyl-L-Tyrosyl-L-Alanyl-L-Tryptophyl-L-Tyrosyl-L-Alanyl-L-Tryptophyl-L-Tyrosyl-L-Prolyl-LProlyl-L-Valyl-L-Valinamide (6).** Using the general SPPS procedure, Rink amide resin was used to produce **6** as a white solid. LRMS (ESI+) m/z calcd for $C_{100}H_{124}N_{20}O_{20}$ $[M+Na]^+$: 1949.1, found: 1948.9.

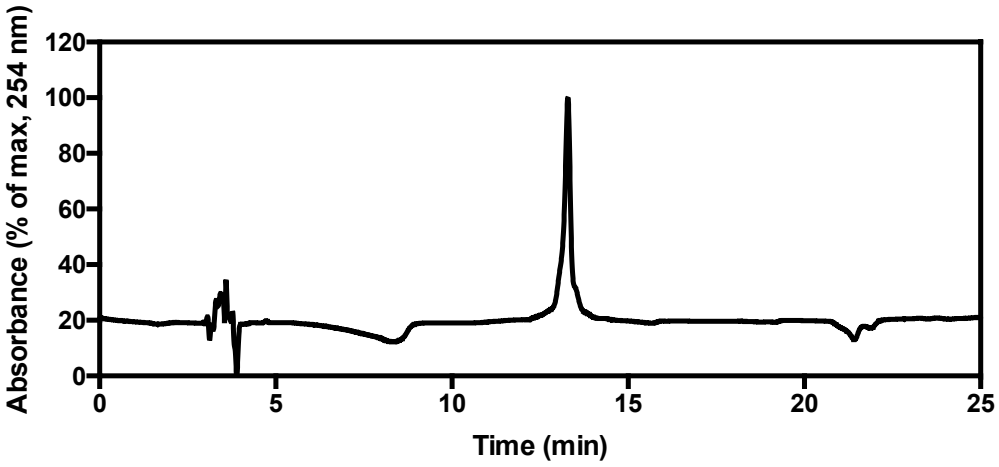

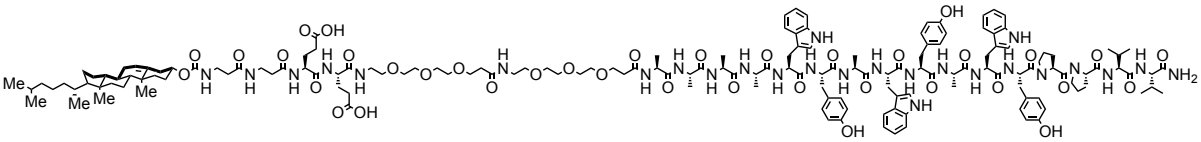

((3β-Cholest-5-en-3-yl)carbonyl)-β-Alanyl-β-Alanyl-L-Glutamyl-L-Glutamyl-mPEG-mPEG-L-Alanyl-L-Alanyl-L-Alanyl-L-Alanyl-L-Tryptophyl-L-Tyrosyl-L-Alanyl-L-Tryptophyl-L-Tyrosyl-L-Alanyl-L-Tryptophyl-L-Tyrosyl-L-Prolyl-LProlyl-L-Valyl-L-Valinamide (7). Using the general SPPS procedure, Rink amide resin was used to produce **7** as a white solid. LRMS (ESI-) m/z calcd for $C_{160}H_{224}N_{26}O_{37}$ $[(M-H)/2]^-$: 1550.8, found: $[(M-H)/2]^-$: 1550.4.

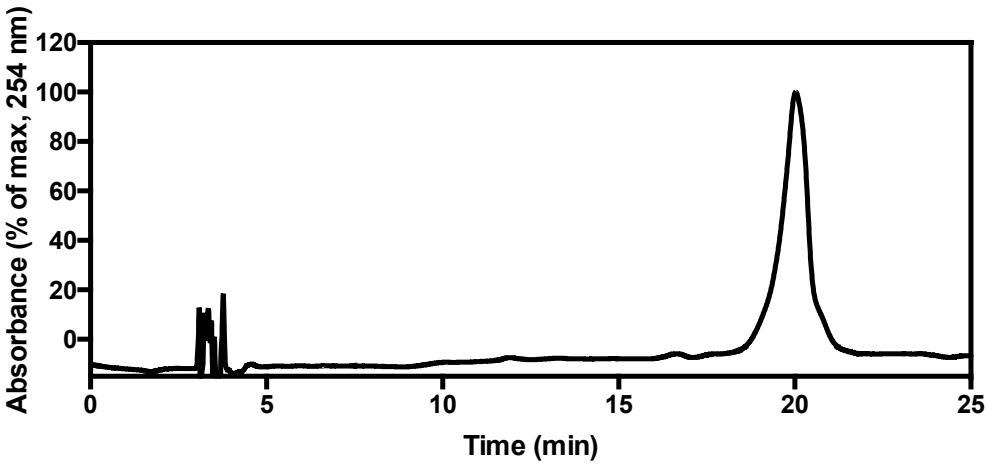

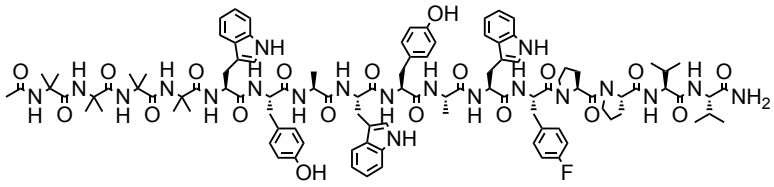

***N*-(Acetyl)-Aminoisobutyl-Aminoisobutyl-Aminoisobutyl-Aminoisobutyl-L-Tryptophyl-L-Tyrosyl-L-Alanyl-L-Tryptophyl-L-Tyrosyl-L-Alanyl-L-Tryptophyl-*p*-Fluoro-L-Phenylalanyl-L-Alanyl-L-Prolyl-L-Prolyl-L-Valyl-L-Valinamide (8).** Using the general SPPS procedure, Rink amide resin was used to produce **8** as a white solid. LRMS (ESI+) m/z calcd for $C_{104}H_{131}FN_{20}O_{19}$ $[M+Na]^+$: 2006.0, found: $[M+Na]^+$: 2006.2.

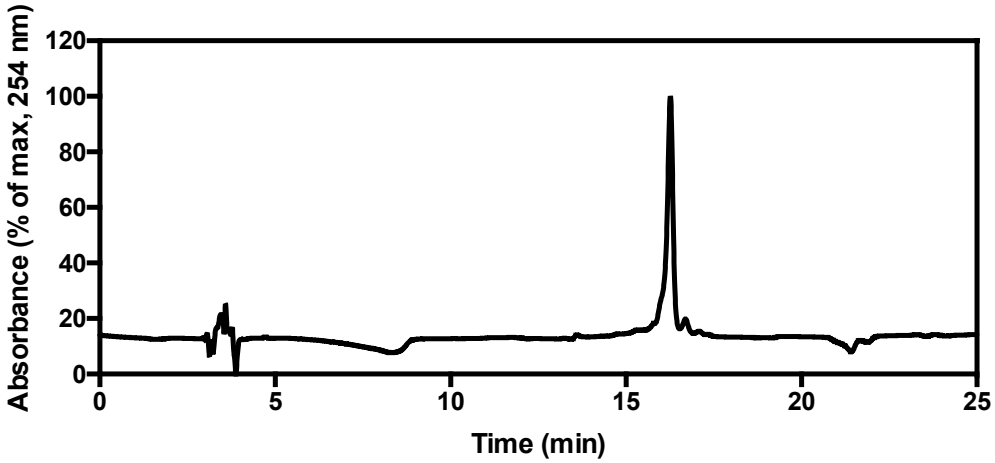

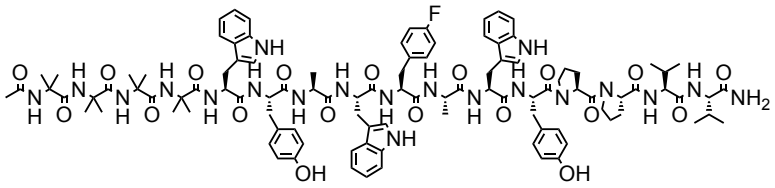

***N*-(Acetyl)-Aminoisobutyl-Aminoisobutyl-Aminoisobutyl-Aminoisobutyl-L-Tryptophyl-L-Tyrosyl-L-Alanyl-L-Tryptophyl-*p*-Fluoro-L-Phenylalanyl-L-Alanyl-L-Tryptophyl-L-Tyrosyl-L-Alanyl-L-Prolyl-L-Prolyl-L-Valyl-L-Valinamide (9).** Using the general SPPS procedure, Rink amide resin was used to produce **9** as a white solid. LRMS (ESI+) m/z calcd for $C_{104}H_{131}FN_{20}O_{19}$ $[M+Na]^+$: 2006.0, found: $[M+Na]^+$: 2006.5.

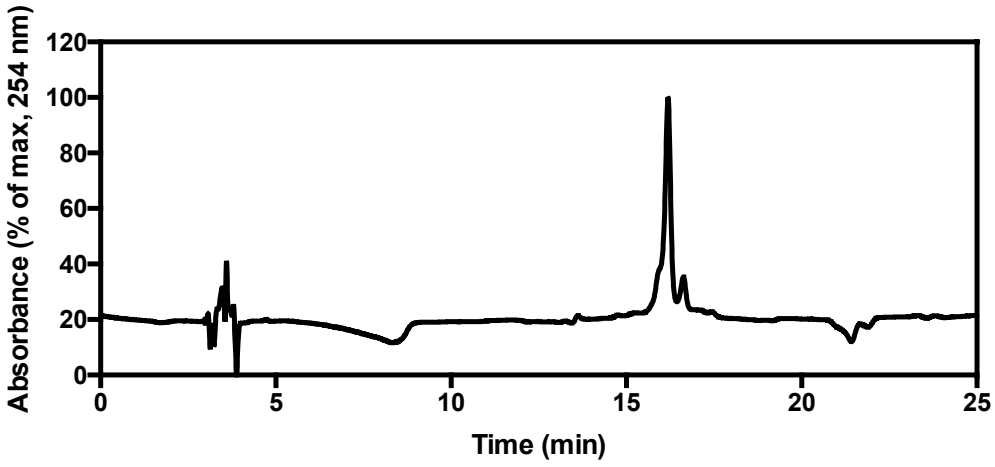

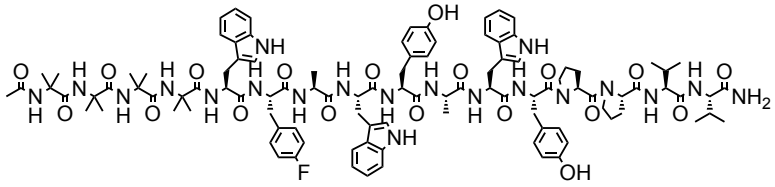

***N*-(Acetyl)-Aminoisobutyl-Aminoisobutyl-Aminoisobutyl-Aminoisobutyl-L-Tryptophyl-*p*-Fluoro-L-Phenylalanyl-L-Alanyl-L-Tryptophyl-L-Tyrosyl-L-Alanyl-L-Tryptophyl-L-Tyrosyl-L-Alanyl-L-Prolyl-L-Prolyl-L-Valyl-L-Valinamide (10).** Using the general SPPS procedure, Rink amide resin was used to produce **10** as a white solid. LRMS (ESI+) m/z calcd for $C_{104}H_{131}FN_{20}O_{19}$ $[M+Na]^+$: 2006.0, found: $[M+Na]^+$: 2006.6.

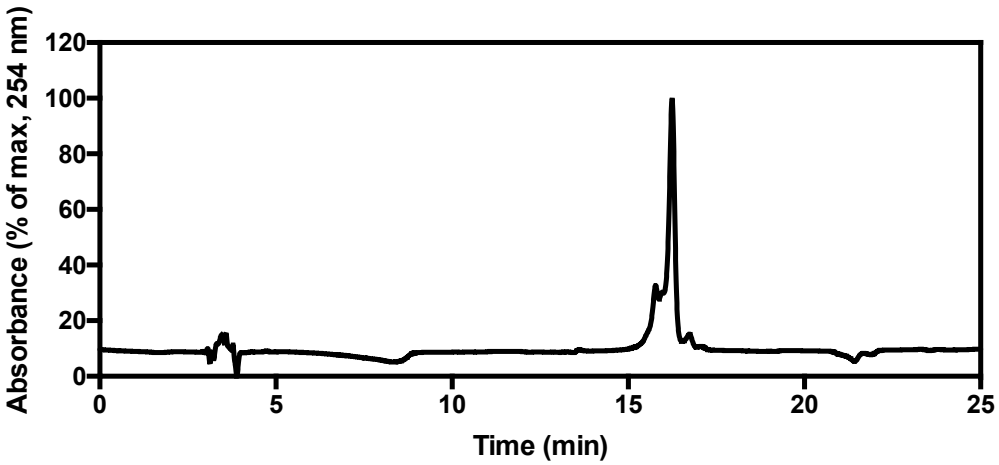

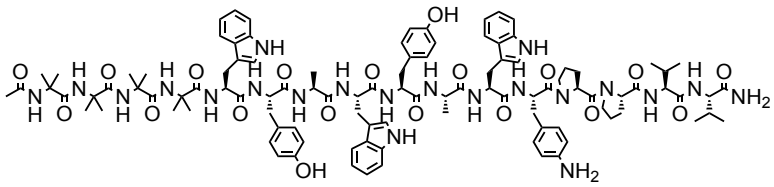

***N*-(Acetyl)-Aminoisobutyl-Aminoisobutyl-Aminoisobutyl-Aminoisobutyl-L-Tryptophyl-L-Tyrosyl-L-Alanyl-L-Tryptophyl-L-Tyrosyl-L-Alanyl-L-Tryptophyl-*p*-Amino-L-Phenylalanyl-L-Alanyl-L-Prolyl-L-Prolyl-L-Valyl-L-Valinamide (11).** Using the general SPPS procedure, Rink amide resin was used to produce **11** as a white solid. LRMS (ESI+) m/z calcd for $C_{104}H_{133}N_{21}O_{19}$ $[M+Na]^+$: 2003.1, found: $[M+Na]^+$: 2003.7.

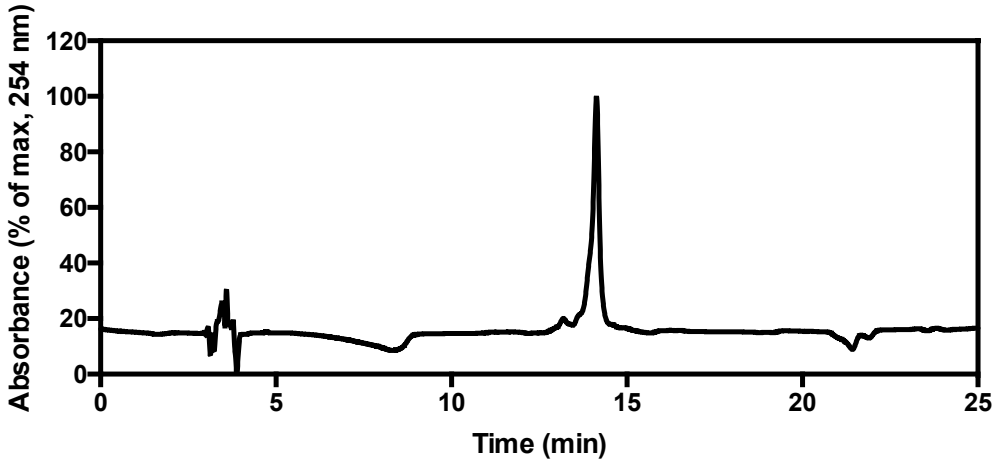

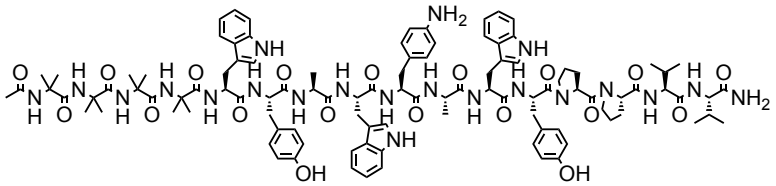

***N*-(Acetyl)-Aminoisobutyl-Aminoisobutyl-Aminoisobutyl-Aminoisobutyl-L-Tryptophyl-L-Tyrosyl-L-Alanyl-L-Tryptophyl-*p*-Amino-L-Phenylalanyl-L-Alanyl-L-Tryptophyl-L-Tyrosyl-L-Alanyl-L-Prolyl-L-Prolyl-L-Valyl-L-Valinamide (12).** Using the general SPPS procedure, Rink amide resin was used to produce **12** as a white solid. LRMS (ESI+) m/z calcd for $C_{104}H_{133}N_{21}O_{19}$ $[M+H]^+$: 1981.3, found: 1981.4.

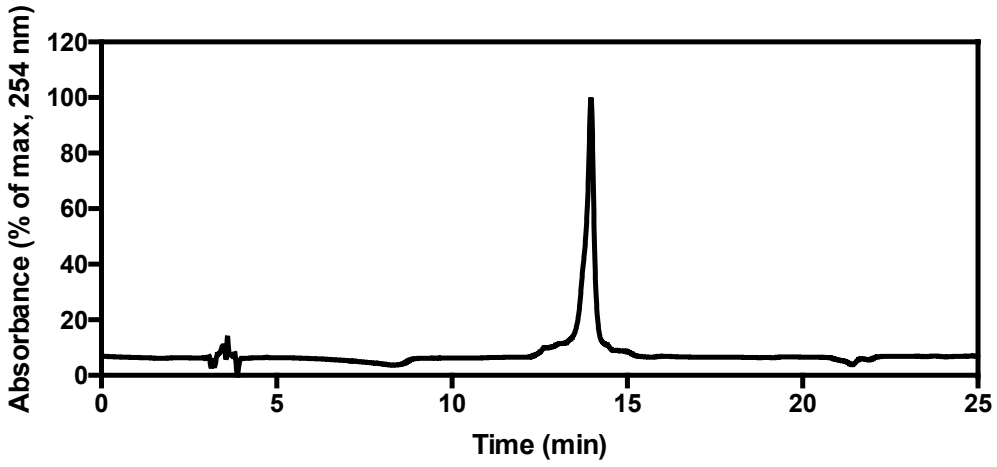

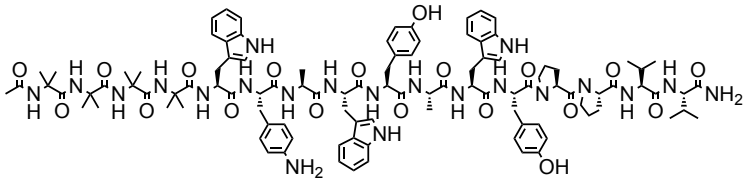

***N*-(Acetyl)-Aminoisobutyl-Aminoisobutyl-Aminoisobutyl-Aminoisobutyl-L-Tryptophyl-*p*-Amino-L-Phenylalanyl-L-Alanyl-L-Tryptophyl-L-Tyrosyl-L-Alanyl-L-Tryptophyl-L-Tyrosyl-L-Alanyl-L-Prolyl-L-Prolyl-L-Valyl-L-Valinamide (13).** Using the general SPPS procedure, Rink amide resin was used to produce **13** as a white solid. LRMS (ESI+) m/z calcd for $C_{104}H_{133}N_{21}O_{19}$ $[M+H]^+$: 1981.3, found: 1981.1.

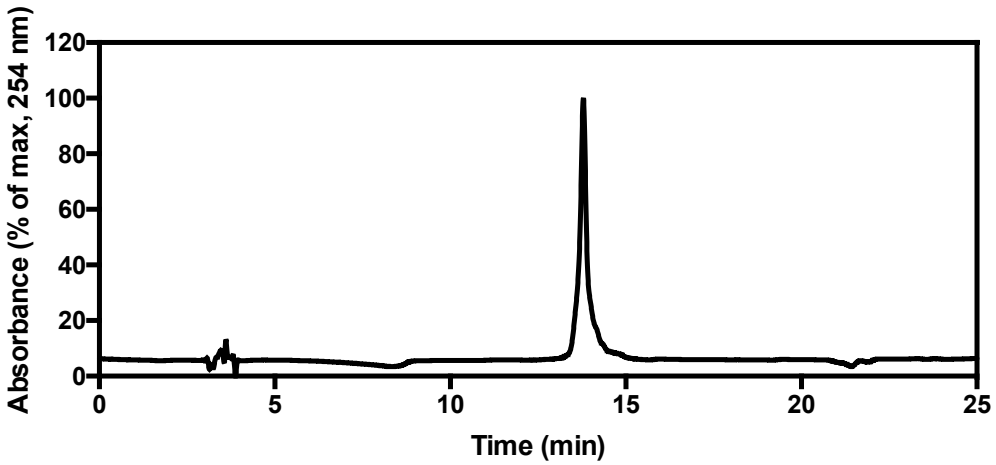

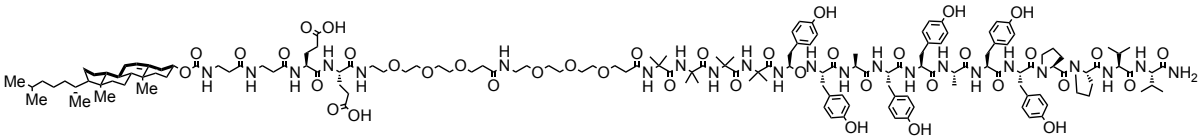

((3β-Cholest-5-en-3-yl)carbonyl)-β-Alanyl-β-Alanyl-L-Glutamyl-L-Glutamyl-mPEG-mPEG-Aminoisobutyl-Aminoisobutyl-Aminoisobutyl-Aminoisobutyl-L-Tyrosyl-L-Tyrosyl-L-Alanyl-L-Tyrosyl-L-Tyrosyl-L-Alanyl-L-Tyrosyl-L-Tyrosyl-L-Prolyl-LProlyl-L-Valyl-L-Valinamide (14). Using the general SPPS procedure, Rink amide resin was used to produce **14** as a white solid. LRMS (ESI+) m/z calcd for $C_{157}H_{229}N_{23}O_{40}$ $[(M+Na)/2]^+$: 1549.8, found: $[(M+Na)/2]^+$: 1549.8.

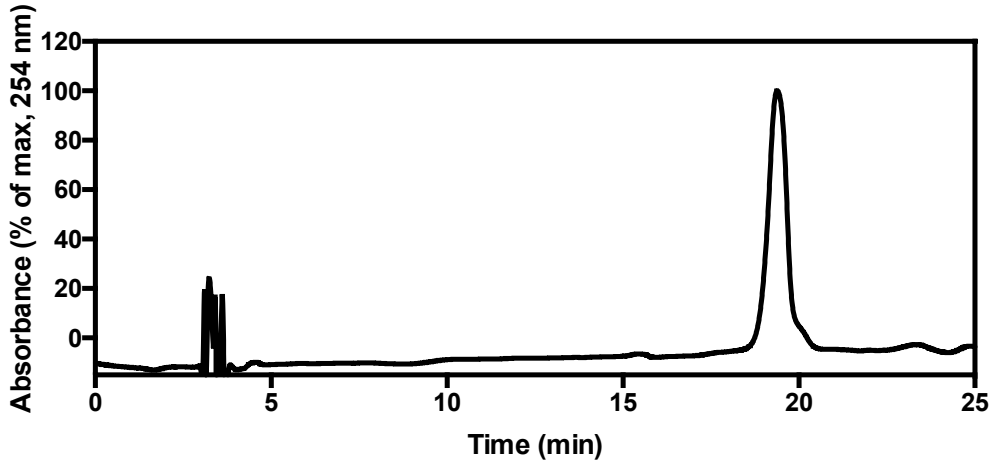

General procedure for the synthesis of endosome disruptors for antibody conjugation

The procedure outlined in *General procedure for solid phase peptide synthesis* was used to generate each peptide. Fmoc-Pacific Blue-L-Lysine was used to incorporate this fluorophore into the structures. As illustrated in Scheme 2-1, after cleavage from the resin and purification by HPLC, each peptide was dissolved in 20% diethylamine in DMF (1 mL) and stirred at room temperature for 1 h. Solvent was removed by vacuum, and the product was dissolved in DMF (1 mL). Disuccinimidyl glutarate (10 eq) and DIEA (10 eq) were added, and the reaction was stirred overnight. The next morning, the solvent was removed by vacuum, and the product was purified by HPLC and lyophilized to give the desired product. The NHS ester of these compounds is prone to hydrolysis, so many of these compounds contain a small amount of the cleaved product, which can be seen as a small peak just before that of the desired product in the analytical HPLC trace. These byproducts would be removed from the antibody-endosome disruptor conjugates by the size exclusion chromatography used to purify the conjugates, so these impurities were not concerning.

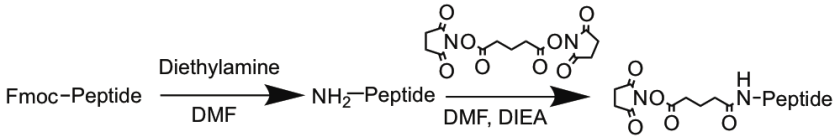

Scheme 2-1. Synthesis of endosome disruptors for antibody conjugation.

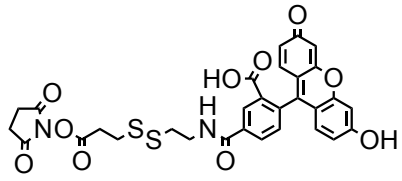

5-((2-((3-((2,5-dioxopyrrolidin-1-yl)oxy)-3-oxopropyl)disulfanyl)ethyl)carbamoyl)-2-(6-hydroxy-3-oxo-3H-xanthen-9-yl)benzoic acid (**15**). Fmoc-3-((2-aminoethyl)disulfanyl)propanoic acid (28 mg, 0.070 mmol) was dissolved in DMF (1 mL) containing 20% piperidine and stirred at 22 °C for 30 min. The solvent was removed under vacuum to provide the primary amine. 5-carboxy fluorescein (17 mg, 0.035 mmol) was dissolved in dry DMF (2 mL) and added to the primary amine along with DIEA (0.2 mL). The reaction was stirred at 22 °C for 16 h. Following completion, the solvent was removed under vacuum, the residue was re-dissolved in DCM containing 5% methanol, applied to a short silica plug, and eluted with 90/10 DCM/MeOH. The solvent was removed to give the crude carboxylic acid product. This product (~15 mg) was dissolved in DMF (2 mL) and EDC (11 mg, 0.06 mmol) and N-hydroxysuccinimide (NHS, 7 mg, 0.06 mmol) were added. The reaction was allowed to stir at 22 °C for 16 h. The solvent was removed under vacuum, and the residue was dissolved in DMSO (2 mL) and purified by preparative RP-HPLC (Gradient: H_2O:CH_3CN (9:1) to (0:100) with added TFA (0.1%) over 20 min). Pure fractions were collected, combined, and dried under vacuum to give **15** (9 mg, 0.014 mmol, 39% overall yield) as a yellow solid. ^{1}H NMR (500 MHz, DMSO-d_6) δ 9.01 (t, J = 5.5 Hz, 1H), 8.46 (s, 1H), 8.25 (d, J = 7.9, 1.6 Hz, 1H), 7.38 (d, J = 8.0 Hz, 1H), 6.69 (d, J = 1.9 Hz, 2H), 6.59 (d, J = 8.6 Hz, 2H), 6.56 – 6.53 (m, 2H), 3.62 (q, J = 6.3 Hz, 2H), 3.13 (t, J = 6.5 Hz, 2H), 3.05 (t, J = 6.9 Hz, 2H), 2.98 (t, J = 6.6 Hz, 2H), 2.54 (s, 4H). ^{13}C NMR (126 MHz, DMSO-d_6) δ 170.1, 168.2, 167.5, 164.8, 159.6, 154.7, 151.8, 136.0, 134.7, 129.2, 126.5, 124.3, 123.3, 112.7, 109.1, 102.3, 40.4, 36.9, 31.9, 30.4, 25.4. HRMS (ESI+) *m/z* calcd for $C_{30}H_{24}N_2O_{10}S_2$ $[M+Na]^+$: 659.0765, found: 659.0740.

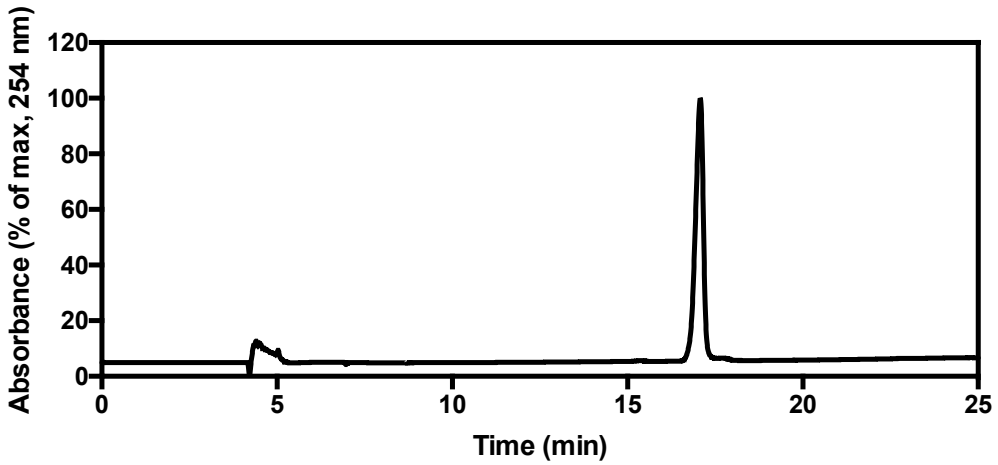

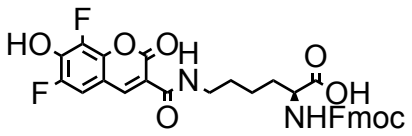

***N*^{2}-(((9H-Fluoren-9-yl)methoxy)carbonyl)-*N*^{6}-(6,8-difluoro-7-hydroxy-2-oxo-2Hchromene-3-carbonyl)-*L*-lysine (41).** As reported in the thesis of Dr. Molly Lee, to a solution of Fmoc-L-Lys-OH (1.76 g, 4.78 mmol) and DIEA (3.3 mL, 18.45 mmol) in DMF (20 mL) was added Pacific Blue NHS ester (1.25 g, 3.69 mmol, synthesized as previously reported[59]). The reaction mixture was stirred at 22 °C overnight. The reaction mixture was added dropwise to cold aq. HCl (1 N, 200 mL). The precipitate formed was filtered, washed with cold aq. HCl (1 N, 25 mL), and dried under vacuum to give **41** as a yellow solid (2.14 g, 98%). 1H NMR (500 MHz, DMSO-d6) δ 8.76 (d, J = 1.4 Hz, 1H), 8.61 (t, J = 5.8 Hz, 1H), 7.86 (dd, J = 7.5, 3.4 Hz, 2H), 7.74-7.64 (m, 3H), 7.39 (tdd, J = 7.6, 3.9, 1.1 Hz, 2H), 7.31 (qd, J = 7.4, 1.2 Hz, 2H), 4.42-4.11 (m, 3H), 3.93 (ddd, J = 10.0, 8.1, 4.5 Hz, 1H), 3.31 (qd, J = 6.9, 2.9 Hz, 2H), 1.89-1.24 (m, 6H). 13C NMR (126 MHz, DMSO-d6) δ 174.0, 161.0, 159.6, 156.2, 148.8 (d, J = 239.9 Hz), 147.1 (d, J = 3.7 Hz), 143.8, 143.8, 140.7, 140.7, 140.5 (d, J = 8.5 Hz), 140.0 (dd, J = 5.1, 2.4 Hz), 138.7 (dd, J = 245.3, 6.5 Hz), 127.6, 127.6, 127.1, 127.1, 127.1, 127.0, 125.3, 125.3, 120.1, 120.1,

116.4, 110.5 (dd, J = 21.2, 2.4 Hz), 109.6 (d, J = 10.2 Hz), 65.6, 53.7, 46.7, 38.9, 30.4, 28.6, 23.1; HRMS (ESI-) *m/z* calcd for $C_{31}H_{25}F_2N_2O_8$ [M-H]$^-$: 591.1579, found: 591.1568.

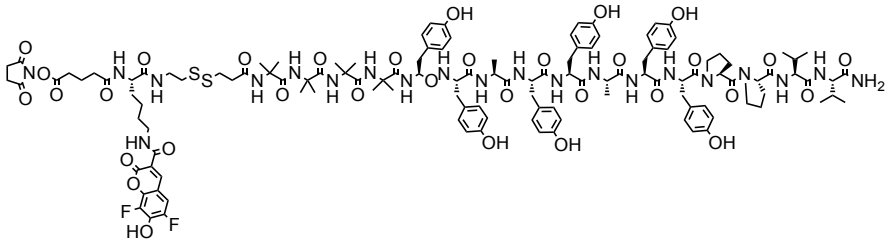

2,5-dioxopyrrolidin-1-yl (2*S*,5*S*,8*S*,11*S*,14*S*,17*S*,20*S*,23*R*,46*R*)-1-((*S*)-2-((*S*)-2-(((*S*)-1-(((*S*)-1-amino-3-methyl-1-oxobutan-2-yl)amino)-3-methyl-1-oxobutan-2-yl)carbamoyl)pyrrolidine-1-carbonyl)pyrrolidin-1-yl)-46-(4-(6,8-difluoro-7-hydroxy-2-oxo-2*H*-chromene-3-carboxamido)butyl)-2,5,11,14,20,23-hexakis(4-hydroxybenzyl)-8,17,26,26,29,29,32,32,35,35-decamethyl-1,4,7,10,13,16,19,25,28,31,34,37,45,48-tetradecaoxo-22-oxa-40,41-dithia-3,6,9,12,15,18,21,24,27,30,33,36,44-tridecaazadopentacontan-52-oate (18). Using the *General procedure for the synthesis of endosome disruptors for antibody conjugation*, Rink amide resin was used to produce **18** as a yellow solid. LRMS (ESI-) m/z calcd for $C_{126}H_{160}F_2N_{21}O_{33}S_2$ [M-H]$^-$: 2583.9, found: 2583.3.

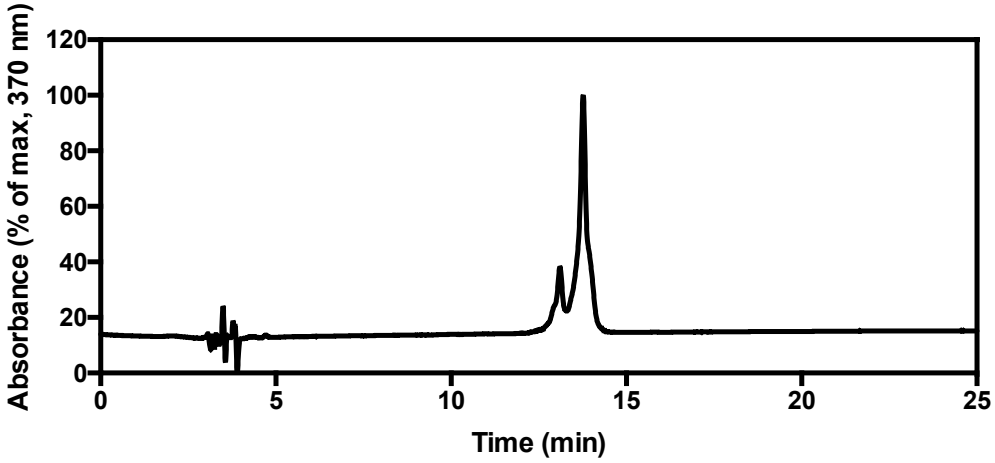

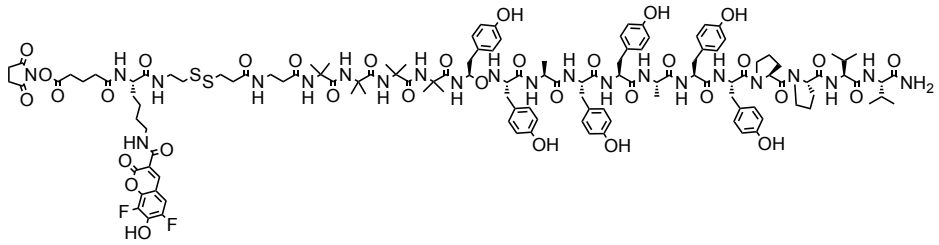

2,5-dioxopyrrolidin-1-yl (2*S*,5*S*,8*S*,11*S*,14*S*,17*S*,20*S*,23*R*,50*S*)-1-((*S*)-2-((*S*)-2-(((*S*)-1-(((*S*)-1-amino-3-methyl-1-oxobutan-2-yl)amino)-3-methyl-1-oxobutan-2-yl)carbamoyl)pyrrolidine-1-carbonyl)pyrrolidin-1-yl)-50-(4-(6,8-difluoro-7-hydroxy-2-oxo-2*H*-chromene-3-carboxamido)butyl)-2,5,11,14,20,23-hexakis(4-hydroxybenzyl)-8,17,26,26,29,29,32,32,35,35-decamethyl-1,4,7,10,13,16,19,25,28,31,34,37,41,49,52-pentadecaoxo-22-oxa-44,45-dithia-3,6,9,12,15,18,21,24,27,30,33,36,40,48,51-pentadecaazahexapentacontan-56-oate (19). Using the *General procedure for the synthesis of endosome disruptors for antibody conjugation*, Rink amide resin was used to produce **19** as a yellow solid. LRMS (ESI-) m/z calcd for $C_{128}H_{164}F_2N_{22}O_{34}S_2$ $[(M+2Na)/2]^-$: 1351.5, found: $[(M+2Na)/2]^-$: 1351.2.

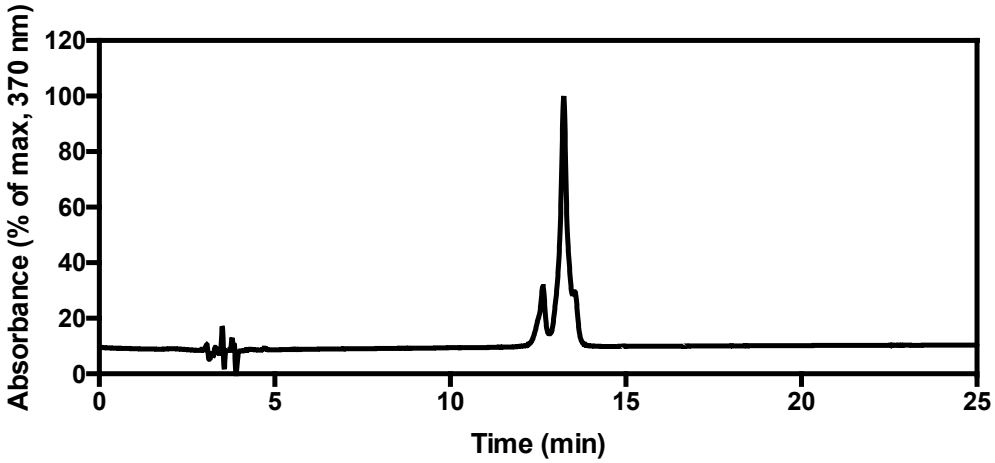

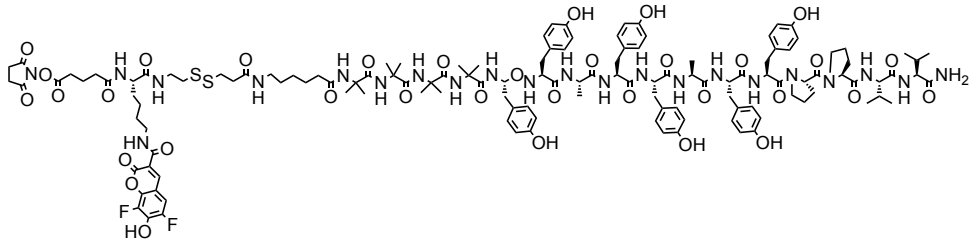

2,5-dioxopyrrolidin-1-yl (2*S*,5*S*,8*S*,11*S*,14*S*,17*S*,20*S*,23*R*,53*S*)-1-((*S*)-2-((*S*)-2-(((*S*)-1-(((*S*)-1-amino-3-methyl-1-oxobutan-2-yl)amino)-3-methyl-1-oxobutan-2-yl)carbamoyl)pyrrolidine-1-carbonyl)pyrrolidin-1-yl)-53-(4-(6,8-difluoro-7-hydroxy-2-oxo-2*H*-chromene-3-carboxamido)butyl)-2,5,11,14,20,23-hexakis(4-hydroxybenzyl)-8,17,26,26,29,29,32,32,35,35-decamethyl-1,4,7,10,13,16,19,25,28,31,34,37,44,52,55-pentadecaoxo-22-oxa-47,48-dithia-3,6,9,12,15,18,21,24,27,30,33,36,43,51,54-pentadecaazanonapentacontan-59-oate (20). Using the *General procedure for the synthesis of endosome disruptors for antibody conjugation*, Rink amide resin was used to produce **20** as a yellow solid. LRMS (ESI-) m/z calcd for $C_{131}H_{170}F_2N_{22}O_{34}S_2$ [(M-H)/2]$^-$: 1348.6, found: [(M-H)/2]$^-$: 1348.9.

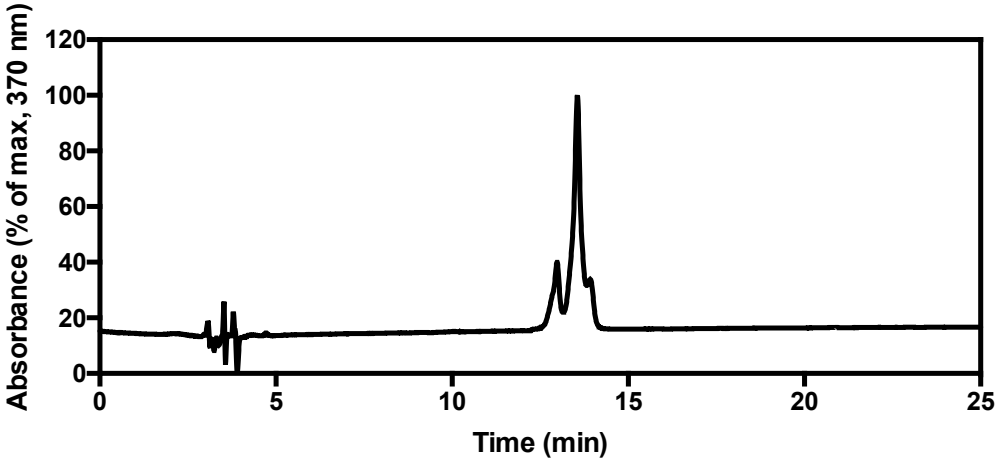

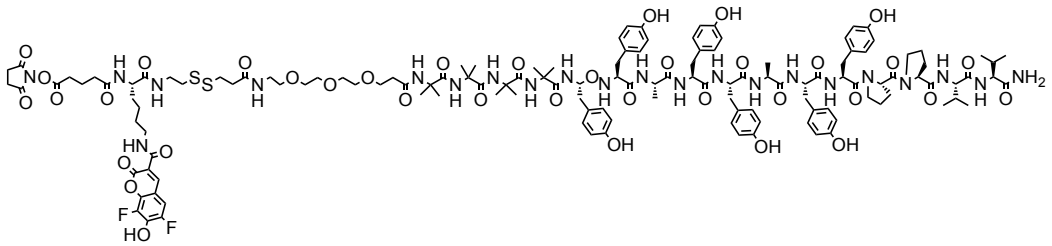

2,5-dioxopyrrolidin-1-yl (2*S*,5*S*,8*S*,11*S*,14*S*,17*S*,20*S*,23*R*,59*S*)-1-((*S*)-2-((*S*)-2-(((*S*)-1-(((*S*)-1-amino-3-methyl-1-oxobutan-2-yl)amino)-3-methyl-1-oxobutan-2-yl)carbamoyl)pyrrolidine-1-carbonyl)pyrrolidin-1-yl)-59-(4-(6,8-difluoro-7-hydroxy-2-oxo-2*H*-chromene-3-carboxamido)butyl)-2,5,11,14,20,23-hexakis(4-hydroxybenzyl)-8,17,26,26,29,29,32,32,35,35-decamethyl-1,4,7,10,13,16,19,25,28,31,34,37,50,58,61-pentadecaoxo-22,40,43,46-tetraoxa-53,54-dithia-3,6,9,12,15,18,21,24,27,30,33,36,49,57,60-pentadecaazapentahexacontan-65-oate (21). Using the *General procedure for the synthesis of endosome disruptors for antibody conjugation*, Rink amide resin was used to produce **21** as a yellow solid. LRMS (ESI-) m/z calcd for $C_{134}H_{176}F_2N_{22}O_{37}S_2$ $[(M+2Na)/2]^-$: 1417.6, found: $[(M+2Na)/2]^-$: 1417.2.

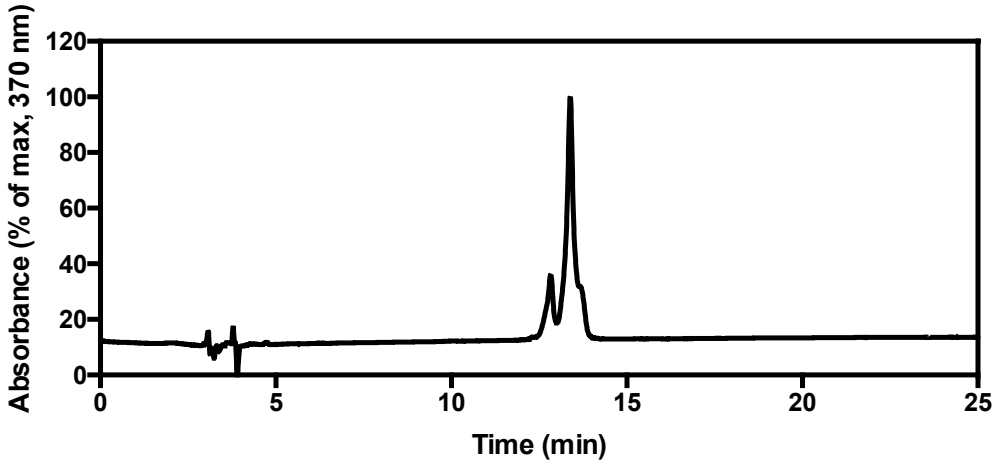

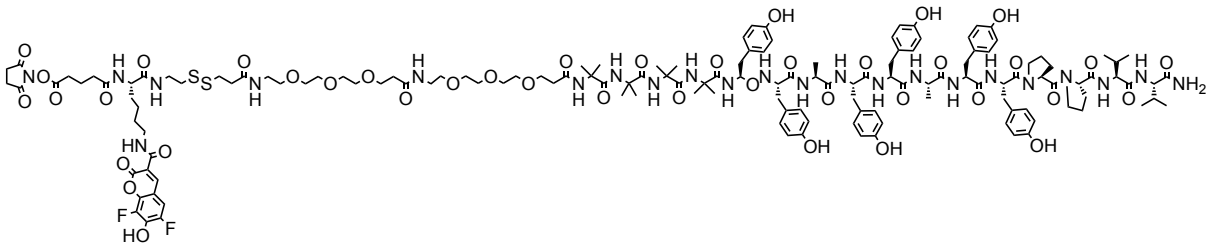

2,5-dioxopyrrolidin-1-yl (2*S*,5*S*,8*S*,11*S*,14*S*,17*S*,20*S*,23*R*,72*S*)-1-((*S*)-2-((*S*)-2-(((*S*)-1-(((*S*)-1-amino-3-methyl-1-oxobutan-2-yl)amino)-3-methyl-1-oxobutan-2-yl)carbamoyl)pyrrolidine-1-carbonyl)pyrrolidin-1-yl)-72-(4-(6,8-difluoro-7-hydroxy-2-oxo-2*H*-chromene-3-carboxamido)butyl)-2,5,11,14,20,23-hexakis(4-hydroxybenzyl)-8,17,26,26,29,29,32,32,35,35-decamethyl-1,4,7,10,13,16,19,25,28,31,34,37,50,63,71,74-hexadecaoxo-22,40,43,46,53,56,59-heptaoxa-66,67-dithia-3,6,9,12,15,18,21,24,27,30,33,36,49,62,70,73-hexadecaazaoctaheptacontan-78-oate (22). Using the *General procedure for the synthesis of endosome disruptors for antibody conjugation*, Rink amide resin was used to produce **22** as a yellow solid. LRMS (ESI+) m/z calcd for $C_{143}H_{193}F_2N_{23}O_{41}S_2$ $[(M+Na)/2]^+$: 1506.7, found: $[(M+2Na)/2]^+$: 1507.1.

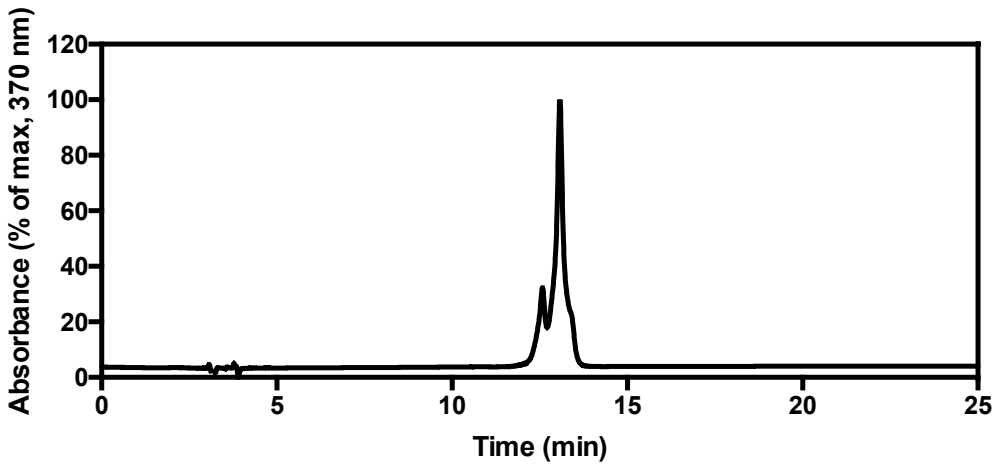

General procedure for the synthesis of membrane anchored endosome disruptors for antibody conjugation

The procedure outlined in *General procedure for solid phase peptide synthesis* was used to generate each peptide. Fmoc-Pacific Blue-L-Lysine (**41**) was used to incorporate this fluorophore into the structures. As illustrated in Scheme 2-2, after cleavage from the resin and purification by HPLC, each peptide was dissolved in ethanol (1 mL). 2,5-dioxopyrrolidin-1-yl 3-(pyridin-2-yldisulfaneyl)propanoate (10 eq) was added, and the reaction was stirred for 16 h. The solution was then concentrated *in vacuo* and purified by preparative HPLC.

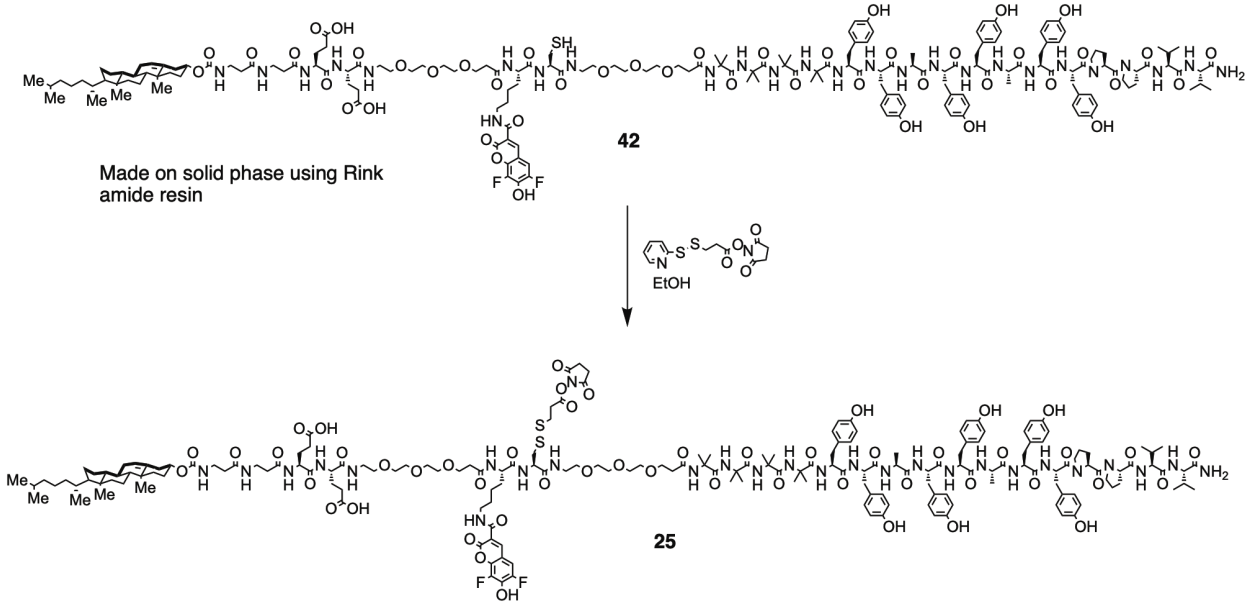

Scheme 2-2. Synthesis of membrane anchored endosome disruptors for antibody conjugation. Synthesis is shown for **25**, but the same method is also used for **28**.

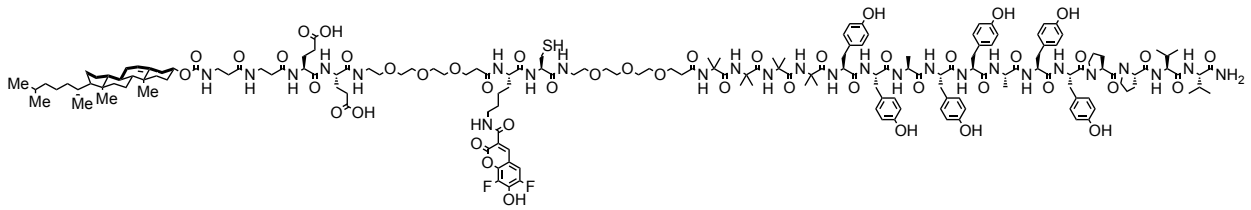

((3β-Cholest-5-en-3-yl)carbonyl)-β-Alanyl-β-Alanyl-L-Glutamyl-L-Glutamyl-mPEG-6-*N*-Pacific-Blue-Lysl-L-Cysteinyl-mPEG-Aminoisobutyl-Aminoisobutyl-Aminoisobutyl-Aminoisobutyl-L-Tyrosyl-L-Tyrosyl-L-Alanyl-L-Tyrosyl-L-Tyrosyl-L-Alanyl-L-Tyrosyl-L-Tyrosyl-L-Prolyl-LProlyl-L-Valyl-L-Valinamide (42). 42 was synthesized using standard SPPS conditions employing Rink amide MBHA resin (EMD or Aapptech, 0.5 mmol/g, 100 mg, 0.05 mmol). The peptide was cleaved from the resin with concurrent removal of *t*-Bu side chain protecting groups by treatment with TFA/TIPS/H2O (90:8:2) with shaking for 2 h. The solution, and the eluent from an additional wash with CH_2Cl_2, was collected. The solution was concentrated *in vacuo* and purified by preparative HPLC to afford **42** as a yellow solid (15 mg, 8% yield). LRMS (ESI+) m/z calcd for $C_{177}H_{248}F_2N_{26}O_{46}S$ $[(M+H)/2]^+$: 1773.6, found: 1773.1.

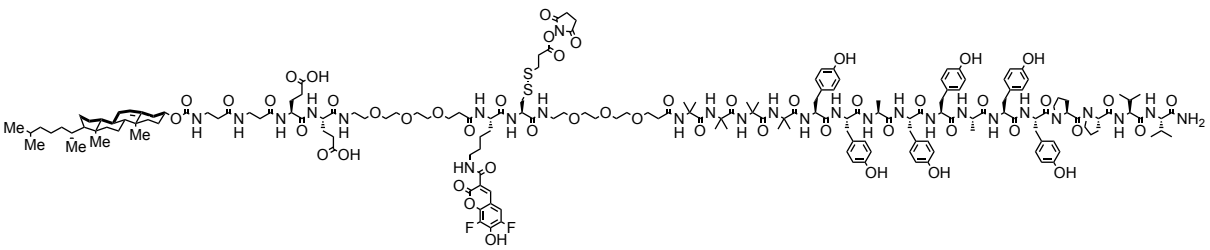

((3β-Cholest-5-en-3-yl)carbonyl)-β-Alanyl-β-Alanyl-L-Glutamyl-L-Glutamyl-mPEG-6-*N*-Pacific-Blue-Lysl-2,5-dioxopyrrolidin-1-yl-(*R*)-3-((2-(λ^2-azaneyl)-3-oxopropyl)disulfaneyl)propanoate-mPEG-Aminoisobutyl-Aminoisobutyl-Aminoisobutyl-Aminoisobutyl-L-Tyrosyl-L-Tyrosyl-L-Alanyl-L-Tyrosyl-L-Tyrosyl-L-Alanyl-L-Tyrosyl-L-Tyrosyl-L-Prolyl-LProlyl-L-Valyl-L-Valinamide (25). Using **42** and the *General procedure for the synthesis of membrane anchored endosome disruptors for antibody conjugation***, 25** was produced as a yellow solid (1.5 mg, 10% yield). LRMS (ESI+) m/z calcd for $C_{184}H_{255}F_2N_{27}O_{50}S_2$ $[(M+H)/2]^+$: 1872.4, found: $[(M+H)/2]^+$: 1872.7.

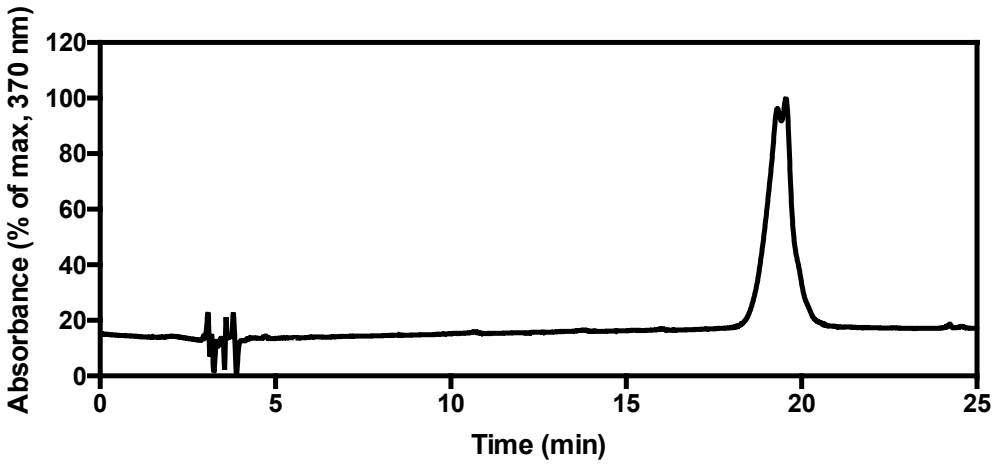

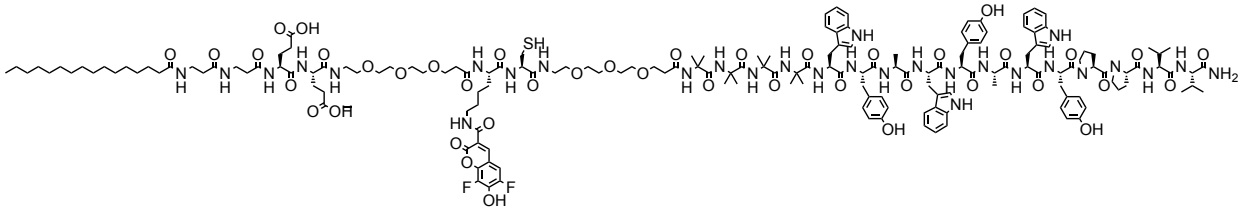

Palmitic-acid-β-Alanyl-β-Alanyl-L-Glutamyl-L-Glutamyl-mPEG-6-*N*-Pacific-Blue-Lysl-L-Cysteinyl-mPEG-Aminoisobutyl-Aminoisobutyl-Aminoisobutyl-Aminoisobutyl-L-Tryptophyl-L-Tyrosyl-L-Alanyl-L-Tryptophyl-L-Tyrosyl-L-Alanyl-L-Tryptophyl-L-Tyrosyl-L-Prolyl-LProlyl-L-Valyl-L-Valinamide (43). The same procedure used to synthesize **42** was used to generate **43** as a yellow solid. LRMS (ESI+) m/z calcd for $C_{171}H_{237}F_2N_{29}O_{42}S$ $[(M+H)/2]^+$: 1719.4, found: $[(M+H)/2]^+$: 1718.8.

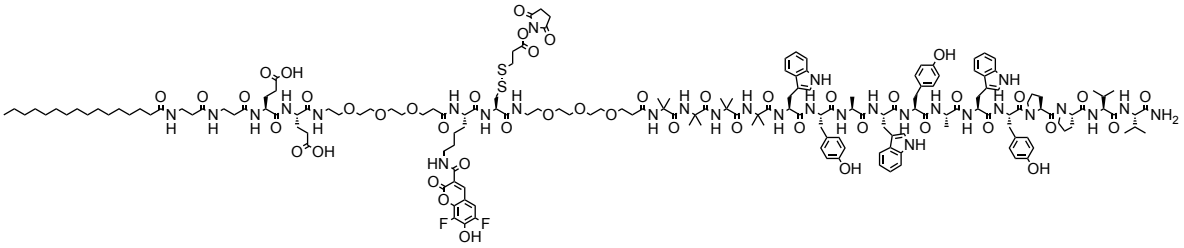

Palmitic-acid-β-Alanyl-β-Alanyl-L-Glutamyl-L-Glutamyl-mPEG-6-*N*-Pacific-Blue-Lysl-2,5-dioxopyrrolidin-1-yl-(*R*)-3-((2-(λ^2-azaneyl)-3-oxopropyl)disulfaneyl)propanoate-mPEG-Aminoisobutyl-Aminoisobutyl-

Aminoisobutyl-Aminoisobutyl-L-Tryptophyl-L-Tyrosyl-L-Alanyl-L-Tryptophyl-L-Tyrosyl-L-Alanyl-L-Tryptophyl-L-Tyrosyl-L-Prolyl-LProlyl-L-Valyl-L-Valinamide (28). The same procedure used to synthesize **25** was used to generate **28** as a yellow solid (1.0 mg, 8% yield). LRMS (ESI-) m/z calcd for $C_{178}H_{244}F_2N_{30}O_{46}S_2$[(M-H)/2]$^-$: 1821.1, found: 1821.0.

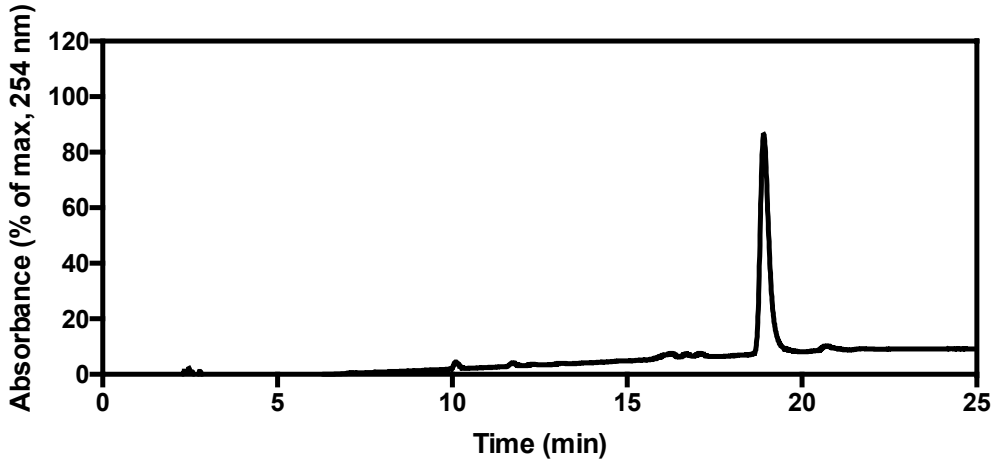

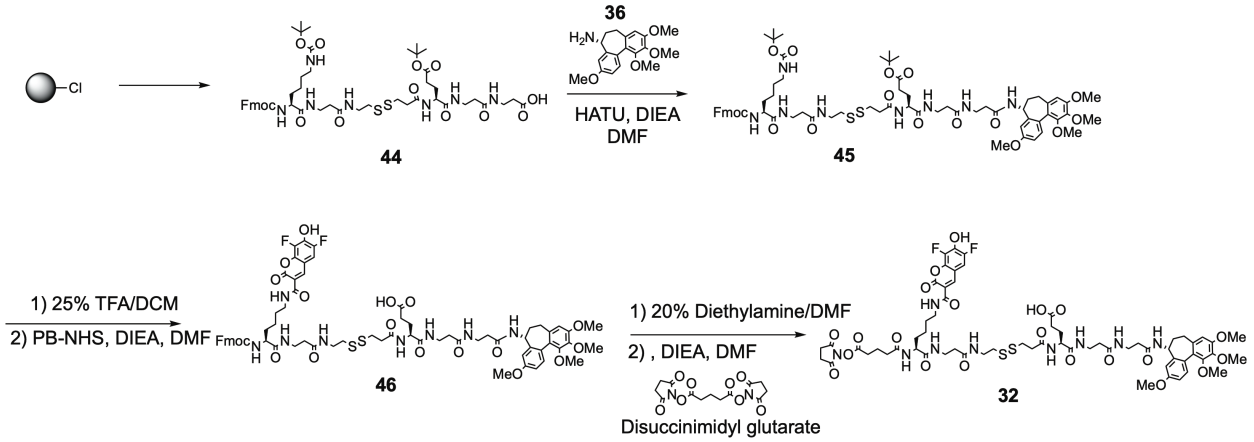

Scheme 2-3. Synthesis of **32**.

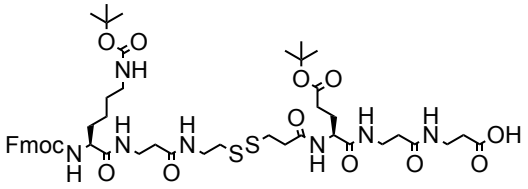

(10*S*,25*S*)-10-((((9*H*-fluoren-9-yl)methoxy)carbonyl)amino)-25-(3-(*tert*-butoxy)-3-oxopropyl)-2,2-dimethyl-4,11,15,23,26,30-hexaoxo-3-oxa-19,20-dithia-5,12,16,24,27,31-hexaazatetratriacontan-34-oic acid (44). 2-Chlorotrityl chloride resin (Aapptec, RTZ001, 0.1 mmol) was loaded with Fmoc-β-Ala-OH (124 mg, 0.4 mmol) under DIEA (143 µL, 0.8 mmol) as a base in DCM/DMF (2 mL/2 mL) overnight on a MiniBlock (600 rpm). After washing with DCM (4 mL, 4x), MeOH (4 mL) was added and stirred for 10 min to cap unreacted 2-CTC resin. Then solvent was drained from the vessel, and the resin was washed with DMF (4 mL, 4x). Cleavage of Fmoc was performed in 20% piperidine/DMF (4 mL) for 4 min twice. After washing with DMF (4 mL, 4x), a solution of HATU (152 mg, 0.4 mmol), Fmoc protected amino acid (0.4 mmol) and DIEA (143 µL, 0.8 mmol) in DMF (4 mL) was added to resin and stirred for 6 hours. The remaining amino acids were coupled on to resin in the same way with the exception of the disulfide linker, which was coupled as the acyl fluoride. Briefly, Fmoc-S-S-COOH (161 mg, 0.4 mmol) was dissolved in dry DCM (2 mL) in a 15 mL plastic conical tube. Drops of dry DMF were added until the solution was clear, followed by addition of DAST (63 µL, 0.48 mmol). The reaction was stirred for 30 min at 0 °C and quenched by ice water. The organic layer was washed with brine and dried over Na_2SO_4. The crude solution was concentrated by rotovap and redissolved in DMF. The resulting solution was added immediately to the resin for conjugation overnight. After all amino acid and linker were successfully installed on the resin, a solution of AcOH/ TFE/DCM (1:2:7, 4 mL) was added to the resin and shaken for 3 hours to cleave the compound. After concentration under rotavap, the crude mixture was purified by HPLC and lyophilized to yield desired compound **44** as white solid (50 mg, 49% yield). ^{1}H NMR (500 MHz, DMSO-d_6) 12.20 (brs, 1H), 8.15-8.00 (m, 2H),

7.96-7.84 (m, 5H), 7.73 (t, *J* = 6.5 Hz, 2H), 7.42 (t, *J* = 7.3 Hz, 3H), 7.33 (t, *J* = 7.7 Hz, 2H), 6.76 (t, *J* = 5.9 Hz, 1H), 4.34-4.13 (m, 5H), 3.97-3.81 (m,2H), 3.47-3.11 (m, 8H), 3.00-2.81 (m, 4H), 2.75 (t, *J* = 6.9 Hz, 2H), 2.56-2.51 (m, 2H), 2.36 (t, *J* = 7.1 Hz, 2H), 2.30-2.11 (m, 6H), 1.93-1.76 (m, 1H), 1.76-1.62 (m, 1H), 1.62-1.43 (m, 2H), 1.37 (s, 9H), 1.36 (s, 9H), 1.29-1.15 (m, 2H). ^{13}C NMR (126 MHz, DMSO-d_6) δ 172.9, 171.9, 171.6, 170.9, 170.4, 170.3, 170.1, 155.9, 155.5, 143.9, 143.8, 140.7, 127.6, 127.0, 125.3, 120.1, 79.6, 77.3, 65.6, 54.7, 51.8, 46.7, 37.9, 37.1, 35.3, 35.2, 35.2, 35.0, 34.9, 34.7, 33.9, 33.8, 31.7, 31.3, 29.2, 28.3, 27.7, 27.5, 22.8. LRMS (ESI+) m/z calcd for $C_{49}H_{71}N_7O_{13}S_2$ $[M+H]^+$: 1030.5, found: 1030.5.

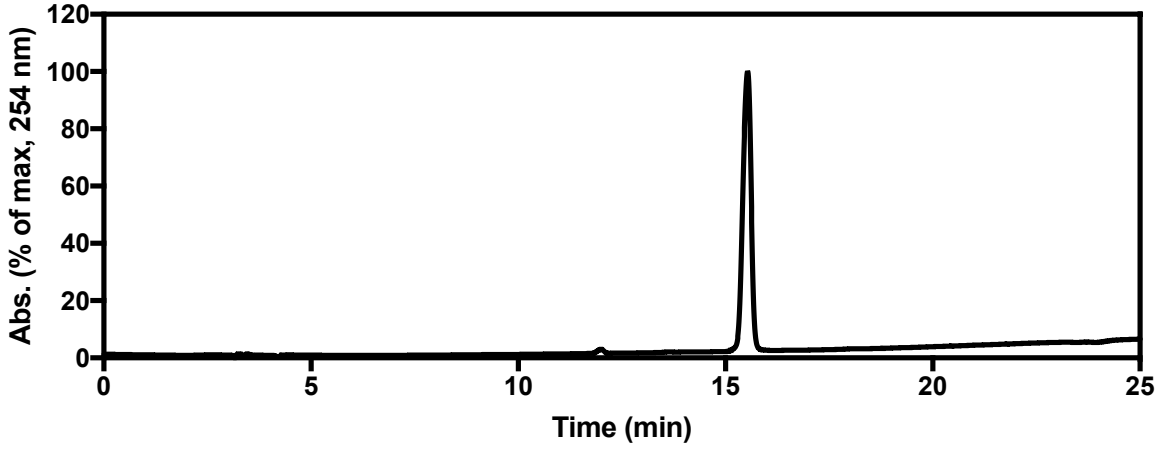

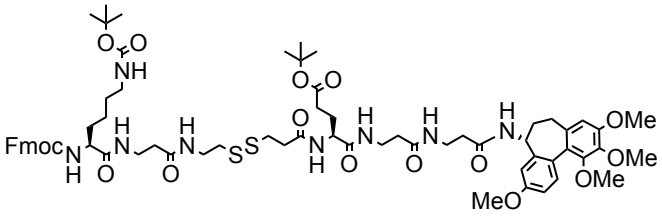

***tert*-butyl-(10*S*,25*S*)-10-((((9*H*-fluoren-9-yl)methoxy)carbonyl)amino)-2,2-dimethyl-4,11,15,23-tetraoxo-25-((3-oxo-3-((3-oxo-3-(((5*R*)-3,9,10,11-tetramethoxy-6,7-dihydro-5*H*-dibenzo[*a*,*c*][7]annulen-5-yl)amino)propyl)amino)propyl)carbamoyl)-3-**

oxa-19,20-dithia-5,12,16,24-tetraazaoctacosan-28-oate (45). To a solution of **44** (40 mg, 0.039 mmol) in dry DMF (2 mL) was added HATU (30 mg, 0.078 mmol), DIEA (35 µL, 0.19 mmol) and **36** (26 mg, 0.078 mmol). The mixture was stirred overnight and concentrated under rotavap. The crude was purified by HPLC and lyophilized to give desired compound **45** as a white solid (38 mg, 73% yield). ^{1}H NMR (500 MHz, DMSO-d_6) 8.39 (d, *J* = 8.4 Hz, 1H), 8.13-8.00 (m, 2H), 7.94-7.84 (m, 5H), 7.72 (t, *J* = 6.6 Hz, 2H), 7.45-7.36 (m, 3H), 7.32 (t, *J* = 7.5 Hz, 2H), 7.24 (d, *J* = 8.1 Hz, 1H), 6.90-6.83 (m, 2H), 6.81-6.69 (m, 2H), 4.52 (dt, *J* = 11.9, 7.6 Hz, 1H), 4.35-4.15 (m, 5H), 3.95-3.84 (m, 2H), 3.82 (s, 3H), 3.77 (s, 3H), 3.77 (s, 3H), 3.47 (s, 3H), 3.34-3.15 (m, 8H), 2.88 (tt, *J* = 6.9, 4.4 Hz, 4H), 2.75 (t, *J* = 7.0 Hz, 2H), 2.59-2.52 (m, 2H), 2.48-2.45 (m, 1H), 2.39-2.27 (m, 2H), 2.27-2.09 (m, 7H), 2.09-1.98 (m, 1H), 1.91-1.76 (m, 2H), 1.72-1.62 (m, 1H), 1.61-1.43 (m, 2H), 1.36 (s, 9H), 1.36 (s, 9H), 1.29-1.14 (m, 2H). ^{13}C NMR (126 MHz, DMSO-d_6) δ 171.9, 171.3, 170.9, 170.4, 170.2, 170.1, 169.6, 158.4, 155.9, 152.1, 150.3, 143.9, 143.8, 141.8, 140.7, 140.6, 134.7, 130.5, 127.6, 127.1, 126.1, 125.3, 124.3, 120.1, 110.8, 109.3, 108.1, 79.7, 77.3, 65.6, 60.5, 55.8, 54.9, 54.7, 51.8, 48.2, 46.7, 38.3, 37.9, 37.1, 35.4, 35.3, 35.3, 35.2, 35.2, 35.1, 34.9, 33.9, 31.7, 31.3, 30.1, 29.2, 28.3, 27.7, 27.5, 22.9. LRMS (ESI+) *m/z* calcd for $C_{68}H_{92}N_8O_{16}S_2$ $[M+H]^+$: 1341.6, found: 1341.7.

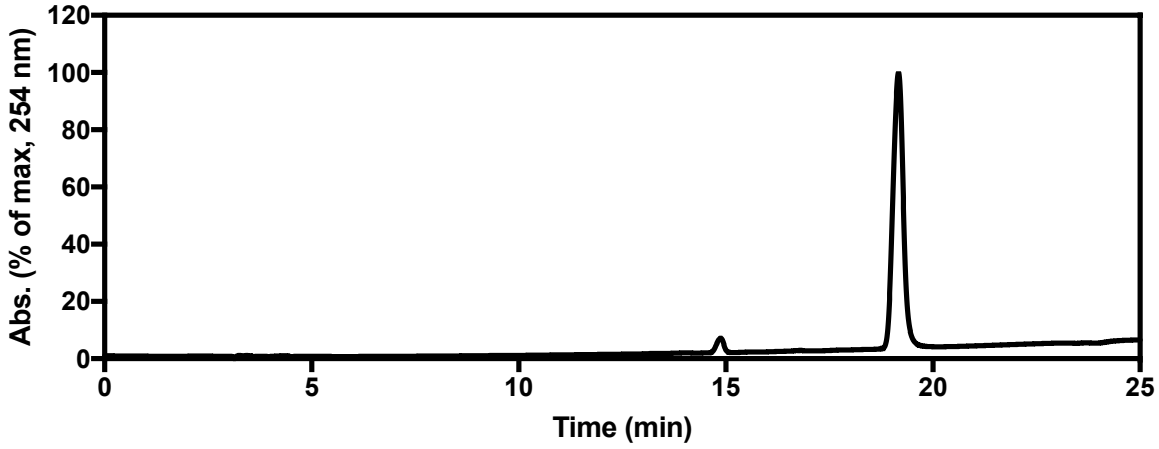

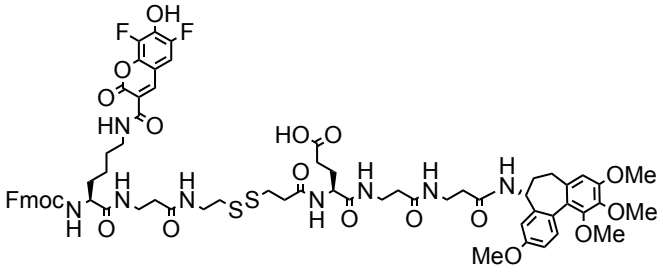

(5*S*,20*S*)-5-(4-(6,8-difluoro-7-hydroxy-2-oxo-2*H*-chromene-3-carboxamido)butyl)-1-(9*H*-fluoren-9-yl)-3,6,10,18-tetraoxo-20-((3-oxo-3-((3-oxo-3-(((5*R*)-3,9,10,11-tetramethoxy-6,7-dihydro-5*H*-dibenzo[*a*,*c*][7]annulen-5-yl)amino)propyl)amino)propyl)carbamoyl)-2-oxa-14,15-dithia-4,7,11,19-tetraazatricosan-23-oic acid (46). 45 (30 mg, 0.022 mmol) was dissolved in 25% TFA/DCM (2 mL) and stirred for 2 hours. The solvent was removed by rotavap and the solid was dissolved in dry DMF (2 mL). Pacific Blue-NHS (11 mg, 0.034 mmol) and DIEA (8 µL, 0.045 mmol) were then added. The solution was stirred overnight. After completion of the reaction, the solvent was removed by rotavap. The crude material was purified by HPLC and lyophilized to give the desired compound **46** as a yellow solid (21 mg, 67% yield). ^{1}H NMR (500 MHz, DMSO-d_6) 12.08 (brs, 1H), 8.75 (s, 1H), 8.59 (t, J = 5.8 Hz, 1H), 8.39 (d, J = 8.4 Hz, 1H), 8.09 (d, J = 8.1 Hz, 1H), 8.04 (t, J = 5.7 Hz, 1H), 7.97-7.88

(m, 3H), 7.85 (dd, *J* = 7.6, 3.8 Hz, 2H), 7.70 (t, *J* = 7.8 Hz, 3H), 7.45 (d, *J* = 8.3 Hz, 1H), 7.42-7.36 (m, 2H), 7.35-7.27 (m, 2H), 7.24 (d, *J* = 8.2 Hz, 1H), 6.90-6.83 (m, 2H), 6.76 (s, 1H), 4.57-4.48 (m, 1H), 4.35-4.26 (m, 1H), 4.23-4.12 (m, 4H), 3.96-3.89 (m, 1H), 3.82 (s, 3H), 3.77 (s, 3H), 3.76 (s, 3H), 3.47 (s, 3H), 3.34-3.14 (m, 10H), 2.94-2.81 (m, 2H), 2.79-2.70 (m, 2H), 2.56-2.51 (m, 2H), 2.48-2.43 (m, 1H), 2.39-2.28 (m, 2H), 2.27-2.10 (m, 7H), 2.09-1.98 (m, 1H), 1.92-1.80 (m, 2H), 1.74-1.58 (m, 2H), 1.58-1.44 (m, 3H), 1.40-1.25 (m, 2H). ^{13}C NMR (126 MHz, DMSO-d_6) δ 173.9, 171.9, 171.0, 170.4, 170.3, 170.1, 169.6, 160.9, 159.6, 158.4, 158.3, 158.0, 157.77, 157.5, 155.9, 152.1, 150.3, 147.9, 147.1, 143.8, 141.8, 140.7, 140.6, 140.5, 134.7, 130.5, 127.6, 127.6, 127.0, 126.1, 125.34, 125.3, 124.3, 120.1, 117.7, 116.4, 110.8, 110.5, 110.4, 109.6, 109.4, 109.3, 108.1, 65.6, 60.5, 55.8, 54.9, 54.5, 51.9, 48.2, 46.7, 38.3, 37.9, 37.1, 35.4, 35.3, 35.3, 35.2, 35.1, 34.9, 33.9, 31.7, 30.2, 30.1, 28.7, 27.5, 23.0. LRMS (ESI+) *m/z* calcd for $C_{69}H_{78}F_2N_8O_{18}S_2$ $[M+H]^+$: 1409.5, found: 1409.5.

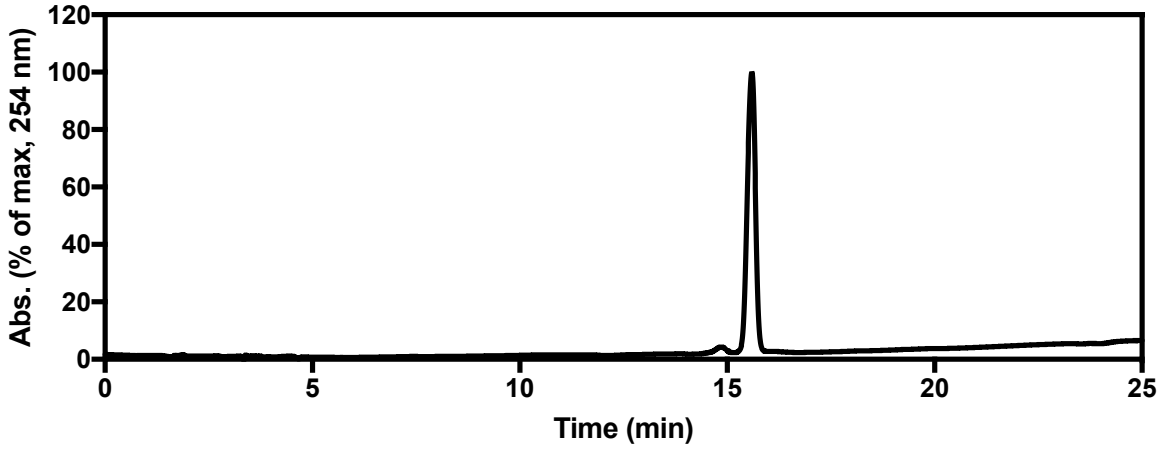

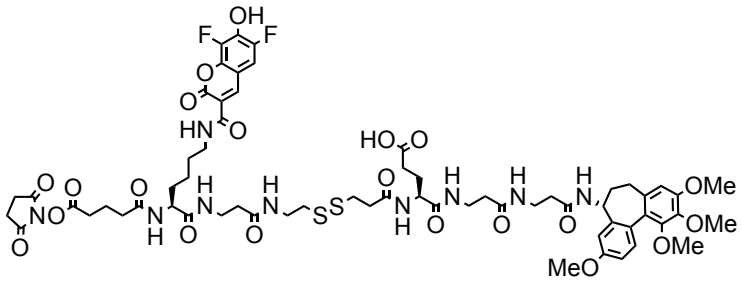

(7*S*,22*S*)-1-(6,8-difluoro-7-hydroxy-2-oxo-2*H*-chromen-3-yl)-7-(5-((2,5-dioxopyrrolidin-1-yl)oxy)-5-oxopentanamido)-1,8,12,20-tetraoxo-22-((3-oxo-3-((3-oxo-3-(((5*R*)-3,9,10,11-tetramethoxy-6,7-dihydro-5*H*-dibenzo[*a*,*c*][7]annulen-5-yl)amino)propyl)amino)propyl)carbamoyl)-16,17-dithia-2,9,13,21-tetraazapentacosan-25-oic acid (32). 46 (15 mg, 0.011mmol) was dissolved in 20% Diethylamine in DMF (1 mL) and stirred for 1 hour. After MS confirmed full cleavage of the Fmoc protecting group, the solvent was removed by rotavap. The crude material was then dissolved in DMF and disuccinimidyl glutarate (35 mg, 0.11 mmol) and DIEA (19 µL, 0.11 mmol) were added. The solution was stirred overnight and concentrated. The crude material was purified by HPLC and lyophilized to give desired product **32** as light yellow solid (7 mg, 47% yield). ^{1}H NMR (500 MHz, DMSO-d_6) 12.07 (brs, 1H), 8.78 (d, J = 1.3 Hz, 1H), 8.58 (t, J = 5.8 Hz, 1H), 8.39 (d, J = 8.4 Hz, 1H), 8.10 (d, J = 8.1 Hz, 1H), 8.04 (t, J = 5.7 Hz, 1H), 7.99-7.83 (m, 4H), 7.75 (dd, J = 10.4, 2.0 Hz, 1H), 7.24 (d, J = 8.1 Hz, 1H), 6.86 (d, J = 8.5 Hz, 2H), 6.76 (s, 1H), 4.60-4.46 (m, 1H), 4.29-4.10 (m, 3H), 3.82 (s, 3H), 3.78 (s, 3H), 3.77 (s, 3H), 3.47 (s, 3H), 3.35-3.14 (m, 11H), 2.92-2.84 (m, 2H), 2.80 (s, 2H), 2.75 (t, J = 6.9 Hz, 2H), 2.67 (t, J = 7.5 Hz, 1H), 2.54 (s, 4H), 2.49-2.44 (m, 1H), 2.39-2.29 (m, 2H), 2.27-2.10 (m, 8H), 2.07-1.99 (m, 1H), 1.92-1.78 (m, 3H), 1.74-1.57 (m, 2H), 1.56-1.43 (m, 3H), 1.37-1.19 (m, 2H). ^{13}C NMR (126 MHz, DMSO-d_6) δ 173.9, 171.7, 171.1, 170.9, 170.4, 170.2, 170.2, 170.2, 170.1, 169.6, 168.7, 160.9, 159.6, 158.4, 158.1,

157.8, 152.1, 150.3, 147.1, 141.8, 140.5, 134.7, 130.5, 126.1, 124.3, 117.5, 116.5, 110.8, 108.1, 99.5, 60.5, 55.8, 54.9, 52.4, 51.9, 48.2, 40.4, 38.3, 37.9, 37.1, 35.4, 35.3, 35.3, 35.2, 35.1, 34.90, 33.8, 33.5, 31.7, 31.4, 30.1, 30.07, 29.6, 28.7, 27.5, 25.4, 22.9, 20.4. LRMS (ESI+) *m/z* calcd for $C_{63}H_{77}F_2N_9O_{21}S_2$ $[M+H]^+$: 1398.5, found: 1398.5.

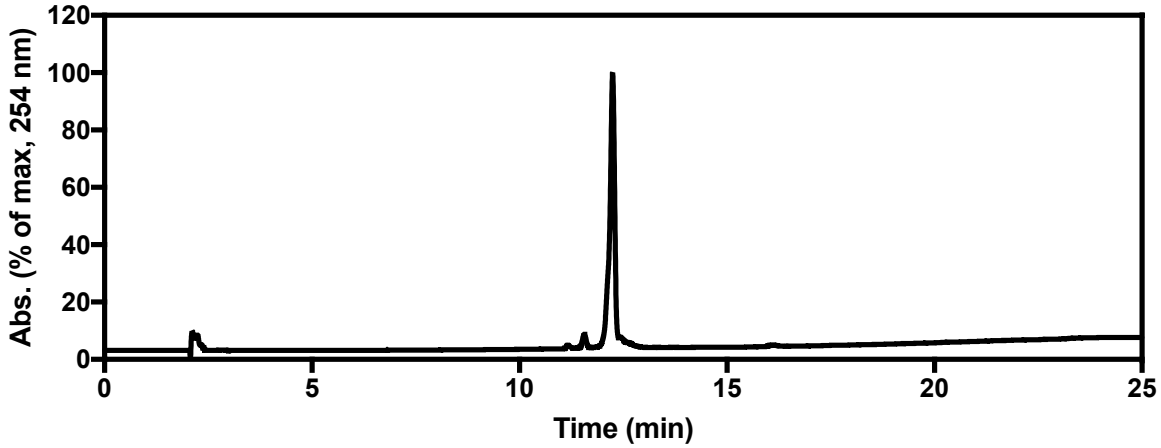

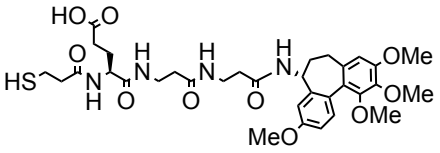

(4*S*)-4-(3-mercaptopropanamido)-5-oxo-5-((3-oxo-3-((3-oxo-3-(((5*R*)-3,9,10,11-tetramethoxy-6,7-dihydro-5*H*-dibenzo[*a*,*c*][7]annulen-5-yl)amino)propyl)amino)propyl)amino)pentanoic acid (37). 46 (6 mg, 0.004 mmol) was dissolved in DMSO (0.4 mL). DL-Dithiothreitol (DTT, 13 mg, 0.085 mmol) was added and the solution was stirred overnight. The next morning, the crude mixture was purified by HPLC and lyophilized to yield **37** as a white solid (2 mg, 68% yield). ^{1}H NMR (500 MHz, DMSO-d_6) δ 8.39 (d, *J* = 8.4 Hz, 1H), 8.10 (d, *J* = 8.0 Hz, 1H), 8.05 (d, *J* = 8.1 Hz, 1H), 7.89 (dt, *J* = 10.9, 5.8 Hz, 2H), 7.24 (d, *J* = 8.1 Hz, 1H), 6.87 (d, *J* = 8.2 Hz, 1H), 6.77 (s, 1H), 4.57 – 4.48 (m, 1H), 4.0 (td, *J* = 8.4, 5.4 Hz, 1H), 3.82 (s, 3H), 3.78 (s, 3H), 3.77 (s,

3H), 3.47, (s, 3H), 3.30 – 3.12 (m, 4H), 2.95 – 2.85 (m, 1H), 2.78 – 2.68 (m, 1H), 2.68 – 2.60 (m, 1H), 2.49 – 2.41 (m, 2H), 2.37 – 2.28 (m, 2H), 2.24 – 2.13 (m, 4H), 2.10 – 1.99 (m, 1H), 1.88 (d, *J* = 6.1 Hz, 2H), 1.77 – 1.63 (m, 2H), 1.30 – 1.21 (m, 1H). ^{13}C NMR (126 MHz, DMSO) δ 173.9, 171.2, 170.4, 170.3, 169.6, 158.4, 152.1, 150.3, 141.8, 140.6, 134.8, 130.5, 126.1, 124.3, 110.8, 109.3 108.0, 60.5, 55.8, 54.9, 51.9, 48.2, 40.0, 39.9, 39.7, 39.5, 39.3, 39.2, 39.0, 38.3, 35.4, 35.3, 35.3, 35.1, 30.2, 30.2, 27.4, 25.2, 19.9. HRMS (ESI+) *m/z* calcd for $C_{33}H_{44}N_4O_{10}S$ $[M+H]^+$: 689.2856, found: 689.2849.

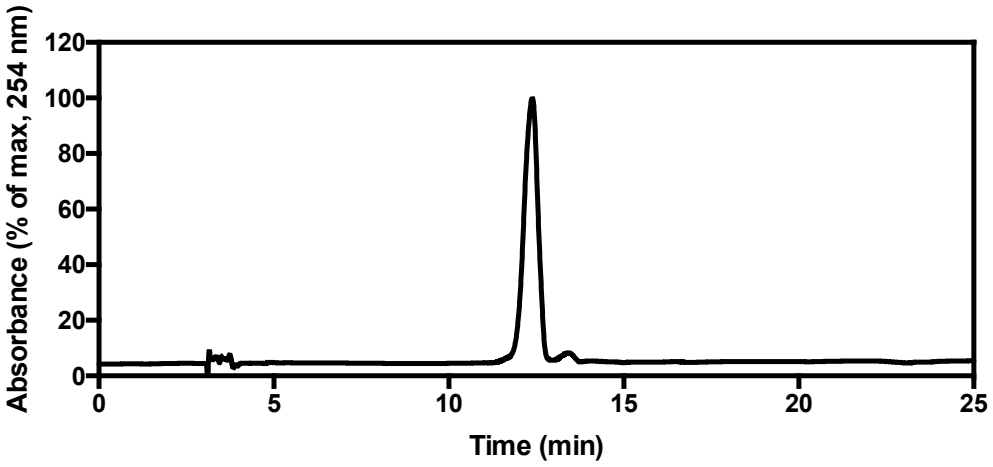

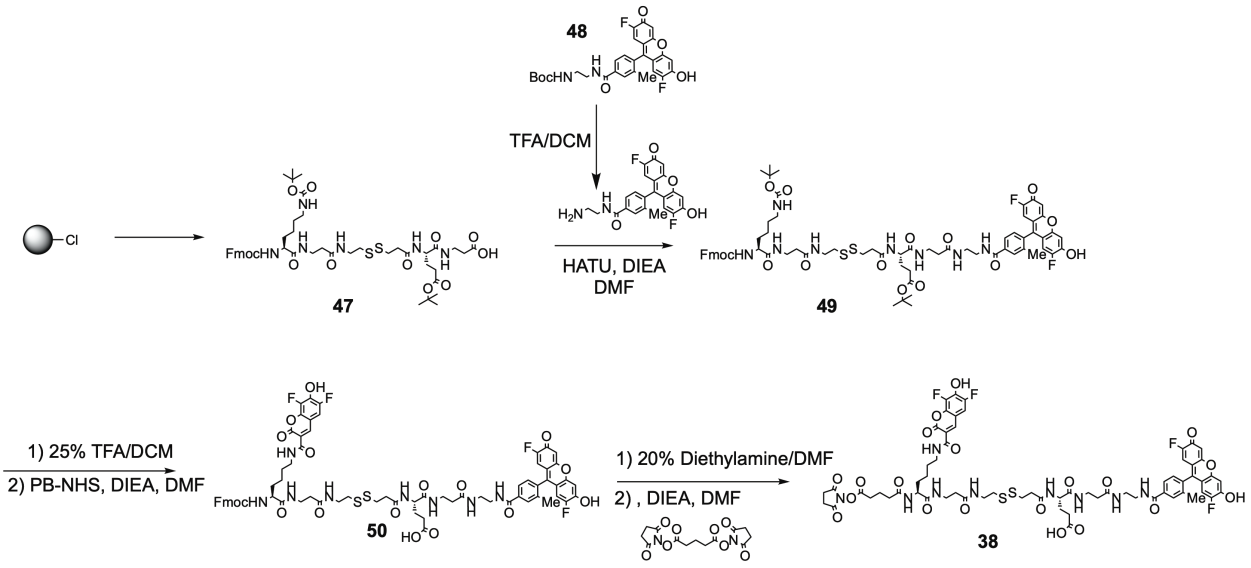

Scheme 2-4. Synthesis of **38**.

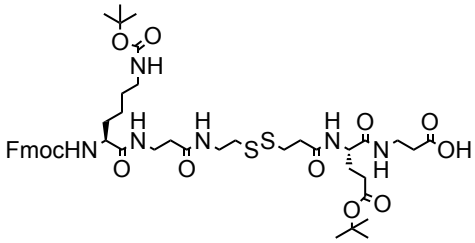

(10*S*,25*S*)-10-((((9*H*-fluoren-9-yl)methoxy)carbonyl)amino)-25-(3-(*tert*-butoxy)-3-oxopropyl)-2,2-dimethyl-4,11,15,23,26-pentaoxo-3-oxa-19,20-dithia-5,12,16,24,27-pentaazatriacontan-30-oic acid (47). 2-Chlorotrityl resin (0.1 mmol) was swelled for 10 min in dry DCM then loaded with Fmoc-β-Ala-OH (124 mg, 0.4 mmol) under DIEA (143 µL, 0.8 mmol) as a base in dry DCM/DMF (2 mL/2 mL) overnight on a MiniBlock (600 rpm). After washing with DCM (4 mL, 4x), MeOH (4 mL) was added and stirred for 10 min to cap unreacted 2-CTC resin. Then solvent was drained, and the resin was washed with DMF (4 mL, 4x). Cleavage of Fmoc was done in 20% piperidine/DMF (4 mL) for 4 min twice. After washing with DMF (4 mL, 4x), a solution of HATU (152 mg, 0.4 mmol), Fmoc protected amino acid (0.4 mmol) and DIEA (143 µL, 0.8 mmol) in DMF (4 mL) was added to resin and stirred for 6 hours. The rest of the amino acids were coupled on to resin in the same way except conjugation of the disulfide linker starts from synthesis of disulfide acyl fluoride. Briefly, Fmoc-S-S-COOH (80 mg, 0.2 mmol) is dissolved in dry DCM (2 mL) in a 15 mL plastic conical tube. Drops of dry DMF were added until the solution cleared, followed by addition of DAST (63 µL, 0.48 mmol). The reaction was stirred for 30 min at 0 °C and quenched by ice water. The organic layer was washed with brine then dried over Na_2SO_4. The crude was concentrated by rotovap and re-dissolved in DMF. The resulting solution was added immediately to the resin for conjugation overnight. After all amino acids were successfully installed on the resin, a solution of AcOH/ TFE/DCM (1:2:7, 4 mL) was added to the resin and shaken for 3 hours to cleave the compound. After

concentration under rotovap, the crude product was purified by HPLC and lyophilized to yield desired compound **47** as white solid (34 mg, 35% yield). ^{1}H NMR (500 MHz, DMSO-d_6) 12.23 (brs, 1H), 8.09 (d, *J* = 8.1 Hz, 1H), 8.05 (t, *J* = 5.7 Hz, 1H), 7.94 (t, *J* = 5.6 Hz, 1H), 7.89 (d, *J* = 7.4 Hz, 3H), 7.72 (t, *J* = 6.5 Hz, 2H), 7.42 (t, *J* = 7.4 Hz, 3H), 7.33 (t, *J* = 7.5 Hz, 2H), 6.75 (t, *J* = 5.9 Hz, 1H), 4.31-4.18 (m, 5H), 3.93-3.84 (m, 2H), 3.35-3.17 (m, 6H), 2.93-2.83 (m, 4H), 2.75 (t, *J* = 6.9 Hz, 2H), 2.54 (q, *J* = 4.0, 3.1 Hz, 2H), 2.37 (t, *J* = 6.9 Hz, 2H), 2.24 (t, *J* = 7.0 Hz, 2H), 2.22-2.15 (m, 2H), 1.88-1.80 (m, 1H), 1.72-1.63 (m, 1H), 1.61 – 1.52 (m, 2H), 1.37 (s, 9H), 1.36 (s, 9H), 1.27-1.16 (m, 1H). ^{13}C NMR (126 MHz, DMSO) δ 172.8, 171.9, 171.6, 171.0, 170.4, 170.1, 155.9, 155.6, 143.9, 143.8, 140.7, 127.6, 127.1, 125.3, 120.1, 79.7, 77.3, 65.6, 54.7, 51.7, 46.7, 40.0, 39.8, 39.7, 39.5, 39.3, 39.2, 39.0, 37.9, 37.1, 35.2, 35.2, 34.9, 34.8, 33.9, 33.7, 31.7, 31.3, 29.2, 283, 27.7, 27.45 22.9. HRMS (ESI+) m/z calcd for $C_{46}H_{66}N_6O_{12}S_2$ $[M+H]^+$: 959.4258, found: 959.4267.

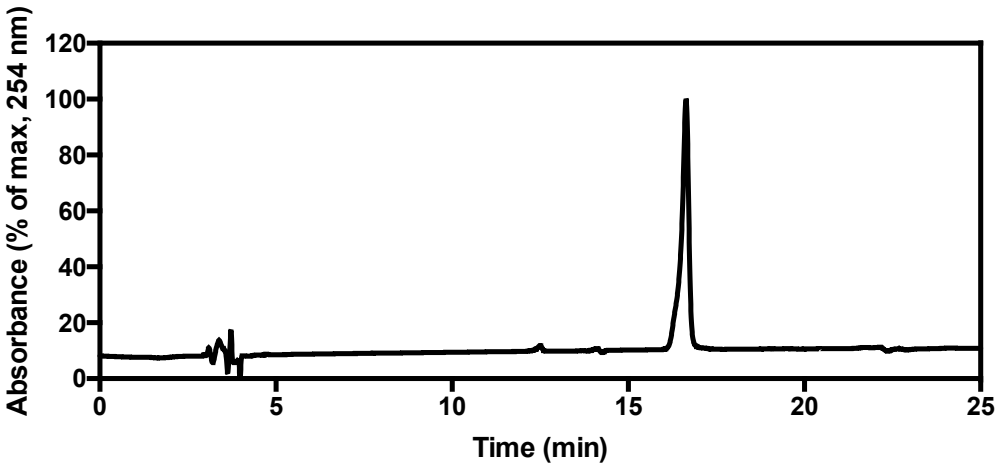

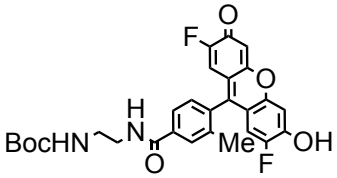

***tert*-Butyl (2-(4-(2,7-difluoro-6-hydroxy-3-oxo-3H-xanthen-9-yl)-3-methylbenzamido)ethyl)carbamate (48).** As reported in the thesis of Dr. Molly Lee, to a solution of 4-Carboxy Pennsylvania Green succinimidyl ester (95 mg, 0.2 mmol), prepared as previously reported,[49] in DMF (1 mL) was added DIEA (125 µL, 0.5 mmol) and N-Boc-ethylenediamine (47 µL, 0.3 mmol). The reaction mixture was stirred at 22 °C for 4 h. The reaction was dried by rotovap followed by purification by column chromatography on silica gel (eluent: DCM/MeOH (15:1) with 1% acetic acid) to afford **48** (78 mg, 75%) as an orange solid. ^{1}H NMR (500 MHz, DMSO-d_6) δ 8.60 (t, J = 5.7 Hz, 1H), 7.96 (s, 1H), 7.88 (d, J = 7.9 Hz, 1H), 7.38 (d, J = 7.9 Hz, 1H), 6.92 (t, J = 5.8 Hz, 1H), 6.84 (d, J = 6.6 Hz, 2H), 6.61 (d, J = 11.1 Hz, 2H), 3.34 (q, J = 6.2 Hz, 2H), 3.15 (q, J = 6.3 Hz, 2H), 2.08 (s, 3H), 1.38 (s, 9H). ^{13}C NMR (126 MHz, DMSO-d_6) δ 165.83, 155.78, 149.38, 149.33, 149.28, 135.93, 135.75, 134.27, 129.53, 129.02, 125.13, 111.35, 105.15, 105.12, 77.69, 40.42, 28.22, 19.08. HRMS (ESI-) m/z calcd for $C_{28}H_{25}F_2N_2O_6$ [M-H]$^-$: 523.1618, found: 523.1668.

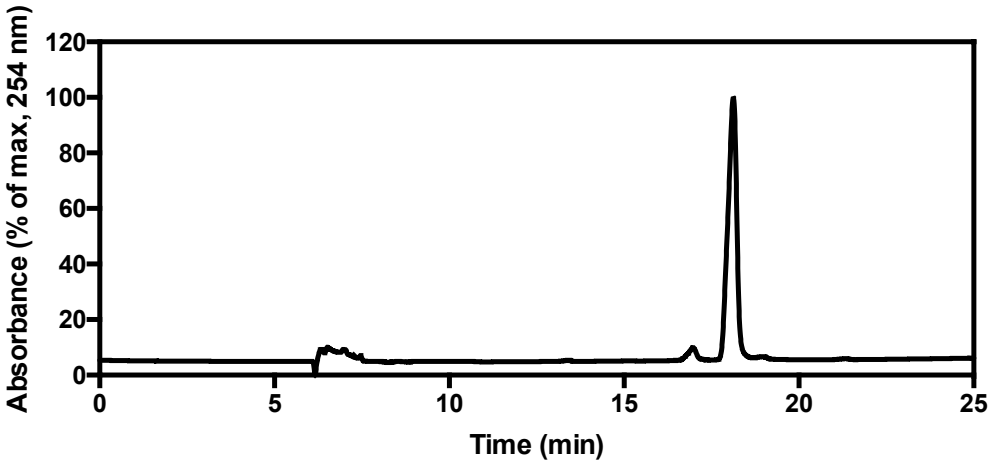

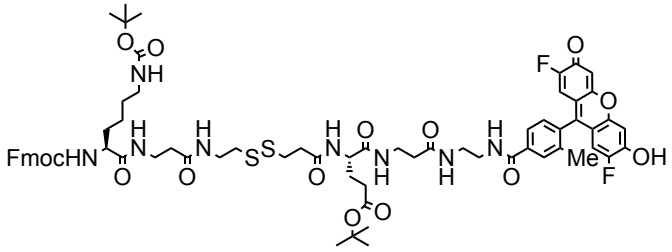

***tert*-butyl (10*S*,25*S*)-10-((((9*H*-fluoren-9-yl)methoxy)carbonyl)amino)-25-((3-((2-(4-(2,7-difluoro-6-hydroxy-3-oxo-3*H*-xanthen-9-yl)-3-methylbenzamido)ethyl)amino)-3-oxopropyl)carbamoyl)-2,2-dimethyl-4,11,15,23-tetraoxo-3-oxa-19,20-dithia-5,12,16,24-tetraazaoctacosan-28-oate (49).** To a solution of **47** (34 mg, 0.035 mmol) in dry DMF (1 mL) was added HATU (27 mg, 0.071 mmol), and DIEA (33 µL, 0.18 mmol). Separately, **48** (37 mg, 0.071 mmol) was treated with a solution of TFA / DCM (0.5 mL, 50:50) for 30 min. The mixture was concentrated under vacuum and washed with DCM (2 mL, 4x) to remove excess TFA. Following deprotection, the amine was dissolved in dry DMF (0.5 mL) and added to the activated acid solution. The mixture was stirred overnight and dried using a Biotage V-10 Touch. The crude product was purified by HPLC and lyophilized to give desired compound **49** as an orange solid (17 mg, 36% yield). ^{1}H NMR (500 MHz, DMSO-d_6) δ 8.67 (t, J = 5.7 Hz, 1H), 8.10 (d, J = 8.0 Hz, 1H), 8.07 – 8.00 (m, 3H), 7.98 – 7.86 (m, 7H), 7.72 (t, J = 6.5 Hz, 2H), 7.45 – 7.35 (m, 4H), 7.32 (t, J = 7.7 Hz, 2H), 6.85 (d, J = 7.0 Hz, 2H), 6.75 (t, J = 5.2 Hz, 1H), 6.61 (d, J = 11.1 Hz, 2H), 4.31 – 4.13 (m, 5H), 3.89 (p, J = 7.2 Hz, 1H), 3.40 – 3.17 (m, 10H), 2.93 – 2.82 (m, 4H), 2.74 (t, J = 6.9 Hz, 1H), 2.59 – 2.51 (m, 1H), 2.34 – 2.12 (m, 6H), 2.08 (s, 3H), 1.88 – 1.79 (m, 1H), 1.75 – 1.64 (m, 1H), 1.62 – 1.47 (m, 2H), 1.36 (s, 9H), 1.35 (s, 9H), 1.27-1.21 (m, 2H). ^{13}C NMR (126 MHz, DMSO-d_6) δ 171.9, 171.6, 171.1, 171.0, 170.6, 170.6, 170.4, 170.2, 165.9, 158.4, 158.1, 157.8, 155.9, 155.6, 143.9, 143.8, 140.7, 136.0, 135.7, 134.3, 129.6, 129.1, 127.6, 127.1, 125.3, 125.1, 120.1, 116.6, 114.3, 105.1, 79.6, 77.3, 65.6,

54.7, 51.8, 46.7, 40.0, 39.8, 39.7, 39.5, 39.3, 39.2, 39.0, 38.3, 37.9, 37.1, 35.4, 35.3, 35.2, 34.9, 33.9, 33.3, 31.7, 31.3, 31.3, 29.2, 28.3, 27.7, 27.5, 22.9, 19.10. LRMS (ESI+) m/z calcd for $C_{46}H_{66}N_6O_{12}S_2$ $[M+H]^+$: 1365.5, found: 1365.5.

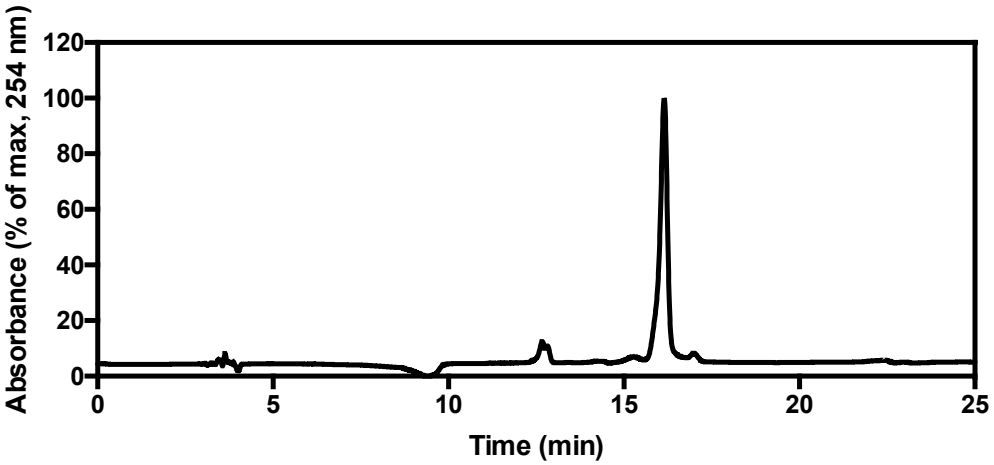

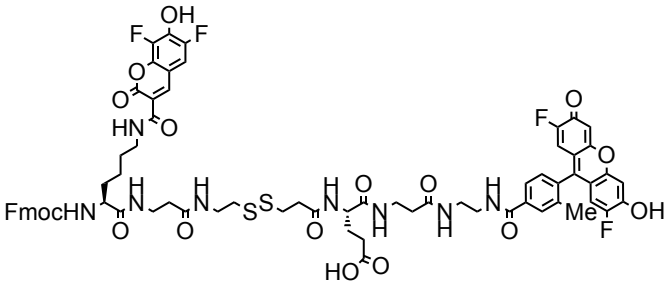

(5*S*,20*S*)-20-((3-((2-(4-(2,7-difluoro-6-hydroxy-3-oxo-3*H*-xanthen-9-yl)-3-methylbenzamido)ethyl)amino)-3-oxopropyl)carbamoyl)-5-(4-(6,8-difluoro-7-hydroxy-2-oxo-2*H*-chromene-3-carboxamido)butyl)-1-(9*H*-fluoren-9-yl)-3,6,10,18-tetraoxo-2-oxa-14,15-dithia-4,7,11,19-tetraazatricosan-23-oic acid (50). 49 (17 mg, 0.012 mmol) was dissolved in 25% TFA/DCM (2 mL) and stirred for 2 hours. The solvent was removed by rotavap, and the compound was washed with DCM to remove all acid (2 ml, 3x). The product was dissolved in dry DMF (1.5 mL). PB-NHS (9 mg, 0.029 mmol) and DIEA (14 µL, 0.080 mmol) were then added. The solution was stirred overnight. After completion of the reaction, the solvent was removed using a Biotage V-10 Touch. The

crude product was purified by HPLC and lyophilized to give the desired compound **50** as a yellow solid (6 mg, 34% yield). ^{1}H NMR (500 MHz, DMSO-d_6) δ 8.74 (s, 1H), 8.67 (t, *J* = 5.6 Hz, 1H), 8.58 (t, *J* = 5.8, 5.3 Hz, 1H), 8.11 (d, *J* = 8.0 Hz, 1H), 8.04 (q, *J* = 6.0 Hz, 2H), 7.98 – 7.90 (m, 3H), 7.89 (d, *J* = 8.1 Hz, 1H), 7.86 – 7.82 (m, 2H), 7.73 – 7.66 (m, 3H), 7.44 (d, *J* = 8.2 Hz, 1H), 7.41 – 7.35 (m, 3H), 7.30 (q, *J* = 6.9 Hz, 2H), 6.84 (s, 1H), 6.61 (d, *J* = 11.1 Hz, 2H), 4.33 – 4.25 (m, 1H), 4.24 – 4.12 (m, 4H), 3.96 – 3.88 (m, 2H), 3.36 (q, *J* = 6.3 Hz, 2H), 3.32 – 3.28 (m, 4H), 3.26 – 3.20 (m, 4H), 2.90 – 2.84 (m, 4H), 2.74 (t, *J* = 6.5 Hz, 2H), 2.56 – 2.52 (m, 2H), 2.29 – 2.17 (m, 6H), 2.08 (s, 3H), 1.93 – 1.79 (m, 1H), 1.78 – 1.66 (m, 1H), 1.65 – 1.58 (m, 1H), 1.57 – 1.45 (m, 3H), 1.39 – 1.20 (m, 3H). LRMS (ESI+) m/z calcd for $C_{70}H_{68}F_4N_8O_{17}S_2$ $[M+H]^+$: 1433.4, found: 1433.4.

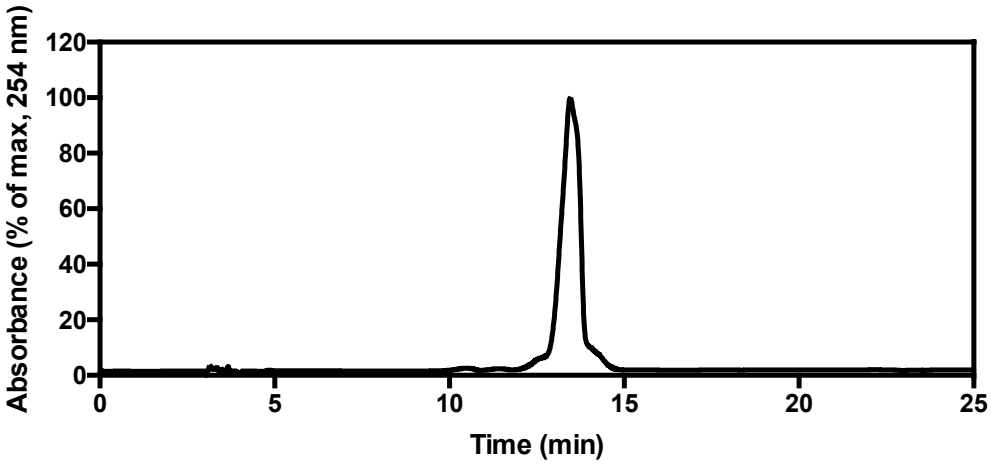

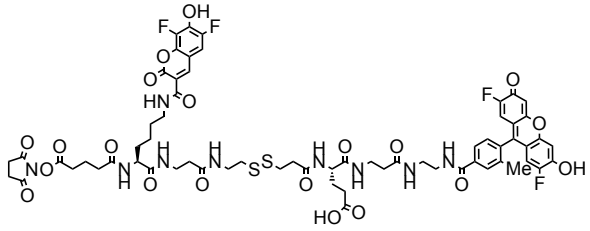

(7*S*,22*S*)-22-((3-((2-(4-(2,7-difluoro-6-hydroxy-3-oxo-3*H*-xanthen-9-yl)-3-methylbenzamido)ethyl)amino)-3-oxopropyl)carbamoyl)-1-(6,8-difluoro-7-hydroxy-2-oxo-2*H*-chromen-3-yl)-7-(5-((2,5-dioxopyrrolidin-1-yl)oxy)-5-oxopentanamido)-

1,8,12,20-tetraoxo-16,17-dithia-2,9,13,21-tetraazapentacosan-25-oic acid (38). 50 (6 mg, 0.004 mmole) was dissolved in 20% Diethylamine in DMF (1 mL) and stirred for 1 hour. After MS confirmed full cleavage of the Fmoc protecting group, the solvent was removed by Biotage V-10. The crude material was then dissolved in DMF (0.45 mL) and disuccinimidyl glutarate (14 mg, 0.04 mmol) and DIEA (7 µL, 0.04 mmol) were added. The solution was stirred overnight and diluted with DMSO (0.45 mL). The crude material was purified by HPLC and lyophilized to give desired product **38** as yellow solid (4 mg, 67% yield). ^{1}H NMR (500 MHz, DMSO-d_6) δ 12.07 (brs, 1H), 8.77 (s, 1H), 8.67 (t, *J* = 6.3 Hz, 1H), 8.57 (t, *J* = 5.6 Hz, 1H), 8.11 (d, *J* = 8.1 Hz, 1H), 8.04 (q, *J* = 5.2 Hz, 2H), 7.98 – 7.86 (m, 4H), 7.74 (dd, *J* = 10.6, 2.1 Hz, 1H), 7.39 (d, *J* = 7.8 Hz, 1H), 6.85 (brs, 1H), 6.61 (d, *J* = 11.0 Hz, 2H), 4.25 – 4.12 (m, 2H), 3.33 – 3.15 (m, 12H), 2.88 (t, *J* = 7.3 Hz, 2H), 2.81 (d, *J* = 4.3 Hz, 4H), 2.77 – 2.72 (m, 2H), 2.71 – 2.64 (m, 1H), 2.59 (s, 2H), 2.54 (s, 2H), 2.40 (t, *J* = 7.3 Hz, 2H), 2.30 – 2.17 (m, 8H), 2.14 (t, *J* = 7.4 Hz, 1H), 2.08 (s, 3H), 1.89 – 1.77 (m, 2H), 1.74 – 1.65 (m, 2H), 1.52 – 1.45 (m, 2H), 1.31 – 1.21 (m, 3H). LRMS (ESI+) m/z calcd for $C_{64}H_{67}F_4N_9O_{20}S_2$ $[M+Na]^+$: 1444.4, found: 1444.4.

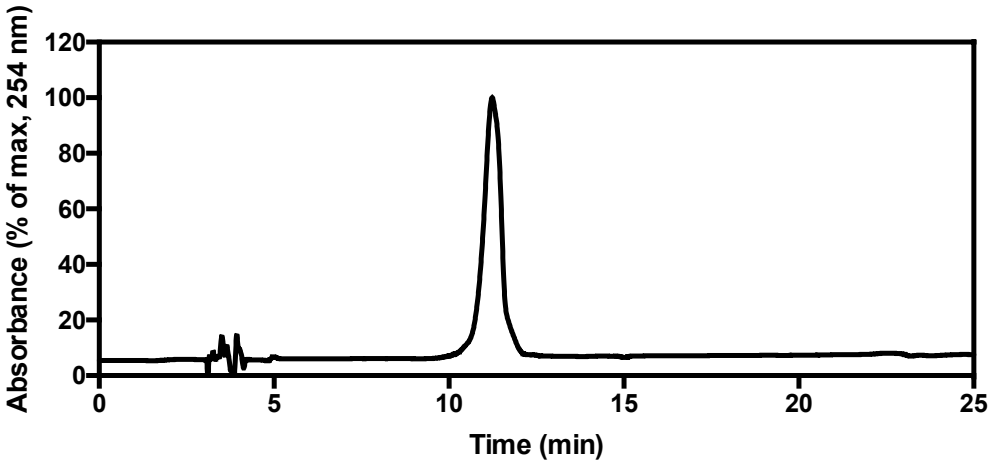

2-7-3. Biological assays and protocols

Cell culture: Jurkat lymphocytes (ATCC TIIB-152), Raji (ATCC CCL-86), Ramos (ATCC CRL-1596), and NCI-N87 cells (ATCC CRL-5822, gift of Dr. Liang Xiu) were cultured in complete media comprising RPMI-1640 (Sigma Aldrich, R8758) supplemented with fetal bovine serum (10%, Hyclone-characterized FBS, SH3039603), penicillin (100 units/mL, Sigma Aldrich P4333), and streptomycin (100 µg/mL, Sigma Aldrich P4333). SkBr3 breast cancer cells (ATCC HTB-30) were cultured in complete media comprising DMEM Nutrient Mixture F-12 Ham (Sigma Aldrich, D8437) supplemented with fetal bovine serum (10%, Hyclone-characterized FBS, SH3039603), penicillin (100 units/mL, Sigma Aldrich P4333), and streptomycin (100 µg/mL, Sigma Aldrich P4333). MDA-MB-468 breast cancer cells (ATCC HTB-132, gift of Dr. Liang Xiu), MDA-MB-231 (ATCC HTB-26), and Mia-Paca-2 (ATCC CRL-1420) were cultured in complete media comprising DMEM (Sigma Aldrich, D6429) supplemented with fetal bovine serum (10%, Hyclone-characterized FBS, SH3039603), penicillin (100 units/mL, Sigma Aldrich P4333), and streptomycin (100 µg/mL, Sigma Aldrich P4333). All cells were grown in T75 flasks (CytoOne CC7682-4875) and incubated at 37 °C with 5% CO_2.

Flow cytometry: A Beckman Coulter Cytoflex S (B2-R0-V2-Y2) flow cytometer or an Accuri C6 flow cytometer were used for cellular analysis. On the Cytoflex, cells were excited with 405 nm and / or 488 nm diode lasers and emitted photons were collected through 450/45 BP (Pacific Blue), 525/40 BP (Fluorescein and Pennsylvania Green), or 690/50 nm BP (PI) filters. FSC threshold was set to 500,000, flow speed was fast, mixing and backflush times were 5 s, and cells were collected until 10,000 cells were collected,

unless otherwise specified. On the Accuri, cells were excited with a 488 nm diode laser and emitted photons were collected through 533/30 BP (Fluorescein and Pennsylvania Green) or 585/40 BP (PI) filters. FSC threshold was set to 500,000, flow speed was fast, and cells were collected until 10,000 cells were collected, unless otherwise specified.

Endosome disruption assays in Jurkat lymphocytes: These assays were performed as reported in the thesis of Dr. David Hymel. Jurkat lymphocytes were suspended at 350,000 cells per mL in media. The fluorescent probe (**1**) was added at 2.5 μM (diluted from a 10 mM DMSO stock). Endosome disruptor was added at various concentrations from 10 nM to 10 μM (diluted from a 1000x DMSO stock). The samples were split into 2 500 μL aliquots in 1.5 mL microcentrifuge tubes (USA Scientific, 1615-5500) to provide replicates and incubated for 14 h in a Big Shot III Hybridization Oven at 37 °C with gentle rotation to maintain cell suspension. Following incubation, the cells were pelleted by centrifugation at 2,000 rpm for 2 minutes, re-suspended in 500 μL media, and incubated at 22 °C for 0.5 h to allow efflux of excess fluorescent probe from the plasma membrane. The cells were washed once more in media and analyzed for cellular fluorescence by flow cytometry using an Accuri C6 flow cytometer. Cells that were treated with **1** but not with endosome disruptor were measured for background fluorescence and subtracted from subsequent fluorescence values. Fluorescence values were normalized to the activity of the published cholesterylamine-PC4 peptide[25] (structure shown in Figure 2-7) and plotted versus concentration. Analysis by non-linear regression in GraphPad Prism 6 provided potency and efficacy values.

Labeling of antibodies with NHS esters: Herceptin (trastuzumab), Erbitux (cetuximab), and Rituxan (rituximab) were all purchased from a pharmacy. Anti-CD44 was provided by Dr. Liang Xiu. Human IgG was purchased as a lyophilized powder (Sigma, I4506). Herceptin was provided as a lyophilized powder mixed 1:1 with stabilizers (α,α-trehalose dihydrate, *L*-histidine, and polysorbate 20). Erbitux and Rituxan were provided as aqueous solutions, Erbitux at 2 mg/mL in solution with sodium chloride, sodium phosphate dibasic heptahydrate, and sodium phosphate monobasic monohydrate and Rituxan at 10 mg/mL in solution with sodium chloride, sodium citrate dihydrate, and polysorbate 80. Anti-CD44 was provided as an aqueous solution at various concentrations.

Herceptin was reconstituted in sterile PBS (pH 7.4) and passed through a spin column packed with Sephadex G25 to remove the stabilizers. Briefly, Sephadex G-25 resin (Superfine, Sigma, S5772) was suspended in PBS (pH 7.4). The resulting slurry (950 µL) was added to a minispin column (USA Scientific, 1415-0600) and centrifuged (16,000 x g, 20 s) to remove the buffer and pack the resin. The antibody solution (no more than 75 µL per column) was loaded onto the packed resin and centrifuged (16,000 x g, 30 s) to separate the protein from the stabilizers. The concentration of Herceptin was then determined by absorbance at 280 nm using the presets for IgG in a Nanodrop 1000 ($\varepsilon_{1\%\ (10\ mg/mL)}$ + 13.7 $Lg^{-1}cm^{-1}$). The concentration was adjusted to 100 µM using sterile PBS. Erbitux, Rituxan, and Anti-CD44 were all concentrated to 100 µM using Amicon Ultra-0.5 Centrifugal Filter Units with MWCO 100K (Millipore, UFC5100) according to the provided manual. IgG was simply reconstituted in sterile PBS (pH 7.4) at 100 µM. Concentrations were all determined using the method described above.

The same basic procedure was used to label all antibodies with all NHS esters. Antibody in PBS (100 μM, 25-300 μL) was aliquoted into a 1.5 mL microcentrifuge tube. 1 M $NaHCO_3$ was added (2.5-30 μL) to achieve a final concentration of 0.1 M. NHS esters were added as DMSO stocks (typically 10 mM, various volumes) to achieve 5-10x excess over the antibody concentration. Many of the endosome disruptors required 10% DMSO to aid solubility. Solutions were incubated for 0.5 h (37 °C) in a Big Shot III Hybridization Oven. To purify the conjugates, Sephadex G25 (small molecules) or G50 (endosome disruptors, centrifuged 1 min to pack) resin was packed into columns as described above for Sephadex G25. The antibody solution was loaded onto the packed resin (no more than 75 μL per column) and centrifuged (16,000 x g, 30 s) to separate the protein from the unconjugated small molecules. This was done twice to ensure full removal of free endosome disruptors and toxins; once was sufficient for small molecule fluorophores. Conjugates being used for toxicity assays or other 72 h assays were sterilized by being passed through 0.22 μm Ultra-MC centrifugal filters (Millipore, UFC30GV0S) by centrifugation (13,000 x g, 3 min).

To purify conjugates of **25**, it was necessary to use ω-Aminopentyl-Agarose (Sigma, A8287). 100 μL of the agarose slurry was transferred to a microspin column (ThermoFisher, 89879), centrifuged at 10,000 x g for 1 min, then rinsed 2x with 50 μL of 10 mM NaOH. The antibody solution was added to the column, incubated at 37 °C in a Big Shot III Hybridization Oven with rotation for 10 min, and then centrifuged at 10,000 x g for 1 min to collect the antibody solution. This solution was then passed through Sephadex G50 as described above to remove any remaining small molecules.

In order to label antibodies with **28**, it was necessary to include 0.4% Triton X-100 (Sigma, T9284) and 30% DMSO in the labeling reaction along with the other components mentioned above. To remove the Triton after labeling, the solution was passed through a 0.5 mL Pierce Detergent Removal Spin Column (ThermoFisher, 87777), following the provided instructions. The detergent-free solution was then passed through Sephadex G50 1x, as described above.

After purification, the degree of labeling (DOL) of each conjugate was determined. This was done by comparing the absorbance at 280 nm and 425 nm or 488 nm (IgG 280 nm $\varepsilon_{1\%\ (10\ mg/mL)}$ = 13.7 $Lg^{-1}cm^{-1}$, Pacific Blue 425 nm ε = 29,500 $M^{-1}cm^{-1}$, Fluorescein 490 nm ε = 70,000 $M^{-1}cm^{-1}$, Pennsylvania Green 490 nm ε = 60,000 $M^{-1}cm^{-1}$), as measured with a Nanodrop 1000 Spectrophotometer. From the absorbance of **32** at 280 nm (4:1 DMSO:PBS), CME contributes an additional 30% of the absorbance of PB at 280 nm, and the concentrations and DOL of **33** and **34** were corrected[61] to account for this contribution.

Analysis of cytotoxicity of antibody-delivered toxins: SkBr3 (HER2+) and MDA-MB-468 (HER2–) cells were used to analyze the toxicity of antibody-toxin conjugates. Cells were plated in the appropriate complete media into CytoOne 96-well tissue culture plates (USA Scientific, CC7682-7596) at 50,000 cells / mL and 200 µL / well and incubated overnight. On the same day, IgG and Herceptin (50 µL each) were labeled with **32** (10x excess), as described above, to yield the IgG conjugate **34** at 57 µM, DOL 5.2 and the Herceptin conjugate **33** at 59 µM and DOL 4.9. The next day, DMSO stocks of *N*-acetyl colchinol methyl ether (CME, **36**, 1 mM, ε = 20,000 $M^{-1}cm^{-1}$ at 262 nm in EtOH), **4** (10

mM, ε = 20,970 $M^{-1}cm^{-1}$ at 280 nm in 4:1 DMSO:PBS), and Chol-SS-CME (**35**, 10 mM, use ε of CME) or **37** (10 mM, use ε of CME) were prepared and normalized using an Agilent 8453 UV-Vis Spectrophotometer and the extinction coefficients listed above. These compounds were serially diluted at a 1:3 ratio to yield 1000x DMSO stocks (0.3-300 μM for **36**, 10-10,000 μM for **4**, **35**, and **37**). These stocks were diluted 1:1000 into the appropriate complete media and vortexed to mix to yield final concentrations of 0.3-300 nM **36** and 10-10,000 nM **4**, **35**, and **37**, all with 0.1% DMSO. Each sample of **35** or **37** diluted in media was prepared at double the volume and split into 2 equal aliquots to yield 2 sets of this compound. 2 μM **4** (2 mM DMSO stock) was added to all tubes of one set. Media was aspirated from each well and replaced with 150 μL of the above treated media in triplicate. Antibody conjugates were serially diluted in the appropriate complete media to yield solutions ranging from 0.03-1,000 nM. Each sample was split into 2 equal aliquots, yielding 2 sets of samples for each conjugate. 2 μM **4** (2 mM DMSO stock) was added to one set of each conjugate. Media was aspirated from each well and replaced with 150 μL treated media in triplicate.

After 72 h incubation, cells were trypsinized and analyzed. Media was aspirated from each well, and each well was washed with 100 μL PBS. 50 μL of trypsin was added to each well, and plates were incubated at 37 °C for 10 min. Trypsin was quenched with 150 μL media containing 3 μM propidium iodide (PI, 3 mM PBS stock, ThermoFisher Scientific, P1304MP), and cells were pipetted up and down to break up clumps. Plates were immediately analyzed using a Beckman Coulter Cytoflex S (B2-R0-V2-Y2) flow cytometer. Cells were collected for 20 s per well. Other settings are described above in **Flow cytometry**. Staining with PI was used to identify populations of live cells. Counts of

viable cells for each treatment, determined in triplicate, were used to generate dose-response curves. These curves were fitted by non-linear regression with an inhibitor vs. response variable 4-parameter model (GraphPad Prism 7) to determine IC_{50} values.

Confocal microscopy: Imaging was performed using an inverted Leica TCS SPE confocal laser-scanning microscope fitted with a Leica 63x oil-immersion objective. Fluorescent probes were excited with either a 405 nm or 488 nm solid-state laser and emitted photons were collected from 425-500 nm or 500-600 nm. Unless otherwise noted, laser power and PMT gain settings were identical for all images acquired within a given experiment to allow accurate comparisons of cellular fluorescence.

Endosome disruption assays analyzed by confocal microscopy: Cells were seeded in the appropriate complete media into 8 Well μ-Slides (Ibidi, 80826, 100,000 cells/mL, 300 μL/well) and allowed to adhere overnight. Each well was washed 1x with media, and then the media was replaced with 150 μL of complete media containing the indicated treatment of vehicle control (0.1% DMSO), cholesterol or antibody-delivered fluorophore, and / or cholesterol or antibody-delivered endosome disruptor at the indicated concentration. Antibodies were labeled as described above. All DMSO stocks were normalized using extinction coefficients and UV-Vis spectroscopy. Cells were incubated for 24 h, washed 1x with media, and then imaged by confocal microscopy as described above.

Fluorescence spectroscopy: Fluorescence spectra were recorded using a Perkin Elmer LS-55 fluorescence spectrometer. Samples were excited at 405 nm or 488 nm and emission was recorded from 425-700 nm or 515–700 nm with a scan speed of 500 nm/min and slit widths of 10 nm.

Kinetic analysis of cleavage of disulfide: Herceptin was labeled with **32** and **38** following the general procedure described above. 10x excess of **32** was used and 4x excess of **38** was used. Conjugates were diluted 1:1000 into 1.5 mL PBS in a 2.0 mL centrifuge tube to yield 25 nM and vortexed to mix. 200 µL of each conjugate was added to each of 6 wells of a black fluorescence Microfluor 1 Flat-Bottom 96-well Plate (Fisher Scientific, 7605). Freshly made dithiothreitol (DTT, 2 µL, 100 mM aqueous stock, Sigma, D0632) was added to 3 wells of each conjugate for a final concentration of 1 mM DTT. The plate was analyzed immediately using a Packard Fusion Universal Microplate Analyzer using a Pacific Blue 405 excitation filter, a Pacific Blue 450 emission filter, top fluorescence with light intensity set to 1, 0.1 s integration, high intensity orbital shaking for 10 s before every reading, and 30 s intervals between readings at 37 °C. Background-subtracted values were curve fitted by non-linear regression with a one-phase association model (GraphPad Prism 6) to determine half-times.

To obtain spectra of the conjugates over time during disulfide cleavage, conjugates were diluted 1:1000 into 0.5 mL PBS in a 1.5 mL centrifuge tube to yield 25 nM and pipetted to mix. The solution was transferred by pipet to a quartz SUPRASIL macro/semi-micro cell (PerkinElmer, B0631132). After preliminary spectra were recorded, DTT (5 µL, 100 mM) was added to the cuvette to yield a final concentration of 1 mM. The solution

was mixed by pipette, and the cap was added to the cuvette to prevent evaporation. The cuvette was then incubated for the indicated amount of time at 37 °C. The solution was mixed before and after each spectrum was recorded. Fluorescence spectra were recorded as described in **Fluorescence spectroscopy**.

Flow cytometry analysis of 39 in SKBR3 over time: SKBR3 cells were plated in complete media into CytoOne 96-well tissue culture plates (USA Scientific, CC7682-7596) at 75,000 cells / mL and 200 µL / well and incubated overnight. On the same day, trastuzumab (300 µL) was labeled with **38** (4x excess) as described above to yield **39** at 62 µM and DOL 2.6. **40** was prepared from **7** by adding 1 mM of DTT to **7** and incubating (37 °C) in a Big Shot III Hybridization Oven for 2 h. Fluorescence emission was monitored over time and the reaction was considered complete when the fluorescent signal stopped increasing (Figure S3). The solution was then purified using Sephadex G25 and filter sterilized as described above to yield **40** at 58 µM and DOL 2.0. **40** was stored at 4 °C overnight before use to give the intra-chain disulfide bonds that were likely cleaved by DTT time to re-form. Trastuzumab (75 µL each) was also singly labeled with Pennsylvania Green NHS and Pacific Blue NHS (2x excess each) to produce trastuzumab-PG (70 µM, DOL 1.5) and trastuzumab-PB (62 µM, DOL 1.7) as controls to check for signal bleed-through for both confocal microscopy and flow cytometry (data not shown).

For analysis with pre-incubation of **4** (data not shown), media in the appropriate wells was replaced with 200 µL complete media containing 2 µM **4** (from a 2 mM DMSO stock). For analysis without pre-incubation, this step was skipped, and cells were treated with all compounds the day after being plated. The next day, sufficient media was prepared of 1

μM of each antibody conjugate with and without 2 μM **4** to dose wells in triplicate with 100 μL for 8 time points. Media was also prepared with 250 nM **1** with and without 2 μM **4** to act as a positive control of endosomal disruption by **4** (data not shown). Media was aspirated from the wells and replaced with 100 μL of the above dosed media in triplicate. Cells were incubated at 4 °C for 0.5 h. Cells were then washed 1x with media, and the media was replaced with 200 μL media, containing 2 μM **4** where appropriate. Wells corresponding to time point t=0 were immediately trypsinized as described in *Analysis of cytotoxicity of antibody delivered toxins*, except without the addition of PI. Cells were analyzed by flow cytometry as described in *Flow cytometry*. Cells were then incubated at 37 °C until the next time point.

To determine the half-life of the release of Pennsylvania Green from the **39**, median blue fluorescent values from each well were collected. The values of **39** with and without **4** were multiplied by 0.83 to correct for the lower efficacy of binding of trastuzumab-PB for HER2 after treatment with DTT. These values divided by the corresponding values of **40** with and without **4** (as a control for complete cleavage of **39**). These ratios were then normalized using the value at t=0 as 0% cleavage and 1 as 100% cleavage. The half-life was determined by curve fitting using the one-phase association model (analysis done in GraphPad Prism 8). The normalized ratios of each time point with and without **4** were compared using unpaired t tests (one per time point) with the assumption that all data were sampled from populations with the same scatter using the Holm-Sidak method with alpha = 5%. No statistically significant differences were found.

Confocal microscopy analysis of 39 in SKBR3 over time: SKBR3 cells were plated in complete media into 8 Well µ-Slides (Ibidi, 80826, 125,000 cells/mL, 300 µL/well) and allowed to adhere overnight. The same batches of antibody conjugates described in *Analysis of cytotoxicity of antibody delivered toxins* were used in this study. For analysis with pre-incubation of **4**, media in the appropriate wells was replaced with 300 µL complete media containing 2 µM **4** (from a 2 mM DMSO stock). For analysis without pre-incubation, this step was skipped, and cells were treated with all compounds the day after being plated. Each well was washed 1x with media, and then the media was replaced with 100 µL of complete media containing 1 µM of the appropriate antibody conjugate or 250 nM **1** with or without 2 µM **4**. **1** was included as a positive control to ensure that **4** was functioning properly (data not shown). Cells were incubated at 4 °C for 0.5 h. Cells were then washed 2x with media (with the exception of cells treated with **1**, which diffuses away over time), and the media was replaced with 300 µL media, containing 2 µM **4** where appropriate. Cells were immediately imaged as described in *Confocal microscopy* for the t=0 time point. Cells were then incubated at 37 °C until the next time point.

Colocalization of 39 with LysoTracker Red DND-99 in SKBR3: Colocalization with LysoTracker was done as a continuation of the assay described in *Confocal microscopy analysis of **39** in SKBR3 over time*. After 72 h of incubation with **39**, 1 µM of Lysotracker Red DND-99 (Molecular Probes, L7528) was added to each appropriate well. Cells were incubated at 37 °C for 0.5 h followed by immediate imaging without washing. Wells containing trastuzumab singly labeled with PB and PG were used to verify no bleed through was being seen between channels (data not shown). Emission windows were

adjusted to achieve this. The final settings used were: Ex. 405 nm, Em. 425-500 nm (Pacific Blue); Ex. 488 nm, Em. 500-550 nm (Pennsylvania Green); Ex. 532 nm, Em. 600-650 nm (LysoTracker Red DND-99). Overlays of the channels were done using the Leica SPE Software. Yellow coloring indicates an overlap of green and red. White coloring indicates an overlap of blue and red.

2-8. References

(1) Pearce, A.; Haas, M.; Viney, R.; Pearson, S. A.; Haywood, P.; Brown, C.; Ward, R., Incidence and severity of self-reported chemotherapy side effects in routine care: A prospective cohort study. *PLoS One* **2017**, *12*, e0184360.

(2) Henry, D. H.; Viswanathan, H. N.; Elkin, E. P.; Traina, S.; Wade, S.; Cella, D., Symptoms and treatment burden associated with cancer treatment: results from a cross-sectional national survey in the U.S. *Support. Care Cancer* **2008**, *16*, 791.

(3) Coates, A.; Abraham, S.; Kaye, S. B.; Sowerbutts, T.; Frewin, C.; Fox, R. M.; Tattersall, M. H., On the receiving end--patient perception of the side-effects of cancer chemotherapy. *Eur. J. Cancer Clin. Oncol.* **1983**, *19*, 203.

(4) Griffin, A. M.; Butow, P. N.; Coates, A. S.; Childs, A. M.; Ellis, P. M.; Dunn, S. M.; Tattersall, M. H., On the receiving end. V: Patient perceptions of the side effects of cancer chemotherapy in 1993. *Ann. Oncol.* **1996**, *7*, 189.

(5) Carelle, N.; Piotto, E.; Bellanger, A.; Germanaud, J.; Thuillier, A.; Khayat, D., Changing patient perceptions of the side effects of cancer chemotherapy. *Cancer* **2002**, *95*, 155.

(6) Russo, S.; Cinausero, M.; Gerratana, L.; Bozza, C.; Iacono, D.; Driol, P.; Deroma, L.; Sottile, R.; Fasola, G.; Puglisi, F., Factors affecting patient's perception of anticancer treatments side-effects: an observational study. *Expert Opin. Drug Saf.* **2014**, *13*, 139.

(7) Adams, G. P.; Weiner, L. M., Monoclonal antibody therapy of cancer. *Nat. Biotechnol.* **2005**, *23*, 1147.

(8) Hansel, T. T.; Kropshofer, H.; Singer, T.; Mitchell, J. A.; George, A. J., The safety and side effects of monoclonal antibodies. *Nat. Rev. Drug Discov.* **2010**, *9*, 325.

(9) Cook-Bruns, N., Retrospective analysis of the safety of Herceptin immunotherapy in metastatic breast cancer. *Oncology* **2001**, *61 Suppl 2*, 58.

(10) Slamon, D. J.; Leyland-Jones, B.; Shak, S.; Fuchs, H.; Paton, V.; Bajamonde, A.; Fleming, T.; Eiermann, W.; Wolter, J.; Pegram, M.; Baselga, J.; Norton, L., Use of chemotherapy plus a monoclonal antibody against HER2 for metastatic breast cancer that overexpresses HER2. *New Engl. J. Med.* **2001**, *344*, 783.

(11) Perez, E. A., Cardiac toxicity of ErbB2-targeted therapies: what do we know? *Clin. Breast Cancer* **2008**, *8 Suppl 3*, S114.

(12) Vu, T.; Claret, F. X., Trastuzumab: updated mechanisms of action and resistance in breast cancer. *Front. Oncol.* **2012**, *2*, 62.

(13) Luque-Cabal, M.; García-Teijido, P.; Fernández-Pérez, Y.; Sánchez-Lorenzo, L.; Palacio-Vázquez, I., Mechanisms Behind the Resistance to Trastuzumab in HER2-Amplified Breast Cancer and Strategies to Overcome It. *Clin. Med. Insights Oncol.* **2016**, *10*, 21.

(14) Cassady, J. M.; Chan, K. K.; Floss, H. G.; Leistner, E., Recent developments in the maytansinoid antitumor agents. *Chem. Pharm. Bull. (Tokyo)* **2004**, *52*, 1.

(15) Lewis Phillips, G. D.; Li, G.; Dugger, D. L.; Crocker, L. M.; Parsons, K. L.; Mai, E.; Blattler, W. A.; Lambert, J. M.; Chari, R. V.; Lutz, R. J.; Wong, W. L.; Jacobson, F. S.; Koeppen, H.; Schwall, R. H.; Kenkare-Mitra, S. R.; Spencer, S. D.; Sliwkowski, M.

X., Targeting HER2-positive breast cancer with trastuzumab-DM1, an antibody-cytotoxic drug conjugate. *Cancer Res.* **2008**, *68*, 9280.

(16) Barok, M.; Tanner, M.; Koninki, K.; Isola, J., Trastuzumab-DM1 causes tumour growth inhibition by mitotic catastrophe in trastuzumab-resistant breast cancer cells in vivo. *Breast Cancer Res.* **2011**, *13*, R46.

(17) Peddi, P. F.; Hurvitz, S. A., Ado-trastuzumab emtansine (T-DM1) in human epidermal growth factor receptor 2 (HER2)-positive metastatic breast cancer: latest evidence and clinical potential. *Ther. Adv. Med. Oncol.* **2014**, *6*, 202.

(18) Uppal, H.; Doudement, E.; Mahapatra, K.; Darbonne, W. C.; Bumbaca, D.; Shen, B. Q.; Du, X.; Saad, O.; Bowles, K.; Olsen, S.; Lewis Phillips, G. D.; Hartley, D.; Sliwkowski, M. X.; Girish, S.; Dambach, D.; Ramakrishnan, V., Potential mechanisms for thrombocytopenia development with trastuzumab emtansine (T-DM1). *Clin. Cancer. Res.* **2015**, *21*, 123.

(19) Donaghy, H., Effects of antibody, drug and linker on the preclinical and clinical toxicities of antibody-drug conjugates. *MAbs* **2016**, *8*, 659.

(20) Kratschmer, C.; Levy, M., Targeted Delivery of Auristatin-Modified Toxins to Pancreatic Cancer Using Aptamers. *Molecular therapy. Nucleic acids* **2018**, *10*, 227.

(21) Polson, A. G.; Calemine-Fenaux, J.; Chan, P.; Chang, W.; Christensen, E.; Clark, S.; de Sauvage, F. J.; Eaton, D.; Elkins, K.; Elliott, J. M.; Frantz, G.; Fuji, R. N.; Gray, A.; Harden, K.; Ingle, G. S.; Kljavin, N. M.; Koeppen, H.; Nelson, C.; Prabhu, S.; Raab, H.; Ross, S.; Slaga, D. S.; Stephan, J. P.; Scales, S. J.; Spencer, S. D.; Vandlen, R.; Wranik, B.; Yu, S. F.; Zheng, B.; Ebens, A., Antibody-drug conjugates for the treatment

of non-Hodgkin's lymphoma: target and linker-drug selection. *Cancer Res.* **2009**, *69*, 2358.

(22) Li, F.; Emmerton, K. K.; Jonas, M.; Zhang, X.; Miyamoto, J. B.; Setter, J. R.; Nicholas, N. D.; Okeley, N. M.; Lyon, R. P.; Benjamin, D. R.; Law, C. L., Intracellular Released Payload Influences Potency and Bystander-Killing Effects of Antibody-Drug Conjugates in Preclinical Models. *Cancer Res.* **2016**, *76*, 2710.

(23) Ritchie, M.; Tchistiakova, L.; Scott, N., Implications of receptor-mediated endocytosis and intracellular trafficking dynamics in the development of antibody drug conjugates. *MAbs* **2013**, *5*, 13.

(24) Lee, B. C.; Chalouni, C.; Doll, S.; Nalle, S. C.; Darwish, M.; Tsai, S. P.; Kozak, K. R.; Del-Rosario, G.; Yu, S. F.; Erickson, H.; Vandlen, R., FRET Reagent Reveals the Intracellular Processing of Peptide-Linked Antibody-Drug Conjugates. *Bioconjug. Chem.* **2018**, *29*, 2468.

(25) Sun, Q.; Cai, S.; Peterson, B. R., Selective disruption of early/recycling endosomes: release of disulfide-linked cargo mediated by a N-alkyl-3beta-cholesterylamine-capped peptide. *J. Am. Chem. Soc.* **2008**, *130*, 10064.

(26) Nakase, I.; Kobayashi, S.; Futaki, S., Endosome-disruptive peptides for improving cytosolic delivery of bioactive macromolecules. *Biopolymers* **2010**, *94*, 763.

(27) Su, X.; Fricke, J.; Kavanagh, D. G.; Irvine, D. J., In vitro and in vivo mRNA delivery using lipid-enveloped pH-responsive polymer nanoparticles. *Mol. Pharm.* **2011**, *8*, 774.

(28) Ren, Y.; Hauert, S.; Lo, J. H.; Bhatia, S. N., Identification and characterization of receptor-specific peptides for siRNA delivery. *ACS nano* **2012**, *6*, 8620.

(29) Febvay, S.; Marini, D. M.; Belcher, A. M.; Clapham, D. E., Targeted cytosolic delivery of cell-impermeable compounds by nanoparticle-mediated, light-triggered endosome disruption. *Nano Lett.* **2010**, *10*, 2211.

(30) Su, X.; Yang, N.; Wittrup, K. D.; Irvine, D. J., Synergistic antitumor activity from two-stage delivery of targeted toxins and endosome-disrupting nanoparticles. *Biomacromolecules* **2013**, *14*, 1093.

(31) Austin, C. D.; De Maziere, A. M.; Pisacane, P. I.; van Dijk, S. M.; Eigenbrot, C.; Sliwkowski, M. X.; Klumperman, J.; Scheller, R. H., Endocytosis and sorting of ErbB2 and the site of action of cancer therapeutics trastuzumab and geldanamycin. *Mol. Biol. Cell* **2004**, *15*, 5268.

(32) Hymel, D.; Cai, S.; Sun, Q.; Henkhaus, R. S.; Perera, C.; Peterson, B. R., Fluorescent mimics of cholesterol that rapidly bind surfaces of living mammalian cells. *Chem. Commun. (Camb.)* **2015**, *51*, 14624.

(33) Polyak, K.; Garber, J., Targeting the missing links for cancer therapy. *Nat. Med.* **2011**, *17*, 283.

(34) Farmer, H.; McCabe, N.; Lord, C. J.; Tutt, A. N.; Johnson, D. A.; Richardson, T. B.; Santarosa, M.; Dillon, K. J.; Hickson, I.; Knights, C.; Martin, N. M.; Jackson, S. P.; Smith, G. C.; Ashworth, A., Targeting the DNA repair defect in BRCA mutant cells as a therapeutic strategy. *Nature* **2005**, *434*, 917.

(35) Yap, T. A.; Sandhu, S. K.; Carden, C. P.; de Bono, J. S., Poly(ADP-ribose) polymerase (PARP) inhibitors: Exploiting a synthetic lethal strategy in the clinic. *CA Cancer J. Clin.* **2011**, *61*, 31.

(36) Hirosue, S.; Weber, T., pH-Dependent lytic peptides discovered by phage display. *Biochemistry* **2006**, *45*, 6476.

(37) Marshall, G. R.; Hodgkin, E. E.; Langs, D. A.; Smith, G. D.; Zabrocki, J.; Leplawy, M. T., Factors governing helical preference of peptides containing multiple alpha,alpha-dialkyl amino acids. *Proc. Natl. Acad. Sci. U. S. A.* **1990**, *87*, 487.

(38) Reddy, V.; Cambridge, G.; Isenberg, D. A.; Glennie, M. J.; Cragg, M. S.; Leandro, M., Internalization of rituximab and the efficiency of B Cell depletion in rheumatoid arthritis and systemic lupus erythematosus. *Arthritis & rheumatology (Hoboken, N.J.)* **2015**, *67*, 2046.

(39) Jones, S. M.; Foreman, S. K.; Shank, B. B.; Kurten, R. C., EGF receptor downregulation depends on a trafficking motif in the distal tyrosine kinase domain. *Am. J. Physiol. Cell Physiol.* **2002**, *282*, C420.

(40) Erickson, H. K.; Park, P. U.; Widdison, W. C.; Kovtun, Y. V.; Garrett, L. M.; Hoffman, K.; Lutz, R. J.; Goldmacher, V. S.; Blattler, W. A., Antibody-maytansinoid conjugates are activated in targeted cancer cells by lysosomal degradation and linker-dependent intracellular processing. *Cancer Res.* **2006**, *66*, 4426.

(41) de Souza, M. C.; Bresolin, I. T.; Bueno, S. M., Purification of human IgG by negative chromatography on omega-aminohexyl-agarose. *J. Chromatogr. B Analyt. Technol. Biomed. Life Sci.* **2010**, *878*, 557.

(42) Ravelli, R. B.; Gigant, B.; Curmi, P. A.; Jourdain, I.; Lachkar, S.; Sobel, A.; Knossow, M., Insight into tubulin regulation from a complex with colchicine and a stathmin-like domain. *Nature* **2004**, *428*, 198.

(43) Brossi, A.; Sharma, P. N.; Atwell, L.; Jacobson, A. E.; Iorio, M. A.; Molinari, M.; Chignell, C. F., Biological effects of modified colchicines. 2. Evaluation of catecholic colchicines, colchifolines, colchicide, and novel N-acyl- and N-aroyldeacetylcolchicines. *J. Med. Chem.* **1983**, *26*, 1365.

(44) Kang, G. J.; Getahun, Z.; Muzaffar, A.; Brossi, A.; Hamel, E., N-acetylcolchinol O-methyl ether and thiocolchicine, potent analogs of colchicine modified in the C ring. Evaluation of the mechanistic basis for their enhanced biological properties. *J. Biol. Chem.* **1990**, *265*, 10255.

(45) Bailly, C.; Bodet-Milin, C.; Rousseau, C.; Faivre-Chauvet, A.; Kraeber-Bodere, F.; Barbet, J., Pretargeting for imaging and therapy in oncological nuclear medicine. *EJNMMI Radiopharm. Chem.* **2017**, *2*, 6.

(46) Goldenberg, D. M.; Sharkey, R. M.; Paganelli, G.; Barbet, J.; Chatal, J. F., Antibody pretargeting advances cancer radioimmunodetection and radioimmunotherapy. *J. Clin. Oncol.* **2006**, *24*, 823.

(47) Steen, E. J. L.; Edem, P. E.; Norregaard, K.; Jorgensen, J. T.; Shalgunov, V.; Kjaer, A.; Herth, M. M., Pretargeting in nuclear imaging and radionuclide therapy: Improving efficacy of theranostics and nanomedicines. *Biomaterials* **2018**, *179*, 209.

(48) Mottram, L. F.; Boonyarattanakalin, S.; Kovel, R. E.; Peterson, B. R., The Pennsylvania Green Fluorophore: a hybrid of Oregon Green and Tokyo Green for the construction of hydrophobic and pH-insensitive molecular probes. *Org. Lett.* **2006**, *8*, 581.

(49) Mottram, L. F.; Maddox, E.; Schwab, M.; Beaufils, F.; Peterson, B. R., A concise synthesis of the Pennsylvania Green fluorophore and labeling of intracellular targets with O6-benzylguanine derivatives. *Org. Lett.* **2007**, *9*, 3741.

(50) Rowland, C. E.; Brown, C. W.; Medintz, I. L.; Delehanty, J. B., Intracellular FRET-based probes: a review. *Methods and applications in fluorescence* **2015**, *3*, 042006.

(51) Zhang, H.; Liu, R.; Tan, Y.; Xie, W. H.; Lei, H.; Cheung, H. Y.; Sun, H., A FRET-based ratiometric fluorescent probe for nitroxyl detection in living cells. *ACS applied materials & interfaces* **2015**, *7*, 5438.

(52) Yang, J.; Chen, H.; Vlahov, I. R.; Cheng, J. X.; Low, P. S., Evaluation of disulfide reduction during receptor-mediated endocytosis by using FRET imaging. *Proc. Natl. Acad. Sci. U. S. A.* **2006**, *103*, 13872.

(53) Erickson, H. K.; Lewis Phillips, G. D.; Leipold, D. D.; Provenzano, C. A.; Mai, E.; Johnson, H. A.; Gunter, B.; Audette, C. A.; Gupta, M.; Pinkas, J.; Tibbitts, J., The effect of different linkers on target cell catabolism and pharmacokinetics/pharmacodynamics of trastuzumab maytansinoid conjugates. *Mol. Cancer Ther.* **2012**, *11*, 1133.

(54) Austin, C. D.; Wen, X.; Gazzard, L.; Nelson, C.; Scheller, R. H.; Scales, S. J., Oxidizing potential of endosomes and lysosomes limits intracellular cleavage of disulfide-based antibody-drug conjugates. *Proc. Natl. Acad. Sci. U. S. A.* **2005**, *102*, 17987.

(55) Phan, U. T.; Arunachalam, B.; Cresswell, P., Gamma-interferon-inducible lysosomal thiol reductase (GILT). Maturation, activity, and mechanism of action. *J. Biol. Chem.* **2000**, *275*, 25907.

(56) Besong, G.; Billen, D.; Dager, I.; Kocienski, P.; Sliwinski, E.; Tai, L. R.; Boyle, F. T., A synthesis of (aR,7S)-(−)-N-acetylcolchinol and its conjugate with a cyclic RGD peptide. *Tetrahedron* **2008**, *64*, 4700.

(57) Nicolaus, N.; Reball, J.; Sitnikov, N.; Velder, J.; Termath, A.; Fedorov, A. Y.; Schmalz, H.-G., A convenient entry to new C-7-modified colchicinoids through azide alkyne [3+2] cycloaddition: application of ring-contractive rearrangements. *Heterocycles* **2011**, *82*, 1585.

(58) Yu, X.; Liu, Q.; Wu, J.; Zhang, M.; Cao, X.; Zhang, S.; Wang, Q.; Chen, L.; Yi, T., Sonication-triggered instantaneous gel-to-gel transformation. *Chemistry* **2010**, *16*, 9099.

(59) Lee, M. M.; Peterson, B. R., Quantification of Small Molecule-Protein Interactions using FRET between Tryptophan and the Pacific Blue Fluorophore. *ACS Omega* **2016**, *1*, 1266.

(60) Kaduk, C.; Wenschuh, H.; Beyermann, M.; Forner, K.; Carpino, L. A.; Bienert, M., Synthesis of Fmoc-amino acid fluorides via DAST, an alternative fluorinating agent. *Lett. Pept. Sci.* **1996**, *2*, 285.

(61) Bhattacharyya, S.; Wang, S.; Reinecke, D.; Kiser, W., Jr.; Kruger, R. A.; DeGrado, T. R., Synthesis and evaluation of near-infrared (NIR) dye-herceptin conjugates as photoacoustic computed tomography (PCT) probes for HER2 expression in breast cancer. *Bioconjug. Chem.* **2008**, *19*, 1186.

Chapter 3

Targeting Fluorescent Sensors to Endoplasmic Reticulum Membranes Enables Detection of Peroxynitrite During Cellular Phagocytosis

3-1. Introduction

Peroxynitrite ($ONOO^-$), an exceptionally strong oxidant, is an inflammatory mediator with important roles in both normal physiology and human pathology.[1,2] In biological systems, this natural product is derived from the diffusion-limited reaction between superoxide radical anion ($O_2^{-\bullet}$), generated by NADPH oxidases (NOX), and nitric oxide free radical ($^\bullet NO$), produced by nitric oxide synthase (NOS) enzymes, among other pathways. In immune cells such as macrophages, for example, the phagocytosis of pathogens and other materials initiates phosphorylation of cytosolic subunits of NADPH oxidase, which causes these subunits to migrate to the membrane of the phagosome to join with other subunits to form the active enzyme complex that then generates superoxide within the phagosome.[3-5] Stimulation of macrophages with molecules such as lipopolysaccharides (LPS) and TNF-α can also lead to superoxide production.[3,5] Activation of macrophages by binding of ligands to pathogen recognition receptors (PPRs) causes macrophages to secrete various cytokines to enlist the help of other immune cells. For example, activated T-helper lymphocytes secrete cytokines such as TNF-α, which can activate inducible nitric oxide synthase (iNOS) in the cytosol of macrophages. This enzyme synthesizes nitric oxide from arginine and NADPH,[5] and as a neutral species, nitric oxide can readily diffuse across cell membranes, allowing it to

move from the cytosol to the phagosome where it can react with superoxide to generate peroxynitrite.[2] Peroxynitrite helps to destroy phagocytosed pathogens.

Although protonated peroxynitrous acid (ONOOH, pKa = 6.8) is highly unstable with a half-life of ~ 1 s at pH 7.4, its conjugate anion $ONOO^-$ is relatively stable, and it can be synthesized[6] and stored at low temperatures. When generated by biological systems, peroxynitrite crosses cell membranes and is thought to diffuse 5–20 microns in its short lifetime.[1] During this time, this oxidant, and its secondary reactive species, can oxidize and damage a wide range of biomolecules, including proteins, lipids, and nucleic acids. Whereas peroxynitrite itself directly modifies some molecules, secondary species produced from this oxidant contribute substantially to its activity. Moieties directly damaged by peroxynitrite include thiols[7] and transition metal centers[8] of proteins. Secondary reactive species result from reaction of peroxynitrite with carbon dioxide, found in millimolar concentrations in cells, to produce unstable nitrosoperoxycarbonate, which quickly decomposes to generate nitrogen dioxide and carbonate radical.[9,10] Additionally, under certain conditions, the protonated form of peroxynitrite, peroxynitrous acid, can generate hydroxyl radical and nitrogen dioxide through homolytic cleavage.[11] All of these species are highly reactive and can damage living systems.

Immune cells such as macrophages use peroxynitrite and other reactive species, in conjunction with acidic pH and enzymes, to destroy phagocytosed pathogens, cancer cells, and other materials. However, peroxynitrite can also damage host cells, and elevated levels have been linked to cardiovascular and neurodegenerative diseases and cancer.[1,2]

The short half-life and low concentrations of cellular peroxynitrite make it difficult to study. Peroxynitrite can be directly monitored using electrochemical detection,[12-16] but these methods do not allow for spatial analysis and require specialized equipment. Indirect methods of detection of peroxynitrite are more commonly used. For example, 3-nitrotyrosine (3NT) has been used as a biomarker of elevated peroxynitrite levels.[11] Although several methods have been developed to detect 3NT,[17-21] other nitrating agents can generate this modification,[22-24] reducing its utility as a selective indicator of peroxynitrite.

To study peroxynitrite in living cells, fluorescence-based methods are of substantial interest. Fluorescent sensors have been previously reported bearing cleavable side chains derived from *p*-hydroxyphenol and *p*-hydroxyaniline,[25] *p*-aminophenol,[26-28] *p*-aminophenyl-trifluoromethylbutanone,[29,30] boronates,[31] indoles,[32,33] and other functional groups such as polymethines.[34] Reversible fluorescent sensors have also been reported.[35] In some cases, these sensors have been targeted to mitochondria,[36-39] and lysosomes.[33] However, detection of low levels of endogenous peroxynitrite, such as those produced during phagocytosis of pathogens by macrophages, remains a challenge. Fluorescent sensors reportedly capable of detecting endogenous peroxynitrite during phagocytosis, such as fluorescein boronate,[39] require not only phagocytosis to function, but also additional stimulation of cells by cytokines such as interferon-gamma (IFN-γ) and lipopolysaccharide (LPS). However, some phagocytes may kill pathogens in vivo in the absence of additional stimulants. To better understand the chemical biology of peroxynitrite, more sensitive sensors are needed.

We report here the development of fluorescent sensors of peroxynitrite that accumulate in the dense tubular membranes of the endoplasmic reticulum (ER).[40] We hypothesized that targeting peroxynitrite sensors to these intracellular membranes might afford highly sensitive sensors because they possess an extensive surface area that is approximately 30 times greater than the plasma membrane. Additionally, the ER is a direct target of peroxynitrite,[41] and ER stress resulting from oxidation is thought to contribute to atherosclerotic lesions. Peroxynitrite can also deplete ER-associated calcium and zinc.[42] Additionally, through mechanisms that are not fully understood, peroxynitrite activates the unfolded protein response (UPR) in this organelle, which is initially cytoprotective, but can lead to apoptosis when prolonged.[42-44]

3-2. Design and synthesis of sensors

Our group has previously developed fluorinated hydrophobic rhodol fluorophores that accumulate within the membranes of the endoplasmic reticulum.[45] The mechanism of this pattern of subcellular localization is not fully understood, but it likely relates to the differences in lipid composition of ER membranes compared to other cell membranes, such as the plasma membrane, that contains substantially more cholesterol.[46] QSAR[47] and microscopy[48] studies indicate that some hydrophobic, amphipathic molecules accumulate in the ER, but this pattern of subcellular localization remains incompletely understood. Here, we combined the design of these fluorinated hydrophobic fluorophores with *p*-aminophenol, a moiety that has previously been reported to react selectively with peroxynitrite (Figure 3-1).[49,50]

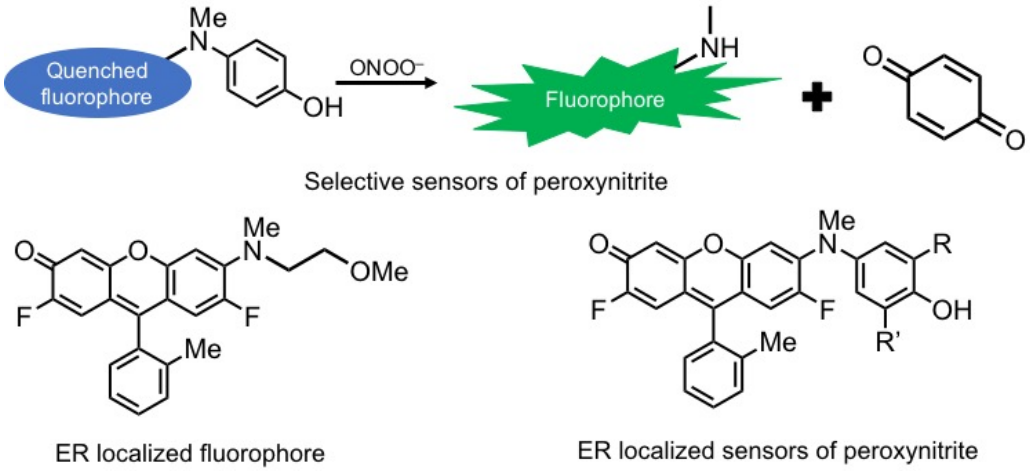

Figure 3-1. Rationale for the design of fluorescent sensors. These sensors were inspired by previous studies that demonstrated that *p*-aminophenol reacts selectively with peroxynitrite.[49,50] Structurally related phenols were appended to fluorinated rhodols previously shown to accumulate in membranes of the endoplasmic reticulum.[45]

Dr. Digamber Rane of the Peterson laboratory synthesized a series of analogues based on this scaffold, utilizing different substituents with different electron withdrawing and donating properties on the phenyl ring (Figure 3-2). These analogues were designed to react with peroxynitrite and undergo *N*-dearylation to yield the highly fluorescent fluorinated rhodol (**59**). These compounds were synthesized from the triflate derivative (**60**) of Pennsylvania Green[51] via Buchwald-Hartwig cross coupling as shown in Scheme 3-1. Additional synthetic details and compound characterization were generated by Dr. Rane and are provided in the Experimental section (3-10).

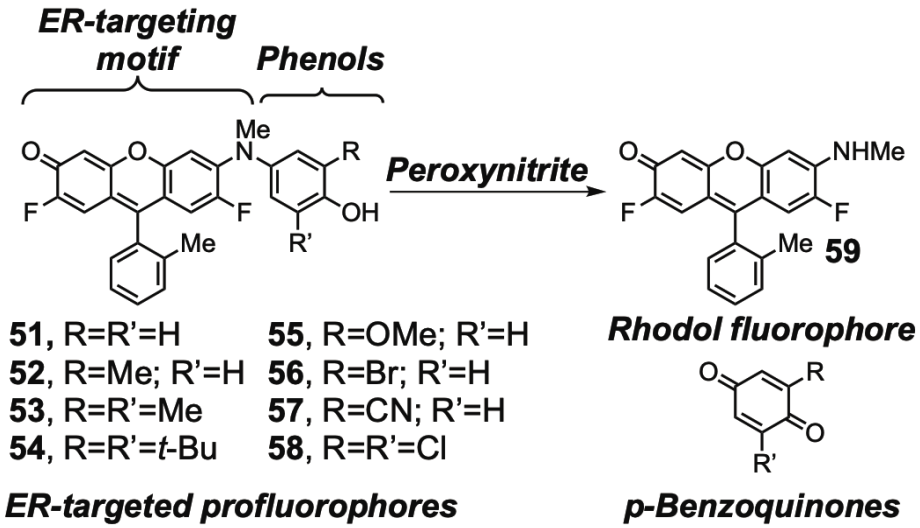

Figure 3-2. Structures of ER-targeted fluorescent sensors and products of oxidative cleavage by peroxynitrite.

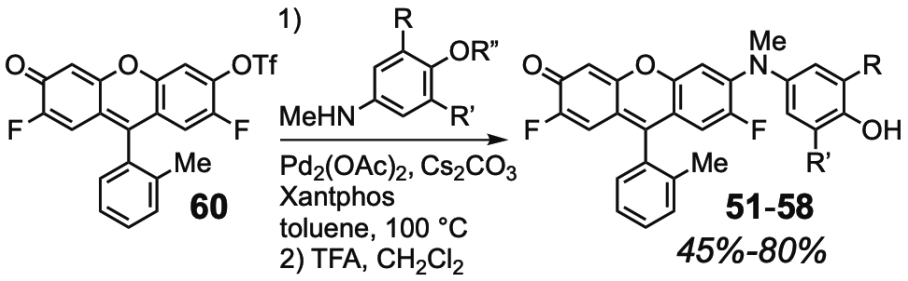

Scheme 3-1. Synthesis of sensors (**51**-**58**). R and R' are defined in Figure 3.2. R"=MOM (for **51-53** and **55-58**) or Boc (for **54**).

3-3. Optical spectroscopic properties of sensors

The spectral properties of these sensors make them ideal for many purposes. The sensors can easily be excited by a 488 nm laser (Figure 3-3), which is common on many confocal microscopes and flow cytometers. Spectra were recorded in *n*-octanol since it is a mimic of a membrane environment. Consistent with prior studies of phenol-linked xanthenes,[28,50,52] the fluorescence emission of **51**–**58** were quenched by up to 1800-fold (for **53**, Φ=0.0004) compared to **59** (Φ=0.72). However, the brightness of these sensors,

calculated as the product of their measured molar extinction coefficients and quantum yields, varied by up to 30-fold (Figure 3-18 in the Experimental section).

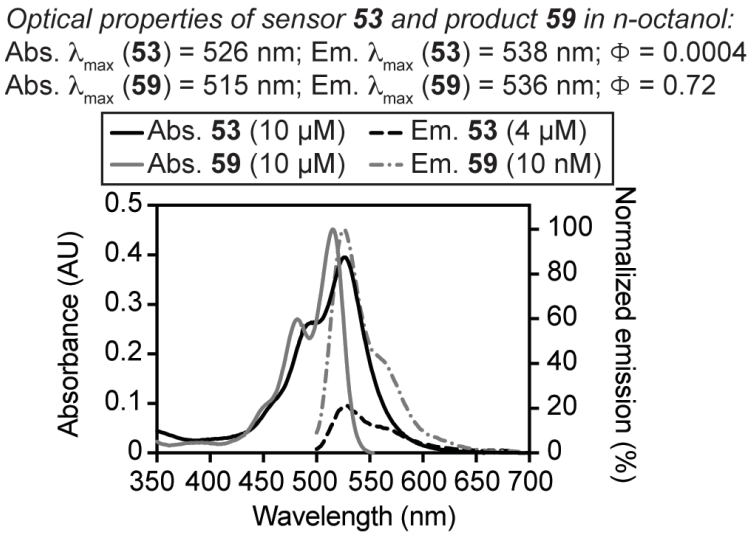

Figure 3-3. Photophysical properties of sensor **53** and the product of oxidative cleavage of the phenol side-chain (**59**) in *n*-octanol.

3-4. Reactivity of sensors with peroxynitrite

To analyze the reactivity of **53** with $ONOO^-$, fluorescence spectra were obtained of **53** after incubation in PBS with increasing equivalents of $ONOO^-$ at room temperature. As seen in Figure 3-4, the fluorescence of the di-methyl sensor increases in a dose-dependent manner after incubation with $ONOO^-$ in PBS. The fluorescence values at 526 nm were then normalized between the minimum intensity (0 nM $ONOO^-$, F_{min}) and the maximum intensity (500 nM $ONOO^-$, F_{max}) and plotted against the concentration of $ONOO^-$ to determine the limit of detection of $ONOO^-$ by **53** (Figure 3-4 B). A 2-fold increase in fluorescence intensity was observed upon treatment with 40 nM peroxynitrite.

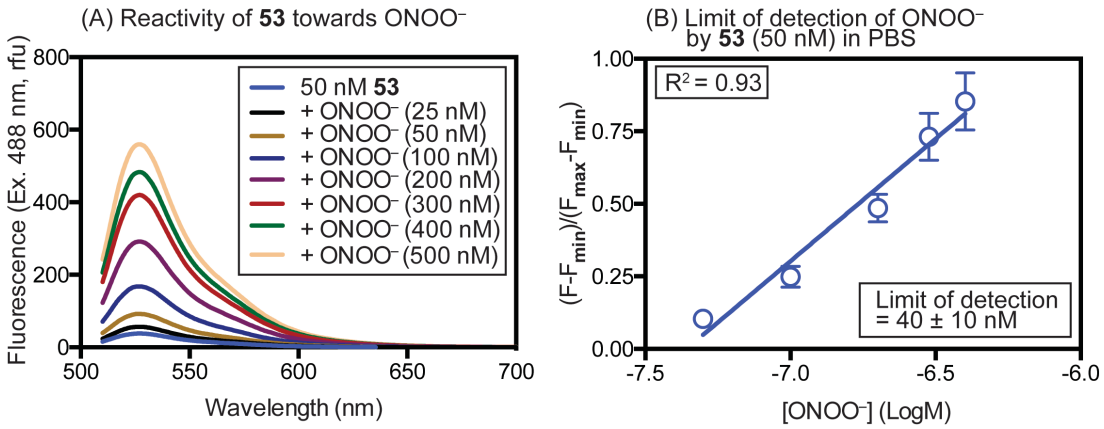

Figure 3-4. Limit of detection of $ONOO^-$ by **53**. (A) Reactivity of **53** towards pure peroxynitrite after 5 min at 23 °C in PBS (pH 7.4) containing DMSO (0.1%). (B) The fluorescence emission at 526 nm from A were normalized and plotted against [$ONOO^-$]. The line crosses the x-axis at ~40 nM, yielding the limit of detection.

3-5. Studies of kinetics of reaction of sensors with SIN-1

To examine the reactivity of **51**–**58** with peroxynitrite in aqueous buffer, we measured kinetic half-times upon treatment with the peroxynitrite generator SIN-1 under pseudo first order conditions (Figure 3-5). Although all of these compounds reacted rapidly with this oxidant to generate a highly fluorescent product, the 2,6-dimethyl-substituted sensor **53** exhibited the fastest kinetics ($t_{1/2}$=49 s), making it of particular interest. Further analysis by HPLC conducted by Dr. Digamber Rane demonstrated that SIN-1 cleanly converted **53** to **59** (Figure 3-6). In Figure 3-5, differences in the brightness achieved by each analogue were observed. This may result from side reactions of less stable benzoquinone fragments after cleavage.

(A) Mechanism of generation of peroxynitrite by SIN-1

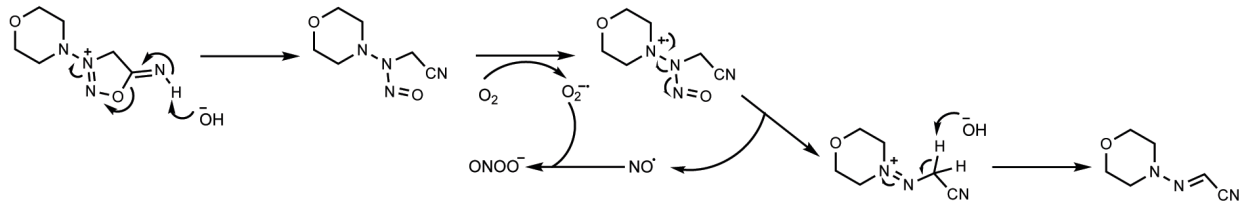

(B) Profiles of reaction of **51**-**58** with SIN-1

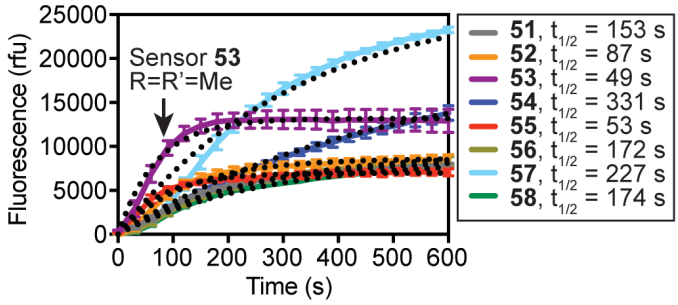

Figure 3-5. (A) Mechanism of generation of peroxynitrite by SIN-1. (B) Profiles of reaction of **51**-**58** (25 nM) with the peroxynitrite generator SIN-1 (1 mM) in phosphate-buffered saline (PBS, pH 7.4). Pseudo first-order half-times ($t_{1/2}$, calculated after subtraction of the background in the absence of SIN-1) are shown. Dotted lines show fits to a one-phase association model.

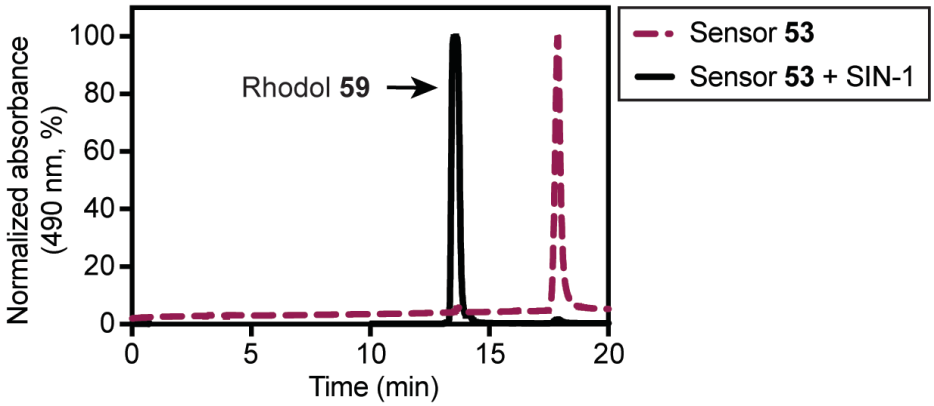

Figure 3-6. Analytical HPLC profile of **53** (5 mM) before and after treatment with SIN-1 (23 mM). Compounds were allowed to react in acetonitrile:PBS (8:2, pH 7.4) for 16 h at 23 °C. The identity of product **59** was verified by comparison with an authentic standard.

Swain-Lupton constants were used to determine if there was a correlation between the properties of the analogues and their rates of reaction with peroxynitrite. The Swain-Lupton constants are expansions of the Hammet constants that splits the electronic

contributions of each substituent into resonance (R) and field (F) effects.[53] For this analysis, an equal contribution from these two effects was assumed. Analysis of the log of the ratio of the rate constant of each analogue compared to that of the parent compound (**51**) of the mono-substituted compounds by the Swain-Lupton method[53] showed a correlation (R^2=0.89, Figure 3-7) between reaction rate constants and the electron density of the phenol, where electron donating substituents accelerate cleavage of the side-chain. The precise mechanism of the reaction between peroxynitrite and the sensors is not fully understood, but it likely involves an intermediate with a positive charge on the amine (Scheme 3-2).

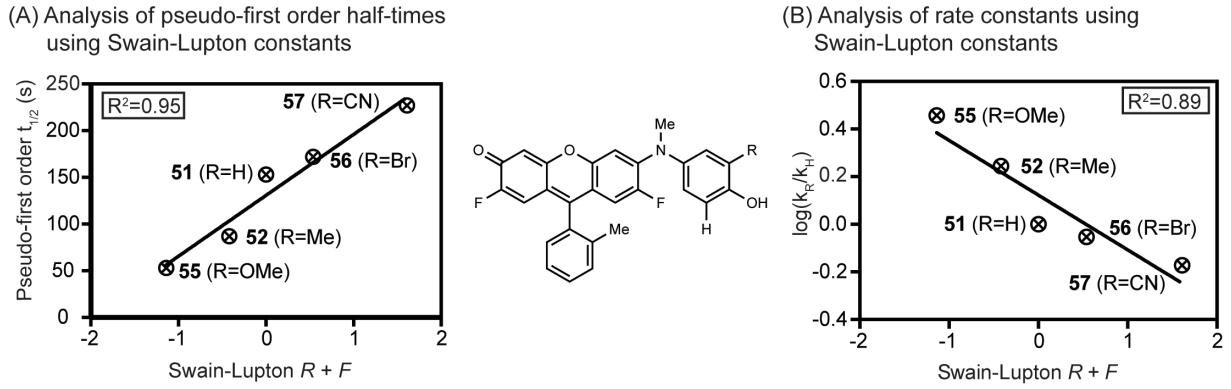

Figure 3-7. Analysis of rate constants using Swain-Lupton constants. (A) A correlation between the pseudo-first order half-times and the electron density of the phenol is observed upon treatment of the mono-substituted sensors (25 nM) with excess SIN-1 (1 mM) in PBS (pH 7.4). Electron donating substituents accelerate cleavage of the side chain. (B) The conventional approach of plotting these constants against $\log(k_R/k_H)$ shows a similar linear relationship.

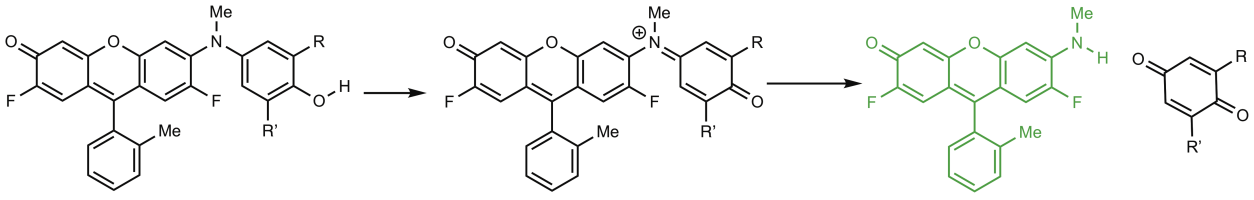

Scheme 3-2. Proposed mechanism of reaction between sensors and peroxynitrite. Electron donating substituents (R and R') stabilize the positive charge on the amine, accelerating the reaction.

5-6. Analysis of the selectivity of sensor 53 towards peroxynitrite

Comparison of the reactivity of **53** with peroxynitrite, hypochlorite, hydroxyl radical, superoxide, peroxides, and nitric oxide, confirmed that this sensor is highly selective for peroxynitrite under biologically-relevant conditions (Figure 3-8). Upon reaction with pure peroxynitrite, a 33-fold increase in fluorescence was observed with addition of one equivalent, and a 140-fold increase with the addition of 10 equivalents of this oxidant. The largest change seen after addition of other oxidants was a 10-fold increase upon the addition of 50 equivalents of hypochlorite. It should be noted that these assays were all done in the presence of 0.1% DMSO, which is known to quench ClO^- [54,55] and enhance the selectivity of reaction of phenols with peroxynitrite.[52] In all of the assays described in this chapter, at least 0.1% (v/v) DMSO was present due to assay design.

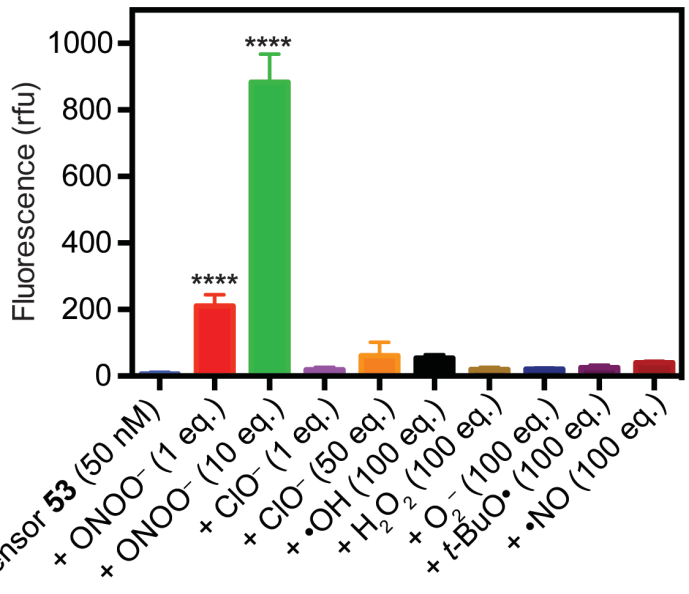

Figure 3-8. Reactivity of **53** towards pure peroxynitrite and other oxidants after 5 min at 23 °C in PBS (pH 7.4) containing DMSO (0.1%). **** indicates $p < 0.0001$. p values are calculated for sensor alone compared to each other column using ordinary one-way ANOVA correcting for multiple comparisons using Sidak's multiple comparisons test with a single pooled variance (GraphPad Prism 6).

3-7. Detection of endogenous peroxynitrite in RAW264.7 cells

To detect peroxynitrite generated during phagocytosis, we treated living RAW 264.7 macrophage cells with amino-TentaGel microspheres (10-micron). As shown in Figure 3-9, these beads were covalently modified with 6-(2,4-dinitrophenylamino)-hexanoic acid (DNP) as a ligand of anti-DNP antibodies (IgG). Beads were additionally modified with the coumarin-derived fluorophore Pacific Blue (PB) to provide a non-IgG-bound control. We hypothesized that treatment of macrophage cells with TentaGel-DNP bound to anti-DNP IgG would lead to recognition of the bead-bound antibodies via Fc receptors, phagocytosis of the beads, and trigger production of cellular peroxynitrite. The proximity of ER-targeted peroxynitrite sensors to phagosomal membranes could facilitate their conversion to the highly fluorescent **59**. In addition, retention of this compound in ER membranes might also enhance sensitivity (Figure 3-9).

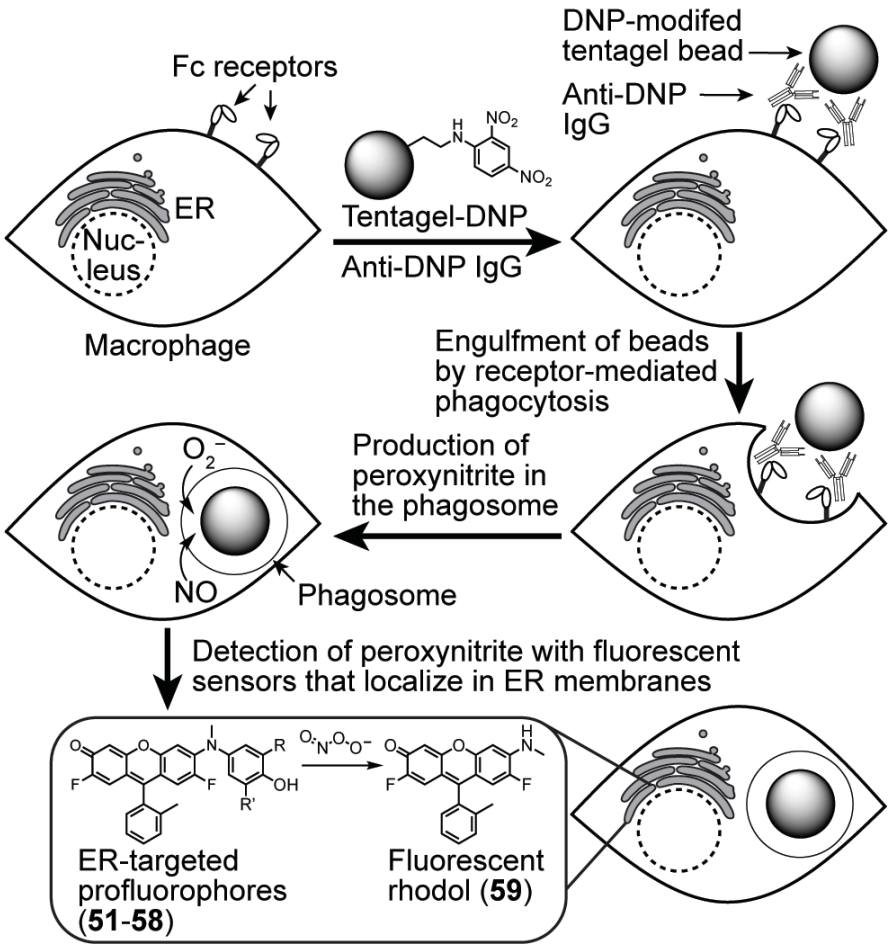

Figure 3-9. Approach for detection of endogenous peroxynitrite in macrophage cells. Receptor-mediated phagocytosis of antibody-bound tentagel beads triggers production of reactive nitrogen species that can be detected by sensors localized in membranes of the endoplasmic reticulum.

We treated living RAW264.7 macrophages with sensors **51**-**58** and quantified cellular fluorescence by flow cytometry (Figure 5-10). To trigger phagocytosis and production of endogenous peroxynitrite, these cells were additionally treated with amino-TentaGel beads modified with the fluorophore Pacific Blue or DNP/Anti-DNP IgG. As a control, fluorescence in cells treated with sensors, beads, and IgG not bound to the beads was also quantified, revealing that the IgG must be bound to the beads to induce an increase in fluorescence (data not shown). This was as expected, since non-opsonized

beads would not be expected to be phagocytosed, even with IgG present in the environment.

As shown in Figure 3-10 (panel A), sensor **53** exhibited the greatest change in fluorescence (10-fold) upon addition of the more immunostimulatory IgG-coated beads. We further compared ER-targeted with two known non-ER-targeted sensors of peroxynitrite: hydroxyphenyl fluorescein (**HPF**)[25] and fluorescein boronate (**FI-B**).[39] Because the fluorescence of **HPF** can be affected by serum proteins,[56] cells were treated with this compound in Hank's balanced salt solution (HBSS). As shown in Figure 3-10 (panel B), both **HPF** and **FI-B** responded to the addition of SIN-1 and could increase cellular fluorescence. However, only the ER-targeted sensor **53** could detect peroxynitrite upon mild treatment of cells with antibody-opsonized TentaGel beads, demonstrating a major advantage of this approach. Additional co-treatment of cells with **53**, IgG-bound beads, and the peroxynitrite decomposition catalyst FeTMPyP decreased cellular fluorescence by over 50%, further supporting selective detection of this specific oxidant by **53**. Importantly, negligible cytotoxicity of **53** was observed at 10 μM after 48 h in culture (Figure 3-11).

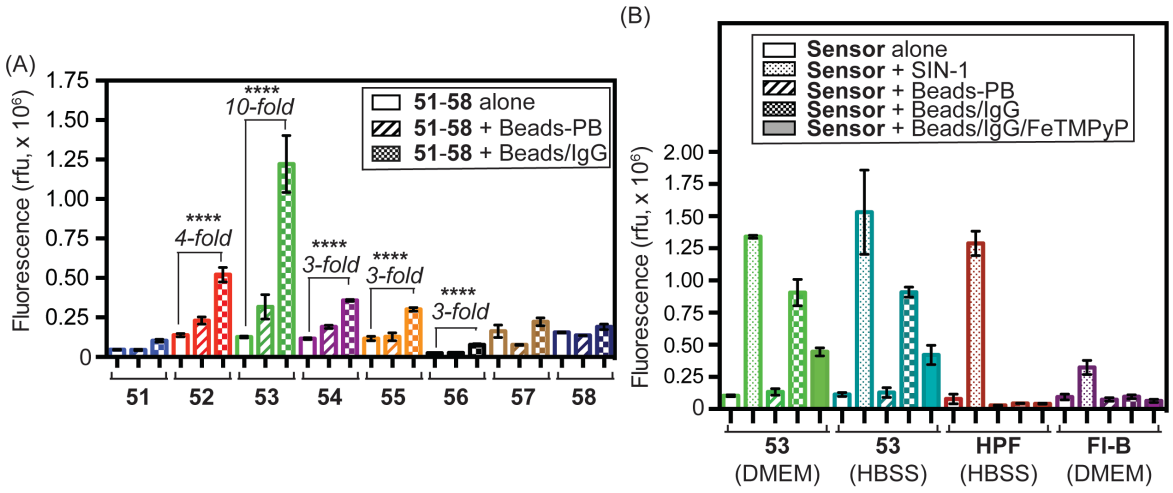

Figure 3-10. (A-B) Analysis of fluorescence of living RAW264.7 macrophages by flow cytometry. Cells were treated (4 h) with sensors **51**-**58** (10 μM) and 10-micron amino-TentaGel beads modified either with Pacific Blue-SE (Beads-PB) or 2,4-DNP-X-SE. To the DNP-modified beads was additionally added rabbit anti-DNP IgG (Beads/IgG), conjugated to Pacific Blue via lysines, to stimulate phagocytosis. In Panel B, cells were treated with **3.3** in DMEM media or HBSS and compared with treatment with hydroxyphenyl fluorescein (**HPF**, 10 μM in HBSS) and fluorescein boronate (**FI-B**, 50 μM in DMEM). [SIN-1] = 50 μM. [FeTMPyP] = 50 μM. * indicates 0.01 < p < 0.05; ** indicates 0.001 < p < 0.01; *** indicates 0.0001 < p < 0.001; **** indicates p < 0.0001. p values are calculated for sensor alone compared to indicated column using ordinary one-way ANOVA correcting for multiple comparisons using Sidak's multiple comparisons test with a single pooled variance (Prism 6).

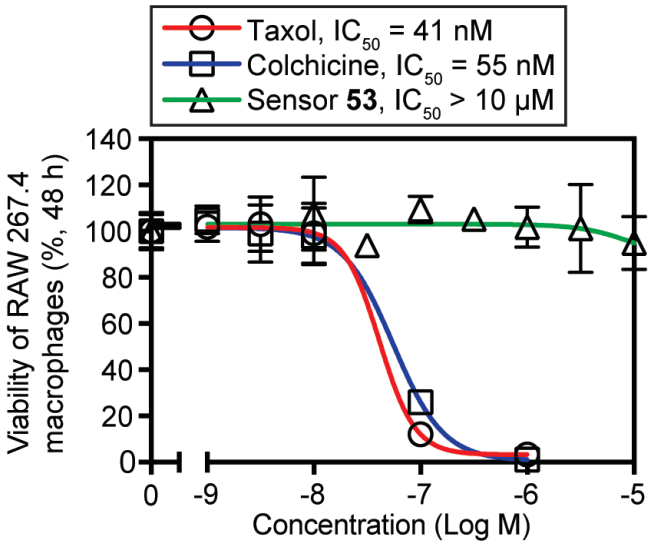

Figure 3-11. Analysis of cytotoxicity of **53** towards RAW264.7 macrophages after 48 h compared with paclitaxel (Taxol) and colchicine as toxic controls.

Additionally, we incubated RAW264.7 macrophages treated with **53** with varying numbers of beads to see if the increase in fluorescence is incremental (Figure 3-12). Even at 600,000 beads/mL, beads modified with PB caused only negligible increases in fluorescence. The opsonized beads, on the other hand, caused incremental increases in fluorescence from 25,000 beads/mL up to 400,000 beads/mL.

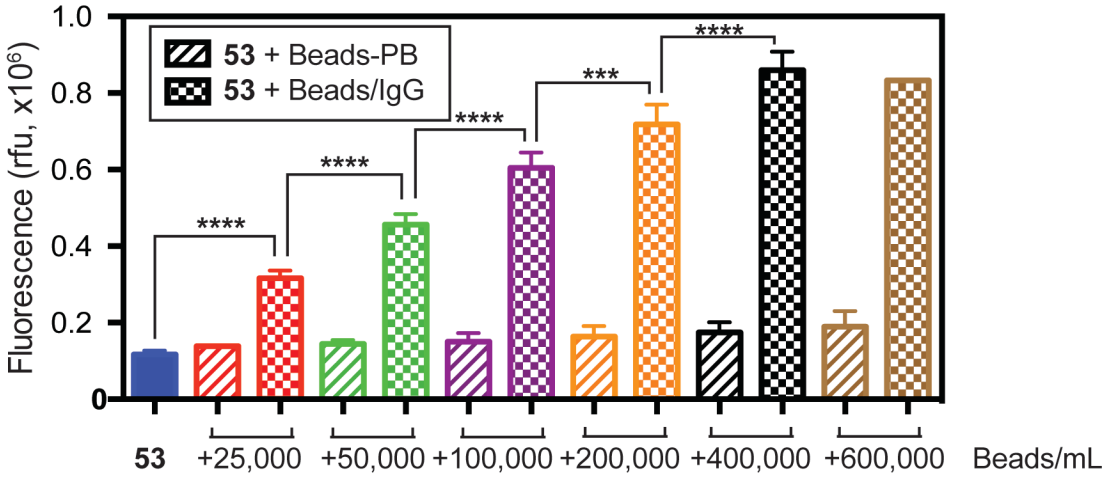

Figure 3-12. Incremental increase in fluorescence of RAW264.7 macrophages incubated with 53 (10 μM, 4h) and increasing numbers of 10-micron amino-TentaGel beads modified either with Pacific Blue-SE (Beads-PB) or DNP-X-SE and bound to Anti-DNP IgG. * indicates $0.01 < p < 0.05$; ** indicates $0.001 < p < 0.01$; *** indicates $0.0001 < p < 0.001$; **** indicates $p < 0.0001$. Statistical analysis was performed using ordinary one-way ANOVA correcting for multiple comparisons using Sidak's multiple comparisons test with a single pooled variance (Prism 6).

3-8. Subcellular localization of sensors

The unique ability of ER-targeted sensors to detect endogenous peroxynitrite during phagocytosis was further investigated by confocal laser scanning microscopy. As shown in Figure 3-13, addition of antibody-opsonized beads to cells treated with **53** resulted in a dramatic increase in localized cytosolic fluorescence. This fluorescence was greatly reduced by co-incubation with the peroxynitrite decomposition catalyst FeTMPyP (Figure 3-14).

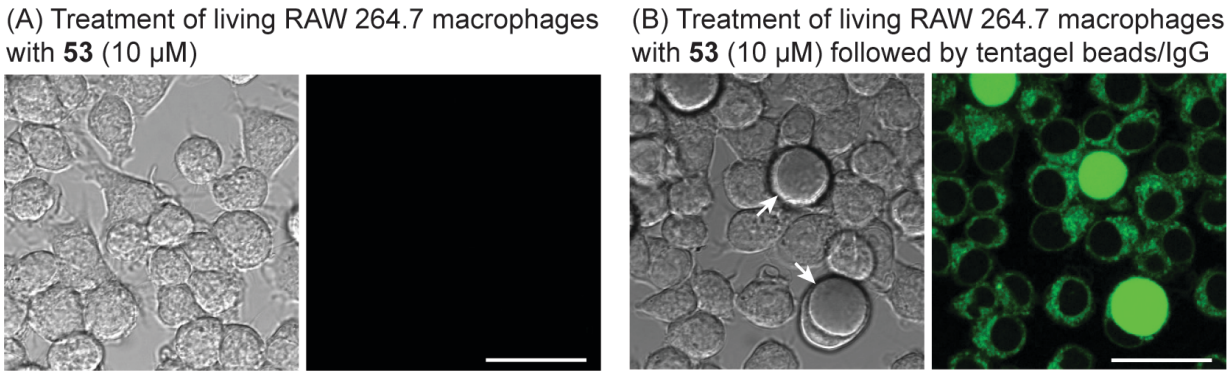

Figure 3-13. (A-B) DIC and confocal laser scanning micrographs of RAW macrophages treated with **53** (4 h). Panel B: Cells were additionally treated with DNP-modified amino tentagel beads (10 microns) bound to anti-DNP IgG. White arrows point at phagocytosed tentagel beads. Scale bar = 25 microns.

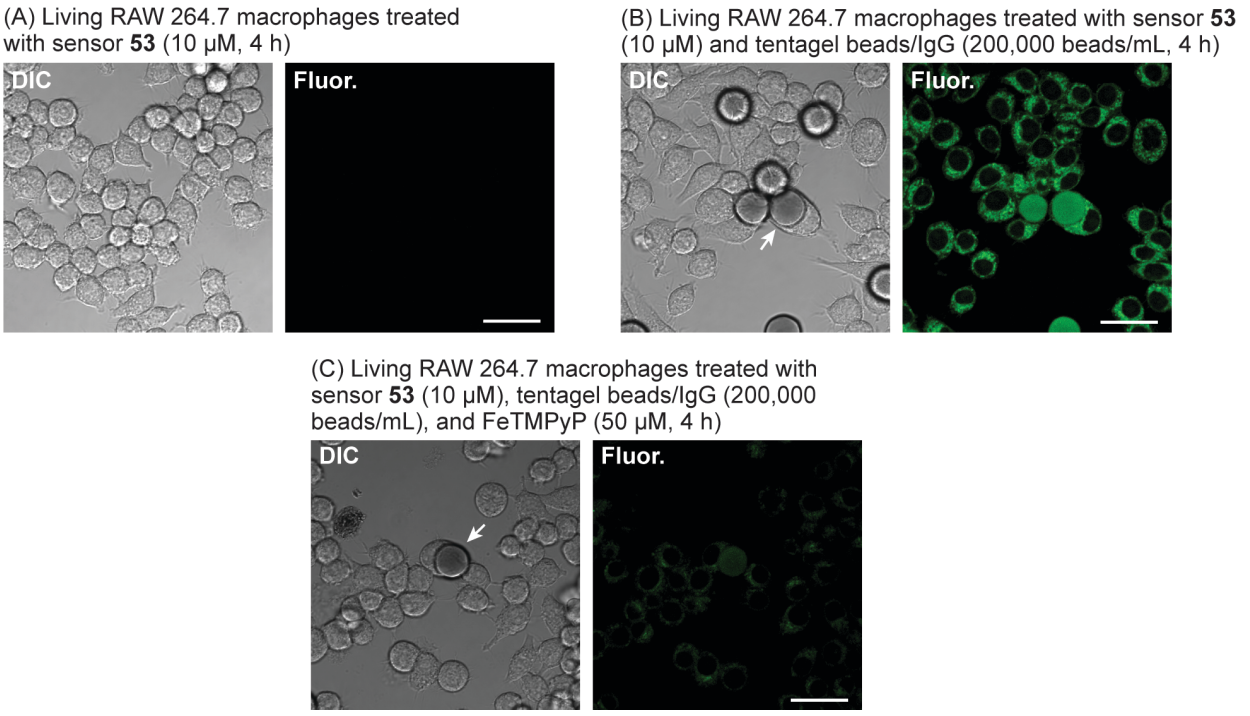

Figure 3-14. (A-C) DIC and confocal laser scanning micrographs of RAW macrophages treated with **53** (4 h). (B) Cells were additionally treated with DNP-modified amino tentagel beads (10 microns) bound to anti-DNP IgG. (C) Cells were additionally treated with DNP-modified amino tentagel beads (10 microns) bound to anti-DNP IgG and FeTMPyP (50 μM). White arrows point at phagocytosed tentagel beads. Scale bar = 25 microns.

As can be seen in both Figure 3-13 B and Figure 3-14 B, the enhanced fluorescence generated upon phagocytosis of the opsonized beads was not localized to macrophages that have phagocytosed beads, but rather was observed throughout the macrophage population. There are several possible explanations for this phenomenon. Perhaps most likely is the rapid exchange of the fluorescent rhodol **59** between cells. In support of this, cellular fluorescence resulting from phagocytosis was best observed in unwashed cells. Washing cells once with media resulted in extensive loss of fluorescence within 10-20 min (Figure 3-15), indicating that efflux of **59** from cellular membranes readily occurs. This dispersed effect could also be caused by the diffusion of peroxynitrite to surrounding cells, given that it is thought to diffuse 5-20 microns within its lifetime.[1] Additionally, activated macrophages release many cytokines including tumor necrosis factor α (TNFα)[57] and interferon-γ (IFN-γ).[58,59] TNFα and IFN-γ, along with many other cytokines, are both able to induce iNOS to synthesize nitric oxide.[5] TNFα has also been shown to enhance the activity of NADPH oxidase when it is activated, leading to increased superoxide production.[5] It is possible that the phagocytosis of the beads was causing the macrophages to release these or other cytokines, which then induced the production of peroxynitrite in neighboring cells.

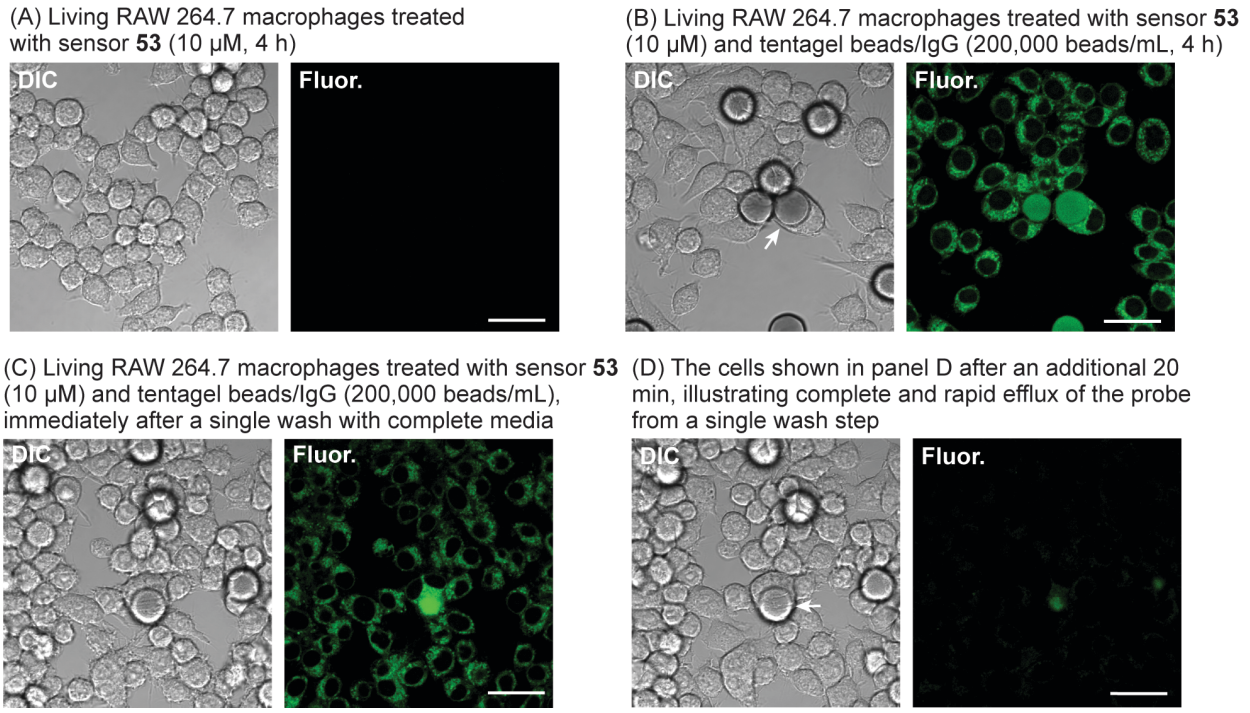

Figure 3-15. (A-D) Confocal laser scanning and DIC micrographs of living RAW264.7 macrophages treated with **53** (10 μM, 4 h). (B) Cells were additionally treated with DNP-modified amino tentagel beads (10 microns) bound to anti-DNP IgG to stimulate phagocytosis, production of peroxynitrite, and generation of the fluorescent rhodol **59**. (C-D) Cells treated with **53** / beads/ IgG for 4 h were washed once with media. Imaging immediately after washing (C) and the same field of cells after 20 min (D) revealed essentially complete loss of cellular fluorescence within 10-20 min. The rapid efflux of rhodol **59** upon washing suggests that this compound can rapidly exchange between cells. White arrows point at phagocytosed beads. Scale bar = 25 microns.

Both the weak intrinsic fluorescence of **53** alone and its highly fluorescent product **59** were confirmed to accumulate in the ER by colocalization with ER tracker blue-white DPX (Figure 3-16). Analysis of images of cells treated with **52**, **53**, and **55** demonstrated that the ratio of cytosolic (ER-associated) to nuclear fluorescence of **53** (ratio = 6.7) is substantially higher compared to **52** (ratio = 3.7) and **55** (ratio = 2.6). These results suggest that the substantially increased efficacy of sensor **53** compared to the similarly reactive sensor **52** is a consequence of the ability of **53** to extensively and selectively accumulate in membranes of the ER.

(A) Treatment of living RAW 267.4 macrophages with sensor **53** and ER tracker blue-white DPX
(Power of 488 nm laser = 25%; gain = 1200; offset = -20%)

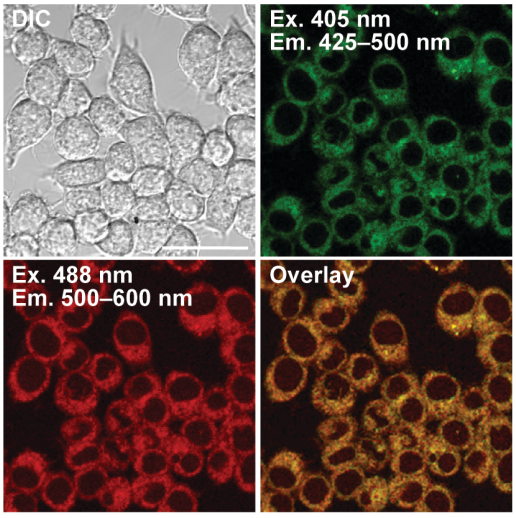

(B) Treatment of living RAW 267.4 macrophages with sensor **53** and ER tracker blue-white DPX followed by stimulation with tentagel beads/IgG
(Power of 488 nm laser = 15%; gain = 850; offset = -20%)

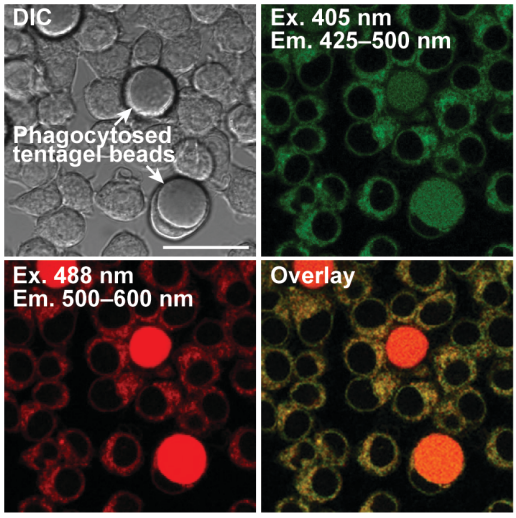

(C) Treatment of living RAW 267.4 macrophages with sensor **52** and ER tracker blue-white DPX
(Power of 488 nm laser = 25%; gain = 1200; offset = -20%)

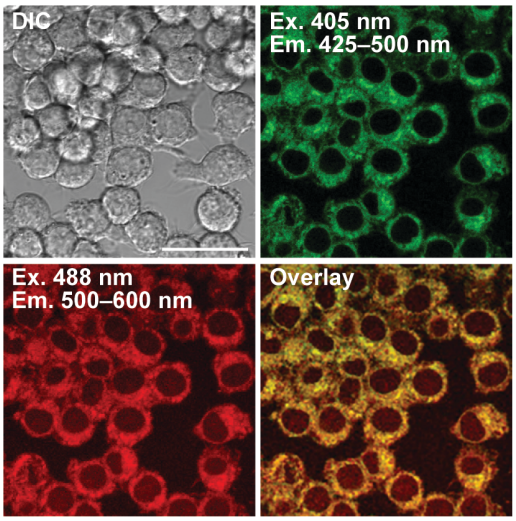

(D) Treatment of living RAW 267.4 macrophages with sensor **55** and ER tracker blue-white DPX
(Power of 488 nm laser = 25%; gain = 1200; offset = -20%)

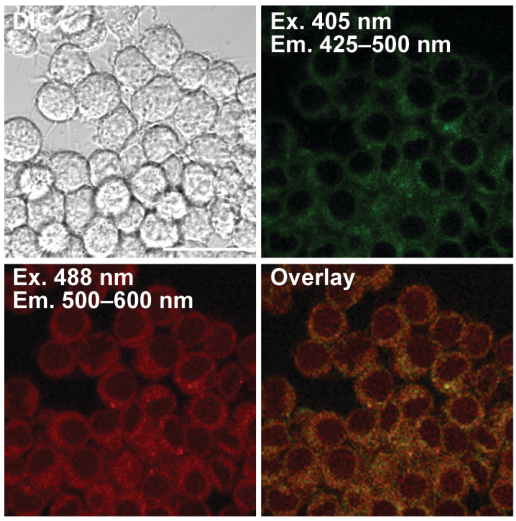

(E)

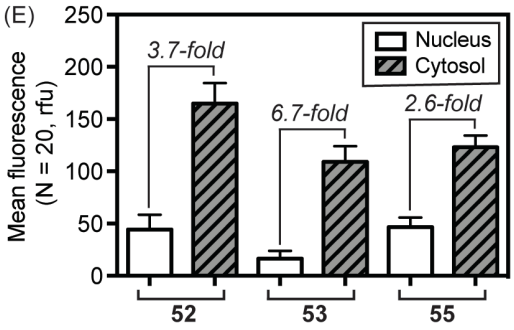

Figure 3-16. Panels A-D: Confocal laser scanning and DIC micrographs of living RAW264.7 macrophages treated with **53**, **52**, and **55** (10 μM, 4 h). Panels A, C, and D: Colocalization of the weak intrinsic fluorescence of **53**, **52**, and **55** with ER tracker blue-white DPX demonstrates accumulation in the ER. Panel B: Cells were treated with **53** and

stimulated with IgG-bound tentagel beads to generate **59**. Imaging at lower laser power and gain and colocalization with ER tracker blue-white confirmed that **59** remains associated with the ER. Panel E: Quantification of cytosolic and nuclear fluorescence of **52**, **53**, and **55**. Sensor **53** shows the greatest selectivity for ER membranes as evidenced by the highest ratio.

This interpretation was further supported by flow cytometry after correcting for differences in brightness. Using this method, **53** was found to accumulate 4-fold more in ER membranes than **55** (Figure 3-17). The association of sensors **51** (cLogP=5.9), **52** (cLogP=6.4), and **53** (cLogP=6.8) with ER membranes was linearly correlated with cLogP (Figure 3-16 B), indicating that increased hydrophobicity provides a driving force for loading of these membranes. However, the more highly hydrophobic di-*t*-butyl-phenol derivative **54** (cLogP=9.2), was less ER-associated than **52**, likely due to lower affinity of branched alkanes for straight-chain fatty acids of lipids of ER membranes. Despite its high hydrophobicity, **58** (cLogP=6.9) showed the lowest association with the ER, likely because its partially-ionized acidic phenol decreases association with membranes. For comparison, the calculated pKa of the phenol of **58** is 7.4, while that of **53** is 11.1 (calculations done using ChemAxon). These trends offer guidelines for the design of other ER-associated sensors.

(A) Analysis of accumulation of sensors (**51**-**58**) in living RAW264.7 macrophages by flow cytometry

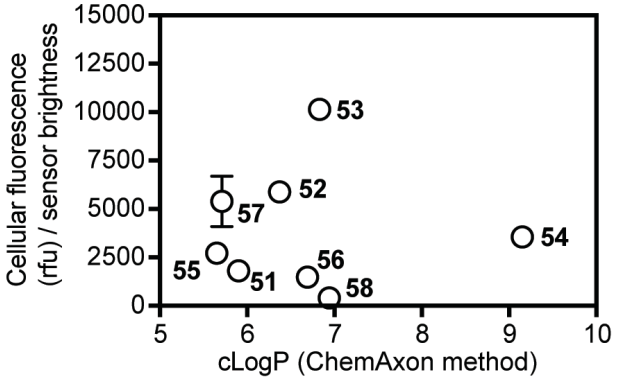

(B) Highly structurally similar sensors (**51**–**53**) show a linear relationship between hydrophobicity and accumulation in membranes of the ER

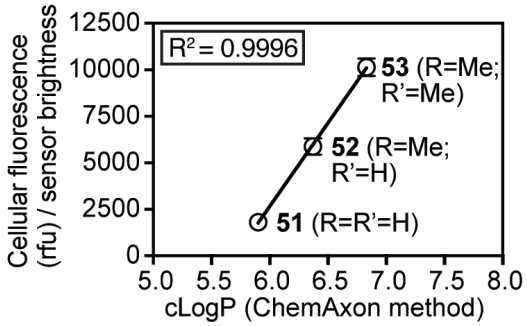

Figure 3-17. Analysis of accumulation of sensors **51**–**58** in ER membranes by flow cytometry. Cellular fluorescence was divided by brightness (quantum yields * molar extinction coefficients) to correct for spectral differences. Sensor **53** shows the greatest cellular fluorescence, resulting from extensive accumulation in membranes of the ER (panel A). For the structurally related sensors **51**–**53**, likely to interact similarly with lipids of the ER, accumulation in membranes of this organelle is linearly correlated with cLogP (panel B). The branched *t*-butyl side chains of **54** lead to lower cellular fluorescence, likely due to decreased affinity for straight-chain lipids of ER membranes. The lowest cellular fluorescence was observed for the dichloro derivative **58**, where the increased acidity of the phenol and subsequent partial ionization in cells is likely to reduce affinity for hydrophobic ER membranes. The steric bulk of the bromo substituent of **56** may contribute to its lower association with ER membranes.

3-9. Conclusions and future directions

We have presented here the design, synthesis, and analysis of endoplasmic reticulum-localized fluorescent sensors of peroxynitrite. These sensors react rapidly and selectively with peroxynitrite and have spectral properties that allow for their use in many systems. Kinetic studies in buffer solutions and flow cytometry-based cell assays were used to select the most effective analogues. In this series of compounds, sensor **53** was found to have the most optimal balance between reaction rate and ER localization and emerged as the best analog.

The extensive and selective association of **53** with membranes of the ER enables this sensor to uniquely detect transient peroxynitrite generated during phagocytosis. Because these convoluted membranes offer a vast intracellular surface area, fluorescent sensors that accumulate in these membranes have potential for highly sensitive detection of a wide variety of transient cellular species.

Additionally, it has been reported that Taxol, an anticancer drug whose mechanism of action is not fully understood, stimulates the production of reactive species such as peroxynitrite in macrophages.[60] The sensors reported here, particularly **53**, could be used

to further investigate the contribution of the activation of macrophages to the mechanism of Taxol. This scaffold is also being used to generate sensors of other reactive species, and the phagocytosis assay is currently being used to screen for compounds that stimulate the generation of peroxynitrite.

3-10. Experimental

3-10-1. General experimental section

All reactions were performed under an inert atmosphere of dry argon or nitrogen either in a flame-dried or oven-dried glassware, or in a glass microwave vial (Biotage, LLC). All anhydrous solvents were either purchased from Sigma Aldrich company or dried via passage through a glass contour solvent system (Pure Process Technology, LLC). All reagents were purchased from TCI, Sigma Aldrich, or Oakwood Products Inc.

Thin-layer chromatography (TLC) was performed using commercial aluminum backed silica plates (TLC Silica gel 60 F254, Analytical Chromatography). Visualization was accomplished with UV light. Flash chromatography was carried out on normal phase using silica gel (230–400 mesh) or by reverse phase on a Combiflash purification system (50g HP C18 gold column).

Nuclear magnetic resonance (NMR) spectra were recorded on either a 400 MHz or 500 MHz Bruker Avance spectrometer with a dual carbon/proton cryoprobe. NMRs were recorded in deuterated chloroform or dimethyl sulfoxide. Chemical shifts are reported in parts per million (ppm) and are referenced to the center line of the solvent (δ 2.50, and 7.26 with respect to dimethyl sulfoxide-d_6, and chloroform-*d* for ^{1}H NMR and ^{19}F NMR and δ 39.52, and 77.16 with respect to dimethyl sulfoxide-d_6, and chloroform-*d*

for ^{13}C NMR). Coupling constants are given in Hertz (Hz). The spin multiplicities are reported as s = singlet, d = doublet, t = triplet, q = quartet, dd = doublet of doublet td = doublet of triplet and m = multiplet. ^{13}C NMR for **51**–**59** was recorded on a 500 MHz Bruker Avance spectrometer using the following acquisition parameters; for **51**, number of scans (ns)= 8000, time domain (td)= 65000, acquisition time (aq)= 1.1 s, relaxation delay (d1)= 0.15 s and temperature (T) = 25.5 °C. For **52**; ns= 1000, td= 65000, aq= 1.1 s, d1= 0.5 s and T= 25.5 °C. For **53**; ns= 14615, td= 32000, aq= 0.55 s, d1= 1.5 s and T= 45 °C. For **54**; ns= 6000, td= 65000, aq= 1.1 s, d1= 0.15 s and T= 25.5 °C. For **55**; ns= 9216, td= 65k, aq= 1.1 s, d1= 0.15 s and T= 25.5 °C. For **56**; ns= 7801, td= 32000, aq= 0.55 s, d1= 0.15 s and T= 60 °C. For **57**; ns= 9211, td= 32000, aq= 0.55 s, d1= 0.15 s and T= 45 °C. For **58**; ns= 7000, td= 32000, aq= 0.55 s, d1= 0.15 s and T= 45 °C. For **59**; ns= 4222, td= 65000, aq= 1.1 s, d1= 0.15 s and T= 60 °C. NMR data analysis used MNova software. HRMS data were collected on an LCT Premier (Waters Corp., Milford MA) time of flight mass spectrometer

3-10-2. Synthetic procedures and compound characterization data

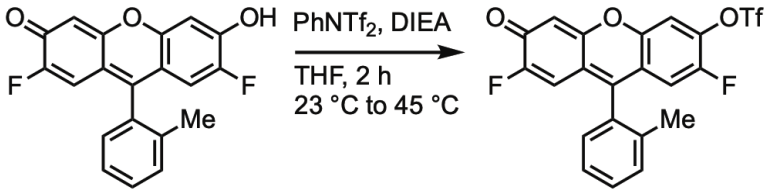

Pennsylvania Green **60**

Scheme 3-3. Synthesis of Pennsylvania Green triflate (**60**).

2,7-difluoro-3-oxo-9-(*o*-tolyl)-3*H*-xanthen-6-yl trifluoromethanesulfonate (**60, Pennsylvania Green triflate**). As shown in Scheme 3-3, the fluorophore Pennsylvania Green (490 mg, 1.44 mmol, 1 equiv., prepared from 2,7-difluoro-3,6-bis[(2-methoxyethoxy)methoxy]-9*H*-xanthene-9-one[61] as previously described,[51] also commercially available from AK Scientific) and *N*-phenyl-bis(trifluoromethanesulfoimide) (1.5 equiv.) were weighted in an oven dried, Ar-flushed round bottom flask equipped with a magnetic stir bar and dissolved in anhydrous THF (~0.15 mM). The mixture was treated with DIEA (2.5 equiv.) and stirred at room temperature (23 °C) for 5 min. This reaction mixture was heated at 45 °C for 2 h. Progress of the reaction was monitored by TLC and upon completion the crude mixture was concentrated to dryness. The residue was re-dissolved in dichloromethane and purified by silica gel chromatography using hexane and ethyl acetate to elute **60** (497 mg, 73% yield).^{1}H NMR (400 MHz, Chloroform-*d*) δ 7.50–7.44 (m, 2H), 7.41–7.33 (m, 2H), 7.09 (dd, *J* = 7.5, 1.3 Hz, 1H), 6.87 (d, *J* = 9.6 Hz, 1H), 6.56 (d, *J* = 10.3 Hz, 1H), 6.51 (d, *J* = 6.7 Hz, 1H), 2.03 (s, 3H); ^{13}C NMR (126 MHz, Chloroform-*d*) δ 176.8 (d, *J* = 21.4 Hz), 157.0 (d, *J* = 272.2 Hz), 156.8, 150.5 (d, *J* = 252.1 Hz), 147.9, 146.7 (d, *J* = 10.0 Hz), 139.2 (d, *J* = 15.8 Hz), 136.2, 131.4, 131.1, 130.7, 129.0, 126.9, 122.0 (d, *J* = 8.2 Hz), 121.1 (d, *J* = 6.9 Hz), 118.77 (d, *J* = 321.1 Hz), 115.1 (d, *J* = 21.7 Hz), 112.8, 110.0 (d, *J* = 22.3 Hz), 107.6 (d, *J* = 4.5 Hz), 19.8; ^{19}F NMR (471 MHz, Chloroform-*d*) δ 27.3, -19.7, -30.0; HRMS calcd. for $C_{21}H_{12}F_5O_5S^+$: 471.0326; Found: 471.0329.

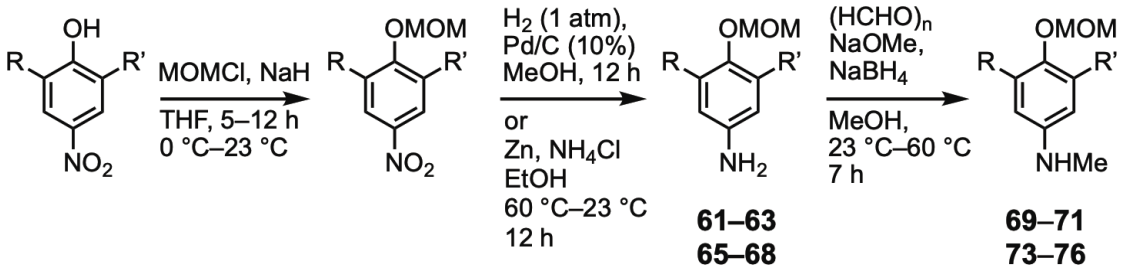

Scheme 3-4. Synthesis of MOM-protected anilines **61**–**63**, **65–71**, and **73–76**.

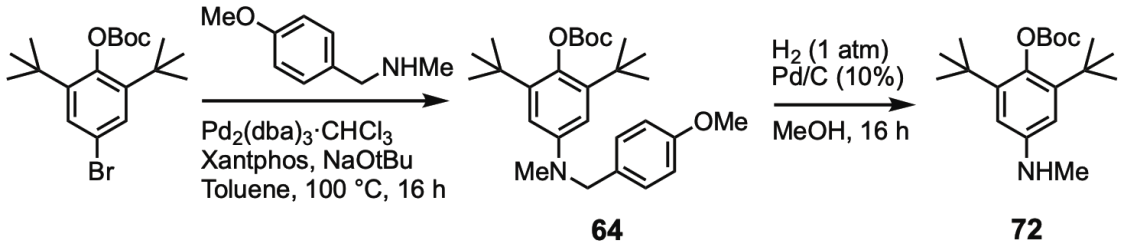

Scheme 3-5. Synthesis of Boc-protected anilines **64** and **72**.

Synthesis of MOM-protected anilines (**61**–**63**, **65**–**71**, and **73**–**76**)**:**

As shown in Scheme 3-4, the nitrophenol (1 equiv.) was weighed out in a flame dried, Ar-flushed round bottom flask equipped with a magnetic stir bar, and anhydrous THF was added (0.25 mM). The solution was cooled to 4 °C and treated with NaH (1.5 equiv.) in several portions over 10–15 min. The suspension was stirred at 4 °C for additional 10 min and then treated dropwise with MOMCl (1.5 equiv.). The reaction mixture was stirred for an additional 10 min. The ice bath was removed, and the reaction mixture was stirred at room temperature for a period of 5–12 h. On completion the reaction was quenched with water and extracted with diethyl ether. The organic layer was dried over $MgSO_4$ and concentrated to dryness. The crude mixture was taken forward to the next step without purification.

Reduction of the nitro group using Pd/C (for **61**–**63**, **65**, and **67**).

As shown in Scheme 3-4, the crude reaction mixture from *Synthesis of MOM-protected anilines* was dissolved in methanol (~0.1 mM) in a round bottom flask equipped with a magnetic stir bar. Pd/C (10%, 0.2 equiv.) was carefully added this solution. The flask was sealed, and the reaction mixture was stirred under H_2 (1 atm). Progress of the reaction was monitored by TLC, and on completion, the crude mixture was filtered through a celite plug. The celite plug was washed with copious amounts of methanol and the combined filtrate was concentrated to dryness. The crude mixture was purified by silica gel chromatography using hexane and ethyl acetate to elute pure products.

Reduction of the nitro group using Zn/NH_4Cl (for **66** and **68**).

As shown in Scheme 3-4, the crude reaction mixture from *Synthesis of MOM-protected anilines* was dissolved in ethanol (~0.2 mM) in a round bottom flask equipped with a magnetic stir bar. Ammonium chloride (10.0 equiv.) was added and the reaction mixture was stirred for 5 min. This suspension was treated with Zn dust (10.0 equiv.) followed by heating in an oil bath at 60 °C for 5 min. This flask was removed from the oil bath and stirred at room temperature for up to 12 h. Progress of the reaction was monitored by TLC, and on completion the crude mixture was filtered through filter agent (Celite 545, Sigma, 419931). The Celite was washed with copious amounts of methanol and the combined filtrate was concentrated to dryness. This crude mixture was re-dissolved in dichloromethane (50 mL) and washed with aqueous NaOH (1N). The aqueous layer was further extracted with dichloromethane (2 X 20 mL). The combined organic layers were

dried over $MgSO_4$, filtered, and concentrated to dryness. The crude residue was further purified by silica gel chromatography using hexane and ethyl acetate as eluents.

Reductive methylation of anilines.[62,63]

As shown in Scheme 3-4, the MOM protected 4-amino phenol (1.0 equiv.) was weighed in a flame dried, Ar-flushed Biotage microwave reaction vial and dissolved in anhydrous methanol (~0.2 mM) at room temperature. The solution was treated with NaOMe (5.0 equiv.) added in a single portion (a slight exotherm was observed). The mixture was stirred, allowed to return to room temperature, and paraformaldehyde (1.4 equiv.) was added. This solution was stirred for 5 h under an atmosphere of Ar. After 5 h, $NaBH_4$ (1.0 equiv.) was added in a single portion, and the vial was sealed and heated at 55 °C for 4 h. This crude mixture was cooled to room temperature, diluted with EtOAc, and extracted with aq. KOH (1N). The organic layer was separated, dried over anhydrous $MgSO_4$, and concentrated to dryness. The crude product was purified by silica gel chromatography using hexane and ethyl acetate as eluents.

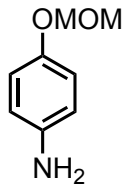

4-(methoxymethoxy)aniline (**61**). As shown in Scheme 3-4, using the method described for *Synthesis of MOM-protected N-methyl anilines* and *reduction of the nitro group using Pd/C*, 1-(methoxymethoxy)-4-nitrobenzene (658 mg, 3.59 mmol) afforded **61** (551 mg, >95% yield over two steps). ^{1}H NMR (400 MHz, Chloroform-*d*) δ 6.90–6.85 (m, 2H), 6.69–

6.63 (m, 2H), 5.08 (s, 2H), 3.47 (s, 3H); ^{13}C NMR (101 MHz, Chloroform-*d*) δ 150.3, 141.4, 118.0, 116.3, 95.6, 55.9; HRMS calcd. for $C_8H_{12}NO_2^+$: 154.0868; Found: 154.0874.

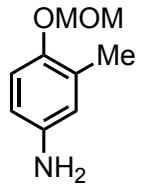

4-(methoxymethoxy)-3-methylaniline (**62**): As shown in Scheme 3-4, using the method described for *Synthesis of MOM-protected N-methyl anilines* and *reduction of the nitro group using Pd/C*, 1-(methoxymethoxy)-2-methyl-4-nitrobenzene (200 mg, 1.30 mmol) afforded **62** (198 mg, 91% yield over two steps). ^{1}H NMR (400 MHz, Chloroform-*d*) δ 6.87 (d, *J* = 8.5 Hz, 1H), 6.53 (d, *J* = 2.9 Hz, 1H), 6.49–6.45 (m, 1H), 5.09 (s, 2H), 3.49 (s, 3H), 3.41 (s, 2H), 2.19 (s, 3H); ^{13}C NMR (101 MHz, Chloroform-*d*) δ 148.7, 141.1, 128.9, 118.2, 116.5, 113.4, 95.8, 56.0, 16.5; HRMS calcd. for $C_9H_{14}NO_2^+$: 168.1025; Found: 168.1021.

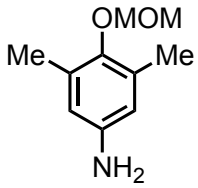

4-(methoxymethoxy)-3,5-dimethylaniline (**63**): As shown in Scheme 3-4, using the method described for *Synthesis of MOM-protected N-methyl anilines* and *reduction of the nitro group using Pd/C*, 2-(methoxymethoxy)-1,3-dimethyl-5-nitrobenzene (300 mg, 1.42 mmol) afforded **63** (292 mg, 90% yield over two steps).^{1}H NMR (400 MHz, Chloroform-*d*)

δ 6.36 (s, 2H), 4.88 (s, 2H), 3.59 (s, 3H), 3.42 (s, 2H), 2.22 (s, 6H); ^{13}C NMR (101 MHz, Chloroform-*d*) δ 147.3, 142.6, 131.9, 115.4, 99.4, 57.4, 17.0; HRMS calcd. for $C_{10}H_{16}NO_2^+$: 182.1181; Found: 182.1187.

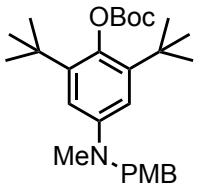

***tert*-butyl (2,6-di-*tert*-butyl-4-((4-methoxybenzyl)(methyl)amino)phenyl) carbonate** (**64**): As shown in Scheme 3-5, 4-bromo-2,6-di-*tert*-butylphenyl *tert*-butyl carbonate[64] (115 mg, 0.3 mmol, 1.0 equiv.), 1-(4-methoxyphenyl)-*N*-methylmethanamine (1.2 equiv.), $Pd_2(dba)_3.CHCl_3$ (0.1 equiv.), xantphos (0.15 equiv.) and Cs_2CO_3 (2.5 equiv.) were weighed in a Biotage microwave reaction vial in a glove box. The mixture was treated with toluene (0.05 mM) and the vial was sealed and removed from the glove box. The reaction mixture was heated in an oil bath at 100 °C for 16 h. The crude mixture was cooled to room temperature and purified by silica gel chromatography using hexane and ethyl acetate as eluents to afford **64** (98 mg, 71% yield). ^{1}H NMR (500 MHz, Chloroform-*d*) δ 7.21 (d, *J* = 8.2 Hz, 2H), 6.86 (d, *J* = 8.6 Hz, 2H), 6.70 (s, 2H), 4.37 (s, 2H), 3.80 (s, 3H), 2.93 (s, 3H), 1.53 (s, 9H), 1.33 (s, 18H); ^{13}C NMR (126 MHz, Chloroform-*d*) δ 158.7, 153.7, 147.4, 142.9, 139.9, 131.7, 128.4, 114.0, 111.0, 82.6, 57.3, 55.4, 38.8, 35.8, 31.6, 28.0; HRMS calcd. for $C_{28}H_{42}NO_4^+$: 456.3114; Found: 456.3116.

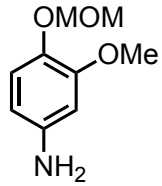

3-methoxy-4-(methoxymethoxy)aniline (**65**): As shown in Scheme 3-4, using the method described for *Synthesis of MOM-protected N-methyl anilines* and *reduction of the nitro group using Pd/C*, 2-methoxy-1-(methoxymethoxy)-4-nitrobenzene (170 mg, 1.0 mmol) afforded **65** (176 mg, >95% yield over two steps). ^{1}H NMR (400 MHz, Chloroform-*d*) δ 6.94 (d, *J* = 8.4 Hz, 1H), 6.30 (d, *J* = 2.6 Hz, 1H), 6.21 (dd, *J* = 8.4, 2.6 Hz, 1H), 5.09 (s, 2H), 3.82 (s, 3H), 3.51 (s, 3H); ^{13}C NMR (101 MHz, Chloroform-*d*) δ 151.1, 142.5, 139.3, 119.3, 106.9, 100.6, 96.8, 56.2, 55.9; HRMS calcd. for $C_9H_{14}NO_3^+$: 184.0974; Found: 184.0990.

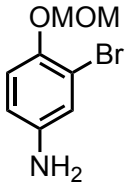

3-bromo-4-(methoxymethoxy)aniline (**66**): This compound was synthesized following procedures described under Scheme 3-4 and was isolated in >95 % yield over two steps. As shown in Scheme 3-4, using the method described for *Synthesis of MOM-protected N-methyl anilines* and *Reduction of the nitro group using Zn/NH₄Cl*, 2-bromo-1-(methoxymethoxy)-4-nitrobenzene (170 mg, 0.45 mmol) afforded **66** (102 mg, >95% yield over two steps). ^{1}H NMR (400 MHz, Chloroform-*d*) δ 6.96 (d, *J* = 8.7 Hz, 1H), 6.90 (d, *J* = 2.8 Hz, 1H), 6.57 (dd, *J* = 8.7, 2.8 Hz, 1H), 5.11 (s, 2H), 3.53 (s, 3H), 3.50 (s, 2H); ^{13}C

NMR (101 MHz, Chloroform-*d*) δ 146.7, 142.6, 119.8, 118.9, 115.2, 114.2, 96.5, 56.5; HRMS calcd. for $C_8H_{11}BrNO_2^+$: 231.9973; Found: 231.9969.

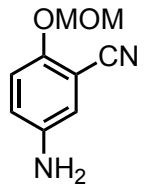

5-amino-2-(methoxymethoxy)benzonitrile (**67**): As shown in Scheme 3-4, using the method described for *Synthesis of MOM-protected N-methyl anilines* and *reduction of the nitro group using Pd/C*, 2-(methoxymethoxy)-5-nitrobenzonitrile (304 mg, 1.85 mmol) afforded **67** (172 mg, 52% yield over two steps). ^{1}H NMR (400 MHz, Chloroform-*d*) δ 7.09–7.00 (m, 1H), 6.88–6.79 (m, 2H), 5.17 (s, 2H), 3.63 (s, 2H), 3.52 (s, 3H); ^{13}C NMR (101 MHz, Chloroform-*d*) δ 152.0, 141.4, 121.3, 118.6, 117.3, 116.7, 103.7, 95.8, 56.5; HRMS calcd. for $C_9H_{11}N2O_2^+$: 179.0821; Found: 179.0855.

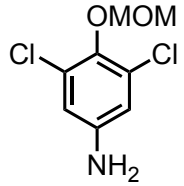

3,5-dichloro-4-(methoxymethoxy)aniline (**68**): As shown in Scheme 3-4, using the method described for *Synthesis of MOM-protected N-methyl anilines* and *Reduction of the nitro group using Zn/NH$_4$Cl*, 1,3-dichloro-2-(methoxymethoxy)-5-nitrobenzene (144 mg, 0.7 mmol) afforded **68** (66 mg, 39% yield over two steps). ^{1}H NMR (400 MHz, Chloroform-*d*) δ 6.61 (s, 2H), 5.06 (s, 2H), 3.67 (s, 3H), 3.63 (bs, 2H); ^{13}C NMR (101 MHz,

Chloroform-*d*) δ 143.8, 141.5, 129.8, 115.2, 99.5, 58.2; HRMS calcd. for $C_8H_{10}Cl_2N_2O_2^+$: 222.0089; Found: 222.0103.

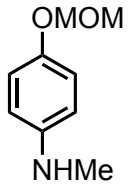

4-(methoxymethoxy)-*N*-methylaniline (**69**): As shown in Scheme 3-4, using the method described for *Reductive methylation of anilines*, **61** (200 mg, 1.30 mmol) afforded **69** (199 mg, 92% yield). ^{1}H NMR (400 MHz, Chloroform-*d*) δ 7.11–6.81 (m, 2H), 6.74–6.43 (m, 2H), 5.08 (s, 2H), 3.48 (s, 3H), 2.81 (s, 3H); ^{13}C NMR (101 MHz, Chloroform-*d*) δ 149.9, 144.3, 118.1, 114.0, 95.8, 55.9, 31.9; HRMS calcd. for $C_9H_{14}NO_2^+$: 168.1025; Found: 168.1027.

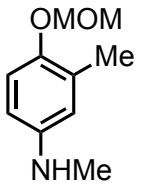

4-(methoxymethoxy)-*N*,3-dimethylaniline (**70**): As shown in Scheme 3-4, using the method described for *Reductive methylation of anilines*, **62** (100 mg, 0.60 mmol) afforded **70** (86 mg, 79% yield). ^{1}H NMR (400 MHz, Chloroform-*d*) δ 6.92 (d, *J* = 8.6 Hz, 1H), 6.46 (d, *J* = 2.8 Hz, 1H), 6.41 (dd, *J* = 8.6, 2.8 Hz, 1H), 5.08 (s, 2H), 3.50 (s, 3H), 3.43 (s, 1H), 2.80 (s, 3H), 2.22 (s, 3H); ^{13}C NMR (101 MHz, Chloroform-*d*) δ 147.9, 144.7, 128.9, 116.8, 115.5, 110.5, 96.0, 56.1, 31.6, 16.7; HRMS calcd. for $C_{10}H_{16}NO_2^+$: 182.1181; Found: 182.1189.

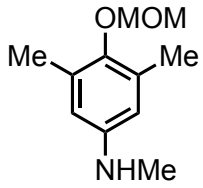

4-(methoxymethoxy)-*N*,3,5-trimethylaniline (**71**): As shown in Scheme 3-4, using the method described for *Reductive methylation of anilines*, **63** (514 mg, 2.84 mmol) afforded **71** (435 mg, 79% yield). ^{1}H NMR (400 MHz, Chloroform-*d*) δ 6.29 (s, 2H), 4.89 (s, 2H), 3.60 (s, 3H), 3.46 (s, 1H), 2.79 (s, 3H), 2.25 (s, 3H); ^{13}C NMR (101 MHz, Chloroform-*d*) δ 146.5, 145.9, 131.8, 112.6, 99.4, 57.4, 31.3, 17.2; HRMS calcd. for $C_{11}H_{18}NO_2^+$: 196.1338; Found: 196.1343

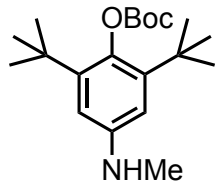

***tert*-butyl (2,6-di-*tert*-butyl-4-(methylamino)phenyl) carbonate** (**72**): As shown in Scheme 3-5, *tert*-butyl (2,6-di-*tert*-butyl-4-((4-methoxybenzyl)(methyl)amino)phenyl) carbonate **64** (50 mg, 0.1 mmol), was dissolved in methanol (~0.1 mM) in a round bottom flask equipped with a magnetic stir bar. Pd/C (10%, 0.2 equiv.) was carefully added to the above solution. The flask was sealed, and the reaction mixture was stirred under H_2 (1 atm). Progress of the reaction was monitored by TLC and on completion the crude mixture was filtered through celite. The celite was washed with copious amounts of methanol and the combined filtrate was concentrated to dryness. The crude mixture was purified by silica gel chromatography using hexane and ethyl acetate for elution of **72** (32 mg, 95% yield). ^{1}H NMR (500 MHz, Chloroform-*d*) δ 6.54 (s, 2H), 2.82 (s, 3H), 1.52 (s, 9H), 1.35

(s, 19H); ^{13}C NMR (126 MHz, Chloroform-*d*) δ 153.7, 146.4, 143.3, 140.2, 110.4, 82.6, 35.6, 31.5, 31.2, 28.0; HRMS calcd. for $C_{20}H_{34}NO_3^+$: 336.2539; Found: 336.2543.

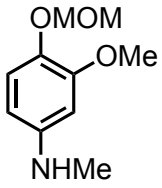

3-methoxy-4-(methoxymethoxy)-*N*-methylaniline (**73**): As shown in Scheme 3-4, using the method described for *Reductive methylation of anilines*, **65** (100 mg, 0.54 mmol) afforded **73** (89 mg, 83% yield). ^{1}H NMR (400 MHz, Chloroform-*d*) δ 6.99 (d, *J* = 8.6 Hz, 1H), 6.22 (d, *J* = 2.6 Hz, 1H), 6.13 (dd, *J* = 8.6, 2.7 Hz, 1H), 5.09 (s, 2H), 3.84 (s, 3H), 3.52 (s, 3H), 2.82 (s, 3H); ^{13}C NMR (101 MHz, Chloroform-*d*) δ 151.3, 146.0, 138.5, 119.5, 103.7, 98.3, 96.9, 56.2, 55.9, 31.5; HRMS calcd. for $C_{10}H_{16}NO_3^+$: 198.1130; Found: 198.1144.

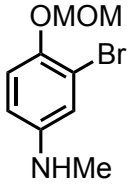

3-bromo-4-(methoxymethoxy)-*N*-methylaniline (**74**): As shown in Scheme 3-4, using the method described for *Reductive methylation of anilines*, **66** (100 mg, 0.43 mmol) afforded **74** (89 mg, 84% yield). ^{1}H NMR (400 MHz, Chloroform-*d*) δ 7.00 (d, *J* = 8.8 Hz, 1H), 6.80 (d, *J* = 2.8 Hz, 1H), 6.49 (dd, *J* = 8.8, 2.9 Hz, 1H), 5.11 (s, 2H), 3.58 (s, 1H), 3.53 (s, 3H), 2.78 (s, 3H); ^{13}C NMR (101 MHz, Chloroform-*d*) δ 145.9, 145.6, 119.3, 116.6,

114.6, 112.6, 96.7, 56.5, 31.2; HRMS calcd. for $C_9H_{13}BrNO_2^+$: 246.0130; Found: 246.0135.

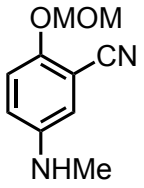

2-(methoxymethoxy)-5-(methylamino)benzonitrile (**75**): As shown in Scheme 3-4, using the method described for *Reductive methylation of anilines*, **67** (150 mg, 0.84 mmol) afforded **75** (149 mg, 92% yield). This compound was synthesized following procedures described under Scheme 3-3 and was isolated in 92% yield. ^{1}H NMR (400 MHz, Chloroform-*d*) δ 7.07 (d, *J* = 8.2 Hz, 1H), 6.78–6.72 (m, 2H), 5.17 (s, 2H), 3.68 (s, 1H), 3.53 (s, 3H), 2.81 (s, 3H); ^{13}C NMR (101 MHz, Chloroform-*d*) δ 151.1, 144.6, 118.9, 117.6, 117.1, 115.1, 103.9, 96.0, 56.5, 31.1; $C_{10}H_{12}N_2O_2^+$: 193.0977; Found: 193.0982.

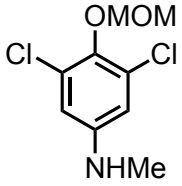

3,5-dichloro-4-(methoxymethoxy)-*N*-methylaniline (**76**): As shown in Scheme 3-4, using the method described for *Reductive methylation of anilines*, **68** (50 mg, 0.22 mmol) afforded **76** (50 mg, 95% yield). ^{1}H NMR (400 MHz, Chloroform-*d*) δ 6.51 (s, 2H), 5.06 (s, 2H), 3.72 (s, 1H), 3.68 (s, 3H), 2.77 (s, 3H); ^{13}C NMR (101 MHz, Chloroform-*d*) δ 146.6, 140.2, 129.8, 112.3, 99.5, 58.2, 30.8;

Buchwald–Hartwig amination of Pennsylvania Green triflate (60) with anilines 69–76: The triflate **60** (1.0 equiv.), amine (1.2 equiv.), $Pd(OAc)_2$ (0.1 equiv.), Xantphos (0.15 equiv.) and Cs_2CO_3 (2.5 equiv.) were weighed in a Biotage microwave reaction vial in a glove box. The mixture was treated with toluene (0.05 mM) and the vial was sealed and removed from the glove box. The reaction mixture was heated in an oil bath at 100 °C for 16 h. The crude mixture was then cooled to room temperature and purified by silica gel chromatography using hexane and ethyl acetate for elution of pure products.

Removal of the MOM/Boc group: The Buchwald-Hartwig amination product was weighed out in a 25 mL scintillation vial wrapped with Al foil and treated with TFA / dichloromethane (3:7). The color of the solution immediately turns magenta upon addition of TFA. The reaction mixture was stirred at room temperature for 2 h. Progress of the reaction was monitored by thin layer chromatography. On complete consumption of starting material, the crude mixture was transferred to a round bottom flask using dichloromethane and was concentrated to dryness. Excess TFA was removed azeotropically using toluene. The crude product re-dissolved in DMSO, purified by reverse phase chromatography using water and acetonitrile (both containing 0.1% TFA) for elution, and yielded pure product as dark red solid upon dissolution in DMSO and subsequent lyophilization.

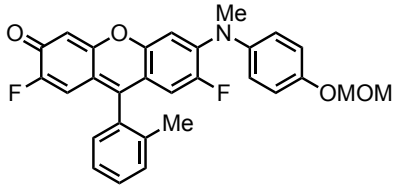

2,7-difluoro-6-((4-(methoxymethoxy)phenyl)(methyl)amino)-9-(*o*-tolyl)-3*H*-xanthen-3-one (**77**): As described under *Buchwald–Hartwig amination of Pennsylvania Green triflate (**60**)*, **69** (47 mg, 0.1 mmol) afforded **77** (39 mg, 72% yield). ^{1}H NMR (500 MHz, DMSO-d_6) δ 7.56–7.48 (m, 2H), 7.43 (td, *J* = 7.4, 1.5 Hz, 1H), 7.34–7.26 (m, 2H), 7.17–7.11 (m, 2H), 7.03–6.97 (m, 2H), 6.56–6.50 (m, 2H), 6.47 (d, *J* = 7.2 Hz, 1H), 5.17 (s, 2H), 3.41 (s, 3H), 3.37 (s, 3H), 2.04 (s, 3H); ^{13}C NMR (126 MHz, DMSO-d_6) δ 174.5 (d, *J* = 20.1 Hz), 157.5, 156.0 (d, *J* = 263.2 Hz), 154.6, 150.7, 150.6 (d, *J* = 247.0 Hz), 150.2 (d, *J* = 11.7 Hz), 143.5 (d, *J* = 10.3 Hz), 142.3 (d, *J* = 2.2 Hz), 136.0, 132.1, 131.1, 130.3, 129.3, 126.8, 125.1, 117.3, 116.0 (d, *J* = 8.3 Hz), 113.2 (d, *J* = 23.9 Hz), 112.8 (d, *J* = 8.4 Hz), 110.2 (d, *J* = 21.2 Hz), 106.3 (d, *J* = 3.2 Hz), 105.9 (d, *J* = 5.4 Hz), 94.5, 56.0, 43.2, 19.6; ^{19}F NMR (376 MHz, Chloroform-*d*) δ -21.69, -24.85; HRMS calcd. for $C_{29}H_{24}F_2NO_4^+$: 488.1673; Found: 488.1665.

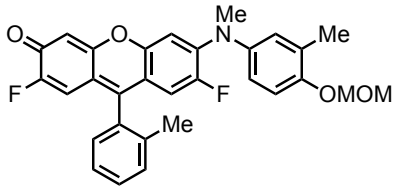

2,7-difluoro-6-((4-(methoxymethoxy)-3-methylphenyl)(methyl)amino)-9-(*o*-tolyl)-3*H*-xanthen-3-one (**78**): As described under *Buchwald–Hartwig amination of Pennsylvania Green triflate (**60**)*, **70** (43 mg, 0.093 mmol) afforded **78** (42 mg, 91% yield). ^{1}H NMR (500 MHz, DMSO-d_6) δ 7.57–7.46 (m, 2H), 7.46–7.42 (m, 1H), 7.30–7.26 (m, 2H), 7.05 (d, *J* = 2.6 Hz, 1H), 7.02–6.92 (m, 2H), 6.56–6.49 (m, 2H), 6.47 (d, *J* = 7.1 Hz, 1H), 5.19 (s, 2H), 3.39 (d, *J* = 7.1 Hz, 6H), 2.15 (s, 3H), 2.04 (s, 3H); ^{13}C NMR (126 MHz, DMSO-d_6) δ 174.5 (d, *J*= 20.2 Hz), 157.5, 156.0 (d, *J*= 262.3 Hz), 152.8, 150.7, 150.6 (d, *J*= 246.7 Hz), 150.3 (dd, *J*= 9.1, 3.0 Hz), 143.6 (d, *J*= 10.1 Hz), 141.9, 136.0, 132.1, 131.1,

130.3, 129.3, 128.2, 126.8, 126.3, 122.4, 115.9 (d, *J*= 8.2 Hz), 115.0, 113.3 (d, *J*= 23.7 Hz), 112.7 (d, *J*= 8.4 Hz), 110.2 (d, *J*= 21.8 Hz), 106.1 (d, *J*= 3.3 Hz), 105.9 (d, *J*= 5.4 Hz), 94.5, 56.1, 43.2, 19.6, 16.6; ^{19}F NMR (376 MHz, Chloroform-*d*) δ -21.98, -25.04; HRMS calcd. for $C_{30}H_{26}F_2NO_4^+$: 502.1830; Found: 502.1826.

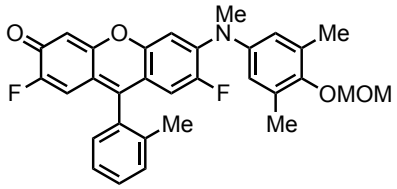

2,7-difluoro-6-((4-(methoxymethoxy)-3,5-dimethylphenyl)(methyl)amino)-9-(*o*-tolyl)-3*H*-xanthen-3-one (**79**): As described under *Buchwald–Hartwig amination of Pennsylvania Green triflate (**60**)*, **71** (47 mg, 0.1 mmol) afforded **79** (46 mg, 89% yield). ^{1}H NMR (400 MHz, DMSO-d_6) δ 7.56–7.48 (m, 2H), 7.44 (td, *J* = 7.2, 1.7 Hz, 1H), 7.34–7.27 (m, 2H), 6.87 (s, 2H), 6.55 (d, *J* = 6.0 Hz, 1H), 6.52 (d, *J* = 4.3 Hz, 1H), 6.47 (d, *J* = 7.2 Hz, 1H), 4.92 (s, 2H), 3.49 (s, 3H), 3.39 (s, 3H), 2.18 (s, 6H), 2.05 (s, 3H); ^{13}C NMR (126 MHz, DMSO-d_6) δ 174.0 (d, *J* = 20.3 Hz), 156.9, 155.4 (d, *J* = 263.0 Hz), 151.5, 150.3 (d, *J* = 246.9 Hz), 150.0, 149.3, 143.3, 142.7 (d, *J* = 10.5 Hz), 135.4, 131.5, 131.4, 130.5, 129.7, 128.7, 126.1, 122.9, 115.6 (d, *J* = 8.2 Hz), 112.7 (d, *J* = 15.2 Hz), 112.5, 109.5 (d, *J* = 21.7 Hz), 106.3 (d, *J* = 3.4 Hz), 105.3 (d, *J* = 5.4 Hz), 98.5, 56.6, 42.2, 18.9, 16.5 (2 carbons); ^{19}F NMR (471 MHz, DMSO-d_6) δ -20.6, -25.8; HRMS calcd. for $C_{31}H_{28}F_2NO_4^+$: 516.1986; Found: 516.1957.

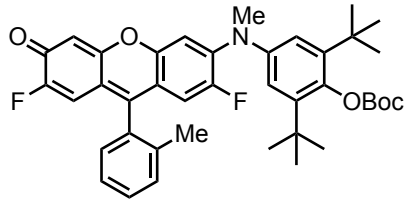

***tert*-butyl(2,6-di-*tert*-butyl-4-((2,7-difluoro-3-oxo-9-(*o*-tolyl)-3*H*-xanthen-6-yl)(methyl)amino) phenyl) carbonate** (**80**): As described under *Buchwald–Hartwig amination of Pennsylvania Green triflate (**60**)*, **72** (22 mg, 0.048 mmol) afforded **80** (27 mg, 87% yield). ^{1}H NMR (400 MHz, Chloroform-d) δ 7.44–7.28 (m, 3H), 7.09 (dd, J = 7.5, 1.4 Hz, 1H), 6.98 (s, 2H), 6.96–6.89 (m, 1H), 6.63 – 6.48 (m, 3H), 3.40 (d, J = 1.7 Hz, 3H), 2.02 (s, 3H), 1.49 (s, 9H), 1.27 (s, 18H).; ^{13}C NMR (126 MHz, Chloroform-d) δ 176.0 (d, *J* = 20.1 Hz), 157.6, 155.5, 153.0, 151.0 (d, *J* = 245.5 Hz), 150.5, 148.8 (d, *J* = 8.9 Hz), 145.8, 144.4, 143.4 (d, *J* = 10.7 Hz), 136.1, 132.3, 131.0, 130.0, 129.0, 126.5, 121.3, 116.9 (d, *J* = 8.4 Hz), 113.7 (d, *J* = 24.4 Hz), 113.3 (d, *J* = 8.9 Hz), 110.1 (d, *J* = 22.1 Hz), 106.6 (d, *J* = 5.0 Hz), 106.3, 83.4, 53.5, 42.5 (d, *J* = 4.5 Hz), 35.9, 31.4, 29.8, 27.9, 19.7; ^{19}F NMR (376 MHz, Chloroform-d) δ -121.01, -124.82; HRMS calcd. for $C_{40}H_{44}F_2NO_5^+$: 656.3188; Found: 656.3140.

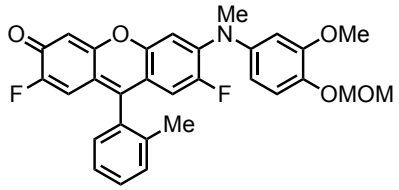

2,7-difluoro-6-((3-methoxy-4-(methoxymethoxy)phenyl)(methyl)amino)-9-(*o*-tolyl)-3*H*-xanthen-3-one (**81**): As described under *Buchwald–Hartwig amination of Pennsylvania Green triflate (**60**)*, **73** (47 mg, 0.1 mmol) afforded **81** (48 mg, 92% yield). ^{1}H NMR (400 MHz, Chloroform-*d*) δ 7.52–7.34 (m, 3H), 7.18–7.11 (m, 2H), 6.94 (d, *J* = 7.3 Hz, 1H), 6.74–6.54 (m, 5H), 5.23 (s, 2H), 3.84 (s, 3H), 3.54 (s, 3H), 3.45 (d, *J* = 1.7 Hz, 3H), 2.09 (s, 3H); ^{13}C NMR (101 MHz, Chloroform-*d*) δ 175.9 (d, *J* = 20.3 Hz), 157.5 (d, *J* = 1.9 Hz), 156.5 (d, *J* = 265.5 Hz), 150.6, 150.5 (d, *J* = 248.4 Hz), 150.4, 149.8 (dd, *J* = 9.3, 2.7 Hz), 144.6, 143.6 (d, *J* = 10.4 Hz), 142.7, 135.9, 132.2, 130.9, 129.9, 128.9,

126.4, 117.1, 116.7 (d, *J* = 8.0 Hz), 116.1 (d, *J* = 1.6 Hz), 113.6 (d, *J* = 24.1 Hz), 113.2 (d, *J* = 8.5 Hz), 110.0 (d, *J* = 22.1 Hz), 108.4, 106.4 (d, *J* = 5.2 Hz), 106.0 (d, *J* = 3.5 Hz), 95.8, 56.4, 56.1, 42.6 (d, *J* = 4.6 Hz), 19.7; ^{19}F NMR (376 MHz, Chloroform-*d*) δ -121.93, -124.74; HRMS calcd. for $C_{30}H_{26}F_2NO_5^+$: 518.1779; Found: 518.1782.

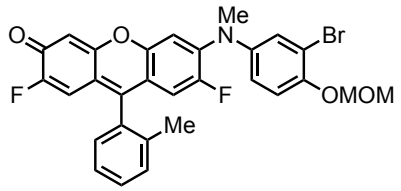

6-((3-bromo-4-(methoxymethoxy)phenyl)(methyl)amino)-2,7-difluoro-9-(*o*-tolyl)-3*H*-xanthen-3-one (**82**): As described under *Buchwald–Hartwig amination of Pennsylvania Green triflate (**60**)*, **74** (32 mg, 0.067 mmol) afforded **82** (22 mg, 57% yield). ^{1}H NMR (400 MHz, Chloroform-*d*) δ 7.43–7.38 (m, 1H), 7.37–7.30 (m, 2H), 7.26 (d, *J* = 2.7 Hz, 1H), 7.07 (dd, *J* = 8.7, 7.0 Hz, 2H), 6.98–6.93 (m, 2H), 6.60 (d, *J* = 12.8 Hz, 1H), 6.54 (d, *J* = 10.9 Hz, 1H), 6.50 (d, *J* = 7.0 Hz, 1H), 5.17 (s, 2H), 3.47 (s, 3H), 3.35 (d, *J* = 1.3 Hz, 3H), 2.03 (s, 3H); ^{13}C NMR (101 MHz, Chloroform-*d*) δ 176.0 (d, *J* = 20.3 Hz), 157.4, 156.5 (d, *J* = 264.9 Hz), 151.3, 151.0 (d, *J* = 249.4 Hz), 150.2, 149.4 (d, *J* = 12.3 Hz), 142.8, 142.6 135.9, 132.0, 130.9, 129.9, 128.9, 128.0, 126.4, 123.2, 117.3 (d, *J* = 8.2 Hz), 116.8, 113.9 (d, *J* = 8.4 Hz), 113.8 (d, *J* = 24.3 Hz), 113.4, 110.0 (d, *J* = 22.1 Hz), 106.9 (d, *J* = 3.0 Hz), 106.5 (d, *J* = 5.0 Hz), 95.4, 56.5, 42.3, 19.6; ^{19}F NMR (376 MHz, Chloroform-*d*) δ -21.32, -24.23; HRMS calcd. for $C_{29}H_{23}BrF_2NO_4^+$: 566.0779; Found: 566.0764.

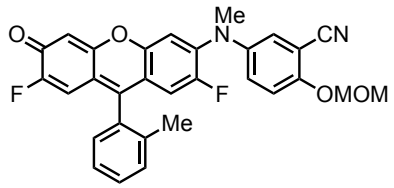

5-((2,7-difluoro-3-oxo-9-(*o*-tolyl)-3*H*-xanthen-6-yl)(methyl)amino)-2-(methoxymethoxy) benzonitrile (**83**): As described under *Buchwald–Hartwig amination of Pennsylvania Green triflate (**60**)*, **75** (47 mg, 0.1 mmol) afforded **83** (44 mg, 86% yield). ^{1}H NMR (400 MHz, DMSO-d_6) δ 7.64 (d, *J* = 2.9 Hz, 1H), 7.57–7.42 (m, 6H), 7.31–7.25 (m, 2H), 6.59 (d, *J* = 13.0 Hz, 1H), 6.55 (d, *J* = 11.4 Hz, 1H), 6.48 (d, *J* = 7.2 Hz, 1H), 5.33 (s, 2H), 3.42 (d, *J* = 1.3 Hz, 3H), 3.32 (s, 3H), 2.06 (s, 3H); ^{13}C NMR (101 MHz, Chloroform-d) δ 176.2 (d, *J* = 20.6 Hz), 157.4, 156.6 (d, *J* = 265.3 Hz), 151.4 (d, *J* = 248.5 Hz), 150.1, 149.2, 142.2 (d, *J* = 1.5 Hz), 141.9 (d, *J* = 10.5 Hz), 136.0, 131.9, 131.0, 130.1, 129.0, 128.5, 126.8, 126.5, 118.0 (d, *J* = 8.5 Hz), 116.4, 115.8, 114.7 (d, *J* = 8.5 Hz), 114.1, 113.9, 110.0 (d, *J* = 22.2 Hz), 107.9 (d, *J* = 3.0 Hz), 106.7 (d, *J* = 5.2 Hz), 103.8, 95.3, 56.8, 42.1, 19.8; ^{19}F NMR (376 MHz, DMSO-d_6) δ -20.37, -25.40; HRMS calcd. for $C_{30}H_{22}F_2N_2O_4^+$: 513.1626; Found: 513.1633.

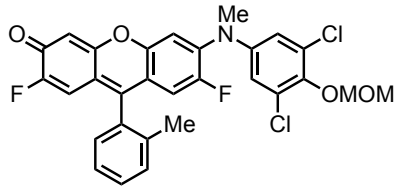

6-((3,5-dichloro-4-(methoxymethoxy)phenyl)(methyl)amino)-2,7-difluoro-9-(*o*-tolyl)-3*H*-xanthen-3-one (**84**): As described under *Buchwald–Hartwig amination of Pennsylvania Green triflate (**60**)*, **76** (47 mg, 0.1 mmol) afforded **84** (38 mg, 67% yield). ^{1}H NMR (400 MHz, Chloroform-d) δ 7.50 (td, J = 7.5, 1.4 Hz, 1H), 7.45–7.38 (m, 2H),

7.23–7.15 (m, 2H), 6.98 (d, J = 0.6 Hz, 2H), 6.74 (d, J = 12.1 Hz, 1H), 6.62 (d, J = 10.7 Hz, 1H), 6.58 (d, J = 6.9 Hz, 1H), 5.16 (s, 2H), 3.69 (d, J = 0.5 Hz, 3H), 3.40 (d, J = 0.8 Hz, 3H), 2.11 (s, 3H).; ^{13}C NMR (101 MHz, Chloroform-d) δ 176.3 (d, *J* = 20.7 Hz), 157.3 (d, *J* = 1.8 Hz), 156.6 (d, *J* = 267.5 Hz), 152.2 (d, *J* = 249.1 Hz), 149.7, 148.8 (dd, *J* = 9.7, 3.1 Hz), 145.5, 144.5 (d, *J* = 1.4 Hz), 141.0 (d, *J* = 12.2 Hz), 135.9, 131.8, 130.9, 130.0, 129.9, 128.9, 126.5, 120.8, 118.5 (d, *J* = 8.4 Hz), 115.8 (d, *J* = 8.4 Hz), 114.1 (d, *J* = 23.8 Hz), 110.1 (d, *J* = 2.4 Hz), 109.9 (d, *J* = 22.2 Hz), 106.7 (d, *J* = 5.0 Hz), 99.5, 58.2, 41.4 (d, *J* = 2.8 Hz), 19.7; ^{19}F NMR (376 MHz, Chloroform-d) δ -22.62, -24.96; HRMS calcd. For $C_{29}H_{22}Cl_2F_2NO_4^+$: 556.0894; Found: 556.0891.

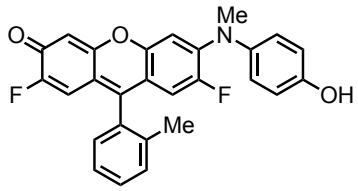

2,7-difluoro-6-((4-hydroxyphenyl)(methyl)amino)-9-(*o*-tolyl)-3*H*-xanthen-3-one (**51**): Compound **77** was deprotected as described under *Removal of the MOM/Boc group* to afford **51** (12 mg, 63% yield). ^{1}H NMR (400 MHz, DMSO-d_6) δ 9.48 (s, 1H), 7.58–7.39 (m, 3H), 7.28 (dd, *J* = 7.5, 1.3 Hz, 1H), 7.17 (d, *J* = 7.5 Hz, 1H), 7.07–6.98 (m, 2H), 6.78–6.69 (m, 2H), 6.55–6.42 (m, 3H), 3.38 (s, 3H), 2.04 (s, 3H); ^{13}C NMR (126 MHz, DMSO-d_6) δ 173.9 (d, *J* = 20.0 Hz), 157.0, 155.5 (d, *J* = 261.8 Hz), 155.3, 150.3, 149.9 (d, *J* = 247.0 Hz), 149.8 (d, *J* = 8.3 Hz), 143.5 (d, *J* = 9.6 Hz), 139.4, 135.5, 131.7, 130.7, 129.8, 128.8, 126.3, 125.2, 115.9, 115.1 (d, *J* = 8.1 Hz), 112.7 (d, *J* = 24.2 Hz), 111.8 (d, *J* = 8.4 Hz), 109.8 (d, *J* = 21.8 Hz), 105.4 (d, *J* = 5.2 Hz), 104.8, 43.0, 19.1; ^{19}F NMR (471 MHz, DMSO-d_6) δ -121.0, -126.3; HRMS calcd. for $C_{27}H_{20}F_2NO_3^+$: 444.1411; Found: 444.1412.

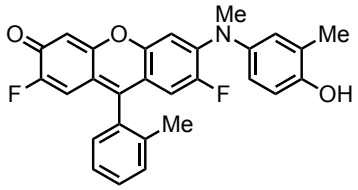

2,7-difluoro-6-((4-hydroxy-3-methylphenyl)(methyl)amino)-9-(*o*-tolyl)-3*H*-xanthen-3-one (**52**): Compound **78** was deprotected as described under *Removal of the MOM/Boc group* to afford **52** (16 mg, 88% yield). ^{1}H NMR (400 MHz, DMSO-d_6) δ 9.39 (s, 1H), 7.55–7.47 (m, 2H), 7.46–7.41 (m, 1H), 7.30–7.24 (m, 1H), 7.14 (d, *J* = 7.4 Hz, 1H), 6.95 (d, *J* = 2.7 Hz, 1H), 6.85 (dd, *J* = 8.5, 2.8 Hz, 1H), 6.74 (d, *J* = 8.5 Hz, 1H), 6.52 (d, *J* = 3.3 Hz, 1H), 6.49 (d, *J* = 5.4 Hz, 1H), 6.45 (d, *J* = 7.2 Hz, 1H), 3.37 (s, 3H), 2.08 (s, 3H), 2.04 (s, 3H); ^{13}C NMR (126 MHz, DMSO-d_6) δ 174.2 (d, *J*= 20.0 Hz), 157.4, 155.9 (d, *J*= 261.4 Hz), 153.9, 150.9, 150.4, 150.3 (d, *J*= 247.7 Hz), 144.1, 139.6, 136.0, 132.1, 131.1, 130.3, 129.3, 126.8, 126.8, 125.3, 122.9, 115.5, 115.4, 113.2 (d, *J*= 24 Hz), 112.2 (d, *J*= 8.4 Hz), 110.2 (d, *J*= 21.7 Hz), 105.8 (d, *J*= 5.7 Hz), 105.1, 43.5, 19.6, 16.5; ^{19}F NMR (376 MHz, DMSO-d_6) δ -121.13, -126.47; HRMS calcd. for $C_{28}H_{22}F_2NO_3^+$: 458.1568; Found: 458.1572.

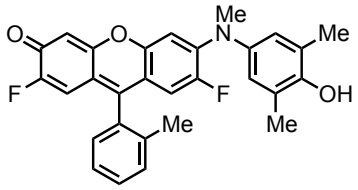

2,7-difluoro-6-((4-hydroxy-3,5-dimethylphenyl)(methyl)amino)-9-(*o*-tolyl)-3*H*-xanthen-3-one (**53**): Compound **79** was deprotected as described under *Removal of the MOM/Boc group* to afford **53** (27 mg, 90% yield). ^{1}H NMR (400 MHz, DMSO-d6) δ 8.29 (s, 1H), 7.59–7.47 (m, 2H), 7.43 (td, J = 7.4, 1.7 Hz, 1H), 7.33–7.25 (m, 1H), 7.13 (d, J =

7.5 Hz, 1H), 6.79 (s, 2H), 6.58 – 6.40 (m, 3H), 3.37 (s, 2H), 2.12 (s, 6H), 2.04 (s, 3H); ^{13}C NMR (126 MHz, DMSO-d_6) δ 173.8 (d, J = 20.0 Hz), 156.8, 155.4 (d, J = 261.8 Hz), 151.1, 150.1, 149.8 (d, J = 245.9 Hz), 149.5 (d, J = 8.2 Hz), 143.5 (d, J = 10.1 Hz), 139.2, 135.4, 131.6, 130.5, 129.6, 128.7, 126.1, 125.2, 123.7, 114.9 (d, J = 8.1 Hz), 112.8 (d, J = 24.2 Hz), 111.6 (d, J = 8.7 Hz), 109.5 (d, J = 21.8 Hz), 105.2 (d, J = 5.6 Hz), 104.6 (d, J = 3.6 Hz), 42.7, 18.9, 16.4; ^{19}F NMR (471 MHz, DMSO-d_6) δ -21.49, -26.38; HRMS calcd. for $C_{29}H_{24}F_2NO_3^+$: 472.1724; Found: 472.1733.

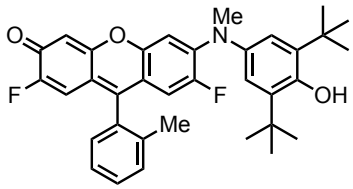

6-((3,5-di-*tert*-butyl-4-hydroxyphenyl)(methyl)amino)-2,7-difluoro-9-(*o*-tolyl)-3*H*-xanthen-3-one (**54**): Compound **80** was deprotected as described under *Removal of the MOM/Boc group* to afford **54** (13 mg, 69% yield). ^{1}H NMR (400 MHz, DMSO-d_6) δ 7.56–7.39 (m, 3H), 7.29 (dd, J = 7.4, 1.2 Hz, 1H), 7.13 (d, J = 7.4 Hz, 1H), 7.03 (s, 1H), 6.91 (s, 2H), 6.52 (s, 1H), 6.49 (d, J = 2.0 Hz, 1H), 6.45 (d, J = 7.2 Hz, 1H), 3.42 (d, J = 1.2 Hz, 3H), 2.03 (s, 3H), 1.34 (s, 18H); ^{13}C NMR (126 MHz, DMSO-d_6) δ 173.9 (d, J = 20.0 Hz), 157.0, 155.4 (d, J = 261.5 Hz), 151.7, 150.4, 149.8 (d, J = 247.4 Hz), 149.7 (dd, J = 8.2, 2.8 Hz), 143.3 (d, J = 9.7 Hz), 140.5, 139.9, 135.5, 131.7, 130.7, 129.8, 128.9, 126.3, 120.1, 115.0 (d, J = 8.2 Hz), 112.6 (d, J = 23.9 Hz), 111.6 (d, J = 8.3 Hz), 109.7 (d, J = 21.7 Hz), 105.4 (d, J = 5.4 Hz), 104.6, 43.0, 34.7 (2 carbons), 30.3 (6 carbons), 19.0; 19F NMR (471 MHz, DMSO) δ -120.72, -126.47; HRMS calcd. for $C_{35}H_{35}F_2NO_3Na^+$: 578.2483; Found: 578.2462.

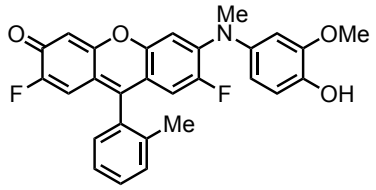

2,7-difluoro-6-((4-hydroxy-3-methoxyphenyl)(methyl)amino)-9-(*o*-tolyl)-3*H*-xanthen-3-one (**55**): Compound **81** was deprotected as described under *Removal of the MOM/Boc group* to afford **55** (25 mg, 90% yield). ^{1}H NMR (400 MHz, DMSO-d_6) δ 9.06 (s, 1H), 7.60–7.47 (m, 2H), 7.46–7.41 (m, 1H), 7.28 (d, *J* = 7.5, 1.3 Hz, 1H), 7.15 (d, *J* = 7.4 Hz, 1H), 6.84 (d, *J* = 2.5 Hz, 1H), 6.73 (d, *J* = 8.4 Hz, 1H), 6.59 (dd, *J* = 8.4, 2.5 Hz, 1H), 6.53 (s, 1H), 6.51 – 6.44 (m, 2H), 3.72 (s, 3H), 3.41 (d, *J* = 1.1 Hz, 3H), 2.04 (s, 3H); ^{13}C NMR (126 MHz, DMSO-d_6) δ 174.8 (d, *J* = 19.9 Hz), 157.0, 155.4 (d, *J* = 261.7 Hz), 150.3, 149.9 (d, *J* = 9.7 Hz), 149.8 (d, *J* = 247.3 Hz), 148.0, 144.7, 143.6 (d, *J* = 9.6 Hz), 139.6, 135.5, 131.7, 130.7, 129.8, 128.8, 126.3, 116.4, 115.5, 115.1 (d, *J* = 8.1 Hz), 112.7 (d, *J* = 24.1 Hz), 111.8 (d, *J* = 8.6 Hz), 109.8 (d, *J* = 22.1 Hz), 109.0, 105.4 (d, = 5.1 Hz), 104.8, 55.7, 42.9, 19.1; ^{19}F NMR (471 MHz, DMSO-d_6) δ -121.3, -126.4.; HRMS calcd. for $C_{28}H_{22}F_2NO_4^+$: 474.1517; Found: 474.1474.

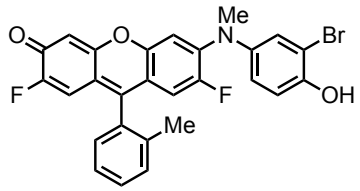

6-((3-bromo-4-hydroxyphenyl)(methyl)amino)-2,7-difluoro-9-(*o*-tolyl)-3*H*-xanthen-3-one (**56**): Compound **82** was deprotected as described under *Removal of the MOM/Boc group* to afford **56** (18 mg, 95% yield). ^{1}H NMR (500 MHz, DMSO-d_6) δ 10.09 (s, 1H),

7.56–7.47 (m, 2H), 7.43 (td, *J* = 7.1, 1.4 Hz, 1H), 7.34 (d, *J* = 2.7 Hz, 1H), 7.27 (dd, *J* = 7.6, 1.4 Hz, 1H), 7.20 (d, *J* = 7.3 Hz, 1H), 7.05 (dd, *J* = 8.7, 2.7 Hz, 1H), 6.93 (d, *J* = 8.6 Hz, 1H), 6.56 – 6.49 (m, 2H), 6.44 (d, *J* = 7.1 Hz, 1H), 3.39 (s, 3H), 2.05 (s, 3H); ^{13}C NMR (126 MHz, DMSO-d_6) δ 173.9 (d, *J* = 20.1 Hz), 156.8, 155.3 (d, *J* = 263.0 Hz), 151.7, 149.9, 149.8 (d, *J* = 247.7 Hz), 149.2 (dd, *J* = 8.9, 2.8 Hz), 142.7 (d, *J* = 10.0 Hz), 140.2, 135.3, 131.4, 130.4, 129.6, 128.6, 127.7, 126.0, 124.0, 116.5, 115.5 (d, *J* = 8.3 Hz), 112.6 (d, *J* = 24.0 Hz), 112.3 (d, *J* = 8.4 Hz), 109.4 (d, *J* = 21.8 Hz), 109.1, 105.6 (d, *J* = 3.2 Hz), 105.2 (d, *J* = 5.4 Hz), 42.37, 18.76; ^{19}F NMR (471 MHz, DMSO-d_6) δ -15.25, -19.69.; HRMS calcd. for $C_{27}H_{19}BrF_2NO_3^+$: 522.0516; Found: 522.0519.

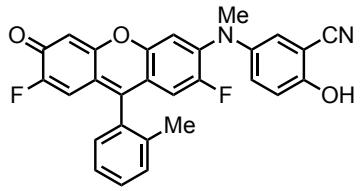

5-((2,7-difluoro-3-oxo-9-(*o*-tolyl)-3*H*-xanthen-6-yl)(methyl)amino)-2-hydroxybenzonitrile (**57**): Compound **83** was deprotected as described under *Removal of the MOM/Boc group* to afford **57** (21 mg, 65% yield). ^{1}H NMR (500 MHz, DMSO-d_6) δ 11.00 (d, J = 1.8 Hz, 1H), 7.57–7.46 (m, 3H), 7.43 (td, J = 7.5, 1.5 Hz, 1H), 7.37–7.25 (m, 3H), 6.98 (d, J = 8.9 Hz, 1H), 6.54 (t, J = 12.0 Hz, 2H), 6.44 (d, J = 7.1 Hz, 1H), 3.39 (s, 3H), 2.05 (s, 3H); ^{13}C NMR (126 MHz, DMSO-d_6) δ 174.0 (d, *J* = 20.2 Hz), 157.4, 156.9, 151.0 (d, *J* = 247.0 Hz), 150.0 (d, *J* = 247.0 Hz), 149.9, 149.3 (d, *J* = 9.6 Hz), 142.3 (d, *J* = 10.0 Hz), 139.6, 135.4, 131.4, 130.5, 130.1, 129.7, 128.7, 127.3, 126.2, 117.0, 116.2, 115.8 (d, *J* = 8.1 Hz), 112.8 (d, *J* = 16.0 Hz), 112.7, 109.6 (d, *J* = 21.8 Hz), 106.2 (d, *J* = 3.1 Hz), 105.3 (d, *J* = 5.4 Hz), 99.1, 42.2, 18.9; ^{19}F NMR (471 MHz, DMSO-d_6) δ -21.05,

-25.66; HRMS calcd. for $C_{28}H_{18}F_2N_2O_3^+$: 469.1364; Found: 469.1359.

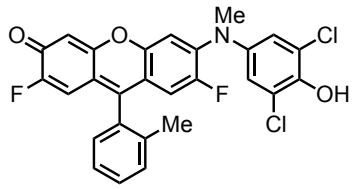

6-((3,5-dichloro-4-hydroxyphenyl)(methyl)amino)-2,7-difluoro-9-(*o*-tolyl)-3*H*-xanthen-3-one (**58**): Compound **84** was deprotected as described under *Removal of the MOM/Boc group* to afford **58** (18 mg, 85% yield). ^{1}H NMR (500 MHz, DMSO-d_6) δ 9.98 (s, 1H), 7.56 – 7.47 (m, 2H), 7.46–7.41 (m, 1H), 7.36 (d, *J* = 7.2 Hz, 1H), 7.28 (d, *J* = 7.6 Hz, 1H), 7.21 (s, 2H), 6.58 (d, *J* = 13.0 Hz, 1H), 6.53 (d, *J* = 11.3 Hz, 1H), 6.45 (d, *J* = 7.1 Hz, 1H), 3.39 (s, 3H), 2.05 (s, 3H); ^{13}C NMR (126 MHz, DMSO-d_6) δ 174.1 (d, *J* = 20.3 Hz), 156.9, 155.5 (d, *J* = 263.4 Hz), 150.4 (d, *J* = 246.0 Hz), 149.8, 149.2 (dd, *J* = 9.0, 2.5 Hz), 146.1, 141.8 (d, *J* = 10.5 Hz), 140.5, 135.5, 131.4, 130.6, 129.7, 128.7, 126.2, 122.9, 122.5, 116.1 (d, *J* = 8.3 Hz), 113.3 (d, *J* = 8.7 Hz), 112.8 (d, *J* = 23.8 Hz), 109.6 (d, *J* = 21.8 Hz), 107.2 (d, *J* = 2.5 Hz), 105.3 (d, *J* = 5.3 Hz), 42.1, 18.9; ^{19}F NMR (471 MHz, DMSO-d_6) δ -15.04, -19.20; HRMS calcd. for $C_{27}H_{18}Cl_2F_2NO_3^+$: 512.0632; Found: 512.0649.

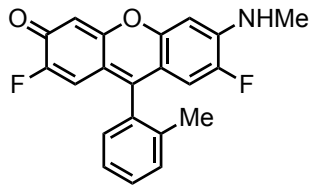

2,7-difluoro-6-(methylamino)-9-(*o*-tolyl)-3*H*-xanthen-3-one (**59**): As described under *Buchwald–Hartwig amination of Pennsylvania Green triflate (**60**)*, commercially available *tert*-butyl methylcarbamate (47 mg, 0.1 mmol) afforded *tert*-butyl (2,7-difluoro-3-oxo-9-(*o*-tolyl)-3*H*-xanthen-6-yl)(methyl)carbamate (17 mg). This compound was deprotected as described under *Removal of the MOM/Boc group* to afford **59** (13 mg, 37% yield, two steps). ^{1}H NMR (500 MHz, DMSO-d_6) δ 7.67 (s, 1H), 7.58–7.48 (m, 2H), 7.44 (t, *J* = 7.4 Hz, 1H), 7.26 (d, *J* = 7.5 Hz, 1H), 6.94 (d, *J* = 7.1 Hz, 1H), 6.64–6.53 (m, 3H), 2.96 (s, 3H), 2.03 (s, 3H); ^{13}C NMR (126 MHz, DMSO-d_6) δ 170.2 (d, *J* = 19.1 Hz), 156.0, 154.3 (d, *J* = 258.0 Hz), 152.7, 152.0 (dd, *J* = 7.0, 4.4 Hz), 148.5 (d, *J* = 244.9 Hz), 145.5 (d, *J* = 15.2 Hz), 135.3, 131.6, 130.4, 129.6, 128.5, 126.0, 113.0 (d, *J* = 8.2 Hz), 110.2 (d, *J* = 21.1 Hz), 110.0 (d, *J* = 21.7 Hz), 109.5 (d, *J* = 8.2 Hz), 104.8 (d, *J* = 5.4 Hz), 96.3 (d, *J* = 4.2 Hz), 29.4, 18.7; ^{19}F NMR (471 MHz, DMSO-d_6) δ -22.35, -27.78; HRMS calcd. for $C_{21}H_{16}F_2NO_2^+$: 352.1149; Found: 352.1152.

3-10-3. Optical spectroscopy

Absorbance spectroscopy: To generate the absorbance spectra (Figure 3-3), a normalized DMSO stock solution of each compound was diluted in *n*-octanol to yield a 10 μM solution, vortexed to mix, and transferred to a Semi-micro quartz cuvette (Sigma Aldrich, Z27667-7). Spectra were recorded from 190–1100 nm using an Agilent 8453 UV-visible spectrometer.

Determination of molar extinction coefficients: Three aliquots of at least 1 mg of each dry powder were carefully weighed and used to make DMSO master stock solutions (1

mM–10 mM) based on molecular weight. Serial dilutions of these master stock solutions were prepared to yield six DMSO stock solutions of various concentrations. Each stock solution was then diluted 1:500 into DMSO, vortexed, and transferred to a semi-micro quartz cuvette (Sigma Aldrich, Z27667-7). Absorbance spectra were recorded using an Agilent 8453 UV-visible Spectrometer. Molar extinction coefficients (ε) were calculated from Beer's Law plots of absorbance versus concentration. Linear least squares fitting of the data including a zero intercept (GraphPad Prism 7) was used to determine the slope, which corresponds to ε. This value was then used to normalize the concentration of all future stock solutions as follows: Absorbance = ε [concentration (M)] L, where L = 1 cm.

Fluorescence spectroscopy: For the fluorescence emission spectra of **53** (Figure 3-3), a DMSO stock solution was prepared for each compound at a fixed concentration (2 mM) determined by absorbance spectroscopy and measured extinction coefficients. This stock solution was diluted in *n*-octanol to yield a 4 μM solution (0.2% DMSO). For the highly fluorescent rhodol **59**, a final concentration of 10 nM (0.1% DMSO) was used. Solutions were pipetted to mix and transferred to a quartz SUPRASIL macro/semi-micro cell (PerkinElmer, B0631132). Fluorescence spectra were recorded using a Perkin Elmer LS-55 fluorescence spectrometer. Samples were excited at 488 nm and emission was recorded from 510–700 nm with a scan speed of 500 nm/min and slit widths of 10 nm.

Determination of quantum yields: Relative quantum yields (ϕ) were determined as previously reported.[65] A normalized DMSO stock solution of each fluorophore was serially diluted to provide five DMSO stock solutions (0.25–2 mM). These were diluted 1:500 in

octanol in triplicate to yield 0.5–4 μM solutions. For fluorescence measurements, solutions were transferred to a Quartz SUPRASIL Macro/Semi-micro Cell (PerkinElmer B0631132) and analyzed using a Perkin Elmer LS-55 Fluorescence Spectrometer. Samples were excited at 488 nm and emission was collected from 510–700 nm with a scan speed of 500 nm/min and 10 nm excitation and emission slit widths. For absorbance measurements, solutions were transferred to a semi-micro quartz cuvette (Sigma Aldrich, Z27667-7) and analyzed using an Agilent 8453 UV-visible Spectrometer. Spectra were recorded from 190 to 1100 nm. The integrated fluorescence emission at each concentration was plotted against the absorbance at 488 nm. Linear least squares fitting of the data including a zero intercept (GraphPad Prism 7) was used to determine the slope, which is proportional to the quantum yield. Quantum yields were calculated as follows:

$$\Phi_x = \frac{\Phi_{st} \cdot Grad_x \cdot \eta^2_x}{Grad_{st} \cdot \eta^2_{st}}$$

where; ϕ_x = quantum yield of the unknown,

ϕ_{st} = quantum yield of the standard,

Grad = slope of the best linear fit,

η = refractive index of the solvent used

Rhodamine 6G, ϕ = 0.96 in octanol,[66] was used as the standard. The *Grad* of Rhodamine 6G was calculated as above, except concentrations of 2–10 nM were used for determining the integrated fluorescence emission, and absorbance values for those concentrations were determined by extrapolation based on absorbance measurements

at higher concentrations. The term η^2_x/η^2_{st} = 1, because all measurements were performed in the same solvent.

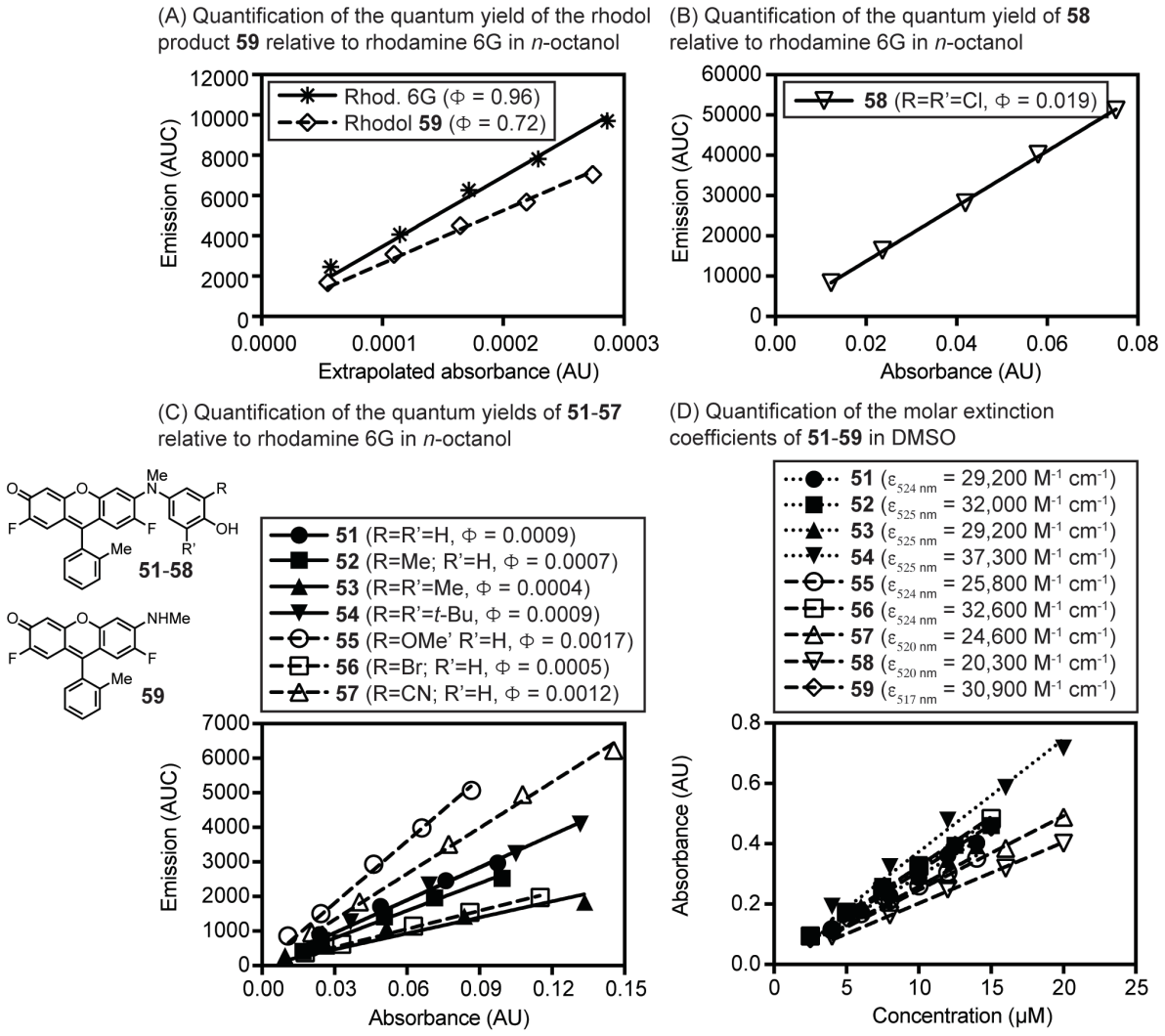

Figure 3-18. Photophysical properties of compounds **51**-**59**. Panels A-C: Determination of quantum yields relative to rhodamine 6G in *n*-octanol. Panel D: Determination of molar extinction coefficients in DMSO.

3-10-4. Studies of kinetics of reaction of sensors with SIN-1

A DMSO stock solution (25 μM) of each compound was prepared and diluted 1:1000 with PBS to yield a 25 nM solution. This solution was vortexed to mix and 200 μL was transferred by micropipette into each of 6 wells of a black fluorescence Microfluor 1

Flat-Bottom 96-well Plate (Fisher Scientific, 7605). A freshly made aqueous stock solution of SIN-1 (2 μL, 100 mM, AdipoGen, AG-CR1-0027-M050) was added to 3 wells of each probe for a final concentration of 1 mM SIN-1. The plate was analyzed immediately using a Packard Fusion Universal Microplate Analyzer using a Fluorescein 485 excitation filter, a Fluorescein 530 emission filter, top fluorescence with light intensity set to 1, 0.1 s integration, high intensity orbital shaking for 10 s before every reading, and 30 s intervals between readings. Efficiency of addition of SIN-1 limited the number of probes analyzed to 3–4 per run. All probes were analyzed on the same day using the same solution of SIN-1. Background-subtracted values were curve fitted by non-linear regression with a one-phase association model (GraphPad Prism 7) to determine half-times.

3-10-5. Determination of the limit of detection of peroxynitrite by 53

A normalized DMSO stock solution of sensor **53** in DMSO (50 μM) was diluted 1:1000 with PBS (pH 7.4) to yield a 50 nM solution (0.1% DMSO). The concentration of a stock solution of pure $ONOO^-$ was measured by absorbance spectroscopy and diluted with aq. NaOH (0.1 M) to provide additional stock solutions. These solutions were diluted 1:1000 into solutions of **53** for analysis in triplicate. These solutions were mixed and incubated at room temperature in the dark for 5 min before being transferred to a quartz cell for analysis by fluorescence spectroscopy. The detection limit of **53** was determined based on a reported method.[38,67] The fluorescence emission at 526 nm were normalized between the minimum intensity (0 nM $ONOO^-$, F_{min}) and the maximum intensity (500 nM $ONOO^-$, F_{max}) using the following equation: $(F-F_{min})/(F_{max}-F_{min})$. These values were

plotted against the concentration of $ONOO^-$ (50 nM–400 nM) and analyzed by linear regression (GraphPad Prism 7) to establish the limit of detection as the x-intercept.

3-10-6. Analysis of selectivity of sensor 53 towards peroxynitrite compared with other oxidants

A normalized DMSO stock solution of sensor **53** in DMSO (50 μM) was diluted 1:1000 with PBS (pH 7.4) to yield a 50 nM solution (0.1% DMSO). RNS and ROS were generated as described below and diluted into the solution in volumes that changed the overall volume by 0.5% or less. These solutions were mixed and incubated at room temperature for 5 min before being transferred to a quartz SUPRASIL Macro/Semi-micro cell (PerkinElmer, B0631132). Fluorescence spectra were recorded using a Perkin Elmer LS-55 fluorescence spectrometer. Samples were excited at 488 nm and emission was recorded from 510–700 nm with a scan speed of 500 nm/min and slit widths of 10 nm. To compare the reactivity of **53** towards different reactive species, fluorescence intensity at 526.5 nm was plotted and analyzed using one-way ANOVA correcting for multiple comparisons using Sidak's multiple comparisons test with a single pooled variance using alpha 0.05 (Prism 6). Comparisons were made between **53** alone and **53** indicated with each indicated species. ******* indicates $0.0001 < p < 0.001$; ******** indicates $p < 0.0001$ (Fgiure 3-8).

Methods for generation of RNS/ROS:

$ONOO^-$: Peroxynitrite ($ONOO^-$) was synthesized by modification of the procedure of Robinson and Beckman.[6] An aqueous solution of hydrogen peroxide (0.6 M, 185 μL) in

hydrochloric acid (0.7 M) was added to aqueous sodium nitrite (0.6 M, 200 µL) at 4 °C. The mixture was made alkaline by rapid addition of aqueous NaOH (3 M, 200 µL). This mixture was treated with manganese dioxide freshly prepared as described by Robinson and Beckman[6] at 4 °C. After 10–15 min, the resulting suspension was filtered to yield a solution of $ONOO^-$ (up to 48 mM). The concentration of $ONOO^-$ was verified by absorbance spectroscopy (ε = 1670 $M^{-1}cm^{-1}$ at 302 nm in aq. NaOH, 0.1 M). $ONOO^-$ was diluted 1:1000 with aq. NaOH (0.1 M) to provide stock solutions. These solutions were diluted into solutions of **53** for analysis.

ClO^-: Commercial bleach was diluted with DI water (1:1000) to generate stock solutions (50 µM and 2.5 mM) that were diluted into solutions of **53**. The concentration was verified by absorbance spectroscopy (ε = 350 $M^{-1}cm^{-1}$ at 209 nm) in water.

•OH: hydroxyl radical was generated using the Fenton reaction.[34] Briefly, an aqueous stock solution of ammonium iron (III) sulfate hexahydrate (5 mM, Alfa Aesar, A12473) and an aqueous stock solution of H_2O_2 (50 mM, see below) were prepared. Each was diluted immediately 1:1000 into the probe solution to yield a final concentration of 5 µM hydroxyl radical.

H_2O_2: 30% hydrogen peroxide (Fisher, BP2633) was diluted in DI water to generate a stock solution (5 mM) that was diluted 1:1000 into a solution of **53**. The concentration was verified by absorbance spectroscopy using ε = 43.6 $M^{-1}cm^{-1}$ at 240 nm in water.

O_2^-: A saturated DMSO stock solution of potassium superoxide (1 mM, Acros, 355420250) was prepared. This solution was diluted 1:200 into the solution of **53** to yield 5 μM superoxide (0.6% DMSO).

t-BuOOH: *tert*-butyl hydroperoxide solution (70%, Alfa Aesar, A13926) was diluted in DI water to yield a 5 mM stock solution that was diluted 1:1000 into the solution of **53**.

NO: A solution of sodium nitroferricyanide (III) dihydrate (5 mM, SNP, Alfa Aesar, A15656) was prepared in PBS and allowed to sit at room temperature for 0.5 h. It was subsequently diluted 1:1000 into the solution of **53**.

Analysis of conversion of 53 to 59 by SIN-1 by HPLC: HPLC profiles were acquired on Agilent 1220 Infinity LC equipped with Agilent PLRP-S reverse phase column (8 μm particle size, 4.6 mm x 250 mm) and diode array detector. Elution was achieved with a gradient of water and acetonitrile (90:10 to 0:100 containing 0.1% TFA) over 25 min.

3-10-7. Biological assays and protocols

Cell culture: RAW264.7 macrophages (ATCC TIB-71) were a kind gift of Prof. Sue Lunte. These cells were cultured in complete media comprising DMEM (Sigma Aldrich D6429) supplemented with fetal bovine serum (10%, Hyclone-characterized FBS, SH3039603), penicillin (100 units/mL, Sigma Aldrich P4333), and streptomycin (100 μg/mL, Sigma Aldrich P4333). Cells were grown in T75 flasks (CytoOne CC7682-4875) and incubated at 37 °C with 5% CO_2.

Flow cytometry: A Beckman Coulter Cytoflex S (B2-R0-V2-Y2) flow cytometer was used for cellular analysis. Cells were excited with 405 nm and / or 488 nm diode lasers and emitted photons were collected through 450/45 BP (Pacific Blue), 525/40 BP (sensors), or 690/50 nm BP (PI) filters. FSC threshold was set to 500,000, flow speed was fast, mixing and backflush times were 5 s, and cells were collected until 10,000 cells were collected, unless otherwise specified. Background fluorescence from treatment with vehicle alone was subtracted from cellular fluorescence for analysis.

Labeling of TentaGel beads: TentaGel M NH_2 microspheres (5 mg, Rapp Polymer, M30102) were allowed to swell in PBS (1 mL, 1 h) while agitated on a Titer Plate Shaker (speed 7). Based on the loading capacity of the beads (0.21 mmol/g), the solution of amines was ca. 1 mM. The solution was split into two aliquots (500 µL each) that were then each diluted to 1 mL (~ 0.5 mM amines). To one aliquot, a solution of *N*-succinimidyl *N*-(2,4-dinitrophenyl)-6-aminocaproate (DNP-X-NHS) (3 µL, 50 mM, Sigma Aldrich, 55472) in DMSO was added. To the other, the *N*-succinimidyl ester of Pacific Blue (Pacific Blue-NHS, prepared as previously described[68] or commercially available) in DMSO (3 µL, 20 mM) was added. The solutions were shaken at room temperature (1 h). The beads were then pelleted by centrifugation on a personal microcentrifuge (USA Scientific Plastics, 2631-006, ~30 s), and the supernatant was removed by pipette. The beads were washed once with EtOH (1 mL) and twice with PBS (pH 7.4, 0.3 mL). The Pacific Blue-labeled beads were diluted to a final volume of 800 µL in PBS and stored at 4 °C until use. The DNP-labeled beads were incubated with rabbit Anti-DNP IgG (50 µL,

Vector Laboratories, SP-0603) additionally labeled with Pacific Blue-NHS (2 μM, DOL 4–5) with shaking at room temperature for 1 h. This antibody was labeled with Pacific Blue on lysines by incubating Anti-DNP (100 μL, 7 μM) with Pacific Blue-NHS (0.2 μL, 20 mM) for 0.5 h (37 °C) in a Big Shot III Hybridization Oven. To purify the conjugate, Sephadex G-25 resin (Superfine, Sigma, S5772) was suspended in PBS (pH 7.4). The resulting slurry (950 μL) was added to a minispin column (USA Scientific, 1415-0600) and centrifuged (16,000 x g, 20 s) to remove the buffer and pack the resin. The antibody solution was loaded onto the packed resin and centrifuged (16,000 x g, 30 s) to separate the protein from the unconjugated Pacific Blue. The DOL was determined by comparing the absorbance at 280 nm and 425 nm (IgG 280 nm $\varepsilon_{1\%\ (10\ mg/mL)}$ = 13.7 $Lg^{-1}cm^{-1}$, Pacific Blue 425 nm ε = 29,500 $M^{-1}cm^{-1}$), as measured with a Nanodrop 1000 Spectrophotometer. The beads were diluted to a final volume of 800 μL of PBS, and stored at 4 °C until needed, but were used within two days to maximize activity. Beads were counted by diluting 20 μL of beads with media (180 μL) in duplicate in a non-treated 96 well plate (USA Scientific Plastics, CC7672-7596). The beads were analyzed by flow cytometry using a Beckman Coulter Cytoflex S flow cytometer. The FSC threshold was set to automatic, flow speed was fast, mixing time was 5 s, backflush time was 5 s, and beads were collected for 20 s. The average of these samples was used to determine to volume of beads to add to cells.

Assays of phagocytosis: RAW264.7 macrophages were seeded on a non-treated 96-well plate (USA Scientific Plastics, CC7672-7596) in complete medium at 40,000 cells in 200 μL per well 16 h prior to treatment. These cells adhere to treated plastic very strongly,

and the use of non-treated plates was required for subsequent release and analysis of cells by flow cytometry. Fluorescent sensors were diluted from DMSO stock solutions into complete media to a final concentration of 10 μM probe and 0.5% DMSO. Because commercial hydroxyphenyl fluorescein (**HPF**, ThermoFisher Scientific) is supplied in DMF, solutions of this probe contained 0.2% DMF instead of DMSO. Components of complete DMEM medium can affect the fluorescence of HPF, so this sensor, and **3.3** for direct comparison, was added to Hank's Balanced Salt Solution (HBSS, Corning, 21-022-CV, pH 7.4) instead of DMEM. Labeled TentaGel beads were added to this complete medium or HBSS (200,000 beads/mL). For the incremental increase assay shown in Figure 3-12, bead counts used are indicated. The original media was carefully removed from all wells by aspiration and replaced with the treatment media containing beads and sensors (200 μL per well) in triplicate. After incubation of treated cells at 37 °C for 4 h, aqueous propidium iodide (20 μL, 30 μM, ThermoFisher Scientific, P1304MP, PI) was added to each well for a final concentration of 3 μM PI. A p200 multichannel pipette was used to release the cells from the plate using sheer force. For comparison of **53** with **HPF** and **FI-B**, treated media or HBSS was aspirated from the wells and replaced with fresh media or HBSS containing PI (3 μM, ThermoFisher Scientific, P1304MP). This was to account for the high background fluorescence of FI-B and to remain consistent with previously reported use of this sensor to detect peroxynitrite.[39] Cells were analyzed by flow cytometry using a Beckman Coulter Cytoflex S flow cytometer. The FSC threshold was set to 500,000, flow speed was fast, mixing time was 5 s, backflush time was 5 s, and cells were collected until 10,000 cells were counted. Viability was determined by gating based on PI staining. The tentagel beads take up significant amounts of PI, making

them brighter than living cells in that channel, allowing for gating to exclude the beads. Additionally, labeling of tentagel beads with Pacific Blue makes them significantly brighter than cells when excited at 405 nm. This allows the 405 channel to be used as secondary assurance that all beads are excluded from gating of live cells. Median values of fluorescence of living cells in the FITC-A channel were compared. Statistical significance was analyzed using one-way ANOVA correcting for multiple comparisons using Sidak's multiple comparisons test with a single pooled variance using alpha 0.05 (Prism 6). Comparisons were made between cells treated with each sensor alone and each indicated treatment. For the incremental assay in Figure 3-12, comparisons were performed between the indicated columns. * indicates $0.01 < p < 0.05$; ** indicates $0.001 < p < 0.01$; *** indicates $0.0001 < p < 0.001$; **** indicates $p < 0.0001$.

Analysis of cytotoxicity: Cells were seeded on a non-treated 96-well plate (USA Scientific Plastics, CC7672-7596) in complete medium at 40,000 cells in 200 µL per well 16 h prior to treatment. This use of non-treated plates was required for subsequent release and analysis of cells by flow cytometry. All compounds were serially diluted in DMSO and added to complete medium to achieve a 1:1000 dilution factor, where possible. Because the solubility of **53** in DMSO is limited to ~2 mM, a final concentration of 0.5% DMSO was used for all samples. The original media was carefully removed from all wells by aspiration and replaced with treatment media (200 µL per well) at the concentrations indicated in triplicate. Plates were incubated for 48 h at 37 °C. The media was then carefully aspirated from each well and replaced with complete media containing propidium iodide (3 µM, ThermoFisher Scientific, P1304MP, PI). The media was pipetted

up and down multiple times to release cells from the plate and to break up clumps of cells. The total living cell-count for each well was determined by flow cytometry using a Beckman Coulter Cytoflex S flow cytometer. The FSC threshold was set to 500,000, flow speed was fast, mixing time was 5 s, backflush time was 5 s, and cells were collected for 20 s per well. Staining with PI was used to identify populations of live cells. Counts of viable cells for each treatment, determined in triplicate, were used to generate dose-response curves. These curves were fitted by non-linear regression with an inhibitor vs. response variable 4-parameter model (GraphPad Prism 7) to determine IC_{50} values.

Confocal microscopy: Imaging was performed using an inverted Leica TCS SPE confocal laser-scanning microscope fitted with a Leica 63x oil-immersion objective. Fluorescent probes were excited with either a 405 nm or 488 nm solid-state laser and emitted photons were collected from 425-500 nm or 500-600 nm. Unless otherwise noted, laser power and PMT gain settings were identical for all images acquired within a given experiment to allow accurate comparisons of cellular fluorescence.

Analysis of subcellular localization: RAW264.7 macrophages were scraped to passage and diluted to 300,000 cells/mL in complete medium. These cells were plated in ibiTreat-coated μ-Slide 8-well (ibidi, 80826) containing 300 μL of media per well and incubated at 37 °C overnight. The next day, the wells were washed once with complete media before treatment with fluorescent probes. Fluorescent sensors in DMSO stock solutions were diluted into complete media and added to cells. ER-Tracker Blue-White DPX (Invitrogen, E12353) was diluted in DMSO to 100 μM followed by 1:1000 dilution

with complete media. FeTMPyP (Cayman Chemical, 75854, 25 mM stock in PBS, pH 7.4) was diluted 1:500 into media containing sensors. Labeled tentagel beads (prepared as described above) were added to cells at 200,000 beads/mL. Cells were incubated for 4 h at 37 °C followed by imaging by confocal microscopy (without washing). To analyze the diffusion of the fluorescent rhodol **59** out of cells, wells treated with **53** / beads / IgG were imaged, washed once with complete media, then imaged again immediately and over a 20 min period. Imaging was performed using an inverted Leica TCS SPE confocal laser-scanning microscope fitted with a Leica 63x oil-immersion objective. Sensors were excited with a 488 nm solid-state laser and emitted photons collected from 500–600 nm. ER-Tracker Blue-White DPX was excited with a 405 nm laser and emitted photons were collected from 425–500 nm. Phagocytosed beads were identified by morphological changes to the cells such as compression of the nucleus around the bead. Addition of the rabbit anti-DNP IgG was necessary for phagocytosis. Antibody-opsonized beads but not Pacific Blue-modified beads were observed to be phagocytosed by microscopy. About 10% of antibody-opsonized beads were phagocytosed. Leica LAS X 2.0.1 software was used to quantify cytosolic and nuclear fluorescence. Regions of interest (ROI) of various sizes were drawn within the cytosol, nucleus, and cell-free regions. Mean fluorescence per pixel was calculated using Leica LAS X 2.0.1 software. ROI from cell-free regions were used to subtract background fluorescence. GraphPad Prism 7 was us to compare the mean fluorescence values (N=20 for each subcellular region).

3-11. References

(1) Szabo, C.; Ischiropoulos, H.; Radi, R., Peroxynitrite: biochemistry, pathophysiology and development of therapeutics. *Nat. Rev. Drug Discov.* **2007**, *6*, 662.

(2) Pacher, P.; Beckman, J. S.; Liaudet, L., Nitric oxide and peroxynitrite in health and disease. *Physiol. Rev.* **2007**, *87*, 315.

(3) Alvarez, M. N.; Peluffo, G.; Piacenza, L.; Radi, R., Intraphagosomal Peroxynitrite as a Macrophage-derived Cytotoxin against Internalized Trypanosoma cruzi: Consequences for Oxidative Killing and Role of Microbial Peroxiredoxins in Infectivity. *J. Biol. Chem.* **2011**, *286*, 6627.

(4) Alvarez, M. N.; Piacenza, L.; Irigoin, F.; Peluffo, G.; Radi, R., Macrophage-derived peroxynitrite diffusion and toxicity to Trypanosoma cruzi. *Arch. Biochem. Biophys.* **2004**, *432*, 222.

(5) Prolo, C.; Alvarez, M. N.; Radi, R., Peroxynitrite, a potent macrophage-derived oxidizing cytotoxin to combat invading pathogens. *BioFactors* **2014**, *40*, 215.

(6) Robinson, K. M.; Beckman, J. S., Synthesis of peroxynitrite from nitrite and hydrogen peroxide. *Methods Enzymol.* **2005**, *396*, 207.

(7) Radi, R.; Beckman, J. S.; Bush, K. M.; Freeman, B. A., Peroxynitrite oxidation of sulfhydryls. The cytotoxic potential of superoxide and nitric oxide. *J. Biol. Chem.* **1991**, *266*, 4244.

(8) Ferrer-Sueta, G.; Radi, R., Chemical biology of peroxynitrite: kinetics, diffusion, and radicals. *ACS Chem. Biol.* **2009**, *4*, 161.

(9) Lymar, S. V.; Hurst, J. K., Rapid reaction between peroxonitrite ion and carbon dioxide: Implications for biological activity. *J. Am. Chem. Soc.* **1995**, *117*, 8867.

(10) Denicola, A.; Freeman, B. A.; Trujillo, M.; Radi, R., Peroxynitrite reaction with carbon dioxide/bicarbonate: kinetics and influence on peroxynitrite-mediated oxidations. *Arch. Biochem. Biophys.* **1996**, *333*, 49.

(11) Bartesaghi, S.; Radi, R., Fundamentals on the biochemistry of peroxynitrite and protein tyrosine nitration. *Redox Biol.* **2018**, *14*, 618.

(12) Xue, J.; Ying, X.; Chen, J.; Xian, Y.; Jin, L., Amperometric ultramicrosensors for peroxynitrite detection and its application toward single myocardial cells. *Anal. Chem.* **2000**, *72*, 5313.

(13) Amatore, C.; Arbault, S.; Bruce, D.; de Oliveira, P.; Erard, L. M.; Vuillaume, M., Characterization of the electrochemical oxidation of peroxynitrite: relevance to oxidative stress bursts measured at the single cell level. *Chemistry* **2001**, *7*, 4171.

(14) Amatore, C.; Arbault, S.; Bouton, C.; Coffi, K.; Drapier, J. C.; Ghandour, H.; Tong, Y., Monitoring in real time with a microelectrode the release of reactive oxygen and nitrogen species by a single macrophage stimulated by its membrane mechanical depolarization. *ChemBioChem* **2006**, *7*, 653.

(15) Amatore, C.; Arbault, S.; Chen, Y.; Crozatier, C.; Tapsoba, I., Electrochemical detection in a microfluidic device of oxidative stress generated by macrophage cells. *Lab Chip* **2007**, *7*, 233.

(16) Hulvey, M. K.; Frankenfeld, C. N.; Lunte, S. M., Separation and detection of peroxynitrite using microchip electrophoresis with amperometric detection. *Anal. Chem.* **2010**, *82*, 1608.

(17) Ohshima, H.; Friesen, M.; Brouet, I.; Bartsch, H., Nitrotyrosine as a new marker for endogenous nitrosation and nitration of proteins. *Food Chem. Toxicol.* **1990**, *28*, 647.

(18) Beckmann, J. S.; Ye, Y. Z.; Anderson, P. G.; Chen, J.; Accavitti, M. A.; Tarpey, M. M.; White, C. R., Extensive nitration of protein tyrosines in human atherosclerosis detected by immunohistochemistry. *Biol. Chem. Hoppe Seyler* **1994**, *375*, 81.

(19) Kaur, H.; Halliwell, B., Evidence for nitric oxide-mediated oxidative damage in chronic inflammation. Nitrotyrosine in serum and synovial fluid from rheumatoid patients. *FEBS Lett.* **1994**, *350*, 9.

(20) van der Vliet, A.; Eiserich, J. P.; Kaur, H.; Cross, C. E.; Halliwell, B., Nitrotyrosine as biomarker for reactive nitrogen species. *Methods Enzymol.* **1996**, *269*, 175.

(21) Leeuwenburgh, C.; Hardy, M. M.; Hazen, S. L.; Wagner, P.; Oh-ishi, S.; Steinbrecher, U. P.; Heinecke, J. W., Reactive nitrogen intermediates promote low density lipoprotein oxidation in human atherosclerotic intima. *J. Biol. Chem.* **1997**, *272*, 1433.

(22) Halliwell, B., What nitrates tyrosine? Is nitrotyrosine specific as a biomarker of peroxynitrite formation in vivo? *FEBS Lett.* **1997**, *411*, 157.

(23) Pfeiffer, S.; Lass, A.; Schmidt, K.; Mayer, B., Protein tyrosine nitration in mouse peritoneal macrophages activated in vitro and in vivo: evidence against an essential role of peroxynitrite. *FASEB J.* **2001**, *15*, 2355.

(24) Ahsan, H., 3-Nitrotyrosine: A biomarker of nitrogen free radical species modified proteins in systemic autoimmunogenic conditions. *Hum. Immunol.* **2013**, *74*, 1392.

(25) Setsukinai, K.; Urano, Y.; Kakinuma, K.; Majima, H. J.; Nagano, T., Development of novel fluorescence probes that can reliably detect reactive oxygen species and distinguish specific species. *J. Biol. Chem.* **2003**, *278*, 3170.

(26) Peng, T.; Wong, N. K.; Chen, X. M.; Chan, Y. K.; Ho, D. H. H.; Sun, Z. N.; Hu, J. J.; Shen, J. G.; El-Nezami, H.; Yang, D., Molecular Imaging of Peroxynitrite with HKGreen-4 in Live Cells and Tissues. *J. Am. Chem. Soc.* **2014**, *136*, 11728.

(27) Peng, T.; Chen, X. M.; Gao, L.; Zhang, T.; Wang, W.; Shen, J. G.; Yang, D., A rationally designed rhodamine-based fluorescent probe for molecular imaging of peroxynitrite in live cells and tissues. *Chem. Sci.* **2016**, *7*, 5407.

(28) Li, J.; Lim, C. S.; Kim, G.; Kim, H. M.; Yoon, J., Highly Selective and Sensitive Two-Photon Fluorescence Probe for Endogenous Peroxynitrite Detection and Its Applications in Living Cells and Tissues. *Anal. Chem.* **2017**, *89*, 8496.

(29) Peng, T.; Yang, D., HKGreen-3: a rhodol-based fluorescent probe for peroxynitrite. *Org. Lett.* **2010**, *12*, 4932.

(30) Yang, D.; Wang, H. L.; Sun, Z. N.; Chung, N. W.; Shen, J. G., A highly selective fluorescent probe for the detection and imaging of peroxynitrite in living cells. *J. Am. Chem. Soc.* **2006**, *128*, 6004.

(31) Sun, X.; Xu, Q.; Kim, G.; Flower, S. E.; Lowe, J. P.; Yoon, J.; Fossey, J. S.; Qian, X.; Bull, S. D.; James, T. D., A water-soluble boronate-based fluorescent probe for

the selective detection of peroxynitrite and imaging in living cells. *Chem. Sci.* **2014**, *5*, 3368.

(32) Zhou, X.; Kwon, Y.; Kim, G.; Ryu, J. H.; Yoon, J., A ratiometric fluorescent probe based on a coumarin-hemicyanine scaffold for sensitive and selective detection of endogenous peroxynitrite. *Biosens. Bioelectron.* **2015**, *64*, 285.

(33) Guo, B. P.; Jing, J.; Nie, L. X.; Xin, F. Y.; Gao, C. C.; Yang, W.; Zhang, X. L., A lysosome targetable versatile fluorescent probe for imaging viscosity and peroxynitrite with different fluorescence signals in living cells. *J. Mater. Chem. B* **2018**, *6*, 580.

(34) Jia, X.; Chen, Q.; Yang, Y.; Tang, Y.; Wang, R.; Xu, Y.; Zhu, W.; Qian, X., FRET-Based Mito-Specific Fluorescent Probe for Ratiometric Detection and Imaging of Endogenous Peroxynitrite: Dyad of Cy3 and Cy5. *J. Am. Chem. Soc.* **2016**, *138*, 10778.

(35) Kaur, A.; Kolanowski, J. L.; New, E. J., Reversible Fluorescent Probes for Biological Redox States. *Angew. Chem. Int. Ed.* **2016**, *55*, 1602.

(36) Sun, C.; Du, W.; Wang, P.; Wu, Y.; Wang, B.; Wang, J.; Xie, W., A novel mitochondria-targeted two-photon fluorescent probe for dynamic and reversible detection of the redox cycles between peroxynitrite and glutathione. *Biochem. Biophys. Res. Commun.* **2017**, *494*, 518.

(37) Sedgwick, A. C.; Han, H. H.; Gardiner, J. E.; Bull, S. D.; He, X. P.; James, T. D., Long-wavelength fluorescent boronate probes for the detection and intracellular imaging of peroxynitrite. *ChemComm* **2017**, *53*, 12822.

(38) Yu, F.; Li, P.; Wang, B.; Han, K., Reversible near-infrared fluorescent probe introducing tellurium to mimetic glutathione peroxidase for monitoring the redox cycles between peroxynitrite and glutathione in vivo. *J. Am. Chem. Soc.* **2013**, *135*, 7674.

(39) Rios, N.; Piacenza, L.; Trujillo, M.; Martinez, A.; Demicheli, V.; Prolo, C.; Alvarez, M. N.; Lopez, G. V.; Radi, R., Sensitive detection and estimation of cell-derived peroxynitrite fluxes using fluorescein-boronate. *Free Radic. Biol. Med.* **2016**, *101*, 284.

(40) Nixon-Abell, J.; Obara, C. J.; Weigel, A. V.; Li, D.; Legant, W. R.; Xu, C. S.; Pasolli, H. A.; Harvey, K.; Hess, H. F.; Betzig, E.; Blackstone, C.; Lippincott-Schwartz, J., Increased spatiotemporal resolution reveals highly dynamic dense tubular matrices in the peripheral ER. *Science* **2016**, *354*, aaf3928.

(41) Dickhout, J. G.; Hossain, G. S.; Pozza, L. M.; Zhou, J.; Lhotak, S.; Austin, R. C., Peroxynitrite causes endoplasmic reticulum stress and apoptosis in human vascular endothelium: implications in atherogenesis. *Arter. Thromb. Vasc. Biol.* **2005**, *25*, 2623.

(42) Lin, W.; Buccella, D.; Lippard, S. J., Visualization of peroxynitrite-induced changes of labile Zn2+ in the endoplasmic reticulum with benzoresorufin-based fluorescent probes. *J. Am. Chem. Soc.* **2013**, *135*, 13512.

(43) Bossy-Wetzel, E.; Talantova, M. V.; Lee, W. D.; Scholzke, M. N.; Harrop, A.; Mathews, E.; Gotz, T.; Han, J.; Ellisman, M. H.; Perkins, G. A.; Lipton, S. A., Crosstalk between nitric oxide and zinc pathways to neuronal cell death involving mitochondrial dysfunction and p38-activated K+ channels. *Neuron* **2004**, *41*, 351.

(44) Mattart, L.; Calay, D.; Simon, D.; Roebroek, L.; Caesens-Koenig, L.; Van Steenbrugge, M.; Tevel, V.; Michiels, C.; Arnould, T.; Boudjeltia, K. Z.; Raes, M., The

peroxynitrite donor 3-morpholinosydnonimine activates Nrf2 and the UPR leading to a cytoprotective response in endothelial cells. *Cell. Signal.* **2012**, *24*, 199.

(45) Meinig, J. M.; Fu, L.; Peterson, B. R., Synthesis of Fluorophores that Target Small Molecules to the Endoplasmic Reticulum of Living Mammalian Cells. *Angew. Chem. Int. Ed. Engl.* **2015**, *54*, 9696.

(46) van Meer, G.; Voelker, D. R.; Feigenson, G. W., Membrane lipids: where they are and how they behave. *Nat. Rev. Mol. Cell Biol.* **2008**, *9*, 112.

(47) Colston, J.; Horobin, R. W.; Rashid-Doubell, F.; Pediani, J.; Johal, K. K., Why fluorescent probes for endoplasmic reticulum are selective: an experimental and QSAR-modelling study. *Biotech. Histochem.* **2003**, *78*, 323.

(48) Terasaki, M.; Song, J.; Wong, J. R.; Weiss, M. J.; Chen, L. B., Localization of endoplasmic reticulum in living and glutaraldehyde-fixed cells with fluorescent dyes. *Cell* **1984**, *38*, 101.

(49) Zhang, H.; Liu, J.; Sun, Y. Q.; Huo, Y.; Li, Y.; Liu, W.; Wu, X.; Zhu, N.; Shi, Y.; Guo, W., A mitochondria-targetable fluorescent probe for peroxynitrite: fast response and high selectivity. *ChemComm* **2015**, *51*, 2721.

(50) Peng, T.; Chen, X.; Gao, L.; Zhang, T.; Wang, W.; Shen, J.; Yang, D., A rationally designed rhodamine-based fluorescent probe for molecular imaging of peroxynitrite in live cells and tissues. *Chem. Sci.* **2016**, *7*, 5407.

(51) Mottram, L. F.; Boonyarattanakalin, S.; Kovel, R. E.; Peterson, B. R., The Pennsylvania Green Fluorophore: a hybrid of Oregon Green and Tokyo Green for the construction of hydrophobic and pH-insensitive molecular probes. *Org. Lett.* **2006**, *8*, 581.

(52) Peng, T.; Wong, N. K.; Chen, X.; Chan, Y. K.; Ho, D. H.; Sun, Z.; Hu, J. J.; Shen, J.; El-Nezami, H.; Yang, D., Molecular imaging of peroxynitrite with HKGreen-4 in live cells and tissues. *J. Am. Chem. Soc.* **2014**, *136*, 11728.

(53) Swain, C. G.; Unger, S. H.; Rosenquist, N. R.; Swain, M. S., Substituent effects on chemical reactivity. Improved evaluation of field and resonance components. *J. Am. Chem. Soc.* **1983**, *105*, 492.

(54) Beilke, M. A.; Collins-Lech, C.; Sohnle, P. G., Effects of dimethyl sulfoxide on the oxidative function of human neutrophils. *J. Lab. Clin. Med.* **1987**, *110*, 91.

(55) Imaizumi, N.; Kanayama, T.; Oikawa, K., Effect of dimethyl sulfoxide as a masking agent for aqueous chlorine in the determination of oxychlorines. *Analyst* **1995**, *120*, 1983.

(56) Indo, H. P.; Davidson, M.; Yen, H. C.; Suenaga, S.; Tomita, K.; Nishii, T.; Higuchi, M.; Koga, Y.; Ozawa, T.; Majima, H. J., Evidence of ROS generation by mitochondria in cells with impaired electron transport chain and mitochondrial DNA damage. *Mitochondrion* **2007**, *7*, 106.

(57) Parameswaran, N.; Patial, S., Tumor necrosis factor-alpha signaling in macrophages. *Crit. Rev. Eukaryot. Gene Expr.* **2010**, *20*, 87.

(58) Darwich, L.; Coma, G.; Pena, R.; Bellido, R.; Blanco, E. J.; Este, J. A.; Borras, F. E.; Clotet, B.; Ruiz, L.; Rosell, A.; Andreo, F.; Parkhouse, R. M.; Bofill, M., Secretion of interferon-gamma by human macrophages demonstrated at the single-cell level after costimulation with interleukin (IL)-12 plus IL-18. *Immunology* **2009**, *126*, 386.

(59) Maggini, J.; Mirkin, G.; Bognanni, I.; Holmberg, J.; Piazzon, I. M.; Nepomnaschy, I.; Costa, H.; Canones, C.; Raiden, S.; Vermeulen, M.; Geffner, J. R.,

Mouse bone marrow-derived mesenchymal stromal cells turn activated macrophages into a regulatory-like profile. *PLoS One* **2010**, *5*, e9252.

(60) Mitchison, T. J., The proliferation rate paradox in antimitotic chemotherapy. *Mol. Biol. Cell* **2012**, *23*, 1.

(61) Woydziak, Z. R.; Fu, L.; Peterson, B. R., Efficient and Scalable Synthesis of 4-Carboxy-Pennsylvania Green Methyl Ester: A Hydrophobic Building Block for Fluorescent Molecular Probes. *Synthesis* **2014**, *46*, 158.

(62) Barluenga, J.; Bayon, A. M.; Asensio, G., A new and specific method for the monomethylation of primary amines. *J. Chem. Soc., Chem. Commun.* **1984**, 1334.

(63) Barluenga, J.; Bayon, A. M.; Asensio, G., Monoalkylation of primary aromatic amines via N-(alkoxymethyl)arylamines. Evidence for the formation of stable monomeric methyleneamines. *J. Chem. Soc., Chem. Commun.* **1983**, 1109.

(64) Hansen, M. M.; Riggs, J. R., A novel protecting group for hindered phenols. *Tetrahedron Lett.* **1998**, *39*, 2705.

(65) Williams, A. T.; Winfield, S. A., Relative Fluorescence Quantum Yields Using a Computer-controlled Luminescence Spectrometer. *Analyst* **1983**, *108*, 1067.

(66) Magde, D.; Wong, R.; Seybold, P. G., Fluorescence quantum yields and their relation to lifetimes of rhodamine 6G and fluorescein in nine solvents: Improved absolute standards for quantum yields. *Photochem. Photobiol.* **2002**, *75*, 327.

(67) Shortreed, M.; Kopelman, R.; Kuhn, M.; Hoyland, B., Fluorescent fiber-optic calcium sensor for physiological measurements. *Anal. Chem.* **1996**, *68*, 1414.

(68) Lee, M. M.; Peterson, B. R., Quantification of Small Molecule-Protein Interactions using FRET between Tryptophan and the Pacific Blue Fluorophore. *ACS Omega* **2016**, *1*, 1266.

Chapter 4

Studies of proximity-driven bioconjugation of antibodies

4-1. Introduction

As described in Chapter 1, antibody drug conjugates (ADCs) are complex therapeutics that use the targeting capabilities of antibodies (mAbs) to deliver toxins to cancer cells. ADCs can overcome resistance to and improve the efficacy of therapeutic antibodies and improve the side effect profile of potent toxins. Each ADC consists of an antibody, a linker, and a toxin, each which must be optimized. When designing linkers, not only the toxin release method, but also the method of conjugation to the antibody must be considered.

Traditionally, the toxins of ADCs are linked to the antibody through either cysteines or lysines. Of the ADCs approved by the United States Food and Drug Administration (FDA) for the treatment of cancer, Adcetris is the only one to use cysteine residues for linkage.[1] Mylotarg,[2] Kadcyla,[3] and Besponsa[4] all link the toxins through lysine residues. Lysine residues are readily available and react quickly with *N*-hydroxysuccinimide (NHS) esters. Immunoglobulin G (IgG) antibodies contain an average of 90 lysines,[5] and random labeling of these residues generates heterogenous ADCs. In contrast, each natural antibody contains only 32 cysteines, 24 of which are involved in intra-chain disulfide bonds and 8 of which are involved in inter-chain disulfide bonds (Figure 4-1). Different methods have been developed to either fully or partially reduce the inter-chain bonds, generating relatively homogenous ADCs with 0, 2, 4, 6, or 8 toxins per antibody.[1,5-7]

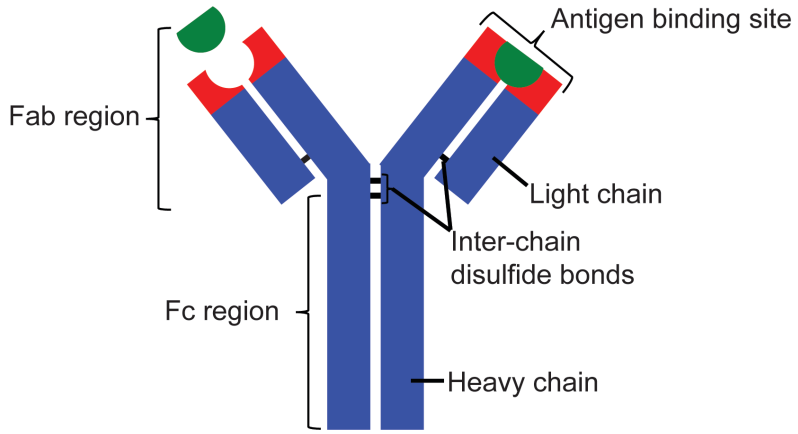

Figure 4-1. Structure of an IgG. Each IgG consists of 2 heavy chains and 2 light chains, held together by 4 inter-chain disulfide bonds. When these disulfides are reduced, hydrophobic interactions and other forces continue to hold these chains together.

Lysine-linked ADCs are heterogenous. As an example, the lysine-linked FDA-approved Kadcyla has an average drug to antibody ratio (DAR) of 3.5, with the number of toxins per antibody ranging from 0 to 8. Peptide mapping has revealed that out of the 88 lysines and 4 N-terminal amines present in the parent antibody Herceptin, 70 sites can be modified.[8] The first ADC to be approved, Mylotarg has a DAR of 3, but consists of ~50% unconjugated antibody and ~50% ADC with a DAR of 6.[9] Besponsa is relatively new, and relatively little information concerning it is available, but according to the information that Pfizer provides to physicians, this ADC has a DAR of 6, with a distribution from 2 to 8.[10] Studies of ADCs undergoing clinical and preclinical evaluation have shown similar heterogeneity, indicating that a single batch of an ADC may contain millions of unique species.[11-13]

This heterogeneity can be problematic for various reasons. Characterization and quality assurance are difficult for ADCs, particularly those generated by linking toxins to lysine residues. For these conjugates, it is necessary to use mass spectrometry and mathematical modeling to estimate the distribution of drug-linked forms, the fraction of

antibodies linked to 0, 1, 2, or more drugs.[6,8,11] For conjugates with linkages via cysteine residues, simpler methods such as hydrophobic interaction chromatography can be used to calculate the drug distribution and potentially separate ADCs of different DARs.[14] The random nature of manufacturing ADCs by linking toxins to lysine residues can lead to batch to batch variability that can impact efficacy and tolerability.

The number and location of toxins attached to an antibody can profoundly affect the efficacy and tolerability of ADCs. In *in vitro* cell culture studies, increasing the DAR of the ADC can decrease its IC_{50}, and a DAR as high as 16 can be achieved in some cases.[14-17] There is a limit to this improvement, and DARs higher than 8 can inhibit antibody binding to antigen,[16] whereas a DAR of 4 results in the highest activity in some cases.[15] High DARs can also lead to aggregation and instability. In an *in vivo* mouse xenograft model, lower DARs have been shown to be associated with enhanced activity.[14] In this mouse xenograft study, an ADC with a DAR of 4 produced equivalent antitumor effects as an ADC with a DAR of 8 while maintaining a better therapeutic index. The ADC with the higher DAR was found to have faster clearance, and therefore lower exposure.[14] The location of toxin attachment can also be important. Attachment within the antigen binding site can affect binding, and differences in the ADC microenvironment, such as solvent accessibility and charge state, can affect linker stability.[18] When the exact number and location of toxins linked to an antibody are not controlled, it is difficult, if not impossible, to control the properties of the ADC and ensure batch to batch equivalence.

For these reasons, there is a push to develop new methods to generate more homogenous ADCs. As mentioned above, cysteine-linked ADCs are less heterogenous than lysine-linked ADCs, but they are still more heterogenous than desired. Additionally,

the traditional method of generating cysteine-linked ADCs, forming thioethers through the reaction of cysteine residues with maleimides, generates ADCs with drugs that can be released by a retro-Michael reaction (Figure 4-2).[18-20] Methods have been reported to improve the stability of this linker[21,22] as well as to use bifunctional linkers to tether toxins while re-forming inter-chain disulfides.[23] Additionally, antibodies have been mutated to contain fewer[24] or additional[18,25-29] cysteines available for modification, providing more control over the DAR and conjugation site of the generated ADC.

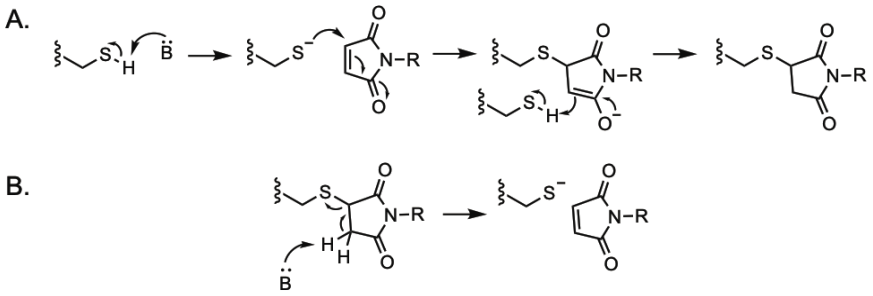

Figure 4-2. Attachment and release of a drug to the cysteine of an antibody through a maleimide linker. (A) Base-catalyzed reaction of the thiol of a cysteine residue with a maleimide linker.[30] (B) Base-catalyzed release of the drug through a retro-Michael reaction. The released drug can then react with other available thiols, commonly a cysteine residue of serum albumin.[18-20]

In addition to improving the more traditional conjugation methods, new methods are being developed. Other natural amino acids such as selenocysteine,[31] tyrosine,[32] and methionine[33] have been incorporated into mAbs to allow for site-specific conjugation of toxins. Unnatural amino acids have also been incorporated into mAbs to generate unique reactive handles for toxin conjugation.[34-38] Various methods have also been developed to modify the glycans attached to antibodies to generate sites of attachment for toxins.[39-43] Transpeptidases such as sortase have been used to link toxins to antibodies, requiring that the recognition sequence of the enzyme be encoded into the sequence of the

antibody using methods such as CRISPR.[44,45] These new methods are contributing to the large number of ADCs in clinical development, but none have yet lead to an FDA-approved therapeutic.

Many of these methods require alterations to the sequence of antibodies, often requiring optimization of each individual antibody and rendering the use of off-the-shelf antibodies impossible. One method being used to circumvent these issues takes advantage of the selective binding between IgG-binding proteins and IgG. This binding brings specific residues of the antibody close to reactive residues on the IgG-binding protein, potentially allowing for proximity-driven labeling of the antibody. Protein A and Protein G are 42-56 kDa bacterial proteins that bind IgG in a specific orientation. Both proteins are composed of small domains (around 6-8 kDa each) that are individually able to bind IgGs and can be produced rapidly in large quantities through bacterial overexpression, cell-free systems, and solid phase peptide synthesis. Modification of these domains with a photoreactive crosslinker and a secondary reactive tag or desired active group such as a fluorophore or toxin allows for the site-selective labeling of unmodified antibodies (Figure 4-3 A).[46-49] A metallopeptide catalyst[50] and the non-canonical amino acid 4-fluorophenyl carbamate lysine[51,52] (Figure 4-3 B) were developed to avoid the use of UV light to induce crosslinking. Each of these methods uses the selective binding of the engineered protein domain to induce proximity-driven, site-specific labeling of various classes of native IgG. Unfortunately, with the exception of the metallopeptide catalyst, each produces an antibody modified with the entire 6-8 kDa peptide domain. These modified antibodies bind their targets in cell culture, but given the importance of Fc receptors, cell surface proteins that bind antibodies at the same sites

bound by these proteins, to their *in vivo* half-lives, it is unclear what effects such large labels will have on bioavailability and clearance rates *in vivo*.

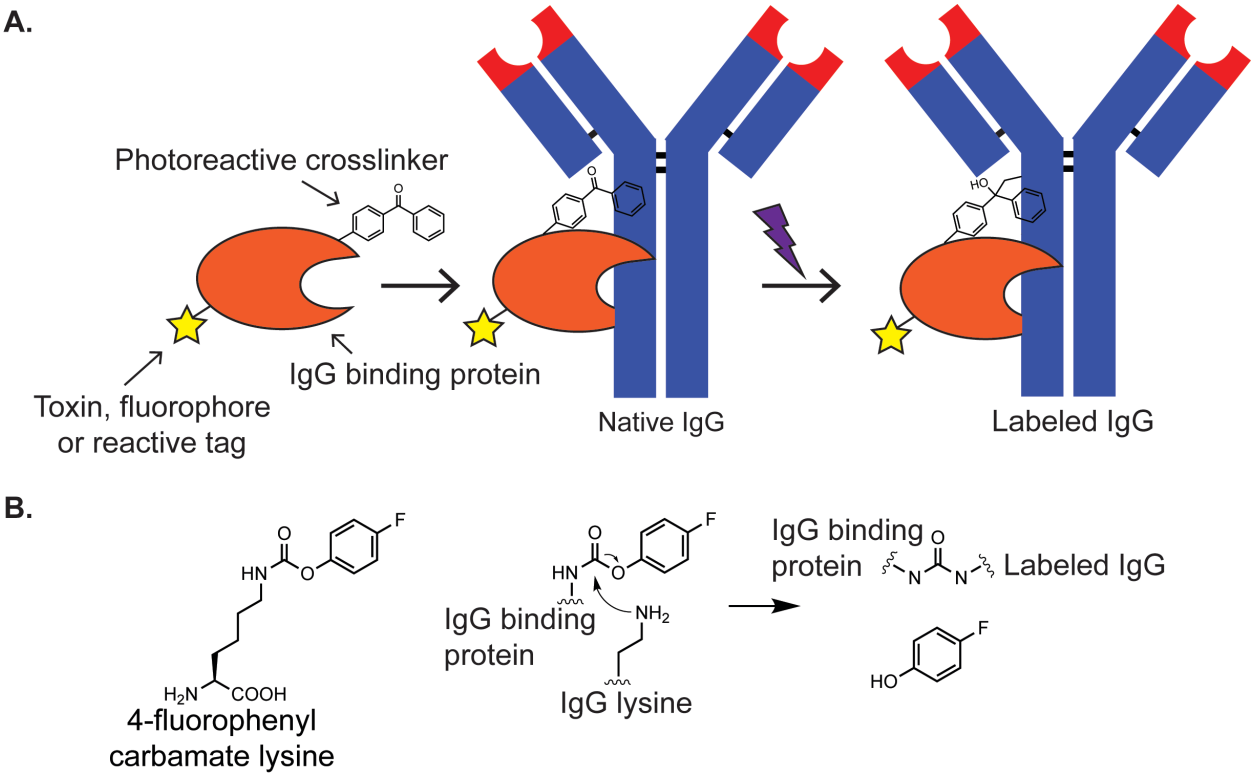

Figure 4-3. Proximity driven labeling of antibodies using antibody binding proteins. Domains of IgG binding proteins such as Protein A and Protein G can be engineered to contain a photoreactive crosslinker or other reactive residue and labeled with toxins, fluorophores, or reactive tags. When these domains are incubated with IgG, the two proteins bind, bringing the reactive tag of the smaller protein into close proximity with specific residues of the IgG, covalently labeling the IgG in a site-specific manner.

Proximity-driven reactions are also used to label proteins with small molecules to enable various experiments. These reactions can be used to label lysines,[53-56] cysteines,[57,58] and other residues[59-64] with small molecules such as fluorophores, biotin, and reactive tags in order to study protein-protein interactions using methods such as fluorescence microscopy and mass spectroscopy. The Peterson Lab has previously demonstrated the selective transfer of a fluorinated pyronin fluorophore from lysines of

the Fc region of human IgG to four homologous lysines out of 118 total lysines of Protein A (SpA).[56] The selectivity of this transfer was hypothesized to be caused by the unique proximity of the involved lysines, as depicted in the X-ray crystal structure of the Fc region of human IgG bound to a fragment of SpA. The selectivity of the proximity-driven reaction engenders the question of whether the opposite reaction might be possible. In other words, could site-specific antibody conjugates be created by first labeling SpA with a transferable tag and then incubating the labeled SpA with IgG?

In this chapter, we explore the use of proximity-driven bioconjugation to create antibody conjugates. SpA and simplified fragments were labeled with a fluorescent tag containing a labile ester and incubated with human IgG. SDS-PAGE, HPLC, and mass spectroscopy were then used to analyze the generated conjugates. We hypothesized that such a system might be used to produce more homogenous antibody conjugates than random lysine labeling reactions.

4-2. Studies using native Protein A

As previously mentioned, Protein A (SpA) is a bacterial protein that binds to human IgG. It is expressed by *Staphylococcus aureus* as both a membrane-bound surface protein and a soluble excreted protein and consists of 5 homologous IgG binding domains, each capable of binding to both the Fc and Fab fragments of IgG from many species of mammals including humans.[65-67] SpA protects *S. aureus* from immune attack through multiple mechanisms, including binding IgG on the surface of the bacteria, which coats the bacteria in IgG incorrectly positioned to bind to Fc receptors on immune cells, and binding to and sequestering IgG in the extracellular space. Both of these actions

prevent the opsonization and phagocytosis of *S. aureus*,[68,69] and have even been shown to protect other bacteria co-cultured with *S. aureus*.[70] Additionally, SpA is used to purify antibodies from complicated mixtures such as serum,[71] and can be used to indirectly label antibodies with fluorophores or other conjugates.

The binding of SpA to IgG is specific and well defined, and several structures of these complexes have been solved.[66,72-74] SpA contains about 60 lysines,[75] some of which are in close proximity to lysines of IgG when the two proteins are bound. Given the evidence that small molecules can be selectively transferred from lysines of human IgG to SpA,[56] we hypothesized that a similar reaction in the opposite direction could be used to selectively label IgG. To test this concept, Dr. Chamani Perera synthesized a set of fluorescent probes including a potentially transferrable probe containing a labile ester bond (**85**) a less reactive amide control (**86**), and a control for random labeling (**87**) (Figure 4-4).

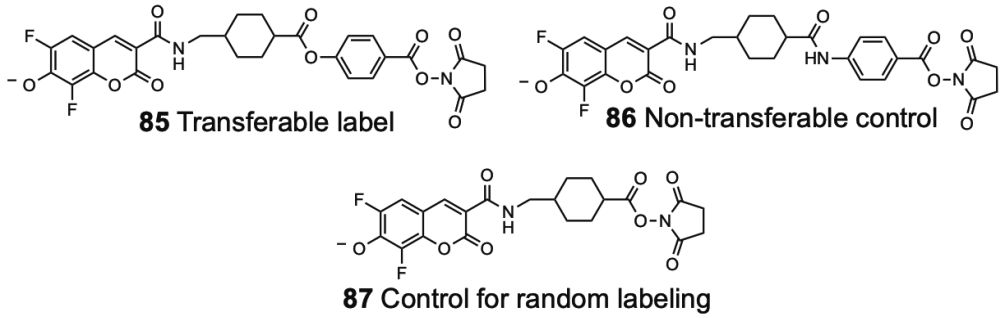

Figure 4-4. Structures of a potentially transferable fluorescent label, a non-transferable amide control, and a control for random labeling.

To study this approach, lysines of SpA were randomly labeled with the NHS esters **85** and **86**. Both SpA conjugates were subsequently incubated overnight with IgG to give the proteins sufficient time to bind and for the transferable label to react with lysines within

close proximity. We hypothesized that we would see transfer of fluorophore from SpA labeled with **85**, but not from the SpA-**86** conjugate. Additionally, IgG was labeled with **87** as a control for random labeling (Figure 4-5).

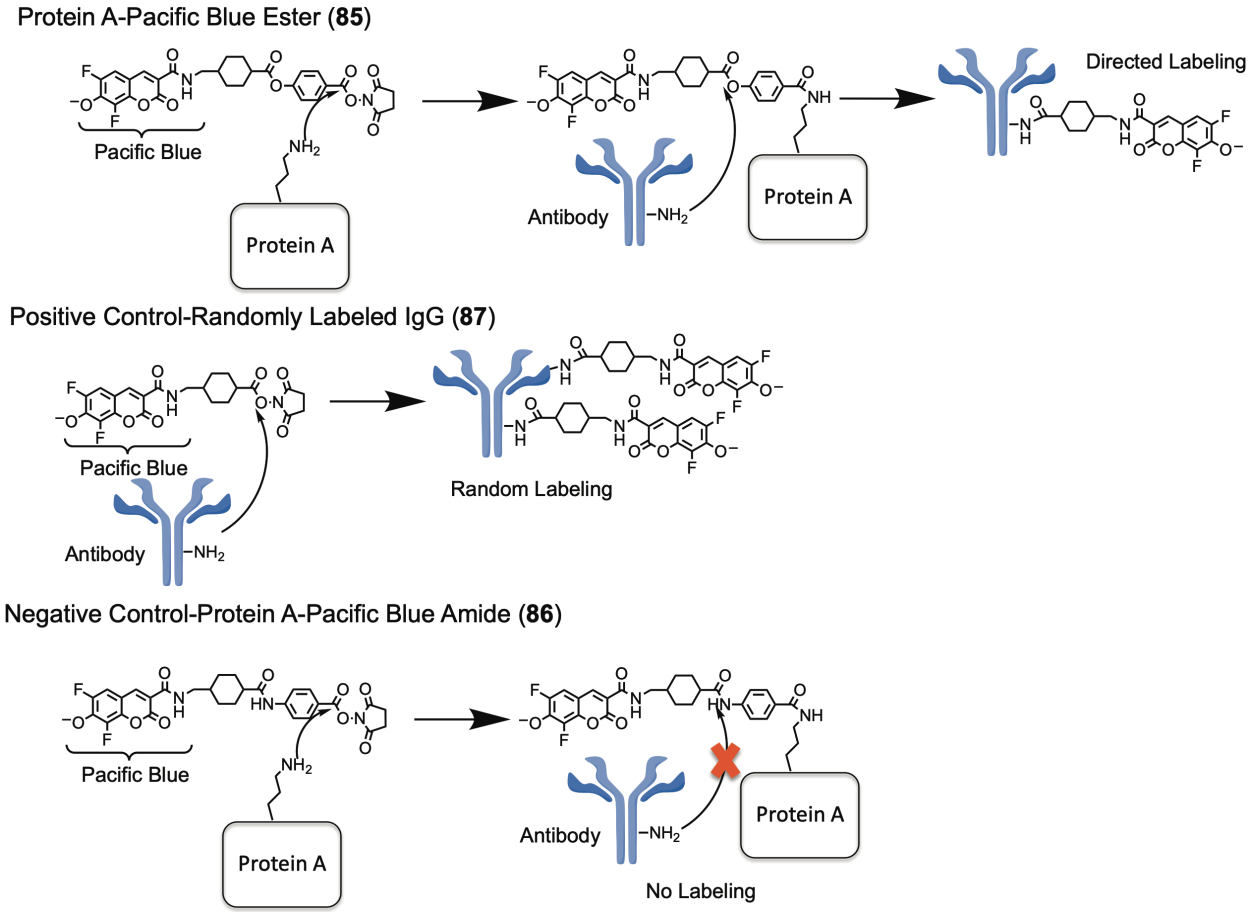

Figure 4-5. Proximity driven bioconjugation of antibodies. We hypothesized that labeling Protein A with **85** followed by incubation with IgG would lead to the directed labeling of the antibody due to the transfer of fluorophore from lysines of Protein A to lysines of IgG brought into close proximity by binding of the two proteins. IgG randomly labeled with **87** acts as a positive control for random labeling of IgG. The SpA-**86** conjugate acts as a negative control since the amide bond tethering the fluorophore to the antibody is not reactive towards amines under these conditions, preventing transfer.

Several methods were used to analyze this system. Sodium dodecyl sulfate-polyacrylamide gel electrophoresis (SDS-PAGE) followed by visualization on a UV transilluminator provided a simple method to examine transfer of fluorescence. As

previously described, SpA was randomly labeled with **85** and **86** and incubated with IgG. These reaction mixtures were analyzed by SDS-PAGE and compared with IgG-**87** as a positive control. The gel was run under reducing conditions to allow analysis of transfer to the separated heavy and light chains of IgG. As can be seen in Figure 4-6, transfer of fluorescence from SpA-**85** to IgG is observed and increases with increasing concentration of SpA-**85**, but this transfer is not observed with SpA-**86**. However, the heavy chain of IgG and SpA run very closely on the gel, and protein diffusion is observed, further complicating the analysis.

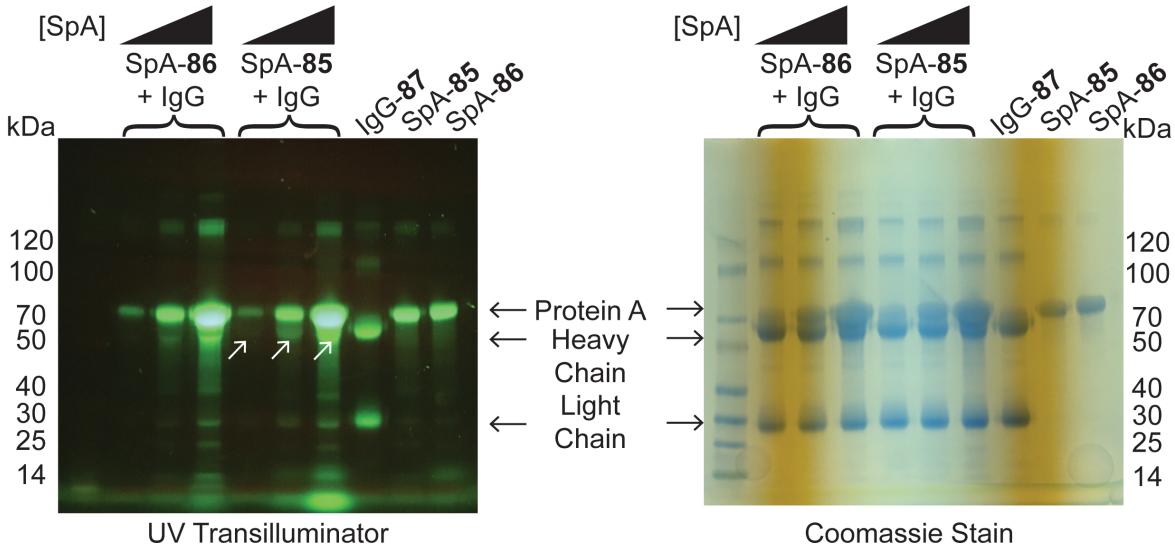

Figure 4-6. SDS-PAGE analysis of the transfer of fluorophore from SpA-**85** to IgG. The image taken on a UV transilluminator (left) shows the transfer of fluorescence from SpA-**85** (indicated with white arrows) to IgG but not from SpA-**86**. This transfer increases with increasing concentration of SpA-**85** and is more pronounced on the heavy chain of IgG. IgG randomly labeled with **87** acts as a positive control for the fluorescent IgG chains. [SpA-**85**/**86**]: 1, 5, 25 μM. [IgG]: 5 μM. SpA-**85** DOL: 4.0. SpA-**86** DOL: 3.6. IgG-**87** DOL: 4.9. Proteins were incubated for 16 h at 37 °C prior to analysis.

Tryptic digestion followed by mass spectroscopy-based protein sequencing was performed in tandem with SDS-PAGE to analyze the transfer of the fluorophore. For this experiment, the monoclonal IgG Herceptin was used in place of pooled human IgG to

increase the homogeneity of the sample. SpA was labeled with both the transferable label (**85**) and the non-transferable control (**86**). Herceptin was added with incubation overnight (16 h), followed by SDS-PAGE analysis of the reaction solution (Figure 4-7). The difference in apparent molecular weight between the SpA used in this experiment and that shown in Figure 4-6 is presumably due to their different sources (recombinant vs. *S. aureus*) and the degradation of this SpA under the reaction conditions. The image of the gel taken on the UV transilluminator suggests that more fluorescence is transferred from SpA-**85** to the heavy chain of Herceptin than to the light chain.

The bands for the heavy chains of both unmodified Herceptin and Herceptin that was incubated with SpA-**85** were excised, digested with trypsin, and analyzed by MS/MS sequencing by Dr. Nadya Galeva of the KU Mass Spectrometry and Analytical Proteomic Laboratory. The MS/MS data was not fully conclusive, due in part to the low efficiency of the label transfer reaction. However, this preliminary data suggests that the fluorophore was transferred to three (Lys246, Lys288, Lys414) out of the 32 lysine residues found in each heavy chain of Herceptin (Figure 4-7). Each modification was observed with at least 90% probability. Of these three residues, one (Lys288) was shown by Hymel *et. al.* to transfer a pyronin molecule to Lys246 of SpA in a similar but reversed experiment as discussed in the Introduction section.[56] The crystal structure of the B domain of SpA bound to IgG (Figure 4-7 B) revealed that Lys288 of IgG is only 9 Å away from SpA Lys246, explaining how Lys288 could be labeled. IgG Lys246 is further away from lysines of SpA (17 Å from SpA Lys246 and 20 Å from SpA Lys218). From this crystal structure it is unclear how IgG Lys414 would be labeled by the proximity driven reaction given its distance from any SpA residues and why IgG Lys248 would not be labeled given that it

closer to SpA than Lys246. However, SpA has also been reported to have some affinity for the Fab fragments of human IgG, and that interaction may contribute to transfer of the fluorophore. Similar analysis of the light chain of Herceptin was not performed.

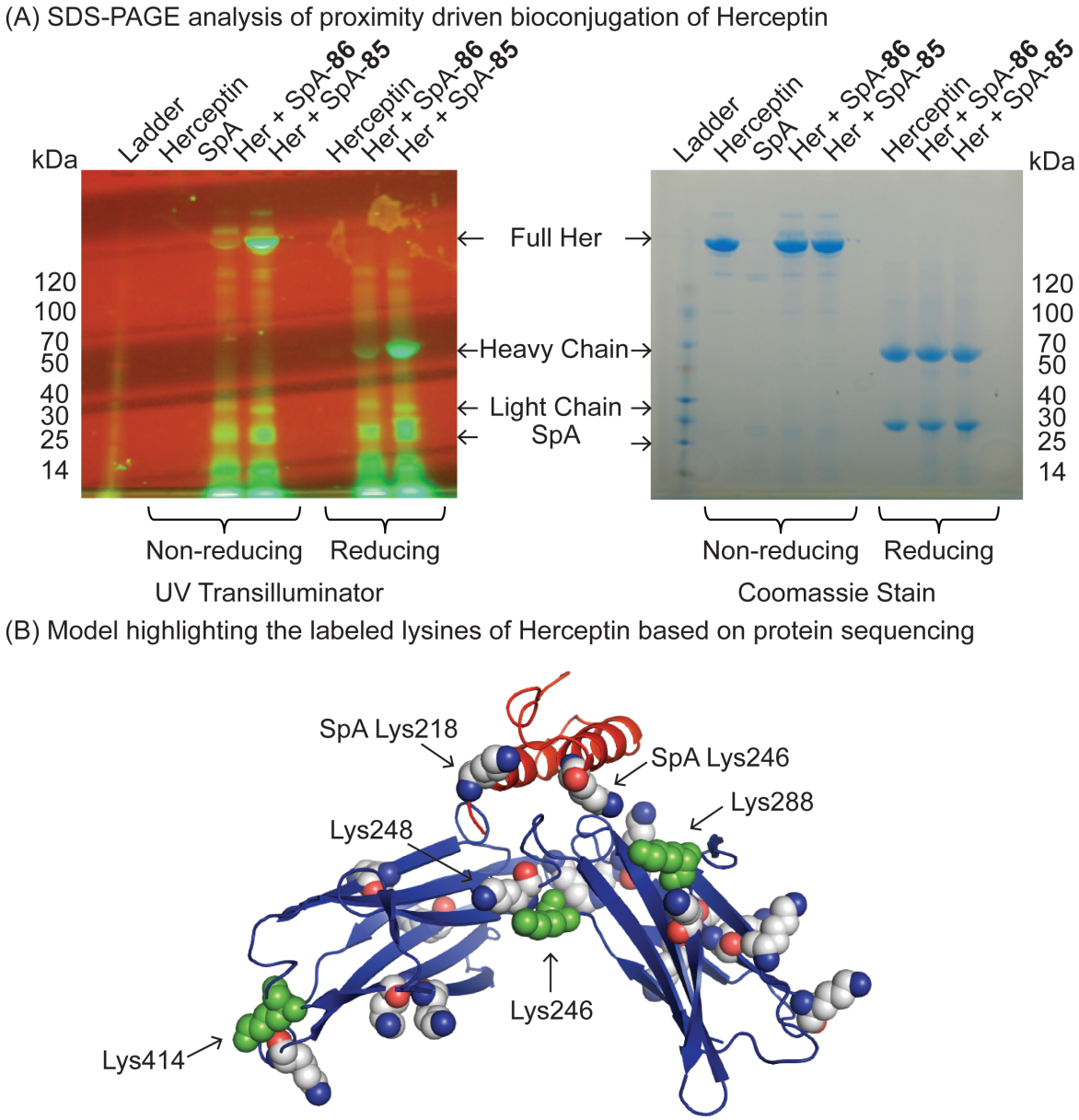

Figure 4-7. Analysis of proximity driven bioconjugation of Herceptin. (A) SDS-PAGE analysis. The image using a UV transilluminator clearly shows the transfer of fluorescence from SpA-**85** to Herceptin but not from SpA-**86**. Transfer appears more prominent to the heavy chain of Herceptin than to the light chain. [SpA-**85**/**86**]: 25 μM. [Herceptin]: 5 μM.

SpA-**85** DOL: 5. SpA-**86** DOL: 5. Proteins were incubated for 16 h at 37 °C. (B) X-ray structure of the Fc region of human IgG (blue) bound to Fragment B of SpA (red, PDB ID 1FC2). Carbohydrates of IgG were omitted for clarity. Lysine residues are shown as CPK models. Lysine residues identified by protein sequencing as possibly being modified by the transferred fluorophore are highlighted in green.

A limitation of the analysis of these reactions was that full peptide coverage of the heavy chain was not achieved. Peptides accounting for 63% of the heavy chain were found, accounting for 19 of the 32 lysine residues. It is possible that other lysines were also modified, reducing the apparent selectivity of the transfer reaction. Herceptin randomly labeled with **87** would have served as an enlightening control but was not analyzed.

To improve this approach, attempts were made to simplify this system. The similarity of molecular weight between SpA and the heavy chain of IgG, along with the diffusion of fluorescence on the SDS-PAGE gels made analysis difficult. Immobilized SpA resin was labeled with **85** and **86** and incubated with IgG, but consistent transfer from only the SpA resin labeled with **85** was not observed. Additionally, Immobilized SpA resin was used to attempt to separate the labeled IgG from the reaction mixture, but once again results were mixed. Because of these issues, and the complexity of SpA itself, a simpler system designed and investigated.

4-3. Studies using simplified variants of Protein A

As previously mentioned, SpA consists of five homologous domains, each of which has affinity for IgG.[65] In 1987, a simplified IgG-binding protein based on the sequence of SpA domain B was generated.[76] The B domain was selected due to its sequence being the closest to the hypothetical consensus sequence of the binding domains and because

of its lack of methionine. The lack of methionine allows the protein to be treated with cyanogen bromide, which cleaves proteins after methionine residues, for immobilization on agarose and other solid supports. The new protein domain, known as the Z domain, also contains a carefully designed glycine to alanine mutation that blocks the sensitivity of the protein to treatment with hydroxylamine, which cleaves asparagine-glycine peptide bonds. Both of the lack of methionine and the point mutation allow for the use of Z domain as a fusion protein that could be cleaved using cyanogen bromide or hydroxylamine.[76] Soon after the development of the Z domain, its dimer the ZZ domain was used as a fusion protein to aid in the expression and purification of human insulin-like growth factor.[77]

The ZZ domain of SpA is much simpler than full length SpA, yet it binds tightly to IgG. SpA is a 45 kDa protein that contains about 60 lysines, whereas the ZZ domain is a 16 kDa protein that contains only 12 lysines. Although SpA and the B domain bind to both the Fc and Fab fragments of IgG, the Z domain only binds to the Fc fragment.[65] Binding to the Fc fragment is more desirable than binding to the Fab fragment because labeling of the Fc fragment is less likely to block binding of the antibody to its target. We hypothesized that the lower number of lysines and simplified binding of this protein to IgG could improve the proposed proximity driven bioconjugation system.

To test this hypothesis, we designed a synthetic gene encoding the SpA ZZ domain (SpA-ZZ-12Lys) as well as a further simplified version with six lysine to arginine mutations, providing a total of 6 lysines (SpA-ZZ-6Lys). The 6 remaining lysines in SpA-ZZ-6Lys correspond to three pairs of homologous residues split between the two fused Z domains (Figure 4-8 A). These were chosen based on a crystal structure of the C domain

of SpA bound to IgG (PDB 4ZNC). This crystal structure shows a more complete structure of SpA that includes more lysines than the structure of the B domain bound to IgG (PDB 1FC2). The C domain is only different from the B domain by five residues, and the structures are highly similar.[74] This structure shows four of the six lysines of the SpA domain. The lysines corresponding to SpA Lys218 and Lys246 are clearly in close proximity to IgG, while Lys260 and Lys261 are not. Additionally, although they are not observed in the structure, it appears that Lys215 would be more likely to interact with IgG than Lys269. For this reason, SpA-ZZ-6Lys was designed to contain lysines 215, 218, and 246. Each gene also includes a single cysteine residue at the C-terminal to allow for attachment to a solid support to potentially simplify analysis of the proximity-driven transfer reaction.

(A) Sequence of SpA and SpA variants

SpA B Domain Sequence (212-269)

Lys215 Lys218 Lys246 Lys260/261 Lys269

ADNKFNKEQQ NAFYEILHLP NLNEEQRNGF IQSLKDDPSQ SANLLAEAKK LNDAQAPK

SpA-ZZ-12Lys Sequence

EFAQHDEA
VDNKFNKEQQ NAFYEILHLP NLNEEQRNAF IQSLKDDPSQ SANLLAEAKK LNDAQAPK
VDNKFNKEQQ NAFYEILHLP NLNEEQRNAF IQSLKDDPSQ SANLLAEAKK LNDAQAPK
VDGGC

SpA-ZZ-6Lys Sequence

EFAQHDEA
VDNKFNKEQQ NAFYEILHLP NLNEEQRNAF IQSLKDDPSQ SANLLAEARR LNDAQAPR
VDNKFNKEQQ NAFYEILHLP NLNEEQRNAF IQSLKDDPSQ SANLLAEARR LNDAQAPR
VDGGC

(B) Crystal structure of the C domain of SpA bound to IgG

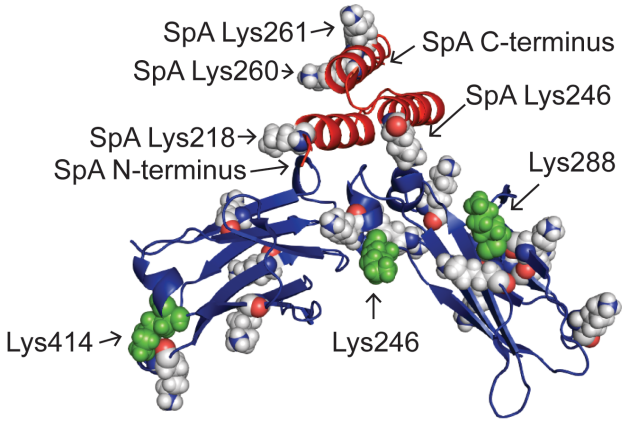

Figure 4-8. (A) Sequence of simplified SpA variants compared to the B Domain of SpA (Uniprot ID P02976). SpA-ZZ-12Lys is identical in sequence to two fused B domains with the exception of the leader sequence at the N terminus, the alanine to valine mutation at the N terminus of each domain, and the addition of a cysteine residue with a short linker at the C terminus. (B) X-ray structure of the Fc region of human IgG (blue) bound to Fragment C of SpA (red, PDB ID 4ZNC). Lysine residues are shown as CPK models. Lysine residues identified by protein sequencing as possibly being modified by the transferred fluorophore are highlighted in green.

The synthetic genes encoding these proteins were ordered from GenScript, cloned into an *E. coli* expression vector, overexpressed, and purified using affinity chromatography. A representative SDS-PAGE analysis of the purification of SpA-ZZ-6Lys is shown in Figure 4-9.

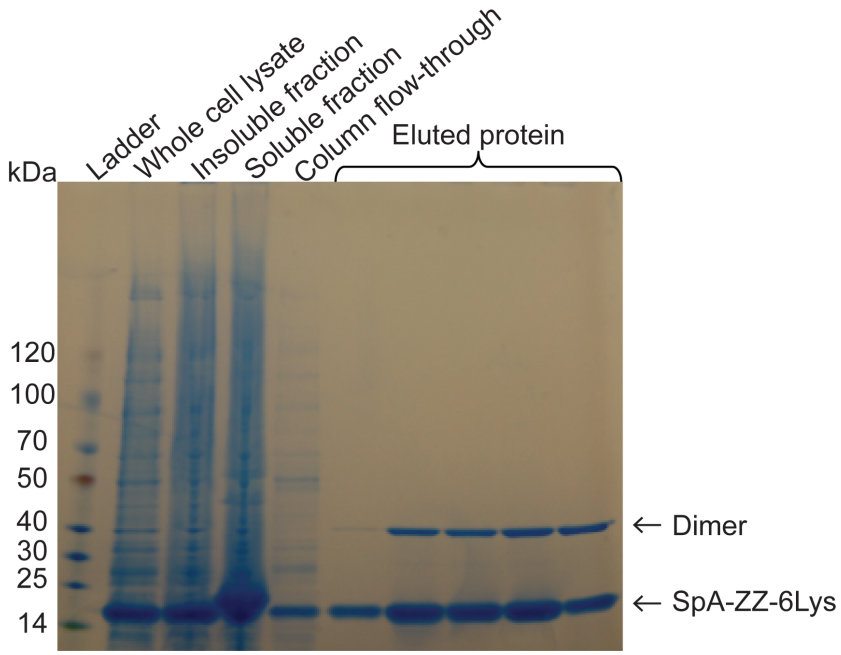

Figure 4-9. Purification of SpA-ZZ-6Lys after overexpression in *E. coli*. SpA-ZZ-6Lys was purified using a Ni-NTA affinity column. Samples from each step of the purification were analyzed using non-reducing SDS-PAGE. The desired protein was collected in good purity with a yield of about 7 mg/L of LB media. A higher yield could potentially have been attained by use of FPLC for purification, as evidenced by the presence of the desired product in the insoluble fraction and the column flow-through.

Comparisons of the simplified SpA-ZZ-12Lys and -6Lys with each other and with full-length SpA by SDS-PAGE did not reveal clear differences. Digestion of the IgG with papain, which cleaves IgG into two Fab fragments and one Fc fragment, after incubation with both SpA-**85** and SpA-ZZ-12Lys-**85** indicated that fluorescence was transferred to both the Fc and Fab portion of the antibody in both cases, although SpA-ZZ-12Lys-**85** might have a slight preference for the Fc portion (Figure 4-10). This preference would be desirable because labeling of the Fc portion of an antibody is less likely to perturb binding between the antibody and its target. Given that the Z domain has been shown to only bind to the Fc portion of the antibody, it is unclear why SpA-ZZ-12Lys-**85** would label both fragments, but non-specific interactions resulting from conjugation may play a role.

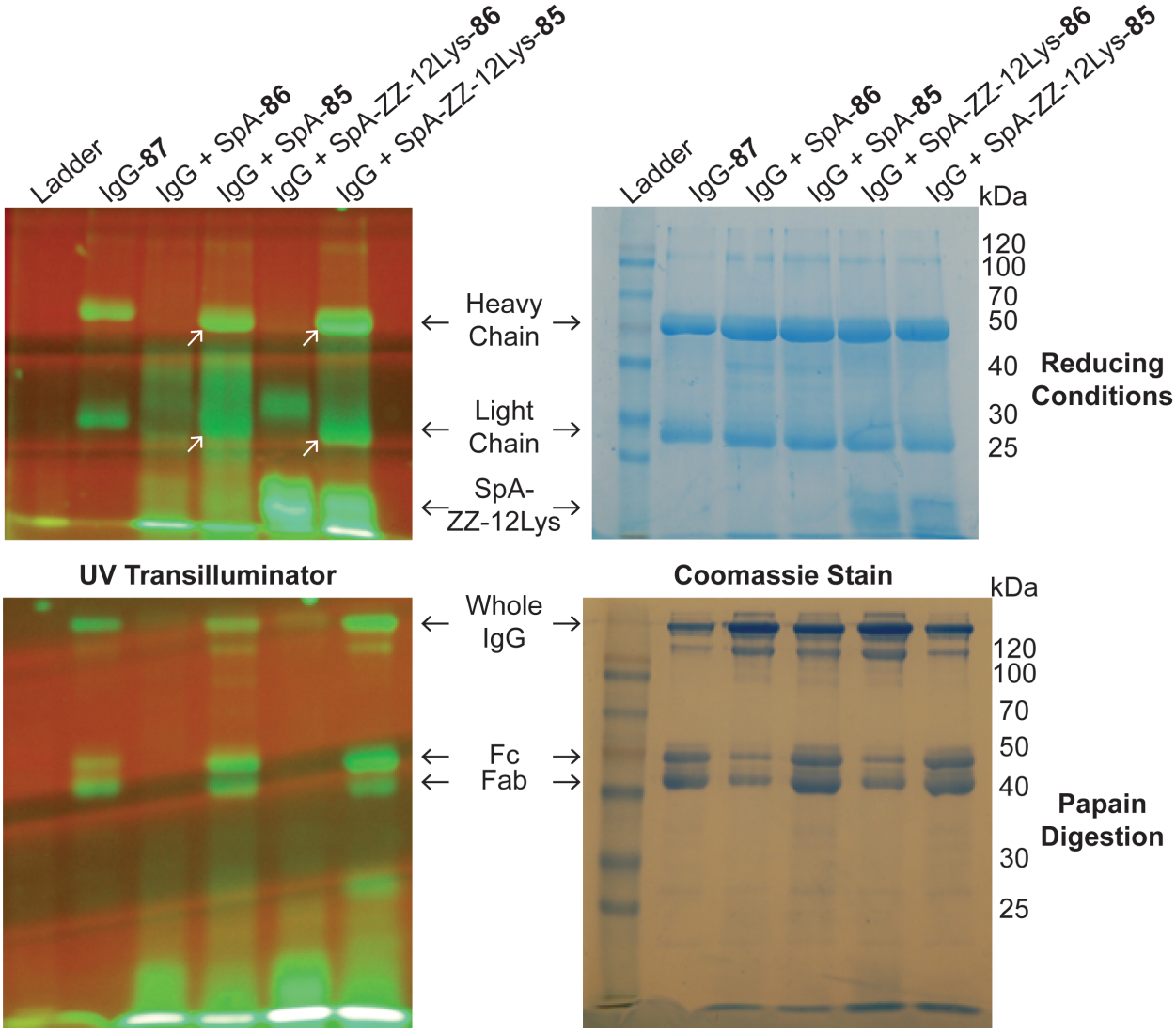

Figure 4-10. SDS-PAGE analysis of proximity-driven bioconjugation of IgG from SpA compared to SpA-ZZ-12Lys. The top panel shows images of a gel run under reducing conditions, while the bottom panel shows a gel of samples digested with papain. Fluorescence is transferred from both SpA-**85** and SpA-ZZ-12Lys-**85** to IgG but not from either protein labeled with **86**. SpA-ZZ-12Lys might preferentially label the Fc fragment of IgG over the Fab fragment when compared to SpA, but the difference is not clear using this analysis method. Labeled SpA was not stable to reaction conditions, leading the smear seen in lanes containing this protein in the images from the UV transilluminator. White arrows indicate fluorescent bands generated by proximity-driven transfer. [SpA-**85**/**86**]: 25 μM. [IgG]: 5 μM. SpA-**85** DOL: 3. SpA-**86** DOL: 4. SpA-ZZ-12Lys-**85**/**86** DOL: difficult to determine due to low extinction coefficient of protein, but comparable between the two samples. IgG-**87** DOL: 2.9. Incubated 16 h, 37 °C.

The differences between transfer from SpA-ZZ-12Lys and -6Lys are also difficult to interpret. As shown in Figure 4-11, transfer happens from both simplified SpA variants labeled with **85** but not with **86**. The transfer might be more robust from the 12Lys variant, but it could also be more selective between the chains from the 6Lys variant. The smearing of the fluorophore on the gel and the close proximity of important bands make comparison by SDS-PAGE difficult. It is possible that mass spectroscopy-based protein sequencing could reveal differences between the proximity-driven fluorescence transfer between the different versions of SpA, but this type of analysis was not performed.

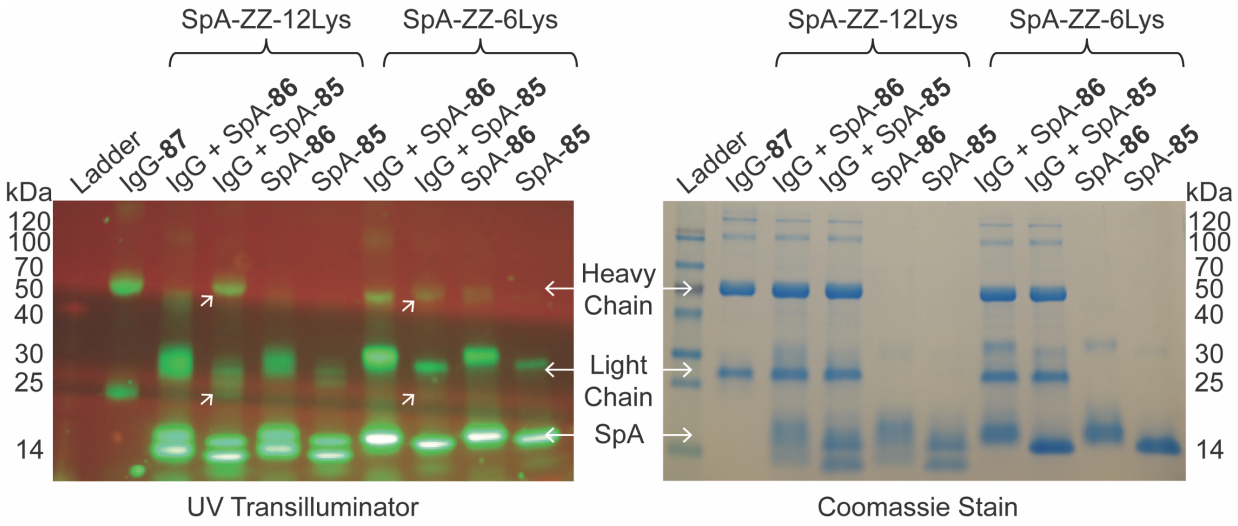

Figure 4-11. SDS-PAGE analysis of proximity-driven bioconjugation of IgG from SpA-ZZ-12Lys compared to SpA-ZZ-6Lys. Fluorescence is transferred from both SpA variants labeled with **85** to IgG but not from either protein labeled with **86**. White arrows indicate fluorescent bands generated by proximity-driven transfer. [SpA-**85**/**86**]: 25 μM. [IgG]: 5 μM. SpA-ZZ-12/6Lys-**85**/**86** DOL: difficult to determine due to low extinction coefficient of protein, but comparable between the four samples. IgG-**87** DOL: 2.9. Incubated for 16 h at 37 °C before analysis.

Attempts were made to use tryptic digestion followed by high performance liquid chromatography (HPLC) to analyze the proximity-driven transfer of fluorophores from

SpA-ZZ-6Lys to Herceptin. However, digests of mixtures of Herceptin and SpA-ZZ-6Lys were too complex to interpret (data not shown). In order to simplify this analysis, transfer from SpA-ZZ-6Lys immobilized through its single cysteine residue on SulfoLink Coupling Resin, an agarose resin activated with iodoacetyl groups, was attempted. Because of the difficulty of properly washing the resin to remove all excess small molecules, transfer was consistently seen from immobilized SpA-ZZ-6Lys labeled with both **85** and **86**. A second method met with slightly more success. Free SpA-ZZ-6Lys labeled with **85** and **86** was incubated with Herceptin. The reaction solution was then added to a microspin column packed with SulfoLink Resin and allowed to equilibrate to encourage the binding of the SpA-ZZ-6Lys to the resin. Herceptin should not have any free cysteines available to react with the resin, so it should bind to a lesser extent and thus be separated from the other protein. Pure Herceptin was eluted from the column, but much Herceptin was lost in the process (Figure 4-12 A). Tryptic digest of Herceptin-**87**, and Herceptin incubated with SpA-ZZ-6Lys-**85** or -**86** followed by HPLC analysis showed a clear difference in the complexity of the labeled proteins when looking at blue fluorescence (Figure 4-12 B). While there are many peaks present in the Herceptin-**87** sample, only a few are seen from Herceptin incubated with SpA-ZZ-6Lys-**85**, one of which is also present in the negative control incubated with SpA-ZZ-6Lys-**86**, indicating that it could be contaminant such as remaining labeled SpA-ZZ-6Lys. This assay shows promise, but an increased yield of the final labeled Herceptin to be digested is needed.

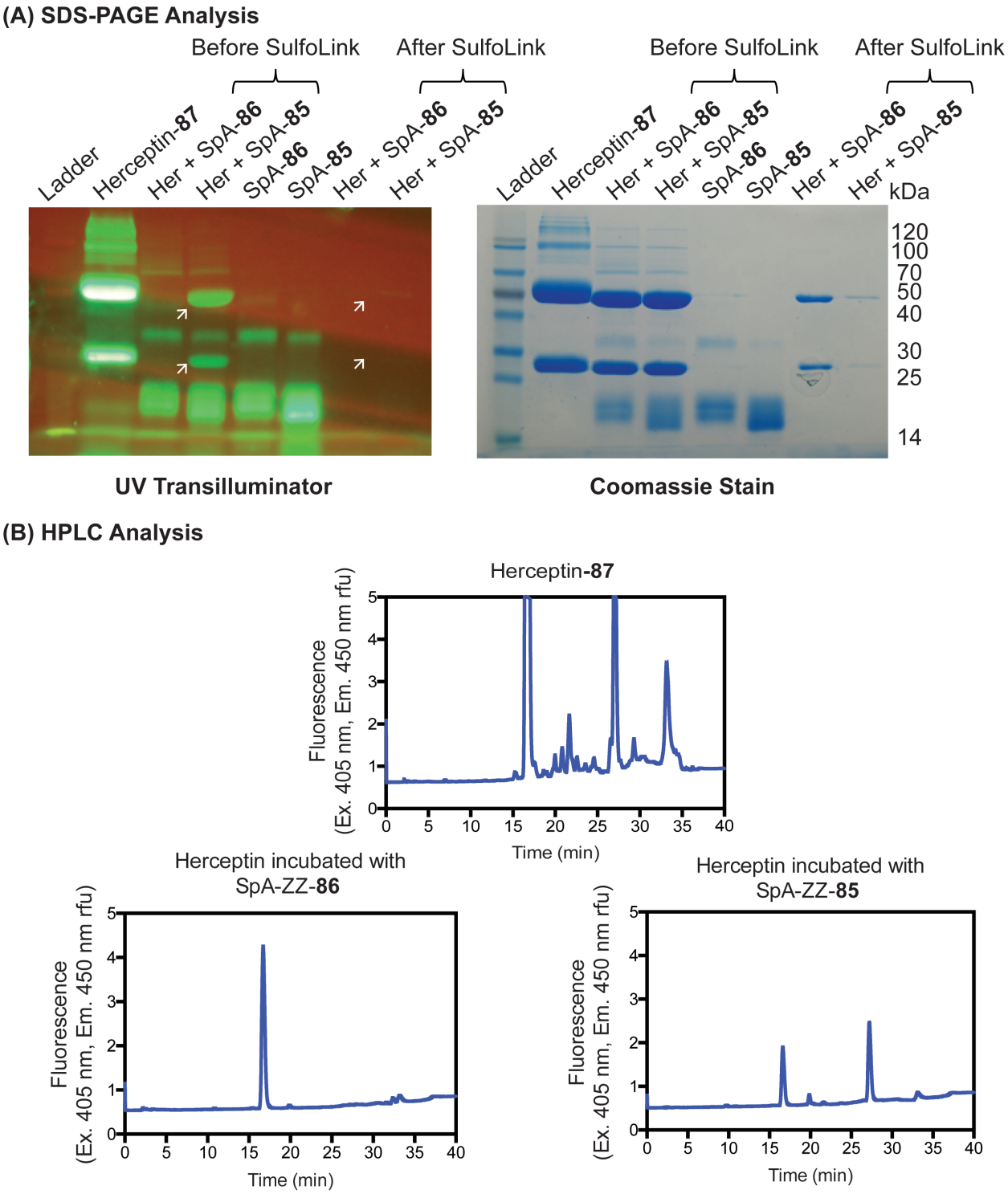

Figure 4-12. SDS-PAGE and HPLC analysis of the proximity-driven transfer of fluorophores from SpA-ZZ-6Lys to Herceptin. Transfer from SpA-ZZ-6Lys-**85** and not from **-86** can be observed, but this assay suffers from loss of Herceptin during purification with SulfoLink Resin, leading to low signal on both the gel and during HPLC analysis. White arrows indicate fluorescent bands generated by proximity-driven transfer.

[Herceptin]: 5 μM. SpA-ZZ-6Lys-**85**/**86** DOL: difficult to determine due to low extinction coefficient of protein, but comparable between the two samples. Her-**87** DOL: 4.0. Incubated for 16 h at 37 °C.

To further simplify the SpA-ZZ-6Lys protein, site-directed mutagenesis was used to generate three separate proteins, each containing only two homologous lysines (Figure 4-13). We hypothesized that this would allow us to determine which lysine residue(s) of SpA-ZZ-6Lys were involved in the proximity-driven transfer reaction. Each new variant was overexpressed in *E. coli* and purified by affinity chromatography to yield samples of high purity (Figure 4-14).

SpA-ZZ-6Lys Sequence

EFAQHDEA
VDNKFNKEQQ NAFYEILHLP NLNEEQRNAF IQSLKDDPSQ SANLLAEARR LNDAQAPR
VDNKFNKEQQ NAFYEILHLP NLNEEQRNAF IQSLKDDPSQ SANLLAEARR LNDAQAPR
VDGGC

SpA-ZZ-2Lys-A Sequence

EFAQHDEA
VDNKFNREQQ NAFYEILHLP NLNEEQRNAF IQSLRDDPSQ SANLLAEARR LNDAQAPR
VDNKFNREQQ NAFYEILHLP NLNEEQRNAF IQSLRDDPSQ SANLLAEARR LNDAQAPR
VDGGC

SpA-ZZ-2Lys-B Sequence

EFAQHDEA
VDNRFNKEQQ NAFYEILHLP NLNEEQRNAF IQSLRDDPSQ SANLLAEARR LNDAQAPR
VDNRFNKEQQ NAFYEILHLP NLNEEQRNAF IQSLRDDPSQ SANLLAEARR LNDAQAPR
VDGGC

SpA-ZZ-2Lys-C Sequence

EFAQHDEA
VDNRFNREQQ NAFYEILHLP NLNEEQRNAF IQSLKDDPSQ SANLLAEARR LNDAQAPR
VDNRFNREQQ NAFYEILHLP NLNEEQRNAF IQSLKDDPSQ SANLLAEARR LNDAQAPR
VDGGC

Figure 4-13. Sequences of SpA-ZZ-2Lys variants A-C. The sequence of these three variants differ only in the position of the two lysine residues.

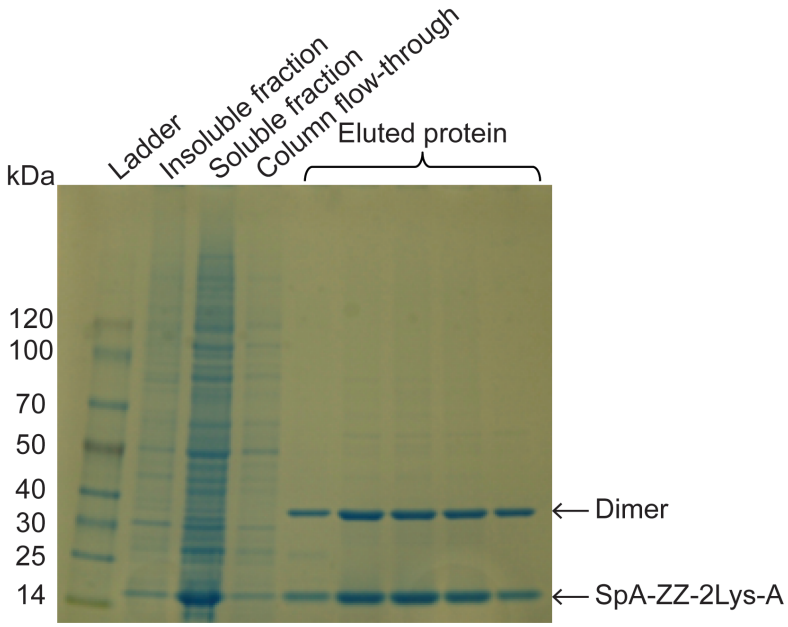

Figure 4-14. Purification of SpA-ZZ-2Lys-A after overexpression in *E. coli*. SpA-ZZ-2Lys-A was purified using a Ni-NTA affinity column. Samples from each step of the purification were analyzed using non-reducing SDS-PAGE. The desired protein was collected in good purity at a yield of about 15 mg/L of LB media.

Each of these simplified SpA-ZZ variants were labeled with **85** and **86** and incubated with Herceptin as previously described. Analysis by SDS-PAGE suggested that transfer did occur from the SpA-ZZ variants labeled with **85** but not from those labeled with **86** (Figure 4-15). However, all signals were weak, and no differences in signal intensity were discernable when pixel density was quantified with Photoshop.

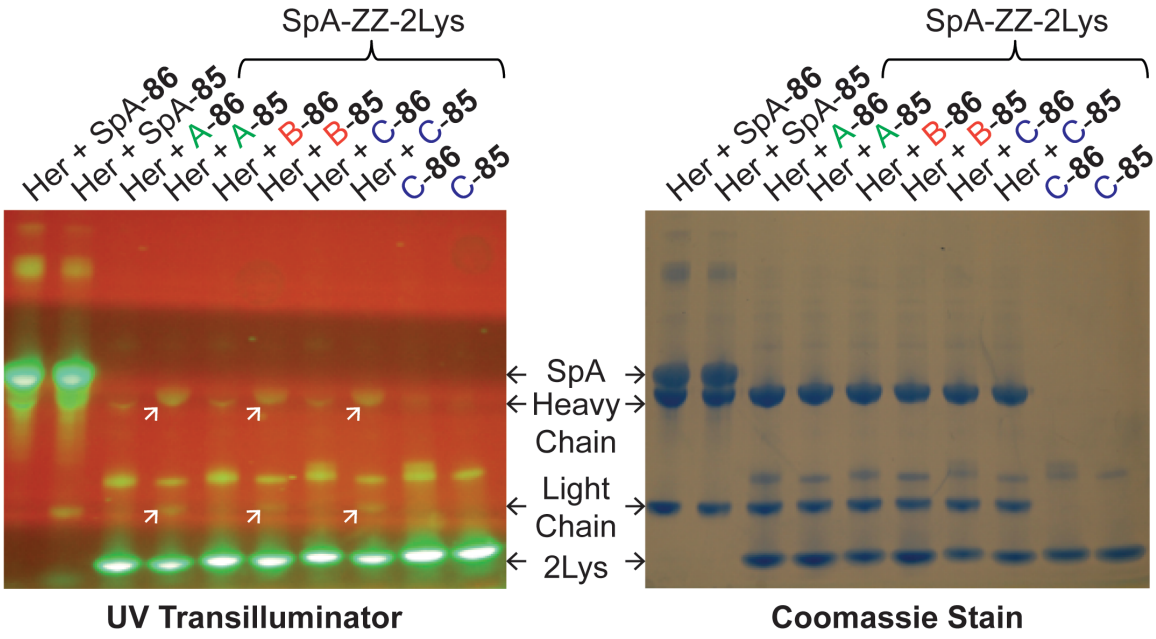

Figure 4-15. SDS-PAGE analysis of proximity-driven bioconjugation of Herceptin from the three SpA-ZZ-2Lys variants (A-C) compared to full SpA. Fluorescence is transferred from all SpA variants labeled with **85** to Herceptin but not from any protein labeled with **86**. White arrows indicate fluorescent bands generated by proximity-driven transfer. [SpA-**85**/**86**]: 25 μM. [Herceptin]: 5 μM. SpA-**85** DOL: 4.7. SpA-**86** DOL: 4.5. SpA-ZZ-2Lys-**85**/**86** DOL: difficult to determine due to low extinction coefficient of protein but assumed to be 2 due to number of lysines present in protein. Proteins were incubated for 16 h at 37 °C.

To further confirm that proximity-driven transfer occured between all three SpA-ZZ-2Lys variants, tryptic digestion followed by HPLC analysis was performed. The SpA-ZZ-2Lys variants were tethered to SulfoLink Resin and labeled with **85** and **86** to allow for separation from the labeled Herceptin. These labeled Herceptin samples, and Herceptin labeled with **87**, were digested with trypsin and then separated by HPLC with fluorescence detection. The chromatograms generated by the three samples that had been incubated with SpA-ZZ-2Lys variants labeled with **85** were nearly identical, and much simpler than that generated from digestion of Herceptin-**87** (Figure 4-16). Additionally, the chromatograms generated by Herceptin incubated with SpA-ZZ-2Lys

variants labeled with the amide control **86** showed very little signal, as would be expected if proximity-driven fluorescence transfer did not occur.

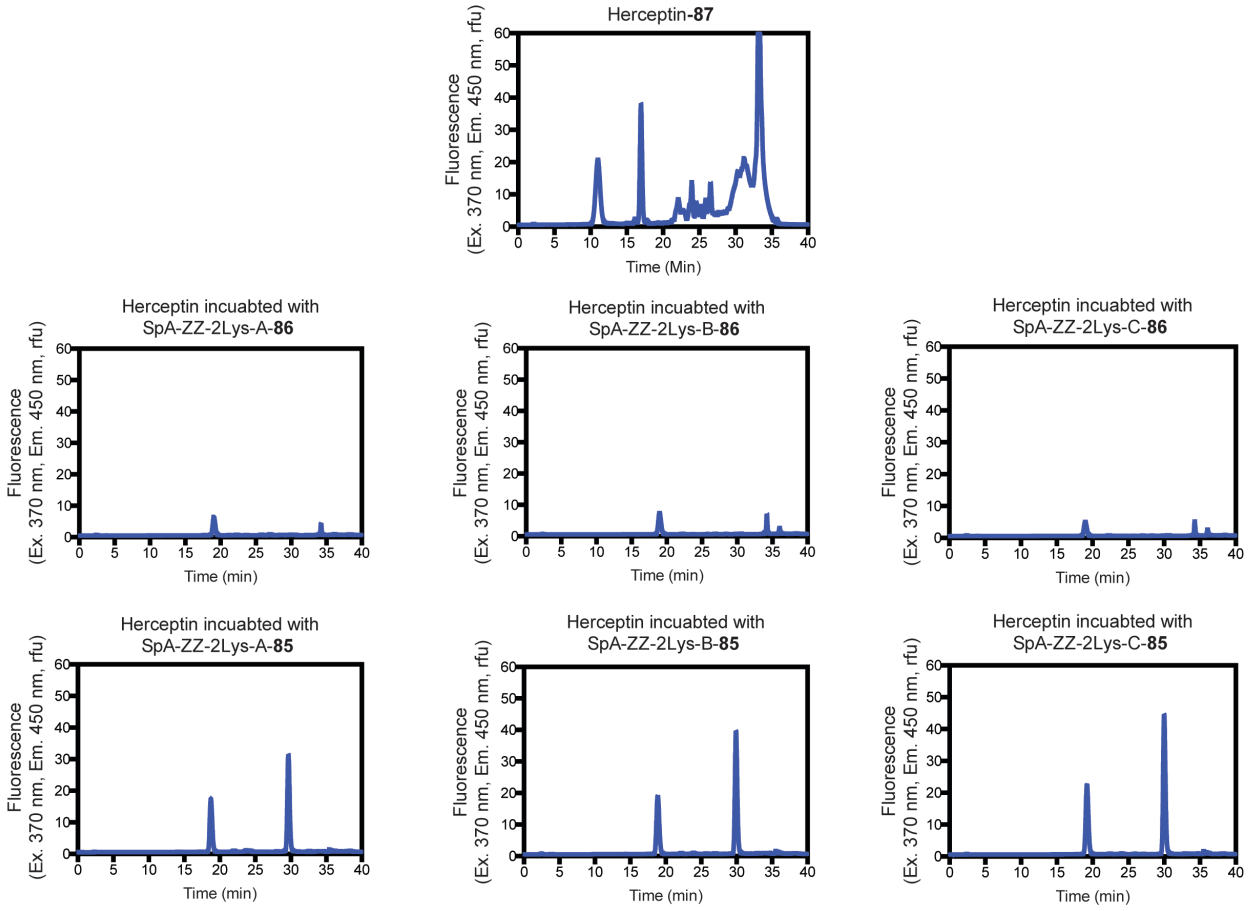

Figure 4-16. HPLC analysis of proximity-driven bioconjugation of Herceptin from the three SpA-ZZ-2Lys variants (A-C). The blue fluorescent signal is produced from Herceptin that was incubated with all SpA variants labeled with **85** while little signal is produced from Herceptin incubated with any variant labeled with **86**. The chromatograms of Herceptin labeled through the proximity-driven reactions are much simpler than that of Herceptin randomly labeled with **87**.

The results of both the SDS-PAGE and HPLC analysis of the proximity-driven bioconjugation of Herceptin by the three SpA-ZZ-2Lys variants support the same conclusion. Fluorophores can be transferred from the lysines of all three 2Lys variants of the ZZ domain of SpA to Herceptin. Specific lysines of Herceptin involved could potentially have been identified using peptide mapping, but this was not performed.

4-4. Conclusions and future directions

We found that Protein A from *S. aureus* can be used to covalently label Herceptin with fluorophores via a proximity-driven reaction. To achieve this, the lysines of SpA, or simplified variants, are randomly labeled with fluorophores that include a linker containing a labile ester bond. The close proximity of lysines of Herceptin when SpA binds to Herceptin drives the transfer of the fluorophores by acylating lysine amines. This system could in theory be used to generate more homogenous antibody drug conjugates, but improvements are necessary to make this approach practical.

First, the selectivity of the system needs to be further explored. Here, a single mass spectroscopy-based peptide sequencing experiment was performed using native SpA as the transfer agent. This experiment would need to be repeated to generate more conclusive and comprehensive results, and similar experiments comparing the selectivity of transfer from each of the simplified SpA variants would also be beneficial. Ideally, peptide sequencing experiments would be performed in tandem with SDS-PAGE analysis to provide both the sequencing data and the visual confirmation using fluorescent gels. These results would be instructive as to which variant(s) provide the most desirable labeling pattern (degree of labeling and label location) and could provide information on the yield of the transfer. Both the SDS-PAGE and HPLC analysis are useful, but peptide sequencing is likely to provide the most valuable information.

Additionally, the affinity of simplified variants of SpA for IgG should be investigated. It is possible that the mutations made to these variants could have affected selectivity and affinity of these mutants for IgG as compared to SpA or the Z domain.[76] Fluorescence

polarization assays might allow quantification of binding of these SpA variants to IgG. Structural studies using X-ray crystallography or NMR spectroscopy could also be used to explore the interactions of these proteins.

The yield of the proximity-driven transfer reaction needs to be improved. This might be achieved by increasing the electrophilicity of the ester of **85** by adding substitutions to the adjacent aromatic ring (Figure 4-17). These probes have been synthesized by Dr. Chamani Perera but were not evaluated. Linker length and hydrophobicity could also be optimized. HPLC analysis of the transfer could be used to compare the relative yields of the transfer reaction to optimize these probes. Transfer yield might also be increased by further optimizing the SpA variants. The results of the peptide sequencing experiments might identify specific lysines involved in the proximity-driven transfer reaction and lead to better designed SpA variants. Here, we demonstrated proof-of-concept that this method for controlling the sites of lysine modification of antibodies is possible, but additional studies are needed to make it practical.

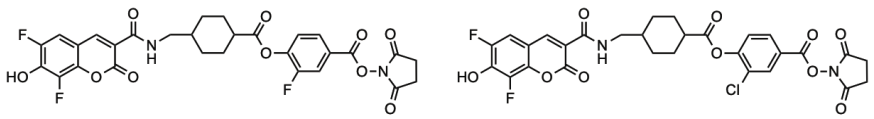

Figure 4-17. Structures of analogues of **85** with esters of increased electrophilicity.

4-5. Experimental

4-5-1. General experimental section

Chemical reagents were purchased from Acros, Aldrich, Alfa Aesar, EMD Biosciences, or TCI America, and were used without further purification. Solvents were from Aldrich or Fisher Scientific. All compounds were synthesized by Dr. Chamani Perera and provided with >90% purity based on analytical HPLC. Column chromatography

employed Silica Gel (SiliCycle, 40-63 μm). Preparative HPLC employed an Agilent 1200 Series preparative pump / gradient extension with a Hamilton PRP-1 (polystyrene-divinylbenzene) reverse-phase preparative column (10-12 μm particle size, 21.5 mm x 25 cm) with a flow rate of 25.0 mL/min. HPLC fractions containing water were dried using a Labconco FreeZone 4.5 lyophilizer. Compounds containing basic amines were isolated as TFA salts. Analytical HPLC traces were acquired using an Agilent 1220 Series binary pump and with diode-array detection at 254 nm. Chromatograms were acquired at room temperature and employed a gradient elution of H_2O:CH_3CN (90:10 to 0:100) with added TFA (0.1%) over 20 min and a 100% CH_3CN wash for an additional 5 min. Purity was determined by integration of the chromatogram. Low-resolution mass spectra (LRMS) were obtained using a Waters Micromass ZQ instrument with ESI+ or ESI-. Peaks are reported as *m/z*. Nuclear magnetic resonance (NMR) spectra were recorded on either a 400 MHz or 500 MHz Bruker Avance spectrometer with a dual carbon/proton cryoprobe. NMRs were recorded in deuterated chloroform or dimethyl sulfoxide. Chemical shifts are reported in parts per million (ppm) and are referenced to the center line of the solvent. Coupling constants are given in Hertz (Hz). The spin multiplicities are reported as s = singlet, d = doublet, t = triplet, q = quartet, dd = doublet of doublet td = doublet of triplet and m = multiplet.

4-5-2. Synthetic procedures and compound characterization data

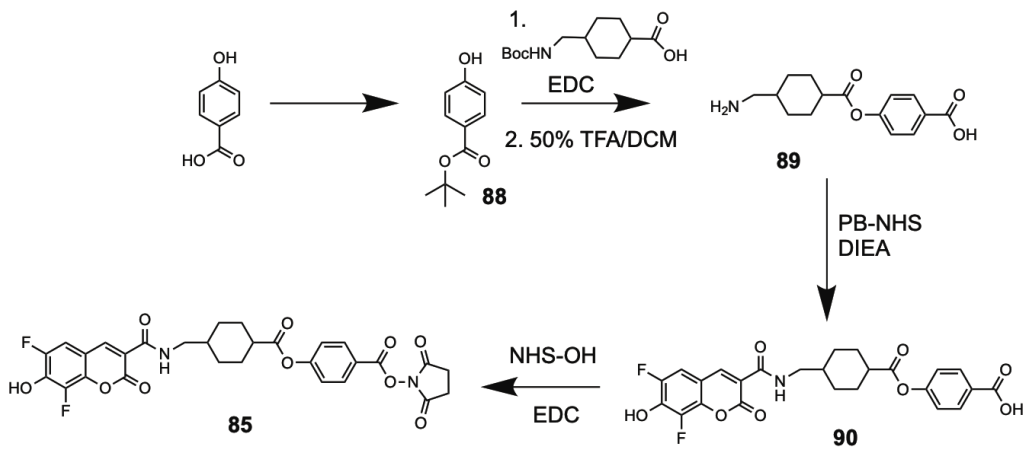

Scheme 1. Synthesis of **85**.

tert-Butyl 4-hydroxybenzoate (88). To a solution of 4-hydroxybenzanoic acid (1 g, 7.2 mmol) in THF (25 mL) was added *t*-butanol (24 mL), DCC (860 mg, 4 mmol) and DAMP (24 mg, 0.2 mmol) and stirred for 6 h. The solvent was removed and purification via flash chromatography provided **88** as a colorless oil (480 mg, 48% yield) ^{1}H NMR (400 MHz; acetone-d_6) δ, 6.9 (d, *J* = 7.1 Hz, 2H), 6.6 (d, *J* = 7.1 Hz, 1H), 3.7 (s, 2H), 1.4 (s, 9H). LRMS (ESI +) *m/z* calcd for $C_{11}H_{14}O_3$ $[M+H]^+$: 195.2, found: 195.3.

4-[4-(aminomethyl)cyclohexanecarbonyl]oxybenzoic acid (89). To a solution of **88** (200 mg, 1.03 mmol) in CH_2Cl_2 (20 mL) was added 4-[[(tert-Butoxycarbonyl)amino]methyl]cyclohexanecarboxylic acid (397 mg, 1.5 mmol) and EDC (464 mg, 2.06 mmol) and the reaction was stirred for 16 h at room temperature. The solvent was removed in *in vacuo* and the resulting crude product was directly purified using flash chromatography (141 mg, 35% yield). ^{1}H NMR (400 MHz; acetone-d_6) δ, 6.9 (d, *J* = 7.1 Hz, 2H), 6.6 (d, *J* = 7.1 Hz, 1H), 2.88 (d, *J* = 7.2 Hz, 2H), 2.27 (m, 1H), 2.06 (m, 1H), 1.62 (m, 2H), 1.52 (m, 4H), 1.46 (s, 6H), 1.42 (s, 9H), 1.38 (m, 2H). LRMS (ESI +) *m/z* calcd for $C_{24}H_{35}NO_6$ $[M+H]^+$: 434.6, found: 434.4. The isolated product was stirred

in a solution of TFA/DCM (1:1) for 2 h to afford compound **89** and was used for the proceeding step without any further purification.

3-(((4-((4-carboxyphenoxy)carbonyl)cyclohexyl)methyl)carbamoyl)-6,8-difluoro-2-oxo-2*H*-chromen-7-olate (90). To a stirred solution of **89** (140 mg, 0.5 mmol) in dry DMF (5 mL) was added Pacific Blue-NHS (109 mg, 0.5 mmol) and DIEA (0.281 mL, 2.5 mmol) and left to stir for 16 h. The solvent was removed, and the resulting crude product was purified using flash chromatography to give 3 as a yellow solid (396 mg, 50% yield). Intermediate **90** was carried on to the next step without any further analysis.

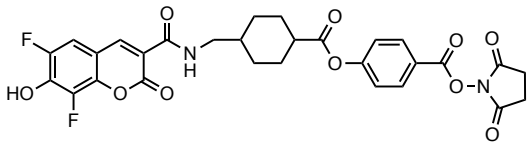

2,5-dioxopyrrolidin-1-yl 4-((4-((6,8-difluoro-7-hydroxy-2-oxo-2*H*-chromene-3-carboxamido)methyl)cyclohexane-1-carbonyl)oxy)benzoate (85). Intermediate **90** (30 mg, 0.06 mmol) was dissolved in dry DMF (3 mL) and added to EDC (23 mg. 0.12 mmol) and NHS-OH (13 mg, 0.12 mmol). The resulting solution was stirred for 4 h, solvent removed and purified by preparative HPLC to give **85** (15 mg, 42% yield) as a yellow solid. ^{1}H NMR (500 MHz, DMSO-d_6) δ 8.78 (s, 1H), 8.64 (t, *J* = 6.0 Hz, 1H), 8.19 – 8.13 (m, 2H), 7.75 (d, *J* = 10.4 Hz, 1H), 7.45 – 7.39 (m, 2H), 3.23 (t, *J* = 6.4 Hz, 2H), 2.90 (s, 3H), 2.65 – 2.56 (m, 1H), 2.13 (d, *J* = 11.4 Hz, 2H), 1.84 (dd, *J* = 13.6, 3.6 Hz, 2H), 1.62 – 1.53 (m, 0H), 1.50 – 1.41 (m, 2H), 1.10 (qd, *J* = 13.1, 3.5 Hz, 2H). ^{13}C NMR (126 MHz, DMSO-d_6) δ 173.22, 170.28, 161.17, 161.12, 159.77, 155.96, 149.94 (d, *J* = 3.4 Hz), 148.02 (d), 147.08, 131.87, 123.15, 121.85, 116.24, 110.53, 110.37, 109.33 (d, *J* = 9.8

Hz), 44.85, 42.33, 36.77, 29.08, 27.88, 25.53. HRMS (ESI-) m/z calcd for $C_{29}H_{24}F_2N_2O_{10}$ $[M-H]^-$: 597.1321, found: 597.1295.

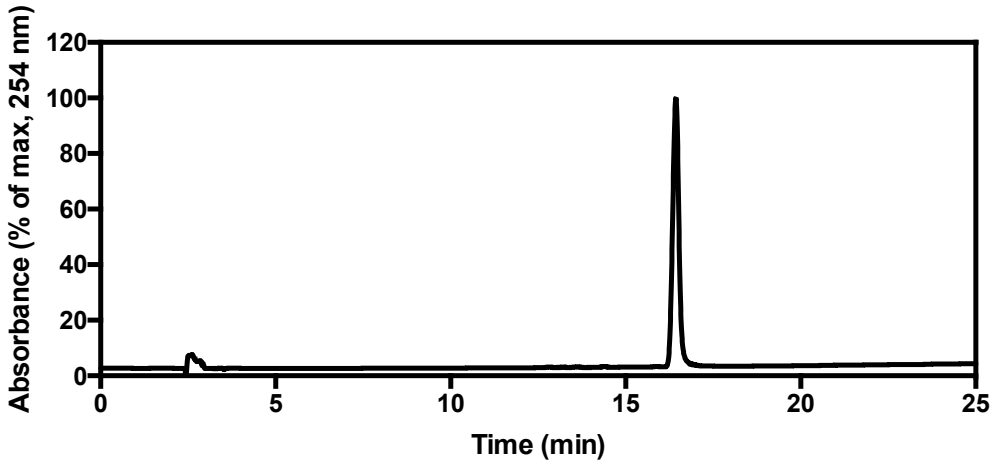

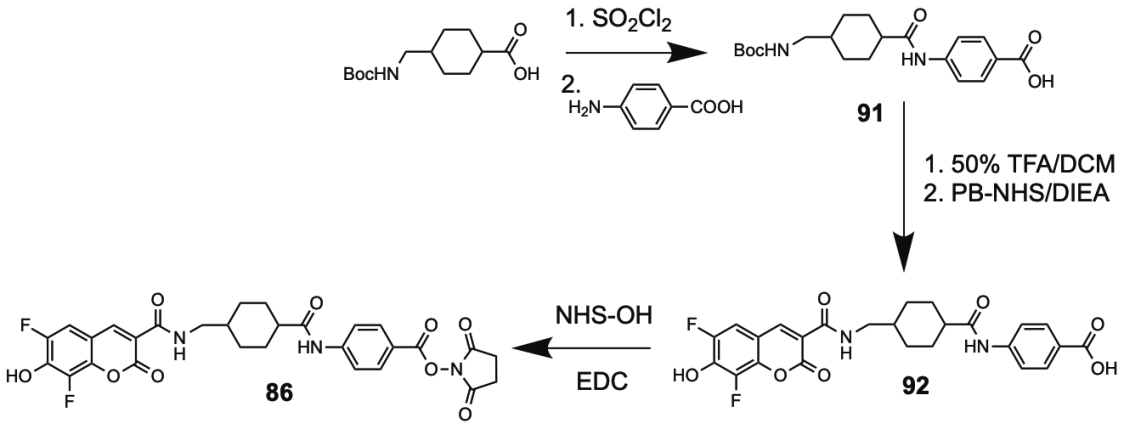

Scheme 3. Synthesis of **86**.

4-(4-(((*tert*-butoxycarbonyl)amino)methyl)cyclohexane-1-carboxamido)benzoic acid (91). Boc-methylamino-cyclohexanecarboxylic acid (0.5 g, 1.9 mmol) was dissolved in THF (10 mL) and $SOCl_2$ (5 mL) was added dropwise over 1 h. The resulting solution was stirred for 2 h, solvent removed and 4-aminobenzolic acid (266 mg, 1.9 mmol) in THF (10 mL) was added. The resulting solution was stirred for 16 h, solvent removed, and purified by flash chromatography to afford **91** as a white solid (460 mg, 65% yield). ^{1}H

NMR (400 MHz; acetone-d_6) δ, 6.9 (d, J = 7.3 Hz, 2H), 6.6 (d, J = 7.3 Hz, 1H), 2.88 (d, J = 7.1 Hz, 2H), 2.27 (m, 1H), 2.06 (m, 1H), 1.62 (m, 2H), 1.52 (m, 4H), 1.42, (s, 9H), 1.38 (m, 2H). LRMS (ESI+) *m/z* calcd for $C_{20}H_{26}N_2O_6$ $[M+H]^+$: 377.5, found: 377.5.

3-(((4-((4-carboxyphenyl)carbamoyl)cyclohexyl)methyl)carbamoyl)-6,8-difluoro-2-oxo-2*H*-chromen-7-olate (92). The same general procedure as that used to synthesize compound **90** was used to produce **92** as a yellow solid (30 mg, 35% yield). Carried onto the next step without further purification. LRMS (ESI+) *m/z* calcd for $C_{25}H_{22}N_2O_7$ $[M+H]^+$: 500.5, found: 500.4.

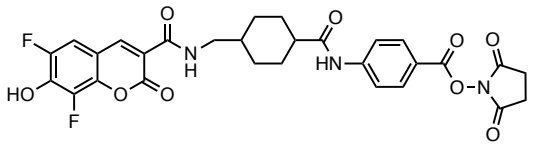

2,5-dioxopyrrolidin-1-yl 4-(4-((6,8-difluoro-7-hydroxy-2-oxo-2*H*-chromene-3-carboxamido)methyl)cyclohexane-1-carboxamido)benzoate (86) The same general procedure as that used to synthesize **85** was used to generate **86** as a yellow solid (10 mg, 42% yield). ^{1}H NMR (500 MHz, DMSO-d_6) δ 10.39 (s, 1H), 8.78 (s, 1H), 8.63 (t, J = 6.1 Hz, 1H), 8.03 (d, J = 8.7 Hz, 2H), 7.86 (d, J = 8.9 Hz, 2H), 7.75 (d, J = 10.4 Hz, 1H), 3.23 (t, J = 6.4 Hz, 2H), 2.88 (s, 4H), 2.40 – 2.32 (m, 1H), 1.94 – 1.87 (m, 2H), 1.86 – 1.79 (m, 2H), 1.49 – 1.36 (m, 2H), 1.10 – 1.00 (m, 2H). ^{13}C NMR (126 MHz, DMSO-d_6) δ 206.50, 175.10, 170.45, 161.23, 161.13, 159.77, 147.07, 145.75, 131.41, 118.80, 117.94, 116.35, 110.55, 110.40, 109.38, 44.99, 44.95, 36.83, 29.37, 28.46, 25.50. HRMS (ESI-) m/z calcd for $C_{29}H_{25}F_2N_3O_9$ $[M-H]^-$: 596.1481, found: 596.1484.

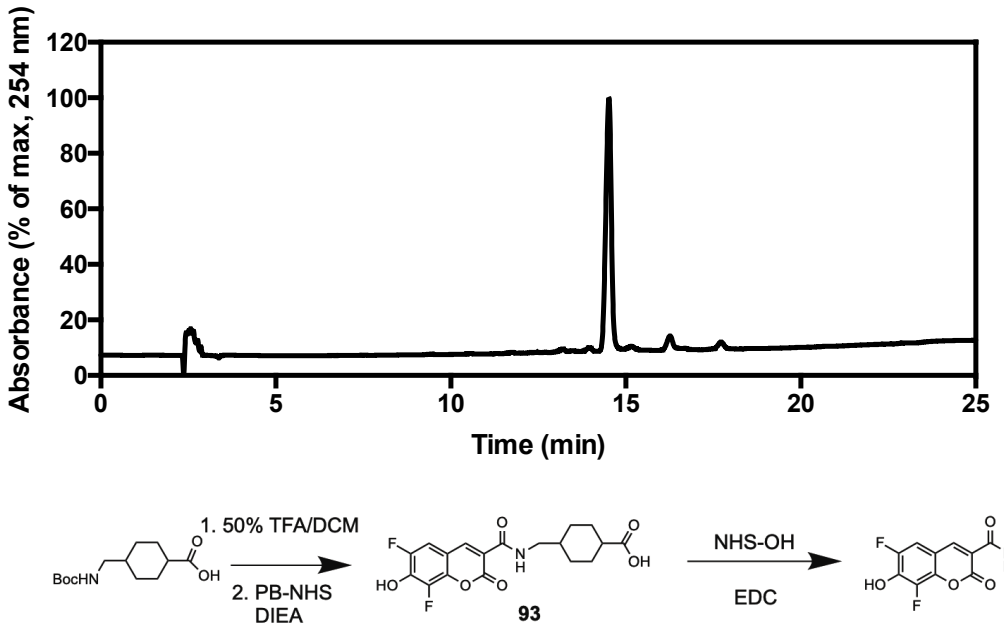

Scheme 3. Synthesis of **87**.

3-(((4-carboxycyclohexyl)methyl)carbamoyl)-6,8-difluoro-2-oxo-2*H*-chromen-7-olate (93). The same procedure used to synthesize compound **92** was used to generate **93** as a yellow solid (60 mg, 42% yield). **93** was carried onto the next step without further characterization. LRMS (ESI+) *m/z* calcd for $C_{18}H_{17}F_2NO_6$ $[M+H]^+$: 382.3, found 382.4.

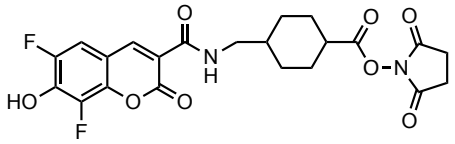

2,5-dioxopyrrolidin-1-yl 4-((6,8-difluoro-7-hydroxy-2-oxo-2*H*-chromene-3-carboxamido)methyl)cyclohexane-1-carboxylate (87). The same procedure used to synthesize compound **86** was used to generate **87** as a yellow solid (15 mg, 40% yield). ^{1}H NMR (500 MHz, DMSO-d_6) δ 8.76 (s, 1H), 8.62 (t, *J* = 6.0 Hz, 1H), 7.73 (d, *J* = 10.5 Hz, 1H), 3.21 (t, *J* = 6.4 Hz, 2H), 2.80 (s, 4H), 2.74 – 2.64 (m, 1H), 2.03 (dd, *J* = 13.6, 3.6 Hz, 2H), 1.81 (dd, 2H), 1.55 (dtd, *J* = 14.8, 11.0, 9.4, 5.3 Hz, 1H), 1.43 (qd, *J* = 13.0, 3.5

Hz, 2H), 1.10 (qd, *J* = 13.1, 3.6 Hz, 2H). ^{13}C NMR (126 MHz, DMSO-d_6) δ 170.93, 170.24, 161.23, 159.79, 147.07, 110.50, 110.33, 44.72, 36.50, 30.68, 28.74, 27.97, 25.43. HRMS (ESI-) m/z calcd for $C_{22}H_{20}F_2N_2O_8$ [M-H]$^-$: 477.1109, found: 477.1119.

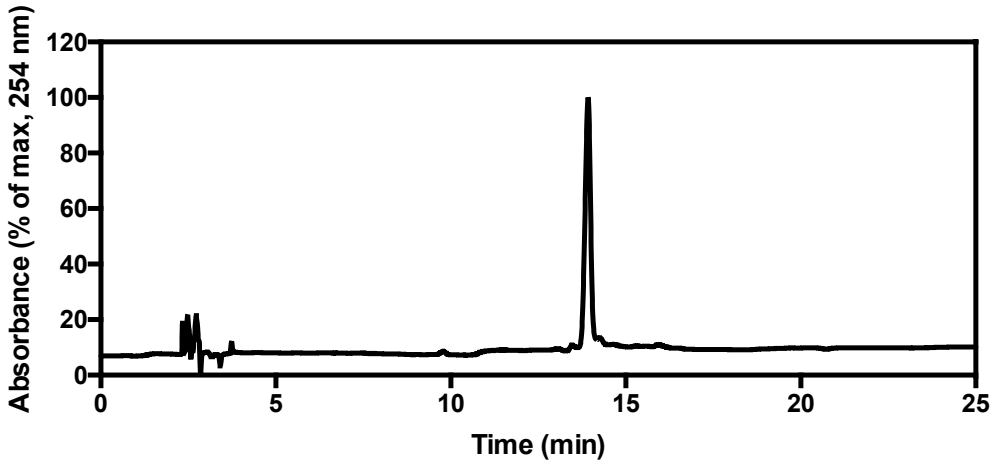

4-5-3. Biological assays and protocols

Labeling of proteins with NHS esters: Protein A (recombinant, Thermo 77673; from *Staphylococcus aureus*, Sigma P6031) was provided as a lyophilized powder. It was reconstituted in sterile PBS (pH 7.4) and the concentration was determined by absorbance at 280 nm using a Nanodrop 1000 and the molecular weight (44,600 Da for recombinant, 42,000 Da for product from *Staph*) and extinction coefficient (ε_{280} = 7,359 $M^{-1}cm^{-1}$) of SpA. Simplified variants of SpA were directly labeled after being dialyzed into PBS and concentrated. Human IgG was purchased as a lyophilized powder (Sigma, I4506) and was also reconstituted in sterile PBS and the concentration determined using the presets for IgG in a Nanodrop 1000 ($\varepsilon_{1\%\ (10\ mg/mL)}$ + 13.7 $Lg^{-1}cm^{-1}$). Herceptin was provided as a lyophilized powder mixed 1:1 with stabilizers (α,α-trehalose dihydrate, *L*-histidine, and polysorbate 20). After Herceptin was reconstituted in sterile PBS it was passed through a spin column packed with Sephadex G25 to remove the stabilizers.

Briefly, Sephadex G-25 resin (Superfine, Sigma, S5772) was suspended in PBS (pH 7.4). The resulting slurry (950 µL) was added to a minispin column (USA Scientific, 1415-0600) and centrifuged (16,000 x g, 20 s) to remove the buffer and pack the resin. The antibody solution (no more than 75 µL per column) was loaded onto the packed resin and centrifuged (16,000 x g, 30 s) to separate the protein from the stabilizers. The concentration of Herceptin was then determined as described for IgG.

Similar procedures were used to label all proteins with all NHS esters. Protein in PBS (100 µM, 25-100 µL) was aliquoted into a 1.5 mL microcentrifuge tube. $NaHCO_3$ was added (1 M, 2.5-10 µL) to achieve a final concentration of 0.1 M. NHS esters were added as DMSO stocks (typically 10 mM, various volumes) to achieve 5-10x excess over the protein concentration. Solutions were incubated for 0.5 h (37 °C) in a Big Shot III Hybridization Oven. To purify the conjugates, Sephadex G25 resin was packed into columns as described above. The protein solution was loaded onto the packed resin (no more than 75 µL per column) and centrifuged (16,000 x g, 30 s) to separate the protein from the unconjugated small molecules.

After purification, the degree of labeling (DOL) of each conjugate was determined. This was done by comparing the absorbance at 280 nm and 425 nm (IgG 280 nm $\varepsilon_{1\%\ (10\ mg/mL)}$ = 13.7 $Lg^{-1}cm^{-1}$, Pacific Blue 425 nm ε = 29,500 $M^{-1}cm^{-1}$), as measured with a Nanodrop 1000 Spectrophotometer. The low extinction coefficient of the simplified variants of SpA made concentration and DOL measurements unreliable, but estimated values were kept consistent throughout individual experiments.

Proximity driven bioconjugation between native SpA and antibody: After SpA was labeled as described above in *Labeling of proteins with NHS esters*, it was incubated overnight with IgG or Herceptin. Briefly, 20 µL reactions were set up in 1.5 mL microcentrifuge tube. Each reaction contained labeled SpA (1, 5, or 25 µM, labeled with **85** or **86**) and IgG or Herceptin (5 µM) diluted with PBS. A tube containing Herceptin (5 µM) or IgG labeled with **87** as a control for random labeling was also prepared, along with tubes of labeled SpA (5 µM). The tubes were incubated overnight (~16 h) in a Big Shot III Hybridization Oven at 37 °C. The next morning, the samples were diluted 1:1 with Laemmli Sample Buffer (2x, BIO RAD, 1610737) containing β-mercaptoethanol (βME, 50 µL into 950 µL sample buffer, Sigma, 63689). Samples were boiled for 5 min and then each sample (25 µL) was loaded onto a Novex NuPAGE 4-12% Bis-Tris Protein Gel (Invitrogen, NP0335). Smart Multi Color Pre-Stained Protein Standard (5 µL, GenScript, M00443) was used as the ladder. Gels were run for 1 h at 180 V and then transferred to DI water and imaged on a UV Transilluminator (VWR Scientific, Model VWR LM-20E). Gels were then stained using InstantBlue Coomassie Protein Stain (expedeon, ISB1L) at room temperature with gentle shaking for at least 1 h. Gels were rinsed with DI water and then imaged using a Visi-White Transilluminator (VWR Scientific, Model VWR TW-26).

Analysis by tryptic digestion followed by mass spectroscopy-based protein sequencing: Tryptic digestion and analysis were performed by Dr. Nadya Galeva of the KU Mass Spectrometry and Analytical Proteomic Laboratory. The gel shown in Figure 4-7 was submitted to Dr. Galeva, who cut out the bands corresponding to the heavy chain of unmodified Herceptin and Herceptin that had been incubated with SpA-**85**. The gel

slices were destained by incubation in 50% acetonitrile/50 mM ammonium bicarbonate for 0.5 h at room temperature. The destaining solution was removed and replaced with 100% acetonitrile to dehydrate the gels. This was incubated for ~5 min or until the gel turned opaque. The open tubes were then incubated at 37 °C for 15 min to dry completely. Dithiothreitol (DTT, 10 mM) in ammonium bicarbonate (0.2 M) was then added and incubated at 37 °C for 0.5 min to reduce the protein. Iodoacetamide was added (final concentration = 20 mM) and samples were incubated for a further 0.5 h at room temperature to alkylate cysteine residues. The gel was then washed twice with DI water and dehydrated by incubation with acetonitrile at room temperature for 5 min followed by 37 °C for 15 min to dry completely. Trypsin (Promega) was added to the samples, which were incubated at 37 °C overnight. Samples were cooled in a freezer for 5 min and then sonicated for 10 min to allow peptides to diffuse out of the gel. Samples were stored at 4 °C prior to analysis by MS/MS sequencing. All MS/MS samples were analyzed using Mascot software (Matrix Science, London, UK; version 2.5.1). Mascot was used to search the SwissProt_2015_01 database (547357 entries) assuming digestion by trypsin. Mascot was searched with a fragment ion mass tolerance of 0.80 Da and a parent ion tolerance of 20 PPM. Carbamidomethyl cysteine was specified in Mascot as a fixed modification. Oxidation of methionine and modification of lysine by transferred fluorophore was specified in Mascot as a variable modification. Scaffold (version 4.8.9, Proteome Software Inc., Portland, OR) was used to validate MS/MS based peptide and protein identifications.

Plasmid propagation: Briefly, DH5α chemically competent *E. coli* (a gift from Dr. Phillip Gao) were transfected with the reconstituted DNA (1 µL, more if concentration was less than ~75 ng/µL) using a traditional heat shock method. An aliquot of bacteria (50 µL) for each plasmid were thawed at room temperature from -80 °C. DNA was added and the 1.5 mL microcentrifuge containing the bacteria, and the tube was flicked to mix. The bacteria were incubated on ice for 0.5 h. The bacteria were then heat shocked by being held in a water bath at 42 °C for 45 s and allowed to recover on ice for 2 min. Pre-warmed (37 °C) LB media (1 mL) was then gently added to each tube, and the cells were incubated at 37 °C with shaking at 190 rpm for 1 h. Bacteria containing each plasmid (150 µL) was then spread onto an LB-agar plate containing 100 µg/mL ampicillin or 50 µg/mL kanamycin, allowed to dry for 5 min right-side-up at room temperature, and then transferred upside to a 37 °C incubator overnight. The next morning, the plates were transferred to a 4 °C refrigerator until they were needed to inoculate liquid cultures. A sterile toothpick or p200 pipet tip was used to transfer a single colony of transfected bacteria into 5 mL of sterile LB media. This was incubated overnight (~16 h) at 37 °C with shaking at 190 rpm until cloudy. A QIAprep Spin Miniprep Kit (QIAGEN, 27104) was used according to the provided protocol to purify the plasmids. Plasmid concentration was determined using the nucleic acid module on a Nanodrop 1000. Confirmation of plasmid was done using standard double restriction digest followed by electrophoresis.

DNA gel electrophoresis: A 1% agarose gel was made by mixing agarose (0.75 g, Sigma, A9539) with homemade Tris base, acetic acid, and EDTA (TAE) buffer (75 mL), heating to just boiling, and pouring into a mold with a comb to form wells. After the gel

set, each sample was diluted with EZ-Vision One DNA Dye as Loading Buffer (Amresco, N472-KIT) and loaded into the gel, along with a 1 kb DNA Ladder (New England BioLabs, N3232S) that was also diluted with EZ-Vision. Gels were run for 1 h at 70 V and visualized using a UV Transilluminator (VWR Scientific, Model VWR LM-20E).

Generation of SpA-ZZ-12Lys and SpA-ZZ-6Lys genes: Both genes were synthesized by GenScript as custom gene inserts containing EcoRI and KpnI restriction sites in the vector pUC57 provided as lyophilized plasmid. The sequence of the SpA-ZZ-12Lys gene was based off of that for Z domain of Protein A.[76] The sequence was optimized for expression in *E. coli* by GenScript using their OptimumGene Codon Optimization Analysis. The final DNA and amino acid sequence of both genes can be found in Appendix C. The sequence of the SpA-ZZ-6Lys gene was based on that of the 12Lys variant, except three of the lysines were mutated to arginines, as shown in Figure 4-8. Upon arrival, plasmids were propagated as described in *Plasmid propagation*.

After the genes were ordered, it was realized that each contained an undesired secretion signal on the N terminus of the protein. These were removed using site-directed mutagenesis. The primers were ordered from Integrated DNA Technologies through their Custom DNA oligos service and were provided lyophilized. The forward primer was 5'-gctacggaattcgcgcagcatgatgaagcg-3' and the reverse primer was 5'-cggagtctcgagtcattaacagccaccatccac-3', where blue coloring indicates the primer end clamp, red the restriction sites (EcoRI and XhoI), and green differences in sequence between the 12Lys and 6Lys variants (bases shown correspond to the sequence of 12Lys). Primers were reconstituted at 100 µM in sterile water and then diluted to 10 µM

for use as primers for polymerase chain reaction (PCR). PCR was performed using *Taq* DNA Polymerase (New England BioLabs, M0273S) using the standard protocol provided with the enzyme. Briefly, the provided Standard *Taq* buffer (1x), dNTPs (200 µM), forward primer (0.5 µM), reverse primer (0.5 µM), template plasmid (1 ng), and *Taq* DNA polymerase (1.25 units) were combined in a PCR tube on ice with enough sterile water to bring the total volume to 50 µL (listed concentrations are final). The PCR tube was then transferred to a pre-heated Biometra T Gradient Thermocycler with a heated lid. The reaction was cycled as described in the table below and then 10 µL of each reaction was analyzed by gel electrophoresis as described in *DNA gel electrophoresis*.

Step	°C	Time (s)	
1	95	30	
2	95	30	Cycle 30x
3	65	20	
4	68	60	
5	68	5 min	
6	4	hold	

The remainder of each successful PCR reaction was purified using a QIAquick Gel Extraction Kit (QIAGEN, 28704) and then digested at 37 °C overnight using EcoRI-HF (New England BioLabs, R3101) and XhoI (New England BioLabs, R0146S). At the same time, plasmid pBP4-3 was digested using the same restriction enzymes. The next day, the DNA was purified using a QIAquick Gel Extraction Kit. The purified PCR product (insert) and cut pBP4-3 vector were ligated using T4 DNA Ligase (New England BioLabs, M0202S). 20 µL reactions were set up in 1.5 mL microcentrifuge tube. Each reaction contained the provided T4 DNA Ligase buffer, 50 ng vector, 25 or 50 ng insert, 1 µL T4

DNA Ligase, and enough sterile water to dilute the solution to 20 µL. Reactions were incubated in a water bath at 16 °C overnight. The next day, the ligation reaction (2-4 µL) was used to transfect DH5α *E. coli* to propagate the plasmids, as described in *Plasmid propagation*. Ligation into pBP4-3 using the above restriction sites generated genes with a His tag at the 3' end. Plasmids were submitted to ACGT, Inc for Single Pass DNA Sequencing using the universal T7 primer (5'-TAA TAC GAC TCA CTA TAG GG-3'). Sequencing results were compared to the expected using Sequencher DNA Sequencing Software. Confirmed plasmids were used to transfect BLE21(DE3) *E. coli* (a gift from Dr. Phillip Gao) for protein production.

Overexpression of SpA-ZZ-12Lys and SpA-ZZ-6Lys in *E. coli*: LB media (2L, 2x 1 L, each in a 2 L flask) was prepared and autoclaved and then cooled to room temperature. The same day, LB (10 mL) was inoculated with a colony of BLE21(DE3) *E. coli* transfected with each plasmid. These cultures were incubated overnight at 37 °C with shaking at 190 rpm. The next morning, ampicillin (100 µg/mL final) and a 10 mL culture were added to each of the 1 L flasks of LB. The cultures were grown at 37 °C with shaking at 190 rpm for about 4 h until the OD_{600} reached ~0.4. The cultures were cooled to 17 °C with continued shaking and then induced with 0.1 mM IPTG. Cultures were incubated at 17 °C overnight (~16 h). The next morning, cells were pelleted by centrifugation at 4,000 rpm for 10 min at 4 °C and resuspended in Lysis Buffer A (100 mM NaH_2PO_4, 10 mM Tris, 8 M urea, pH 8). Cells were then frozen at -80 °C for 45 min to begin lysing the cells. After thawing in cool water, the solution was vortexed until no longer viscous. A small aliquot of this solution was saved for SDS-PAGE analysis. The solution was then pelleted by

centrifugation at 19,500 rpm for 30 min at 4 °C. A small aliquot of both the soluble and insoluble fraction was saved for SDS-PAGE. The soluble fraction was then added to HisPur Ni-NTA Resin (Thermo, 88221) in an Econo-Column Chromatography Column (BIO RAD). The column and slurry were gently shaken at 17 °C for 1 h. The column was then drained and rinsed with Lysis Buffer A and Buffer B (Buffer A at pH 6.3) and the protein was eluted with Buffer C (A at pH 5.9) and Buffer D (A at pH 4.5). Absorbance spectroscopy with a Nanodrop 1000 was used to determine which fractions contained protein. Fractions of interest were analyzed by SDS-PAGE as described in *Proximity driven bioconjugation between native SpA and antibody*, except without the addition of βME or visualization on a UV transilluminator. Fractions containing the desired protein were pooled and concentrated to about 0.5 mL using Amicon Ultra Centrifugal Filters (MWCO 10 kDa, Millipore, UFC801024) at 4 °C. The protein was then dialyzed with PBS using Slide-A-Lyzer Dialysis Cassettes (MWCO 10 kDa, Thermo, P166384). 400 mL of PBS was used and changed 3x. A Nanodrop 1000 was used to determine the concentration of each protein (MW 16,174 Da, ε = 2,980 $M^{-1}cm^{-1}$).

Papain digestion of IgG: Papain digestion was used to generate Fab and Fc fragments of antibodies. Briefly, papain (Sigma, P4762) was activated by diluting 1 µL of the enzyme solution into 9 µL of papain buffer (1 mM EDTA, 50 mM phosphate buffer pH 7, 10 mM cysteine) and incubating at 37 °C for 10 min. This activated papain solution (1 µL, 2% w/w of the antibody) was then added to 20 µL of each proximity driven bioconjugation reaction mixture (typically containing 5 µM IgG and 25 µM of a SpA variant), mixed, and incubated at 37 °C for 2 h before analysis by SDS-PAGE as described above.

Clean-up of PDB reactions with SulfoLink Resin: In order to analyze the PDB reactions by HPLC, Herceptin needed to be separated from the SpA variants. The SpA variants were designed to each contain a single cysteine residue, so SulfoLink Coupling Resin (Thermo, 20401) was used to remove the SpA variants. PDB reactions were carried out as described above and cleaned up after overnight incubation at 37 °C. SulfoLink was shaken to resuspend the beads in the provided solution. 60 µL of this slurry for each reaction to be cleaned was transferred to a Pierce Micro-Spin Column (Thermo, 89879). The columns were centrifuged (16,000 x g, 1 min) to dry the resin, and then the resin was washed with 200 µL PBS twice. 25 µL of each PDB reaction was then added to the dry resin and incubated in a Big Shot III Hybridization Oven at 37 °C for 0.5 h. The columns were then centrifuged to elute Herceptin.

Tryptic digest of Herceptin for HPLC analysis: The Herceptin solution to be digested was first denatured and reduced. To do this, the antibody solution was mixed with an equal volume of a solution of guanidine hydrochloride (12 M, GDN) with Tris (100 mM). The GDN is not soluble at this concentration at room temperature, so this solution was heated until completely dissolved before adding to the antibody solution. DTT was then added to a final concentration of 4 mM. This was incubated at about 75 °C for 0.5 h. While this was incubating, trypsin (lyophilized, sequencing grade, Promega, PRV5111) was activated by dissolving it in the provided resuspension solution (50 mM acetic acid) to a concentration of 0.1 mg/mL and then incubating it at 30 °C for 0.5 h. The antibody solution was then mixed with 5x its volume of 50 mM Tris, 2 mM $CaCl_2$ to reduce the concentration

of GDN from 6 M to 1 M to prevent denaturing the trypsin. Trypsin (1:50 w/w of the Herceptin) was then added to the antibody solution and incubated at 37 °C for 1 h. Digested samples were stored on ice until ready for analysis.

HPLC analysis of digested Herceptin: After Herceptin was digested with trypsin, it was analyzed using HPLC. Analysis was performed using an Agilent 1100 Series quaternary pump and a Hamilton PRP-1 (polystyrene-divinylbenzene) reverse phase analytical column (7 µm particle size, 4 mm x 25 cm) with fluorescence detection with emission at 450 nm and excitation at either 370 (Figure 4-14) or 405 (Figure 4-12) nm. The gradient used was H_2O:CH_3CN with added TFA (0.1%) 90:10 to 60:40 over 30 min and then 60:40 to 0:100 over 5 min and a 100% CH_3CN wash for 5 min. The excitation wavelength was switched from 405 to 370 nm to account for the shift in the absorbance maximum of Pacific Blue in the presence of 0.1% TFA.

Generation of SpA-ZZ-2Lys variant genes: The plasmid for SpA-ZZ-6Lys was used as the template for mutagenesis to generate all three 2Lys variants. The site-directed mutagenesis method based off of the QuikChange Site-Directed Mutagenesis Kits published by Zheng *et. al.*[78] was used. Though the original sequences of the two Z domains of SpA-ZZ-6Lys were nearly identical, the optimization done by GenScript caused the two sequences to be different enough that a separate set of primers was needed to mutate each lysine (6 sets were needed instead of just 3 sets, Figure 4-16). These primer sets were designed to mutate each lysine to an arginine and were ordered

from Integrated DNA Technologies and are listed below. Point mutations used to mutate lysines to arginines are indicated in red.

SpA-ZZ-6Lys Sequence

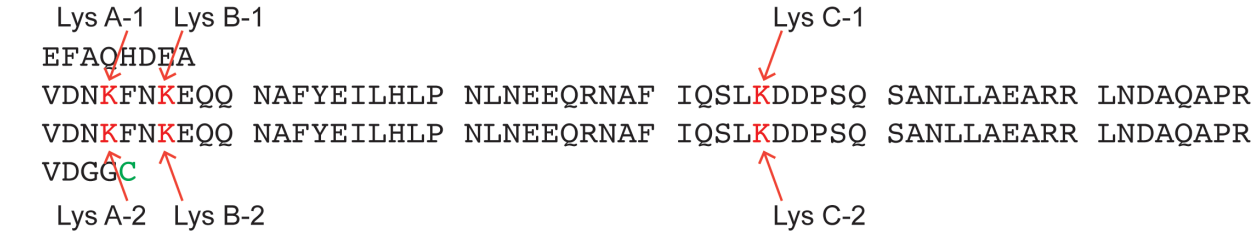

Figure 4-18. Sequence of SpA-ZZ-6Lys with each lysine named.

Lysine	Forward Primer	Reverse Primer
A-1	5′-GTG GAT AAC CGA TTC AAC AAA GAA CAG CAA AAC-3′	5′-C TTT GTT GAA TCG GTT ATC CAC CGC TTC ATC-3′
A-2	5′-GTT GAC AAT CGA TTT AAT AAA GAA CAA CAA AAC-3′	5′-C TTT ATT AAA TCG ATT GTC AAC ACG CGG AGC-3′
B-1	5′-C CGA TTC AAC CGA GAA CAG CAA AAC GCC TTC-3′	5′-G CTG TTC TCG GTT GAA TCG GTT ATC CAC-3′
B-2	5′-C AAT CGA TTT AAT CGA GAA CAA CAA AAC GCG-3′	5′-G TTG TTC TCG ATT AAA TCG ATT GTC AAC ACG -3′
C-1	5′-CAA AGC CTG CGA GAT GAC CCG AGC CAG TCT GC-3′	5′-CGG GTC ATC TCG CAG GCT TTG GAT AAA TGC-3′
C-2	5′-CAG TCT CTG CGA GAC GAC CCG AGT CAG TCC GC-3′	5′-CGG GTC GTC TCG CAG AGA CTG AAT GAA CGC-3′

Attempts were made to perform PCR using multiple sets of primers at the same time, but this was mostly unsuccessful, so most mutations were done sequentially. PCR was performed using Phusion High-Fidelity DNA Polymerase (New England BioLabs, M0530S) following the instructions provided on the product insert. Reactions components were prepared in PCR tubes on ice, mixed, and transferred to a pre-heated Biometra T Gradient Thermocycler with a heated lid. 5x Phusion HF Buffer, dNTPs (200 μM), forward primer (0.5 μM), reverse primer (0.5 μM), template plasmid (10 ng), and Phusion DNA polymerase (1 units) were combined in a PCR tube on ice with enough sterile water to bring the total volume to 50 μL (listed concentrations are final). DMSO (1.5 μL) was added

when reactions did not work on the first try. Tubes were cycled as indicated below, though Step 3 ranged from 65-70 °C.

Step	°C	Time (s)	
1	98	30	
2	98	10	Cycle 35x
3	67	10	
4	72	60	
5	72	5 min	
6	4	hold	

After cycling, each reaction (10 µL) was analyzed by gel electrophoresis as described above. Successful reactions were digested with DpNI (New England BioLabs, R0176S) to remove the methylated template DNA. To do this, 10x CutSmart Buffer (4 µL, New England BioLabs, B7204S) and DpNI (0.4 µL) were added to 40 µL of reaction mixture and incubated at 37 °C for 2 h. After digestion, this solution (5 µL) was used to transfect DH5α *E. coli* as described above. Inoculated plates that grew colonies were then used to inoculate liquid LB media to collect plasmids, as described above.

This general method was used to generate all three SpA-ZZ-2Lys variants, named A-C for the lysine residues each still contains. Plasmids were submitted to ACGT, Inc for Single Pass DNA Sequencing using the universal T7 primer (5'-TAA TAC GAC TCA CTA TAG GG-3'). Sequencing results were compared to the expected using Sequencher DNA Sequencing Software. Confirmed plasmids were used to transfect BLE21(DE3) *E. coli* (a gift from Dr. Phillip Gao) for protein production.

Overexpression of SpA-ZZ-2Lys Variants: LB media (200 mL) was prepared and autoclaved for each variant and then cooled to room temperature. The same day, 5 mL of LB was inoculated with a colony of BLE21(DE3) *E. coli* transfected with each plasmid. These cultures were incubated overnight at 37 °C with shaking at 190 rpm. The next morning, ampicillin (100 µg/mL final) and 2 mL out of the 5 mL culture were added to each of the 200 mL flasks of LB. The cultures were grown at 37 °C with shaking at 190 rpm for about 4 h until the OD_{600} reached ~0.4. The cultures were then induced with IPTG (0.4 mM) and incubated for a further 3 h. Cells were pelleted by centrifugation (4,000 rpm for 10 min at 4 °C), the supernatant was removed, and cell pellets were frozen at -80 °C overnight. Purification was done using buffers containing urea instead of guanidine hydrochloride (Gdn) because the Gdn method did not generate pure protein. The next morning, cell pellets were thawed in warm water and then resuspended in Buffer 1 (6 mL, 10 mM Tris, 100 mM NaH_2PO_4, 8 M urea, pH 8). Cells were vortexed to lyse and then centrifuged (12,500 rpm, 45 min at 4 °C). The supernatant was added to HisPur Ni-NTA Resin (Thermo, 88221) in a small Econo-Column Chromatography Column (BIO RAD). The column and slurry were gently shaken at 4 °C for 1 h. The column was then drained and rinsed with Buffer 1 and Buffer 2 (Buffer 1 at pH 6.3) and the protein was eluted with Buffer 3 (1 at pH 5.9) and Buffer 4 (1 at pH 4.5). Absorbance spectroscopy with a Nanodrop 1000 was used to determine which fractions contained protein. Fractions of interest were analyzed by SDS-PAGE as described in *Proximity driven bioconjugation between native SpA and antibody*, except without the addition of βME and visualization using a UV transilluminator. Fractions containing the desired protein were pooled and concentrated to about 0.5 mL using Amicon Ultra Centrifugal Filters (MWCO 10 kDa,

Millipore, UFC801024). The protein was then dialyzed with PBS using Slide-A-Lyzer Dialysis Cassettes (MWCO 10 kDa, Thermo, P166384). PBS (1 L) was used and changed 4x. A Nanodrop 1000 was used to determine the concentration of each protein (MW 16,174 Da, ε = 2,980 $M^{-1}cm^{-1}$).

PDB with SpA-ZZ-2Lys variants attached to SulfoLink: This method was used to simplify HPLC analysis of Herceptin labeled through PDB. First, each SpA-ZZ-2Lys variant was tethered to SulfoLink Coupling Resin (Thermo, 20401) through its single cysteine residue. This was done by agitating the SulfoLink until resuspended and then transferring 600 µL of the slurry to a 1.5 mL microcentrifuge tube. The SulfoLink was pelleted by centrifugation (14,000 rpm, 1 min) and then washed 3x with 600 µL 100 mM Tris, 10 mM EDTA. The SulfoLink was then resuspended in 600 µL of this buffer and split into 3 tubes of 200 µL each and pelleted again. The supernatant was removed and replaced with a solution of each 2Lys variant. These variants were overexpressed as described above and then 100 µL of each was diluted with 100 µL 100 mM Tris, 10 mM EDTA with 25 mM TCEP. The 2Lys variants and SulfoLink solutions were shaken at room temperature for 15 min and then incubated at room temperature for a further 30 min without shaking. The SulfoLink was pelleted by centrifugation and then washed 2x with the Tris/EDTA buffer to remove unbound 2Lys. 200 µL of 50 mM Tris, 5 mM EDTA, 50 mM cysteine was added to each tube and shaken at room temperature for 15 min and then incubated at room temperature for a further 30 min without shaking to cap any free binding groups on the resin. The resin was then washed 3x with 200 µL PBS and stored at 4 °C until needed.

Each immobilized SpA-ZZ-2Lys variant was then labeled with **85** and **86**. This was done by taking each of the 3 200 µL aliquot of immobilized 2Lys and splitting it into 2 Pierce Micro-Spin Columns (Thermo, 89879). These columns were centrifuged (16,000 x g, 1 min) to pack and dry the resin. 150 µL PBS, 15 µL 1 M $NaHCO_3$, and 15 µL of 10 mM DMSO stock of **85** or **86** were combined. 55 µL of these mixtures was added to each Micro-Spin Column. The columns were capped and incubated for 40 min at 37 °C in a Big Shot II Hybridization Oven. Then, the columns were centrifuged to dry and rinsed with 100 µL PBS. 100 µL PBS was then added to each and incubated for 5 min at room temperature followed by 2 more rinses with PBS. The labeled resin was then resuspended in 100 µL PBS and transferred to microcentrifuge tubes.

To run the PDB reactions, each tube of labeled SulfoLink Resin was pipetted to resuspend. 25 µL of each resin was transferred to a Pierce Micro-Spin Column and centrifuged (13,000 rpm, 1 min) to dry and rinsed 2x with 150 µL PBS. 25 µL of 10 µM Herceptin was then added to each column. The columns were capped and incubated in a Big Shot II Hybridization Oven at 37 °C overnight. The next morning, the columns were centrifuged to elute the Herceptin, which was digested and analyzed by HPLC as described above.

4-6. References

(1) Senter, P. D.; Sievers, E. L., The discovery and development of brentuximab vedotin for use in relapsed Hodgkin lymphoma and systemic anaplastic large cell lymphoma. *Nat. Biotechnol.* **2012**, *30*, 631.

(2) Bross, P. F.; Beitz, J.; Chen, G.; Chen, X. H.; Duffy, E.; Kieffer, L.; Roy, S.; Sridhara, R.; Rahman, A.; Williams, G.; Pazdur, R., Approval summary: gemtuzumab ozogamicin in relapsed acute myeloid leukemia. *Clin Cancer Res* **2001**, *7*, 1490.

(3) Lewis Phillips, G. D.; Li, G.; Dugger, D. L.; Crocker, L. M.; Parsons, K. L.; Mai, E.; Blattler, W. A.; Lambert, J. M.; Chari, R. V.; Lutz, R. J.; Wong, W. L.; Jacobson, F. S.; Koeppen, H.; Schwall, R. H.; Kenkare-Mitra, S. R.; Spencer, S. D.; Sliwkowski, M. X., Targeting HER2-positive breast cancer with trastuzumab-DM1, an antibody-cytotoxic drug conjugate. *Cancer Res* **2008**, *68*, 9280.

(4) Lamb, Y. N., Inotuzumab Ozogamicin: First Global Approval. *Drugs* **2017**, *77*, 1603.

(5) Jain, N.; Smith, S. W.; Ghone, S.; Tomczuk, B., Current ADC Linker Chemistry. *Pharm. Res.* **2015**, *32*, 3526.

(6) Wakankar, A.; Chen, Y.; Gokarn, Y.; Jacobson, F. S., Analytical methods for physicochemical characterization of antibody drug conjugates. *mAbs* **2011**, *3*, 161.

(7) Sun, M. M.; Beam, K. S.; Cerveny, C. G.; Hamblett, K. J.; Blackmore, R. S.; Torgov, M. Y.; Handley, F. G.; Ihle, N. C.; Senter, P. D.; Alley, S. C., Reduction-alkylation strategies for the modification of specific monoclonal antibody disulfides. *Bioconjug. Chem.* **2005**, *16*, 1282.

(8) Kim, M. T.; Chen, Y.; Marhoul, J.; Jacobson, F., Statistical modeling of the drug load distribution on trastuzumab emtansine (Kadcyla), a lysine-linked antibody drug conjugate. *Bioconjug. Chem.* **2014**, *25*, 1223.

(9) Kunz, A., Moran, J., Rubino, J., Jain, N., Vidunas, E., Simpson, E., Robbins, P., Merchant, N., DiJoseph, J., Ruppen, M., Damle, N., and Popplewell, A., Calicheamicin derivative-carrier conjugates, U.S. Patent 8,153,768 B2, April 10, 2012.

(10) "Besponsa (inotuzumab ozogamicin)." *Pfizer.* <https://www.pfizermedicalinformation.com/en-us/besponsa/>.

(11) Wang, L.; Amphlett, G.; Blattler, W. A.; Lambert, J. M.; Zhang, W., Structural characterization of the maytansinoid-monoclonal antibody immunoconjugate, huN901-DM1, by mass spectrometry. *Protein Sci.* **2005**, *14*, 2436.

(12) Lu, S. X.; Takach, E. J.; Solomon, M.; Zhu, Q.; Law, S. J.; Hsieh, F. Y., Mass spectral analyses of labile DOTA-NHS and heterogeneity determination of DOTA or DM1 conjugated anti-PSMA antibody for prostate cancer therapy. *J. Pharm. Sci.* **2005**, *94*, 788.

(13) Lazar, A. C.; Wang, L.; Blattler, W. A.; Amphlett, G.; Lambert, J. M.; Zhang, W., Analysis of the composition of immunoconjugates using size-exclusion chromatography coupled to mass spectrometry. *Rapid Commun. Mass Spectrom.* **2005**, *19*, 1806.

(14) Hamblett, K. J.; Senter, P. D.; Chace, D. F.; Sun, M. M.; Lenox, J.; Cerveny, C. G.; Kissler, K. M.; Bernhardt, S. X.; Kopcha, A. K.; Zabinski, R. F.; Meyer, D. L.; Francisco, J. A., Effects of drug loading on the antitumor activity of a monoclonal antibody drug conjugate. *Clin. Cancer. Res.* **2004**, *10*, 7063.

(15) Chari, R. V.; Martell, B. A.; Gross, J. L.; Cook, S. B.; Shah, S. A.; Blattler, W. A.; McKenzie, S. J.; Goldmacher, V. S., Immunoconjugates containing novel maytansinoids: promising anticancer drugs. *Cancer Res.* **1992**, *52*, 127.

(16) Firestone, R. A.; Willner, D.; Hofstead, S. J.; King, H. D.; Kaneko, T.; Braslawsky, G. R.; Greenfield, R. S.; Trail, P. A.; Lasch, S. J.; Henderson, A. J.; Casazza, A. M.; Hellström, I.; Hellström, K. E., Synthesis and antitumor activity of the immunoconjugate BR96-Dox. *J. Controlled Release* **1996**, *39*, 251.

(17) King, H. D.; Dubowchik, G. M.; Mastalerz, H.; Willner, D.; Hofstead, S. J.; Firestone, R. A.; Lasch, S. J.; Trail, P. A., Monoclonal antibody conjugates of doxorubicin prepared with branched peptide linkers: inhibition of aggregation by methoxytriethyleneglycol chains. *J. Med. Chem.* **2002**, *45*, 4336.

(18) Shen, B. Q.; Xu, K.; Liu, L.; Raab, H.; Bhakta, S.; Kenrick, M.; Parsons-Reponte, K. L.; Tien, J.; Yu, S. F.; Mai, E.; Li, D.; Tibbitts, J.; Baudys, J.; Saad, O. M.; Scales, S. J.; McDonald, P. J.; Hass, P. E.; Eigenbrot, C.; Nguyen, T.; Solis, W. A.; Fuji, R. N.; Flagella, K. M.; Patel, D.; Spencer, S. D.; Khawli, L. A.; Ebens, A.; Wong, W. L.; Vandlen, R.; Kaur, S.; Sliwkowski, M. X.; Scheller, R. H.; Polakis, P.; Junutula, J. R., Conjugation site modulates the in vivo stability and therapeutic activity of antibody-drug conjugates. *Nat. Biotechnol.* **2012**, *30*, 184.

(19) Alley, S. C.; Benjamin, D. R.; Jeffrey, S. C.; Okeley, N. M.; Meyer, D. L.; Sanderson, R. J.; Senter, P. D., Contribution of linker stability to the activities of anticancer immunoconjugates. *Bioconjug. Chem.* **2008**, *19*, 759.

(20) Baldwin, A. D.; Kiick, K. L., Tunable degradation of maleimide-thiol adducts in reducing environments. *Bioconjug. Chem.* **2011**, *22*, 1946.

(21) Christie, R. J.; Fleming, R.; Bezabeh, B.; Woods, R.; Mao, S.; Harper, J.; Joseph, A.; Wang, Q.; Xu, Z. Q.; Wu, H.; Gao, C.; Dimasi, N., Stabilization of cysteine-linked antibody drug conjugates with N-aryl maleimides. *J. Control. Release* **2015**, *220*, 660.

(22) Tumey, L. N.; Charati, M.; He, T.; Sousa, E.; Ma, D.; Han, X.; Clark, T.; Casavant, J.; Loganzo, F.; Barletta, F.; Lucas, J.; Graziani, E. I., Mild method for succinimide hydrolysis on ADCs: impact on ADC potency, stability, exposure, and efficacy. *Bioconjug. Chem.* **2014**, *25*, 1871.

(23) Behrens, C. R.; Ha, E. H.; Chinn, L. L.; Bowers, S.; Probst, G.; Fitch-Bruhns, M.; Monteon, J.; Valdiosera, A.; Bermudez, A.; Liao-Chan, S.; Wong, T.; Melnick, J.; Theunissen, J. W.; Flory, M. R.; Houser, D.; Venstrom, K.; Levashova, Z.; Sauer, P.; Migone, T. S.; van der Horst, E. H.; Halcomb, R. L.; Jackson, D. Y., Antibody-Drug Conjugates (ADCs) Derived from Interchain Cysteine Cross-Linking Demonstrate Improved Homogeneity and Other Pharmacological Properties over Conventional Heterogeneous ADCs. *Mol. Pharm.* **2015**, *12*, 3986.

(24) McDonagh, C. F.; Turcott, E.; Westendorf, L.; Webster, J. B.; Alley, S. C.; Kim, K.; Andreyka, J.; Stone, I.; Hamblett, K. J.; Francisco, J. A.; Carter, P., Engineered antibody-drug conjugates with defined sites and stoichiometries of drug attachment. *Protein Eng. Des. Sel.* **2006**, *19*, 299.

(25) Junutula, J. R.; Raab, H.; Clark, S.; Bhakta, S.; Leipold, D. D.; Weir, S.; Chen, Y.; Simpson, M.; Tsai, S. P.; Dennis, M. S.; Lu, Y.; Meng, Y. G.; Ng, C.; Yang, J.; Lee, C. C.; Duenas, E.; Gorrell, J.; Katta, V.; Kim, A.; McDorman, K.; Flagella, K.; Venook, R.; Ross, S.; Spencer, S. D.; Lee Wong, W.; Lowman, H. B.; Vandlen, R.; Sliwkowski, M.

X.; Scheller, R. H.; Polakis, P.; Mallet, W., Site-specific conjugation of a cytotoxic drug to an antibody improves the therapeutic index. *Nat. Biotechnol.* **2008**, *26*, 925.

(26) Junutula, J. R.; Flagella, K. M.; Graham, R. A.; Parsons, K. L.; Ha, E.; Raab, H.; Bhakta, S.; Nguyen, T.; Dugger, D. L.; Li, G.; Mai, E.; Lewis Phillips, G. D.; Hiraragi, H.; Fuji, R. N.; Tibbitts, J.; Vandlen, R.; Spencer, S. D.; Scheller, R. H.; Polakis, P.; Sliwkowski, M. X., Engineered thio-trastuzumab-DM1 conjugate with an improved therapeutic index to target human epidermal growth factor receptor 2-positive breast cancer. *Clin. Cancer. Res.* **2010**, *16*, 4769.

(27) Shinmi, D.; Taguchi, E.; Iwano, J.; Yamaguchi, T.; Masuda, K.; Enokizono, J.; Shiraishi, Y., One-Step Conjugation Method for Site-Specific Antibody-Drug Conjugates through Reactive Cysteine-Engineered Antibodies. *Bioconjug. Chem.* **2016**, *27*, 1324.

(28) Frutos, S.; Hernandez, J. L.; Otero, A.; Calvis, C.; Adan, J.; Mitjans, F.; Vila-Perello, M., Site-Specific Antibody Drug Conjugates Using Streamlined Expressed Protein Ligation. *Bioconjug. Chem.* **2018**, *29*, 3503.

(29) Kumar, A.; Kinneer, K.; Masterson, L.; Ezeadi, E.; Howard, P.; Wu, H.; Gao, C.; Dimasi, N., Synthesis of a heterotrifunctional linker for the site-specific preparation of antibody-drug conjugates with two distinct warheads. *Bioorg. Med. Chem. Lett.* **2018**, *28*, 3617.

(30) Northrop, B. H.; Frayne, S. H.; Choudhary, U., Thiol–maleimide “click” chemistry: evaluating the influence of solvent, initiator, and thiol on the reaction mechanism, kinetics, and selectivity. *Polymer Chemistry* **2015**, *6*, 3415.

(31) Li, X.; Nelson, C. G.; Nair, R. R.; Hazlehurst, L.; Moroni, T.; Martinez-Acedo, P.; Nanna, A. R.; Hymel, D.; Burke, T. R., Jr.; Rader, C., Stable and Potent Selenomab-Drug Conjugates. *Cell chemical biology* **2017**, *24*, 433.

(32) Bruins, J. J.; Westphal, A. H.; Albada, B.; Wagner, K.; Bartels, L.; Spits, H.; van Berkel, W. J. H.; van Delft, F. L., Inducible, Site-Specific Protein Labeling by Tyrosine Oxidation-Strain-Promoted (4 + 2) Cycloaddition. *Bioconjug. Chem.* **2017**, *28*, 1189.

(33) Lin, S.; Yang, X.; Jia, S.; Weeks, A. M.; Hornsby, M.; Lee, P. S.; Nichiporuk, R. V.; Iavarone, A. T.; Wells, J. A.; Toste, F. D.; Chang, C. J., Redox-based reagents for chemoselective methionine bioconjugation. *Science* **2017**, *355*, 597.

(34) Tian, F.; Lu, Y.; Manibusan, A.; Sellers, A.; Tran, H.; Sun, Y.; Phuong, T.; Barnett, R.; Hehli, B.; Song, F.; DeGuzman, M. J.; Ensari, S.; Pinkstaff, J. K.; Sullivan, L. M.; Biroc, S. L.; Cho, H.; Schultz, P. G.; DiJoseph, J.; Dougher, M.; Ma, D.; Dushin, R.; Leal, M.; Tchistiakova, L.; Feyfant, E.; Gerber, H. P.; Sapra, P., A general approach to site-specific antibody drug conjugates. *Proc. Natl. Acad. Sci. U. S. A.* **2014**, *111*, 1766.

(35) VanBrunt, M. P.; Shanebeck, K.; Caldwell, Z.; Johnson, J.; Thompson, P.; Martin, T.; Dong, H.; Li, G.; Xu, H.; D'Hooge, F.; Masterson, L.; Bariola, P.; Tiberghien, A.; Ezeadi, E.; Williams, D. G.; Hartley, J. A.; Howard, P. W.; Grabstein, K. H.; Bowen, M. A.; Marelli, M., Genetically Encoded Azide Containing Amino Acid in Mammalian Cells Enables Site-Specific Antibody-Drug Conjugates Using Click Cycloaddition Chemistry. *Bioconjug. Chem.* **2015**, *26*, 2249.

(36) Zimmerman, E. S.; Heibeck, T. H.; Gill, A.; Li, X.; Murray, C. J.; Madlansacay, M. R.; Tran, C.; Uter, N. T.; Yin, G.; Rivers, P. J.; Yam, A. Y.; Wang, W. D.; Steiner, A. R.; Bajad, S. U.; Penta, K.; Yang, W.; Hallam, T. J.; Thanos, C. D.; Sato,

A. K., Production of site-specific antibody-drug conjugates using optimized non-natural amino acids in a cell-free expression system. *Bioconjug. Chem.* **2014**, *25*, 351.

(37) Axup, J. Y.; Bajjuri, K. M.; Ritland, M.; Hutchins, B. M.; Kim, C. H.; Kazane, S. A.; Halder, R.; Forsyth, J. S.; Santidrian, A. F.; Stafin, K.; Lu, Y.; Tran, H.; Seller, A. J.; Biroc, S. L.; Szydlik, A.; Pinkstaff, J. K.; Tian, F.; Sinha, S. C.; Felding-Habermann, B.; Smider, V. V.; Schultz, P. G., Synthesis of site-specific antibody-drug conjugates using unnatural amino acids. *Proc. Natl. Acad. Sci. U. S. A.* **2012**, *109*, 16101.

(38) Jackson, D.; Atkinson, J.; Guevara, C. I.; Zhang, C.; Kery, V.; Moon, S. J.; Virata, C.; Yang, P.; Lowe, C.; Pinkstaff, J.; Cho, H.; Knudsen, N.; Manibusan, A.; Tian, F.; Sun, Y.; Lu, Y.; Sellers, A.; Jia, X. C.; Joseph, I.; Anand, B.; Morrison, K.; Pereira, D. S.; Stover, D., In vitro and in vivo evaluation of cysteine and site specific conjugated herceptin antibody-drug conjugates. *PLoS One* **2014**, *9*, e83865.

(39) Okeley, N. M.; Toki, B. E.; Zhang, X.; Jeffrey, S. C.; Burke, P. J.; Alley, S. C.; Senter, P. D., Metabolic engineering of monoclonal antibody carbohydrates for antibody-drug conjugation. *Bioconjug. Chem.* **2013**, *24*, 1650.

(40) Li, X.; Fang, T.; Boons, G. J., Preparation of well-defined antibody-drug conjugates through glycan remodeling and strain-promoted azide-alkyne cycloadditions. *Angew. Chem. Int. Ed. Engl.* **2014**, *53*, 7179.

(41) Zhou, Q.; Stefano, J. E.; Manning, C.; Kyazike, J.; Chen, B.; Gianolio, D. A.; Park, A.; Busch, M.; Bird, J.; Zheng, X.; Simonds-Mannes, H.; Kim, J.; Gregory, R. C.; Miller, R. J.; Brondyk, W. H.; Dhal, P. K.; Pan, C. Q., Site-specific antibody-drug conjugation through glycoengineering. *Bioconjug. Chem.* **2014**, *25*, 510.

(42) Zhu, Z.; Ramakrishnan, B.; Li, J.; Wang, Y.; Feng, Y.; Prabakaran, P.; Colantonio, S.; Dyba, M. A.; Qasba, P. K.; Dimitrov, D. S., Site-specific antibody-drug conjugation through an engineered glycotransferase and a chemically reactive sugar. *mAbs* **2014**, *6*, 1190.

(43) van Geel, R.; Wijdeven, M. A.; Heesbeen, R.; Verkade, J. M.; Wasiel, A. A.; van Berkel, S. S.; van Delft, F. L., Chemoenzymatic Conjugation of Toxic Payloads to the Globally Conserved N-Glycan of Native mAbs Provides Homogeneous and Highly Efficacious Antibody-Drug Conjugates. *Bioconjug. Chem.* **2015**, *26*, 2233.

(44) Xu, Y.; Jin, S.; Zhao, W.; Liu, W.; Ding, D.; Zhou, J.; Chen, S., A Versatile Chemo-Enzymatic Conjugation Approach Yields Homogeneous and Highly Potent Antibody-Drug Conjugates. *Int. J. Mol. Sci.* **2017**, *18*.

(45) Khoshnejad, M.; Brenner, J. S.; Motley, W.; Parhiz, H.; Greineder, C. F.; Villa, C. H.; Marcos-Contreras, O. A.; Tsourkas, A.; Muzykantov, V. R., Molecular engineering of antibodies for site-specific covalent conjugation using CRISPR/Cas9. *Sci. Rep.* **2018**, *8*, 1760.

(46) Jung, Y.; Lee, J. M.; Kim, J. W.; Yoon, J.; Cho, H.; Chung, B. H., Photoactivable antibody binding protein: site-selective and covalent coupling of antibody. *Anal. Chem.* **2009**, *81*, 936.

(47) Konrad, A.; Karlstrom, A. E.; Hober, S., Covalent immunoglobulin labeling through a photoactivable synthetic Z domain. *Bioconjug. Chem.* **2011**, *22*, 2395.

(48) Hui, J. Z.; Tamsen, S.; Song, Y.; Tsourkas, A., LASIC: Light Activated Site-Specific Conjugation of Native IgGs. *Bioconjug. Chem.* **2015**, *26*, 1456.

(49) Kanje, S.; von Witting, E.; Chiang, S. C.; Bryceson, Y. T.; Hober, S., Site-Specific Photolabeling of the IgG Fab Fragment Using a Small Protein G Derived Domain. *Bioconjug. Chem.* **2016**, *27*, 2095.

(50) Ohata, J.; Ball, Z. T., A Hexa-rhodium Metallopeptide Catalyst for Site-Specific Functionalization of Natural Antibodies. *J. Am. Chem. Soc.* **2017**, *139*, 12617.

(51) Yu, C.; Tang, J.; Loredo, A.; Chen, Y.; Jung, S. Y.; Jain, A.; Gordon, A.; Xiao, H., Proximity-Induced Site-Specific Antibody Conjugation. *Bioconjug. Chem.* **2018**, *29*, 3522.

(52) Xuan, W.; Shao, S.; Schultz, P. G., Protein Crosslinking by Genetically Encoded Noncanonical Amino Acids with Reactive Aryl Carbamate Side Chains. *Angew. Chem. Int. Ed. Engl.* **2017**, *56*, 5096.

(53) Fernandez-Suarez, M.; Chen, T. S.; Ting, A. Y., Protein-protein interaction detection in vitro and in cells by proximity biotinylation. *J. Am. Chem. Soc.* **2008**, *130*, 9251.

(54) Hughes, C. C.; Yang, Y. L.; Liu, W. T.; Dorrestein, P. C.; La Clair, J. J.; Fenical, W., Marinopyrrole A target elucidation by acyl dye transfer. *J. Am. Chem. Soc.* **2009**, *131*, 12094.

(55) Slavoff, S. A.; Liu, D. S.; Cohen, J. D.; Ting, A. Y., Imaging protein-protein interactions inside living cells via interaction-dependent fluorophore ligation. *J. Am. Chem. Soc.* **2011**, *133*, 19769.

(56) Hymel, D.; Woydziak, Z. R.; Peterson, B. R., Detection of Protein–Protein Interactions by Proximity-Driven SNAr Reactions of Lysine-Linked Fluorophores. *J. Am. Chem. Soc.* **2014**, *136*, 5241.

(57) Tsukiji, S.; Miyagawa, M.; Takaoka, Y.; Tamura, T.; Hamachi, I., Ligand-directed tosyl chemistry for protein labeling in vivo. *Nat. Chem. Biol.* **2009**, *5*, 341.

(58) Chen, Z.; Jing, C.; Gallagher, S. S.; Sheetz, M. P.; Cornish, V. W., Second-generation covalent TMP-tag for live cell imaging. *J. Am. Chem. Soc.* **2012**, *134*, 13692.

(59) Amini, F.; Kodadek, T.; Brown, K. C., Protein affinity labeling mediated by genetically encoded peptide tags. *Angew. Chem. Int. Ed. Engl.* **2002**, *41*, 356.

(60) Liu, B.; Archer, C. T.; Burdine, L.; Gillette, T. G.; Kodadek, T., Label transfer chemistry for the characterization of protein-protein interactions. *J. Am. Chem. Soc.* **2007**, *129*, 12348.

(61) Andrews, S. S.; Hill, Z. B.; Perera, B. G.; Maly, D. J., Label transfer reagents to probe p38 MAPK binding partners. *Chembiochem* **2013**, *14*, 209.

(62) Bhogal, M. S.; Lanyon-Hogg, T.; Johnston, K. A.; Warriner, S. L.; Baker, A., Covalent Label Transfer between Peroxisomal Importomer Components Reveals Export-driven Import Interactions. *J. Biol. Chem.* **2016**, *291*, 2460.

(63) Yang, Y.; Song, H.; He, D.; Zhang, S.; Dai, S.; Lin, S.; Meng, R.; Wang, C.; Chen, P. R., Genetically encoded protein photocrosslinker with a transferable mass spectrometry-identifiable label. *Nature communications* **2016**, *7*, 12299.

(64) Matsuo, K.; Nishikawa, Y.; Masuda, M.; Hamachi, I., Live-Cell Protein Sulfonylation Based on Proximity-driven N-Sulfonyl Pyridone Chemistry. *Angew. Chem. Int. Ed. Engl.* **2018**, *57*, 659.

(65) Jansson, B.; Uhlen, M.; Nygren, P. A., All individual domains of staphylococcal protein A show Fab binding. *FEMS Immunol. Med. Microbiol.* **1998**, *20*, 69.

(66) Gouda, H.; Shiraishi, M.; Takahashi, H.; Kato, K.; Torigoe, H.; Arata, Y.; Shimada, I., NMR study of the interaction between the B domain of staphylococcal protein A and the Fc portion of immunoglobulin G. *Biochemistry* **1998**, *37*, 129.

(67) Forsgren, A.; Sjoquist, J., "Protein A" from S. aureus. I. Pseudo-immune reaction with human gamma-globulin. *J. Immunol.* **1966**, *97*, 822.

(68) Peterson, P. K.; Verhoef, J.; Sabath, L. D.; Quie, P. G., Effect of protein A on staphylococcal opsonization. *Infect. Immun.* **1977**, *15*, 760.

(69) Foster, T. J., Immune evasion by staphylococci. *Nat. Rev. Microbiol.* **2005**, *3*, 948.

(70) Armbruster, C. R.; Wolter, D. J.; Mishra, M.; Hayden, H. S.; Radey, M. C.; Merrihew, G.; MacCoss, M. J.; Burns, J.; Wozniak, D. J.; Parsek, M. R.; Hoffman, L. R., Staphylococcus aureus Protein A Mediates Interspecies Interactions at the Cell Surface of Pseudomonas aeruginosa. *mBio* **2016**, *7*.

(71) Hjelm, H.; Hjelm, K.; Sjoquist, J., Protein A from Staphylococcus aureus. Its isolation by affinity chromatography and its use as an immunosorbent for isolation of immunoglobulins. *FEBS Lett.* **1972**, *28*, 73.

(72) Deisenhofer, J., Crystallographic refinement and atomic models of a human Fc fragment and its complex with fragment B of protein A from Staphylococcus aureus at 2.9- and 2.8-A resolution. *Biochemistry* **1981**, *20*, 2361.

(73) Graille, M.; Stura, E. A.; Corper, A. L.; Sutton, B. J.; Taussig, M. J.; Charbonnier, J. B.; Silverman, G. J., Crystal structure of a Staphylococcus aureus protein A domain complexed with the Fab fragment of a human IgM antibody: structural basis for

recognition of B-cell receptors and superantigen activity. *Proc. Natl. Acad. Sci. U. S. A.* **2000**, *97*, 5399.

(74) Deis, L. N.; Wu, Q.; Wang, Y.; Qi, Y.; Daniels, K. G.; Zhou, P.; Oas, T. G., Suppression of conformational heterogeneity at a protein-protein interface. *Proc. Natl. Acad. Sci. U. S. A.* **2015**, *112*, 9028.

(75) Uhlen, M.; Guss, B.; Nilsson, B.; Gatenbeck, S.; Philipson, L.; Lindberg, M., Complete sequence of the staphylococcal gene encoding protein A. A gene evolved through multiple duplications. *J. Biol. Chem.* **1984**, *259*, 1695.

(76) Nilsson, B.; Moks, T.; Jansson, B.; Abrahmsen, L.; Elmblad, A.; Holmgren, E.; Henrichson, C.; Jones, T. A.; Uhlen, M., A synthetic IgG-binding domain based on staphylococcal protein A. *Protein Eng.* **1987**, *1*, 107.

(77) Moks, T.; Abrahmsen, L.; Holmgren, E.; Bilich, M.; Olsson, A.; Uhlen, M.; Pohl, G.; Sterky, C.; Hultberg, H.; Josephson, S.; et al., Expression of human insulin-like growth factor I in bacteria: use of optimized gene fusion vectors to facilitate protein purification. *Biochemistry* **1987**, *26*, 5239.

(78) Zheng, L.; Baumann, U.; Reymond, J. L., An efficient one-step site-directed and site-saturation mutagenesis protocol. *Nucleic Acids Res.* **2004**, *32*, e115.

Appendix A. NMR Spectra of Compounds

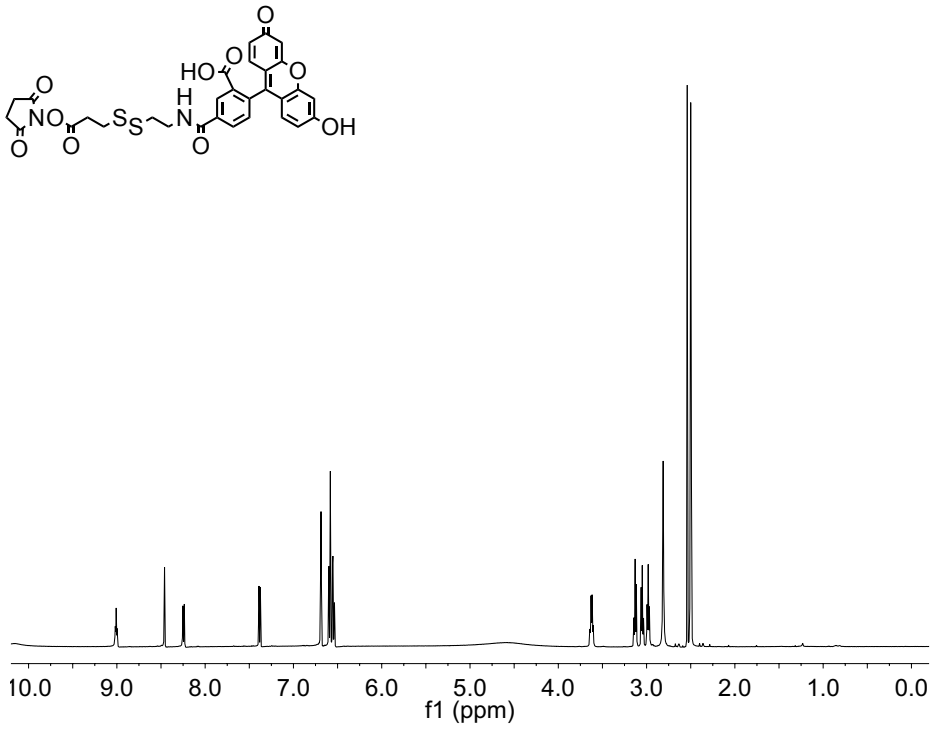

Figure 5-1. ^{1}H NMR (500 MHz, DMSO-d_6) spectrum of **15**.

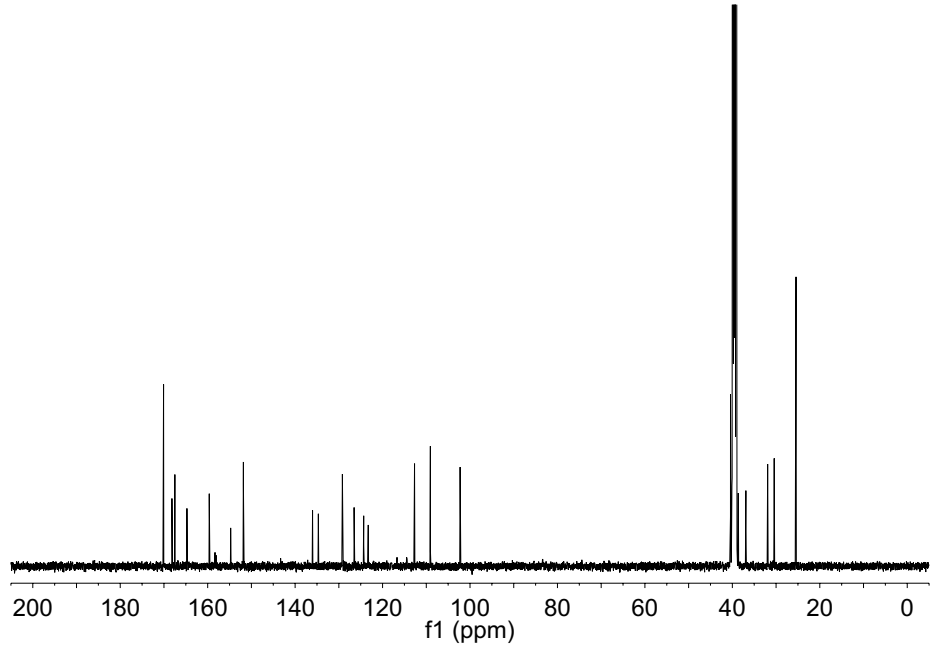

Figure 5-2. ^{13}C NMR (126 MHz, DMSO-d_6) spectrum of **15**.

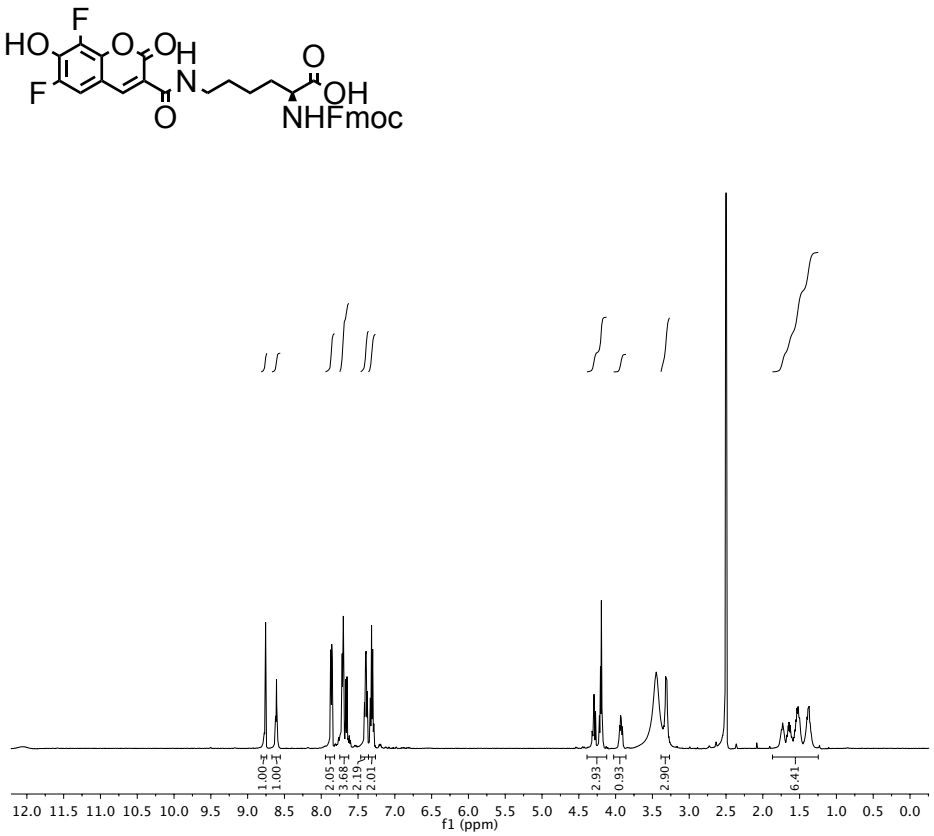

Figure 5-3. ^{1}H NMR (500 MHz, DMSO-d_6) spectrum of **41**.

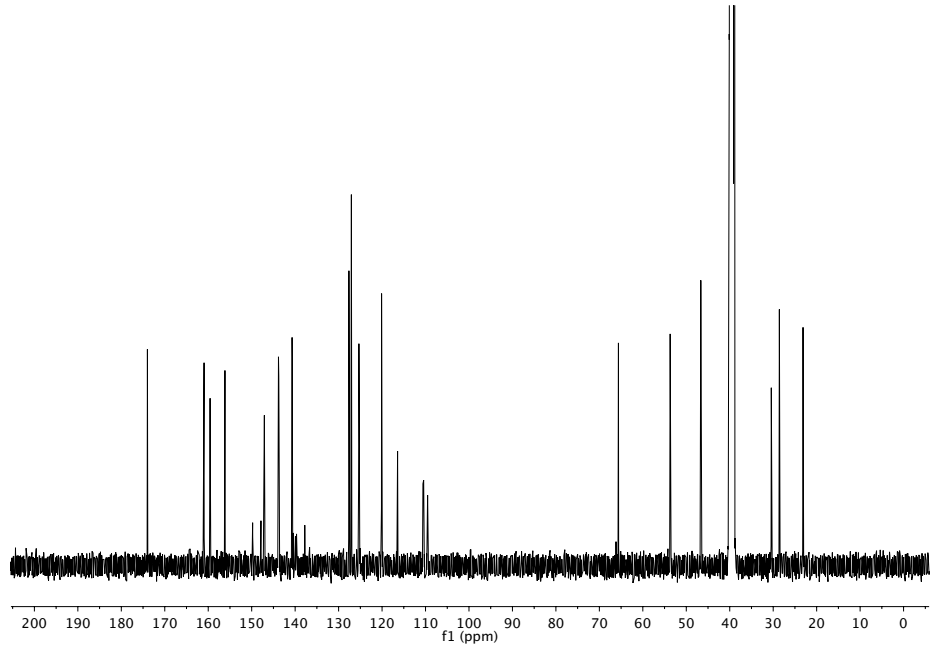

Figure 5-4. ^{13}C NMR (126 MHz, DMSO-d_6) spectrum of **41**.

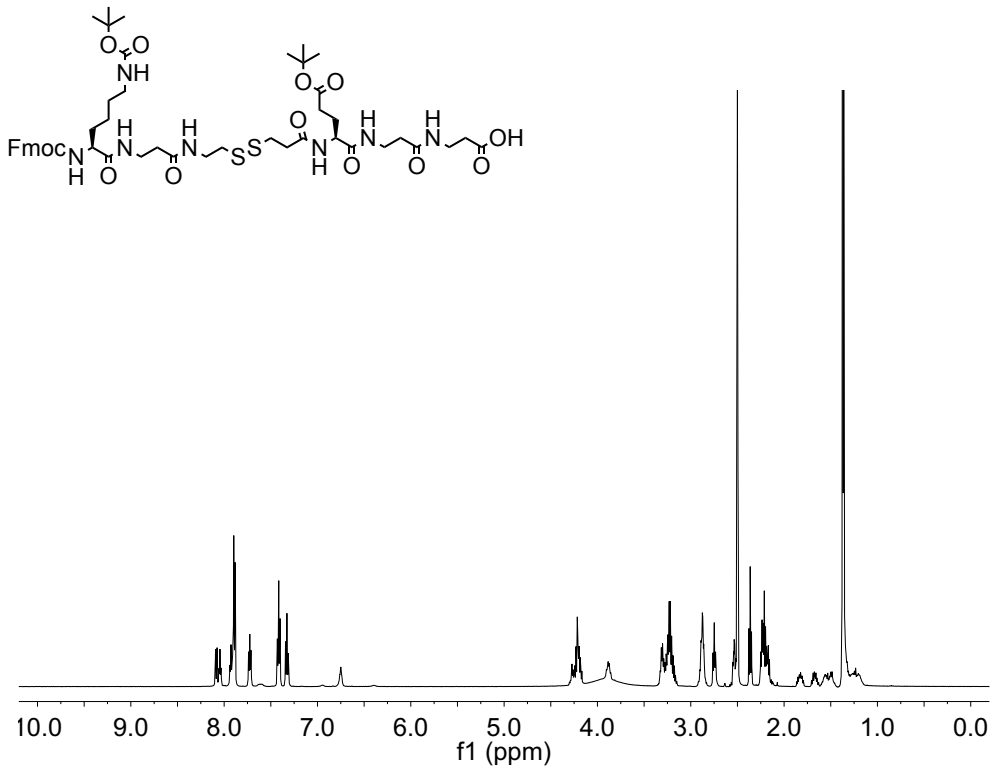

Figure 5-5. ^{1}H NMR (500 MHz, DMSO-d_6) spectrum of **44**.

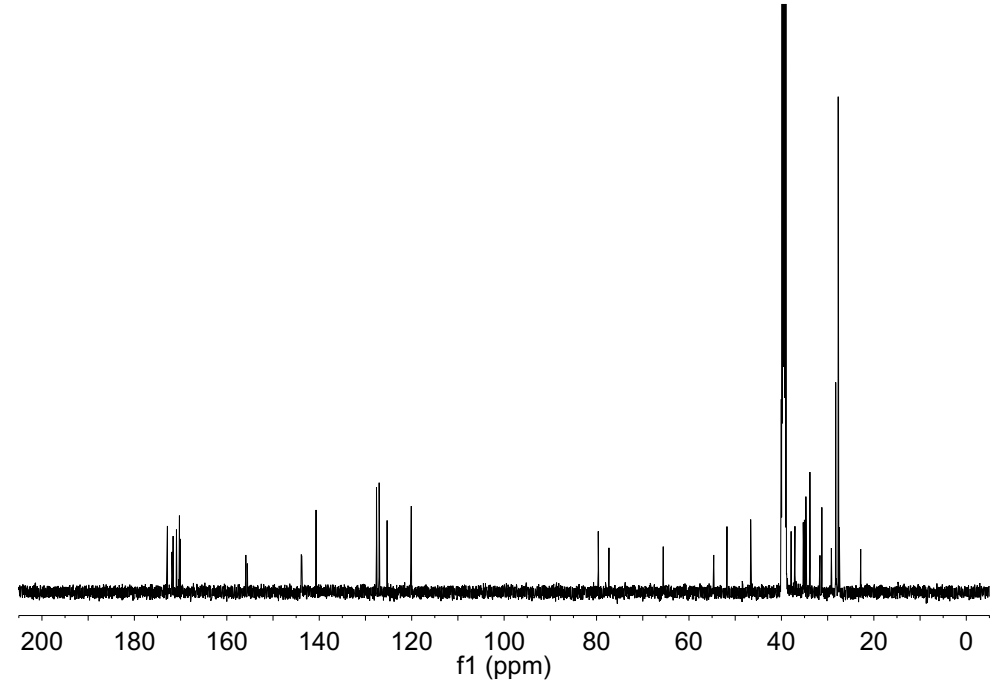

Figure 5-6. ^{13}C NMR (126 MHz, DMSO-d_6) spectrum of **44**.

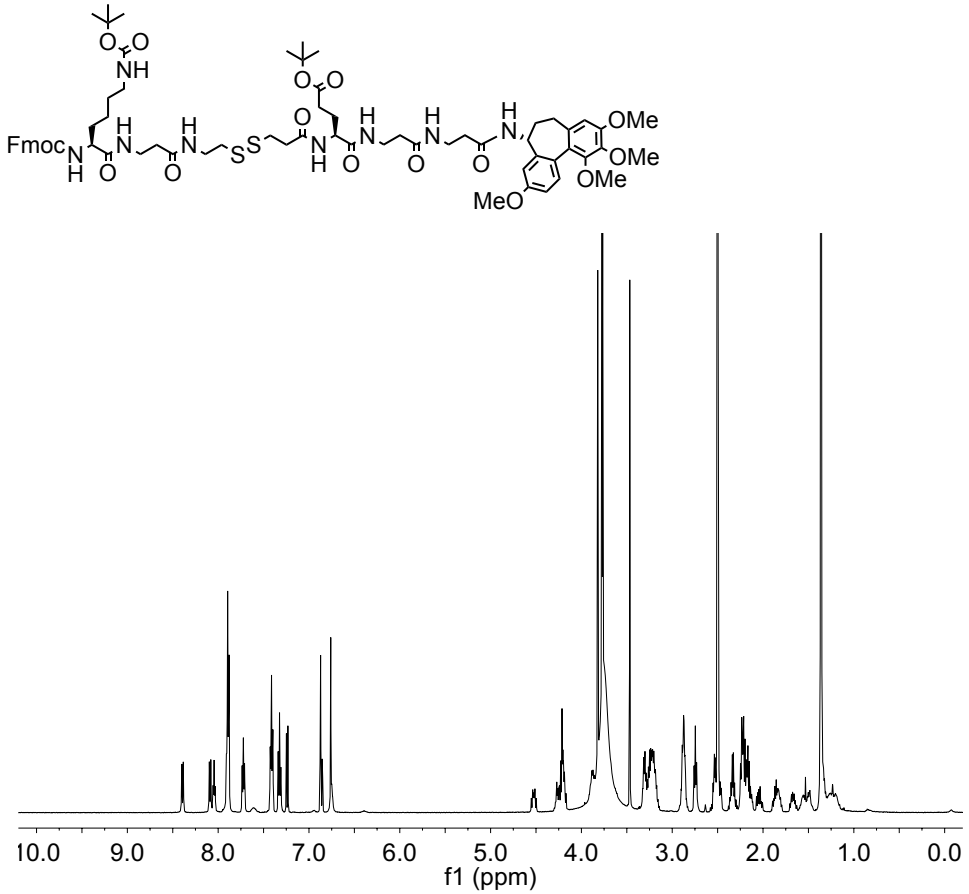

Figure 5-7. ^{1}H NMR (500 MHz, DMSO-d_6) spectrum of **45**.

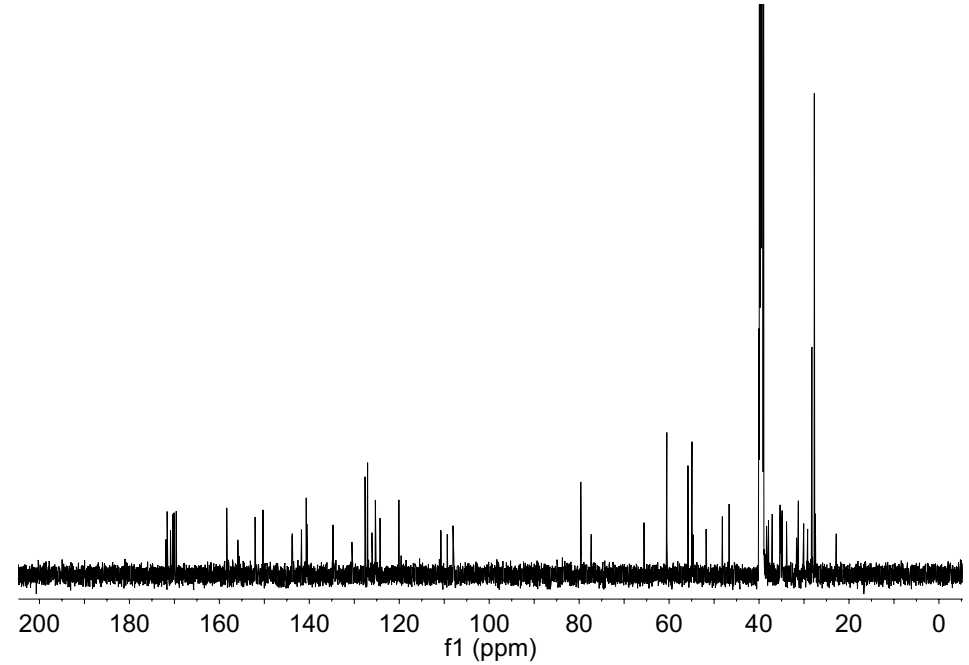

Figure 5-8. ^{13}C NMR (126 MHz, DMSO-d_6) spectrum of **45**.

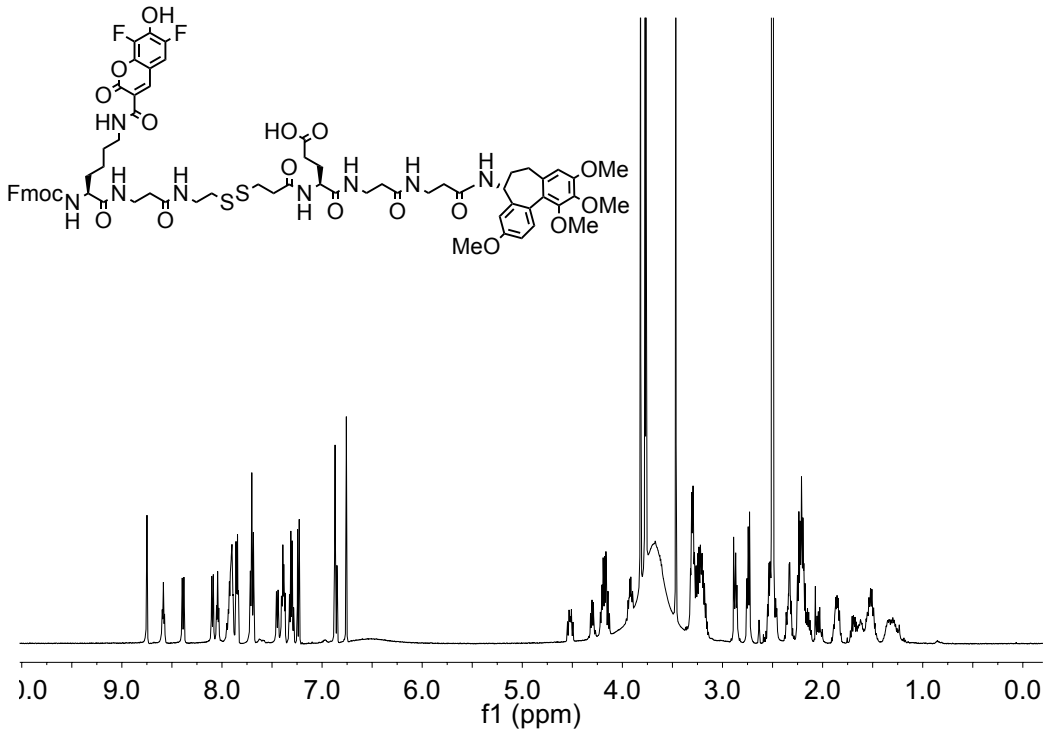

Figure 5-9. ^{1}H NMR (500 MHz, DMSO-d_6) spectrum of **46**.

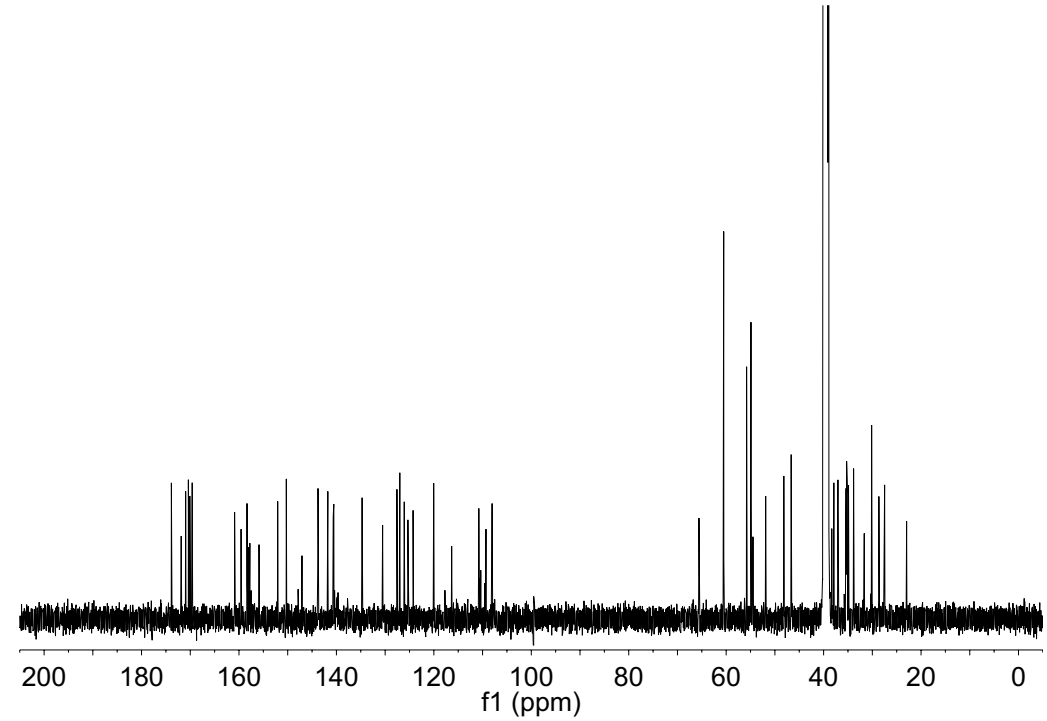

Figure 5-10. ^{13}C NMR (126 MHz, DMSO-d_6) spectrum of **46**.

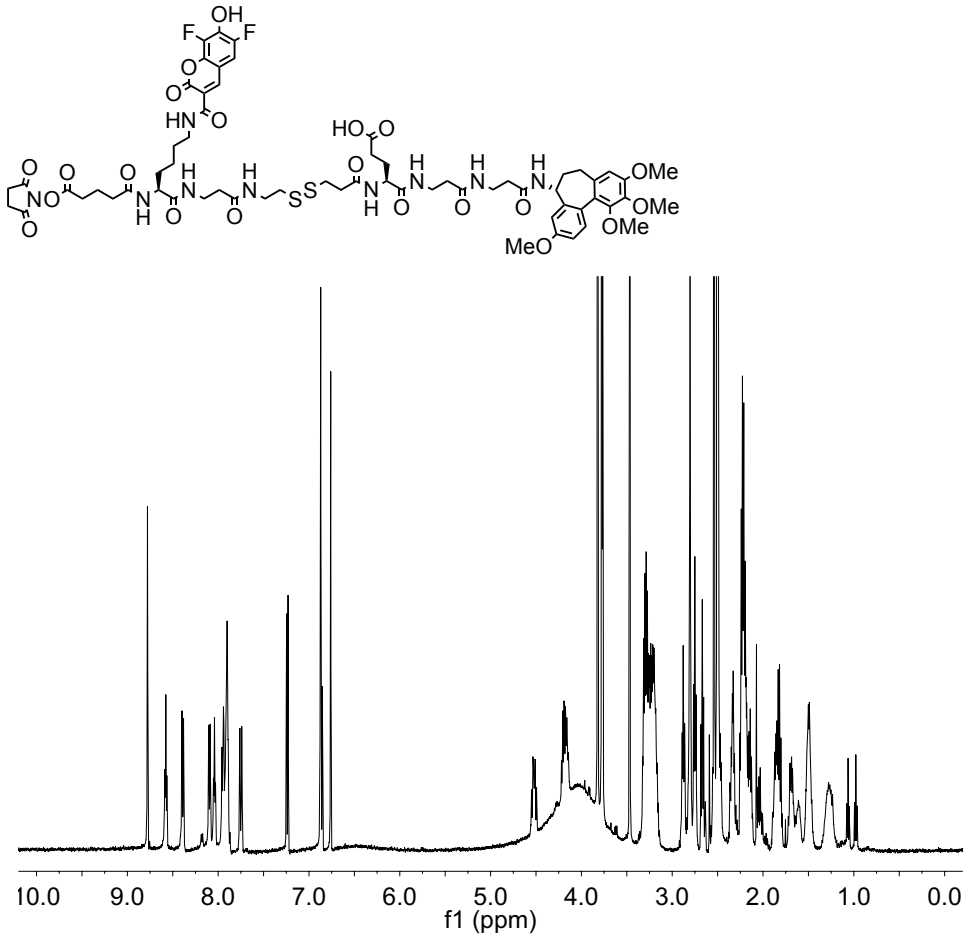

Figure 5-11. ^{1}H NMR (500 MHz, DMSO-d_6) spectrum of **32**.

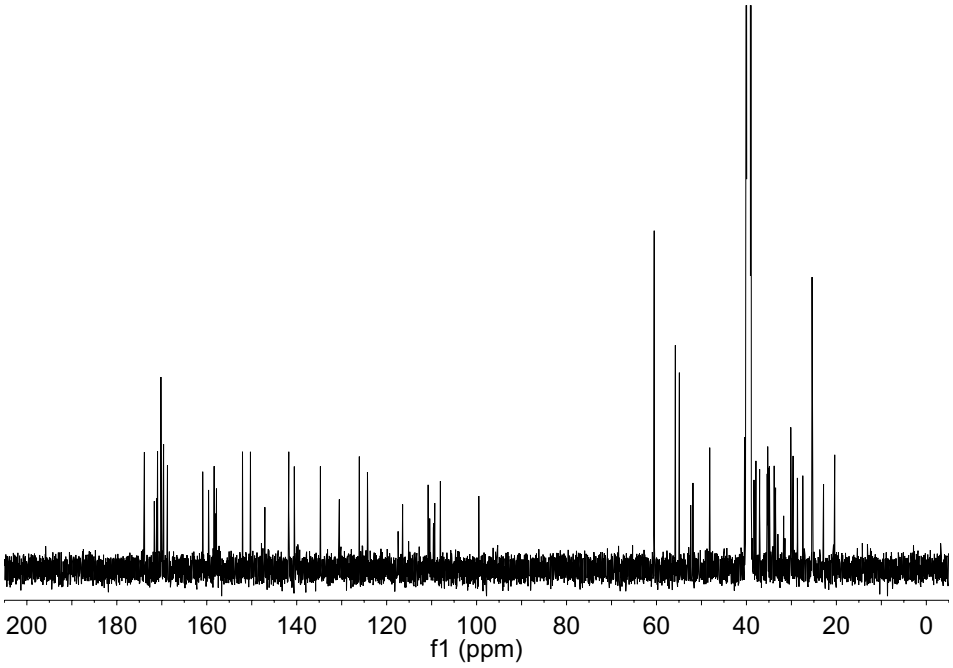

Figure 5-12. ^{13}C NMR (126 MHz, DMSO-d_6) spectrum of **32**.

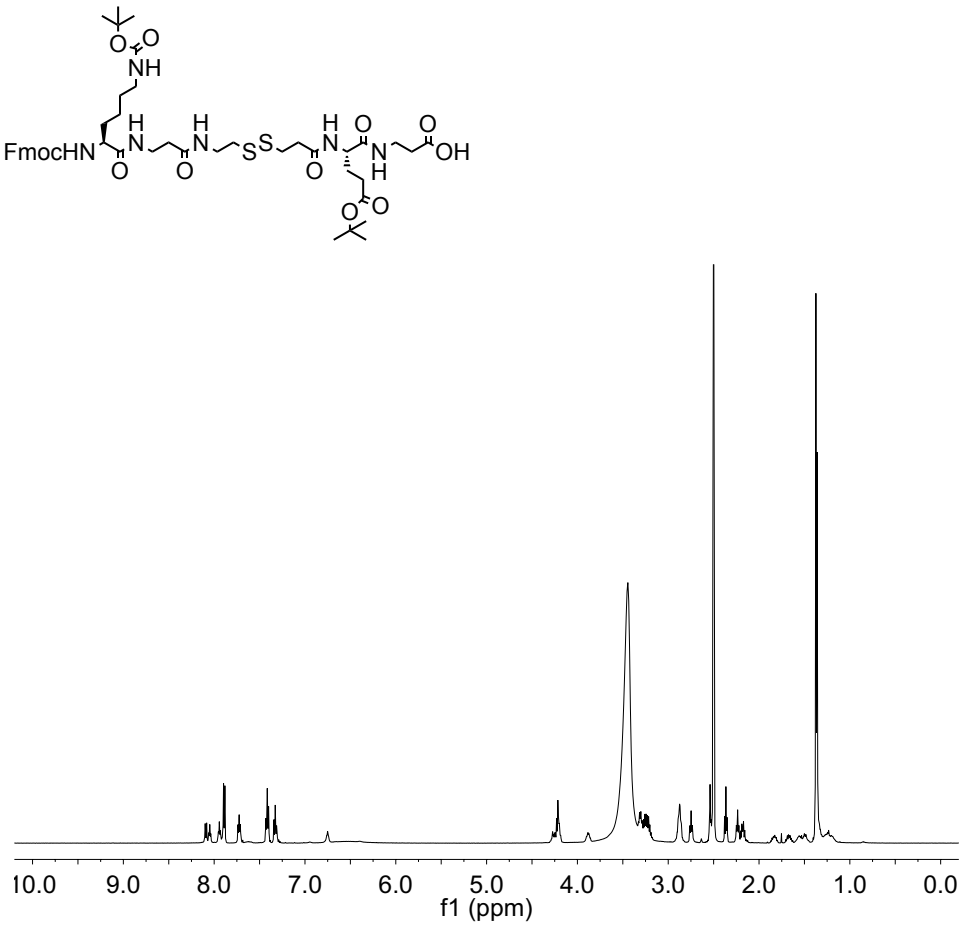

Figure 5-13. ^{1}H NMR (500 MHz, DMSO-d_6) spectrum of **47.**

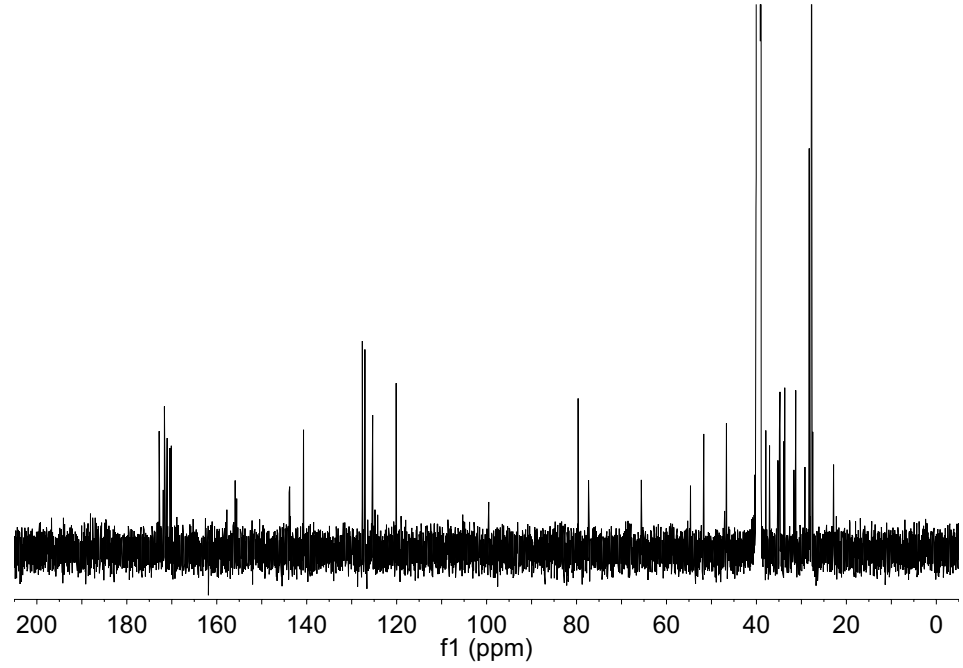

Figure 5-14. ^{13}C NMR (126 MHz, DMSO-d_6) spectrum of **47.**

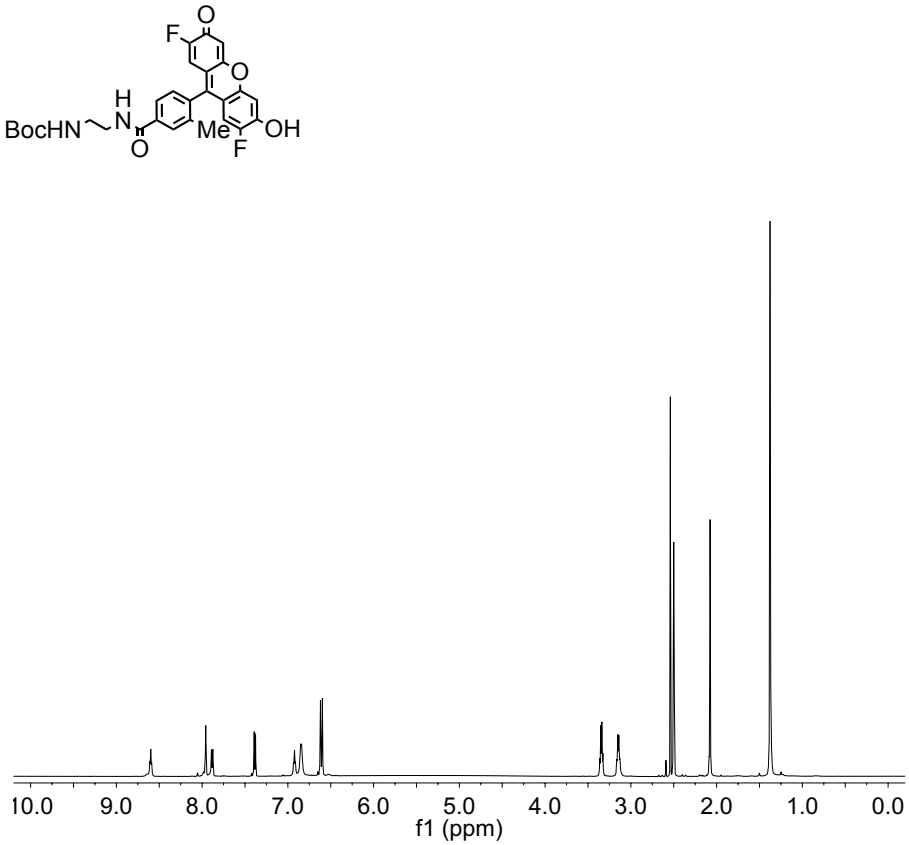

Figure 5-15. ^{1}H NMR (500 MHz, DMSO-d_6) spectrum of **48**.

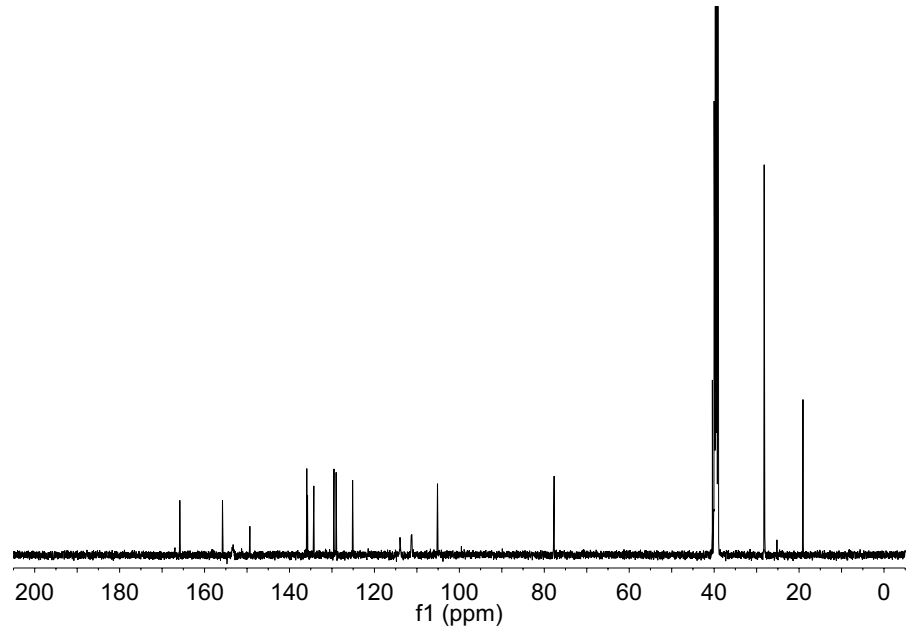

Figure 5-16. ^{13}C NMR (126 MHz, DMSO-d_6) spectrum of **48**.

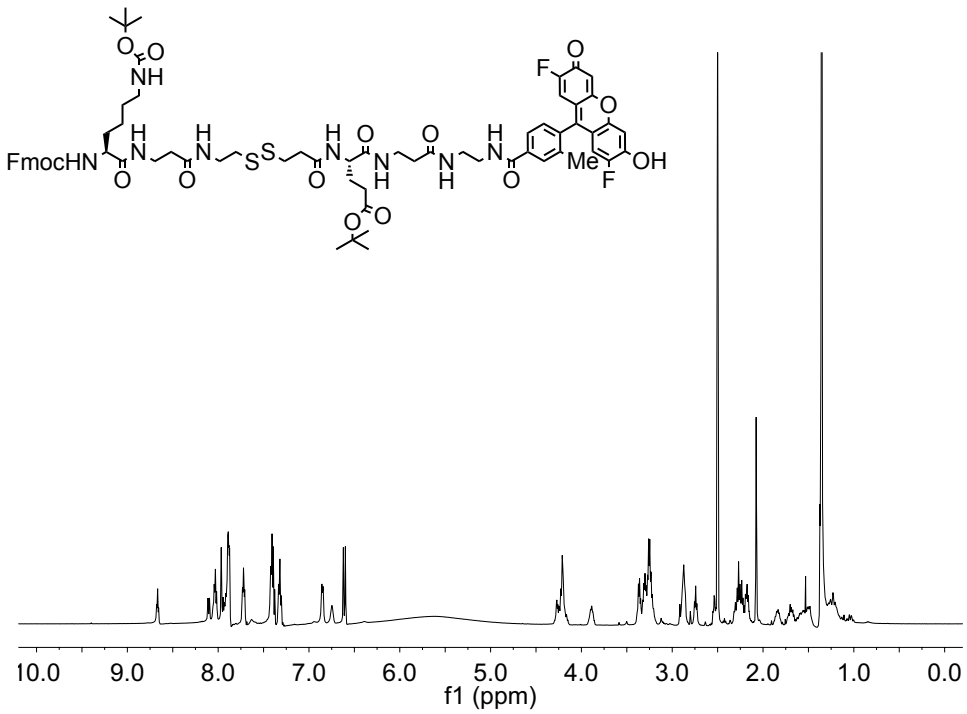

Figure 5-17. ^{1}H NMR (500 MHz, DMSO-d_6) spectrum of **49.**

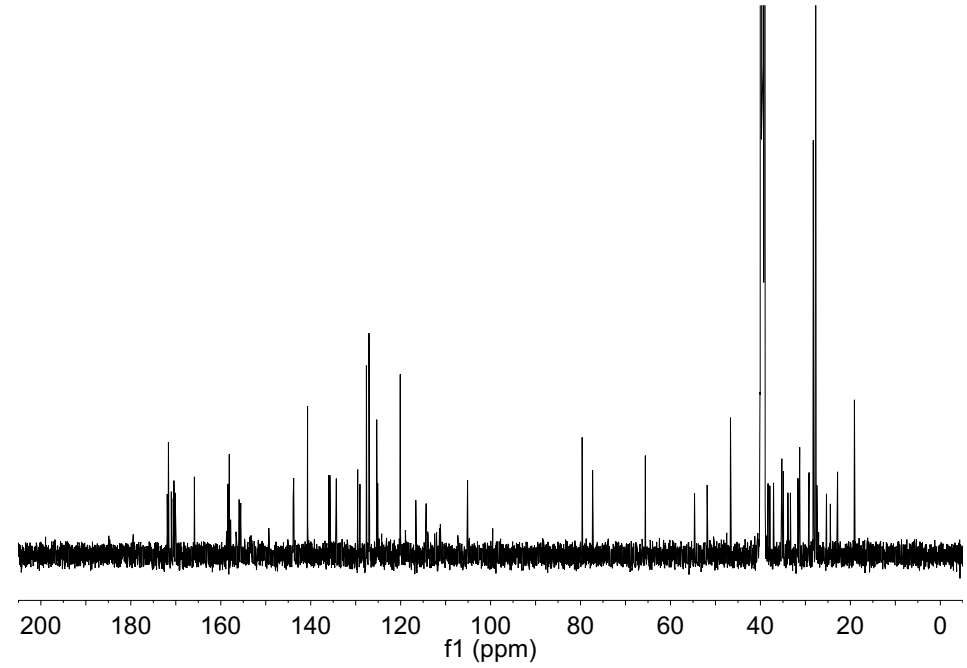

Figure 5-18. ^{13}C NMR (126 MHz, DMSO-d_6) spectrum of **49.**

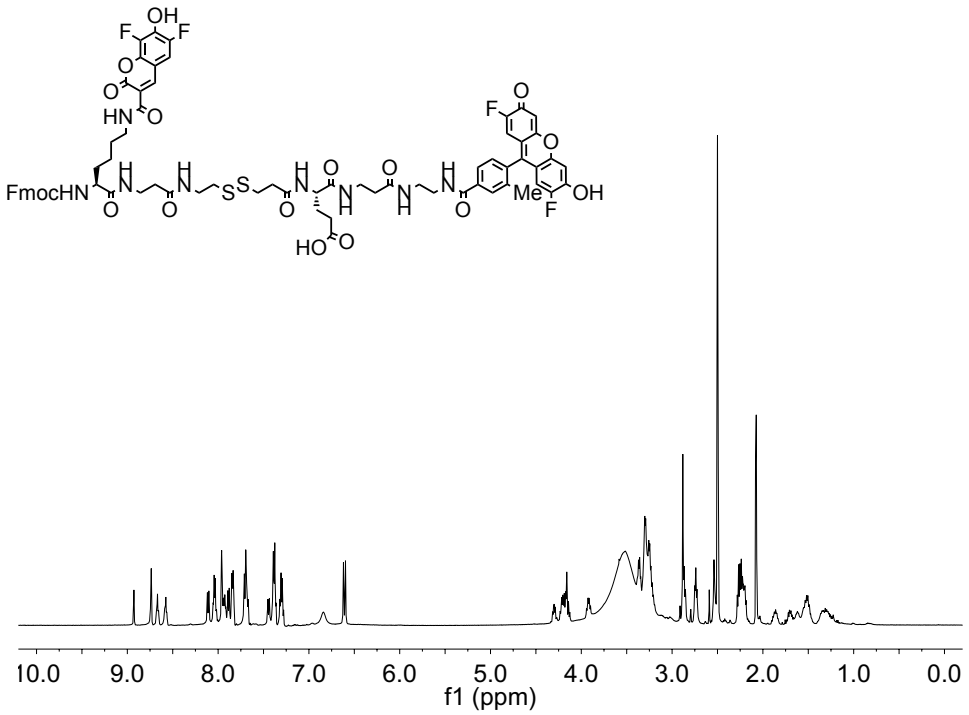

Figure 5-19. ^{1}H NMR (500 MHz, DMSO-d_6) spectrum of **50**.

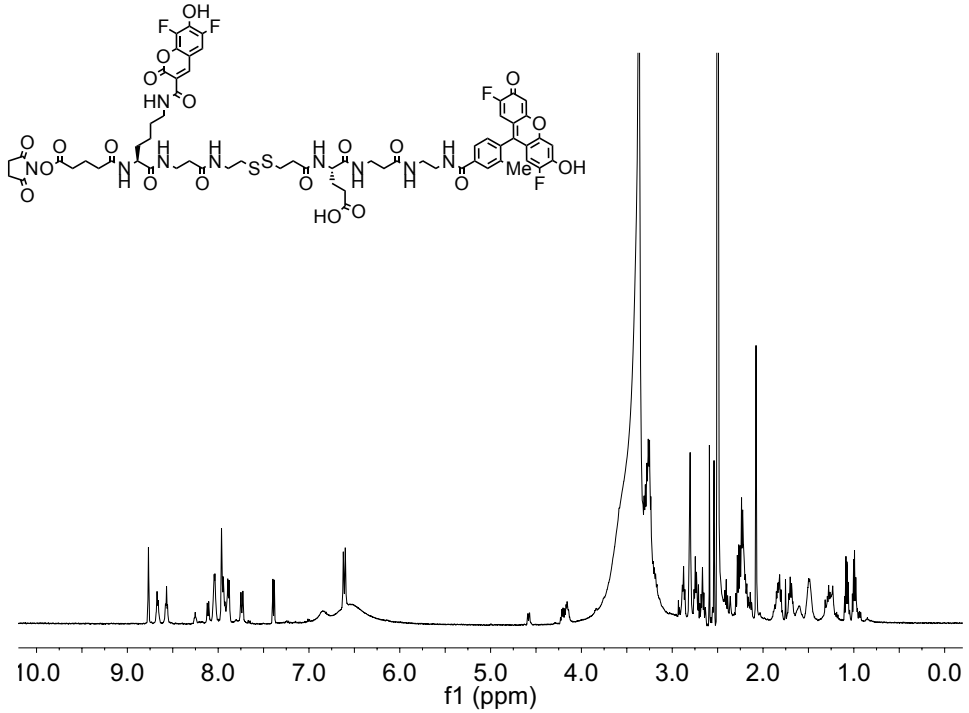

Figure 5-20. ^{1}H NMR (500 MHz, DMSO-d_6) spectrum of **38**.

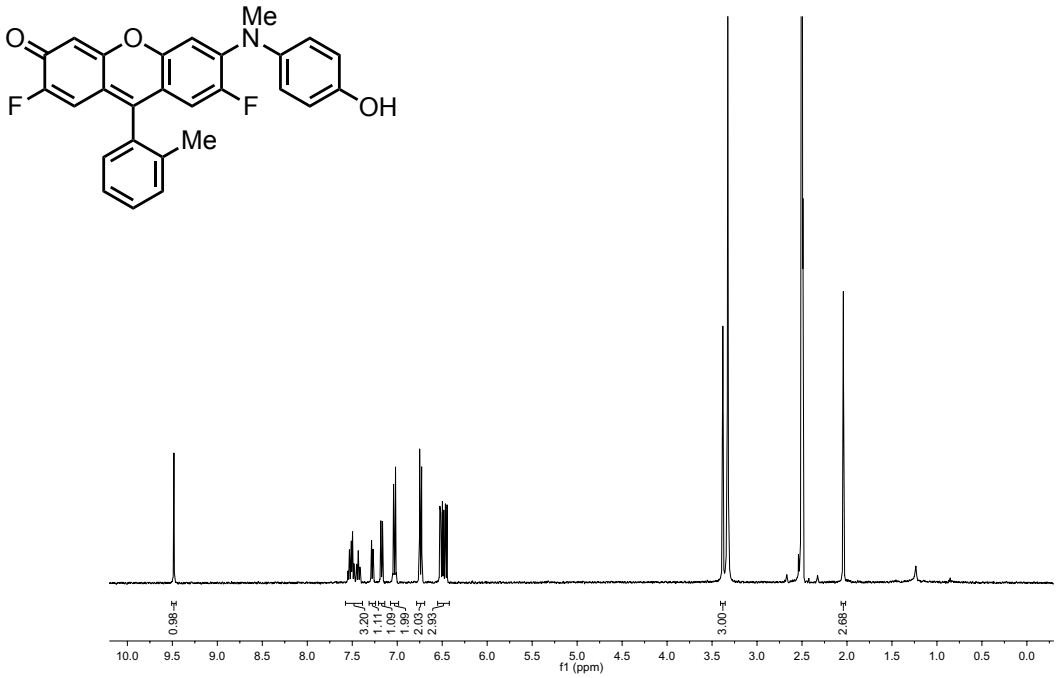

Figure 5-21. ^{1}H NMR (400 MHz, DMSO-d_6) spectrum of **51**.

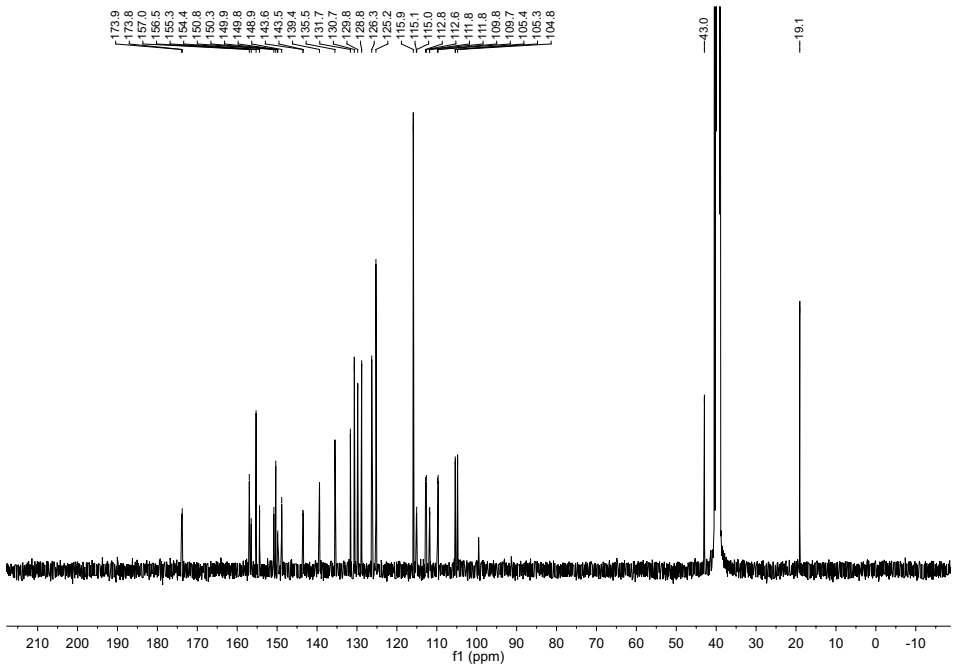

Figure 5-22. ^{13}C NMR (126 MHz, DMSO-d_6) spectrum of **51**.

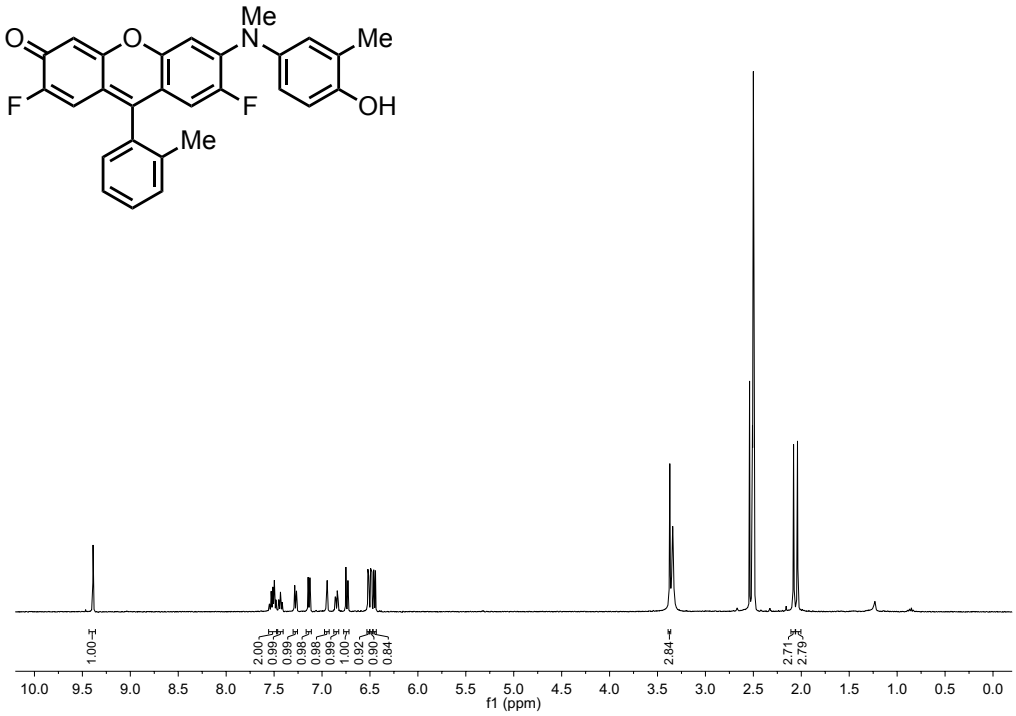

Figure 5-23. ^{1}H NMR (400 MHz, DMSO-d_6) spectrum of **52**.

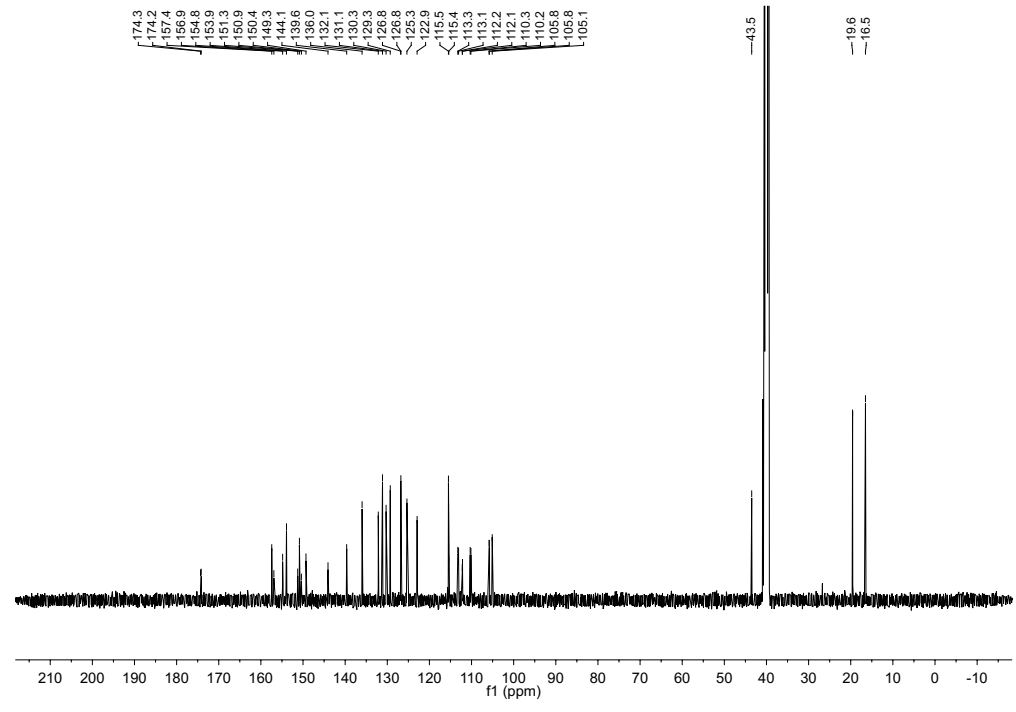

Figure 5-24. ^{13}C NMR (126 MHz, DMSO-d_6) spectrum of **52**.

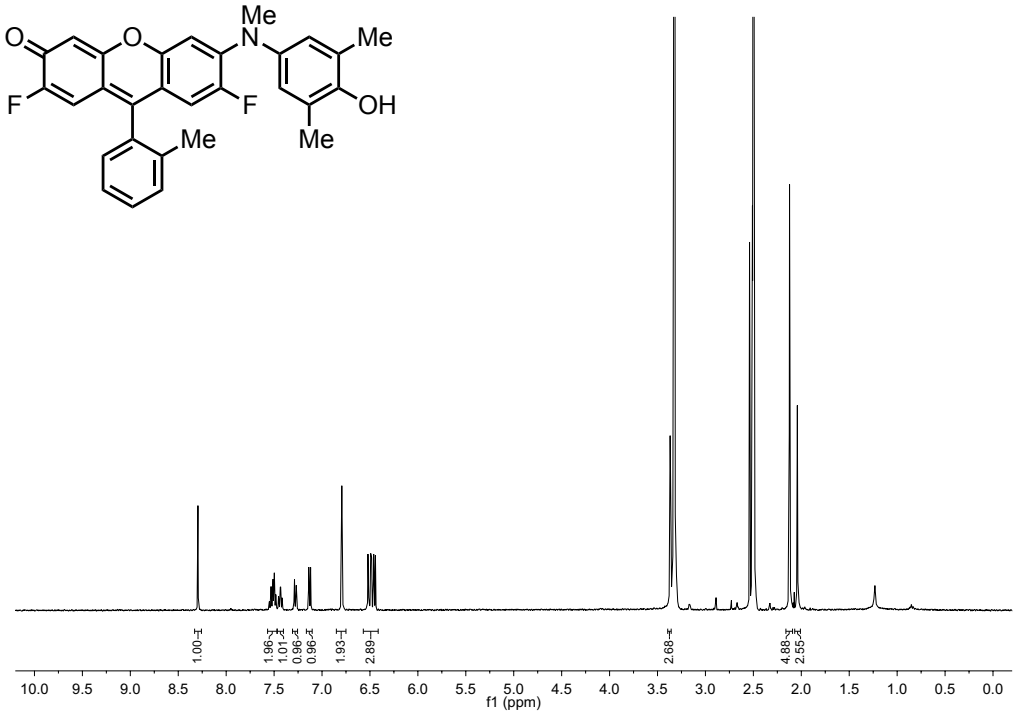

Figure 5-25. ^{1}H NMR (400 MHz, DMSO-d_6) spectrum of **53**.

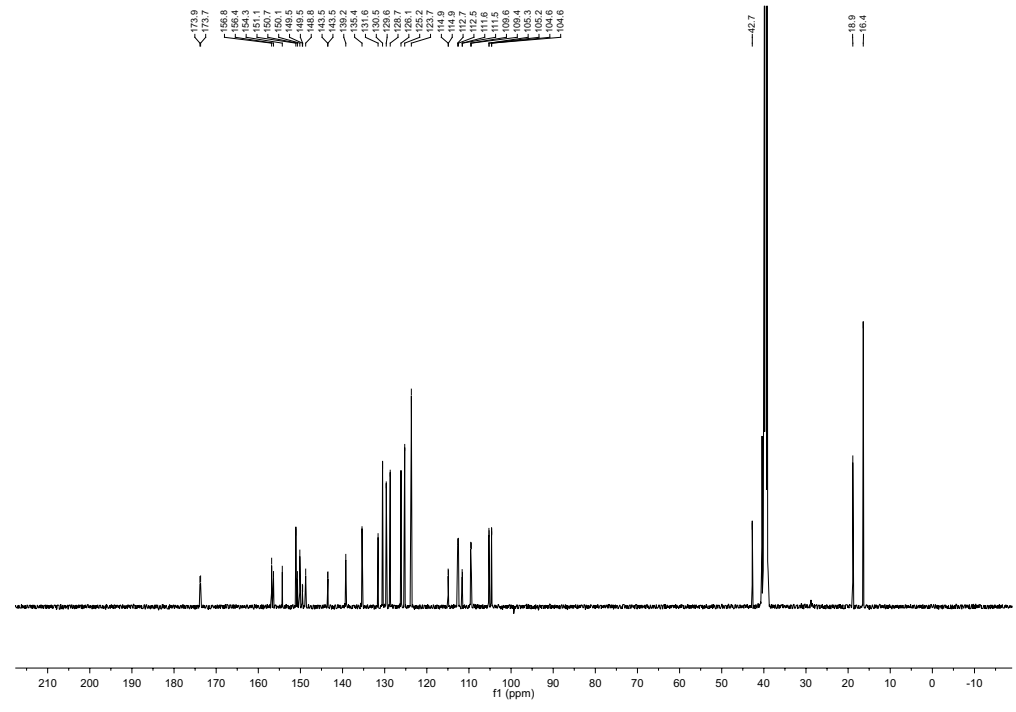

Figure 5-26. ^{13}C NMR (126 MHz, DMSO-d_6) spectrum of **53**.

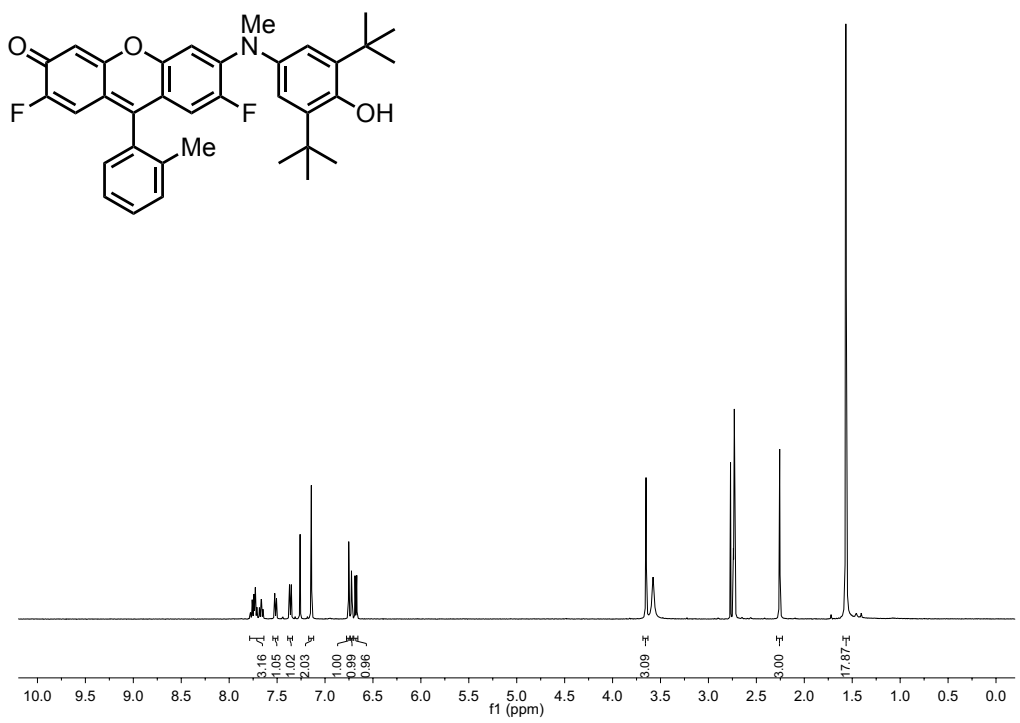

Figure 5-27. ^{1}H NMR (400 MHz, DMSO-d_6) spectrum of **54**.

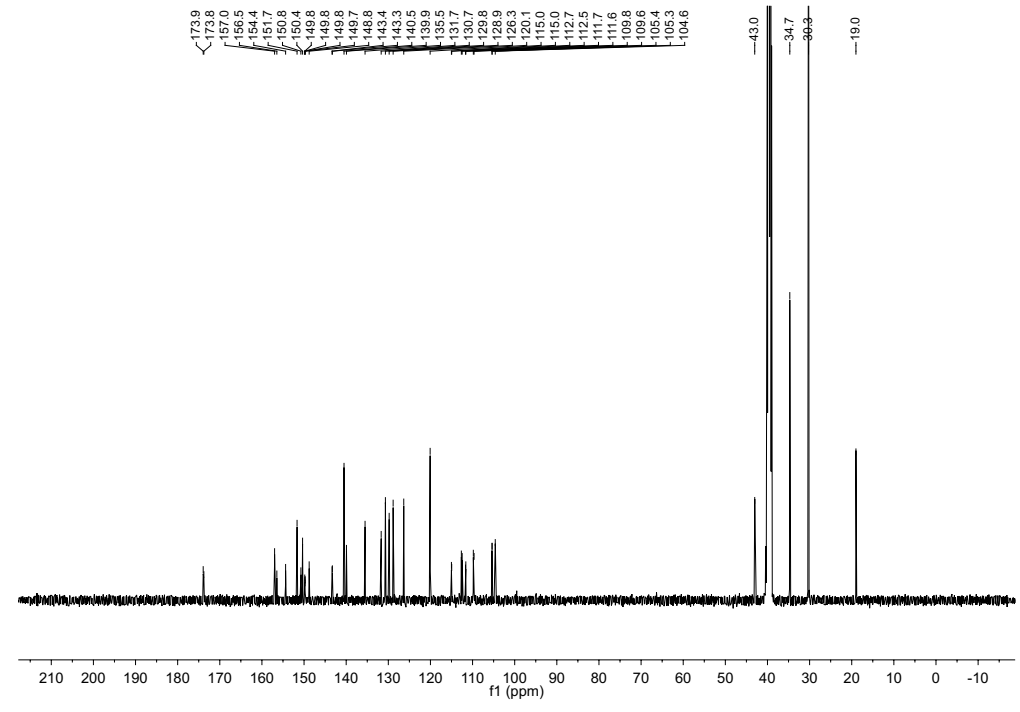

Figure 5-28. ^{13}C NMR (126 MHz, DMSO-d_6) spectrum of **54**.

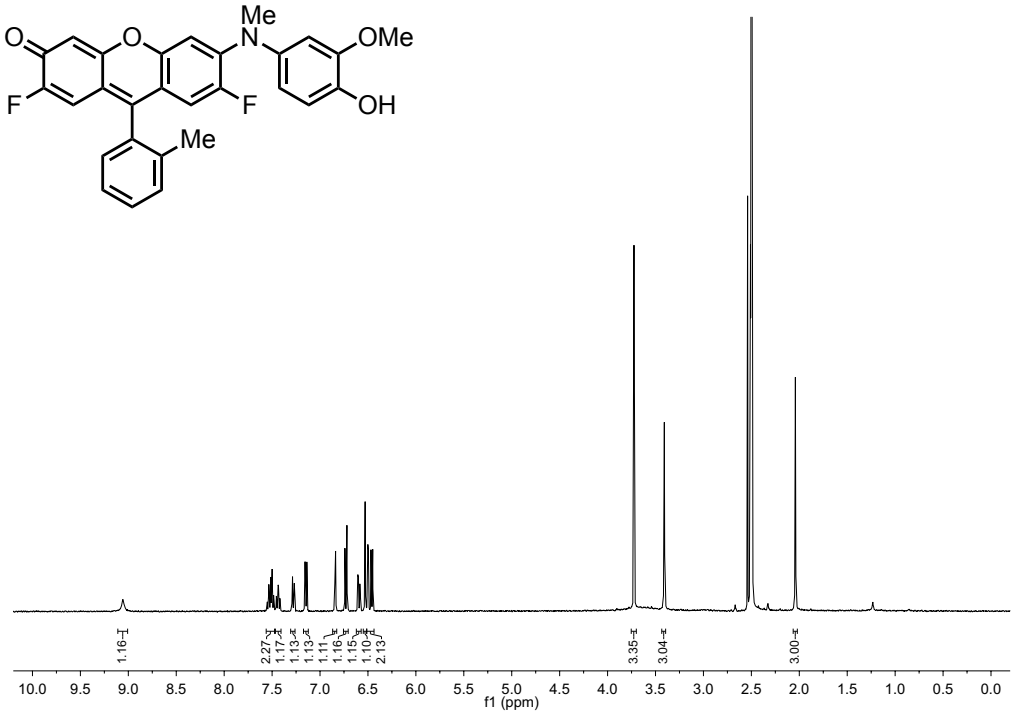

Figure 5-29. ^{1}H NMR (400 MHz, DMSO-d_6) spectrum of **55**.

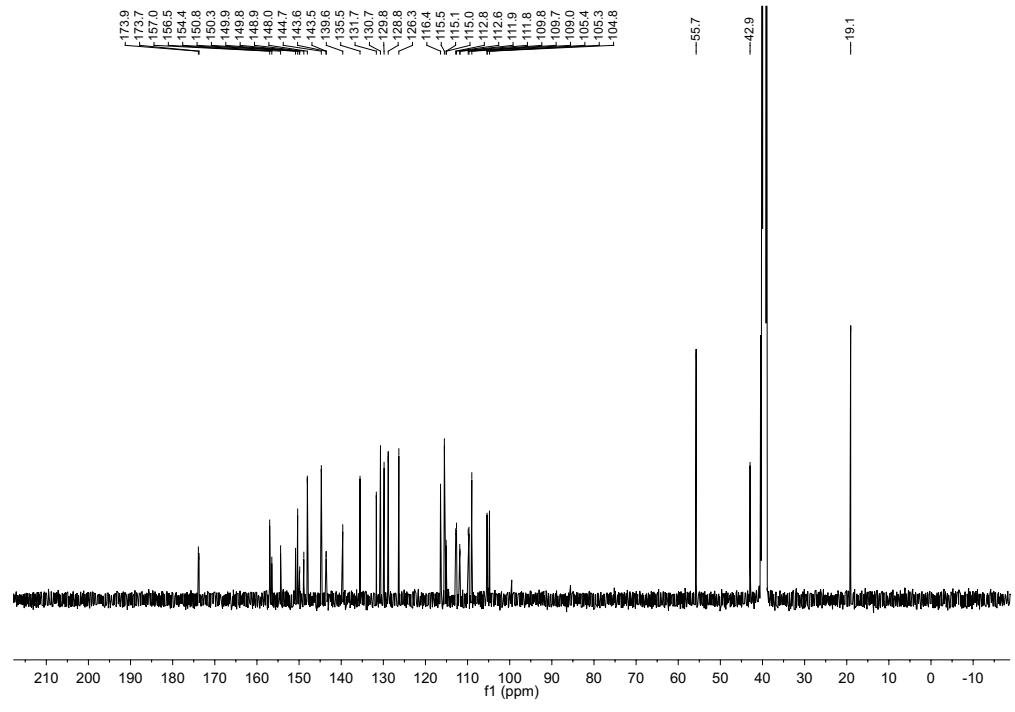

Figure 5-30. ^{13}C NMR (126 MHz, DMSO-d_6) spectrum of **55**.

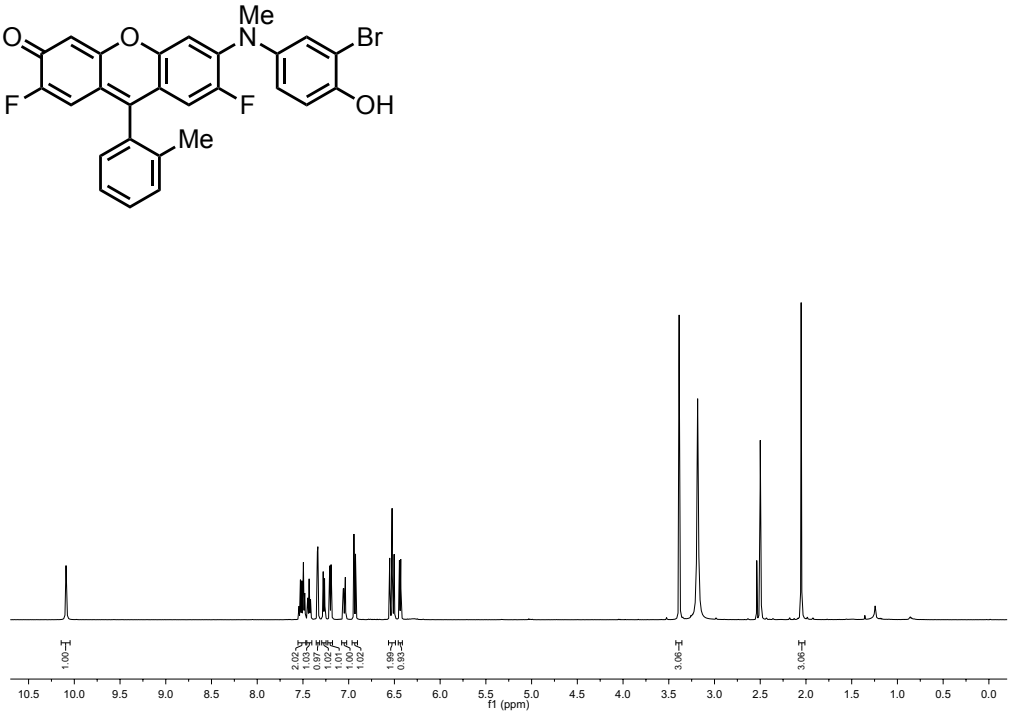

Figure 5-31. ^{1}H NMR (500 MHz, DMSO-d_6) spectrum of **56**.

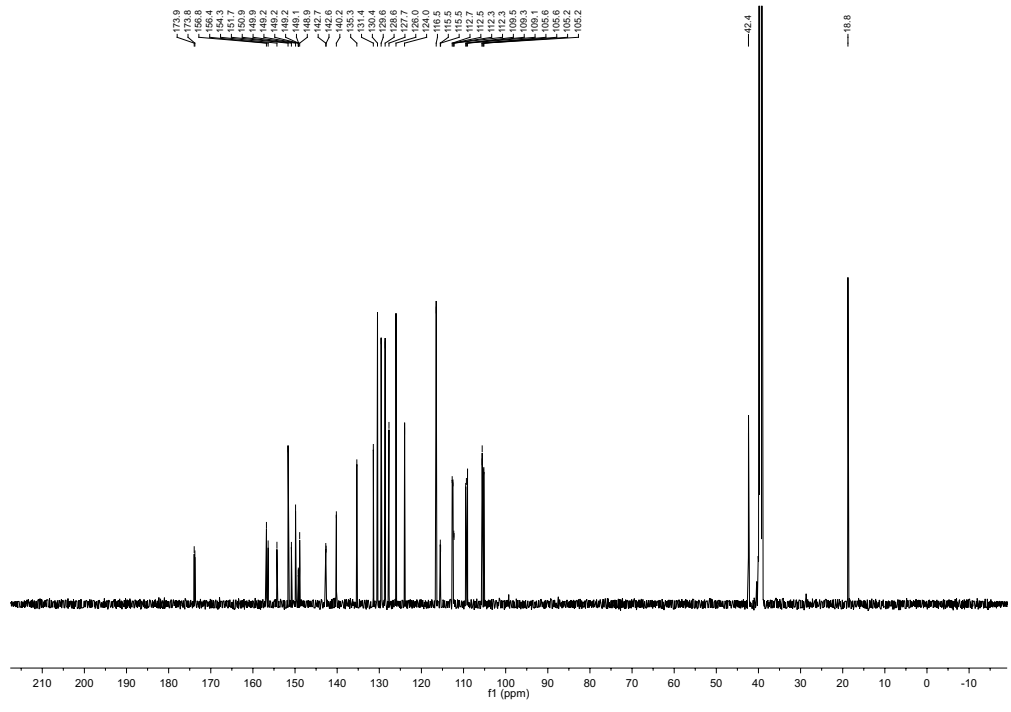

Figure 5-32. ^{13}C NMR (126 MHz, DMSO-d_6) spectrum of **56**.

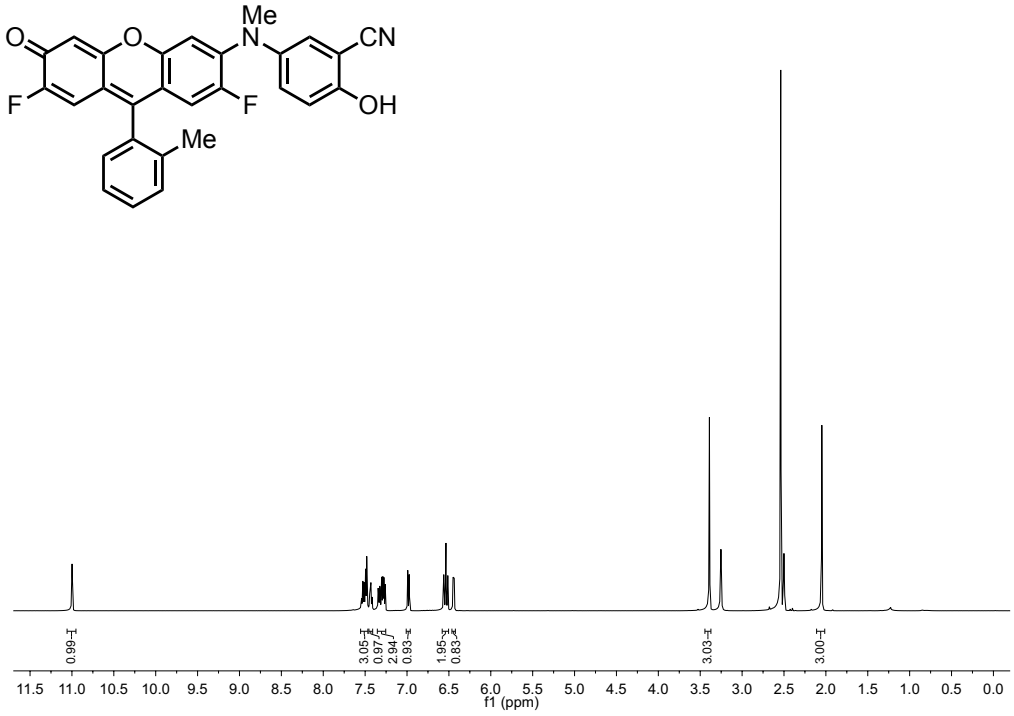

Figure 5-33. ^{1}H NMR (500 MHz, DMSO-d_6) spectrum of **57**.

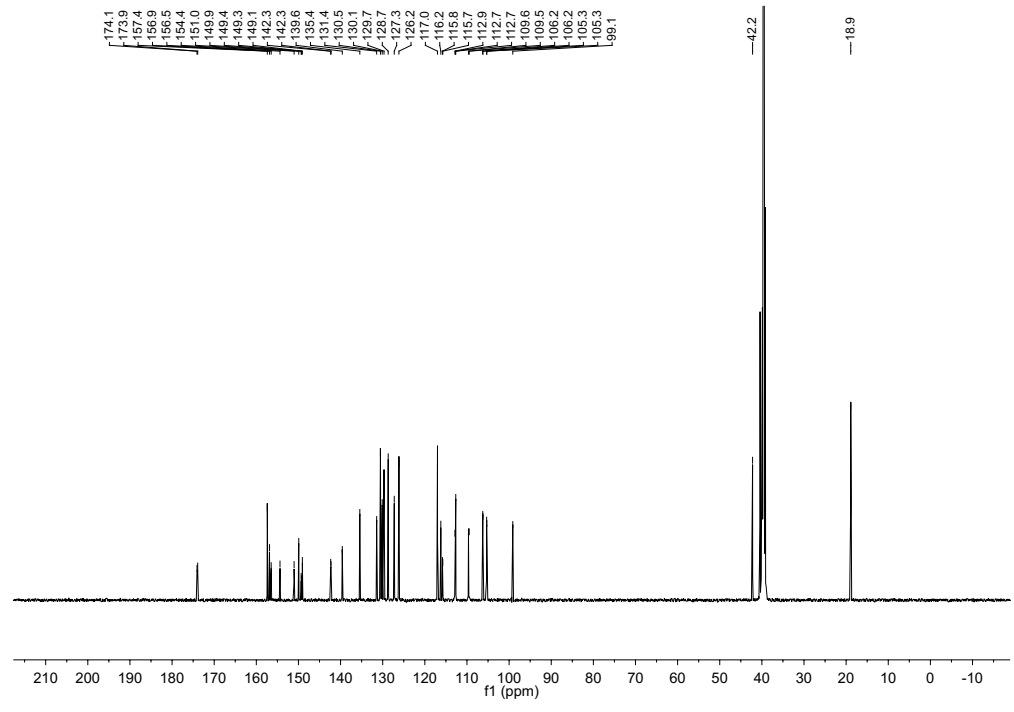

Figure 5-34. ^{13}C NMR (126 MHz, DMSO-d_6) spectrum of **57**.

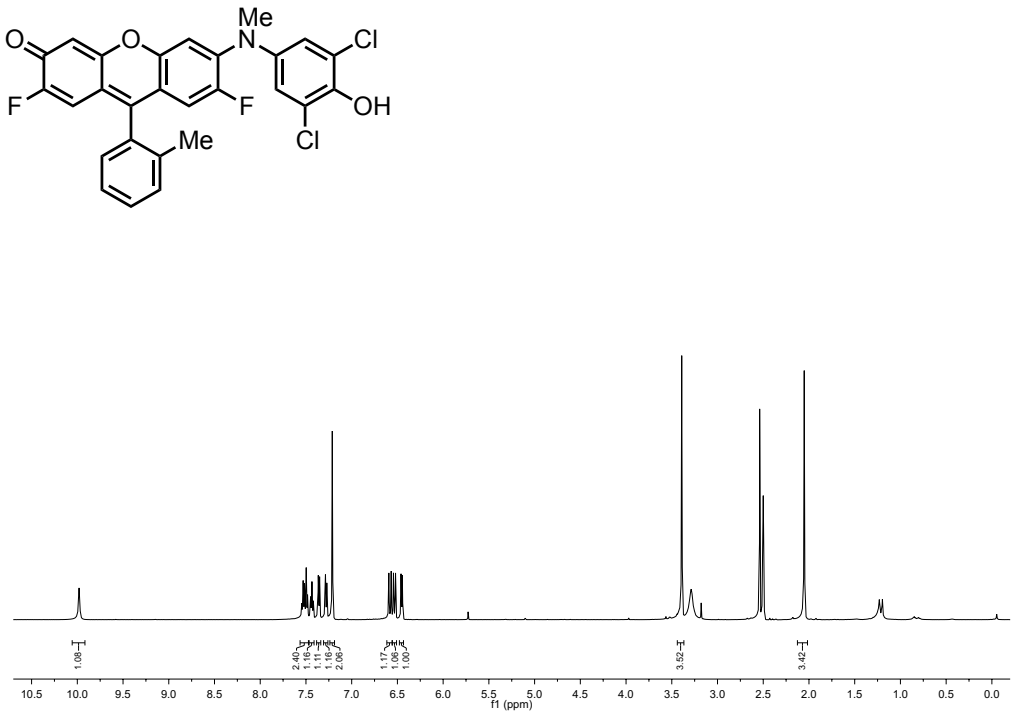

Figure 5-35. ^{1}H NMR (500 MHz, DMSO-d_6) spectrum of **58**.

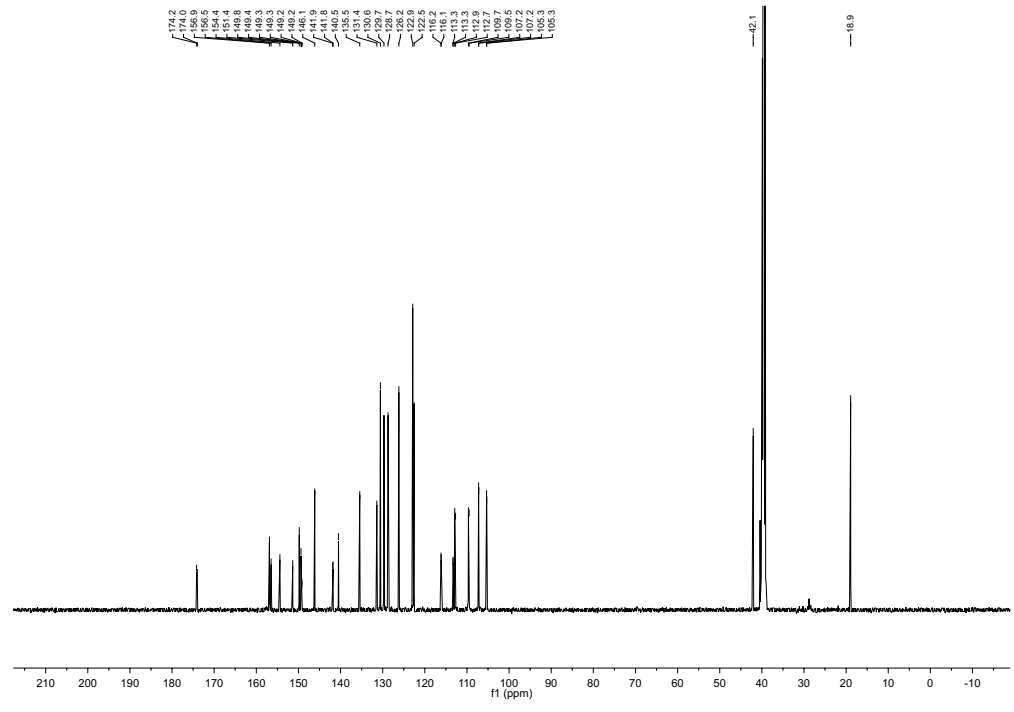

Figure 5-36. ^{13}C NMR (126 MHz, DMSO-d_6) spectrum of **58**.

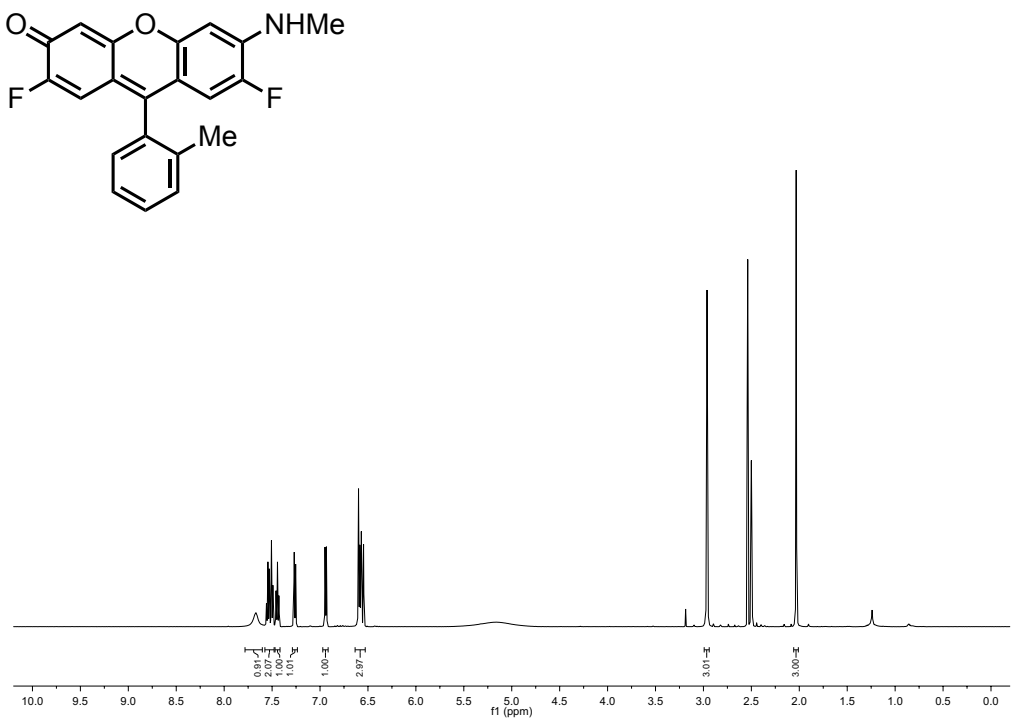

Figure 5-37. ^{1}H NMR (500 MHz, DMSO-d_6) spectrum of **59**.

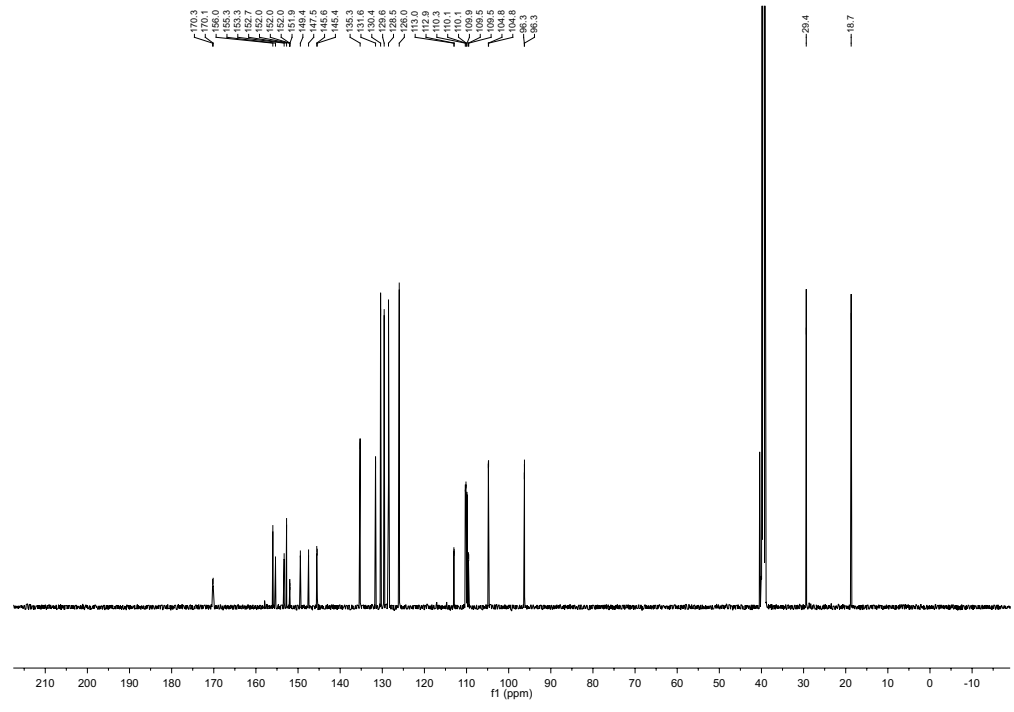

Figure 5-38. ^{13}C NMR (126 MHz, DMSO-d_6) spectrum of **59**.

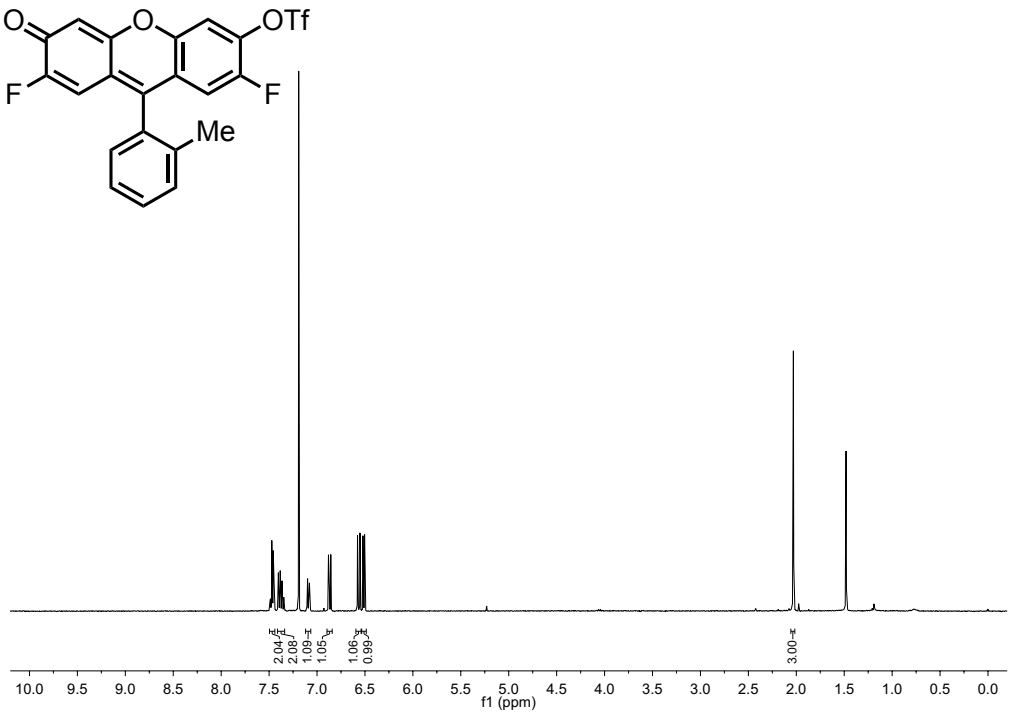

Figure 5-39. ^{1}H NMR (400 MHz, Chloroform-*d*) spectrum of **60**.

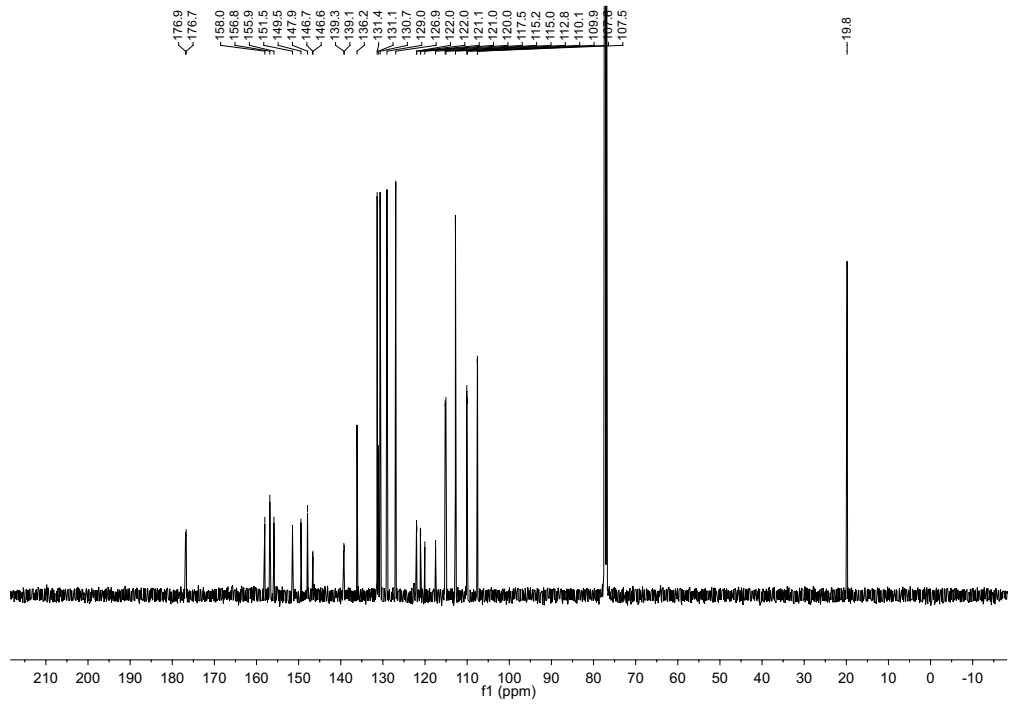

Figure 5-40. ^{13}C NMR (126 MHz, Chloroform-*d*) spectrum of **60**.

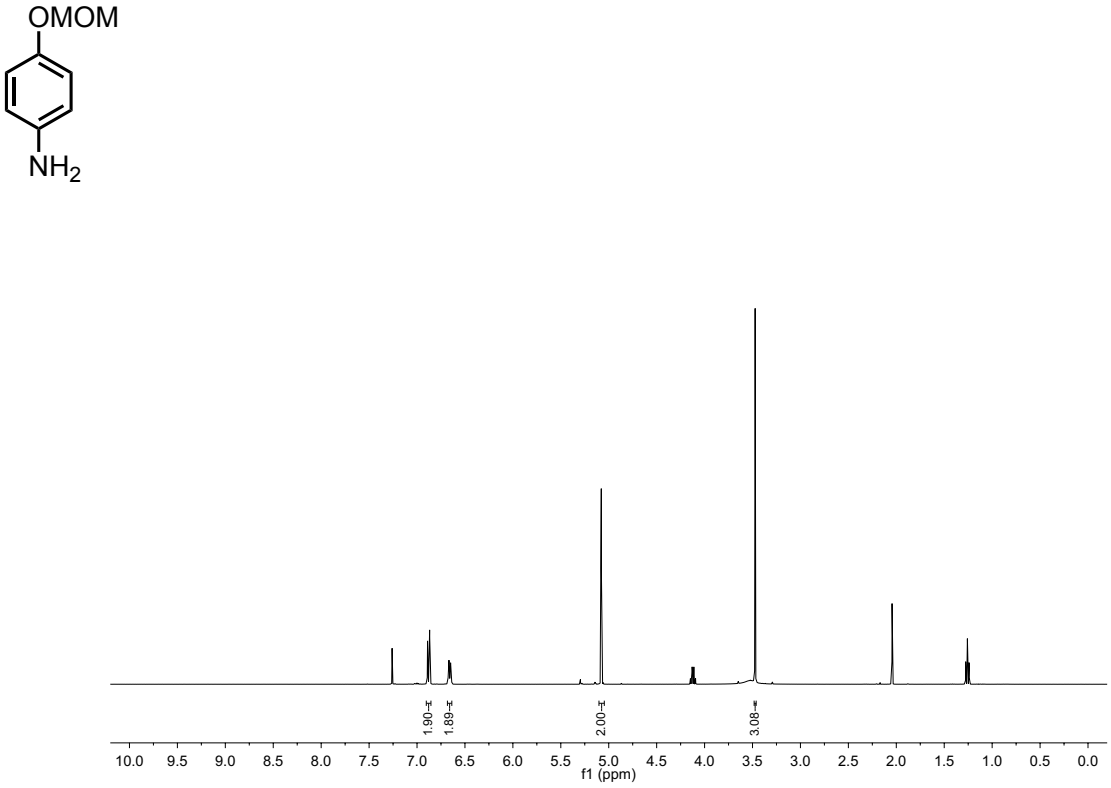

Figure 5-41. ^{1}H NMR (400 MHz, Chloroform-*d*) spectrum of **61**.

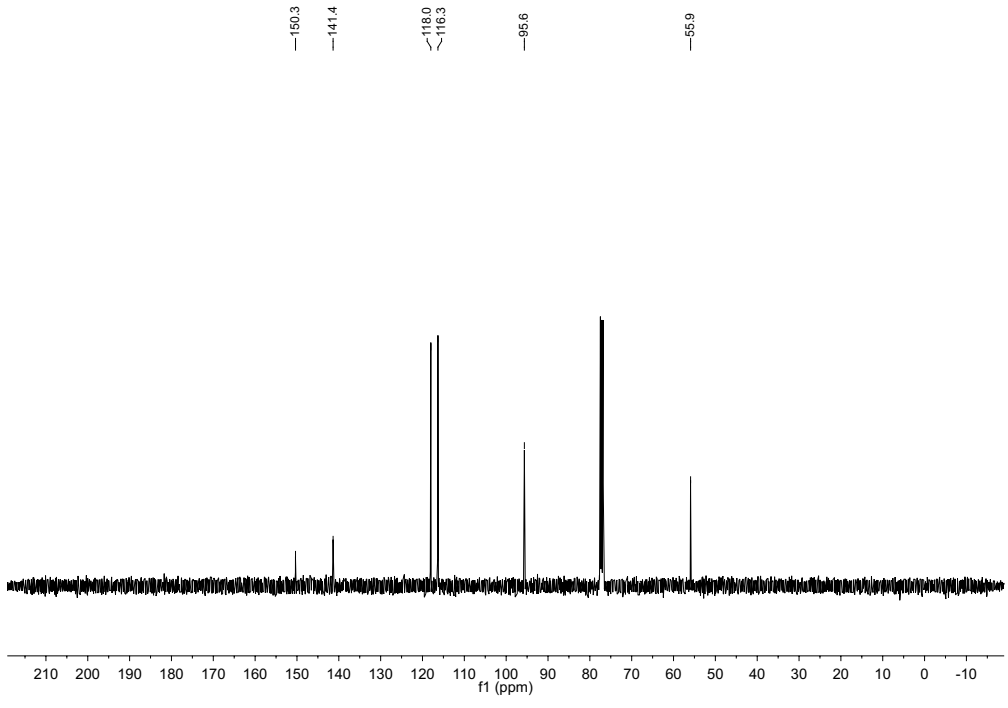

Figure 5-42. ^{13}C NMR (101 MHz, Chloroform-*d*) spectrum of **61**.

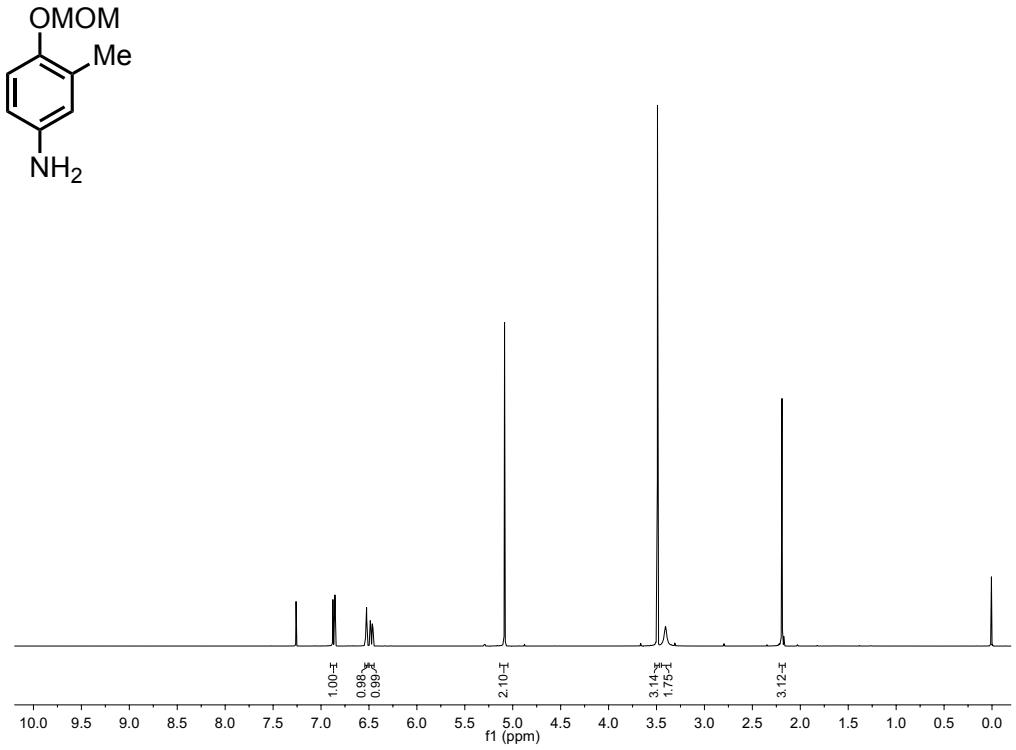

Figure 5-43. ^{1}H NMR (400 MHz, Chloroform-*d*) spectrum of **62**.

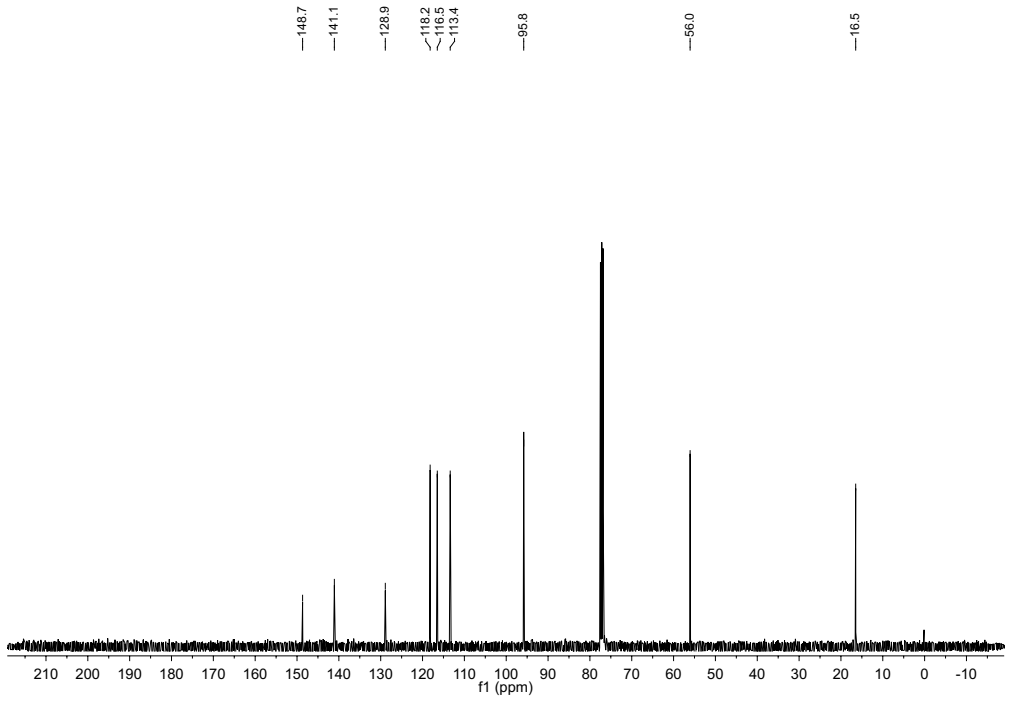

Figure 5-44. ^{13}C NMR (101 MHz, Chloroform-*d*) spectrum of **62**.

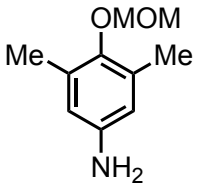

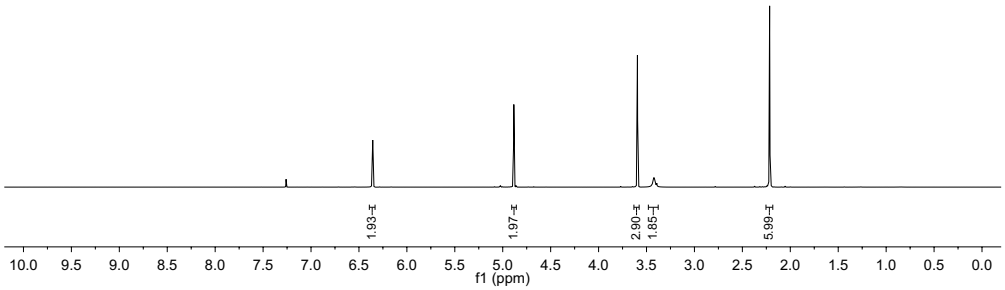

Figure 5-45. ^{1}H NMR (400 MHz, Chloroform-*d*) spectrum of **63**.

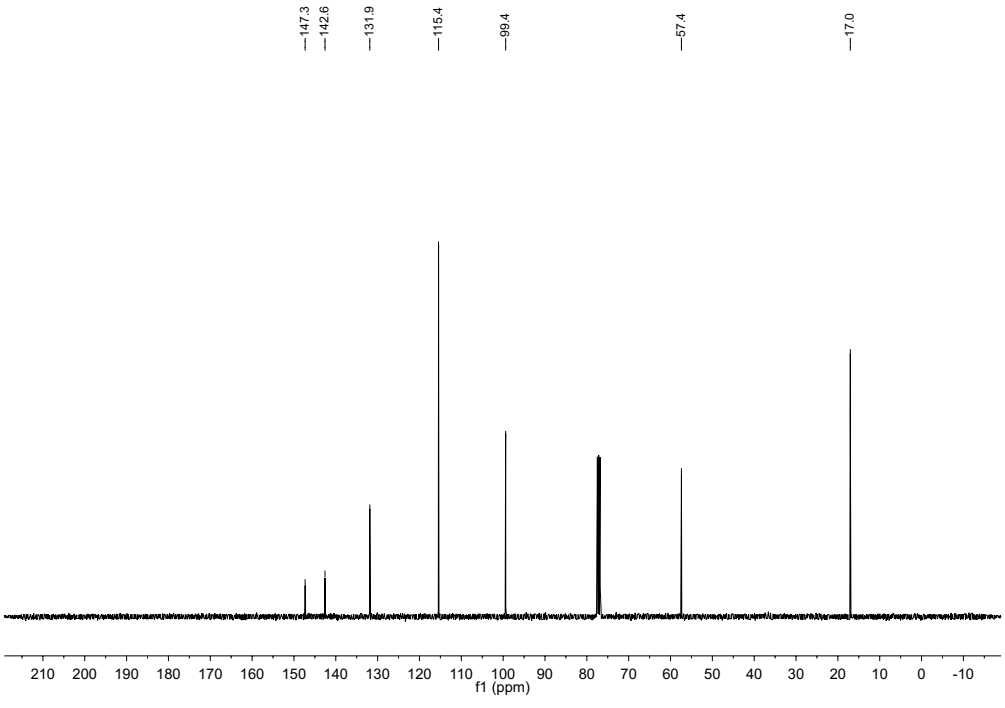

Figure 5-46. ^{13}C NMR (101 MHz, Chloroform-*d*) spectrum of **63**.

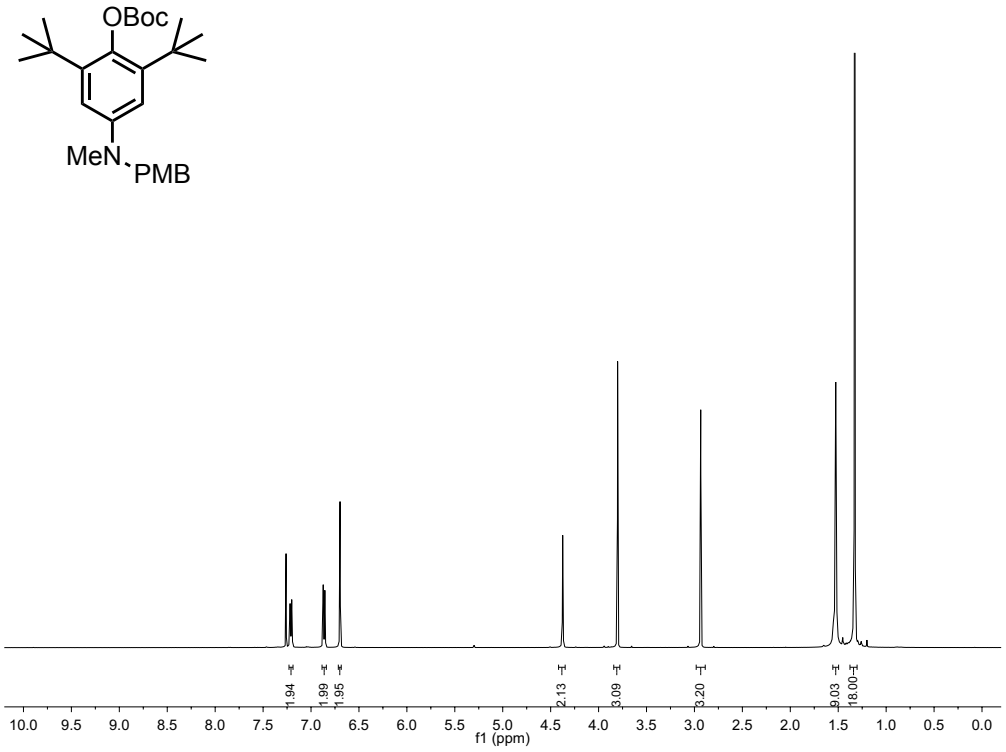

Figure 5-47. ^{1}H NMR (500 MHz, Chloroform-*d*) spectrum of **64**.

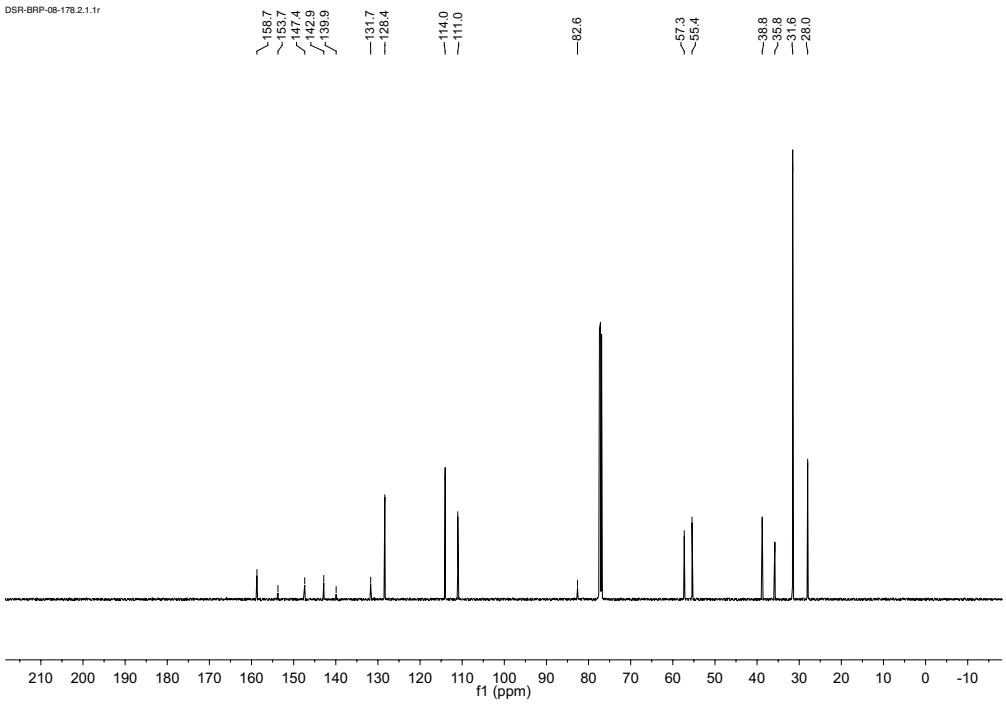

Figure 5-48. ^{13}C NMR (126 MHz, Chloroform-*d*) spectrum of **64**.

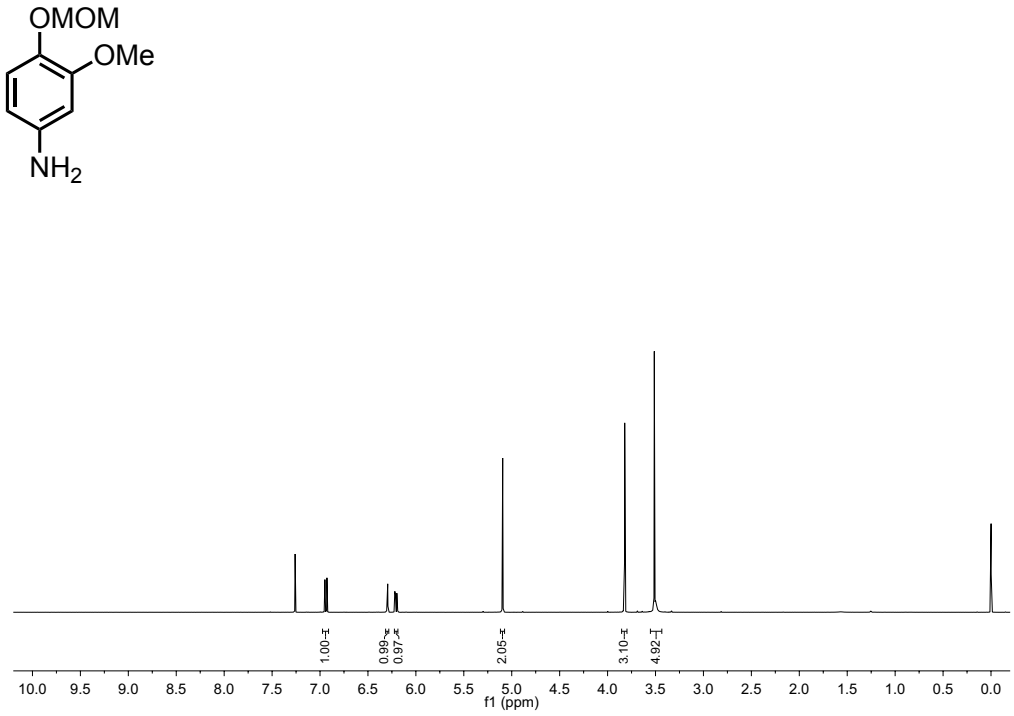

Figure 5-49. ^{1}H NMR (400 MHz, Chloroform-*d*) spectrum of **65**.

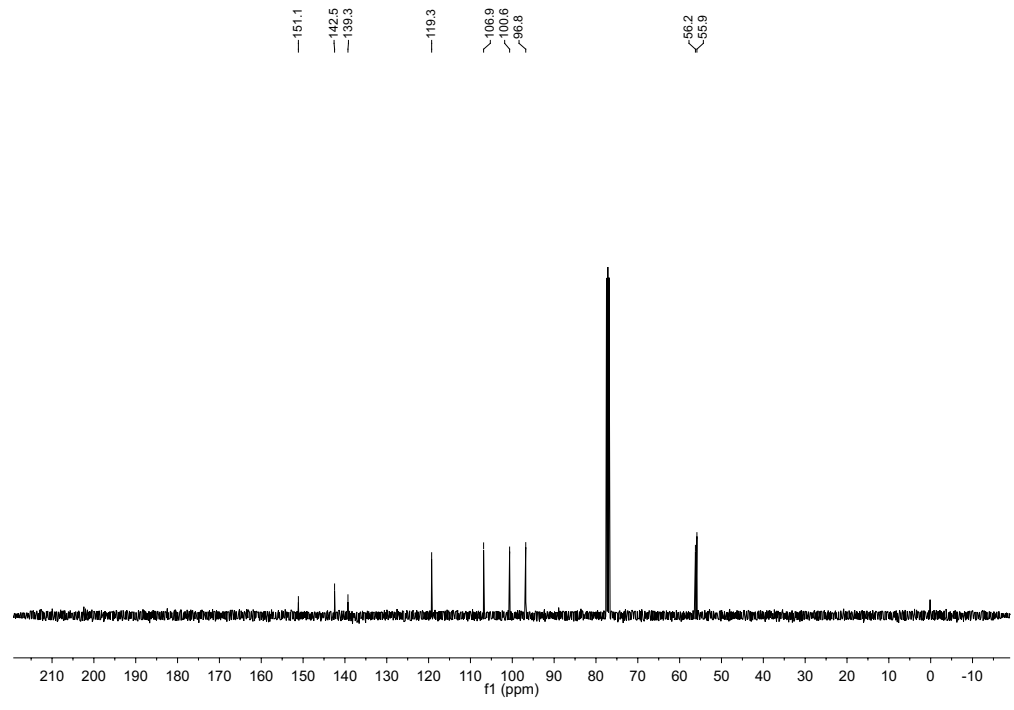

Figure 5-50. ^{13}C NMR (101 MHz, Chloroform-*d*) spectrum of **65**.

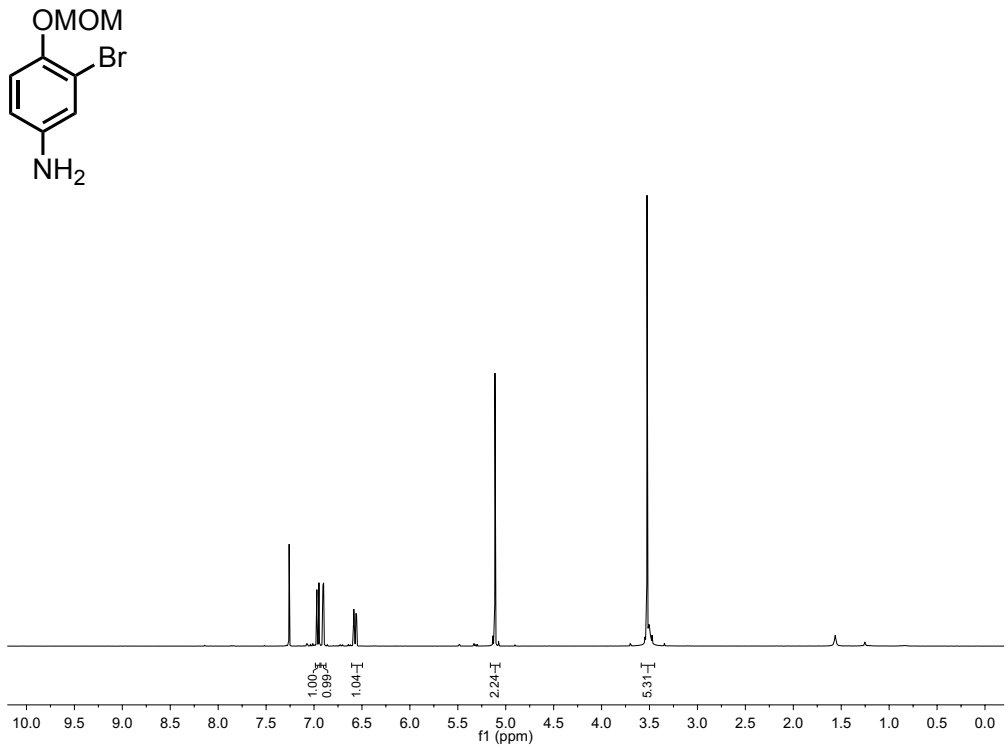

Figure 5-51. ^{1}H NMR (400 MHz, Chloroform-*d*) spectrum of **66**.

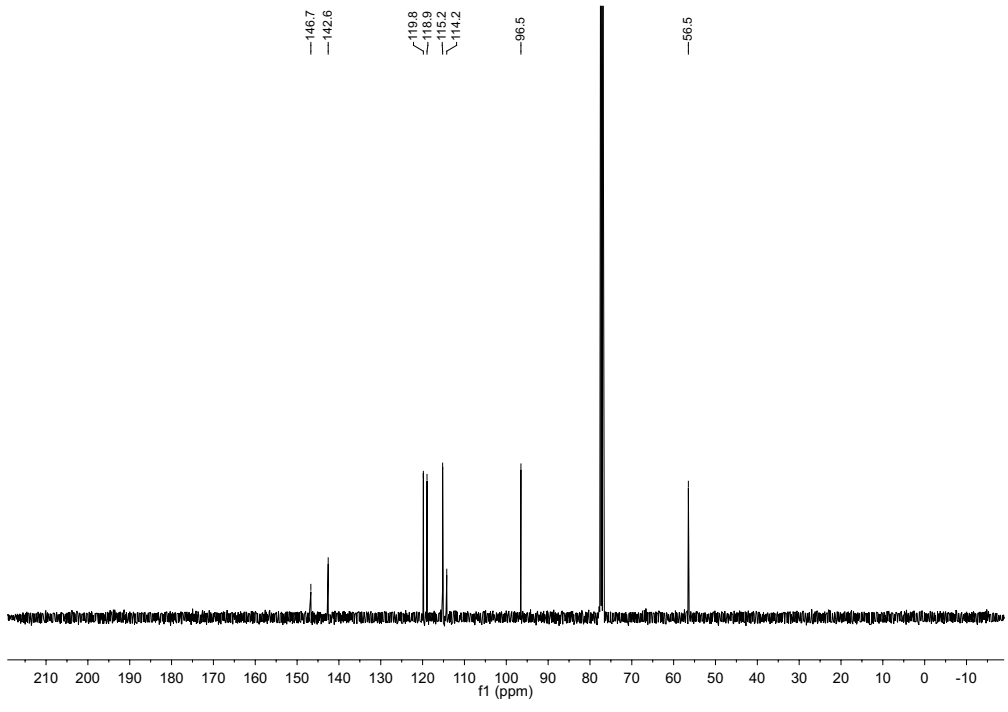

Figure 5-52. ^{13}C NMR (101 MHz, Chloroform-*d*) spectrum of **66**.

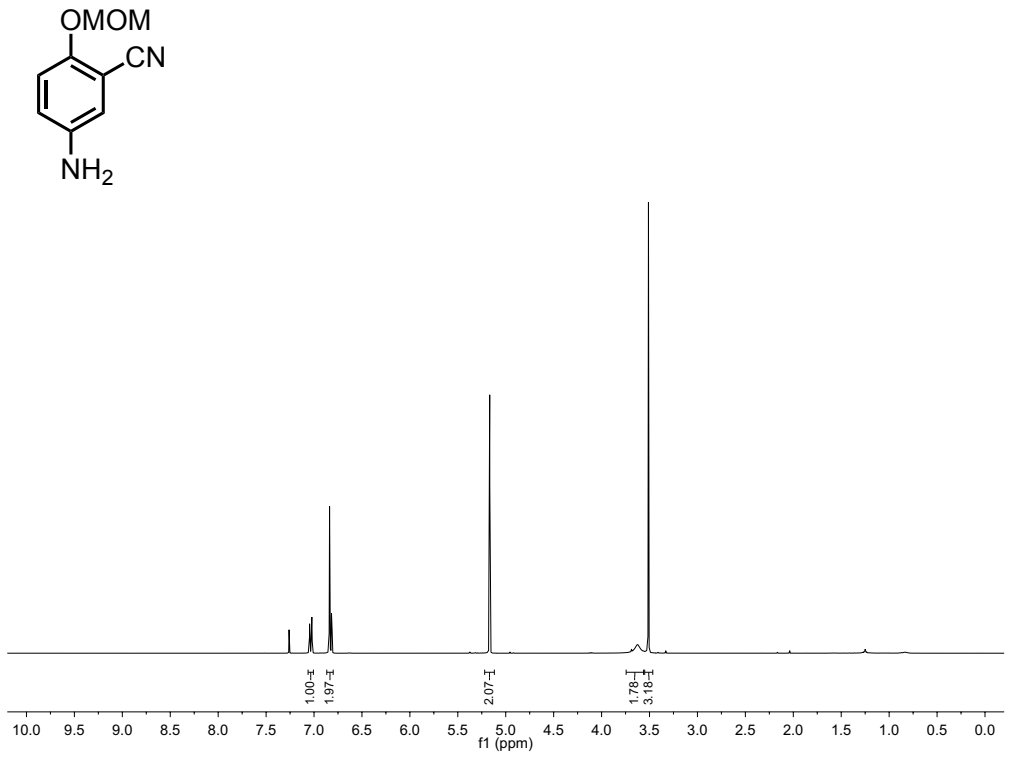

Figure 5-53. ^{1}H NMR (400 MHz, Chloroform-*d*) spectrum of **67**.

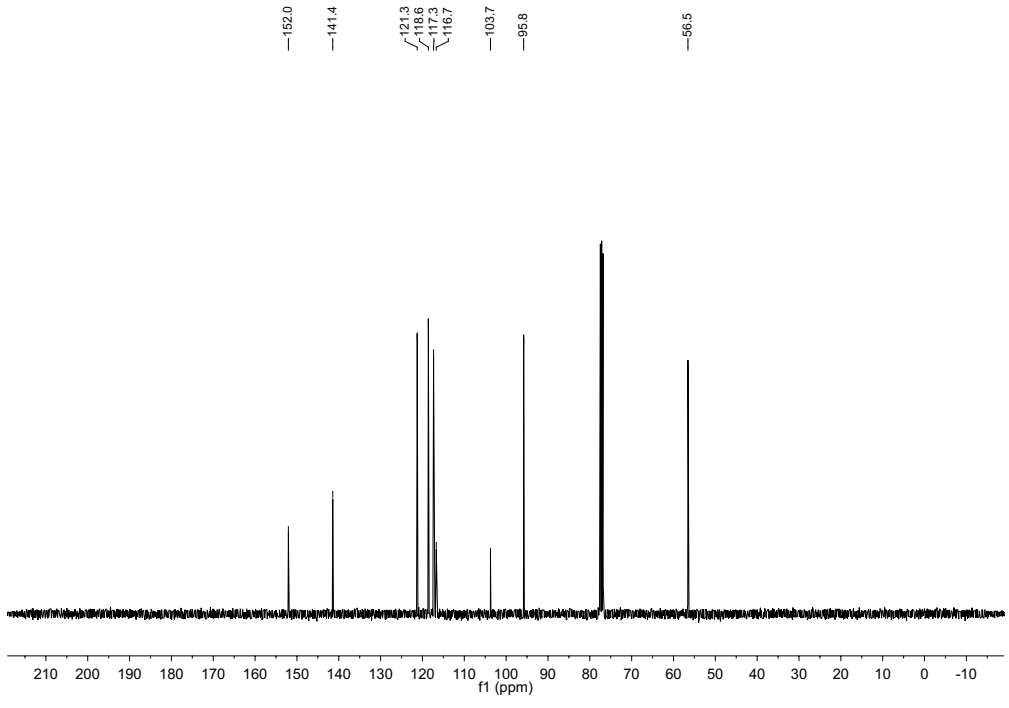

Figure 5-54. ^{13}C NMR (101 MHz, Chloroform-*d*) spectrum of **67**.

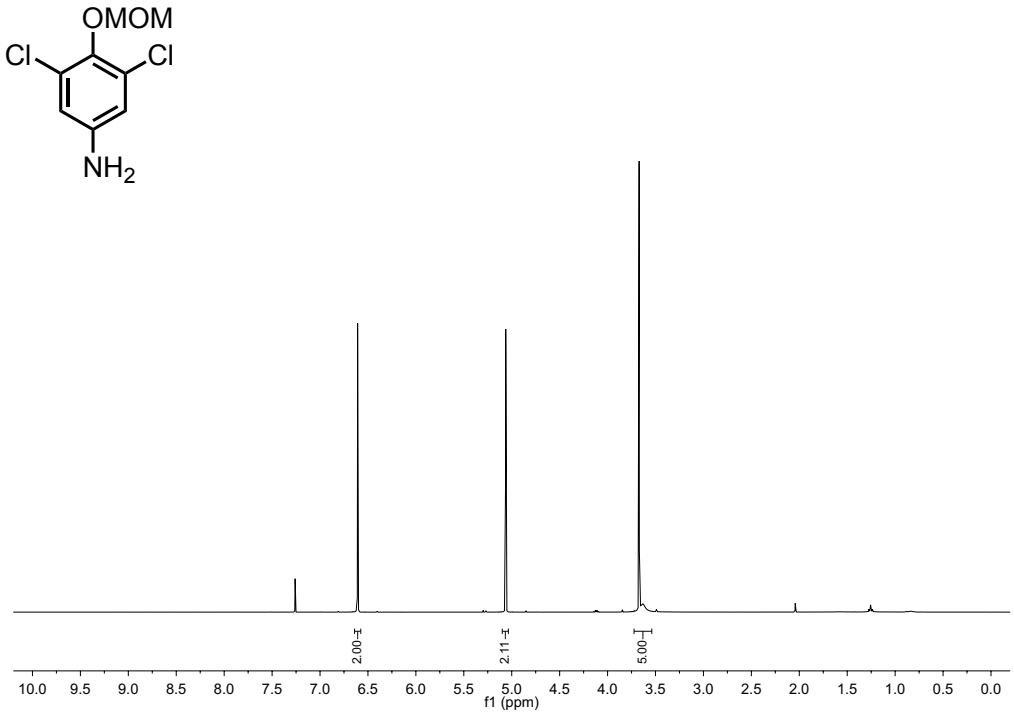

Figure 5-55. ^{1}H NMR (400 MHz, Chloroform-*d*) spectrum of **68**.

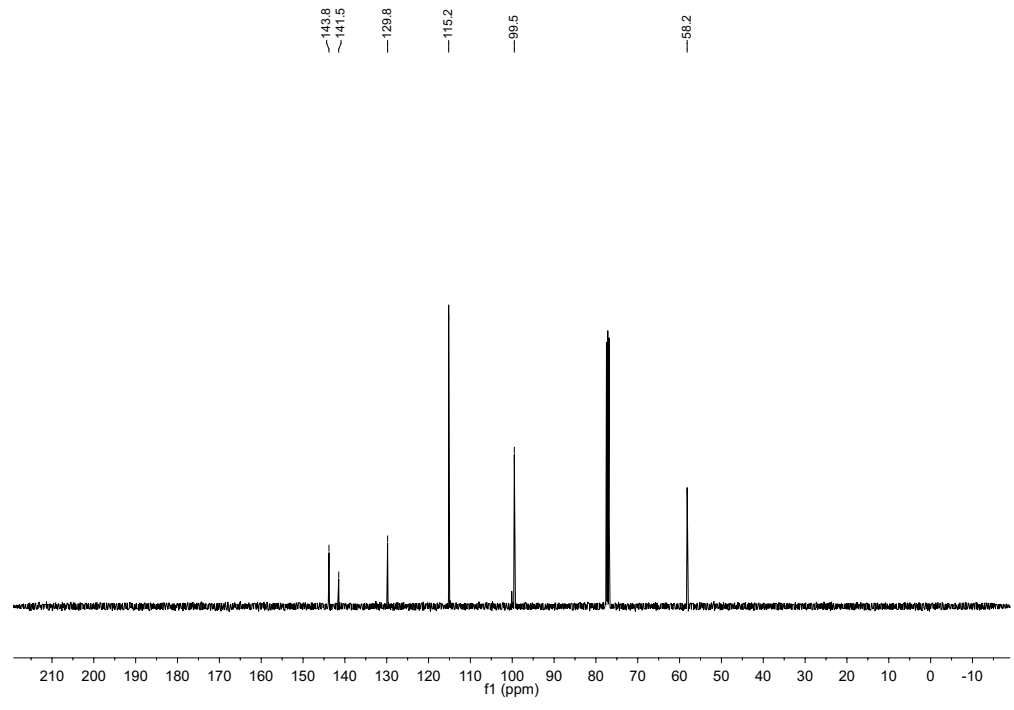

Figure 5-56. ^{13}C NMR (101 MHz, Chloroform-*d*) spectrum of **68**.

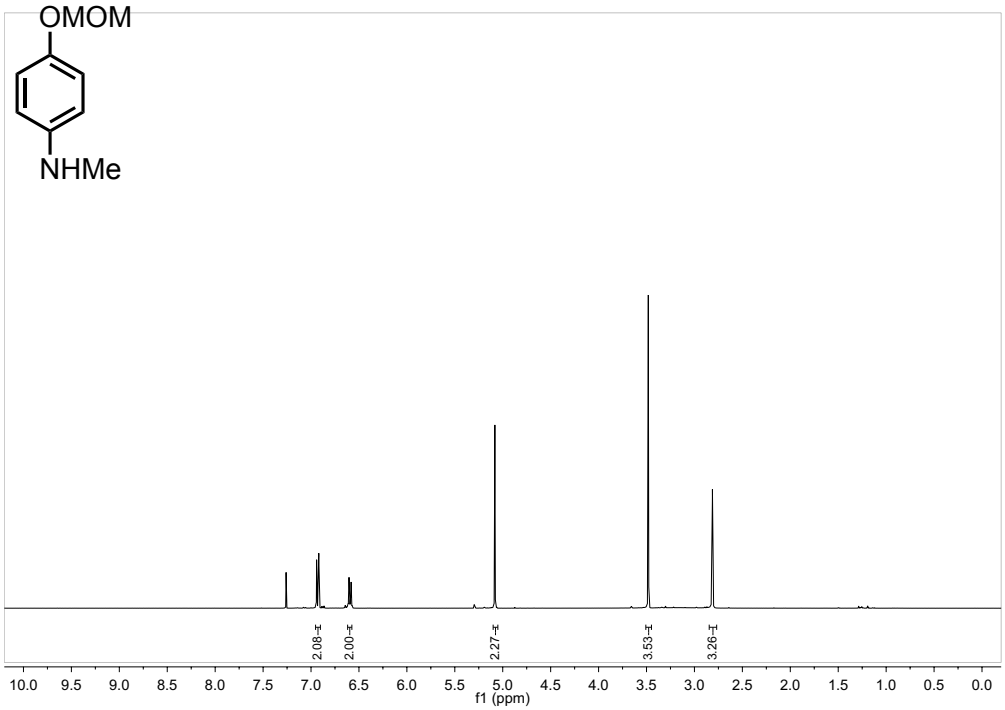

Figure 5-57. ^{1}H NMR (400 MHz, Chloroform-*d*) spectrum of **69**.

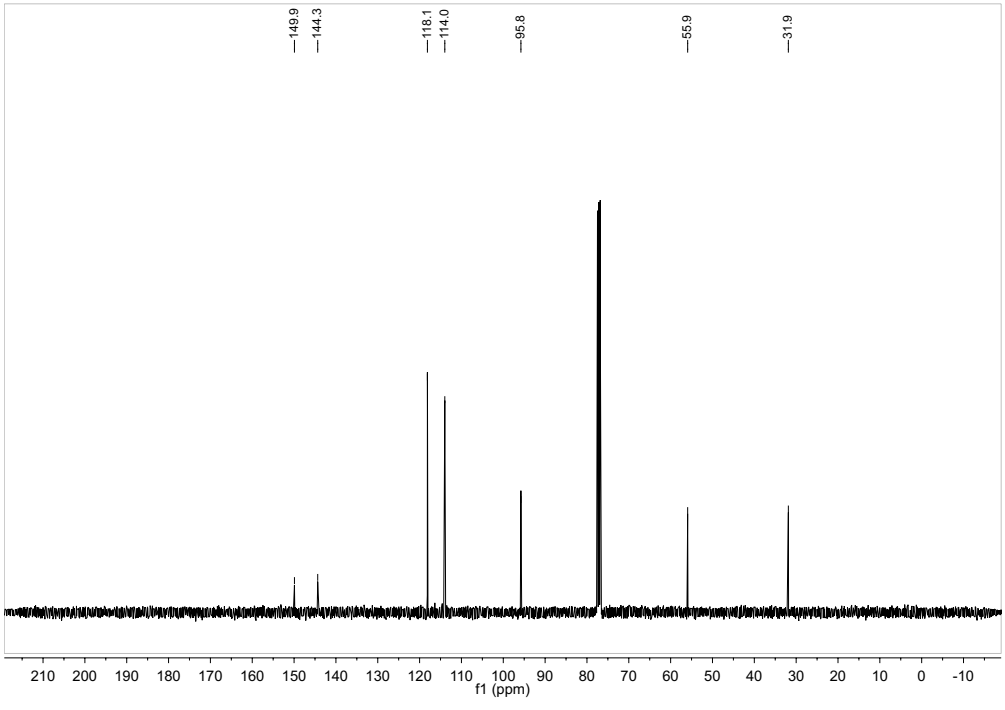

Figure 5-58. ^{13}C NMR (101 MHz, Chloroform-*d*) spectrum of **69**.

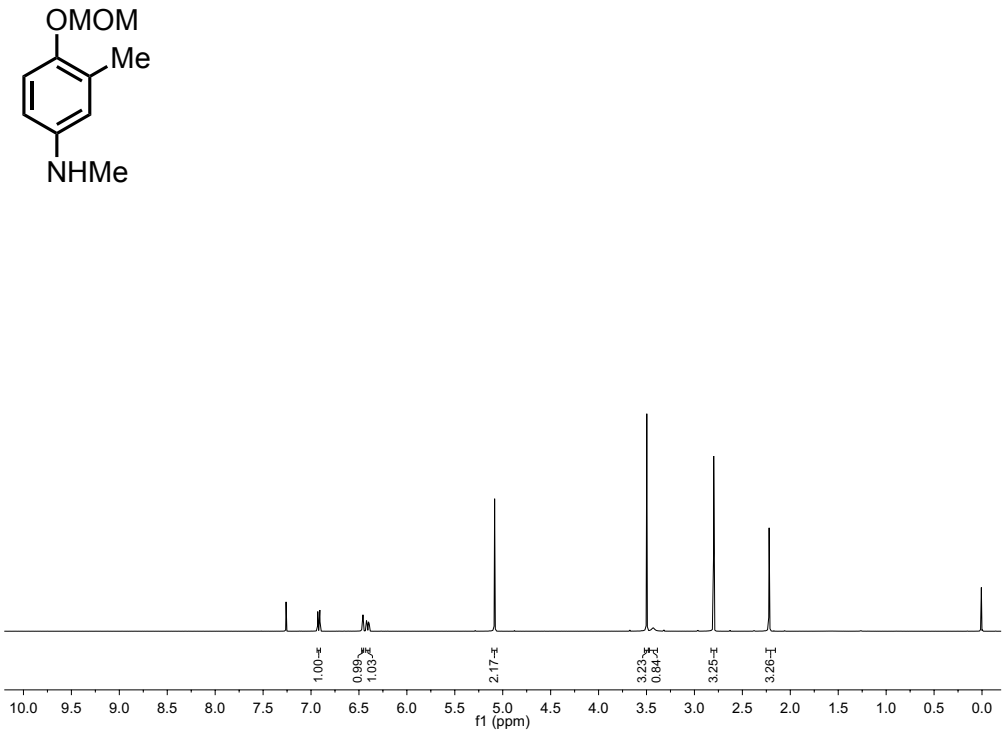

Figure 5-59. ^{1}H NMR (400 MHz, Chloroform-*d*) spectrum of **70**.

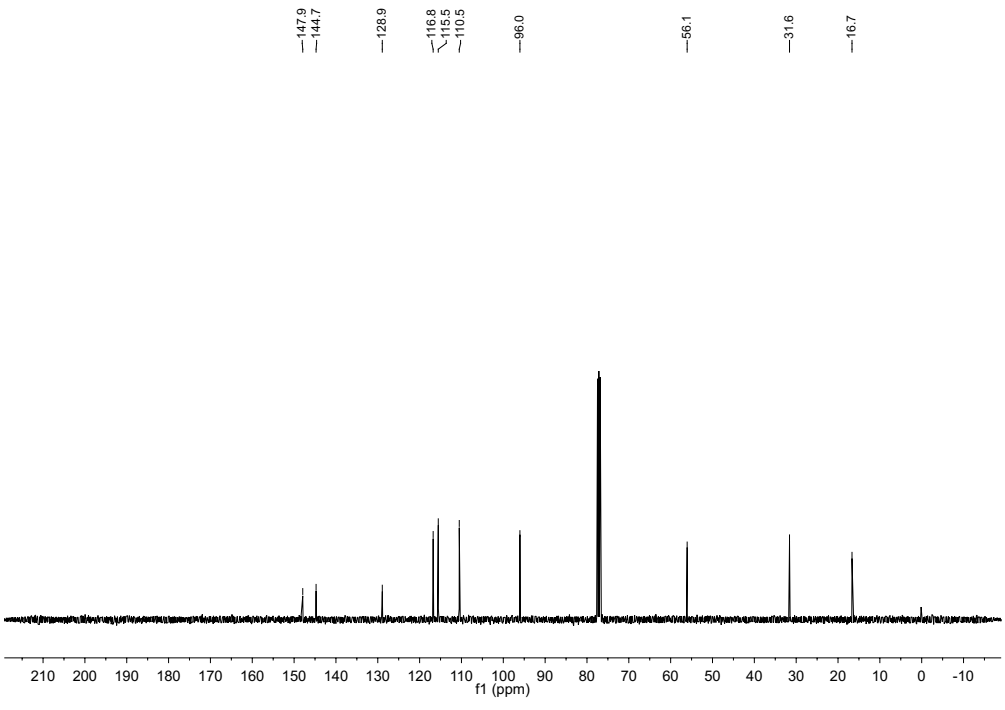

Figure 5-60. ^{13}C NMR (101 MHz, Chloroform-*d*) spectrum of **70**.

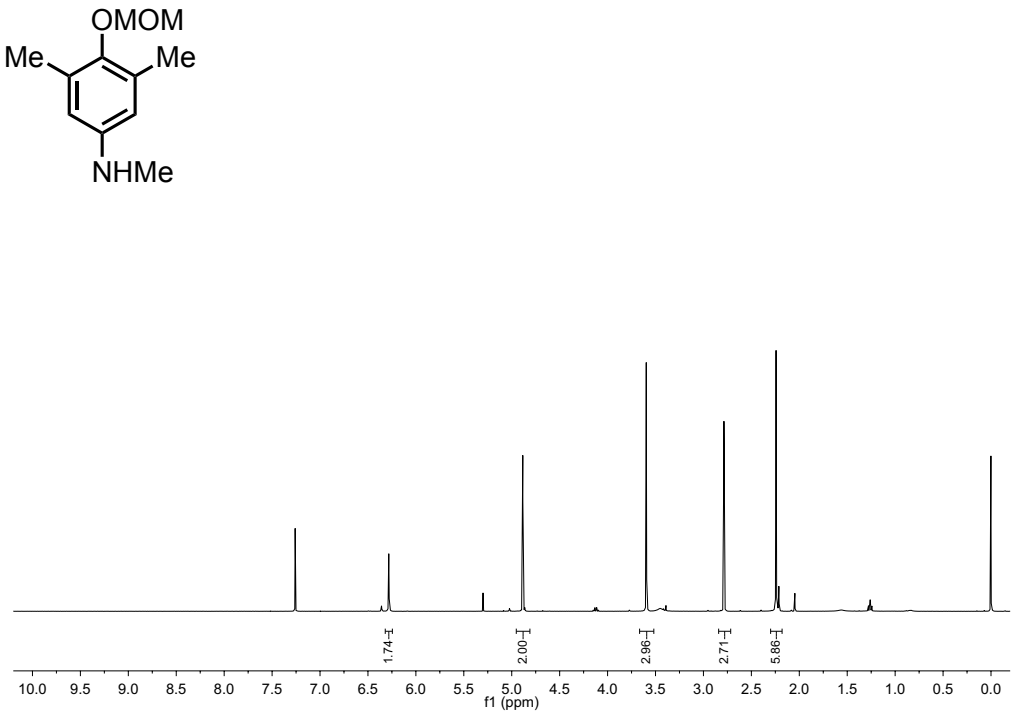

Figure 5-61. ^{1}H NMR (400 MHz, Chloroform-*d*) spectrum of **71**.

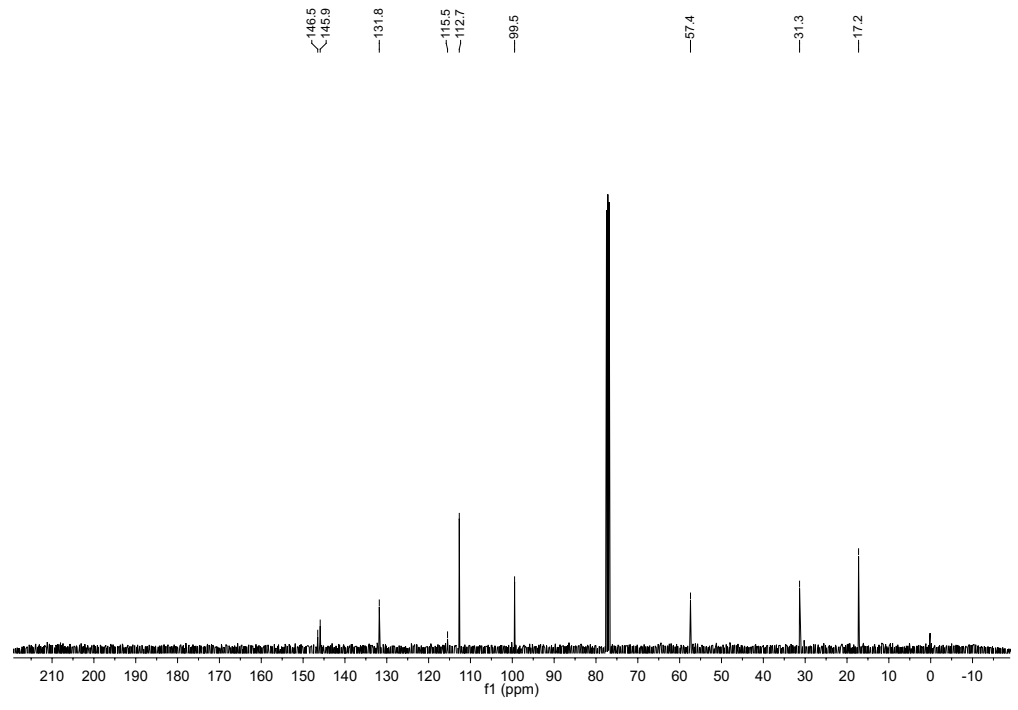

Figure 5-62. ^{13}C NMR (101 MHz, Chloroform-*d*) spectrum of **71**.

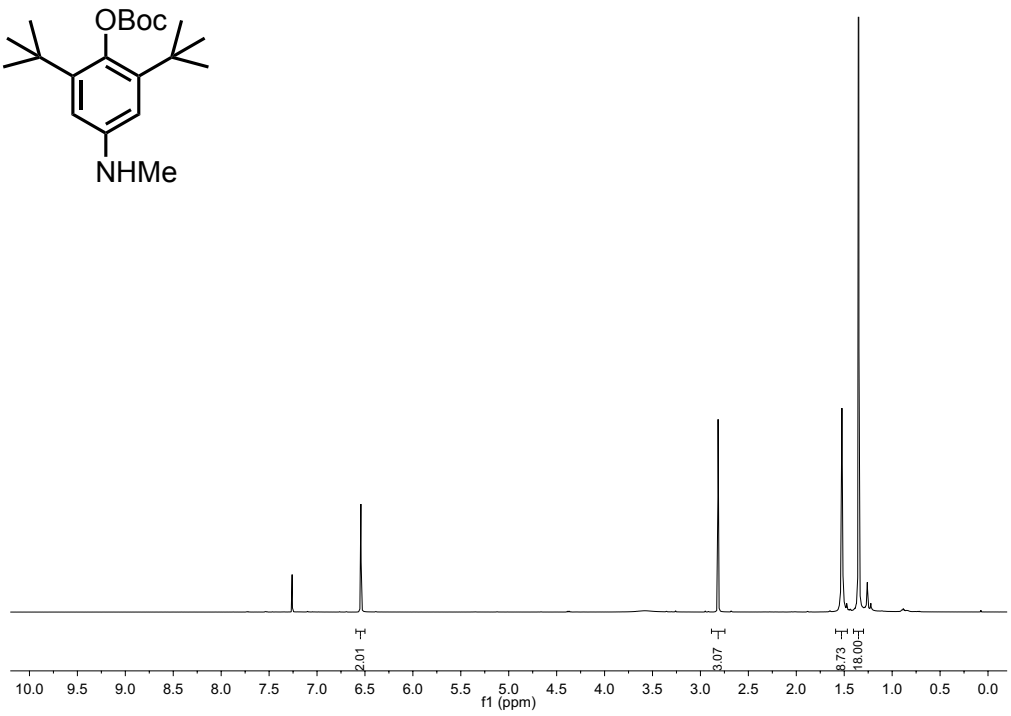

Figure 5-63. ^{1}H NMR (500 MHz, Chloroform-*d*) spectrum of **72**.

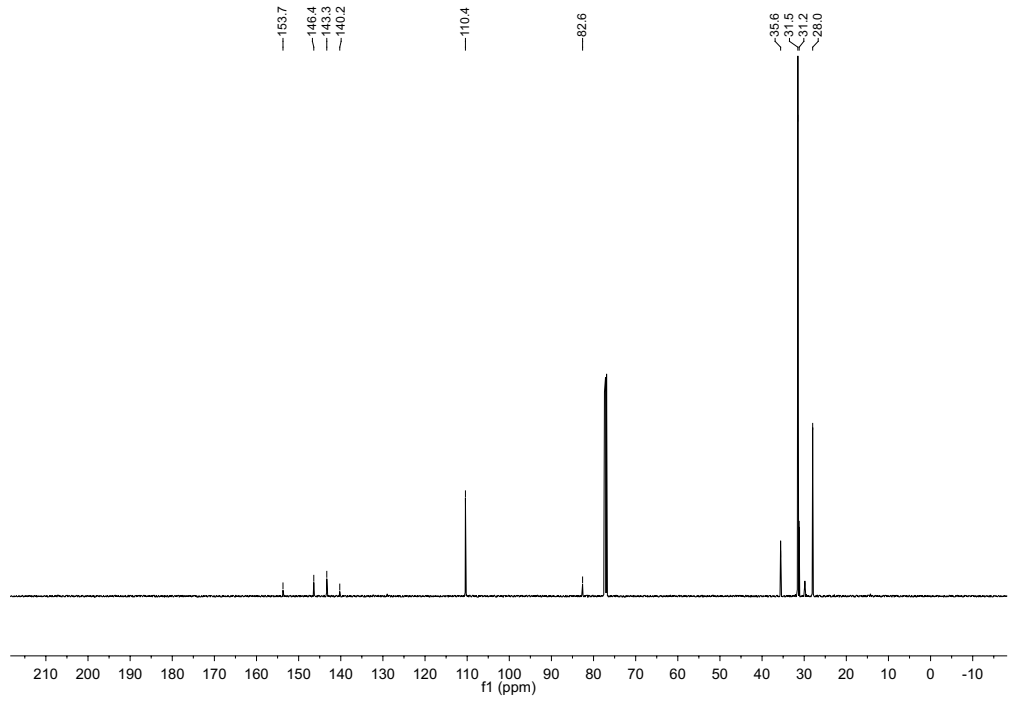

Figure 5-64. ^{13}C NMR (126 MHz, Chloroform-*d*) spectrum of **72**.

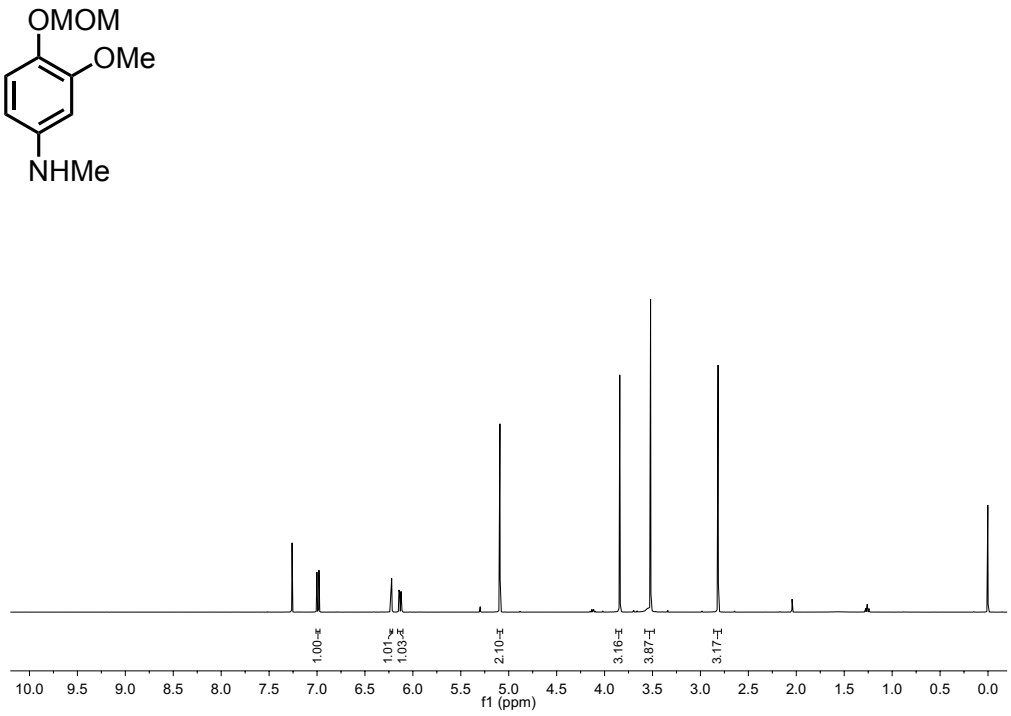

Figure 5-65. ^{1}H NMR (400 MHz, Chloroform-*d*) spectrum of **73**.

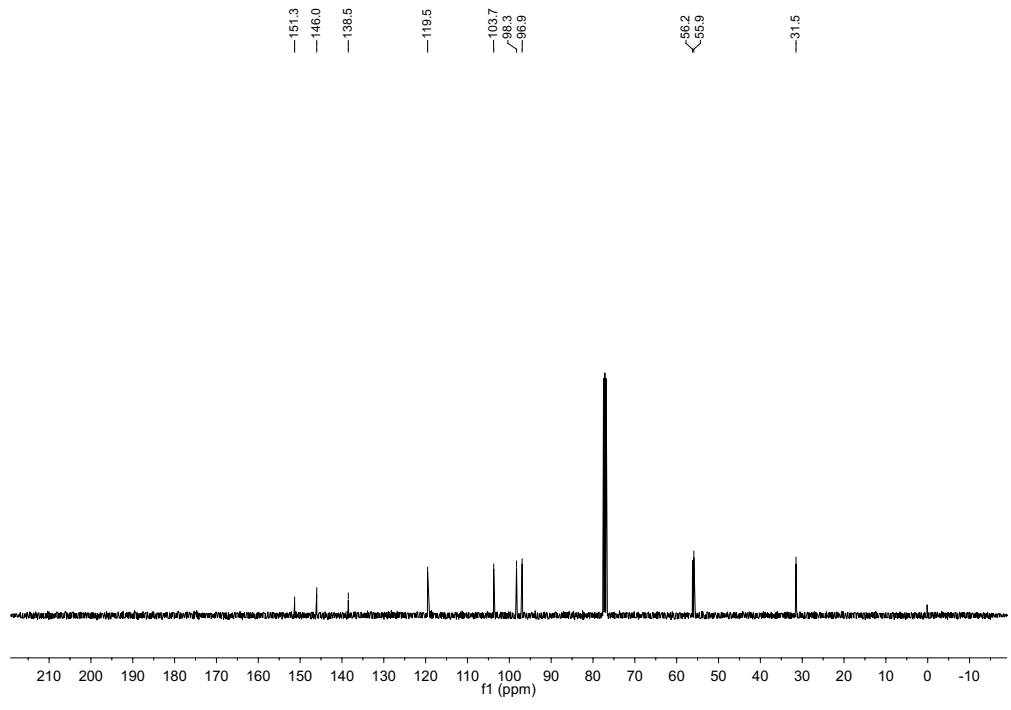

Figure 5-66. ^{13}C NMR (101 MHz, Chloroform-*d*) spectrum of **73**.

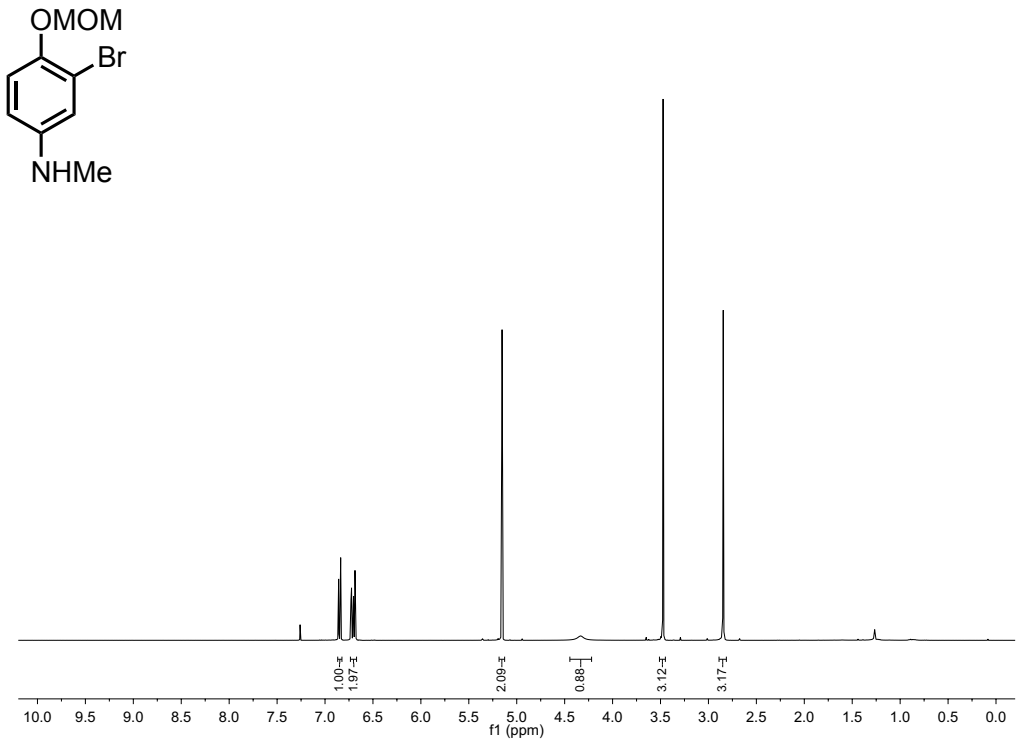

Figure 5-67. ^{1}H NMR (400 MHz, Chloroform-*d*) spectrum of **74**.

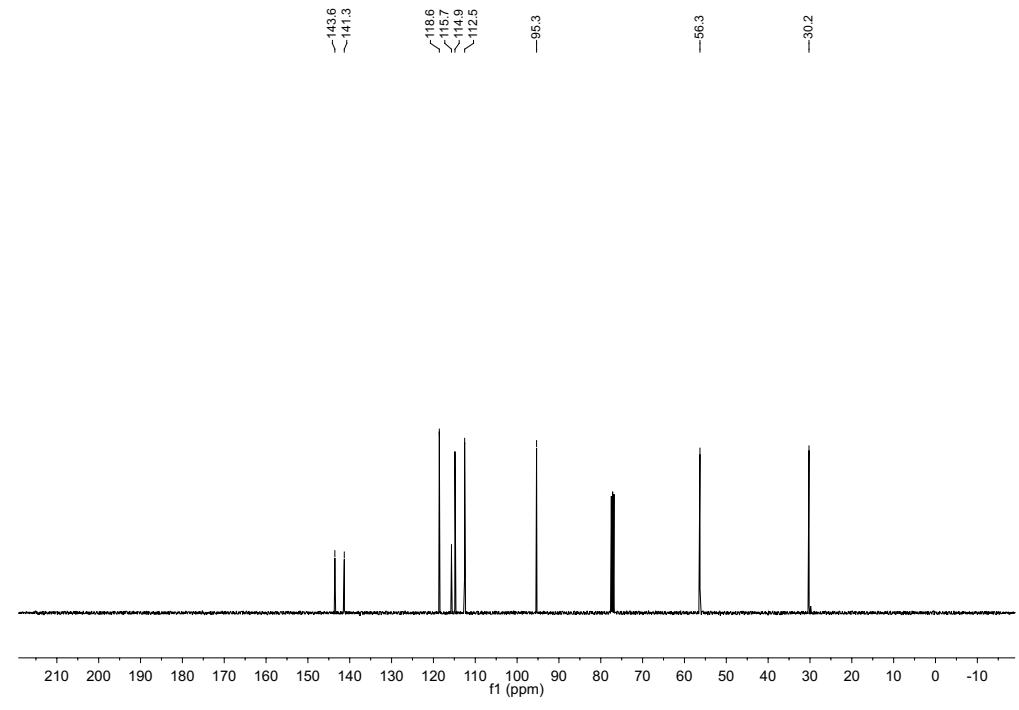

Figure 5-68. ^{13}C NMR (101 MHz, Chloroform-*d*) spectrum of **74**.

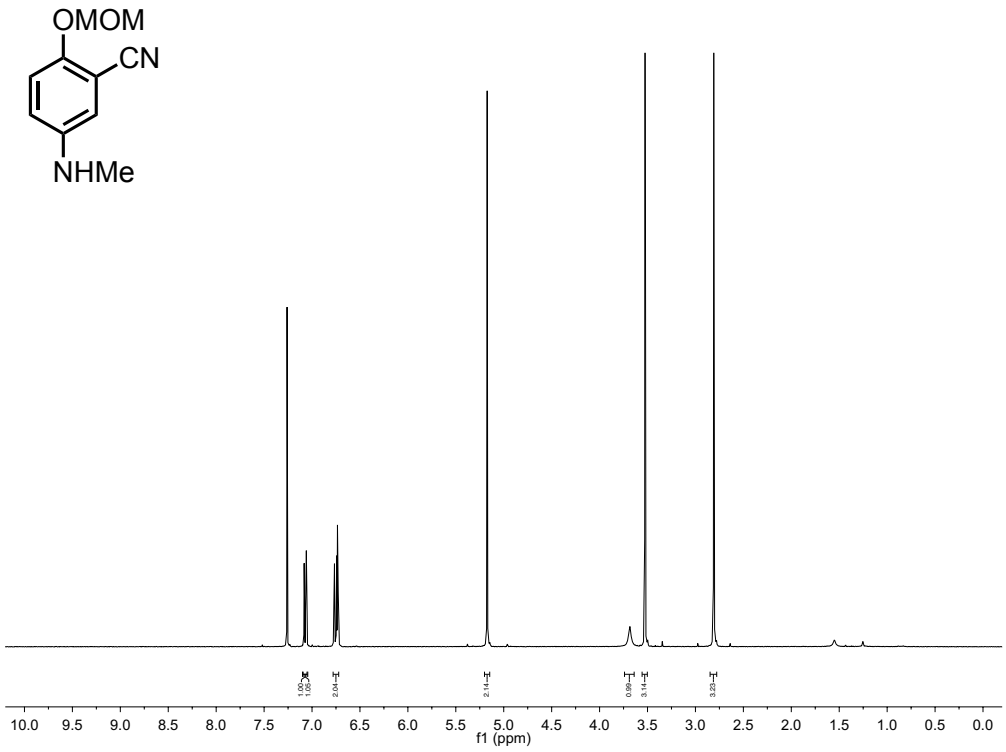

Figure 5-69. ^{1}H NMR (400 MHz, Chloroform-*d*) spectrum of **75**.

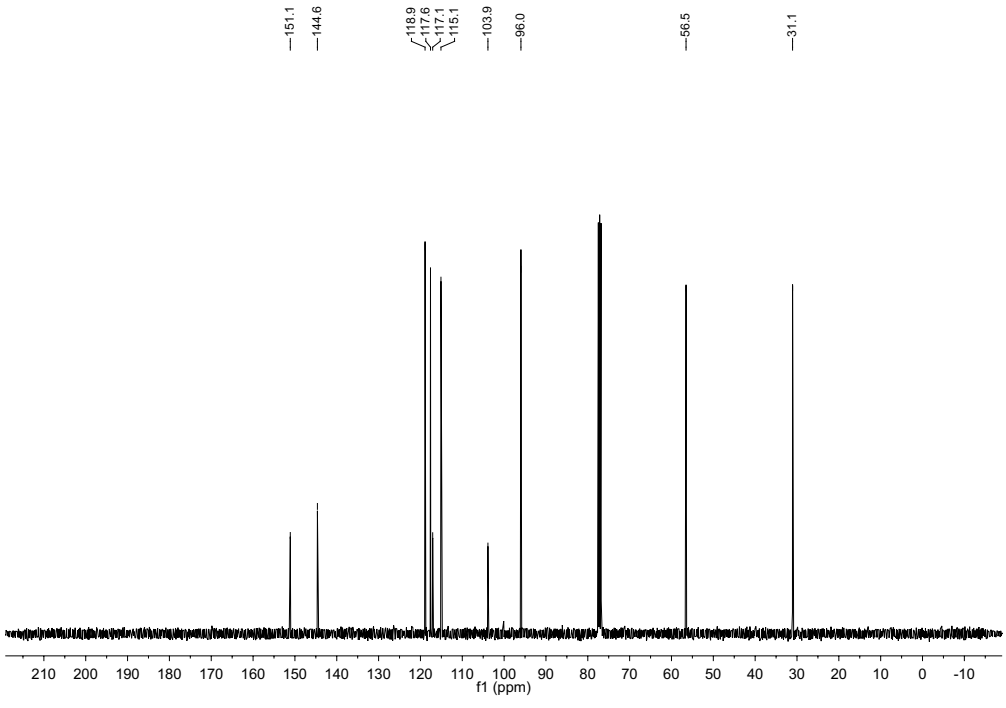

Figure 5-70. ^{13}C NMR (101 MHz, Chloroform-*d*) spectrum of **75**.

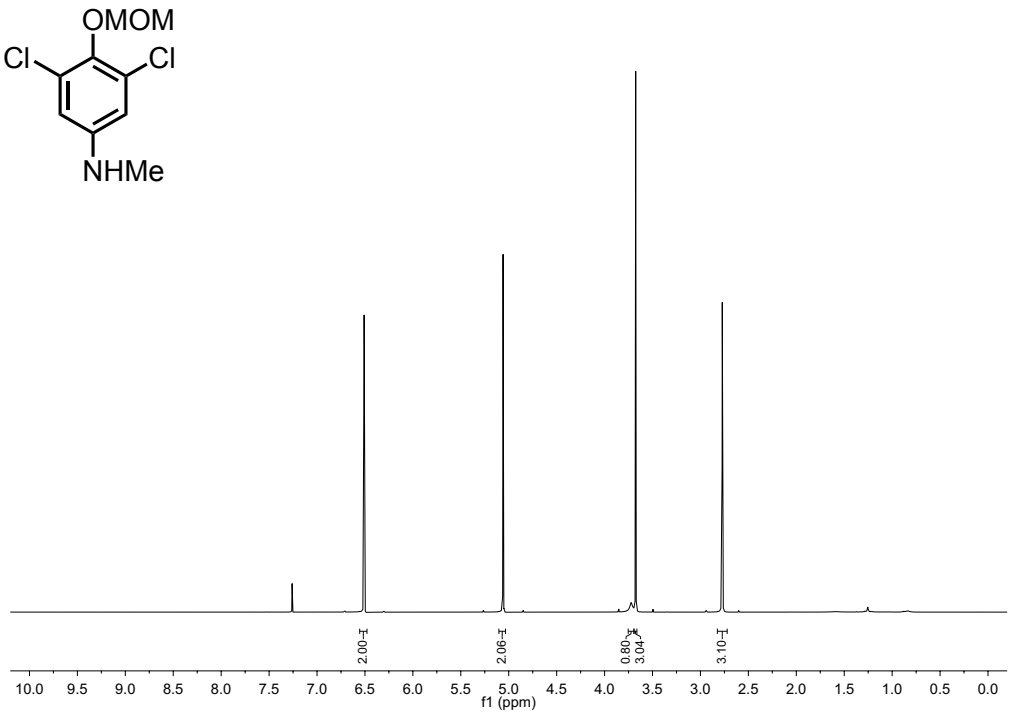

Figure 5-71. ^{1}H NMR (400 MHz, Chloroform-*d*) spectrum of **76**.

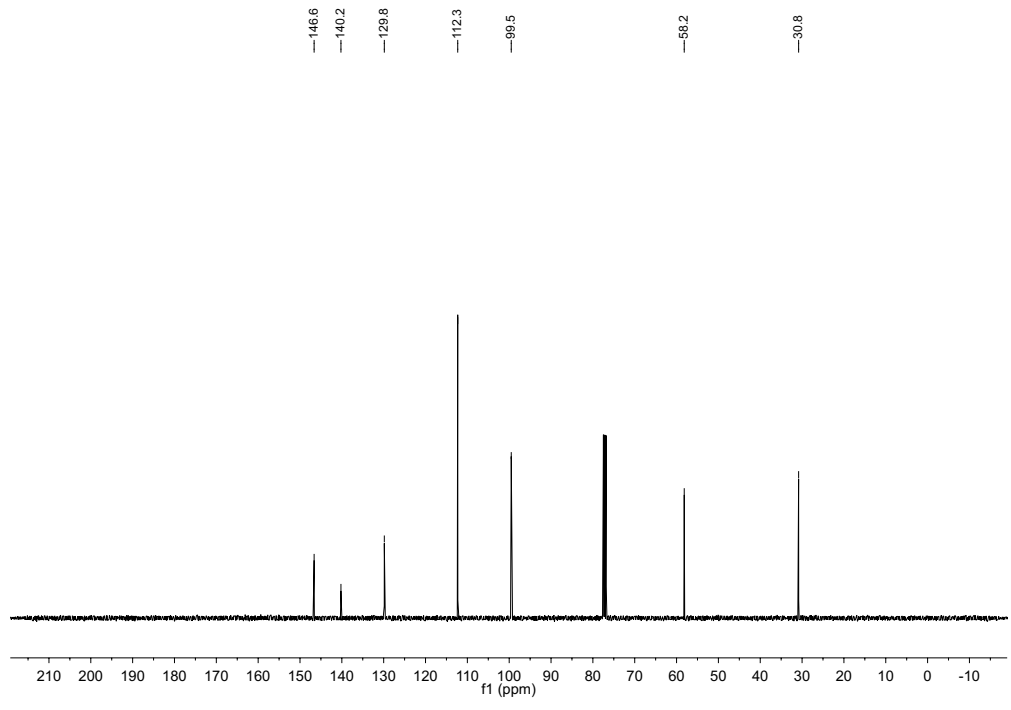

Figure 5-72. ^{13}C NMR (101 MHz, Chloroform-*d*) spectrum of **76**.

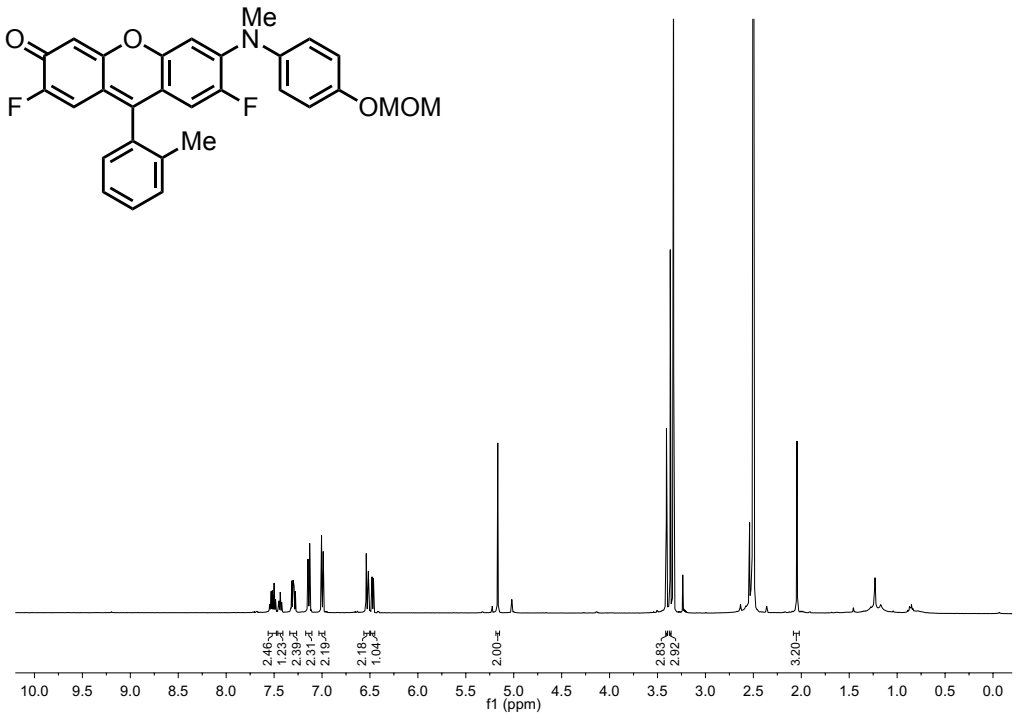

Figure 5-73. ^{1}H NMR (500 MHz, DMSO-d_6) spectrum of **77**.

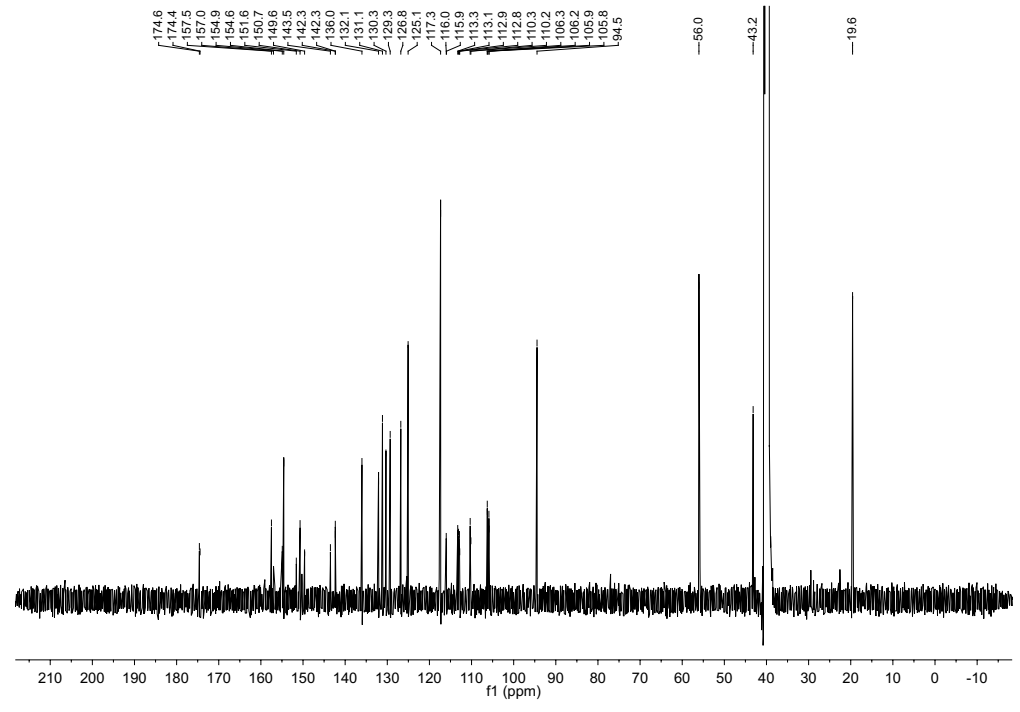

Figure 5-74. ^{13}C NMR (126 MHz, DMSO-d_6) spectrum of **77**.

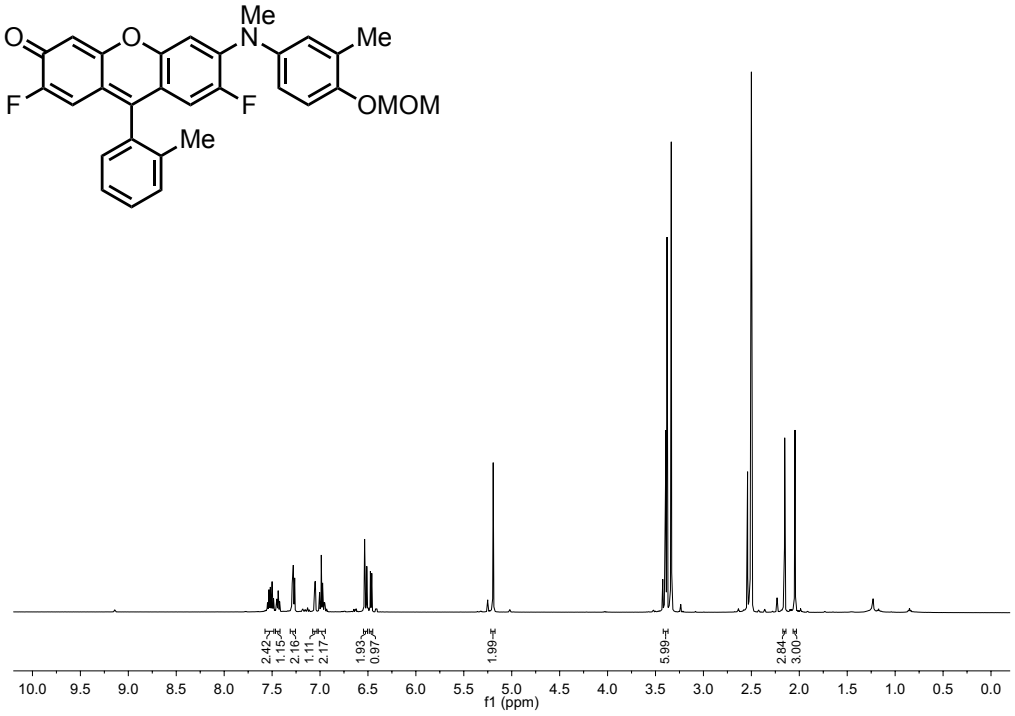

Figure 5-75. ^{1}H NMR (500 MHz, DMSO-d_6) spectrum of **78**.

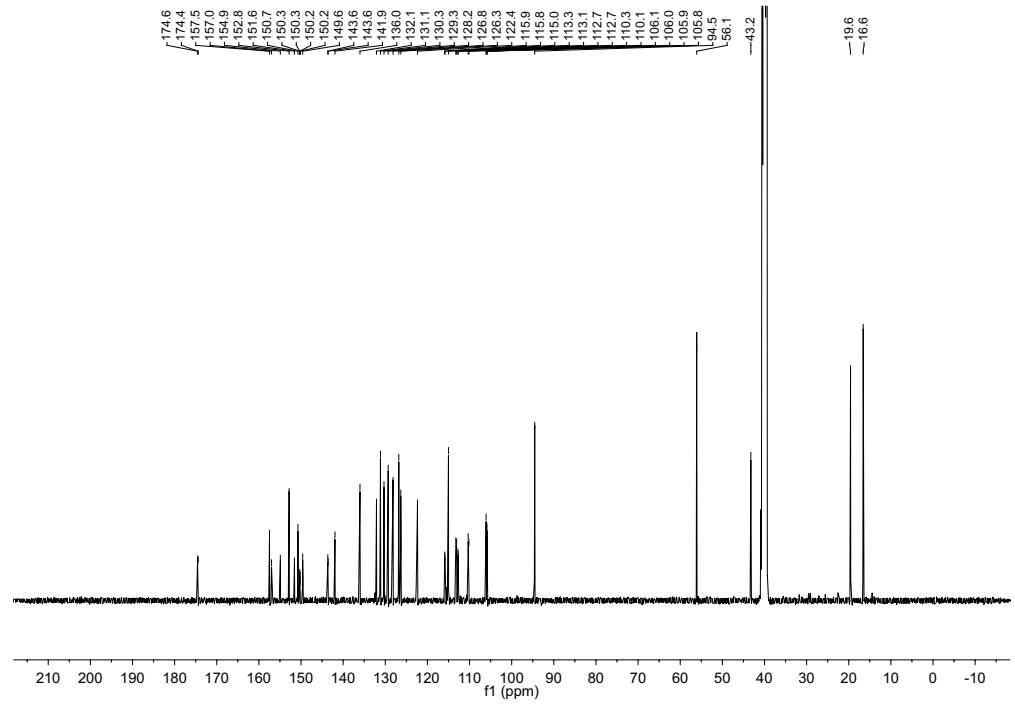

Figure 5-76. ^{13}C NMR (126 MHz, DMSO-d_6) spectrum of **78**.

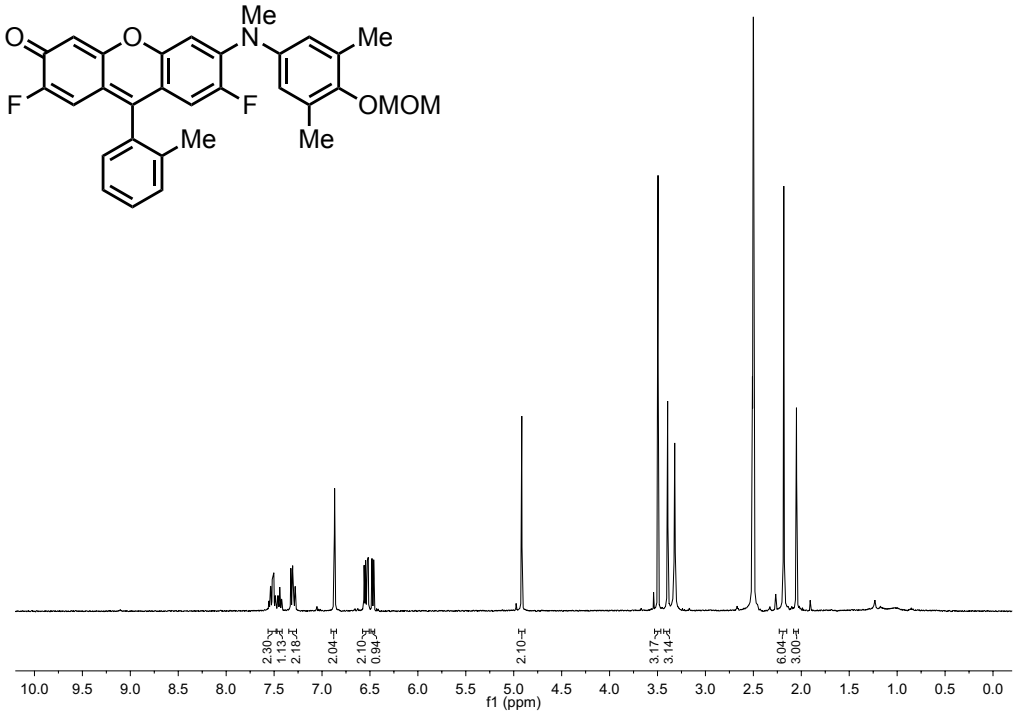

Figure 5-77. ^{1}H NMR (400 MHz, DMSO-d_6) spectrum of **79**.

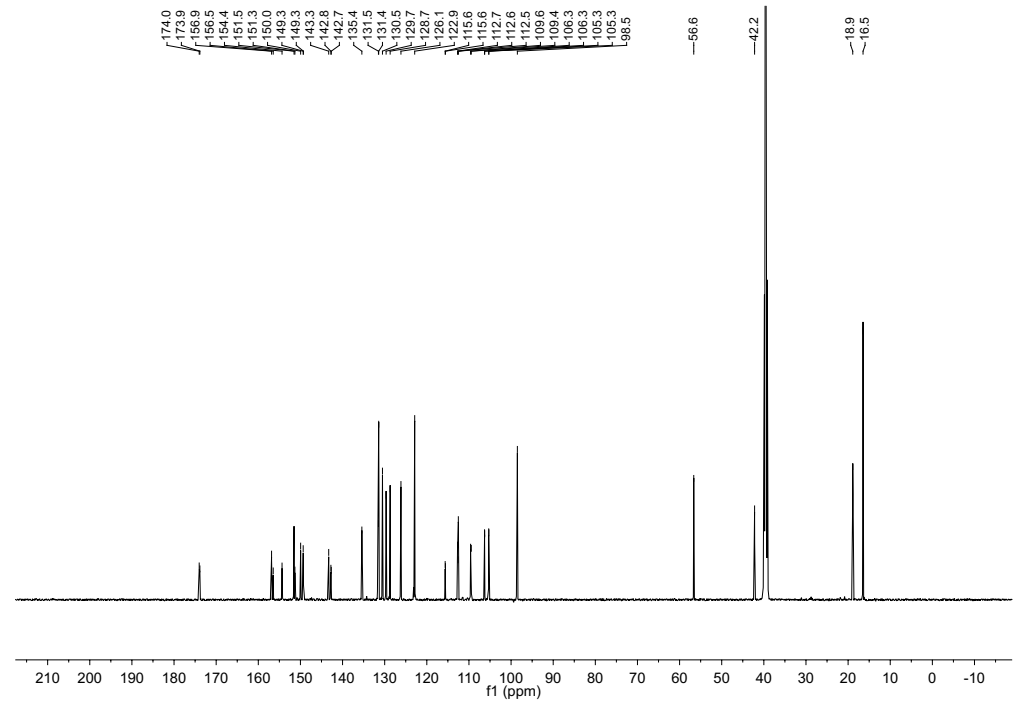

Figure 5-78. ^{13}C NMR (126 MHz, DMSO-d_6) spectrum of **79**.

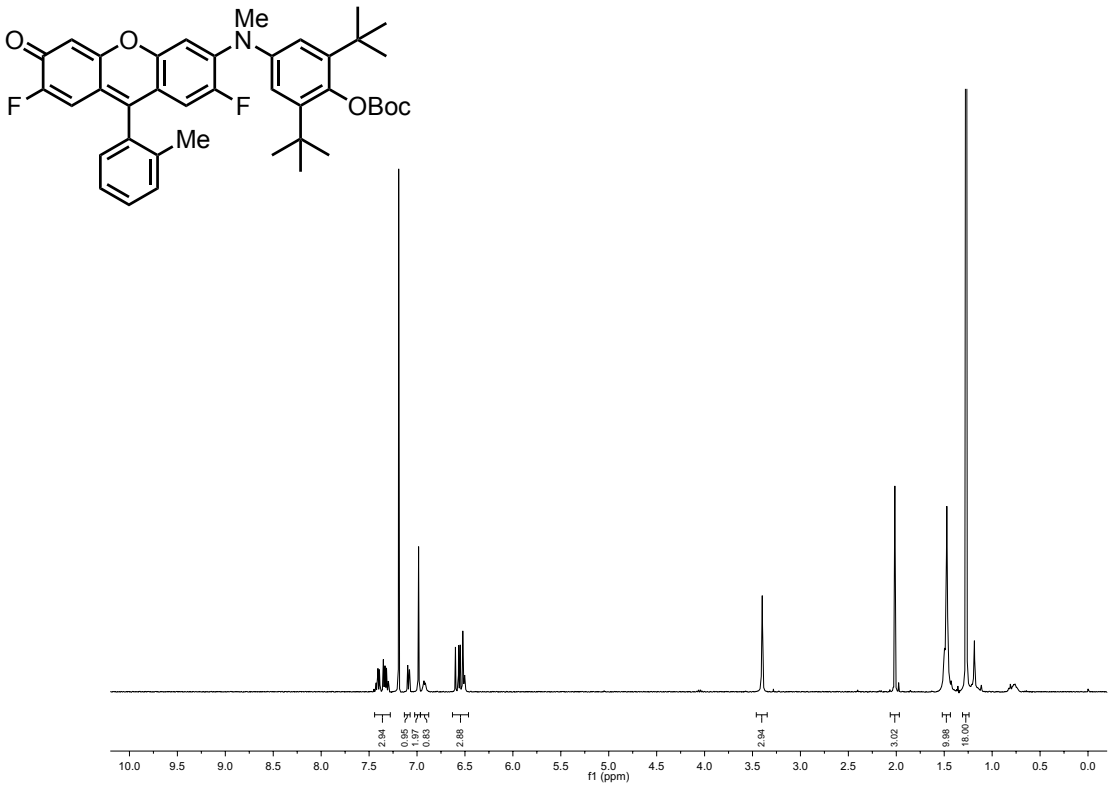

Figure 5-79. ^{1}H NMR (400 MHz, Chloroform-*d*) spectrum of **80**.

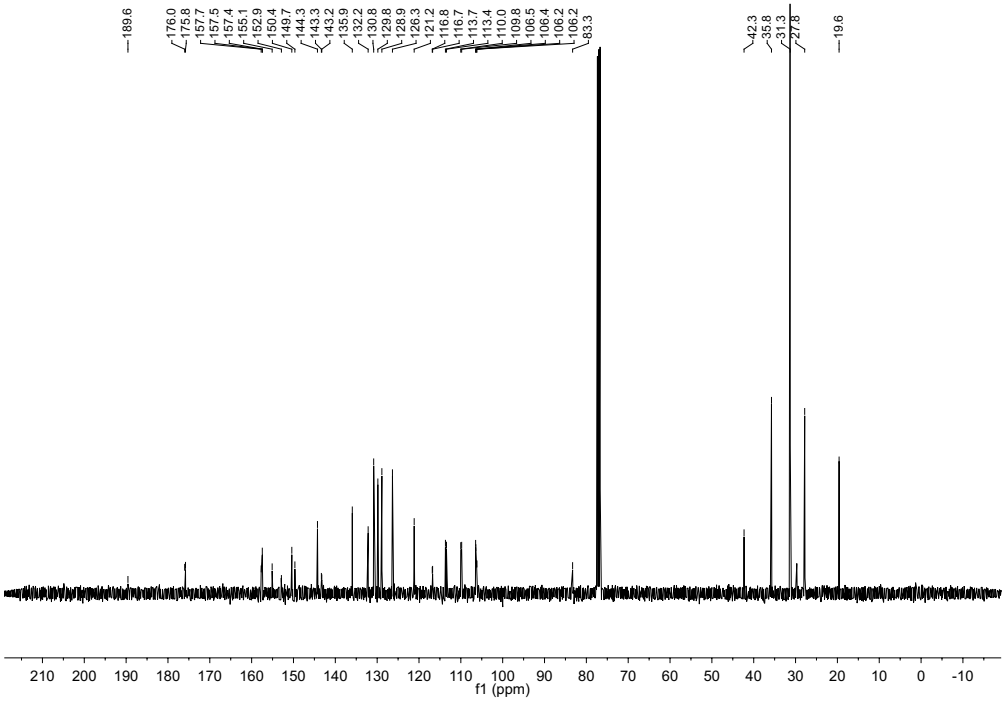

Figure 5-80. ^{13}C NMR (126 MHz, Chloroform-*d*) spectrum of **80**.

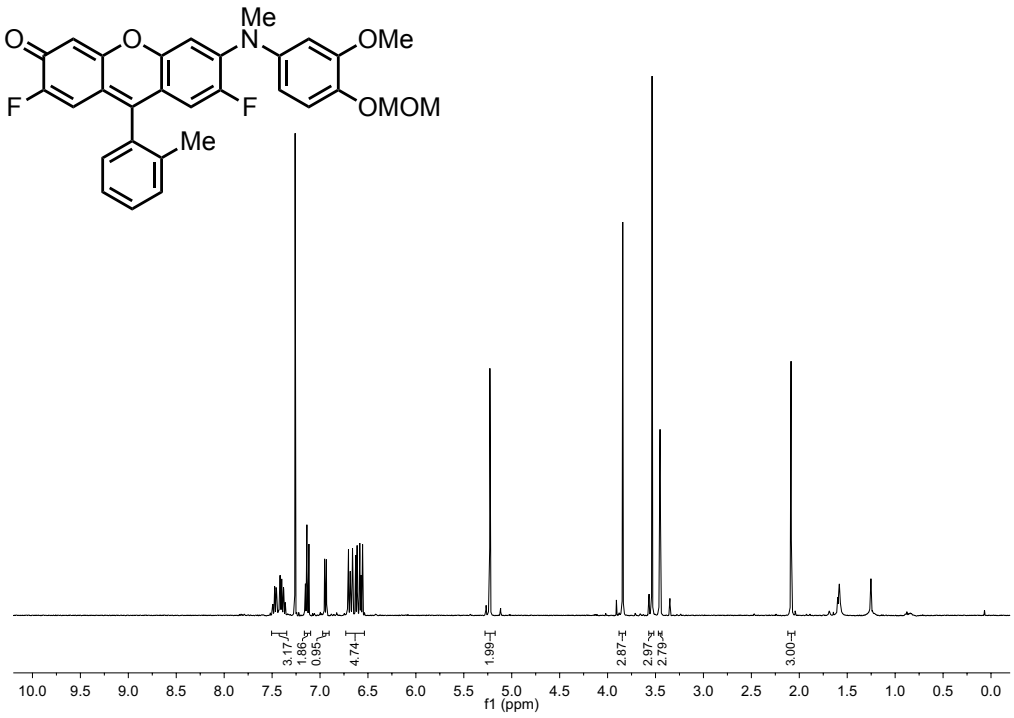

Figure 5-81. ^{1}H NMR (400 MHz, Chloroform-*d*) spectrum of **81**.

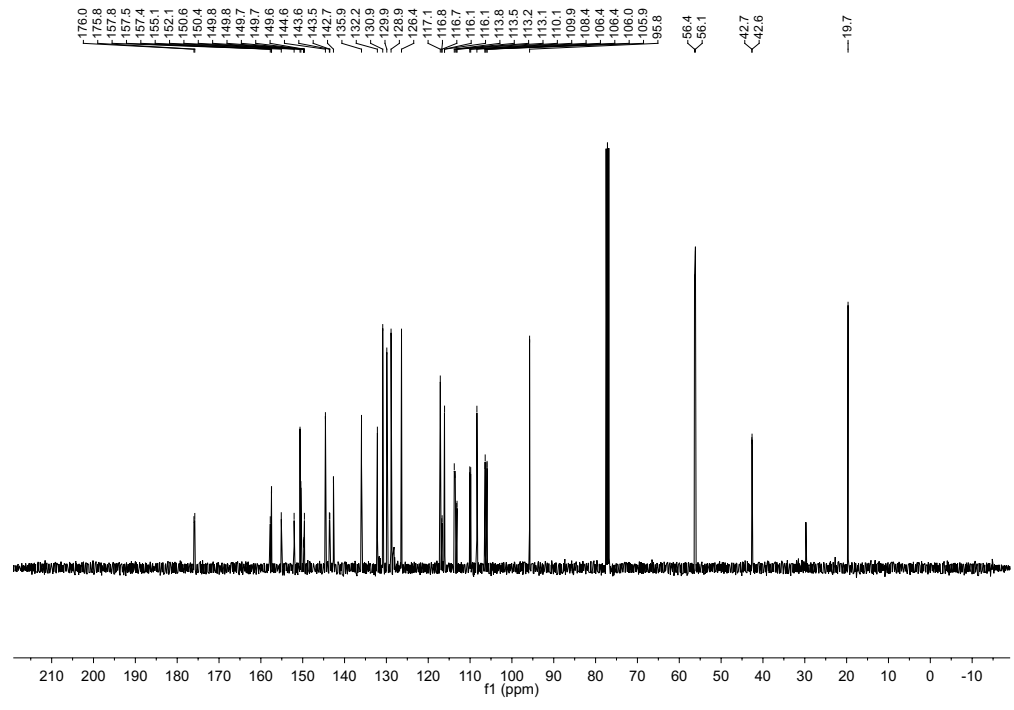

Figure 5-82. ^{13}C NMR (101 MHz, Chloroform-*d*) spectrum of **81**.

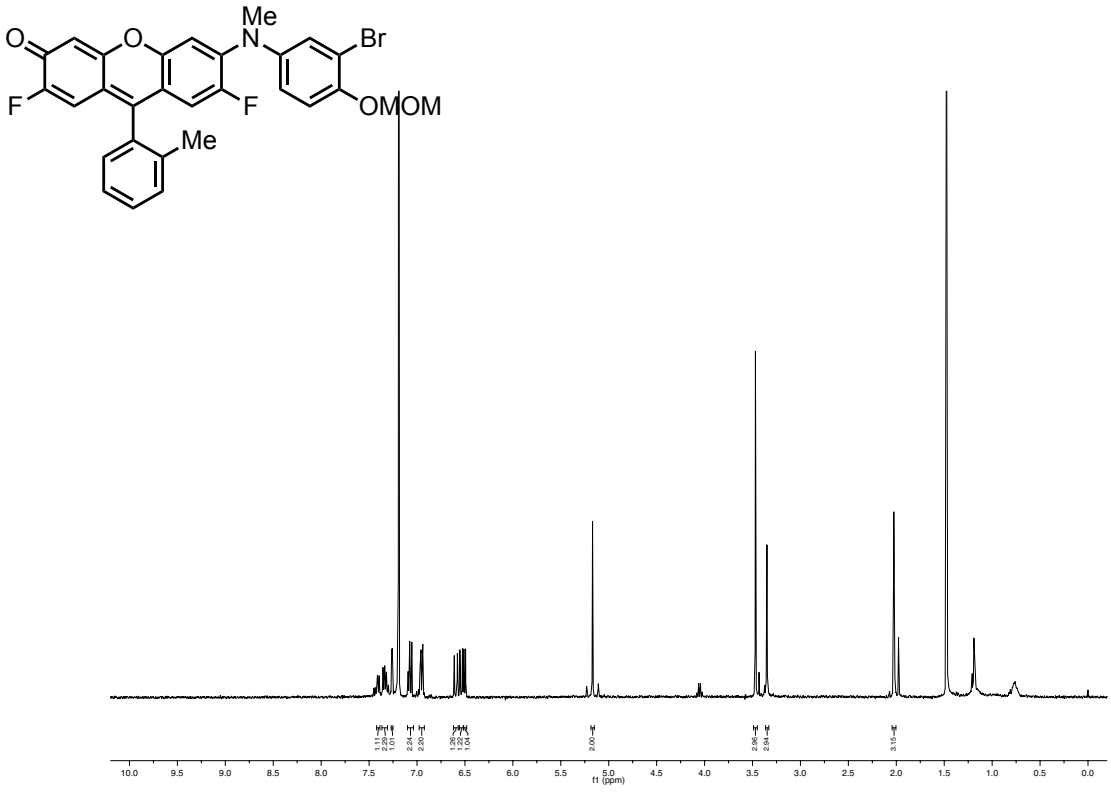

Figure 5-83. ^{1}H NMR (400 MHz, Chloroform-*d*) spectrum of **82**.

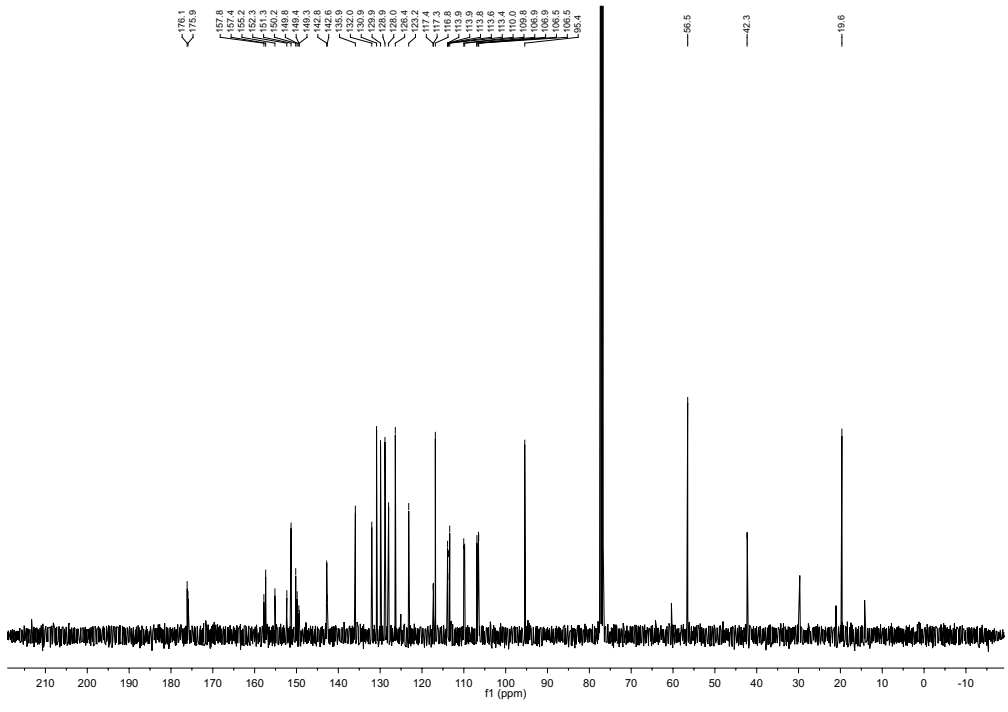

Figure 5-84. ^{13}C NMR (101 MHz, Chloroform-*d*) spectrum of **82**.

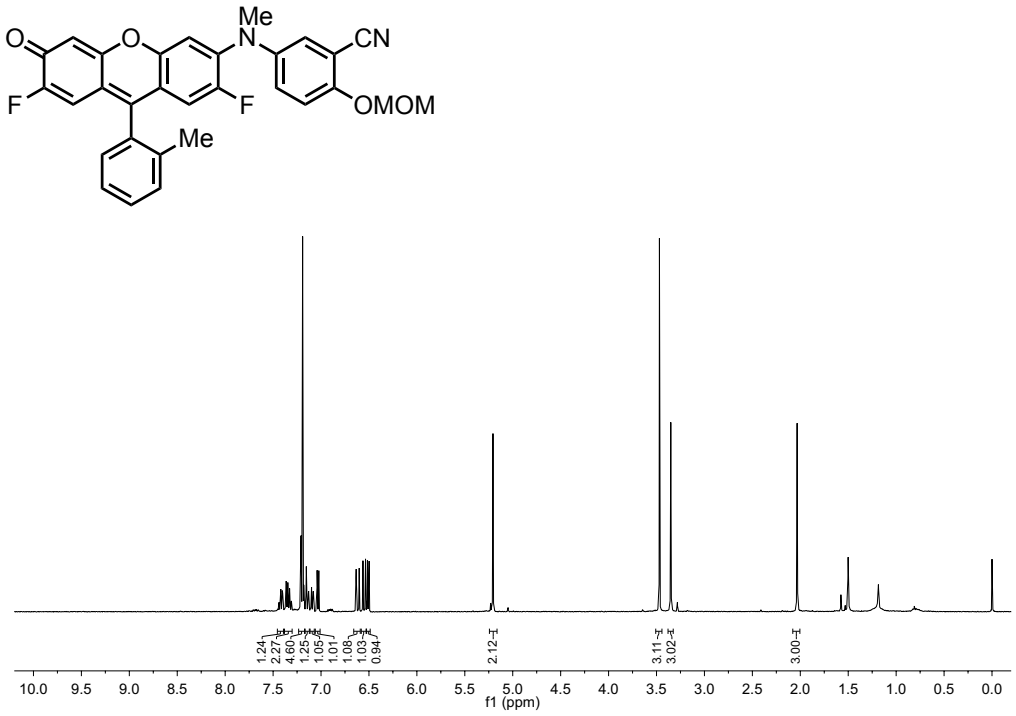

Figure 5-85. ^{1}H NMR (400 MHz, DMSO-d_6) spectrum of **83**.

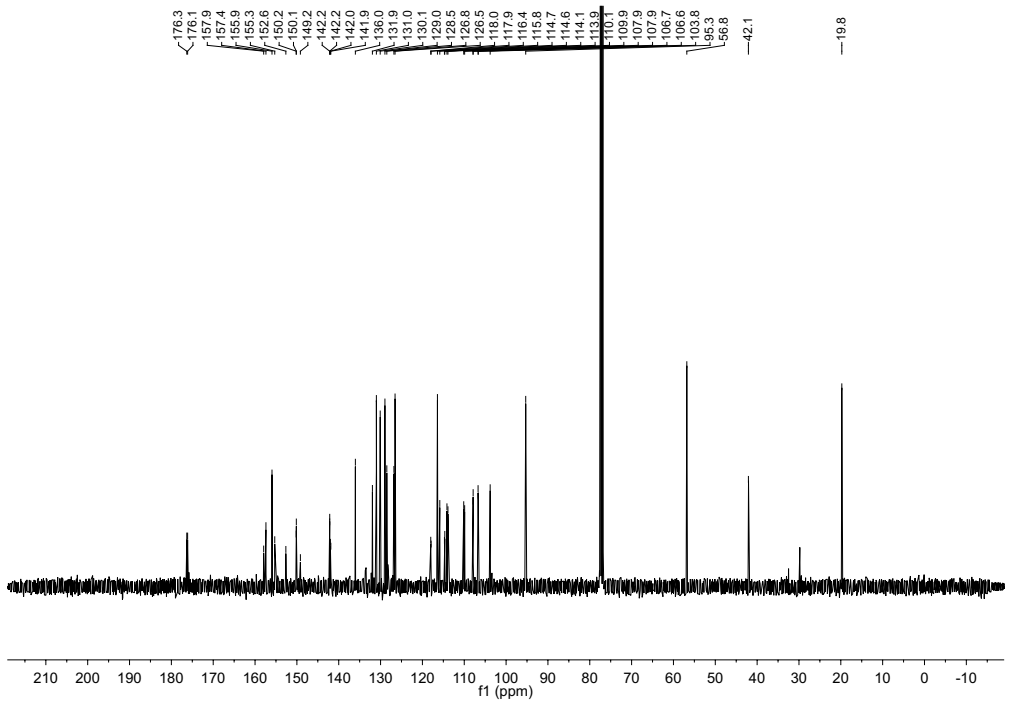

Figure 5-86. ^{13}C NMR (101 MHz, Chloroform-*d*) spectrum of **83**.

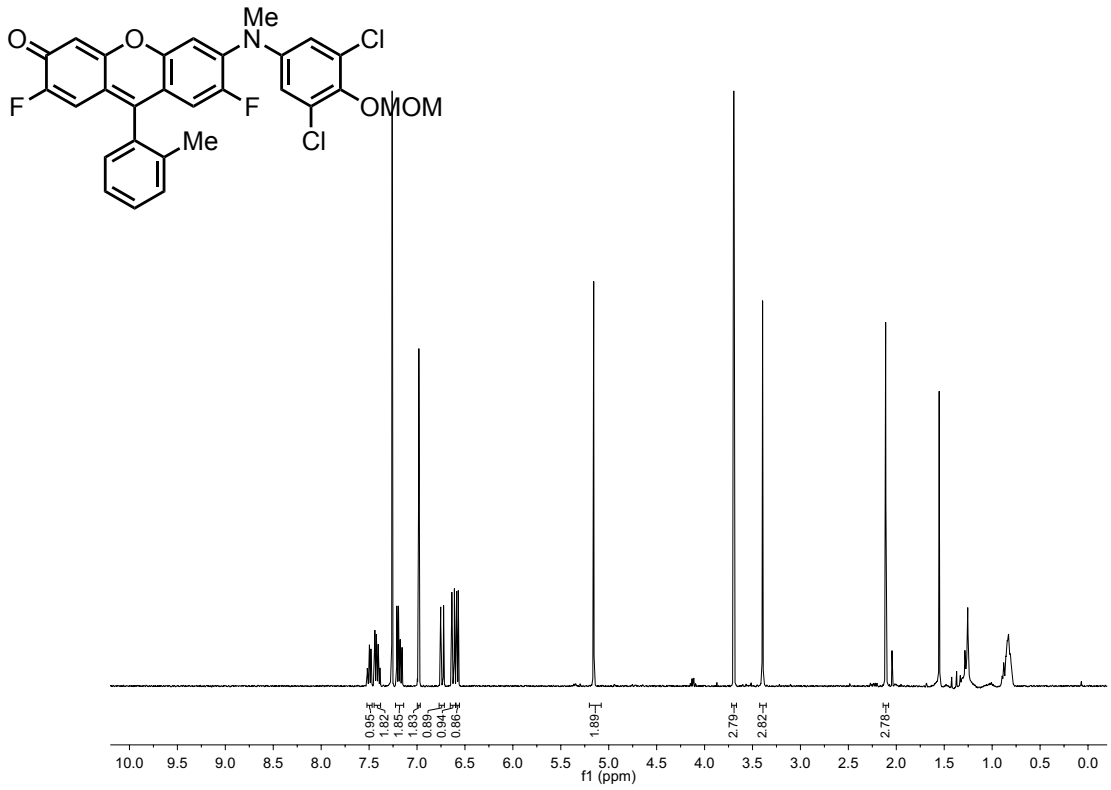

Figure 5-87. ^{1}H NMR (400 MHz, Chloroform-*d*) spectrum of **84**.

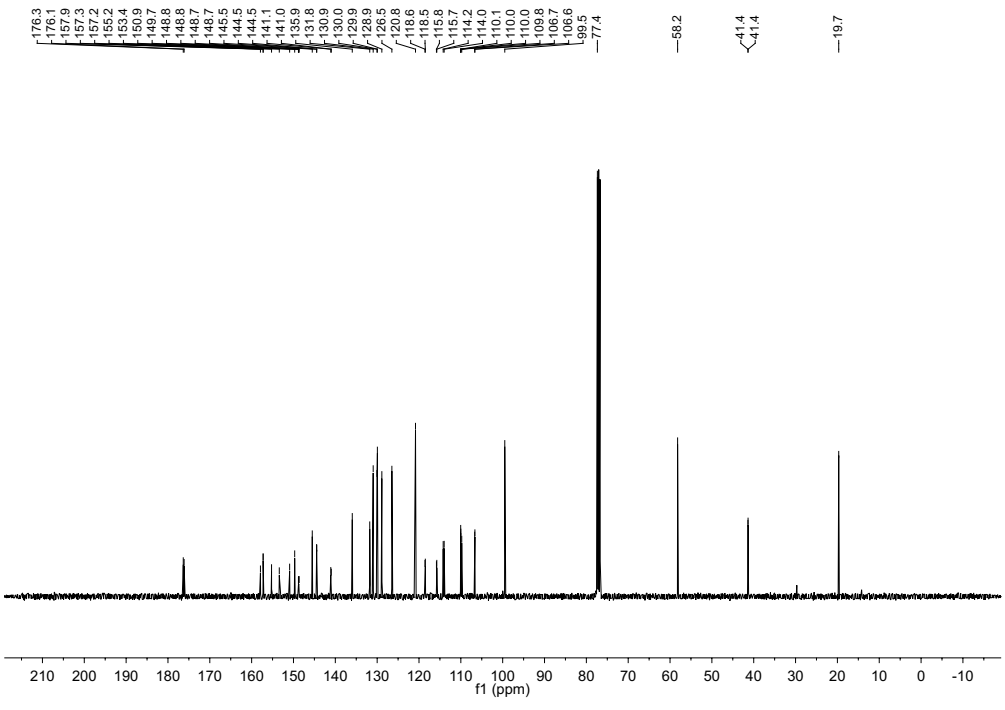

Figure 5-88. ^{13}C NMR (101 MHz, Chloroform-*d*) spectrum of **84**.

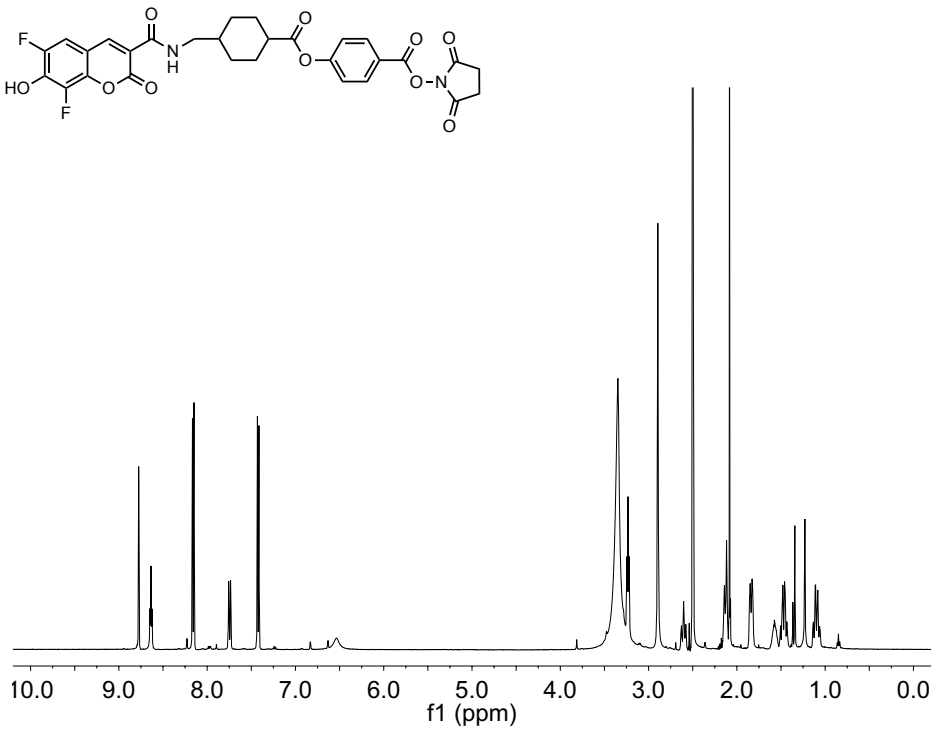

Figure 5-89. ^{1}H NMR (500 MHz, DMSO-d_6) spectrum of **85**.

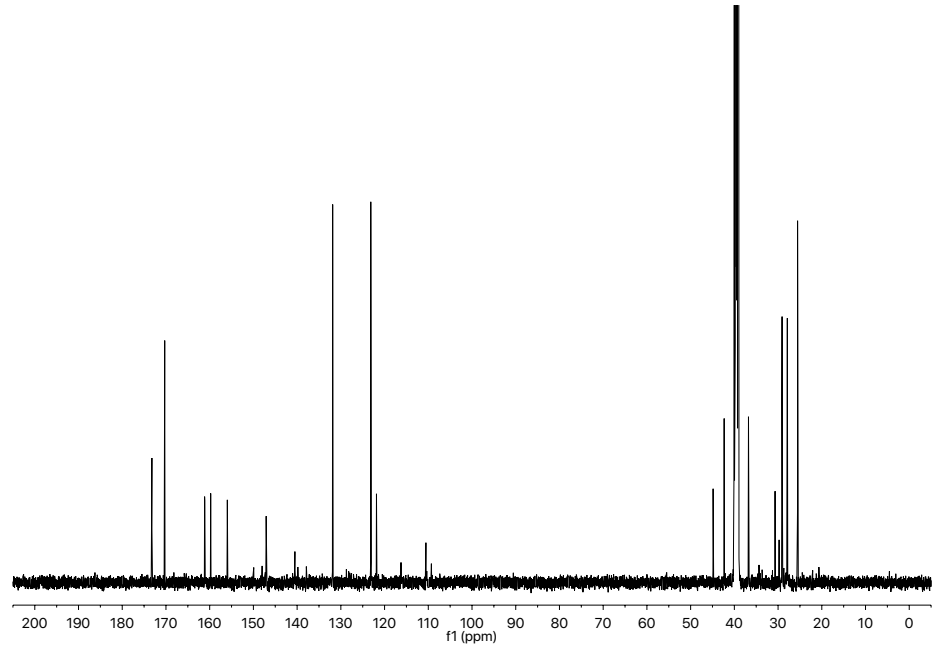

Figure 5-90. ^{13}C NMR (126 MHz, DMSO-d_6) spectrum of **85**.

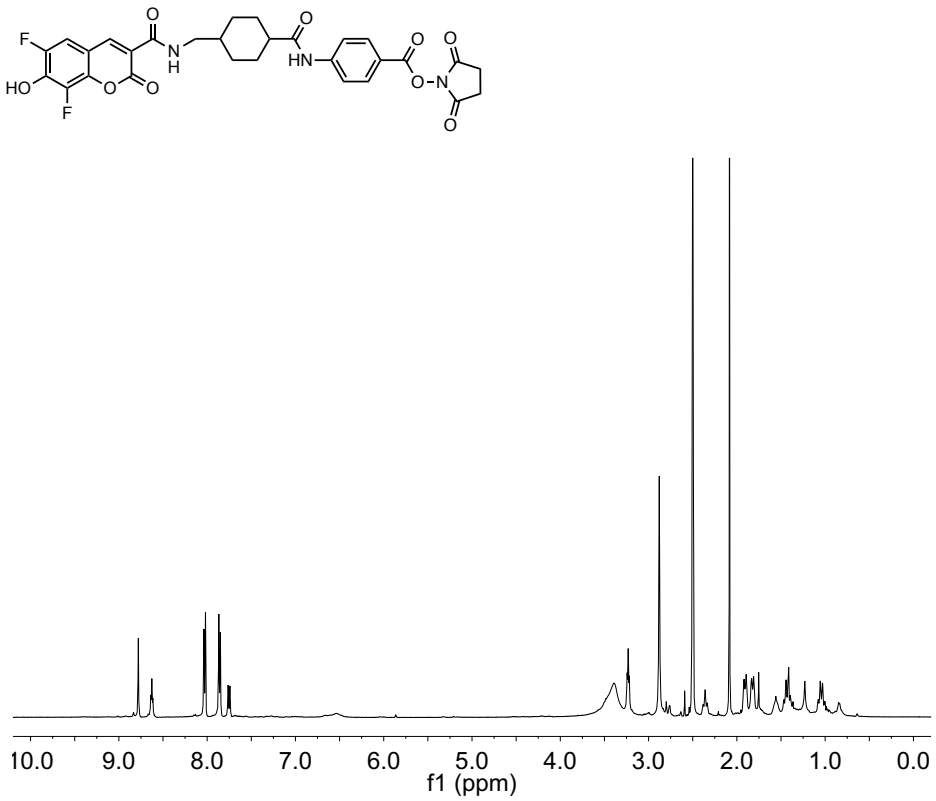

Figure 5-91. ^{1}H NMR (500 MHz, DMSO-d_6) spectrum of **86**.

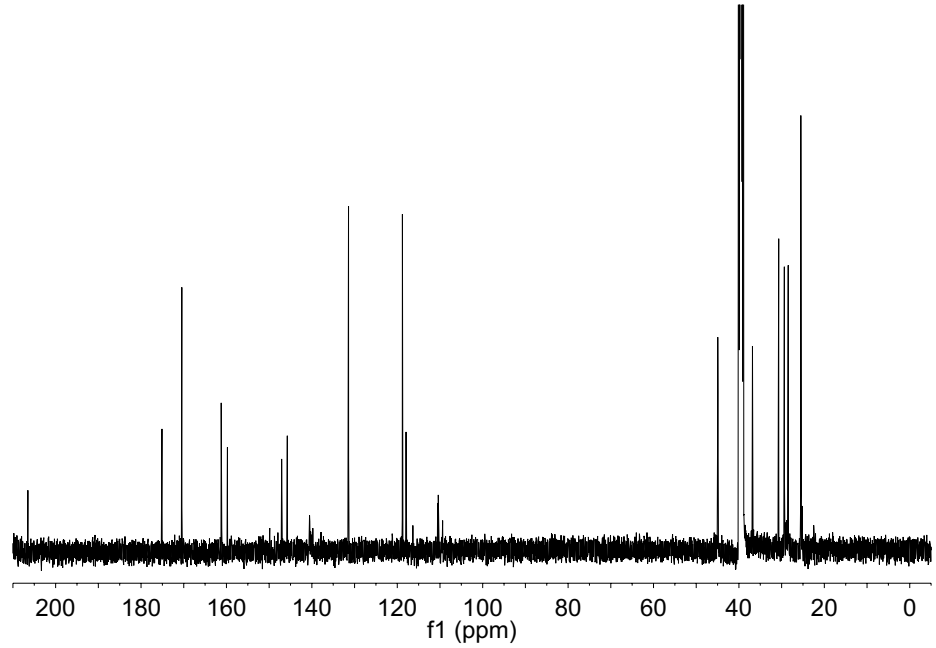

Figure 5-92. ^{13}C NMR (126 MHz, DMSO-d_6) spectrum of **86**.

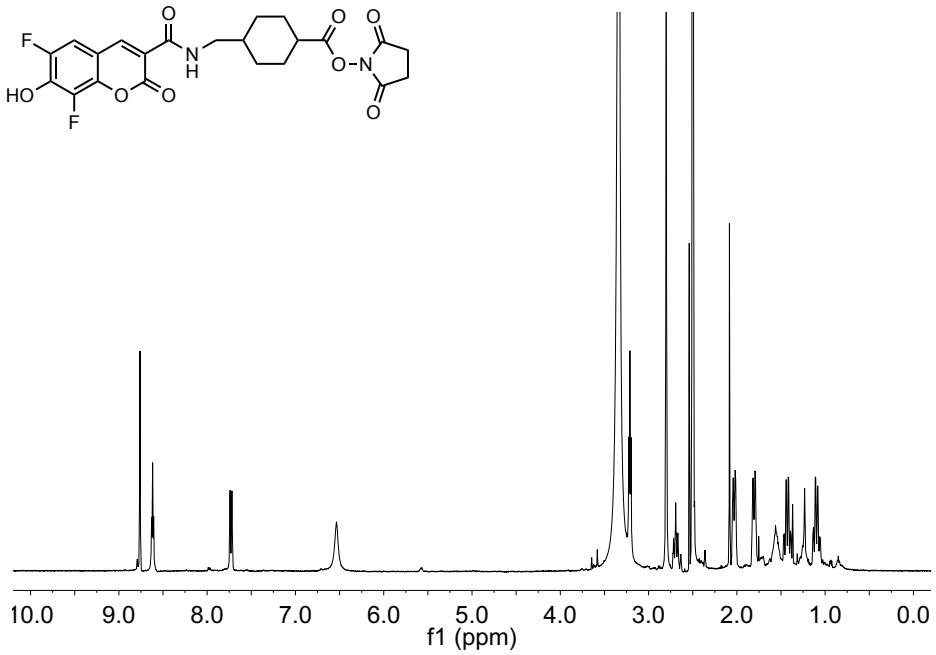

Figure 5-93. ^{1}H NMR (500 MHz, DMSO-d_6) spectrum of **87**.

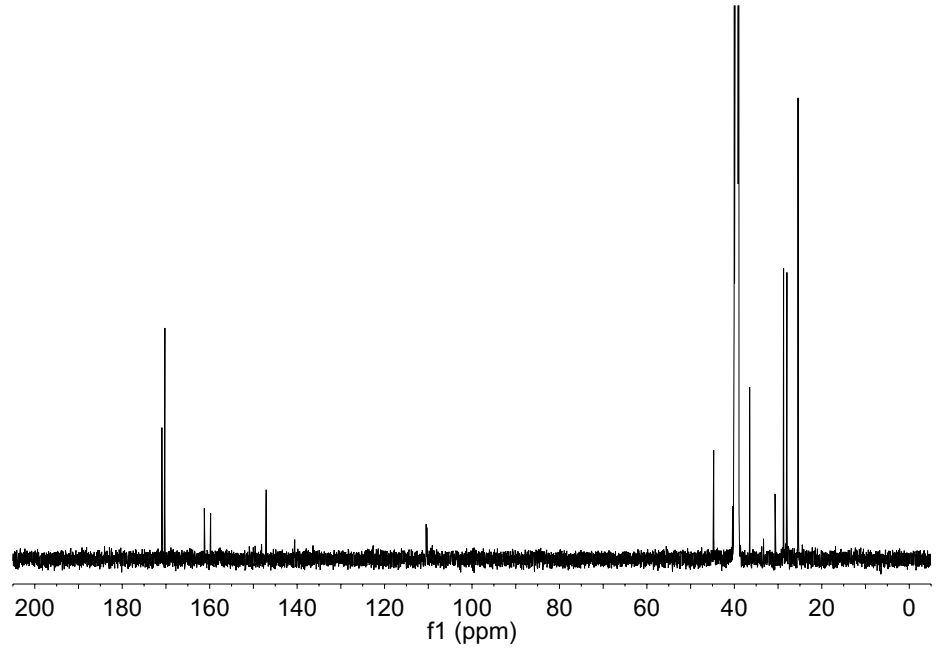

Figure 5-94. ^{13}C NMR (126 MHz, DMSO-d_6) spectrum of **87**.

Appendix B. List of cell lines used

Cell Line	Media	Growth	Organism	Tissue Type	Source	Notes
Jurkat	RPMI-1640 + 10% FBS + Pen/Strep	Suspension	Human	T-cell Lymphocyte	ATCC	ATCC #TIB-152
SkBr3	DMEM/F12K +10% FBS + Pen/Strep	Adherent	Human	Breast	ATCC	ATCC #HTB-30
MDA-MB-231	DMEM + 10% FBS + Pen/Strep	Adherent	Human	Breast	ATCC	ATCC #HTB-26
MDA-MB-468	DMEM + 10% FBS + Pen/Strep	Adherent	Human	Breast	Liang Xu (KU) via ATCC	ATCC #HTB-132
NCI-N87	RPMI-1640 + 10% FBS + Pen/Strep	Adherent	Human	Stomach	Liang Xu (KU) via ATCC	ATCC #CRL-5822
Mia-Paca-2	DMEM + 10% FBS + Pen/Strep	Adherent	Human	Pancreatic	ATCC	ATCC #CRL-1420
Raji	RPMI-1640 + 10% HI FBS + Pen/Strep	Suspension	Human	B Lymphocyte	ATCC	ATCC #CCL-86
Ramos	RPMI-1640 + 10% HI FBS + Pen/Strep	Suspension	Human	B Lymphocyte	ATCC	ATCC #CRL-1596
RAW264.7	DMEM + 10% FBS + Pen/Strep	Adherent	Mouse	Macrophage	Sue Lunte (KU) via ATCC	ATCC #TIB-71

Appendix C. List of plasmids used

Name	Gene Product	Gene Species	Vector	Type	Source
pBP4-3	n/a	n/a	pBP4-3	Bacterial Expression Vector	Peterson Lab
Sec-SpA-ZZ-12Lys	SpA-ZZ-12Lys w/secretion signal	*Staphylococcus aureus*	pUC57	Cloning Vector	GenScript
Sec-SpA-ZZ-6Lys	SpA-ZZ-6Lys w/secretion signal	*Staphylococcus aureus*	pUC57	Cloning Vector	GenScript
SpA-ZZ-12Lys	SpA-ZZ-12Lys w/o secretion signal	*Staphylococcus aureus*	pBP4-3	Bacterial Expression Vector	Cloning
SpA-ZZ-6Lys	SpA-ZZ-6Lys w/o secretion signal	*Staphylococcus aureus*	pBP4-3	Bacterial Expression Vector	Cloning
SpA-ZZ-2Lys-A	SpA-ZZ-2Lys-A	*Staphylococcus aureus*	pBP4-3	Bacterial Expression Vector	Mutation of SpA-ZZ-6Lys
SpA-ZZ-2Lys-B	SpA-ZZ-2Lys-B	*Staphylococcus aureus*	pBP4-3	Bacterial Expression Vector	Mutation of SpA-ZZ-6Lys
SpA-ZZ-2Lys-C	SpA-ZZ-2Lys-C	*Staphylococcus aureus*	pBP4-3	Bacterial Expression Vector	Mutation of SpA-ZZ-6Lys

Appendix D. Sequences of genes synthesized by GenScript

SpA-ZZ-12Lys

DNA sequence (optimized portion in black):

GAA TTC GGC GTG GGC ATT GCG AGC GTG ACC CTG GGC ACC CTG CTG ATT
AGC GGC GGC GTG ACC CCG GCG GCG AAC GCG GCG CAG CAT GAT GAA GCG
GTG GAT AAT AAA TTC AAC AAG GAA CAG CAG AAC GCC TTC TAT GAA ATT
CTG CAT CTG CCG AAC CTG AAC GAA GAA CAG CGT AAC GCG TTT ATT CAG
AGC CTG AAA GAC GAT CCT AGC CAG AGC GCG AAC CTG CTT GCG GAA GCG
AAG AAA CTG AAC GAT GCG CAG GCG CCG AAA GTG GAT AAC AAA TTT AAC
AAA GAA CAG CAG AAC GCG TTT TAT GAA ATT CTG CAT CTG CCG AAC CTG
AAC GAA GAA CAG CGT AAC GCG TTT ATT CAG AGC CTG AAA GAT GAT CCG
AGC CAG AGC GCG AAC CTG CTG GCG GAA GCG AAA AAA CTG AAC GAT GCG
CAG GCG CCG AAA GTG GAT GGT GGC TGT TAA TGA CTC GAG GGG GTA CC

Amino acid sequence (lysines in red):

E F G V G I A S V T L G T L L I S G G V T P A A N A A Q H D E A V
D N K F N K E Q Q N A F Y E I L H L P N L N E E Q R N A F I Q S L
K D D P S Q S A N L L A E A K K L N D A Q A P K V D N K F N K E Q
Q N A F Y E I L H L P N L N E E Q R N A F I Q S L K D D P S Q S A
N L L A E A K K L N D A Q A P K V D G G C Stop Stop L E G V

SpA-ZZ-6Lys

DNA sequence (optimized portion in black):

GAA TTC GGC GTC GGT ATC GCA AGC GTG ACC CTG GGC ACC CTG CTG ATT
AGC GGC GGC GTG ACC CCG GCG GCA AAT GCT GCT CAA CAT GAT GAA GCG
GTG GAT AAC AAA TTC AAC AAA GAA CAG CAA AAC GCC TTC TAT GAA ATT
CTG CAT CTG CCG AAC CTG AAT GAA GAA CAG CGT AAT GCA TTT ATC CAA
AGC CTG AAA GAT GAC CCG AGC CAG TCT GCT AAC CTG CTG GCG GAA GCG
CGT CGC CTG AAC GAT GCA CAG GCT CCG CGT GTT GAC AAT AAA TTT AAT
AAA GAA CAA CAA AAC GCG TTC TAC GAA ATT CTG CAC CTG CCG AAT CTG
AAC GAA GAA CAG CGC AAC GCG TTC ATT CAG TCT CTG AAA GAC GAC CCG
AGT CAG TCC GCC AAT CTG CTG GCC GAA GCC CGT CGC CTG AAT GAT GCC
CAA GCG CCG CGT GTG GAT GGT GGT TGT TAA TGA CTC GAG GGG GTA CC

Amino acid sequence (lysines in red):

E F G V G I A S V T L G T L L I S G G V T P A A N A A Q H D E A V
D N K F N K E Q Q N A F Y E I L H L P N L N E E Q R N A F I Q S L
K D D P S Q S A N L L A E A R R L N D A Q A P R V D N K F N K E Q
Q N A F Y E I L H L P N L N E E Q R N A F I Q S L K D D P S Q S A
N L L A E A R R L N D A Q A P R V D G G C Stop Stop L E G V